

FEBRUARY 2020

AJNR

VOLUME 41 • PP 191-368

AJNR

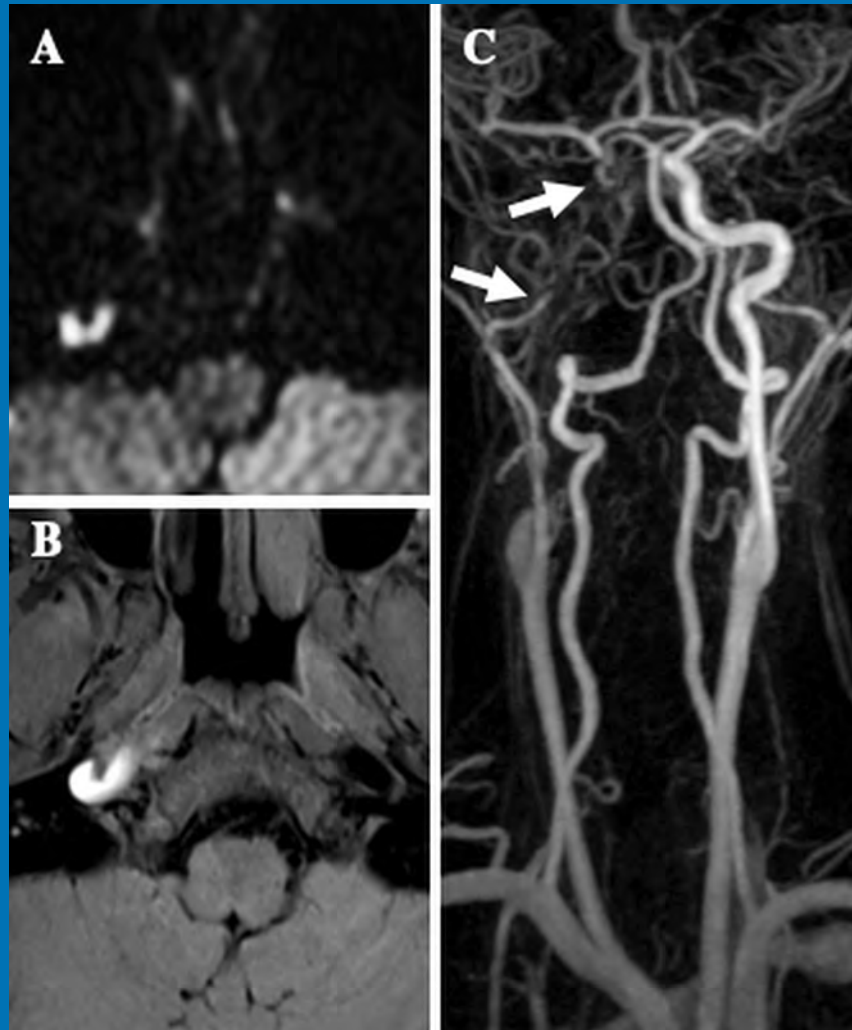
AMERICAN JOURNAL OF NEURORADIOLOGY

FEBRUARY 2020
VOLUME 41
NUMBER 2
WWW.AJNR.ORG

THE JOURNAL OF DIAGNOSTIC AND
INTERVENTIONAL NEURORADIOLOGY

Review of round window pathologies
Multiphase color maps for acute stroke
Treatment decisions for M2 occlusions
Delayed diagnosis of spinal dural fistula

Official Journal ASNR • ASFNR • ASHNR • ASPNR • ASSR





ONE AND DONE

INDICATIONS FOR USE:

The WEB Aneurysm Embolization System is indicated for use at the middle cerebral artery (MCA) bifurcation, internal carotid artery (ICA) terminus, anterior communicating artery (AComm) complex, or basilar artery apex for the endovascular treatment of adult patients with saccular, wide neck bifurcation intracranial aneurysms with dome diameter from 3 mm to 10 mm and either neck size 4 mm or greater or the dome-to-neck ratio is greater than 1 and less than 2.

The WEB Aneurysm Embolization System is contraindicated for patients with known bacterial infection that may interfere with or negatively affect the implantation procedure and patients with known hypersensitivity to nickel. For complete indications, contraindications, potential complications, warnings, precautions, and instructions, see instructions for use (IFU provided with the device).

The VIA® Catheter is intended for the introduction of non-liquid interventional devices (such as stents/_ow diverters) and infusion of diagnostic (such as contrast media) or non-liquid therapeutic agents into the neuro, peripheral, and coronary vasculature. The VIA Catheter is contraindicated for use with liquid embolic materials, such as n-butyl 2-cyanoacrylate or ethylene vinyl alcohol & DMSO (dimethyl sulfoxide). The VIA Catheter is contraindicated for use in the pediatric population (<22 yrs of age).

Caution: Federal law restricts these devices to sale by or on the order of a physician.

WEB[®]

Aneurysm Embolization System

MicroVention[®] delivers the first intrasaccular solution for wide neck bifurcation aneurysms.

The **world leader**
and **first**
PMA - approved
device in an
important new
category of
intrasaccular
flow disruptors.

The WEB[®] System is a safe
and effective single-device
solution for treating wide
neck bifurcation aneurysms.



SL Device



SLS Device

Contact a MicroVention sales associate to learn more
about integrating the WEB[®] device into your practice.



**MicroVention Worldwide
Innovation Center**

35 Enterprise
Aliso Viejo, CA 92656 USA

MicroVention UK Limited

MicroVention Europe, S.A.R.L.

MicroVention Deutschland GmbH

microvention.com

PH +1.714.247.8000

PH +44 (0) 191 258 6777

PH +33 (1) 39 21 77 46

PH +49 211 210 798-0

DOTAREM[®]

(gadoterate meglumine) Injection

REAL-WORLD TESTED.
**REAL-WORLD
PROVEN.**

The Dotarem[®] safety profile has been tested and proven in both studies and 30 years of global clinical use.*



0.007% Spontaneously Reported
Worldwide Adverse Events.
(>50 million doses)³⁻¹⁰

Dotarem remains an industry standard for contrast imaging with a low incidence of immediate adverse events for patients of all ages.²⁻¹⁰

1 Dotarem[®]
The first and only macrocyclic
and ionic GBCA molecule.¹

A low incidence of adverse events can help your patient focus on what matters most in their life.

Guerbet | 

COMMITTED



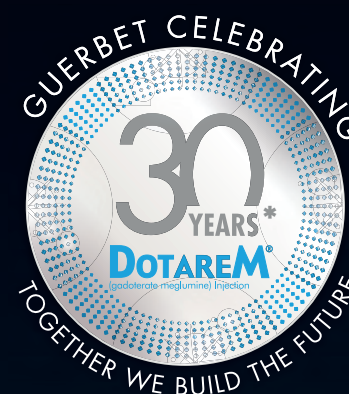


IMPORTANT SAFETY INFORMATION¹

WARNING: NEPHROGENIC SYSTEMIC FIBROSIS (NSF)

Gadolinium-based contrast agents (GBCAs) increase the risk for NSF among patients with impaired elimination of the drugs. Avoid use of GBCAs in these patients unless the diagnostic information is essential and not available with non-contrast MRI or other modalities. NSF may result in fatal or debilitating fibrosis affecting the skin, muscle and internal organs.

- The risk for NSF appears highest among patients with:
 - Chronic, severe kidney disease (GFR < 30 mL/min/1.73m²), or
 - Acute kidney injury.
- Screen patients for acute kidney injury and other conditions that may reduce renal function. For patients at risk for chronically reduced renal function (e.g. age > 60 years, hypertension, diabetes), estimate the glomerular filtration rate (GFR) through laboratory testing.
- For patients at highest risk for NSF, do not exceed the recommended DOTAREM dose and allow a sufficient period of time for elimination of the drug from the body prior to any re-administration.



Indications and Usage

DOTAREM[®] (gadoterate meglumine) injection is a prescription gadolinium-based contrast agent indicated for intravenous use with magnetic resonance imaging (MRI) in brain (intracranial), spine and associated tissues in adult and pediatric patients (including term neonates) to detect and visualize areas with disruption of the blood brain barrier (BBB) and/or abnormal vascularity.

Contraindications

History of clinically important hypersensitivity reactions to DOTAREM.

Warnings and Precautions

- Hypersensitivity Reactions: Anaphylactic and anaphylactoid reactions have been reported with DOTAREM, involving cardiovascular, respiratory, and/or cutaneous manifestations. Some patients experienced circulatory collapse and died. In most cases, initial symptoms occurred within minutes of DOTAREM administration and resolved with prompt emergency treatment.
- Before DOTAREM administration, assess all patients for any history of a reaction to contrast media, bronchial asthma and/or allergic disorders. These patients may have an increased risk for a hypersensitivity reaction to DOTAREM.
- Administer DOTAREM only in situations where trained personnel and therapies are promptly available for the treatment of hypersensitivity reactions, including personnel trained in resuscitation.
- Gadolinium Retention: Gadolinium is retained for months or years in several organs. The highest concentrations have been identified in the bone, followed by brain, skin, kidney, liver and spleen. The duration of retention also varies by tissue, and is longest in bone. Linear GBCAs cause more retention than macrocyclic GBCAs.
- Consequences of gadolinium retention in the brain have not been established. Adverse events involving multiple organ systems have been reported in patients with normal renal function without an established causal link to gadolinium retention.
- Acute Kidney Injury: In patients with chronically reduced renal function, acute kidney injury requiring dialysis has occurred with the use of GBCAs. The risk of acute kidney injury may increase with increasing dose of the contrast agent; administer the lowest dose necessary for adequate imaging.
- Extravasation and Injection Site Reactions: Ensure catheter and venous patency before the injection of DOTAREM. Extravasation into tissues during DOTAREM administration may result in tissue irritation.

Adverse Reactions

- The most common adverse reactions associated with DOTAREM in clinical trials were nausea, headache, injection site pain, injection site coldness and rash.
- Serious adverse reactions in the Postmarketing experience have been reported with DOTAREM. These serious adverse reactions include but are not limited to: arrhythmia, cardiac arrest, respiratory arrest, pharyngeal edema, laryngospasm, bronchospasm, coma and convulsion.

Use in Specific Populations

- **Pregnancy:** GBCAs cross the human placenta and result in fetal exposure and gadolinium retention. Use only if imaging is essential during pregnancy and cannot be delayed.
- **Lactation:** There are no data on the presence of gadoterate in human milk, the effects on the breastfed infant, or the effects on milk production. However, published lactation data on other GBCAs indicate that 0.01 to 0.04% of the maternal gadolinium dose is present in breast milk.
- **Pediatric Use:** The safety and efficacy of DOTAREM at a single dose of 0.1 mmol/kg has been established in pediatric patients from birth (term neonates \geq 37 weeks gestational age) to 17 years of age based on clinical data. The safety of DOTAREM has not been established in preterm neonates. No cases of NSF associated with DOTAREM or any other GBCA have been identified in pediatric patients age 6 years and younger.

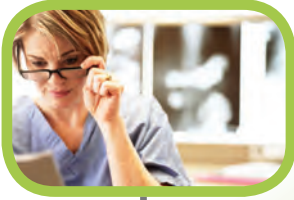
You are encouraged to report negative side effects of prescription drugs to the FDA. Visit www.fda.gov/medwatch or call 1-800-FDA-1088.

Please see the full Prescribing Information, including the patient Medication Guide, for additional important safety information.

^{*}Dotarem was launched globally in 1989 and approved by the FDA for use in the US in 2013.

References:

1. Dotarem [package insert]. Princeton, NJ: Guerbet LLC; July 2019.
2. Internal data as of May 2019.
3. de Kerviler E et al. Adverse reactions to gadoterate meglumine: review of over 25 years of clinical use and more than 50 million doses. *Invest Radiol.* 2016 Sep;51(9):544-51.
4. Briand et al. Efficacy and safety of the macrocyclic complex Gd-DOTA in Children: Results of a Multi-Centre Study. *Proceedings of the 29th Congress of the European Society of Pediatric Radiology.* 1992; 128
5. Briand Y. Daily Paediatric Use of MRI Contrast Agents: Results of a Multi-Centre Survey. *Proceedings of the 29th Congress of the European Society of Pediatric Radiology.* 1992.
6. Ishiguchi T & Takahashi S. Safety of gadoterate meglumine (Gd-DOTA) as a contrast agent for magnetic resonance imaging: results of a post-marketing surveillance study in Japan. *Drugs R D.* 2010;10(3):133-45.
7. Emond S & Brunelle F. Gd-DOTA administration at MRI in children younger than 18 months of age: immediate adverse reactions. *Pediatr Radiol.* 2011 Nov;41(11):1401-6.
8. Maurer M et al. Tolerability and diagnostic value of gadoterate acid in the general population and in patients with risk factors: results in more than 84,000 patients. *Eur J Radiol.* 2012 May;81(5):885-90.
9. Soyer et al. Observational Study on the Safety Profile of Gadoterate Meglumine in 35,499 Patients: The SECURE Study. *J. Magn. Reson. Imag.* 2017; 45, 988-997
10. Radbruch A et al. Gadolinium retention in the dentate nucleus and globus pallidus is dependent on the class of contrast agent. *Radiology.* 2015 Jun;275(3):783-97.



Simplify the MOC Process



Manage your CME Credits Online

CMEgateway.org

Available to Members of Participating Societies

American Board of Radiology (ABR)
American College of Radiology (ACR)
American Roentgen Ray Society (ARRS)
American Society of Neuroradiology (ASNR)
Commission on Accreditation of Medical
Physics Educational Programs, Inc. (CAMPEP)
Radiological Society of North America (RSNA)
Society of Interventional Radiology (SIR)
SNM
The Society for Pediatric Radiology (SPR)

It's Easy and Free!

Log on to CME Gateway to:

- View or print reports of your CME credits from multiple societies from a single access point.
- Print an aggregated report or certificate from each participating organization.
- Link to SAMs and other tools to help with maintenance of certification.

American Board of Radiology (ABR) participation!

By activating ABR in your organizational profile, your MOC-fulfilling CME and SAM credits can be transferred to your own personalized database on the ABR Web site.

Sign Up Today!

go to CMEgateway.org

AJNR

AMERICAN JOURNAL OF NEURORADIOLOGY

FEBRUARY 2020
VOLUME 41
NUMBER 2
WWW.AJNR.ORG

Publication Preview at www.ajnr.org features articles released in advance of print. Visit www.ajnrblog.org to comment on AJNR content and chat with colleagues and AJNR's News Digest at <http://ajnrdigest.org> to read the stories behind the latest research in neuroimaging.

191 **PERSPECTIVES** *M. Hauben*

REVIEW ARTICLE

 192 **The Forgotten Second Window: A Pictorial Review of Round Window Pathologies** *J.C. Benson, et al.* **HEAD & NECK**

PRACTICE PERSPECTIVES

   200 **Displaying Multiphase CT Angiography Using a Time-Variant Color Map: Practical Considerations and Potential Applications in Patients with Acute Stroke** *J.M. Ospel, et al.*

GENERAL CONTENTS

   206 **Assessment of a Bayesian Vitrea CT Perfusion Analysis to Predict Final Infarct and Penumbra Volumes in Patients with Acute Ischemic Stroke: A Comparison with RAPID** *R.A. Rava, et al.* **ADULT BRAIN**

213 **Predictive Value of Noncontrast Head CT with Negative Findings in the Emergency Department Setting** *A.L. Callen, et al.* **ADULT BRAIN**

 219 **Visualization of Lenticulostriate Arteries on CT Angiography Using Ultra-High-Resolution CT Compared with Conventional-Detector CT** *K. Murayama, et al.* **ADULT BRAIN**

   224 **A Method to Estimate Brain Volume from Head CT Images and Application to Detect Brain Atrophy in Alzheimer Disease** *V. Adduru, et al.* **ADULT BRAIN**

231 **Metal Artifact Reduction in Head CT Performed for Patients with Deep Brain Stimulation Devices: Effectiveness of a Single-Energy Metal Artifact Reduction Algorithm** *Y. Nagayama, et al.* **ADULT BRAIN**

   238 **Spiral T1 Spin-Echo for Routine Postcontrast Brain MRI Exams: A Multicenter Multireader Clinical Evaluation** *M.B. Ooi, et al.* **ADULT BRAIN**

 246 **MR Diffusional Kurtosis Imaging–Based Assessment of Brain Microstructural Changes in Patients with Moyamoya Disease before and after Revascularization** *P.-G. Qiao, et al.* **ADULT BRAIN FUNCTIONAL**

255 **Effects of Susceptibility Artifacts on Perfusion MRI in Patients with Primary Brain Tumor: A Comparison of Arterial Spin-Labeling versus DSC** *H. Maral, et al.* **ADULT BRAIN FUNCTIONAL**

AJNR (Am J Neuroradiol ISSN 0195–6108) is a journal published monthly, owned and published by the American Society of Neuroradiology (ASNR), 800 Enterprise Drive, Suite 205, Oak Brook, IL 60523. Annual dues for the ASNR include approximately 21% for a journal subscription. The journal is printed by Cadmus Journal Services, 5457 Twin Knolls Road, Suite 200, Columbia, MD 21045; Periodicals postage paid at Oak Brook, IL and additional mailing offices. Printed in the U.S.A. POSTMASTER: Please send address changes to American Journal of Neuroradiology, P.O. Box 3000, Denville, NJ 07834, U.S.A. Subscription rates: nonmember \$410 (\$480 foreign) print and online, \$320 online only; institutions \$470 (\$540 foreign) print and basic online, \$935 (\$1000 foreign) print and extended online, \$380 online only (basic), extended online \$825; single copies are \$35 each (\$40 foreign). Indexed by PubMed/MEDLINE, BIOSIS Previews, Current Contents (Clinical Medicine and Life Sciences), EMBASE, Google Scholar, HighWire Press, Q-Sensei, RefSeek, Science Citation Index, SCI Expanded, Meta/CZI, ReadCube, and Semantic Scholar. Copyright © American Society of Neuroradiology.

	262	How Do Physicians Approach Intravenous Alteplase Treatment in Patients with Acute Ischemic Stroke Who Are Eligible for Intravenous Alteplase and Endovascular Therapy? Insights from UNMASK-EVT <i>J.M. Ospel, et al.</i>	INTERVENTIONAL		
	268	Impact of Aortic Arch Anatomy on Technical Performance and Clinical Outcomes in Patients with Acute Ischemic Stroke <i>J.A. Knox, et al.</i>	INTERVENTIONAL		
	274	DWI-Based Algorithm to Predict Disability in Patients Treated with Thrombectomy for Acute Stroke <i>H. Raoult, et al.</i>	INTERVENTIONAL		
	280	Endovascular Treatment Decisions in Patients with M2 Segment MCA Occlusions <i>M. Almekhlafi, et al.</i>	INTERVENTIONAL		
		286	Delayed Leukoencephalopathy: A Rare Complication after Coiling of Cerebral Aneurysms <i>A. Ikemura, et al.</i>	INTERVENTIONAL ADULT BRAIN	
	293	Intra-Arterial Verapamil Treatment in Oral Therapy–Refractory Reversible Cerebral Vasoconstriction Syndrome <i>J.M. Ospel, et al.</i>	INTERVENTIONAL		
		300	Artery of Davidoff and Schechter Supply in Dural Arteriovenous Fistulas <i>K.D. Bhatia, et al.</i>	INTERVENTIONAL	
	305	Asymptomatic Cerebral Vasoconstriction after Carotid Artery Stenting <i>C.H. Kang, et al.</i>	INTERVENTIONAL		
	310	Characterization of Carotid Plaque Components by Quantitative Susceptibility Mapping <i>M. Azuma, et al.</i>	EXTRACRANIAL VASCULAR		
	318	Standard Diffusion-Weighted Imaging in the Brain Can Detect Cervical Internal Carotid Artery Dissections <i>G. Adam, et al.</i>	EXTRACRANIAL VASCULAR ADULT BRAIN		
	323	MRI Patterns of Extrapontine Lesion Extension in Diffuse Intrinsic Pontine Gliomas <i>L. Makepeace, et al.</i>	PEDIATRICS		
	331	Frequency, Extent, and Correlates of Superficial Siderosis and Ependymal Siderosis in Premature Infants with Germinal Matrix Hemorrhage: An SWI Study <i>M.S. Albayram, et al.</i>	PEDIATRICS		
	338	Macrocerebellum in Achondroplasia: A Further CNS Manifestation of <i>FGFR3</i> Mutations? <i>H.M. Pascoe, et al.</i>	PEDIATRICS		
			343	Considerations for Mean Upper Cervical Cord Area Implementation in a Longitudinal MRI Setting: Methods, Interrater Reliability, and MRI Quality Control <i>C. Chien, et al.</i>	SPINE
		351	Renal Excretion of Contrast on CT Myelography: A Specific Marker of CSF Leak <i>S. Behbahani, et al.</i>	SPINE	
	357	Long-Term Outcome of Patients with Spinal Dural Arteriovenous Fistula: The Dilemma of Delayed Diagnosis <i>F. Jablawi, et al.</i>	SPINE		
	364	Differentiation between Tuberculous and Pyogenic Spondylodiscitis: The Role of the Anterior Meningovertebral Ligament in Patients with Anterior Epidural Abscess <i>S.B. Strauss, et al.</i>	SPINE		

ONLINE FEATURES

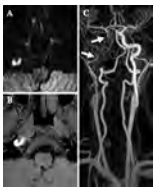
LETTERS

- E4 **Intraoperative MR and Synthetic Imaging** *M.I. Vargas, et al.*
- E7 **Comments on “Prolonged Microgravity Affects Human Brain Structure and Function”** *J.J. Bevelacqua, et al.*
- E8 **Reply** *D.R. Roberts, et al.*
- E9 **Erratum**

BOOK REVIEWS

R.M. Quencer, Section Editor

Please visit www.ajnrblog.org to read and comment on Book Reviews.



DWI (A) and fat-saturated TIWI (B) show a right carotid dissection as a crescent-shaped increased signal. MR angiography (C) shows near-occlusion of the arterial lumen.

 Indicates Editor's Choices selection

 Indicates Fellows' Journal Club selection

 Indicates open access to non-subscribers at www.ajnr.org

 Indicates article with supplemental on-line table

 Indicates article with supplemental on-line photo

 Indicates article with supplemental on-line video

 Evidence-Based Medicine Level 1

 Evidence-Based Medicine Level 2

EDITOR-IN-CHIEF

Jeffrey S. Ross, MD

Professor of Radiology, Department of Radiology,
Mayo Clinic College of Medicine, Phoenix, AZ

SENIOR EDITORS

Harry J. Cloft, MD, PhD

Professor of Radiology and Neurosurgery,
Department of Radiology, Mayo Clinic College of
Medicine, Rochester, MN

Christopher G. Filippi, MD

Professor and Vice Chair of Biomedical and
Translational Science,
Donald and Barbara Zucker School of Medicine at
Hofstra/Northwell,
Lenox Hill Hospital and Greenwich Village
Healthplex, New York, NY

Thierry A.G.M. Huisman, MD

Radiologist-in-Chief, Texas Children's Hospital,
Houston, TX

Yvonne W. Lui, MD

Associate Professor of Radiology,
Chief of Neuroradiology,
New York University School of Medicine,
New York, NY

C.D. Phillips, MD, FACR

Professor of Radiology, Weill Cornell Medical
College, Director of Head and Neck Imaging,
New York-Presbyterian Hospital, New York, NY

Lubdhra M. Shah, MD, MS

Professor of Radiology and Director of Spine
Imaging, University of Utah Department of
Radiology and Imaging Sciences, Salt Lake City, UT

Charles M. Strother, MD

Professor of Radiology, Emeritus, University of
Wisconsin, Madison, WI

STATISTICAL SENIOR EDITOR

Bryan A. Comstock, MS

Senior Biostatistician,
Department of Biostatistics,
University of Washington, Seattle, WA

ARTIFICIAL INTELLIGENCE DEPUTY EDITOR

Peter D. Chang, MD

Assistant Professor-in-Residence,
Departments of Radiological Sciences,
Computer Sciences, and Pathology,
Director, Center for Artificial Intelligence in
Diagnostic Medicine (CAIDM),
University of California, Irvine, Irvine, CA

EDITORIAL BOARD

Ashley H. Aiken, Atlanta, GA

Lea M. Alhilali, Phoenix, AZ

Kubilay Aydin, Istanbul, Turkey

John D. Barr, Dallas, TX

Ari Blitz, Baltimore, MD

Barton F. Branstetter IV, Pittsburgh, PA

Jonathan L. Brisman, Lake Success, NY

Keith Cauley, Danville, PA

James Y. Chen, San Diego, CA

Asim F. Choudhri, Memphis, TN

Daniel Chow, Irvine, CA

J. Matthew Debnam, Houston, TX

Seena Dehkharghani, New York, NY

Yonghong Ding, Rochester, MN

Clifford J. Eskey, Hanover, NH

Saeed Fakhra, Phoenix, AZ

Massimo Filippi, Milan, Italy

Nils D. Forkert, Calgary, Alberta, Canada

Wende N. Gibbs, Phoenix, AZ

Christine M. Glastonbury, San Francisco, CA

John L. Go, Los Angeles, CA

Philipp Göltz, Erlangen, Germany

Allison Grayev, Madison, WI

Brent Griffith, Detroit, MI

Ajay Gupta, New York, NY

Rakesh Kumar Gupta, Haryana, India

Lothi Hacein-Bey, Sacramento, CA

Christopher P. Hess, San Francisco, CA

Andrei Holodny, New York, NY

Benjamin Huang, Chapel Hill, NC

Mahesh V. Jayaraman, Providence, RI

Valerie Jewells, Chapel Hill, NC

Christof Karmonik, Houston, TX

Timothy J. Kaufmann, Rochester, MN

Hillary R. Kelly, Boston, MA

Toshibumi Kinoshita, Akita, Japan

Kenneth F. Layton, Dallas, TX

Alexander Lerner, Los Angeles, CA

Michael Lev, Boston, MA

Karl-Olof Lovblad, Geneva, Switzerland

Franklin A. Marden, Chicago, IL

Joseph C. McGowan, Merion Station, PA

Stephan Meckel, Freiburg, Germany

Christopher J. Moran, St. Louis, MO

Takahisa Mori, Kamakura City, Japan

Suresh Mukherji, Ann Arbor, MI

Alexander J. Nemeth, Chicago, IL

Renato Hoffmann Nunes, Sao Paulo, Brazil

Sasan Partovi, Cleveland, OH

Laurent Pierot, Reims, France

Jay J. Pillai, Baltimore, MD

Whitney B. Pope, Los Angeles, CA

Joana Ramalho, Lisbon, Portugal

Otto Rapalino, Boston, MA

Álex Rovira-Cañellas, Barcelona, Spain

Paul M. Ruggieri, Cleveland, OH

Amit M. Saindane, Atlanta, GA

Maksim Shapiro, New York, NY

Timothy Shepherd, New York, NY

Mark S. Shiroishi, Los Angeles, CA

Bruno P. Soares, Baltimore, MD

Maria Vittoria Spampinato, Charleston, SC

Khin Khin Tha, Sapporo, Hokkaido, Japan

Krishnamoorthy Thamburaj, Hershey, PA

Cheng Hong Toh, Taipei, Taiwan

Aquila S. Turk, Greenville, SC

Anja G. van der Kolk, Utrecht, the Netherlands

Willem Jan van Rooij, Tilburg, Netherlands

Arastoo Vossough, Philadelphia, PA

Elysa Widjaja, Toronto, Ontario, Canada

Max Wintermark, Stanford, CA

Ronald L. Wolf, Philadelphia, PA

Kei Yamada, Kyoto, Japan

Carlos Zamora, Chapel Hill, NC

Vahe M. Zohrabian, New Haven, CT

EDITORIAL FELLOW

Hediyeh Baradaran, Salt Lake City, UT

SPECIAL CONSULTANTS TO THE EDITOR

AJNR Blog Editor

Neil Lall, Denver, CO

Case of the Month Editor

Nicholas Stence, Aurora, CO

Case of the Week Editors

Juan Pablo Cruz, Santiago, Chile

Sapna Rawal, Toronto, Ontario, Canada

Classic Case Editor

Sandy Cheng-Yu Chen, Taipei, Taiwan

Health Care and Socioeconomics Editor

Pina C. Sanelli, New York, NY

Physics Editor

Greg Zaharchuk, Stanford, CA

Podcast Editor

Wende N. Gibbs, Phoenix, AZ

Twitter Editor

Roger Jordan, Houston, TX

Official Journal:

American Society of Neuroradiology

American Society of Functional Neuroradiology

American Society of Head and Neck Radiology

American Society of Pediatric Neuroradiology

American Society of Spine Radiology

Founding Editor

Juan M. Taveras

Editors Emeriti

Mauricio Castillo, Robert I. Grossman,

Michael S. Huckman, Robert M. Quencer

Managing Editor

Karen Halm

Assistant Managing Editor

Laura Wilhelm

Editorial Assistant

Margaret B. Sabato

Executive Director, ASNR

Mary Beth Hepp

We're Inside Every Great Neuroradiologist!

ASNR MEMBERS RECEIVE

American Journal of Neuroradiology (AJNR)

The leading neuroradiology research journal, published monthly

Neurographics

Bimonthly educational journal with CME for members

ASNR Annual Meeting

Discounts for members on the field's premier conference

eCME

Online collection of lectures and articles with SA-CME and Category 1 credit

Advocacy

Coding/reimbursement, quality standards and practice guidelines; demonstrating neuroradiology's value!

Networking

Access to 5,000 peers

... And More!

Join the leaders in neuroradiology today!

Learn more at www.asnr.org/join

ASNR

American Society of Neuroradiology

800 Enterprise Dr., Suite 205, Oak Brook, IL 60523 • (630)574-0220 • membership@asnr.org • www.asnr.org

AJNR *go green*

***AJNR* urges American Society of Neuroradiology members to reduce their environmental footprint by voluntarily suspending their print subscription.**

The savings in paper, printing, transportation, and postage directly fund new electronic enhancements and expanded content.

The digital edition of *AJNR* presents the print version in its entirety, along with extra features including:

- Publication Preview
- Case Collection
- Podcasts
- The *AJNR* News Digest
- The *AJNR* Blog

It also reaches subscribers much faster than print. An electronic table of contents will be sent directly to your mailbox to notify you as soon as it publishes.

Readers can search, reference, and bookmark current and archived content 24 hours a day on www.ajnr.org.

ASNR members who wish to opt out of print can do so by using the *AJNR* Go Green link on the *AJNR* Website (<http://www.ajnr.org/content/subscriber-help-and-services>). Just type your name in the email form to stop print and spare our ecosystem.

CALL FOR AJNR EDITORIAL FELLOWSHIP CANDIDATES

ASNR and AJNR are pleased once again to join efforts with other imaging-related journals that have training programs on editorial aspects of publishing for trainees or junior staff (<5 years on staff), including Radiology (Olmsted fellowship), AJR (Figley and Rogers fellowships), JACR (Bruce J. Hillman fellowship), and Radiologia.

2020 Candidate Information and Requirements

GOALS

- Increase interest in editorial and publication-related activities in younger individuals.
- Increase understanding and participation in the AJNR review process.
- Incorporate into AJNR's Editorial Board younger individuals who have previous experience in the review and publication process.
- Fill a specific need in neuroradiology not offered by other similar fellowships.
- Increase the relationship between "new" generation of neuroradiologists and more established individuals.
- Increase visibility of AJNR among younger neuroradiologists.

ACTIVITIES OF THE FELLOWSHIP

- Serve as Editorial Fellow for one year. This individual will be listed on the masthead as such.
- Review at least one manuscript per month for 12 months. Evaluate all review articles submitted to AJNR.
- Learn how electronic manuscript review systems work.
- Be involved in the final decision of selected manuscripts together with the Editor-in-Chief.
- Participate in all monthly Senior Editor telephone conference calls.
- Participate in all meetings of the Editors during the annual meetings of ASNR and RSNA and the Radiology Editors Forum as per candidate's availability. The Foundation of the ASNR will provide \$2000 funding for this activity.
- Evaluate progress and adjust program to specific needs in annual meeting or telephone conference with the Editor-in-Chief.
- Embark on an editorial scientific or bibliometric project that will lead to the submission of an article to AJNR or another appropriate journal as determined by the Editor-in-Chief. This project will be presented by the Editorial Fellow at the ASNR annual meeting.
- Serve as liaison between AJNR and ASNR's Young Professionals Network. Participate in meetings and telephone calls with this group. Design one electronic survey/year, polling the group regarding readership attitudes and wishes.
- Recruit trainees as reviewers as determined by the Editor-in-Chief.
- Organize and host a Fellows' Journal Club podcast.
- Serve as Guest Editor for an issue of AJNR's News Digest with a timely topic.

QUALIFICATIONS

- Be a fellow in neuroradiology from North America, including Canada (this may be extended to include other countries).
- Be a junior faculty neuroradiology member (<5 years) in either an academic or private environment.
- Be an "in-training" or member of ASNR in any other category.

APPLICATION

- Include a short letter of intent with statement of goals and desired research project. CV must be included.
- Include a letter of recommendation from the Division Chief or fellowship program director. A statement of protected time to perform the functions outlined is desirable.
- Applications will be evaluated by AJNR's Senior Editors prior to the ASNR meeting. The name of the selected individual will be announced at the meeting.
- Applications should be received by March 2, 2020 and sent to Ms. Karen Halm, AJNR Managing Editor, electronically at khalm@asnr.org.



Title: Chrysler Building Reflections. I exclusively shot film at the time I took this image, which was quite a few years ago. I never record the camera and film specifications, though at that time I was shooting with a Nikon N80 with an AF Zoom Nikkor 24-85 mm, f/2.8-4DIF lens, and using Kodak Portra. The glass curtain walls of international style architecture provide large, unadorned reflective surfaces that are heat tempered. Thermal tempering can induce deviations from flatness in the glass, known as warps, overall and local bows, and local and roller wave distortions. Depending on the surrounding structures reflected from the glass, which in this case is the iconic Chrysler Building, an infinite number of phantasmagoric images appear, one continuously morphing into another with slight shifts in perspective. It is interesting to this fan of distorted reflections that these deviations from flatness are typically discussed as defects in the construction materials literature, while actually not-to-be missed opportunities to create modern art images, underscoring a core message of photography: stop, or at least slow down, and contemplate our amazing world.

Manfred Hauben, MD, MPH Pfizer Inc and NYU Langone Health, New York City

The Forgotten Second Window: A Pictorial Review of Round Window Pathologies

J.C. Benson, F. Diehn, T. Passe, J. Guerin, V.M. Silvera, M.L. Carlson, and J. Lane



ABSTRACT

SUMMARY: The round window serves to decompress acoustic energy that enters the cochlea via stapes movement against the oval window. Any inward motion of the oval window via stapes vibration leads to outward motion of the round window. Occlusion of the round window is a cause of conductive hearing loss because it increases the resistance to sound energy and consequently dampens energy propagation. Because the round window niche is not adequately evaluated by otoscopy and may be incompletely exposed during an operation, otologic surgeons may not always correctly identify associated pathology. Thus, radiologists play an essential role in the identification and classification of diseases affecting the round window. The purpose of this review is to highlight the developmental, acquired, neoplastic, and iatrogenic range of pathologies that can be encountered in round window dysfunction.

ABBREVIATIONS: LO = labyrinthitis ossificans; RW = round window

The round window (RW) serves as a boundary between the basal turn of the cochlea anteriorly and the round window niche posteriorly.¹ It, along with the oval window, is 1 of 2 natural openings between the inner and middle ear. The round window is often overshadowed by the “first window” (the oval window) and pathologic “third windows” (eg, superior semicircular canal dehiscence). Nevertheless, numerous developmental, acquired, neoplastic, and iatrogenic processes can affect the round window membrane and niche. Any of these can cause conductive hearing loss because occlusion of the round window prevents propagation of acoustic energy along the cochlear axis.² In operative interventions in which a primary goal of surgery is to improve conductive hearing loss or access the round window region for cochlear implantation, accurate preoperative identification of round window abnormalities is essential to first determine whether surgery is a worthwhile endeavor and subsequently to guide the surgical strategy. In this article, the various pathologic entities and surgical

considerations of the round window that can be encountered on imaging are reviewed.

Physiology and Functionality

The inner ear “windows” refer to openings in the otic capsule that connect the fluid in the inner ear to either the middle ear or intracranial space.³ The 2 primary natural openings are the oval and round windows.³ Other windows include the cochlear and vestibular aqueducts and tiny foramina that transmit vessels and/or nerves to the inner ear and adjacent structures (eg, the petromastoid canal and singular canal).

Functionally, the role of the oval and round windows is related to sound transmission: Vibratory acoustic energy enters through the oval window, is transmitted through the cochlea, and exits into the middle ear cavity via the round window.³ The fluid in the cochlea through which sound is transmitted is functionally incompressible due to the surrounding osseous structures.⁴ Movement of the cochlear fluid is thereby dependent on the mobility of the round and oval window membranes: Inward displacement of the oval window membrane via the stapes by ossicular vibration is matched by outward round window membrane displacement.⁴

Developmental Anomalies

Normal Anatomy. The round window is located along the posterior aspect of the cochlear promontory and measures 1.5–2.1 mm horizontally, 1.9 mm vertically, and 0.65 mm in thickness (Fig 1).^{1,5} The round window membrane is thicker along its edges and

Received July 24, 2019; accepted after revision November 2.

From the Departments of Neuroradiology (J.C.B., F.D., T.P., J.G., V.M.S., J.L.) and Otolaryngology–Head and Neck Surgery (M.L.C.), Mayo Clinic, Rochester, Minnesota.

Internal departmental funding was used without commercial sponsorship or support.

Please address correspondence to John C. Benson, MD, 200 1st St. SW, Rochester MN 55905; e-mail: Benson.john3@mayo.edu

Indicates open access to non-subscribers at www.ajnr.org

<http://dx.doi.org/10.3174/ajnr.A6356>

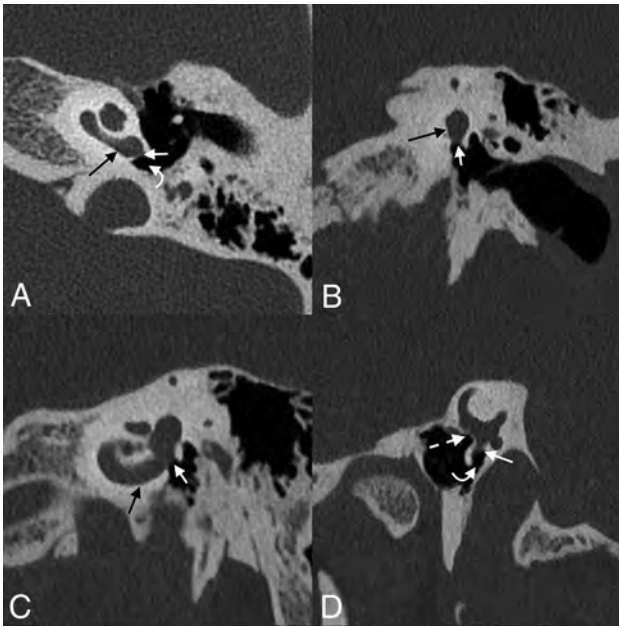


FIG 1. Normal round window anatomy. Axial (A), coronal (B), Stenvers (C), and Pöschl (D) images centered on the round window membrane (straight white arrows), situated between the basal turn of the cochlea (black arrows) and the round window niche of the middle ear (curved white arrows). The oval window is closely adjacent (dashed arrow).

thinner in the middle and is made up of 3 layers: 2 epithelial layers facing the inner and middle ear, respectively, and connective tissue in the core.⁶ Contrary to its name, the shape of the round window is typically skewed, ovoid, and nonplanar according to a recent study.⁷ The round window niche is primarily defined by the relatively thin overhanging bone that naturally extends from the promontory. This overhanging bone may obscure complete direct visualization of the round window membrane during routine middle ear surgery and cochlear implantation (Fig 2).⁸ In addition, most ears have a thin layer of mucosa covering the round window membrane, often called a “pseudomembrane,” that blocks direct visualization of the window if not removed.

Round Window Stenosis and Atresia. Round window absence is a rare abnormality that may be seen in conjunction with various syndromes, including incomplete partition anomalies, mandibulofacial dysostosis, and Coloboma of the eye, Heart defects, Atresia of the choanae, Retardation of growth and/or development, Genital and/or urinary abnormalities, and Ear abnormalities and deafness (CHARGE) syndrome, in addition to cases of aural atresia (Fig 3).^{9–11} In very rare cases, it may also occur without an associated syndrome (Fig 4).^{12,13} Some authors have posited that such nonsyndromic cases may represent an inherited autosomal dominant genetic disorder with variable penetrance.¹⁰ Even in nonsyndromic cases, few reports exist of round window atresia as an isolated finding; most of these patients have associated middle ear or pinna abnormalities.¹⁰

Patients with round window atresia typically have a mixed but predominantly conductive hearing loss, with an associated typical

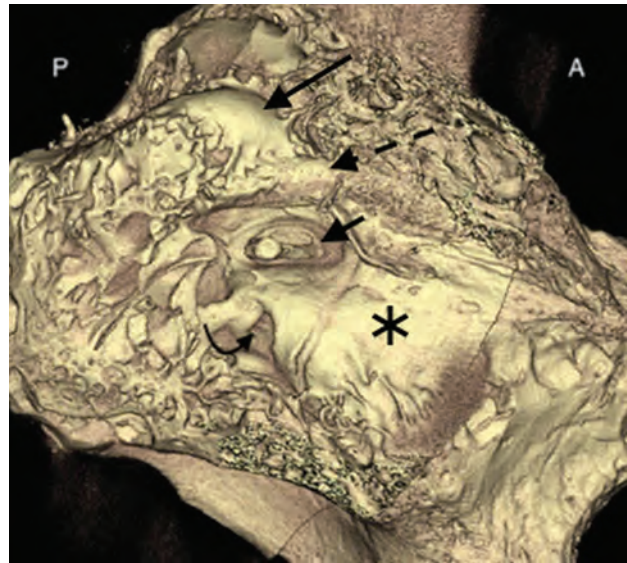


FIG 2. Surface-rendered image of a microCT (GE Healthcare, Milwaukee, Wisconsin) of the temporal bone shows the relationship of the round window niche (curved arrow) to the adjacent anatomic structures. Also seen are the lateral semicircular canal (long straight arrow), facial nerve canal (dashed arrow), stapes and oval window (short arrow), and cochlear promontory (asterisk). A indicates anterior; P, posterior.

air-bone gap of 30–40 dB.¹⁴ Attempts to surgically recreate the round window do not always produce substantial gains in hearing.¹⁴ The reasons remain uncertain because few such surgical

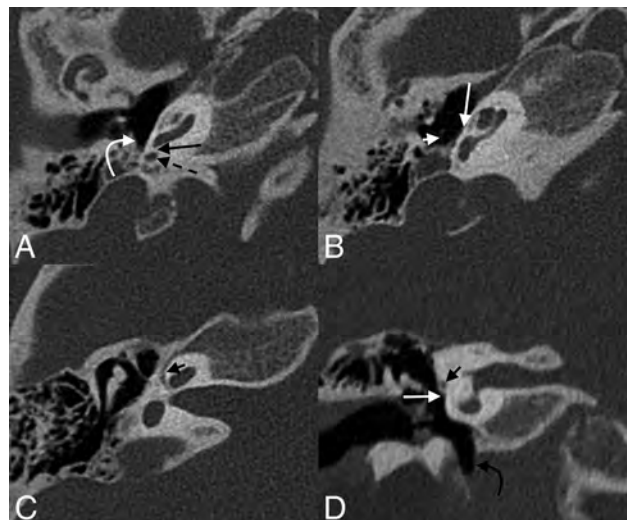


FIG 3. A 5-year-old girl with round window atresia in the setting of CHARGE syndrome. Axial (A–C) and coronal (D) images of the right temporal bone demonstrate complete absence of the round window (long black arrow, A); the round window niche is hypoplastic and surrounded by bone (dashed arrow, A), adjacent to a preserved sinus tympani (curved white arrow, A). Multiple other anomalies are the following: The stapes is dysmorphic with absence of the neck, crura, and footplate (short white arrow, B); the oval window is absent (long white arrow, B and D); the facial nerve canal is diminutive (short black arrow, C) and inferiorly displaced (short black arrow, D); and the hypotympanum is enlarged (curved black arrow, D). The semicircular canals are absent.

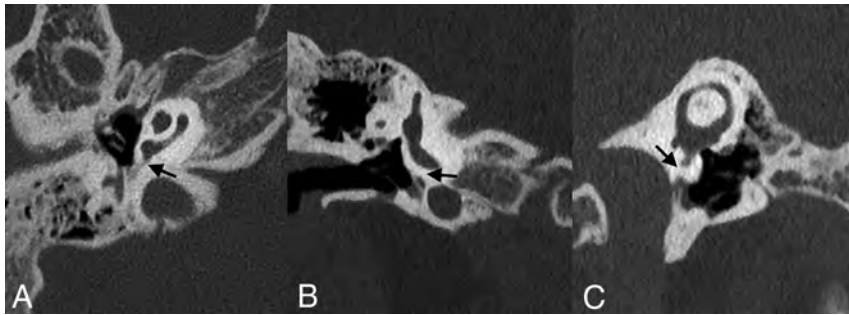


FIG 4. Nonsyndromic round window atresia. Axial (A), coronal (B), and Pöschl (C) views of the right temporal bone of a 10-year-old girl demonstrate an ossification at the expected location of the round window membrane (arrows). The patient had no known syndromic association.

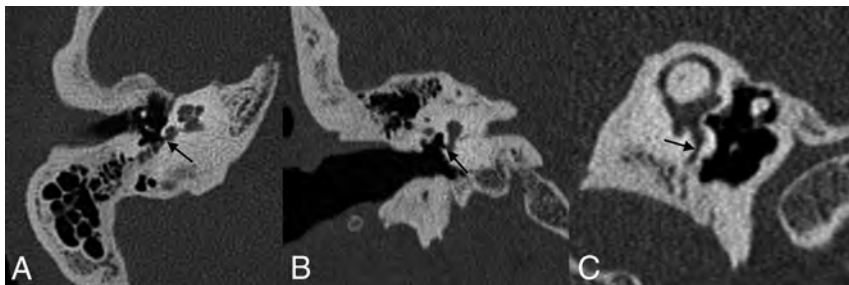


FIG 5. Round window stenosis. A 52-year-old woman with profound bilateral hearing loss. Axial (A), coronal (B), and Pöschl (C) images of the right temporal bone demonstrate advanced stenosis of the round window (arrows).



FIG 6. Round window niche occlusion. A 48-year-old woman who presented with fullness in the right ear and conductive hearing loss following a bout of flulike symptoms. Axial (A), Pöschl (B), and coronal (C) images of the right temporal bone demonstrate a tiny focus of debris adjacent to the right round window membrane (straight arrow) within the round window niche (curved arrow), possibly sequelae of her recent inflammatory illness.

case reports exist. However, the inconsistent results may be related to the presence of associated anomalies such as congenital stapes fixation, otosclerosis, or re-ossification following an operation.

Unfortunately, because surgeons often have incomplete exposure of the round window niche during routine otologic procedures and because of its rarity, round window atresia can easily be overlooked intraoperatively.¹⁴ It also is frequently missed on imaging, and many patients with round window atresia are not diagnosed until middle ear exploration.¹⁰ Close attention must therefore be paid to the morphology of the round window and

round window niche on imaging performed for conductive or mixed hearing loss.

Stenosis of the round window membrane and/or recess is more common than complete round window absence. Like round window atresia, stenosis of the round window can have syndromic associations and contribute to hearing loss.¹⁵ The lower limit of normal size for the round window niche is generally cited as being 1.5 mm.¹ Nevertheless, imaging characteristics of stenotic recesses can be quite variable, ranging from mild to severe (Fig 5).

Acquired Abnormalities

Acquired abnormalities that affect the round window include a range of traumatic, inflammatory, and iatrogenic processes. Otitis media associated with mucosal thickening and effusion may obscure the round window or adjacent niche (Fig 6). Less commonly, barotrauma or increased pressure may cause the round window membrane to rupture, leading to perilymph fistula with sensorineural hearing loss and vertigo.¹⁷⁻¹⁹ Temporal bone fractures through the round window may disrupt the membrane. Several primary osseous processes such as Paget disease, fibrous dysplasia, otosyphilis, and osteogenesis imperfecta can affect the temporal bone, including the annular ring of the round window.^{15,20,21} Below, several of the most common causes of acquired abnormalities of the round window are discussed, with imaging correlates.

Labyrinthitis Ossificans. Labyrinthitis ossificans (LO) refers to ossification within the membranous labyrinth, most frequently occurring within the scala tympani.²² Typically, LO is secondary to

inflammatory changes from infection such as suppurative otitis media, labyrinthitis, or meningitis, though trauma and otosclerosis have also been indicated as inciting processes.^{23,24} In cases of LO associated with bacterial meningitis, the basal turn of the cochlea is often preferentially affected because infection may spread from the subarachnoid space through the cochlear aqueduct to the proximal scala tympani (though spread may also occur through the modiolus).²⁵ In some cases, LO may involve the round window, involvement thought to occur when the inciting event is otitis media or meningitis that spreads through the round window along the scala tympani (Fig 7).²⁶ The etiology of

LO cannot be predicted on the basis of mineralization patterns seen on CT.²⁷ LO is associated with the development of sensorineural hearing loss and may render cochlear implantation more challenging and outcomes less rewarding.^{28,29} Extensive LO may preclude the placement of a cochlear implant. Expected CT findings of LO involving the round window include thickening/high attenuation along the membrane, likely with coexistent ossific material in the basal turn of the cochlea or elsewhere in the membranous labyrinth. In the early stages of labyrinthitis, fibrosis may be evident only on heavily weighted T2 imaging, where low signal is seen within or partially replacing normally high-signal perilymph.

Otosclerosis. Otosclerosis is an acquired condition in which spongiotic bone replaces mature endochondral bone of the otic capsule.³⁰ Typically, otosclerosis involves the oval window and stapes footplate in the region of the fissula ante fenestram.^{30,31} Fenestral otosclerosis may also secondarily involve the round window in approximately 3%–13% of cases.^{32,33} Isolated round

window otosclerosis has been reported, though the prevalence is rare (approximately 0.3% of cases).³² Nevertheless, secondary involvement or isolated involvement of the round window by otosclerosis is an important radiologic observation because it portends a poorer chance of surgical success.³⁰ Specifically, round window involvement diminishes the movement of perilymphatic fluid following stapedectomy and prosthesis placement, the surgery typically used in cases of otosclerosis.^{34,35}

The appearance of otosclerosis on imaging depends on the disease phase. In the active (otospongiotic) stage, the affected bone surrounding the round window will appear lucent and demineralized (Fig 8).^{36,37} Later on, these areas are replaced by sclerotic bone during the nonactive (otosclerotic) stage.³⁷ As this replacement occurs, the round window membrane may become thickened or irregular. Heaped-up osseous plaques may narrow the round window or adjacent niche.³⁴

Mansour et al³² categorized otosclerosis of the round window on the basis of the extent of involvement of the membrane and adjacent structures. Under this classification scheme, RW-I represented hypodensities about the round window edge, RW-II had partial thickening of the membrane, RW-III showed global membrane thickening with a persistent air-filled recess, RW-IV had obliteration of the recess, and RW-V demonstrated overgrowth of otosclerotic foci. Predictably, higher grades of round window involvement were found to be associated with more severe hearing loss, likely related to increased impedance within the scala tympani.³²

Jugular Bulb Dehiscence and Diverticula. The positional anatomy of the jugular bulb is variable throughout a person's life.³⁸ Jugular bulb abnormalities consequently develop with time and are typically acquired by the fourth decade of life.³⁸ High-riding jugular bulbs are found in approximately 8% of patients, both on pathologic specimens and CT images.³⁸ Dehiscent jugular bulbs and jugular bulb diverticula are more rare, occurring at a rate of 2.6% and 1.2%, respectively.^{39,40}

High-riding jugular bulbs, dehiscent bulbs, and jugular diverticula are often asymptomatic.⁴¹ However, they may also present with pulsatile tinnitus or, less commonly, conductive hearing loss, likely related to encroachment by the bulb on the round window, ossicular chain, or tympanic membrane (Fig 9).^{41,42} The incidence in which the round window membrane is specifically involved is rare; 1 histologic analysis of temporal bones identified 2 such cases in 1579 specimens (0.1%).⁴³

Imaging findings vary on the basis of the type of jugular bulb abnormality. High-riding bulbs typically occur as an isolated finding, in which the dome of the jugular bulb is within 2 mm of the internal auditory canal (IAC) floor (though definitions vary).^{44,45} A high-riding bulb may extend further superolaterally, erode the sigmoid plate, and protrude into the middle ear cavity; this dehiscence is best seen on CT as thinning and/or absence of bone between the bulb and middle ear structures.⁴⁴

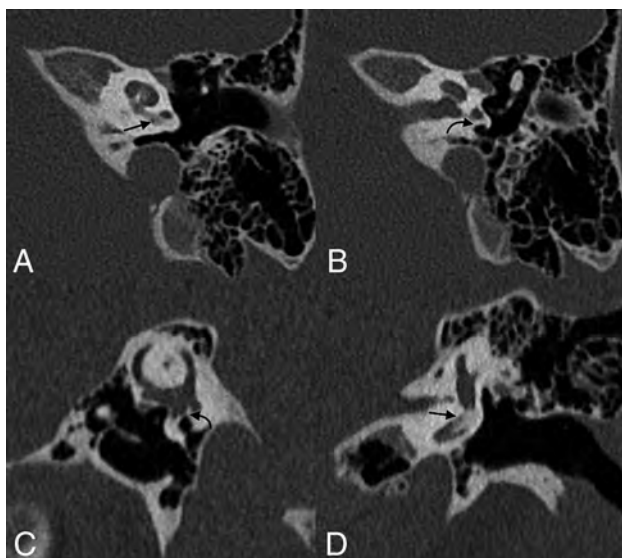


FIG 7. Labyrinthitis ossificans with round window involvement. Axial (A and B), Pöschl (C), and coronal (D) images of the left temporal bone of a 5-year-old with a history of prior tympanoplasty tube placements. Labyrinthitis ossificans is seen in the basal turn of the cochlea (straight arrows, A and D) with mineralization of the round window (curved arrows, B and C).

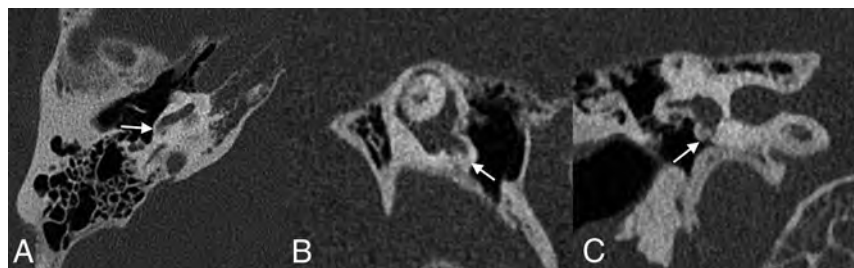


FIG 8. Otosclerosis with round window involvement. Axial (A), Pöschl (B), and coronal (C) images of the right temporal bone demonstrate bony changes compatible with otosclerosis adjacent to the round window, with marked narrowing of the round window niche (arrows).

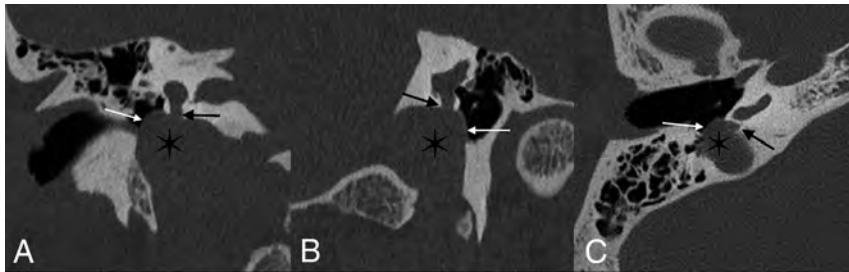


FIG 9. Jugular bulb anomalies. Coronal (A), Pöschl (B), and axial (C) images demonstrate a high-riding jugular bulb (asterisk) that extends into the round window niche (straight black arrows). The bony margins overlying the jugular bulb within the middle window are markedly thinned, compatible with dehiscence (white arrows).

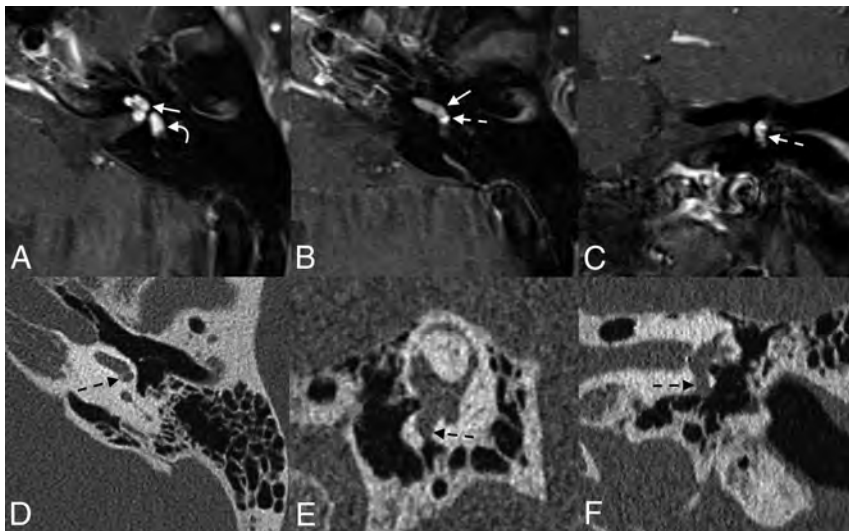


FIG 10. Intralabyrinthine schwannoma with involvement of the round window. Axial (A and B) and coronal (C) contrast-enhanced TIWI shows an avidly enhancing mass in the left cochlea (straight arrows) and vestibule (curved arrow), compatible with a schwannoma. The mass extends through the round window membrane and into the round window niche (dashed arrows), better demonstrated on the follow-up axial (D), Pöschl (E), and coronal (F) CT images.

Finally, diverticula will appear as distinct outpouchings from the bulb. Any jugular bulb anomaly seen on CT should be closely examined for the presence of abutment of the bulb on the round window membrane, niche, or other middle ear structures.

Neoplastic Processes. Several neoplastic processes may affect the round window membrane or round window niche. Some, such as metastases and primary osseous tumors, are centered in the bone; secondary round window involvement by these lesions depends on their size and location. Notably, most primary osteodystrophies and osseous neoplasms spare the otic capsule, given divergent embryology and composition. Other tumors have an anatomic proclivity to involve the round window membrane. For example, intralabyrinthine schwannomas may extend through the round window membrane into the niche (Fig 10).^{46,47} CT images of such patients may demonstrate a soft-tissue mass within the niche; visualization of the entire lesion often requires MR imaging.

Jugulotympanic paragangliomas—comprising glomus jugulare and glomus tympanicum tumors—may also involve the

round window.^{48,49} Glomus tympanicum tumors arise from the tympanic nerve (Jacobson nerve) and grow within and along the cochlear promontory; if large enough, they may extend into and occlude the round window niche.⁴⁸ Glomus jugulare tumors begin within the jugulare foramen. Although histologically benign, glomus jugulare tumors are locally destructive and can erode into adjacent middle ear structures such as the round window niche (Fig 11).

Surgical Considerations

Surgical Access and Round Window Visualization. Several conditions may require surgical dissection at the round window niche. Most commonly, the niche is accessed during cochlear implantation. Most cases are performed using a standard cortical mastoidectomy with facial recess. The bony overhang of the round window niche is then drilled to allow direct round window membrane visualization during electrode insertion. Conversely, when surgical access of the round window or niche is performed to treat infectious or neoplastic middle ear processes, the region is typically visualized via a transcanal approach. In addition, there are uncommon situations in which round window occlusion is performed to treat traumatic perilymphatic fistulas or superior canal dehiscence syndrome. In these cases, the middle ear is typically accessed via a transcanal approach, the round window is visualized with an operating

microscope or endoscope, and fascia with or without cartilage is packed in the round window niche.

Recently, endoscopes have gained popularity in otologic surgery. Endoscopy allows superior visualization around corners, particularly during removal of a cholesteatoma in the sinus tympani and anterior epitympanum. Thus, endoscopes are sometimes used to augment microscopic techniques in complex cases. However, for visualization and access of the round window, the use of an endoscope does not carry a substantial advantage over microscope visualization in most cases⁵⁰ because the round window niche is readily seen when performing either transcanal or transmastoid-facial recess surgery via a direct line of sight.

Postoperative Changes in Third-Window Lesions. Third-window lesions refer to any range of pathology that creates an abnormal connection between the inner ear and either the middle ear or the intracranial cavity.⁵¹ Acoustic energy is lost through these windows, often causing a so-called “pseudoconductive” hearing loss, which manifests as increased bone and decreased air

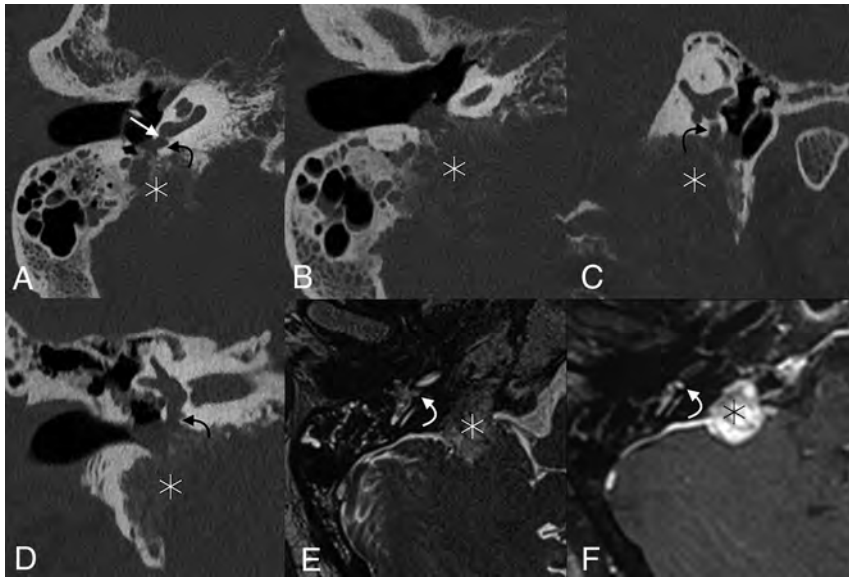


FIG 11. Glomus jugulare tumor with round window obstruction. Axial (A and B), Pöschl (C), and coronal (D) CT images of the right temporal bone show a permeative destructive mass centered in the right jugular foramen (asterisk), which extends into the right middle ear and fills the round window niche (curved arrows); opacification of the niche extends up to the round window membrane (straight arrow). Axial T2 sampling perfection with application-optimized contrasts by using different flip angle evolutions (SPACE sequence; Siemens, Erlangen, Germany) (E) and T1WI with gadolinium (F) also show the mass (asterisk) and round window niche occlusion (curved arrows).

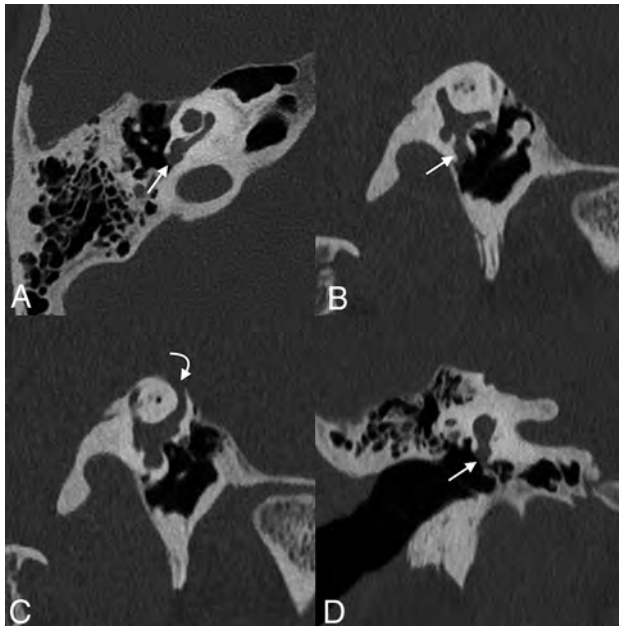


FIG 12. Postoperative changes of round window niche occlusion for superior semicircular canal dehiscence. Axial (A), Pöschl (B and C), and coronal (D) images of the right temporal bone demonstrate a soft-tissue opacity corresponding to a mixed temporalis fascia and irradiated rib cartilage against the round window and within the adjacent niche (straight arrow). There is frank dehiscence of the superior semicircular canal (curved arrow).

conduction.^{3,52} There are many such connections: vestibular aqueduct enlargement, semicircular canal dehiscence, and any other type of osseous thinning between the inner ear and adjacent

vascular or nervous channels.⁵² Patients can present with Tullio phenomenon (vertigo symptoms induced by loud noises) or Hennebert sign (similar symptoms induced by increases in pressure within the ear canal) due to deflection of the superior canal cupula by endolymphatic fluid escaping the osseous defect.⁵³⁻⁵⁵

For cases of superior semicircular canal dehiscence, surgical plugging of the pathologic osseous defect can be completed, either via a middle cranial fossa craniotomy or transmastoid approach.^{55,56} Alternatively, the round window can be targeted; surgeons may reinforce the round window with overlying tissue (eg, fascia, cartilage, fat) or occlude the round window niche (Fig 12).^{55,57-60} Currently, most authors favor the former approach over the latter; although round window occlusion is considered low-risk, this strategy may induce conductive hearing loss. Furthermore, the theoretic physiologic justification for this approach is lacking because occlusion of the round window

should theoretically create preferential shunting toward the pathologic third window.^{20,61,62}

Cochlear Implant. Cochlear implants may be inserted through a cochleostomy adjacent to the round window or directly through the round window membrane.^{63,64} Most surgeons surveyed in 2007 preferred the former approach, though these decisions may be based on historical presumptions; early multichannel leads were thought to traumatize the cochlea if placed through the round window.^{65,66} A more recent survey found that today most surgeons prefer round window membrane electrode insertions, given the natural and less traumatic access provided to the scala tympani—the preferred location of electrode placement.⁶⁷ A recent study found no difference in the number of audiometric outcomes or postoperative complications among groups undergoing electrode placement via either approach; however, most cochlear implant surgeons now prefer the round window approach when trying to preserve any residual natural acoustic hearing.^{66,67}

Regardless of the cochlear entry point, complications do occur. The electrode can kink, flip over at its tip, or migrate.^{68,69} Postoperative imaging can also demonstrate various degrees of electrode displacement, including within the semicircular canal, internal carotid artery, internal auditory canal, and vestibule.^{69,70} Across time, electrodes may also migrate from their initial position (Fig 13). Postoperative images should be evaluated in the context of the surgical approach (ie, via the round window or adjacent cochleostomy) and should include an assessment of electrode position, integrity, and change since prior examinations.

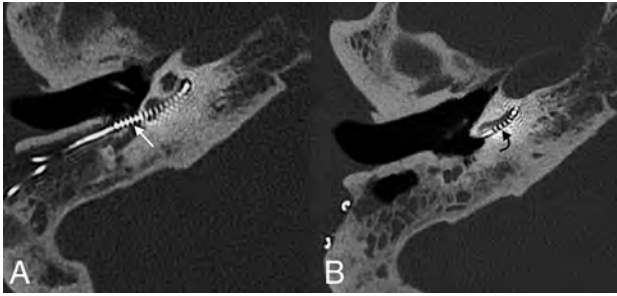


FIG 13. A 64-year-old woman who had poor progress of hearing following the placement of a cochlear implant. Axial CT image at the time of presentation (A) shows that the electrode array is retracted from its expected location, with multiple electrode leads located outside of the cochlea (*straight white arrow*). Follow-up imaging after surgical revision (B) shows normal positioning of the implant, with the first electrode located approximately 4 mm past the round window (*curved black arrow*).

CONCLUSIONS

Numerous acquired and developmental processes may affect the round window, presenting with varying clinical symptoms. Such cases can be challenging to radiologists who are unfamiliar with the local anatomy and pathologies. Nevertheless, because the round window and round window niche are often anatomically obscured during an operation, imaging plays a uniquely important role. Thus, radiologists should scrutinize the round window and familiarize themselves with the anomalies and disease processes that may be encountered in this important anatomic region.

REFERENCES

1. Veillon F, Riehm S, Emachescu B, et al. **Imaging of the windows of the temporal bone.** *Semin Ultrasound CT MR* 2001;22:271–80 CrossRef Medline
2. Curtin HD. **Imaging of conductive hearing loss with a normal tympanic membrane.** *AJR Am J Roentgenol* 2016;206:49–56 CrossRef Medline
3. Merchant SN, Rosowski JJ. **Conductive hearing loss caused by third-window lesions of the inner ear.** *Otol Neurotol* 2008;29:282–89 CrossRef Medline
4. Stenfelt S, Goode RL. **Bone-conducted sound: physiological and clinical aspects.** *Otol Neurotol* 2005;26:1245–46 CrossRef Medline
5. Paparella MM, Oda M, Hiraide F, et al. **Pathology of sensorineural hearing loss in otitis media.** *Ann Otol Rhinol Laryngol* 1972;81:632–47 CrossRef Medline
6. Goycoolea MV, Lundman L. **Round window membrane: structure function and permeability—a review.** *Microsc Res Tech* 1997;36:201–11 CrossRef Medline
7. Atturo F, Barbara M, Rask-Andersen H. **Is the human round window really round? An anatomic study with surgical implications.** *Otol Neurotol* 2014;35:1354–60 CrossRef Medline
8. Roland PS, Wright CG, Isaacson B. **Cochlear implant electrode insertion: the round window revisited.** *Laryngoscope* 2007;117:1397–1402 CrossRef Medline
9. Vesseur AC, Verbist BM, Westerlaan HE, et al. **CT findings of the temporal bone in CHARGE syndrome: aspects of importance in cochlear implant surgery.** *Eur Arch Otorhinolaryngol* 2016;273:4225–40 CrossRef Medline
10. Borrmann A, Arnold W. **Non-syndromal round window atresia: an autosomal dominant genetic disorder with variable penetrance?** *Eur Arch Otorhinolaryngol* 2007;264:1103–08 CrossRef Medline

11. Morimoto AK, Wiggins RH, Hudgins PA, et al. **Absent semicircular canals in CHARGE syndrome: radiologic spectrum of findings.** *AJNR Am J Neuroradiol* 2006;27:1663–71 Medline
12. Martin C, Tringali S, Bertholon P, et al. **Isolated congenital round window absence.** *Ann Otol Rhinol Laryngol* 2002;111:799–801 CrossRef Medline
13. Clifford AR, Fagan PA, Doust BD. **Isolated congenital round window absence.** *J Laryngol Otol* 1990;104:980–81 CrossRef Medline
14. Linder TE, Ma F, Huber A. **Round window atresia and its effect on sound transmission.** *Otol Neurotol* 2003;24:259–63 CrossRef Medline
15. Alkadhi H, Rissmann D, Kollias SS. **Osteogenesis imperfecta of the temporal bone: CT and MR imaging in Van der Hoeve-de Kleyn syndrome.** *AJNR Am J Neuroradiol* 2004;25:1106–09 Medline
16. Lemmerling M, Foer Bd. *Temporal Bone Imaging.* Berlin: Springer-Verlag; 2014
17. Choo YB. **Microscopic characteristics of round window problems in otology.** *Laryngoscope* 1984;94:1–9 CrossRef Medline
18. Lyons GD, Dodson ML, Casey DA, et al. **Round window rupture secondary to acoustic trauma.** *South Med J* 1978;71:71–73 CrossRef Medline
19. Al Felasi M, Pierre G, Mondain M, et al. **Perilymphatic fistula of the round window.** *Eur Ann Otorhinolaryngol Head Neck Dis* 2011;128:139–41 CrossRef Medline
20. Andreu-Arasa VC, Sung EK, Fujita A, et al. **Otosclerosis and dysplasias of the temporal bone.** *Neuroimaging Clin N Am* 2019;29:29–47 CrossRef Medline
21. Ogungbemi A, Dudau C, Morley S, et al. **Computed tomography features of luetic osteitis (otosyphilis) of the temporal bone.** *J Laryngol Otol* 2014;128:185–88 CrossRef Medline
22. deSouza C, Paparella MM, Schachern P, et al. **Pathology of labyrinthine ossification.** *J Laryngol Otol* 1991;105:621–24 CrossRef Medline
23. Kaya S, Paparella MM, Cureoglu S. **Pathologic findings of the cochlea in labyrinthitis ossificans associated with the round window membrane.** *Otolaryngol Head Neck Surg* 2016;155:635–40 CrossRef Medline
24. d'Archembeau O, Parizel PM, Koekelkoren E, et al. **CT diagnosis and differential diagnosis of otodystrophic lesions of the temporal bone.** *Eur J Radiol* 1990;11:22–30 CrossRef Medline
25. Du Y, Wu X, Li L. **Mechanisms of bacterial meningitis-related deafness.** *Drug Discov Today Dis Mech* 2006;3:115–18 CrossRef
26. Suga F, Lindsay JR. **Labyrinthitis ossificans due to chronic otitis media.** *Ann Otol Rhinol Laryngol* 1975;84:37–44 CrossRef Medline
27. Buch K, Baylous B, Fujita A, et al. **Etiology-specific mineralization patterns in patients with labyrinthitis ossificans.** *AJNR Am J Neuroradiol* 2019;40:551–57 CrossRef Medline
28. Swartz JD, Mandell DM, Faerber EN, et al. **Labyrinthine ossification: etiologies and CT findings.** *Radiology* 1985;157:395–98 CrossRef Medline
29. Green JD, Marion MS, Hinojosa R. **Labyrinthitis ossificans: histopathologic consideration for cochlear implantation.** *Otolaryngol Head Neck Surg* 1991;104:320–26 CrossRef Medline
30. Thomson S, Madani G. **The windows of the inner ear.** *Clin Radiol* 2014;69:e146–52 CrossRef Medline
31. Wichova H, Alvi S, Boatright C, et al. **High-resolution computed tomography of the inner ear: effect of otosclerosis on cochlear aqueduct dimensions.** *Ann Otol Rhinol Laryngol* 2019;128:749–54 CrossRef Medline
32. Mansour S, Nicolas K, Ahmad HH. **Round window otosclerosis: radiologic classification and clinical correlations.** *Otol Neurotol Off Neurotol* 2011;32:384–92 CrossRef Medline
33. Lagleyre S, Sorrentino T, Calmels M-N, et al. **Reliability of high-resolution CT scan in diagnosis of otosclerosis.** *Otol Neurotol* 2009;30:1152–59 CrossRef Medline
34. Purohit B, Hermans R, Op de Beeck K. **Imaging in otosclerosis: a pictorial review.** *Insights Imaging* 2014;5:245–52 CrossRef Medline

35. Bae YJ, Shim YJ, Choi BS, et al. **“Third window” and “single window” effects impede surgical success: analysis of retrofenestral otosclerosis involving the internal auditory canal or round window.** *J Clin Med* 2019;8 CrossRef Medline
36. Batson L, Rizzolo D. **Otosclerosis: an update on diagnosis and treatment.** *JAAPA* 2017;30:17–22 CrossRef Medline
37. Wolfowitz A, Luntz M. **Impact of imaging in management of otosclerosis.** *Otolaryngol Clin North Am* 2018;51:343–55 CrossRef Medline
38. Friedmann DR, Eubig J, Winata LS, et al. **Prevalence of jugular bulb abnormalities and resultant inner ear dehiscence: a histopathologic and radiologic study.** *Otolaryngol Head Neck Surg* 2012;147:750–56 CrossRef Medline
39. Woo CK, Wie CE, Park SH, et al. **Radiologic analysis of high jugular bulb by computed tomography.** *Otol Neurotol* 2012;33:1283–87 CrossRef Medline
40. Bilgen C, Kirazli T, Ogut F, et al. **Jugular bulb diverticula: clinical and radiologic aspects.** *Otolaryngol Head Neck Surg* 2003;128:382–86 CrossRef Medline
41. Koo YH, Lee JY, Lee JD, et al. **Dehiscent high-riding jugular bulb presenting as conductive hearing loss: a case report.** *Medicine (Baltimore)* 2018;97:e11067 CrossRef Medline
42. Weiss RL, Zahtz G, Goldofsky E, et al. **High jugular bulb and conductive hearing loss.** *Laryngoscope* 1997;107:321–27 CrossRef Medline
43. Kuhn MA, Friedmann DR, Winata LS, et al. **Large jugular bulb abnormalities involving the middle ear.** *Otol Neurotol* 2012;33:1201–06 CrossRef Medline
44. Friedmann DR, Eubig J, Winata LS, et al. **A clinical and histopathologic study of jugular bulb abnormalities.** *Arch Otolaryngol Head Neck Surg* 2012;138:66–71 CrossRef Medline
45. Rauch SD, Xu WZ, Nadol JB. **High jugular bulb: implications for posterior fossa neurotologic and cranial base surgery.** *Ann Otol Rhinol Laryngol* 1993;102:100–07 CrossRef Medline
46. Mafee MF, Lachenauer CS, Kumar A, et al. **CT and MR imaging of intralabyrinthine schwannoma: report of two cases and review of the literature.** *Radiology* 1990;174:395–400 CrossRef Medline
47. Noguchi Y, Takahashi M, Momiyama N, et al. **Intralabyrinthine schwannoma extending into the round window niche and internal auditory canal [in Japanese].** *Nippon Jibiinkoka Gakkai Kaiho* 2012;115:687–692 CrossRef Medline
48. Carlson ML, Sweeney AD, Pelosi S, et al. **Glomus tympanicum: a review of 115 cases over 4 decades.** *Otolaryngol Head Neck Surg* 2015;152:136–42 CrossRef Medline
49. Singh VK, Badhwar S, D’Souza J, et al. **Glomus tympanicum.** *Med J Armed Forces India* 2004;60:200–03 CrossRef Medline
50. Fujita T, Shin JE, Cunnane M, et al. **Surgical anatomy of the human round window region: implication for cochlear endoscopy through the external auditory canal.** *Otol Neurotol Off Neurotol* 2016;37:1189–94 CrossRef Medline
51. Ho ML. **Third window lesions.** *Neuroimaging Clin N Am* 2019;29:57–92 CrossRef Medline
52. Ho ML, Moonis G, Halpin CF, et al. **Spectrum of third window abnormalities: semicircular canal dehiscence and beyond.** *AJNR Am J Neuroradiol* 2017;38:2–9 CrossRef Medline
53. Kaski D, Davies R, Luxon L, et al. **The Tullio phenomenon: a neurologically neglected presentation.** *J Neurol* 2012;259:4–21 CrossRef Medline
54. Yu A, Teich DL, Moonis G, et al. **Superior semicircular canal dehiscence in East Asian women with osteoporosis.** *BMC Ear Nose Throat Disord* 2012;12:8 CrossRef Medline
55. Silverstein H, Van Ess MJ. **Complete round window niche occlusion for superior semicircular canal dehiscence syndrome: a minimally invasive approach.** *Ear Nose Throat J* 2009;88:1042–56 CrossRef Medline
56. Spasic M, Trang A, Chung LK, et al. **Clinical characteristics of posterior and lateral semicircular canal dehiscence.** *J Neurol Surg B Skull Base* 2015;76:421–25 CrossRef Medline
57. Nikkar-Esfahani A, Whelan D, Banerjee A. **Occlusion of the round window: a novel way to treat hyperacusis symptoms in superior semicircular canal dehiscence syndrome.** *J Laryngol Otol* 2013;127:705–07 CrossRef Medline
58. Chemtob RA, Noij KS, Qureshi AA, et al. **Superior canal dehiscence surgery outcomes following failed round window surgery.** *Otol Neurotol* 2019;40:535–42 CrossRef Medline
59. Suzuki M, Okamoto T, Ushio M, et al. **Two cases of Tullio phenomenon in which oval and round window reinforcement surgery was effective.** *Auris Nasus Larynx* 2019;46:636–40 CrossRef Medline
60. Wegner I, Eldaebes M, Landry TG, et al. **Effect of round window reinforcement on hearing: a temporal bone study with clinical implications for surgical reinforcement of the round window.** *Otol Neurotol* 2016;37:598–601 CrossRef Medline
61. Silverstein H, Kartush JM, Parnes LS, et al. **Round window reinforcement for superior semicircular canal dehiscence: a retrospective multi-center case series.** *Am J Otolaryngol* 2014;35:286–93 CrossRef Medline
62. Palma Diaz M, Cisneros Lesser JC, Vega Alarcón A. **Superior semicircular canal dehiscence syndrome: diagnosis and surgical management.** *Int Arch Otorhinolaryngol* 2017;21:195–98 CrossRef Medline
63. Deep NL, Dowling EM, Jethanamest D, et al. **Cochlear implantation: an overview.** *J Neurol Surg Part B Skull Base* 2019;80:169–77 CrossRef Medline
64. Paprocki A, Biskup B, Kozłowska K, et al. **The topographical anatomy of the round window and related structures for the purpose of cochlear implant surgery.** *Folia Morphol (Warsz)* 2004;63:309–12 Medline
65. Adunka OF, Buchman CA. **Scala tympani cochleostomy, I: results of a survey.** *Laryngoscope* 2007;117:2187–94 CrossRef Medline
66. Gudis DA, Montes M, Bigelow DC, et al. **The round window: is it the “cochleostomy” of choice? Experience in 130 consecutive cochlear implants.** *Otol* 2012;33:1497–1501 CrossRef Medline
67. Carlson ML, O’Connell BP, Lohse CM, et al. **Survey of the American Neurotology Society on Cochlear Implantation, Part 2: surgical and device-related practice patterns.** *Otol Neurotol* 2018;39:e20–27 CrossRef Medline
68. Sabban D, Parodi M, Blanchard M, et al. **Intra-cochlear electrode tip fold-over.** *Cochlear Implants Int* 2018;19:225–29 CrossRef Medline
69. Vogl TJ, Tawfik A, Emam A, et al. **Pre-, intra- and post-operative imaging of cochlear implants.** *Rofa* 2015;187:980–89 CrossRef Medline
70. Jain R, Mukherji SK. **Cochlear implant failure: imaging evaluation of the electrode course.** *Clin Radiol* 2003;58:288–93 CrossRef Medline

Displaying Multiphase CT Angiography Using a Time-Variant Color Map: Practical Considerations and Potential Applications in Patients with Acute Stroke

J.M. Ospel, O. Volny, W. Qiu, M. Najm, N. Kashani, M. Goyal, and B.K. Menon



ABSTRACT

SUMMARY: Various imaging protocols exist for the identification of vessel occlusion and assessment of collateral flow in acute stroke. CT perfusion is particularly popular because the color maps are a striking visual indicator of pathology. Multiphase CTA has similar diagnostic and prognostic ability but requires more expertise to interpret. This article presents a new multiphase CTA display format that incorporates vascular information from all phases of the multiphase CTA series in a single time-variant color map, thereby facilitating multiphase CTA interpretation, particularly for less experienced readers. Exemplary cases of multiphase CTA from this new display format are compared with conventional multiphase CTA, CT perfusion, and follow-up imaging to demonstrate how time-variant multiphase CTA color maps facilitate assessment of collateral flow, detection of distal and multiple intracranial occlusions, differentiation of pseudo-occlusion from real occlusion, and assessment of flow relevance of stenoses, ante- and retrograde flow patterns, and clot permeability.

ABBREVIATIONS: ACA = anterior cerebral artery; mCTA = multiphase CT angiography; PCA = posterior cerebral artery

Since the publication of multiple recent trials attesting to the benefit of thrombolysis and thrombectomy even in patients presenting late after stroke onset, fast and reliable detection of cerebrovascular pathology is ever more important. Several ongoing trials are using imaging to further expand treatment indications in patients with acute stroke. Imaging protocols designed for patients with acute stroke, therefore, need to be reliable in detecting and measuring a whole host of cerebrovascular pathology, including arterial flow dynamics across time, pial

collateral status, distal arterial occlusions, and thrombus characteristics such as extent and permeability, carotid pseudo-occlusions, and venous thrombus, to name a few. Because acute stroke is a time-sensitive state in which any delay in decision-making affects patient outcome, such imaging protocols need to be easy to interpret for the average stroke physician in a small hospital. These imaging protocols also need to be easy to acquire and process without being affected too much by patient motion, a common occurrence when imaging patients with stroke.

Multiphase CTA (mCTA) provides time-resolved images of the cerebral vasculature that satisfy many of the above requirements for use in patients with acute stroke. The current display format of mCTA consists of 3 gray-scale images of the cerebral vasculature displayed side by side; visualization requires the reader to link these images together and scroll through them simultaneously. Interpretation, therefore, requires some degree of expertise. The technique was, however, used as a selection criterion for endovascular treatment in patients with acute ischemic stroke with large-vessel occlusions presenting <12 hours from symptom onset in the Endovascular Treatment for Small Core and Proximal Occlusion Ischemic Stroke (ESCAPE) trial and is being used in the ongoing Safety and Efficacy of NA-1 in Subjects Undergoing Endovascular Thrombectomy for Stroke (ESCAPE-NA1; NCT02930018) and the A Randomized Controlled Trial of TNK-tPA Versus Standard of Care for Minor Ischemic Stroke With Proven Occlusion (TEMPO 2; NCT02398656) trials. Good collaterals as determined on CTA have also been shown to

Received October 9, 2019; accepted after revision November 19.

From the Division of Neuroradiology, Clinic of Radiology and Nuclear Medicine (J.M.O.), University Hospital Basel, University of Basel, Basel, Switzerland; Departments of Clinical Neurosciences (J.M.O., O.V., W.Q., M.N., M.G.) and Radiology (N.K., M.G.), University of Calgary, Calgary, Alberta, Canada; International Clinical Research Centre (O.V.), Stroke Research Program, St. Anne's University Hospital, Brno, Czech Republic; and Departments of Radiology and Clinical Neurosciences, Radiology and Community Health Sciences (B.K.M.), Cumming School of Medicine, University of Calgary, Foothills Medical Centre, Calgary, Alberta, Canada.

Paper previously presented as an educational exhibit at: Annual Meeting of the Radiological Society of North America, December 1–6, 2019; Chicago, Illinois.

Please address correspondence to Bijoy K. Menon, MD, Departments of Radiology and Clinical Neurosciences, Radiology and Community Health Sciences, Cumming School of Medicine, University of Calgary, Foothills Medical Centre, 1403 29th St NW, Calgary, AB Canada T2N 2T9; e-mail: docbijoymenon@gmail.com; @johanna_ospel

Indicates open access to non-subscribers at www.ajnr.org

Indicates article with supplemental on-line appendix and table.

Indicates article with supplemental on-line photos.

<http://dx.doi.org/10.3174/ajnr.A6376>

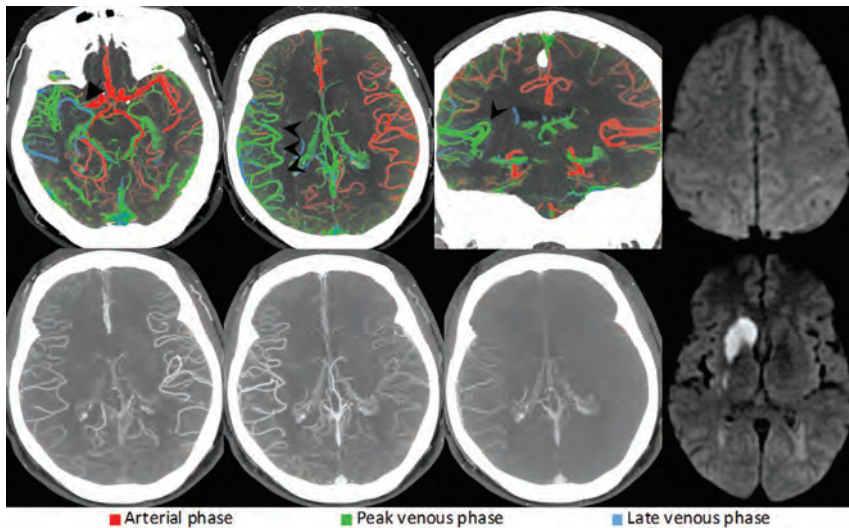


FIG 1. Right-sided M1 segment MCA occlusion (*arrow*). ColorViz summation maps (*upper row*) show predominantly green vessels in the affected territory (*arrowheads*), indicating a 1-phase delay; The vessel extent is identical to that of the unaffected hemisphere. The findings are consistent with good pial artery filling and collateral flow. Corresponding conventional mCTA images are displayed in the *lower row*. The patient received intravenous alteplase, and follow-up MR imaging 24 hours after symptom onset (*upper and lower right*) shows infarction of the caudate head and lentiform nucleus only, with sparing of the cortex.

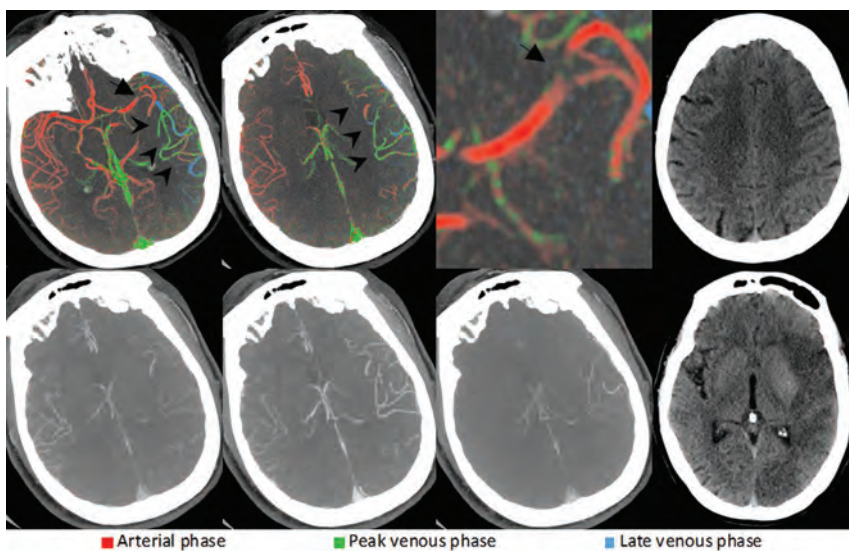


FIG 2. Left-sided M1 segment MCA occlusion (*arrow*). ColorViz summation maps (*upper row*) show predominantly green vessels (*arrowheads*) in the affected territory, indicating a 1-phase delay. However, the vessel extent is reduced compared with the unaffected hemisphere. Hence, the findings are consistent with intermediate pial artery filling and collateral flow. Corresponding conventional mCTA images are displayed in the *lower row*. The patient was treated with intravenous alteplase, and follow-up CT after 24 hours (*upper and lower right*) reveals an incomplete infarction pattern. While the insula, M1, and M2 regions are infarcted, the M3, M4, M5, and M6 regions are spared. Infarction is also present in the left PCA territory, indicating a fetal left PCA origin.

correlate with reduced infarct volume in patients presenting beyond 6 hours.¹ Most interesting, no association between collateral status and outcome was noted in this study.¹ CTP, another imaging technique with time-resolved images of parenchymal

blood flow but with more complex acquisition and postprocessing, is considered easier to interpret because the display format is a single color-coded cerebral map of estimated blood flow and predicted tissue fate. This feature is in spite of obvious disadvantages of CTP, including longer image-acquisition times, susceptibility to patient motion, more radiation exposure, an additional contrast dose, a lack of whole-brain coverage, and complex and heterogeneous postprocessing algorithms. mCTA, on the other hand, requires no postprocessing, has a lower radiation dose, and can be acquired in <30 seconds (as opposed to CTP, which requires continuous scanning for 45–90 seconds), thereby minimizing motion artifacts.

In this primarily descriptive article, we present the case for a novel mCTA display format that encodes vascular information from all mCTA phases into a single color-coded map using a simple algorithm, thereby combining the indicator effect of color with the technical advantages of mCTA.

Patient Cohort

Imaging data were obtained from the Precise and Rapid Assessment of Collaterals Using Multi-phase CTA in the Triage of Patients With Acute Ischemic Stroke for IA Therapy¹ a prospective observational multicenter study that seeks to analyze the incremental value of mCTA and CTP in acute ischemic stroke ($n=596$). The local institutional ethics boards (University of Calgary, Foothills Medical center) approved the study. Patient baseline characteristics from this study are summarized in the On-line Table.

Image Acquisition and Interpretation

The details about the multiphase CTA acquisition technique, parameters, and image interpretation can be found in the On-line Appendix. Color-coded

mCTA summation maps presented here were created on a workstation using the FastStroke research prototype (GE Healthcare, Milwaukee, Wisconsin), a CT image-analysis software package that is intended to display the full set of imaging information of

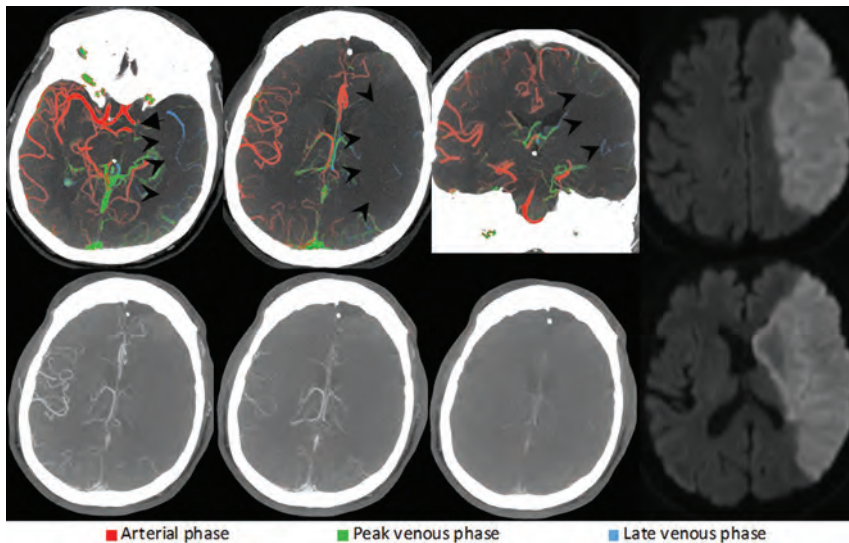


FIG 3. Left-sided ICA carotid L-occlusion (*arrow*). ColorViz summation maps (*upper row*) show a severely reduced vessel extent compared with the unaffected hemisphere (*arrowheads*). The few visible opacified vessels are predominantly blue, suggesting a 2-phase delay. This is consistent with poor pial artery filling and collateral flow. The patient was treated with antithrombotic therapy, and follow-up MR imaging after 24 hours (*upper and lower right*) shows complete infarction of the left MCA territory.

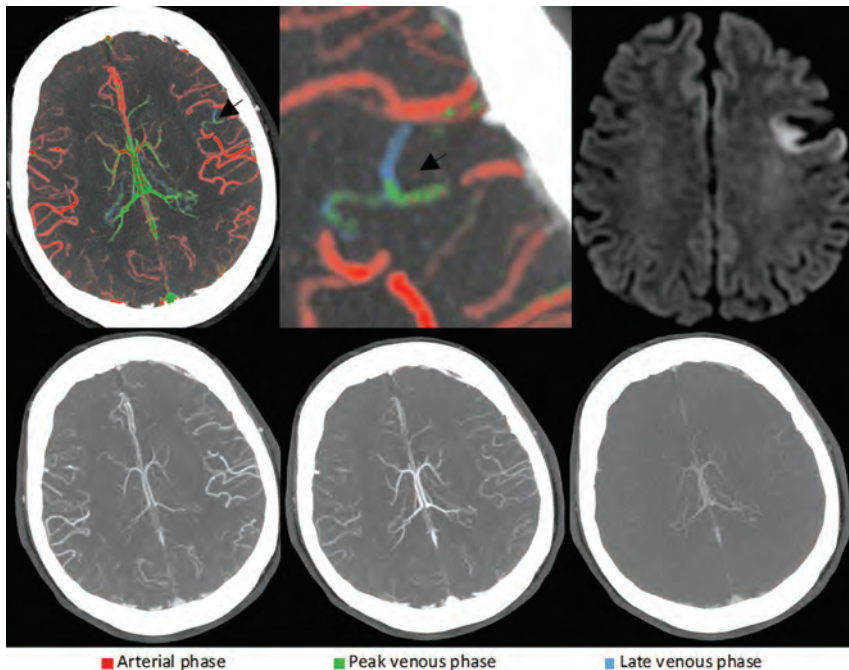


FIG 4. Left-sided M4 segment MCA occlusion. ColorViz summation images (*upper row*) show a focal area with blue and green vessels in the left frontal lobe (*black arrows*), ie, an area with delayed pial artery filling and washout, suggestive of a distal vessel occlusion. The thrombus itself cannot be visualized; the occlusion was detected on the basis of arterial flow information only. Corresponding conventional mCTA images in the *lower row* also show a slight delay in left frontal pial artery filling and washout; however, the occlusion is not as easily appreciable as in the color-coded summation maps. The patient received intravenous alteplase. Follow-up MR imaging after 24 hours (*upper right*) shows an acute left frontal lobe infarction, thereby confirming the suspected site of intracranial occlusion.

an advanced stroke CT imaging protocol (noncontrast CT, multiphase CTA, and CTP) in 1 single optimized, progressive workflow. The software fuses the vascular information from the different CTA phases (maximum of 9 phases) into a single color-coded view called ColorViz. It uses the original multiphase CTA thin slices to automatically display MIPs of the axial, coronal, sagittal, and oblique reformations. Colors are assigned on the basis of the timing and extent of contrast enhancement in the vessels and on a per-patient adaptive threshold technique; vessels maximally enhancing during the pre-venous phase appear red; those that enhance in venous phase and venous phase are displayed in green and blue, respectively. The overall and phase-specific extent of pial enhancement can then be quantified and compared with other territories in the contralateral hemisphere. Postprocessing is fully automated with the color-coded maps being available for review within 5–10 seconds. For evaluation of the vessel extent, the summation map can be switched to a single-color mode. Hence, the color display of the vasculature provides the full set of information about the dynamics and extent of pial artery filling from all mCTA phases in 1 single series. This feature expedites assessment of the intracranial vasculature compared with the conventional mCTA display format.

Evaluating Pial Arterial Filling/ Collateral Flow

mCTA is a reliable tool for assessment of pial artery filling in acute stroke imaging. Several studies (some single-center) have shown that it reduces interrater reliability and has excellent predictive validity with regard to clinical outcome.^{2,3} It has, therefore, been used in past⁴ and in ongoing clinical stroke trials such as ESCAPE NA1 and TEMPO 2. Pial artery filling is evaluated by assessing the extent of arterial filling and delay in that filling compared with the opposite side. A third metric is delayed washout of contrast within the pial arteries over the 3

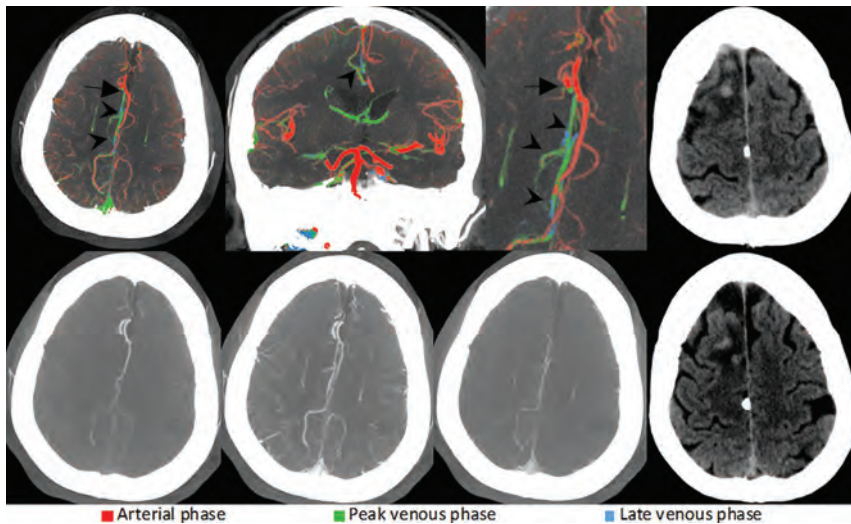


FIG 5. Right-sided A2 segment ACA occlusion (*arrows*). ColorViz summation images (*upper row*) show green and blue vessels distal to the occlusion (*arrowheads*), indicating impaired arterial filling within the right ACA territory. Corresponding conventional mCTA images are shown in the *lower row*. The patient received intravenous alteplase. Follow-up CT after 24 hours (*upper and lower right*) shows infarction in the right ACA territory.

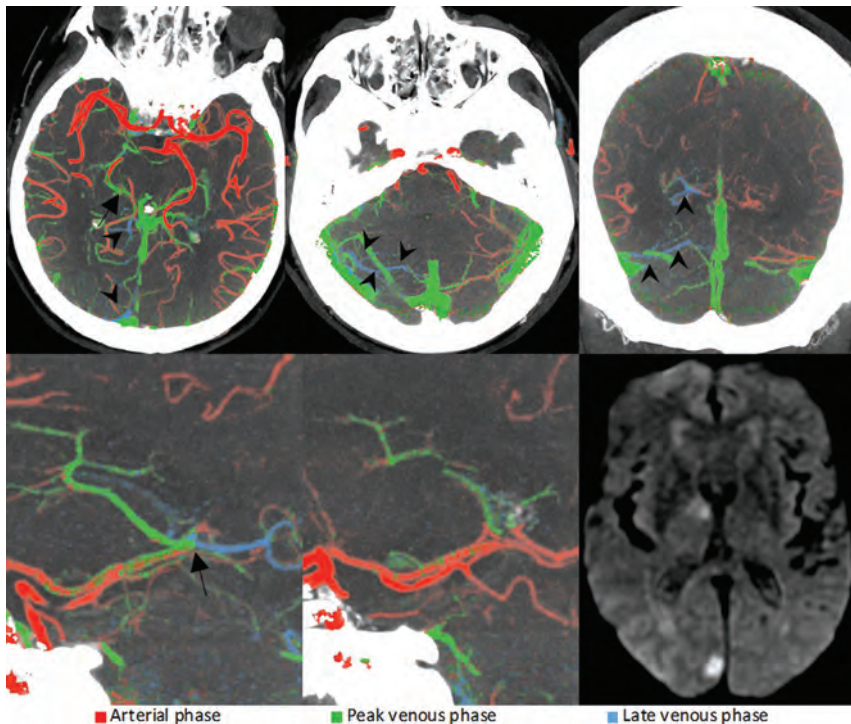


FIG 6. Right-sided fetal PCA occlusion (*arrows*). As opposed to the left PCA (*lower middle image*), the right distal PCA (*lower left image*) is blue in the color-coded summation images, suggestive of impaired filling of the distal vessel. The delayed arterial filling leads to a subsequent delay in venous filling in the posterior fossa on the affected side (*arrowheads*), a useful feature that is often encountered in posterior circulation occlusions and can help to identify the site of occlusion. Mechanical thrombectomy was performed. Follow-up MR imaging after 24 hours (*lower right*) reveals small right-sided occipital and thalamic infarct.

phases. Although pial artery filling and collateral flow are relatively easy to assess on conventional mCTA, the color-coded summation maps (ColorViz) further facilitate interpretation by combining all information into a single image and using a color-coded display format. Image-interpretation time is a few seconds for color-coded mCTA summation maps, as opposed to approximately 1 minute for conventional mCTA maps. An exemplary method for assessing collaterals on ColorViz based on assessing delay, extent, and washout within pial arteries is shown in Fig 1.

To assess pial artery filling using ColorViz, one visually determines the predominant vessel color (the color that is present in >40% of the vessels) in the affected territory. Under normal circumstances, predominantly red vessels (such as the vessels on the contralateral side in Figs 1–3) indicate no delay, predominantly green vessels indicate a 1-phase delay (Fig 2), and predominantly blue vessels, a 2-phase delay (Fig 3). The absence of visible vessels in the affected territory indicates “no filling.” Because diseases such as congestive heart failure can lead to a reduction in cardiac output and systemic flow delays, the predominant color in the unaffected hemisphere is also assessed and compared with the predominant color in the affected side. Of note, this correction cannot be applied to conditions that cause unilateral flow delays, such as flow-limiting proximal ICA stenosis, a limitation of mCTA. The extent of pial artery filling is scored in a single color mode by comparing vessel extent in the affected territory with that in the contralateral hemisphere. Differentiation of veins and arteries is based on their distinct flow characteristics (veins are usually displayed in green or blue because they enhance in the peak venous and late venous phases), filling direction, morphology, and anatomic location. The affected hemisphere may be considered to have good collateral flow if pial vessels distal to the occlusion are well-seen and are predominantly red or green (Fig 1).

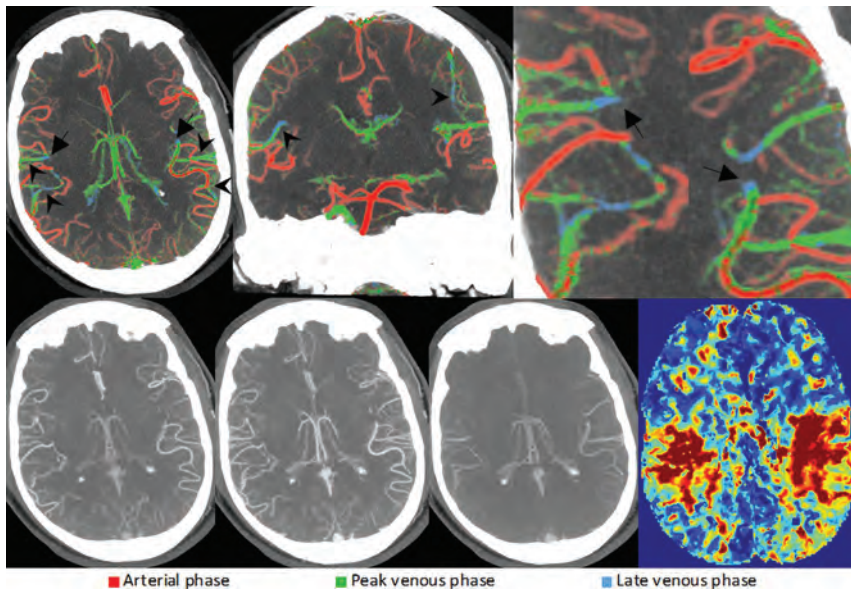


FIG 7. Bilateral M3 segment MCA occlusions (*arrows*) visualized through changes in the pial artery color compared with the surrounding pial arteries. Some cortical MCA branches of both hemispheres are depicted in green and blue (*arrowheads*), consistent with bilateral occlusions. Due to the symmetry of the occlusions, they are difficult to appreciate on conventional mCTA (*lower row*). CTP (*lower right*) shows prolonged time-to-maximum times in the affected territories, confirming the suspected occlusions.

Intermediate pial artery filling and collateral flow are present if either pial artery extent, pial artery filling, or both are moderately reduced in the affected territory (Fig 2). Most frequently, intermediate collateral flow manifests as green vessels (indicating a 1-phase delay) and reduced pial artery extent compared with the unaffected hemisphere.

Complete absence of pial artery filling or severely reduced extent and a 2-phase filling delay (ie, predominantly blue vessels) or complete absence of vessel opacification distal to the occlusion is considered poor pial artery filling (Fig 3).

Increasing Sensitivity in Vessel Occlusion Detection

While large-vessel occlusions are relatively easy to spot on single-phase CTA, distal occlusions are often missed.^{5,6} Both CTP (by detecting ischemia in the color maps) and mCTA (through delayed collateral filling and washout) have been shown to improve distal-vessel-occlusion detection compared with single-phase CTA alone.⁵⁻⁷ The additional color-indicator effect that is achieved using a color-coded display format and the ability to merge the vascular information in 1 rather than 3 series further facilitate detection of distal vessel occlusions on mCTA. The hallmark of distal occlusion in color-coded mCTA maps is areas of delayed flow manifesting as pial vessels in green and blue within 1 vascular territory (Fig 4).

Another advantage of color-coded mCTA summation maps is in detecting distal anterior cerebral artery (ACA) and posterior cerebral artery (PCA) occlusions (Figs 5 and 6). In theory, ACA and PCA occlusions can be easily detected on CTP by detecting perfusion abnormalities in the affected territories. However, the ACA and PCA territories are often not

fully covered by the 4-, 8-, or 10-cm CTP slab that is frequently used with older generation scanners. Furthermore, mCTA does not succumb to skull base artifacts to the same extent as CTP and can therefore better visualize the posterior circulation. A particularly useful feature for posterior circulation occlusions is the venous filling delay in the posterior fossa, which results in a subsequent delay of venous filling, manifesting as an increased number of veins depicted in blue (Fig 6).

Detection of Multiple Intracranial Thrombi

Detecting intracranial thrombi other than the large-vessel occlusion that is easily identified is important because it may influence acute treatment strategies⁸ and ultimately affect patient outcomes.⁹ Color-coded mCTA is able to detect multiple intracranial occlusions in either the same (Fig 7) or different (On-line Fig 1) vascular territories.

CONCLUSIONS

Color-coded mCTA summation maps may facilitate easier assessment of acute stroke pathology, including better assessment of collateral status, distal occlusions, carotid pseudo-occlusions, intracranial stenosis, and thrombus permeability. ColorViz may be particularly useful for less experienced readers. Future work will, however, need detailed quantitative validation of each of the imaging constructs that ColorViz mCTA provides in patients with acute stroke.

Disclosures: Johanna M. Ospel—*RELATED: Grant:* Freiwillige Akademische Gesellschaft Basel, Julia-Bangerter-Rhyner Foundation, University of Basel Research Foundation, *Comments:* research scholarships. Ondrej Volny—*RELATED: Grant:* National Program of Sustainability II, Czech Republic, grant No. LQ1605.* Mayank Goyal—*RELATED: Other:* GE Healthcare, *Comments:* licensing agreement for systems of acute stroke diagnosis; *UNRELATED: Consultancy:* Medtronic, Stryker, MicroVention, Mentice, *Comments:* advice on acute stroke intervention; *Grants/Grants Pending:* Stryker, *Comments:* unrestricted research grant for the UNMASK-EVT study.* Bijoy K. Menon—*OTHER RELATIONSHIPS:* patent on systems of triage in acute stroke, stock ownership in Circle Neurovascular. *Money paid to the institution.

REFERENCES

- de Havenon A, Mlynash M, Kim-Tenser MA, et al. **Results from DEFUSE 3: good collaterals are associated with reduced ischemic core growth but not neurologic outcome.** *Stroke* 2019;50:632–38 CrossRef Medline
- Menon BK, d'Este CD, Qazi EM, et al. **Multiphase CT angiography: a new tool for the imaging triage of patients with acute ischemic stroke.** *Radiology* 2015;275:510–20 CrossRef Medline
- Garcia-Tornel A, Carvalho V, Boned S, et al. **Improving the evaluation of collateral circulation by multiphase computed tomography angiography in acute stroke patients treated with endovascular**

- reperfusion therapies. *Interv Neurol* 2016;5:209–17 CrossRef Medline
4. Goyal M, Demchuk AM, Menon BK, et al. **Randomized assessment of rapid endovascular treatment of ischemic stroke.** *N Engl J Med* 2015;372:1019–30 CrossRef Medline
 5. Volny O, Cimflova P, Kadlecova P, et al. **Single-phase versus multiphase CT angiography in middle cerebral artery clot detection—benefits for less experienced radiologists and neurologists.** *J Stroke Cerebrovasc Dis* 2017;26:19–24 CrossRef Medline
 6. Yu AY, Zerna C, Assis Z, et al. **Multiphase CT angiography increases detection of anterior circulation intracranial occlusion.** *Neurology* 2016;87:609–16 CrossRef Medline
 7. Becks MJ, Manniesing R, Vister J, et al. **Brain CT perfusion improves intracranial vessel occlusion detection on CT angiography.** *J Neuroradiol* 2019;46:124–29 CrossRef Medline
 8. Liebeskind DS, Bracard S, Guillemin F, et al. **eTICI reperfusion: defining success in endovascular stroke therapy.** *J Neurointerv Surg* 2019;11:433–38 CrossRef Medline
 9. Ganesh A, Al-Ajlan FS, Sabiq F, et al. **Infarct in a new territory after treatment administration in the ESCAPE Randomized Controlled Trial (Endovascular Treatment for Small Core and Anterior Circulation Proximal Occlusion with Emphasis on Minimizing CT to Recanalization Times).** *Stroke* 2016;47:2993–98 CrossRef Medline

Assessment of a Bayesian Vitrea CT Perfusion Analysis to Predict Final Infarct and Penumbra Volumes in Patients with Acute Ischemic Stroke: A Comparison with RAPID

R.A. Rava, K.V. Snyder, M. Mokin, M. Waqas, A.B. Allman, J.L. Senko, A.R. Podgorsak, M.M. Shiraz Bhurwani, Y. Hoi, A.H. Siddiqui, J.M. Davies, E.I. Levy, and C.N. Ionita



ABSTRACT

BACKGROUND AND PURPOSE: Brain CTP is used to estimate infarct and penumbra volumes to determine endovascular treatment eligibility for patients with acute ischemic stroke. We aimed to assess the accuracy of a Bayesian CTP algorithm in determining penumbra and final infarct volumes.

MATERIALS AND METHODS: Data were retrospectively collected for 105 patients with acute ischemic stroke (55 patients with successful recanalization [TICI 2b/2c/3] and large-vessel occlusions and 50 patients without interventions). Final infarct volumes were calculated using DWI and FLAIR 24 hours following CTP imaging. RAPID and the Vitrea Bayesian CTP algorithm (with 3 different settings) predicted infarct and penumbra volumes for comparison with final infarct volumes to assess software performance. Vitrea settings used different combinations of perfusion maps (MTT, TTP, CBV, CBF, delay time) for infarct and penumbra quantification. Patients with and without interventions were included for assessment of predicted infarct and penumbra volumes, respectively.

RESULTS: RAPID and Vitrea default setting had the most accurate final infarct volume prediction in patients with interventions ([Spearman correlation coefficient, mean infarct difference] default versus FLAIR: [0.77, 4.1 mL], default versus DWI: [0.72, 4.7 mL], RAPID versus FLAIR: [0.75, 7.5 mL], RAPID versus DWI: [0.75, 6.9 mL]). Default Vitrea and RAPID were the most and least accurate in determining final infarct volume for patients without an intervention, respectively (default versus FLAIR: [0.76, -0.4 mL], default versus DWI: [0.71, -2.6 mL], RAPID versus FLAIR: [0.68, -49.3 mL], RAPID versus DWI: [0.65, -51.5 mL]).

CONCLUSIONS: Compared with RAPID, the Vitrea default setting was noninferior for patients with interventions and superior in penumbra estimation for patients without interventions as indicated by mean infarct differences and correlations with final infarct volumes.

ABBREVIATIONS: AIS = acute ischemic stroke; FIV = final infarct volume; MAE = mean absolute error; Tmax = time until the residue function reaches its peak

CTP is an imaging technique used to quantify infarct and penumbra tissue in patients with acute ischemic stroke (AIS) evaluated for endovascular thrombectomy.¹ CTP hemodynamic features include CBV, CBF, TTP, MTT, time until residue

function reaches its peak (Tmax), and delay time, which are compared between contralateral hemispheres to identify ischemic tissues.² Various perfusion thresholds can be used for each hemodynamic parameter to identify tissues as infarct and penumbra.³ Infarct is irreversibly damaged tissue that cannot recover in the event of reperfusion. Penumbra represents tissue deficient in blood flow but that can be salvaged through reperfusion.² As recommended by the American Heart Association, ischemic volume estimations should be used for selection of patients with AIS for mechanical thrombectomy when symptom onset is beyond 6 hours.⁴

Bayesian CTP software, based on a probabilistic approach, has been developed in Vitrea (Vital Images, Minnetonka, Minnesota) and Olea Sphere (Olea Medical, La Ciotat, France). This method relies on adjacent perfusion scan regions to calculate hemodynamic maps and implements postprocessing noise reduction.⁵ Quantitative analysis provided by Bayesian CTP maps allows

Received September 20, 2019; accepted after revision December 4.

From the Departments of Biomedical Engineering (R.A.R., A.B.A., J.L.S., A.R.P., M.M.S.B., C.N.I.), Neurosurgery (K.V.S., M.W., A.R.P., A.H.S., J.M.D., E.I.L., C.N.I.), Medical Physics (A.R.P.), and Bioinformatics (J.M.D.), University at Buffalo, Buffalo, New York; Canon Stroke and Vascular Research Center (R.A.R., K.V.S., M.W., A.B.A., J.L.S., A.R.P., M.M.S.B., A.H.S., J.M.D., E.I.L., C.N.I.), Buffalo, New York; Department of Neurosurgery (M.M.), University of South Florida, Tampa, Florida; and Canon Medical Systems USA (Y.H.), Tustin, California.

This research was funded by Canon Medical Systems USA.

Please address correspondence to Ryan A. Rava, BS, Department of Biomedical Engineering, University at Buffalo, 875 Ellicott St, Buffalo, NY 14203; e-mail: ryanrava@buffalo.edu

Indicates article with supplemental on-line table.

Indicates article with supplemental on-line photos.

<http://dx.doi.org/10.3174/ajnr.A6395>

infarct and penumbra volume estimations using all CTP parameters, including the normally excluded MTT temporal parameter.⁶ Investigation of thresholds using various parameters for the Bayesian algorithm has yet to be conducted. Investigations are necessary due to discrepancies in CTP thresholds across perfusion map calculation methods and vendors.⁷ In particular, Vitrea software allows 3 predefined threshold settings, each using distinct combinations of perfusion maps and contralateral hemisphere thresholds, for infarct and penumbra quantification as well as user-defined ROIs to outline ischemic regions.

In this study, we aimed to investigate the effects of 3 preset Bayesian CTP threshold settings for predicting final infarct volumes (FIVs) by comparing them with DWI and FLAIR in patients with AIS. Additionally, we compared performances of Vitrea and RAPID (iSchemaView, Menlo Park, California), a clinically studied CTP software, in quantifying infarct and penumbra volumes.^{8,9} The variability of user-defined ROIs was investigated for determining ischemic regions in the Vitrea software.

MATERIALS AND METHODS

Image and Data Collection

The University at Buffalo review board approval was obtained, and informed consent was waived for this Health Insurance Portability and Accountability Act retrospective study. Inclusion criteria were patients with AIS who underwent CTP evaluation on arrival at the stroke center and DWI and FLAIR 24 hours following CTP imaging. Before CTP imaging, patients underwent non-contrast CT to rule out hemorrhagic stroke, and scan results were considered for clinical decision-making. Between March and August 2019, one hundred five consecutive patients were split into intervention and nonintervention cohorts. Intervention cases ($n = 55$) were required to have an emergent large-vessel occlusion and to have undergone mechanical thrombectomy. Nonintervention cases ($n = 50$) were patients with large- and small-vessel occlusions who received neither thrombectomy nor tPA. Patients with and without interventions were included for evaluation of CTP infarct and penumbra volume predictions, respectively. For patients with interventions, TICI scores were measured by 2 independent operators not involved in data collection. All patients with interventions received successful reperfusion (TICI 2b/2c/3).

CTP data were obtained from two 2012 Aquilion ONE CT units (Canon Medical Systems, Otawara, Japan). CTP protocol involved acquisition of 19 scans, each with 320 images with 0.5-mm resolution. A total dose-length product of 13,739 mGy*cm and CT dose index volumes ranging from 15.3 to 44.4 mGy for each scan volume were used. Contrast was 50 mL of iohexol (Omnipaque 350; GE Healthcare, Piscataway, New Jersey) at a 5-mL/s injection rate. In the stroke work-up, reconstructed CTP volumes are provided within 5 minutes from the start of scanning.

DWI and FLAIR were performed using a Vantage Titan 1.5T MR imaging unit (Canon Medical Systems). DWI and FLAIR protocols involved TEs of 100 and 120 ms and TRs of 8,165 and 10,000 ms, respectively.

CTP Infarct Quantification

CBV, CBF, MTT, TTP, and delay time perfusion maps were calculated using the Vitrea 7.10 Bayesian algorithm. Stroke

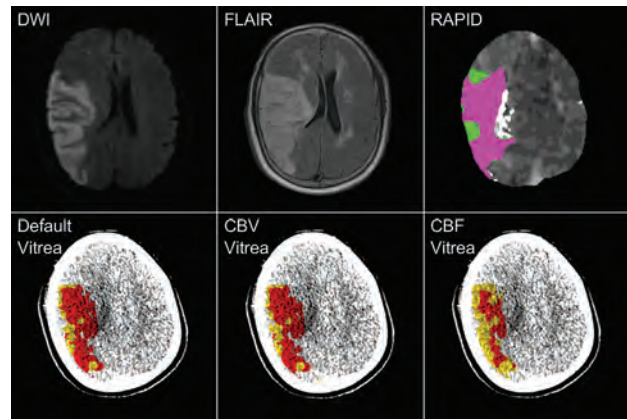


FIG 1. Ground truth infarct labels with the hyperintensified regions in the DWI and FLAIR identifying infarct. Default, CBV, and CBF Vitrea perfusion analysis demonstrates infarct as red and penumbra as yellow, while RAPID perfusion analysis represents infarct as pink and penumbra as green. For this nonintervention case, there is agreement between Vitrea and RAPID infarct volumes and their respective locations within the MR imaging scans. Final infarct volumes for each MR imaging method and CTP software (summation of infarct and penumbra due to it being a nonintervention case) are as follows: DWI = 135.0 mL, FLAIR = 167.6 mL, default Vitrea = 132.4 mL, CBV Vitrea = 141.2 mL, CBF Vitrea = 115.3 mL, RAPID = 176.0 mL.

regions were outlined throughout perfusion volumes. Three different combinations of perfusion map thresholds comparing contralateral hemispheres within Vitrea were used for infarct and penumbra quantification. Default Bayesian setting contralateral hemisphere thresholds were the following: A 38% reduction in CBV (with 5.3-second increase in TTP or 55% reduction in MTT) indicated infarct while a 5.3-second increase in TTP or 58% reduction in CBF or a 5.8-second increase in delay time (without CBV reduction) indicated penumbra. Reduction in MTT can occur within regions of deep infarction or when the CT scan starts too early, resulting in a truncated time-density curve.¹⁰ The CBV Bayesian setting, which use CBV to quantify infarct, thresholds were the following: A 38% reduction in CBV (with a 5.3-second increase in TTP or 55% reduction in MTT) indicated infarct; a 5.3-second increase in TTP or 76% reduction in CBF or 82% increase in MTT (without CBV reduction) indicated penumbra; and delay time was not used. The CBF Bayesian setting, which used CBF to determine infarct, thresholds were the following: A 72% reduction in CBF (with a 3.9-second increase in TTP) indicated infarct; a 3.9-second increase in TTP indicated penumbra; and MTT, CBV, and delay time were not used in volume quantifications. These 3 threshold combinations were predefined within Vitrea by the manufacturer, and contralateral hemisphere voxels exceeding these thresholds were classified as infarct or penumbra, accordingly. Infarct and penumbra volumes and penumbra-to-infarct ratios were recorded for automated- and user-segmented Vitrea analysis of stroke regions.

RAPID analysis was conducted offsite by sending CTP volumes from the CT scanner to iSchemaView and receiving predicted ischemic volumes through the PACS of the hospital. With RAPID, infarct is tissue with CBF <30% compared with the contralateral hemisphere and penumbra is volume of tissue with a Tmax of >6 seconds. Fig 1 compares all 3 Vitrea settings and

Table 1: Characteristics and outcomes of patients with ischemic stroke

Characteristic	All (n = 105)	Endovascular Intervention (n = 55)	Nonintervention (n = 50)
Male sex (%)	46.7% (49/105)	50.9% (28/55)	42.0% (21/50)
Age (mean) (yr)	67.1 ± 14.7	64.8 ± 16.3	69.6 ± 12.6
NIHSS score (median) (IQR)	11.0 (6.0–17.0)	12.0 (9.0–19.0)	6.5 (4.0–14.8)
Site of occlusion			
Middle cerebral artery	72.4% (76/105)	76.3% (42/55)	68.0% (34/50)
Posterior cerebral artery	12.4% (13/105)	7.3% (4/55)	18.0% (9/50)
Internal carotid artery	11.4% (12/105)	10.9% (6/55)	12.0% (6/50)
Basilar artery	3.8% (4/105)	5.5% (3/55)	2.0% (1/50)
Time from onset of stroke to perfusion imaging (median) (IQR) (min)	267.0 (116.0–710.0)	171.0 (91.0–364.0)	629.0 (147.5–976.8)
Time from onset of stroke to reperfusion (median) (IQR) (min)	–	243.0 (157.5–526.0)	–
Time from perfusion imaging to recanalization (median) (IQR) (min)	–	64.0 (52.0–104.0)	–
Default Vitrea infarct volume (median) (IQR) (mL)	6.7 (2.0–24.0)	4.7 (1.3–19.4)	6.8 (3.3–25.4)
CBV Vitrea infarct volume (median) (IQR) (mL)	6.5 (1.0–17.3)	4.0 (0.7–15.9)	8.5 (3.2–21.0)
CBF Vitrea infarct volume (median) (IQR) (mL)	2.5 (0.1–15.4)	0.3 (0.0–8.4)	6.6 (1.4–18.4)
RAPID infarct volume (median) (IQR) (mL)	6.0 (0.0–17.0)	0.0 (0.0–16.5)	28.0 (4.0–90.0)
Posttreatment reperfusion			
TICI 2b	–	38.2% (21/55)	–
TICI 2c	–	25.5% (14/55)	–
TICI 3	–	36.4% (20/55)	–
Final FLAIR MR imaging infarct volume (median) (IQR) (mL)	9.8 (3.2–25.1)	11.8 (4.4–32.4)	7.4 (2.7–18.4)
Final DWI MR imaging infarct volume (median) (IQR) (mL)	9.8 (2.3–25.7)	11.8 (3.2–36.0)	6.7 (2.0–17.7)

Note:—IQR indicates interquartile range; –, indicates data that was not obtained for the nonintervention patients and that cannot be quantified for all patients.

RAPID with DWI and FLAIR in predicting FIVs for the same patient without an intervention.

Final Infarct Volume

DWI and FLAIR were used as FIV ground truths because they are common standards for computing FIVs. DWI and FLAIR give accurate representations of infarct by locating regions of restricted diffusion and hyperintense lesions, respectively.^{11,12} Because DWI has shown lesion reversal in instances of rapid reperfusion, FLAIR MR imaging was the main infarct ground truth.¹³ Infarct volumes from DWI were quantified using 162% differences in intensities across hemispheres as demonstrated previously.¹⁴ FLAIR data were loaded into 3D Slicer software (<http://www.slicer.org>), and infarct was segmented and quantified using thresholding in which gray-scale pixel values of >80 indicate regions of infarct.¹⁵ For nonintervention cases, FIVs were compared against summations of infarct and penumbra because the entirety of penumbra should convert to infarct when no treatment occurs.¹⁶ Although vascular reperfusion may occur from embolus breakage leading to penumbra being salvaged.

Statistical Analysis

Frequency distributions for categoric data and summary statistics for continuous variables were tabulated for analyzed data. For intervention and nonintervention subgroups, differences

in infarct between predicted CTP and ground truth DWI and FLAIR volumes were determined. For patients without interventions, infarct was estimated as a summation of infarct and penumbra because all penumbra should convert to infarct. Mean absolute errors (MAEs) for each subgroup were calculated for all CTP threshold combinations. Shapiro-Wilk tests were conducted assessing the normality of infarct volume data. Regression analysis was performed to compare FIVs with predicted CTP volumes for intervention and nonintervention groups. Results were represented as scatterplots, and Spearman correlation coefficients were calculated. Software-processing times to predict ischemic volumes were determined. Vitrea and RAPID processing times were defined as the time from loading CTP volumes into Vitrea until the perfusion maps were generated and time from CTP scan completion until RAPID perfusion maps were uploaded to the PACS of the hospital, respectively. Interreader variability was assessed across 5 Vitrea users to determine the mean difference and MAE of segmented infarcts.

RESULTS

Patient Demographic Analysis

Predicted infarct volumes and patient characteristics are presented in Table 1. Tabulated data include separation into 55 intervention and 50 nonintervention cases. In Table 1, age is normally distributed, while all other continuous variables are

Table 2: Mean difference and MAE between final infarct using DWI and FLAIR and predicted infarct using CTP software

Parameter/Final Infarct Predictor	Perfusion Software	Endovascular Intervention	Nonintervention
Mean infarct difference (mL) DWI	Default Vitrea	4.7	-2.6
	CBV Vitrea	9.7	-0.3
	CBF Vitrea	14.1	1.4
	RAPID	7.5	-51.5
FLAIR	Default Vitrea	4.1	-0.4
	CBV Vitrea	9.1	1.9
	CBF Vitrea	13.5	3.6
	RAPID	6.9	-49.3
Mean absolute error (mL) DWI	Default Vitrea	13.0	9.6
	CBV Vitrea	13.6	12.8
	CBF Vitrea	20.5	9.1
	RAPID	14.5	53.1
FLAIR	Default Vitrea	12.7	10.9
	CBV Vitrea	13.4	13.3
	CBF Vitrea	20.3	10.9
	RAPID	14.7	51.1

non-normally distributed on the basis of Shapiro-Wilks testing ($P < .05$). Normally and non-normally distributed data are represented as mean \pm SD and median (interquartile range), respectively. Student *t*, Mann-Whitney-Wilcoxon, and χ^2 *P* values for normally distributed continuous, non-normally distributed continuous, and categorical data, respectively, are given in Table 1 to determine the statistical significance among the subcategories.

Software Analysis

Differences in the amount of predicted CTP and MR imaging FIVs using all software are shown in Table 2 with MAEs for intervention and nonintervention categories. Shapiro-Wilk testing indicated no statistical evidence ($P > .05$) suggesting that infarct difference values are non-normally distributed for all threshold settings. For patients with interventions, Student *t* analysis showed no statistical differences in MAEs in each tested software against FLAIR and DWI. For nonintervention cases, Student *t* analysis of MAEs showed statistically significant differences ($P < .05$) between RAPID and all Vitrea settings for FLAIR and DWI. Fig 2 shows that regression plots of the default Vitrea setting predicted infarct versus DWI and FLAIR FIV for intervention and nonintervention categories. The default setting frequently showed the lowest mean infarct difference, lowest MAE, and highest correlations with final infarct volumes. Regression plots for RAPID-predicted infarct-versus-MR imaging FIV measurements are shown in On-line Fig 1. Shapiro-Wilk testing indicated that infarct volume calculations were non-normally distributed, all with $P < .05$. Spearman correlations for each CTP setting against final DWI and FLAIR infarct measurements for patients with and without interventions are shown in Table 3. The On-line Table shows mean infarct differences and MAEs between automated Vitrea analysis for each setting and follow-up MR imaging. Mean penumbra-to-infarct ratios for patients with and without interventions using each CTP software are as follows: (intervention, nonintervention): default = (5.6, 1.4), CBV = (8.6, 2.3),

CBF = (17.4, 2.3), RAPID = (2.8, 9.2). Ninety-five percent CIs for processing times of Vitrea and RAPID software were 186.2 ± 5.3 seconds and 885.6 ± 66.1 seconds, respectively.

Interreader Variability Analysis

Interreader variability studies demonstrated a mean difference of 0.6 mL and an MAE of 3.1 mL in user-segmented regions of infarct in Vitrea software. No statistical significance was demonstrated among user-segmented infarct volumes ($P = .97$).

DISCUSSION

This study provided an analysis for the effects of perfusion-parameter and threshold selection on ischemic

tissue quantification in Bayesian CTP software. Comparisons with DWI, FLAIR, and RAPID were used to quantify these effects. Accurate quantification of penumbra is crucial because treatment decisions are based on the size of salvageable penumbra. Studies have shown that accurately quantifying infarct has directly indicated clinical outcome in patients with stroke.¹⁷ For instance, infarct overestimation can result in patients being excluded from reperfusion treatments, while infarct underestimation can increase the likelihood of poor clinical outcomes due to hemorrhage following revascularization procedures. Although optimal perfusion parameters for identifying infarct are patient-specific, infarct underestimation is preferred because it allows patients to reobtain lost neurologic function through enrollment in endovascular procedures.³

Differences in predicted volume and FIV along with MAEs for patients with interventions indicate the Vitrea default setting as optimal for Bayesian CTP software. Discrepancies in MR imaging and CTP infarct measurements may be due to the 24-hour delay between MR imaging and CTP imaging, allowing tissue to convert from penumbra to infarct at a rate of 10.1 mL/h in patients with hypoperfusion intensity ratios of >0.5 .¹⁸ The hypoperfusion intensity ratio represents the ratio of severely hypoperfused tissue to the volume of tissue with any hypoperfusion.¹⁹ Vitrea software was compared with RAPID and proved to be noninferior as seen by similar infarct differences and correlations with final infarct volumes.

For patients without interventions, default Bayesian was the most accurate for determining final infarct volumes. These patients did not receive mechanical thrombectomy or tPA because of minimal penumbra or contraindications to thrombolysis. Typically, endovascular interventions are not performed unless there is at least a 2:1 penumbra-to-infarct mismatch.²⁰ In this instance, tissue originally determined as penumbra on perfusion imaging would die and show up as infarct on follow-up MR imaging.²¹ Additionally, all penumbra converts to infarct in patients who delay initial perfusion imaging, indicated by the statistical

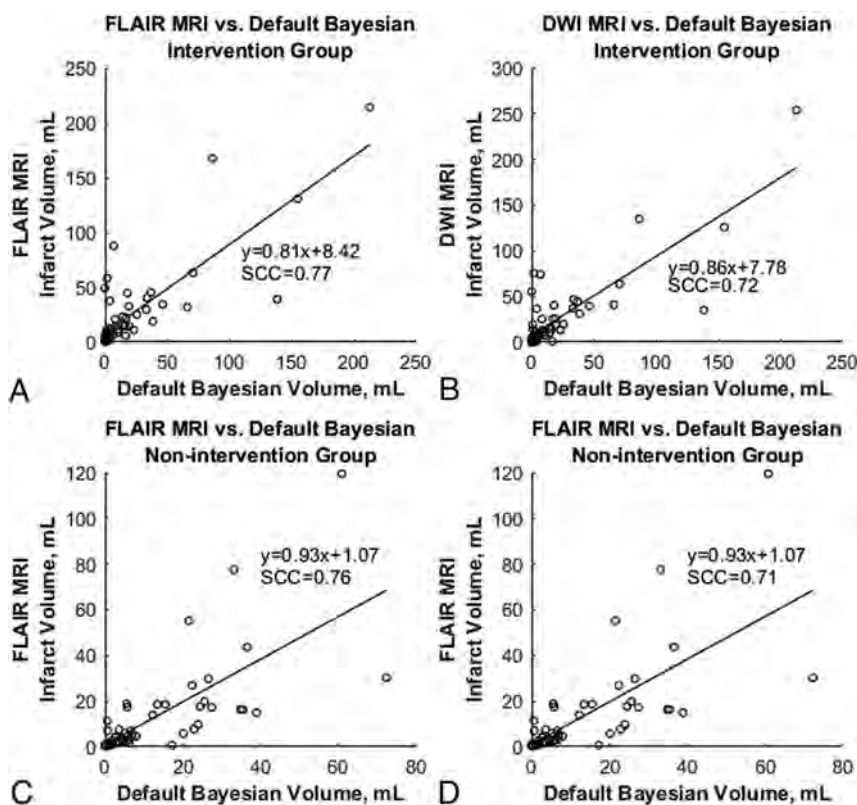


FIG 2. Correlation between final DWI and FLAIR infarct and predicted CTP infarct volumes for the default CTP software. *A* and *B*, Relationship between final (FLAIR and DWI) and predicted infarct volumes for intervention cases. *C* and *D*, The same relationship for nonintervention cases.

Table 3: Spearman correlation coefficients between predicted CTP infarct and final DWI and FLAIR infarct

Parameter/Final Infarct Predictor	Perfusion Software	Endovascular Intervention	Nonintervention
Spearman correlation coefficient			
DWI	Default Vitrea	0.72	0.71
	CBV Vitrea	0.71	0.58
	CBF Vitrea	0.53	0.67
FLAIR	RAPID	0.75	0.65
	Default Vitrea	0.77	0.76
	CBV Vitrea	0.72	0.64
	CBF Vitrea	0.53	0.69
	RAPID	0.75	0.68

significance between patients with and without interventions from the onset of stroke to perfusion imaging in Table 1. This significant difference could affect penumbra estimation results for patients without interventions. This possibility is due to most patients coming for perfusion imaging after all penumbra has turned to infarct, indicating that CTP software is only predicting infarct as opposed to an inclusion of infarct and penumbra in some cases. Patients without interventions, additionally, show lower median infarct volumes compared with patients with interventions due to inclusion of patients with small-vessel occlusion in the nonintervention category. NIHSS scores are statistically different between patients with and without interventions because the nonintervention group included patients with small-vessel occlusion, who have lower

NIHSS scores. Due to the default Vitrea algorithm indicating accurate infarct results before thrombectomy, it can be deduced that estimated infarct, not including penumbra, is accurate for nonintervention cases. This deduction, therefore, validates that penumbra estimations are accurate for patients without interventions because combined infarct and penumbra volumes agree with MR imaging infarct volumes.

Strong agreement of mean differences and correlations between RAPID- and Bayesian CTP-predicted infarct volumes with MR imaging FIVs for patients with interventions is significant due to ongoing discrepancies between CTP software in calculating infarct volume. A recent study showed that infarct predictions using IntelliSpace Portal (Philips Healthcare, Best, the Netherlands) and syngo.via (Siemens, Erlangen, Germany) CTP software did not correlate well with RAPID.²² This finding prevents a common standard from being established for when vascular interventions should be performed in patients with AIS.

For patients with interventions, significant differences are seen in summed infarct and penumbra estimations with FIVs due to the overestimation of penumbra by RAPID. These infarct differences are in the negative direction, indicating that predicted CTP-summed infarct and penumbra are larger than the FIV. Furthermore, the large penumbra-to-infarct ratio for patients without interventions using RAPID indicates that most estimated infarct and penumbra summation is penumbra, showing that penumbra is causing the overestimation. This overestimation could be due to the use of Tmax to calculate penumbra in RAPID. The Tmax parameter is known to be sensitive to changes in the shape of the arterial input function, which is used to generate the Tmax parameter through deconvolution. Quantum noise can significantly alter the shape of the arterial input function, impacting the Tmax parameter and amount of quantified penumbra.²³ In a previous study using the Tmax parameter, lesion volumes differed by 13% depending on the amount of quantum noise present.²⁴

A potential reason that infarct volumes calculated using Bayesian CTP software indicated strong agreement with final DWI and FLAIR infarct volumes was the allowed user interaction

to segment regions affected by the occlusion. This segmentation allows exclusion of erroneous infarct volumes occurring around the skull due to improper software segmentation as seen in Online Fig 2. In Bayesian CTP software, it is evident which regions correspond to these erroneous volumes as demonstrated by inter-reader variability results indicating no statistical significance in infarct segmentation among 5 users.

Vitreia Bayesian CTP software has demonstrated great efficiency, with processing time being 12 minutes faster than with RAPID on average. Processing time included transfer time of RAPID perfusion maps to the PACS of the hospital. Because RAPID analysis was conducted offsite, transfer speeds may have hindered the rate that CTP data were analyzed.

Limitations of this study include no independent method to verify penumbra volumes. However, because mean penumbra-to-infarct ratios for each CTP software were above the Endovascular Therapy Following Imaging Evaluation for Ischemic Stroke 3 (DEFUSE 3) trial threshold of 1.5, some validity can be added to the penumbra estimations because each software is capable of determining patients' eligible for thrombectomy.⁹ Furthermore, this study is limited by the heterogeneous mixture of patients within the nonintervention group because it includes patients with large- and small-vessel occlusions, along with patients outside the tPA treatment window. Inclusion of patients with small-vessel occlusion can affect infarct estimation results because CTP does not pick up small infarcts well.

Additional limitations to this study are that it included only 10 patients with infarct measurements of >50 mL and did not evaluate spatial overlap of predicted and final infarct volumes. Furthermore, this study did not test all potential perfusion map thresholds. Possibly, an even more optimal grouping of infarct predictive perfusion thresholds exists. Use of DWI and FLAIR as FIVs is another limitation because each MR imaging method could present different ground truth infarct volumes, but FLAIR should be used as the main ground truth due to reversibility of lesions shown in DWI.¹³ The assumption that all penumbra turns to infarct in patients in this study is another limitation because it is possible that emboli could break apart, leading to reperfusion in patients without interventions. Last, this study did not include outside validation sets, yet it was conducted within a comprehensive stroke center that receives hundreds of cases of AIS per year.

CONCLUSIONS

The Vitrea default setting proved to be noninferior to RAPID as seen by similar calculated infarct differences and correlations with FIVs for patients with interventions. Additionally, the default Bayesian Vitrea setting appeared to estimate penumbra volumes more accurately than RAPID as indicated by lower infarct differences and higher correlations for the patients without interventions.

Disclosures: Ryan A. Rava—RELATED: Grant: James H. Cummings Foundation Inc*; Other: Canon Medical Systems Inc. Maxim Mokin—UNRELATED: Consultancy: Medtronic, Canon Medical Systems Inc; Stock/Stock Options: Serenity Medical, VICIS. Ariana B. Allman—RELATED: Grant: James H. Cummings Foundation Inc*; Other: Canon Medical Systems Inc.* Mohammad Mahdi Shiraz Bhurwani—RELATED: Grant: James H. Cummings Foundation Inc*; Other: Canon Medical

Systems Inc.* Yiemeng Hoi—UNRELATED: Employment: Canon Medical Systems Inc. Adnan H. Siddiqui—UNRELATED: Consultancy: Amnis Therapeutics, Boston Scientific, Canon Medical Systems Inc, Cerebrotech Medical Systems, Cerenovus, Corindus Inc, ENDOSTREAM MEDICAL LTD, Guidepoint Global, Imperative Care, Integra Medical Services, Medtronic, MicroVention, Northwest University Data and Safety Monitoring Board Chair for the HEAT Trial, Penumbra, Q'Apel Medical, Rapid Medical, Rebound Therapeutics Corp, Serenity Medical, Silk Road Medical, StimMed, Stryker, Three Rivers Medical, VasSol, W.L. Gore & Associates; Stock/Stock Options: Amnis Therapeutics, Blinktbi, Buffalo Technology Partners LLC, Cardinal Consultants LLC, Cerebrotech Medical Systems, Cognition Medical, ENDOSTREAM MEDICAL LTD, Imperative Care, International Medical Distribution Partners, Neurovascular Diagnostics Inc, Q'Apel Medical, Rebound Therapeutics Corp, Rist Neurovascular, Serenity Medical, Silk Road Medical, Spinnaker Medical Consultants, StimMed, Synchron, Three Rivers Medical, Viseon Spine; Other: National Principal Investigator/Steering Committees: Cerenovus NAPA trial and ARISE II trial; Medtronic SWIFT PRIME and SWIFT DIRECT trials; MicroVention FRED trial and CONFIDENCE study; MUSC POSITIVE trial; Penumbra 3D Separator trial, COMPASS trial, INVEST trial. Jason M. Davies—RELATED: Grant: James H. Cummings Foundation Inc*; UNRELATED: Consultancy: Medtronic; Grants/Grants Pending: National Institutes of Health—National Institute of Neurological Disorders and Stroke; Stock/Stock Options: Rist Neurovascular, Cerebrotech Medical Systems. Elad I. Levy—UNRELATED: Board Membership: Stryker, NeXtGen Biologics, MedX, Cognition Medical, ENDOSTREAM MEDICAL LTD*; Consultancy: Claret Medical, GLG Consulting, Guidepoint Global, Imperative Care, Medtronic, Rebound Therapeutics, StimMed*; Stock/Stock Options: NeXtGen Biologics, RAPID Medical, Claret Medical, Cognition Medical, Imperative Care, Rebound Therapeutics Corp, StimMed, Three Rivers Medical*; Other: Medtronic. Comments: honorarium.* Ciprian N. Ionita—RELATED: Grant: Canon Medical Systems Inc, National Institutes of Health*; UNRELATED: Grants/Grants Pending: National Institutes of Health, James H. Cummings Foundation Inc.* Jillian L. Senko—RELATED: Grant: James H. Cummings Foundation Inc*; Other: Canon Medical Systems Inc.* *Money paid to the institution.

REFERENCES

1. Koenig M, Klotz E, Luka B, et al. **Perfusion CT of the brain: diagnostic approach for early detection of ischemic stroke.** *Radiology* 1998;209:85–93 CrossRef Medline
2. Miles K, Eastwood JD, Konig M. *Multidetector Computed Tomography in Cerebrovascular Disease: CT Perfusion Imaging.* New York: Taylor & Francis Ltd; 2007
3. Mokin M, Levy EI, Saver JL, et al; SWIFT PRIME Investigators. **Predictive value of RAPID assessed perfusion thresholds on final infarct volume in SWIFT PRIME (Solitaire With the Intention for Thrombectomy as Primary Endovascular Treatment).** *Stroke* 2017; 48:932–38 CrossRef Medline
4. Powers WJ, Rabinstein AA, Ackerson T, et al; American Heart Association Stroke Council. **2018 guidelines for the early management of patients with acute ischemic stroke: a guideline for health-care professionals from the American Heart Association/American Stroke Association.** *Stroke* 2018;49:e46–110 CrossRef Medline
5. Nael K, Mossadeghi B, Boutelier T, et al. **Bayesian estimation of cerebral perfusion using reduced-contrast-dose dynamic susceptibility contrast perfusion at 3T.** *AJNR Am J Neuroradiol* 2015;36:710–18 CrossRef Medline
6. Lansberg MG, Christensen S, Kemp S, et al; CT Perfusion to Predict Response to Recanalization in Ischemic Stroke Project (CRISP) Investigators. **Computed tomographic perfusion to predict response to recanalization in ischemic stroke.** *Ann Neurol* 2017;81:849–56 CrossRef Medline
7. Bathla G, Limaye K, Policeni B, et al. **Achieving comparable perfusion results across vendors: the next step in standardizing stroke care: a technical report.** *J Neurointerv Surg* 2019;11:1257–60 CrossRef Medline
8. Saver JL, Goyal M, Bonafe A, et al; SWIFT PRIME Investigators. **Solitaire™ with the Intention for Thrombectomy as Primary Endovascular Treatment for Acute Ischemic Stroke (SWIFT PRIME) trial: protocol for a randomized, controlled, multicenter study comparing the Solitaire revascularization device with IV tPA with IV tPA alone in acute ischemic stroke.** *Int J Stroke* 2015;10:439–48 CrossRef Medline
9. Albers GW, Lansberg MG, Kemp S, et al. **A multicenter randomized controlled trial of endovascular therapy following imaging**

- evaluation for ischemic stroke (DEFUSE 3). *Int J Stroke* 2017; 12:896–905 CrossRef Medline
10. Kudo K, Sasaki M, Yamada K, et al. **Differences in CT perfusion maps generated by different commercial software: quantitative analysis by using identical source data of acute stroke patients.** *Radiology* 2010;254:200–09 CrossRef Medline
 11. Kamran S, Bates V, Bakshi R, et al. **Significance of hyperintense vessels on FLAIR MRI in acute stroke.** *Neurology* 2000;55:265–69 CrossRef Medline
 12. Ho CY, Hussain S, Alam T, et al. **Accuracy of CT cerebral perfusion in predicting infarct in the emergency department: lesion characterization on CT perfusion based on commercially available software.** *Emerg Radiol* 2013;20:203–22 CrossRef Medline
 13. Inoue M, Mlynash M, Christensen S, et al; DEFUSE 2 Investigators. **Early DWI reversal following endovascular reperfusion is typically transient in patients imaged 3–6 hours after onset.** *Stroke* 2014;45:1024–28 CrossRef Medline
 14. Madai VI, Galinovic I, Grittner U, et al. **DWI intensity values predict FLAIR lesions in acute ischemic stroke.** *PLoS One* 2014;9:e92295 CrossRef Medline
 15. Isa I, Sulaiman S, Abdullah M, et al. **Assessing intensity of white matter hyperintensity and normal appearing white matter in healthy adults.** In: *Proceedings of the 2016 IEEE EMBS Conference on Biomedical Engineering and Sciences (IECBES)*, Kuala Lumpur, Malaysia; December 4–7, 2016
 16. Chavez JC, Hurko O, Barone FC, et al. **Pharmacologic interventions for stroke: looking beyond the thrombolysis time window into the penumbra with biomarkers, not a stopwatch.** *Stroke* 2009;40:558–63 CrossRef Medline
 17. Gasparotti R, Grassi M, Mardighian D, et al. **Perfusion CT in patients with acute ischemic stroke treated with intra-arterial thrombolysis: predictive value of infarct core size on clinical outcome.** *AJNR Am J Neuroradiol* 2009;30:722–27 CrossRef Medline
 18. Guenego A, Mlynash M, Christensen S, et al. **Hypoperfusion ratio predicts infarct growth during transfer for thrombectomy.** *Ann Neurol* 2018;84:616–20 CrossRef Medline
 19. Bang O, Saver J, Alger J, et al; UCLA Collateral Investigators. **Determinants of the distribution and severity of hypoperfusion in patients with ischemic stroke.** *Neurology* 2008;71:1804–11 CrossRef Medline
 20. Mokin M, Ansari SA, McTaggart RA, et al; Society of Neuro-Interventional Surgery. **Indications for thrombectomy in acute ischemic stroke from emergent large vessel occlusion (ELVO): report of the SNIS Standards and Guidelines Committee.** *J Neurointerv Surg* 2019;11:215–20 CrossRef Medline
 21. Legrand L, Tisserand M, Turc G, et al. **Do FLAIR vascular hyperintensities beyond the DWI lesion represent the ischemic penumbra?** *AJNR Am J Neuroradiol* 2015;36:269–74 CrossRef Medline
 22. Koopman MS, Berkhemer OA, Geuskens R, et al; MR CLEAN Trial Investigators. **Comparison of three commonly used CT perfusion software packages in patients with acute ischemic stroke.** *J Neurointerv Surg* 2019;11:1249–56 CrossRef Medline
 23. Wouters A, Christensen S, Straka M, et al. **A comparison of relative time to peak and Tmax for mismatch-based patient selection.** *Front Neurol* 2017;8:539 CrossRef Medline
 24. Christensen S, Mishra N, Straka M, et al. **Abstract W P28: precision of Tmax and CBF lesion volume estimates in CT perfusion imaging.** *Stroke* 2018;45:AWP28

Predictive Value of Noncontrast Head CT with Negative Findings in the Emergency Department Setting

A.L. Callen, D.S. Chow, Y.A. Chen, H.R. Richelle, J. Pao, M. Bardis, B.D. Weinberg, C.P. Hess, and L.P. Sugrue

ABSTRACT

BACKGROUND AND PURPOSE: Noncontrast head CTs are routinely acquired for patients with neurologic symptoms in the emergency department setting. Anecdotally, noncontrast head CTs performed in patients with prior negative findings with the same clinical indication are of low diagnostic yield. We hypothesized that the rate of acute findings in noncontrast head CTs performed in patients with a preceding study with negative findings would be lower compared with patients being imaged for the first time.

MATERIALS AND METHODS: We retrospectively evaluated patients in the emergency department setting who underwent noncontrast head CTs at our institution during a 4-year period, recording whether the patient had undergone a prior noncontrast head CT, the clinical indication for the examination, and the examination outcome. Positive findings on examinations were defined as those that showed any intracranial abnormality that would necessitate a change in acute management, such as acute hemorrhage, hydrocephalus, herniation, or interval worsening of a prior finding.

RESULTS: During the study period, 8160 patients in the emergency department setting underwent a total of 9593 noncontrast head CTs; 88.2% (7198/8160) had a single examination, and 11.8% (962/8160) had at least 1 repeat examination. The baseline positive rate of the “nonrepeat” group was 4.3% (308/7198). The 911 patients in the “repeat” group with negative findings on a baseline/first CT had a total of 1359 repeat noncontrast head CTs during the study period. The rate of positive findings for these repeat examinations was 1.8% (25/1359), significantly lower than the 4.3% baseline rate ($P < .001$). Of the repeat examinations that had positive findings, 80% (20/25) had a study indication that was discordant with that of the prior examination, compared with only 44% (593/1334) of the repeat examinations that had negative findings ($P < .001$).

CONCLUSIONS: In a retrospective observational study based on approximately 10,000 examinations, we found that serial noncontrast head CT examinations in patients with prior negative findings with the same study indication are less likely to have positive findings compared with first-time examinations or examinations with a new indication. This finding suggests a negative predictive value of a prior noncontrast head CT examination with negative findings with the same clinical indication.

ABBREVIATIONS: ED = emergency department; NCHCT = noncontrast head CT

Use of CT in the emergency department (ED) has grown dramatically in recent years.¹⁻⁵ Factors contributing to this growth include greater availability of CT and an increased reliance on imaging for initial patient triage and evaluation.^{1,2} In

patients presenting to the ED with neurologic symptoms, noncontrast head CT (NCHCT) is the diagnostic tool of choice to exclude acute intracranial pathology and its use has grown apace with other CT imaging.¹⁻³

In the absence of focal neurologic deficits, however, the diagnostic yield of NCHCT in the emergency setting is relatively low. For example, in patients presenting with syncope or dizziness, positive findings on NCHCT range from 2% to 7%.^{6,7} In addition, anecdotally, many neuroradiologists will attest that the yield is even lower in patients who have had a recent study with negative findings for a similar indication. This perception is

Received August 7, 2017; accepted after revision December 6, 2019.

From the Neuroradiology Section (A.L.C., C.P.H., L.P.S.), Department of Radiology and Biomedical Imaging, University of California, San Francisco, San Francisco, California; Neuroradiology Section (D.S.C., H.R.R., J.P., M.B.), Department of Radiology, University of California, Irvine, Irvine, California; Trillium Health Partners (Y.A.C.), University of Toronto, Toronto, Ontario, Canada; and Radiology and Imaging Sciences (B.D.W.), Emory University, Atlanta, Georgia.

Dr Chow was the *AJNR* Editorial Fellow during this study, and this is work related to his bibliometric study.

Previously presented at: Annual Meeting of the American Society of Neuroradiology and the Foundation of the ASNR Symposium, April 22–27, 2017; Long Beach, California under the title “Use and Yield of Repeat Noncontrast CT Head Exams in the Emergency Department.”

Please address correspondence to Leo P. Sugrue, MD, PhD, Neuroradiology Section, L-352, University of California, San Francisco, 505 Parnassus Ave, San Francisco, CA 94143; e-mail: leo.sugrue@ucsf.edu
<http://dx.doi.org/10.3174/ajnr.A6408>

undoubtedly shaped by experience with a subset of patients, so-called “frequent flyers,” who present repeatedly to the ED with similar symptoms and undergo head CTs on each presentation.⁸⁻¹⁰

Concerns about repeat imaging are not limited to these extreme cases. For example, a recent single-institution study found that up to one-third of ED CT examinations ordered were for patients who had a recent, potentially redundant, CT examination.¹¹ Data from the Center for Information Technology Leadership estimates that approximately 14% of imaging studies, reflecting up to \$20 billion in annual health care expenditure, may reflect unnecessary duplicate imaging.⁸ Beyond financial considerations, there is increasing recognition that repeat CT imaging may tangibly increase cancer risk, especially in younger patients,^{1,8,12} with estimates that up to 1.5%–2% of cancers in the United States may be caused by health care–related exposure to ionizing radiation.^{12,13} In addition, excessive diagnostic testing may lead to incidental findings, which may initiate costly and, at times, unnecessary work-ups.

Prior work evaluating the use of chest CTs to rule out an acute pulmonary embolism demonstrated that repeat examinations performed within 90 days have a much lower rate of positive findings.¹⁴ However, little-to-no quantitative data are available regarding the relative diagnostic value of repeat head CT imaging in the emergency setting.

The goal of this study was to quantify the predictive value of a prior negative head CT in the ED. We hypothesized that there would be a lower rate of acute findings for NCHCTs performed in patients who had a recent study with negative findings compared with patients who were being imaged for the first time or with a new clinical indication.

MATERIALS AND METHODS

Patient Selection

After institutional review board approval of this Health Insurance Portability and Accountability Act–compliant study, we conducted a retrospective query of the Radiology Information Systems data base at The University of California, San Francisco from January 2013 to December 2016. Informed consent was not required, and no financial support was received in this study. We included all noncontrast head CTs ordered by our emergency department that were identified by the Current Procedural Terminology (CPT) code 70450 “CT of the head without contrast.” Noncontrast head CTs performed as part of Code Stroke studies that included CT angiography and/or perfusion were not included. Our analysis was limited to adult patients, defined as 18 of age or older. We conducted a retrospective review of medical records to determine patient demographic information, including sex and age. We divided patients who underwent a single CT examination or multiple examinations during the study period into “nonrepeat” and “repeat” groups, respectively. For patients in the repeat group, we recorded the time interval between the first (baseline) and repeat examinations. Study indications included in the clinical history by the ordering provider were recorded for each examination. If the study indication for the repeat examination was discordant

with the baseline examination, this discordance was recorded as well.

Imaging Techniques

All imaging was performed on a 64-section CT imaging system (Discovery CT750 HD; GE Healthcare, Milwaukee, Wisconsin) with an effective axial section thickness of 0.625 mm, reformatted in bone and soft-tissue windows in sagittal and coronal planes. All studies were interpreted by members of the neuroradiology faculty as part of the normal daily clinical workflow. The “Impression” section of the generated study reports served as the basis for categorizing a study as having positive or negative findings as further detailed below.

Definition of Examinations with Positive and Negative Findings

Given the large number of cases, we used an automated classification workflow to identify examinations with negative findings. Specifically, the “Impression” section of each report was searched for the following keywords: “No acute,” “No significant,” “No interval,” “No new,” “No hemorrhage, hydrocephalus, herniation,” and so forth. These examinations were categorized as negative. Reports that could not be classified automatically were manually reviewed by a board-certified neuroradiologist (D.S.C., L.P.S., Y.A.C.) to determine whether they should be categorized as negative or positive. Positive was defined as any intracranial abnormality that would necessitate a change in acute management, including hemorrhage (both extra-axial and parenchymal), hydrocephalus, herniation, mass effect, or interval worsening of a prior finding. Finally, all “Impressions” were manually compared with their category to ensure the accuracy of classification.

Study Indication

History or study indication or both were provided in the form of free text by the ordering clinician. At the time of analysis, we reviewed the history/indication provided for each study and used it to classify study indications according to a set of categories that covered the range of indications encountered in the data. This set of indications included the following: altered mental status, trauma, cancer, headache, seizure, vertigo, nausea, fever, syncope, psychosis, numbness, altered speech, weakness, facial droop, visual abnormalities, substance use, hydrocephalus, hypertension, and intracranial pressure/hemorrhage. A single study could be assigned ≥ 1 indication. When repeat studies were performed on the same patient, the clinical indications were compared between baseline and repeat examinations. Examination indications were considered concordant if the same study indication categories were used. Indications were considered discordant if different or additional categories were used. For example, if 2 studies had indications of “trauma, headache” and “headache” alone, the study indications were considered discordant.

Data Collection and Validation

The rates of positive findings were compared for the nonrepeat and repeat groups, defined above. For the repeat group, we specifically examined the rate of positive findings for the first (baseline) examination and the rate of positive findings for subsequent repeat examinations in patients whose findings on the first/

Table 1: Patient demographics and outcomes/indications for first examination in patients undergoing a single (nonrepeat) or serial (repeat) NCHCT examinations

	Nonrepeat (n = 7198)	Repeat (n = 962)	P
Demographic information			
Proportion of men	0.478	0.486	.973
Age (yr)	57.9	64.1	<.001
Rate of positive findings on the first examination (%) (No.)	4.3 (308)	5.3 (51)	.16
Proportion of men	0.522	0.529	.995
Age (yr)	63.5	64.2	.832
Indications for positive first examination (%) (No.)			
Altered mental status	37.0 (114)	31.4 (16)	.442
Headache	17.2 (53)	19.6 (10)	.677
Trauma	17.2 (53)	39.2 (20)	<.001
Other	28.6 (88)	9.8 (5)	.005

baseline examination were negative. We recorded both the examination indication and findings for all examinations with positive findings in both the nonrepeat and repeat groups.

Statistical Tests

The 2-sample test for proportions and the χ^2 assessment were performed using MedCalc for Windows, Version 12.2.1 (MedCalc Software, Mariakerke, Belgium). A *P* value < .05 was considered statistically significant.

RESULTS

Demographic Data

In total, 9593 CT examinations were identified among 8160 unique patients who met the inclusion and exclusion criteria during the study period (Table 1). Of unique patients, 88.2% (7198/8160) had a single examination and 11.8% (962/8160) had at least 1 repeat examination. The mean age of patients in the repeat group was significantly higher compared with patients in the nonrepeat group (64.1 versus 57.9 years, *P* < .001). There was no significant difference in sex between the 2 groups (*P* = .97).

Positive Rate of Initial CT Examinations

A positive finding was identified in 4.4% (384/8160) of all first/baseline head CT examinations. There was no significant difference in the positive rate between patients in the nonrepeat group and the first examination of patients in the repeat group (4.3% [308/7198] versus 5.3% [51/962], *P* = .16). Among baseline studies with positive findings from the nonrepeat and repeat groups, there was no significant difference in either patient age (*P* = .99) or sex (*P* = .83) (Table 1).

The most common indications for positive findings on baseline CT examinations in the nonrepeat group were altered mental status (37.0%, 114/308), headache (17.2%, 53/308), trauma (17.2%, 53/308), and miscellaneous categories (28.6%, 88/308). For the repeat group, the most common indications for positive findings on baseline CT examinations were altered mental status (31.4%, 16/51), trauma (39.2%, 20/51), and headache (19.6%, 10/51). Among baseline studies with positive findings, there was no significant difference in the proportion of examinations with

altered mental status or headache as the indication between the nonrepeat and repeat groups (*P* = .442 and *P* = .677, respectively). However, there was a significantly higher proportion of baseline examinations with positive findings with trauma as the indication in the repeat group (*P* = .003).

Assessment of Patients with Repeat Examinations

As described above, 962 patients underwent repeat head CT examinations during the study period; of these, 94.7% (911/962) had negative findings on the first (baseline) examination. A total of 1359 follow-up or repeat CTs were performed in these 911 patients. The average number of repeat examinations acquired per patient was 1.49 examinations, and the mean follow-up interval was 6.5 months. The proportions of patients with 1, 2, 3, and >3 repeat head CTs were, respectively, 73.7% (671/911), 15.8% (144/911), 6.2% (56/911), and 1.2% (40/911) (Fig 1). Of note, 3 patients had >10 studies with a maximum of 17. There was no significant difference in the rate of positivity in patients who had only 1 repeat compared with patients who had >1 repeat examination (20/671 [3%] versus 5/240 [2%], *P* = .45).

A positive finding was identified in 1.8% (25/1359) of all repeat head CTs that followed a first examination with negative findings, significantly different from the 4.3% positive rate in the nonrepeat group (*P* < .001) and the 5.3% positive rate for the first examination in the repeat group (*P* < .001) (Fig 2). Of patients in the repeat group who converted from negative to positive, the proportions who converted on the first, second, or third repeat examination were 80% (20/25), 16% (4/25), and 4% (1/25), respectively. Across the time scales relevant to this study, the interval between the first examination with negative findings and the follow-up did not substantially impact the probability of the repeat examination findings being positive: The proportions of repeat examinations with positive findings obtained within 30 days, 60 days, and 90 days of an initial negative head CT were 1.5% (5/344), 1.8% (8/491), and 1.7% (9/605), respectively (Table 2). For each interval, the proportion of examinations with positive findings was significantly lower than the 4.3% baseline positive rate. The 5 cases with positive findings obtained within 30 days of an initial head CT with negative findings included an acute on chronic subdural hemorrhage in a patient with altered mental status, new hemorrhagic metastasis in a patient with known metastatic lung cancer, new hydrocephalus in a patient with known leptomeningeal carcinomatosis, new subdural hemorrhage following a fall in an elderly patient, and new parenchymal hematoma in a patient on anticoagulation.

Across the 1359 repeat examinations, the proportion of examinations with positive findings varied by indication as follows (note that a given examination could have >1 indication): altered mental status 3% (8/300), trauma 2% (12/716), cancer 2% (1/44), headache 4% (2/252), seizure 0% (0/117), vertigo 2% (1/53), nausea 0% (0/32), fever 0% (0/8), syncope 2% (1/42), psychosis 0% (0/8), numbness 0% (0/21), altered speech 0% (0/22), weakness 5% (3/65), facial droop 0% (0/13), visual abnormalities 17% (1/6), substance use 0% (0/5), hydrocephalus 0% (0/6), hypertension 0% (0/1), and intracranial pressure/hemorrhage 0% (0/1).

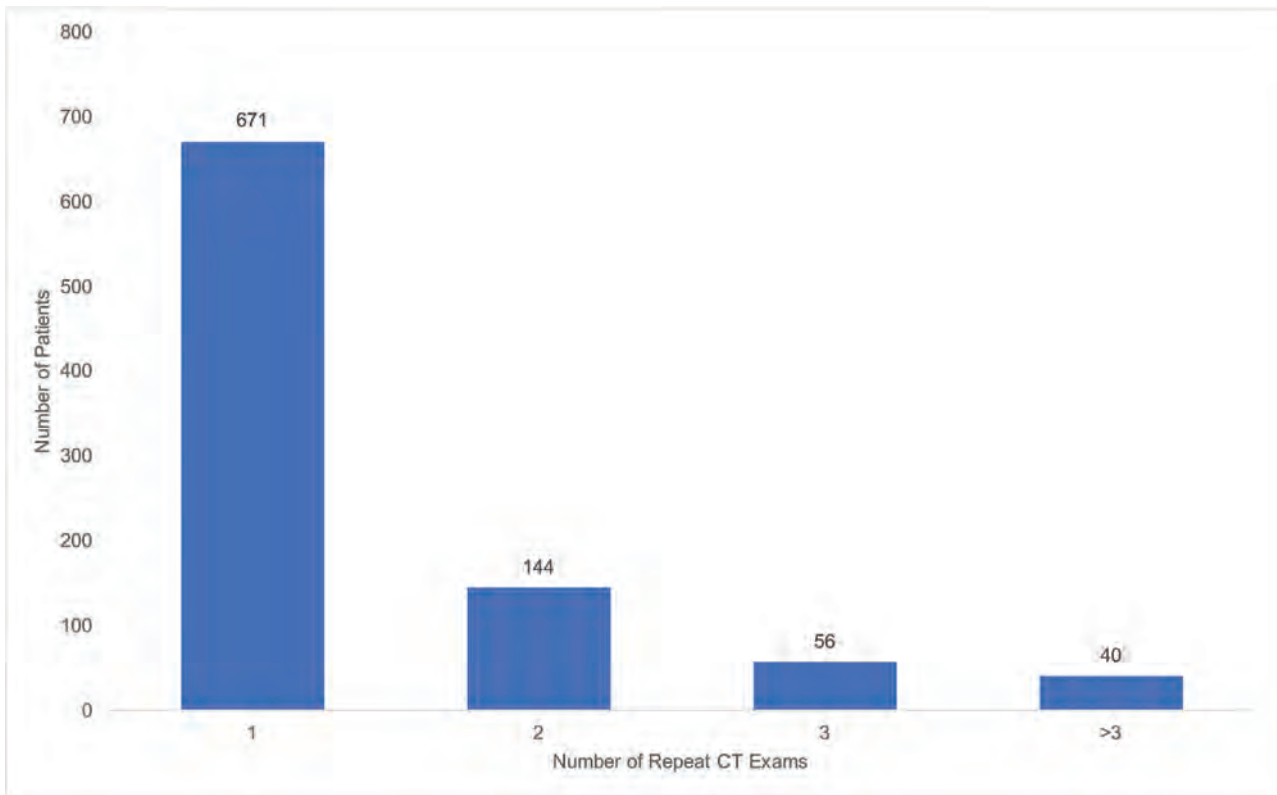


FIG 1. Histogram showing the number of patients in the repeat group who had 1, 2, 3, and >3 repeat NCHCT examinations during the study period.

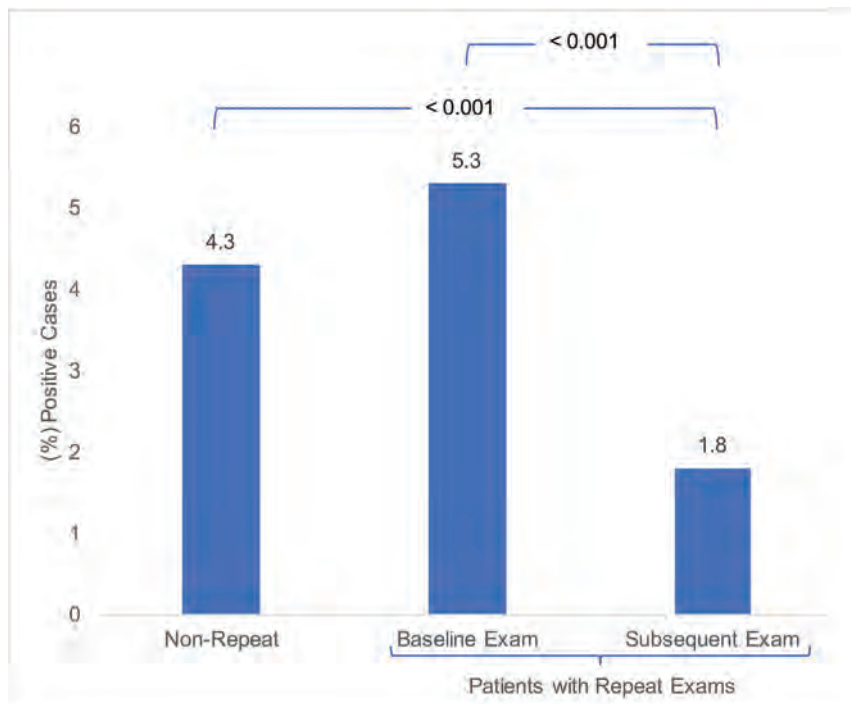


FIG 2. Rate of positive findings in first/baseline-versus-subsequent examinations. Repeat NCHCT examinations that followed a prior examination with negative findings had a much lower rate of positive findings (1.8%) than examinations in the nonrepeat group (4.3%) or the first examination of patients in the repeat group (5.3%). There was no significant difference between the rate of positive findings in the nonrepeat group and the first/baseline examination in the repeat group.

On a per-patient basis, 2.7% (25/911) of patients in the serially imaged group with negative findings on a first head CT ultimately went on to have at least 1 follow-up head CT with positive findings. Because it may include multiple follow-up examinations, this per-patient rate is higher than the positive rate for a single follow-up study; nevertheless, it is still significantly lower than the positive rate for the nonrepeat group ($P = .02$) and for the first examination in the serially imaged group ($P = .004$).

Comparison of Clinical Indications between Study Groups

Across all studies (baseline plus repeats), the most common indications for both positive and negative findings on CT examinations were similar. For positive findings, the most common indications were altered mental status (36%, 130/359), trauma (20%, 73/359), and headache (18%, 63/359). For negative findings, the most common indications were trauma (3341/

Table 2: Outcome of repeat examination by interval since the examination with negative findings^a

Interval between CTs	No. of Positive Examinations	Total Repeat Examinations	% Positive	P Value ^b
<30 days	5	344	1.5	.011
<60 days	8	491	1.8	.007
<90 days	9	605	1.7	.002
<120 days	10	690	1.6	<.001
<180 days	11	804	1.5	<.001
>180 days	25	1359	1.8	<.001

^a Outcome of repeat NCHCT examinations as a function of the interval (in days) since the prior examination with negative findings. The proportion of repeat examinations with positive findings remained between 1.5% and 1.8% (and significantly lower than the 4.3% positive rate of first/baseline examinations) for the durations (up to 1 year) considered in this study.

^b The P value was taken against the 4.3% rate of first/baseline examinations.

9234, 36%), headache (1932/9234, 21%), and altered mental status (1686/9234, 18%).

Of the 911 patients who had negative findings on the baseline examination, there were 1359 total repeat examinations. Of the total 1359 repeat examinations, 613 (45%) had indications discordant with their baseline examination, and 746 (55%) had indications concordant with their baseline examination. The discordant repeat examinations had a significantly greater proportion of positive findings than in the concordant group, with 20/613 (3%) having positive findings, compared with only 5/746 (0.7%) in the concordant group ($P < .001$). It follows that repeat examinations with positive findings tended to have a clinical indication discordant with the baseline examination. Specifically, of the follow-up examinations that had positive findings, 20/25 (80%) had indications discordant with the baseline examination. Of the follow-up examinations that had negative findings, 593/1334 (44%) had an indication discordant with the baseline examination ($P < .001$).

DISCUSSION

NCHCT examinations performed in the emergency department setting with the same study indication were significantly less likely to have positive findings if the patient had a recent prior NCHCT with negative findings. Among nearly 10,000 examinations performed during a 4-year period at a single academic medical center, we found that NCHCTs had positive findings in only 1.8% of patients who had a recent prior NCHCT with negative findings, compared with 4.3% in first-time (baseline) examinations, and they had positive findings in only 0.7% in patients for whom the indications for the baseline and repeat examinations were the same. This result corroborates prior work suggesting that NCHCT examinations performed in the emergency setting in patients without focal neurologic deficits largely have negative findings,^{6,7} while extending the result to suggest that at a statistical level, there is a negative predictive value for a recent examination with negative findings with the same clinical indication.

We hypothesized that a repeat study that had the same clinical indication as its prior baseline examination would be associated with a lower rate of positive findings than a repeat study with a different indication. This hypothesis was confirmed by the data, with 80% of repeat examinations with positive findings having a

different clinical indication compared with the baseline examination, while only 44% of repeat examinations with negative findings had a different clinical indication.

We also hypothesized that the negative predictive effect of a prior study with negative findings might decline and the rate of positive findings might return to that of first-time examinations as the interval between a negative baseline and follow-up examination increased. At <30 days of follow-up, the positive rate was 1.5%, significantly lower than the first-time examination rate of 4.3%. Somewhat surprising, positive rates for follow-up examinations remained low (<2%, and significantly lower than that of first-time examinations) even as the time since the baseline study with negative findings increased up to 12 months. This finding suggests that the negative predictive effect of a NCHCT with negative findings is long-lasting, at least for the month-to-year time scale evaluated in this study.

The current study did not explore why a prior NCHCT with negative findings performed for the same indication has a negative predictive value. We speculate that for some patients presenting with vague neurologic symptoms, there may be no underlying anatomic/imaging correlate for their presenting symptom. For others, an anatomic correlate may exist, but CT may not be sensitive enough to detect it, meaning that the yield for repeat CT imaging for the same indication will remain low. These latter patients might benefit from a more sensitive diagnostic evaluation with MR imaging as has been shown to be the case in patients who present with dizziness.⁷ Developing criteria to reliably discriminate between these 2 groups will be an important goal for future work.

During the past decade, many factors have contributed to the increased use of CT examinations in the emergency department setting. These include increased availability of CT; technologic advances that have reduced scan time, radiation dose, and cost; system-based cost-saving and outcome-focused initiatives that have emphasized earlier and more accurate diagnosis; as well as a general fear on the part of providers of missing something in an era of increasing malpractice litigation.^{2,15,16} At a population level, CT scans undoubtedly help ED physicians arrive at earlier and more accurate diagnoses. Similarly, at a population level, increased CT imaging has a measurable cost, both in exposure to ionizing radiation and its associated cancer risk and in increased health care dollars spent on studies with limited diagnostic yield.

While crucially important from a public health and medical economics perspective, the cost-benefit of CT imaging at the population level does not necessarily help the practicing emergency department physician or radiologist determine the relative cost/benefit of a CT examination in any given patient. Our current results suggest that information easily available from the electronic medical record, such as the outcome and indications of prior imaging, has potential value in stratifying patients with respect to the appropriateness of NCHCT imaging. Such information, combined with decision-support systems, could be used to facilitate more personalized and effective imaging decisions.¹⁷⁻¹⁹ Indeed, a prior retrospective study of ED CT use suggested that simply alerting ED physicians to the existence of prior relevant CT imaging could alter ordering practice.¹¹

Our study has at least 2 important limitations. First, as a single-institution retrospective study, our results may not reflect the ordering practices or patient demographics of other centers and did not consider examinations that our patients may have undergone at other institutions during the study period. Second, our results suggest that the examination indication impacts the prior probability that a repeat examination will have positive findings. However, even though our study included ~10,000 patients, the low overall rate of CT examinations with positive findings precluded an analysis of the relationship between specific indications and positive findings on baseline and repeat examinations. Going forward, our goal is to conduct a larger multicenter study to validate these results across institutions and provide sufficient power to answer these more nuanced questions.

CONCLUSIONS

We investigated the rate of positive findings in repeat noncontrast head CTs performed on patients presenting to the ED who had prior negative findings on NCHCT with the same or different indications and compared it with the rate of positive findings in patients being imaged for the first time. In this retrospective observational study based on approximately 10,000 eligible examinations, we found that, overall, serial NCHCT examinations in patients with a prior study with negative findings are much less likely to be positive compared with first-time examinations. Most important, this difference depends on whether the prior study had the same clinical indication. This finding suggests that when a patient returns to the emergency department with the same neurologic symptom, a repeat NCHCT may be of limited diagnostic benefit.

Disclosures: Leo P. Sugrue—UNRELATED: Board Membership: Research Radiology, Inc; Stock/Stock Options: Research Radiology, Inc.

REFERENCES

- Hess EP, Haas LR, Shah ND, et al. **Trends in computed tomography utilization rates: a longitudinal practice-based study.** *J Patient Saf* 2014;10:52–58 CrossRef Medline
- Larson DB, Johnson LW, Schnell BM, et al. **National trends in CT use in the emergency department: 1995–2007.** *Radiology* 2011;258:164–73 CrossRef Medline
- Hussein W, Mullins PM, Alghamdi K, et al. **Trends in advanced computed tomography use for injured patients in United States emergency departments: 2007–2010.** *Acad Emerg Med* 2015;22:663–69 CrossRef Medline
- Levin DC, Rao VM, Parker L, et al. **Continued growth in emergency department imaging is bucking the overall trends.** *J Am Coll Radiol* 2014;11:1044–47 CrossRef Medline
- Levin DC, Parker L, Rao VM. **Recent trends in imaging use in hospital settings: implications for future planning.** *J Am Coll Radiol* 2017;14:331–36 CrossRef Medline
- Mitsunaga MM, Yoon HC. **Journal club: head CT scans in the emergency department for syncope and dizziness.** *AJR Am J Roentgenol* 2015;204:24–28 CrossRef Medline
- Lawhn-Heath C, Buckle C, Christoforidis G, et al. **Utility of head CT in the evaluation of vertigo/dizziness in the emergency department.** *Emerg Radiol* 2013;20:45–49 CrossRef Medline
- Kamat AB, Midgley S, Kimbrell K. **Duplication of radiology imaging studies in the emergency department: what is the cost?** *Emerg Med J* 2015;32:144–48 CrossRef Medline
- Anandalwar SP, Mau CY, Gordhan CG, et al. **Eliminating unnecessary routine head CT scanning in neurologically intact mild traumatic brain injury patients: implementation and evaluation of a new protocol.** *J Neurosurg* 2016;125:667–73 CrossRef Medline
- Grover CA, Close RJ, Villarreal K, et al. **Emergency department frequent user: pilot study of intensive case management to reduce visits and computed tomography.** *West J Emerg Med* 2010;11:336–43 Medline
- Wasser EJ, Prevedello LM, Sodickson A, et al. **Impact of a real-time computerized duplicate alert system on the utilization of computed tomography.** *JAMA Intern Med* 2013;173:1024–26 CrossRef Medline
- Brenner DJ, Hall EJ. **Computed tomography: an increasing source of radiation exposure.** *N Engl J Med* 2007;357:2277–84 CrossRef Medline
- Smith-Bindman R, Miglioretti DL, Johnson E, et al. **Use of diagnostic imaging studies and associated radiation exposure for patients enrolled in large integrated health care systems, 1996–2010.** *JAMA* 2012;307:2400–09 CrossRef Medline
- Kline JA, Courtney DM, Beam DM, et al. **Incidence and predictors of repeated computed tomographic pulmonary angiography in emergency department patients.** *Ann Emerg Med* 2009;54:41–48 CrossRef Medline
- Griffey RT, Jeffe DB, Bailey T. **Emergency physicians' attitudes and preferences regarding computed tomography, radiation exposure, and imaging decision support.** *Acad Emerg Med* 2014;21:768–77 CrossRef Medline
- Baker LC, Atlas SW, Afendulis CC. **Expanded use of imaging technology and the challenge of measuring value.** *Health Aff (Millwood)* 2008;27:1467–78 CrossRef Medline
- Marin JR, Mills AM. **Developing a research agenda to optimize diagnostic imaging in the emergency department: an executive summary of the 2015 Academic Emergency Medicine Consensus Conference.** *Acad Emerg Med* 2015;22:1363–71 CrossRef Medline
- Dunne RM, Ip IK, Abbett S, et al. **Effect of evidence-based clinical decision support on the use and yield of CT pulmonary angiographic imaging in hospitalized patients.** *Radiology* 2015;276:167–74 CrossRef Medline
- Sistrom CL, Dang PA, Weilburg JB, et al. **Effect of computerized order entry with integrated decision support on the growth of outpatient procedure volumes: seven-year time series analysis.** *Radiology* 2009;251:147–55 CrossRef Medline

Visualization of Lenticulostriate Arteries on CT Angiography Using Ultra-High-Resolution CT Compared with Conventional-Detector CT

K. Murayama, S. Suzuki, H. Nagata, J. Oda, I. Nakahara, K. Katada, K. Fujii, and H. Toyama



ABSTRACT

BACKGROUND AND PURPOSE: The newly developed ultra-high-resolution CT is equipped with a 0.25-mm detector, which has one-half the conventional section thickness, one-half the in-plane detector element width, and one-half the reconstructed pixel width compared with conventional-detector CT. Thus, the ultra-high-resolution CT scanner should provide better image quality for microvasculature than the conventional-detector CT scanners. This study aimed to determine whether ultra-high-resolution CT produces superior-quality images of the lenticulostriate arteries compared with conventional-detector CT.

MATERIALS AND METHODS: From February 2017 to June 2017, thirteen patients with aneurysms (4 men, 9 women; mean age, 61.2 years) who underwent head CTA with both ultra-high-resolution CT and conventional-detector CT were enrolled. Two board-certified radiologists determined the number of all lenticulostriate arteries on the CTA coronal images of the MCA M1 segment reconstructed from 512 matrixes on conventional-detector CT and 1024 matrixes on ultra-high-resolution CT.

RESULTS: There were statistically more lenticulostriate arteries identified on ultra-high-resolution CT (average, 2.85 ± 0.83 ; 95% CI, 2.509–3.183) than on conventional-detector CT (average, 2.17 ± 0.76 ; 95% CI, 1.866–2.480) ($P = .009$) in 16 of the total 26 MCA M1 segments.

CONCLUSIONS: Improvements in lenticulostriate artery visualization were the result of the combined package of the ultra-high-resolution CT scanner plus the ultra-high-resolution scanning protocol, which includes higher radiation doses with lower than the national diagnostic reference levels and stronger adaptive iterative dose-reduction processing. This package for ultra-high-resolution CT is a simple, noninvasive, and easily accessible method to evaluate microvasculature such as the lenticulostriate arteries.

ABBREVIATIONS: AIDR = adaptive iterative dose reduction; C-CT = conventional-detector CT; C-CTA = conventional CTA; CTDI_{vol} = volume CT dose index; LSA = lenticulostriate artery; UHR = ultra-high-resolution

The lenticulostriate arteries (LSAs) are perforating arteries that originate in the MCA and supply the basal ganglia. Accurately assessing the variation and structure of the LSAs reduces the likelihood of postoperative complications when performing resections of insular gliomas and when clipping or

coiling MCA M1–2 segment aneurysms.^{1,2} It is also clinically important to evaluate the features of the LSAs in patients with symptomatic intracranial atherosclerotic stenosis to determine the best therapeutic strategy.³ However, although conventional-detector CT (C-CT), which uses a detector with a range of 0.5 mm, has been used to image the proximal side of the LSA,⁴ it is not easy to image the entire LSA from the proximal-to-distal side using C-CT.

In 2005, Canon Medical Systems and the National Cancer Center, Japan, jointly developed a prototype ultra-high-resolution CT system (UHR-CT; TSX-304R; Canon Medical Systems, Otawara, Japan). The UHR-CT was equipped with a 0.25-mm detector, which has one-half the conventional section thickness, one-half the in-plane detector element width, and one-half the reconstructed pixel width compared with the C-CT. Kakinuma et al⁵ reported that the prototype UHR-CT scanner had significantly better image quality for lung nodules than the C-CT scanners. Clinical studies that have tested phantoms using the

Received November 2, 2018; accepted after revision November 12, 2019.

From the Joint Research Laboratory of Advanced Medical Imaging (K.M.), Departments of Radiology (S.S., H.N., K.K., H.T.) and Comprehensive Strokeology (J.O., I.N.), Fujita Health University, Aichi, Japan; and Canon Medical Systems (K.F.), Otawara, Japan.

This work was supported by Grants-in-Aid for Scientific Research (KAKENHI) 18K07694.

Paper previously presented at: Annual Meeting of the Japan Radiological Society, April 12–15, 2018; Yokohama, Japan.

Please address correspondence to Kazuhiro Murayama, MD, PhD, Joint Research Laboratory of Advanced Medical Imaging, Fujita Health University, 1-98 Dengakugakubo, Kutsukake-cho Toyoake, Aichi, 470-1101, Japan; e-mail: kmura@fujita-hu.ac.jp

Indicates open access to non-subscribers at www.ajnr.org

<http://dx.doi.org/10.3174/ajnr.A6377>

production version of the UHR-CT (Aquilion Precision; Canon Medical Systems) have reported that a higher image quality could be obtained compared with C-CT.^{6,7} Another such study that imaged the artery of Adamkiewicz reported improved images.⁸ On the basis of these findings, we predicted that UHR-CTA will have improved imaging quality of the LSAs that exceeds that of conventional CTA (C-CTA). Therefore, the goal of this study was to investigate whether UHR-CTA produced superior images of the LSAs compared with C-CTA.

MATERIALS AND METHODS

Subjects

Our institutional review board (Fujita Health University) approved this opt-out research design. Opt-out opportunities were provided to all participants included in this retrospective study. Forty-two consecutive patients with intracranial aneurysms who underwent intracranial UHR-CTA between February 2017 and June 2017 and who underwent C-CTA using 320-row detector CT during a follow-up study (14–373 days later; mean interval, 224 days) were selected. Twenty-nine patients were excluded for the following reasons: unavailable datasets, the scanning parameters differing from those defined in the protocol, insufficient scanning range for evaluating the LSAs, and enhanced adaptive iterative dose reduction 3D (AIDR 3D; Canon Medical Systems)^{9,10} not used for the denoising procedure. Therefore, 13 patients (4 men and 9 women; age range, 35–74 years; mean age, 61.2 years) with 26 bilateral MCA M1 segments were enrolled in this study.

CTA Protocols for UHR-CT and C-CT

Contrast-enhanced volume data for UHR-CTA were acquired with a 160-detector row UHR-CT scanner (Aquilion Precision) using helical scanning. The UHR-CT scanner used in this study is a medical device with certification as a CT scanner that is safe for clinical use. The other scan parameters were as follows: section thickness of 0.25 mm, tube voltage of 120 kV, automatic exposure control tube current SD of 5, pitch factor of 0.625, reconstructed FOV size of 190–240 mm, and gantry rotation speed of 1 s/rotation. Contrast-enhanced volume data for C-CTA were acquired with a 320-row detector CT scanner (Aquilion ONE; Canon Medical Systems) using nonhelical scanning. The other scan parameters were as follows: section thickness of 0.5 mm, tube voltage of 120 kV, automatic exposure control tube current SD of 3–5, pitch factor of 0.625, reconstructed FOV size of 180–240 mm, and gantry rotation speed of 1 s/rotation. The contrast medium volume was calculated on the basis of each patient's body weight, and 250 mg I/kg of iopamidol (Iopamiron 370; Bayer Healthcare, Osaka, Japan) was injected intravenously as a bolus for a fixed infusion duration of 10 seconds, followed by an intravenous bolus injection of 30 mL of physiologic saline solution at the same rate as the contrast medium.

Image Postprocessing and Data Analysis

The CTA coronal MIP images of 20-mm thick MCA M1 segments were reconstructed from a pixel matrix of 512 × 512 for C-CTA with a 0.5-mm thickness and a pixel matrix of 1024 × 1024 for UHR-CTA with a 0.25-mm thickness with a strong

AIDR 3D. C-CTA was reconstructed with a weak AIDR 3D using the analysis software installed in the CT console. Previous studies evaluating the LSAs on MR imaging and CTA determined the number of LSA branches within 5 mm from the MCA and the number of branches beyond 5 mm.^{11,12} The number of LSAs, defined as those longer than 5 mm, were analyzed.¹² Two board-certified radiologists (K.M. with 14 years of experience; S.S. with 14 years of experience) participated as observers. A standard window level and width were applied during reader observations. The observers were allowed to freely vary window levels and widths.

Statistical Analysis

We compared the mean visible number of LSAs recorded by 2 blinded and independent observers between the C-CTA and UHR-CTA images. A Wilcoxon matched-pairs signed rank test was used to calculate *P* values for comparisons. For all statistical analyses, a *P* value of <.05 indicated a statistically significant between-group difference. The statistical analyses were performed using commercially available statistical software (GraphPad Prism software, Version 6, GraphPad Software, San Diego, California; BellCurve for Excel, Version 2.11, Social Survey Research Information, Tokyo, Japan).

Radiation Dose

The estimated volume CT dose index (CTDI_{vol}) for CTA displayed on the CT scanner console was recorded for each patient. The estimated dose-length product was calculated as CTDI_{vol} × Scan Length. The radiation dose was also compared against the diagnostic reference level of the Japan Network for Research and Information on Medical Exposure (J-RIME) (<http://www.radher.jp/J-RIME/report/DRLhoukokusyoEng.pdf>). The J-RIME is the network used to collect data related to medical exposure and to construct a framework within Japan for appropriate medical radiation doses. The J-RIME suggested that national diagnostic reference levels established in 2015 for routine brain CT examination were 85 mGy (CTDI_{vol}) and 1350 mGy × cm (dose-length product).

RESULTS

The number of LSAs determined by the 2 observers is summarized in Fig 1. There were statistically more LSAs identified on UHR-CT (average, 2.85 ± 0.83; 95% CI, 2.509–3.183) than on C-CT (average, 2.17 ± 0.76; 95% CI, 1.866–2.480) (*P* = .009). There were also more LSAs identified on UHR-CT than on C-CT in 16 of the total 26 MCA M1 segments. Figures 2 and 3 show representative images that clearly show bilateral LSAs from the proximal-to-distal tip in UHR-CTA compared with LSAs imaged by C-CTA, respectively.

The CTDI_{vol} obtained with C-CT was 9.7–37.7 mGy (mean, 27.2 mGy), whereas it was 44.7–63.1 mGy (mean, 53.8 mGy) with UHR-CT. The estimated dose-length product range was calculated as CTDI_{vol} × Scan Length, which was determined as 124.9–488.1 mGy × cm (mean, 266.5 mGy × cm) with C-CT and 685.8–942.5 mGy × cm (mean, 740.8 mGy × cm) with UHR-CT. The radiation doses for both C-CT and UHR-CT

attributable to the spatial resolution of the UHR-CT and its associated reduction in the partial volume effects for the following reasons: First, UHR-CT provides significantly higher quality images of intracranial CTA using detectors with half the thickness in the z-axis direction (0.25 mm × 160 detectors) and twice as many channels in the x- and y-axis directions (1792 channels) on the super-high-resolution data-acquisition mode compared with C-CT. Second, the focal spot size of the UHR x-ray tubes (0.4 × 0.5 mm) is smaller than that of C-CT x-ray tubes (0.9 × 0.8 mm). Finally, UHR-CTA is reconstructed by a higher resolution matrix (1024 × 1024) compared with C-CTA (matrix size, 512 × 512). On the basis of these factors, UHR-CT appears to provide significantly higher quality images of intracranial CTA than C-CT. Thus, UHR-CTA allows us to accurately assess the variation and structure of LSAs.

Differences in the imaging quality of C-CTA and UHR-CTA include the difference between helical and nonhelical scanning in addition to the spatial resolution as mentioned above; these differences influence the image quality of contrast-enhanced images.^{19–21} Because UHR-CT must use helical scanning, UHR-CTA image homogeneity with helical scans can be inferior to that of C-CTA with nonhelical scanning.²² Furthermore, it may be difficult to obtain images with optimal contrast-enhanced timing because UHR-CTA requires a longer scanning time. UHR-CTA is significantly superior to C-CTA for imaging the LSAs despite these disadvantages; this difference implies the greater advantages of UHR-CTA compared with C-CTA. In some cases, the number of LSAs on UHR-CT was the same or fewer than on C-CT for the following reasons: CTA scanning on UHR-CT must use the super-high-resolution mode, which has the smallest size of scan focus. The super-high-resolution mode has the technical upper limit of radiation output power; therefore, all cases showed nearly the same values for CTDI and dose-length product. As a result, we predicted that this occurred when the radiation doses were not sufficient for UHR-CT imaging to visualize LSAs in some cases.

This study has several limitations. First, a small number of subjects were included in this retrospective analysis; future prospective studies should include more subjects. Second, the scan protocols such as the FOV, reconstruction, and AIDR 3D were not the same between UHR-CTA and C-CTA. It was difficult to scan all CTA images using completely identical conditions between UHR-CTA and C-CTA because these scan protocols were optimized individually for the equipment for each C-CT and UHR-CT. Third, C-CT scans were obtained at a radiation dose range (9.7–37.7 mGy CTDI_{vol}) that is much lower than the 85-mGy diagnostic reference level. There was a possibility that LSAs were poorly visualized in C-CT simply because of the lower dose and correspondingly higher image noise levels. The comparisons between C-CT and UHR-CT should be performed at the same radiation dose. Fourth, UHR-CTA was compared with C-CTA, with C-CTA performed an average of 224 days after the initial CTA. We detected no new lesions between the scans on CT; however, the visualization of the LSAs on the follow-up scans could be affected by pathologic changes or morphologic changes.

CONCLUSIONS

Improvement in LSA visualization was the result of the combined package of the UHR-CT scanner plus the UHR scanning protocol, which includes a higher radiation dose with lower than the national diagnostic reference levels and stronger AIDR processing. This package for UHR-CT is a simple, noninvasive, and easily accessible method to evaluate microvasculature such as the LSAs.

Disclosures: Kazuhiro Murayama—RELATED: Grant: Grants-in-Aid for Scientific Research (KAKENHI).* Ichiro Nakahara—UNRELATED: Consultancy: Kaneka Medix (Japan), Terumo (Japan), Nipro Corporation (Japan). Kazuhiro Katada—RELATED: Consultancy: Canon Medical Systems; Grants/Grants Pending: Canon Medical Systems.* Kenji Fujii—RELATED: Employment: Canon Medical Systems. *Money paid to the institution.

ACKNOWLEDGMENT

The authors would like to thank Maruzen-Yushodo Co Ltd (<https://kw.maruzen.co.jp/kousei-honyaku/>) for the English language editing.

REFERENCES

1. Steno A, Jezberova M, Holly V, et al. **Visualization of lenticulostriate arteries during insular low-grade glioma surgeries by navigated 3D ultrasound power Doppler: technical note.** *J Neurosurg* 2016; 125:1016–23 CrossRef Medline
2. Moshel YA, Marcus JD, Parker EC, et al. **Resection of insular gliomas: the importance of lenticulostriate artery position.** *J Neurosurg* 2008;109:825–34 CrossRef Medline
3. Wang M, Wu F, Yang Y, et al. **Quantitative assessment of symptomatic intracranial atherosclerosis and lenticulostriate arteries in recent stroke patients using whole-brain high-resolution cardiovascular magnetic resonance imaging.** *J Cardiovasc Magn Reson* 2018;20:35 CrossRef Medline
4. Gotoh K, Okada T, Satogami N, et al. **Evaluation of CT angiography for visualisation of the lenticulostriate artery: difference between normotensive and hypertensive patients.** *Br J Radiology* 2012;85: e1004–08 CrossRef Medline
5. Kakinuma R, Moriyama N, Muramatsu Y, et al. **Ultra-high-resolution computed tomography of the lung: image quality of a prototype scanner.** *PLoS One* 2015;10:e0137165 CrossRef Medline
6. Yanagawa M, Hata A, Honda O, et al. **Subjective and objective comparisons of image quality between ultra-high-resolution CT and conventional area detector CT in phantoms and cadaveric human lungs.** *Eur Radiol* 2018;28:5060–68 CrossRef Medline
7. Hata A, Yanagawa M, Honda O, et al. **Effect of matrix size on the image quality of ultra-high-resolution CT of the lung: comparison of 512 × 512, 1024 × 1024, and 2048 × 2048.** *Acad Radiol* 2018;25:869–76 CrossRef Medline
8. Yoshioka K, Tanaka R, Takagi H, et al. **Ultra-high-resolution CT angiography of the artery of Adamkiewicz: a feasibility study.** *Neuroradiology* 2018;60:109–15 CrossRef Medline
9. Matsuki M, Murakami T, Juri H, et al. **Impact of adaptive iterative dose reduction (AIDR) 3D on low-dose abdominal CT: comparison with routine-dose CT using filtered back projection.** *Acta Radiol* 2013;54:869–75 CrossRef Medline
10. Feger S, Rief M, Zimmermann E, et al. **The impact of different levels of adaptive iterative dose reduction 3D on image quality of 320-row coronary CT angiography: a clinical trial.** *PLoS One* 2015;10: e0125943 CrossRef Medline
11. Okuchi S, Okada T, Ihara M, et al. **Visualization of lenticulostriate arteries by flow-sensitive black-blood MR angiography on a 1.5 T MRI system: a comparative study between subjects with and without stroke.** *AJNR Am J Neuroradiol* 2013;34:780–84 CrossRef Medline

12. Gotoh K, Okada T, Miki Y, et al. **Visualization of the lenticulostriate artery with flow-sensitive black-blood acquisition in comparison with time-of-flight MR angiography.** *J Magn Reson Imaging* 2009;29:65–69 CrossRef Medline
13. Akashi T, Taoka T, Ochi T, et al. **Branching pattern of lenticulostriate arteries observed by MR angiography at 3.0 T.** *Jpn J Radiol* 2012;30:331–35 CrossRef Medline
14. Chen YC, Li MH, Li YH, et al. **Analysis of correlation between the number of lenticulostriate arteries and hypertension based on high-resolution MR angiography findings.** *AJNR Am J Neuroradiol* 2011;32:1899–1903 CrossRef Medline
15. Okuchi S, Okada T, Fujimoto K, et al. **Visualization of lenticulostriate arteries at 3T: optimization of slice-selective off-resonance sinc pulse-prepared TOF-MRA and its comparison with flow-sensitive black-blood MRA.** *Acad Radiol* 2014;21:812–16 CrossRef Medline
16. Cho ZH, Kang CK, Han JY, et al. **Observation of the lenticulostriate arteries in the human brain in vivo using 7.0T MR angiography.** *Stroke* 2008;39:1604–06 CrossRef Medline
17. Yashiro S, Kameda H, Chida A, et al. **Evaluation of lenticulostriate arteries changes by 7 T magnetic resonance angiography in type 2 diabetes.** *J Atheroscler Thromb* 2018;25:1067–75 CrossRef Medline
18. Park JC, Shim JH, Lee DH, et al. **Three-dimensional angiographic evaluation of middle cerebral artery trunk aneurysms: demonstration of the close relationship between the early frontal cortical branches and lateral lenticulostriate arteries.** *World Neurosurg* 2016;91:383–89 CrossRef Medline
19. Saake M, Goelitz P, Struffert T, et al. **Comparison of conventional CTA and volume perfusion CTA in evaluation of cerebral arterial vasculature in acute stroke.** *AJNR Am J Neuroradiol* 2012;33:2068–73 CrossRef Medline
20. Honda O, Yanagawa M, Hata A, et al. **Influence of gantry rotation time and scan mode on image quality in ultra-high-resolution CT system.** *Eur J Radiol* 2018;103:71–75 CrossRef Medline
21. Jeon SK, Choi YH, Cheon JE, et al. **Unenhanced 320-row multidetector computed tomography of the brain in children: comparison of image quality and radiation dose among wide-volume, one-shot volume, and helical scan modes.** *Pediatr Radiol* 2018;48:594–601 CrossRef Medline
22. Honda O, Takenaka D, Matsuki M, et al. **Image quality of 320-detector row wide-volume computed tomography with diffuse lung diseases: comparison with 64-detector row helical CT.** *J Comput Assist Tomogr* 2012;36:505–11 CrossRef Medline

A Method to Estimate Brain Volume from Head CT Images and Application to Detect Brain Atrophy in Alzheimer Disease

V. Adduru, S.A. Baum, C. Zhang, M. Helguera, R. Zand, M. Lichtenstein, C.J. Grissenaue, and A.M. Michael



ABSTRACT

BACKGROUND AND PURPOSE: Total brain volume and total intracranial volume are important measures for assessing whole-brain atrophy in Alzheimer disease, dementia, and other neurodegenerative diseases. Unlike MR imaging, which has a number of well-validated fully-automated methods, only a handful of methods segment CT images. Available methods either use enhanced CT, do not estimate both volumes, or require formal validation. Reliable computation of total brain volume and total intracranial volume from CT is needed because head CTs are more widely used than head MRIs in the clinical setting. We present an automated head CT segmentation method (CTseg) to estimate total brain volume and total intracranial volume.

MATERIALS AND METHODS: CTseg adapts a widely used brain MR imaging segmentation method from the Statistical Parametric Mapping toolbox using a CT-based template for initial registration. CTseg was tested and validated using head CT images from a clinical archive.

RESULTS: CTseg showed excellent agreement with 20 manually segmented head CTs. The intraclass correlation was 0.97 ($P < .001$) for total intracranial volume and 0.94 ($P < .001$) for total brain volume. When CTseg was applied to a cross-sectional Alzheimer disease dataset (58 with Alzheimer disease patients and 58 matched controls), CTseg detected a loss in percentage total brain volume (as a percentage of total intracranial volume) with age ($P < .001$) as well as a group difference between patients with Alzheimer disease and controls ($P < .01$). We observed similar results when total brain volume was modeled with total intracranial volume as a confounding variable.

CONCLUSIONS: In current clinical practice, brain atrophy is assessed by inaccurate and subjective “eyeballing” of CT images. Manual segmentation of head CT images is prohibitively arduous and time-consuming. CTseg can potentially help clinicians to automatically measure total brain volume and detect and track atrophy in neurodegenerative diseases. In addition, CTseg can be applied to large clinical archives for a variety of research studies.

ABBREVIATIONS: AD = Alzheimer disease; BET = Brain Extraction Tool; ICC = intraclass correlation coefficient; TBV = total brain volume; TIV = total intracranial volume; TPM = tissue probability map

Total brain volume (TBV) is an important measure for assessing brain atrophy in aging and neurodegenerative diseases.¹ TBV is estimated from MR or x-ray CT brain images by segmenting the brain parenchyma using manual or automated methods. Automated methods are preferred due to efficiency, reliability, and reproducibility. A number of automated segmentation methods are available for MR images that are extensively applied in

the clinical domain.² In the clinical setting, CT is more widely used than MR imaging due to faster acquisition speed, a smaller number of contraindications, lower cost, and its ability to answer a range of clinical questions.³ However, only a handful of automated segmentation methods exist for head CT images.

Several existing methods in CT segmentation are either semiautomated^{4,5} or targeted toward a specific brain region⁶⁻⁸ or disease condition.^{5,9} Methods available for segmenting CT

Received May 14, 2019; accepted after revision November 20.

From the Duke Institute for Brain Sciences (V.A., A.M.M.), Duke University, Durham, North Carolina; Neuroscience Institute (V.A., C.Z., R.Z., M.L., C.J.G., A.M.M.), Geisinger Health System, Danville, Pennsylvania; Chester F. Carlson Center for Imaging Science (V.A., S.A.B., C.Z., M.H., A.M.M.), Rochester Institute of Technology, Rochester, New York; Faculty of Science (S.A.B.), University of Manitoba, Winnipeg, Manitoba, Canada; and Instituto Tecnológico José Mario Molina Pasquel y Henríquez (M.H.), Lagos de Moreno, Jalisco, Mexico.

This study was supported by the Geisinger Health System Foundation.

Please address correspondence to Andrew M. Michael, PhD, Duke Institute for Brain Sciences, Duke University, Durham, NC 27708; e-mail: andrew.michael@duke.edu

Indicates open access to non-subscribers at www.ajnr.org

Indicates article with supplemental on-line appendix and tables.

Indicates article with supplemental on-line photos.

<http://dx.doi.org/10.3174/ajnr.A6402>

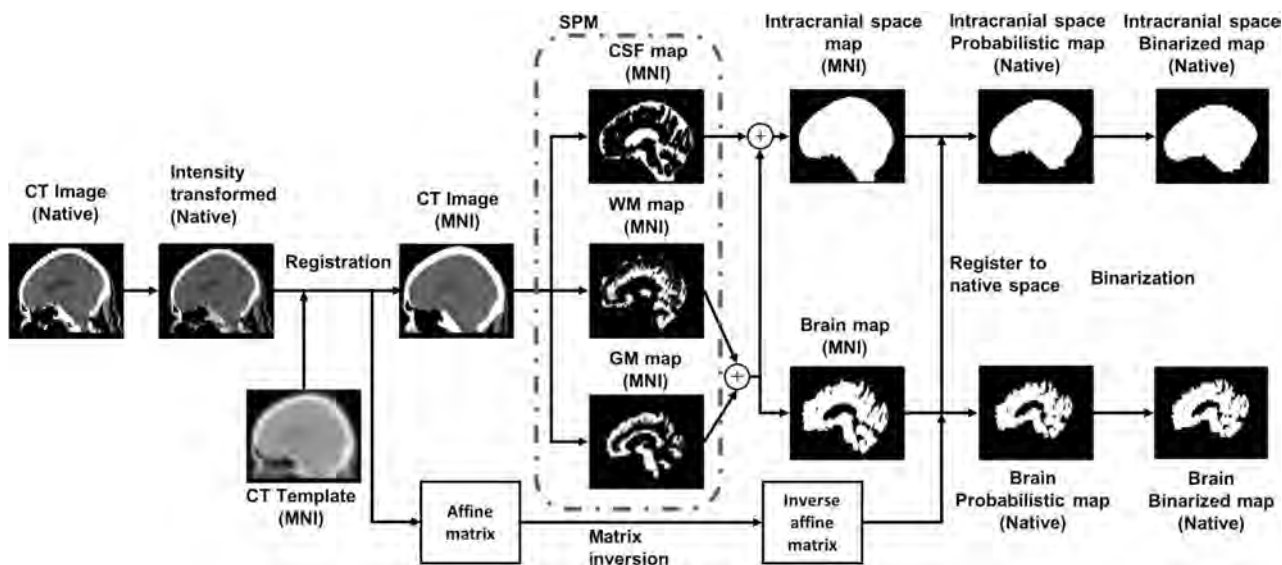


FIG 1. CTSeg pipeline for intracranial space and brain parenchyma segmentation from head CT images. Within parentheses is the 3D coordinate space of the image. MNI indicates Montreal Neurological Institute.

images to measure global volume metrics such as total intracranial volume (TIV) and TBV from images with no detectable pathology were not formally validated.¹⁰⁻¹² Some well-validated methods segment only TIV^{13,14} but not TBV. However, TBV is more indicative of disease conditions in neurodegenerative diseases,¹⁵ and TIV is used merely as a nuisance variable for normalization purposes. Manniesing et al⁴ estimated TBV using head CT but used enhanced CT images.⁴ However, their method cannot be applied to single-time-point CT images with no image enhancement. Irimia et al¹⁶ adapted SPM12 (<http://www.fil.ion.ucl.ac.uk/spm/>),¹⁷ a widely used MR imaging-based segmentation method, for CT segmentation and validated it by comparing it with MR images segmented using FreeSurfer (<http://surfer.nmr.mgh.harvard.edu>). However, they validated only the accuracy of ventricular CSF and not TIV or TBV.

We present a fully-automated CT segmentation (CTSeg; <https://github.com/NuroAI/CTSeg>) method for brain segmentation and estimation of TBV and TIV from nonenhanced single-time-point head CT images by adapting SPM12. CTSeg was validated for brain segmentation and TBV and TIV estimation by comparing it with manual segmentation ($n = 20$). Additionally, we present a clinical application in which CTSeg is used to show TBV differences in Alzheimer disease (AD) ($n = 116$).

MATERIALS AND METHODS

Subjects

This study was reviewed and approved by the Geisinger Health System institutional review board. CT images were originally collected as part of patients' routine clinical care but were fully de-identified. We created 2 datasets: 1) a manual segmentation dataset ($n = 20$, subjects free of brain abnormalities) and 2) an AD dataset ($n = 167$, subjects with and without a diagnosis of AD). Fifteen subjects with AD had catheters and were removed from further analysis. The AD dataset that was further analyzed consisted of 152 subjects.

Manual Segmentation Dataset. A total of 20 subjects (mean age, 66 years; age range, 32–89 years; 10 women) were randomly selected for manual segmentation of the intracranial space and the brain parenchyma. These subjects were free of brain abnormalities and were unremarkable according to the radiology reports. Additionally, through visual inspection, we confirmed that the images were free of artifacts.

AD Dataset. The initial cross-sectional AD dataset consisted of 62 subjects (mean age, 77 years; age range, 68–83 years; 41 women) with a diagnosis of AD and 90 controls (mean age, 78 years; age range, 68–83 years; 64 women) who did not have a diagnosis of AD. Subjects with AD and controls were selected on the basis of the International Classification of Disease, Ninth Revision (ICD-9-CM 331.0) codes.¹⁸ All CT images were free of artifacts, and the radiology reports of the images confirmed no acute pathologies or brain abnormalities. A retrospective evaluation indicated that the controls had undergone a CT scan following headaches or head injury. The CT images were acquired using multiple CT scanners, and details of the scanner models and imaging parameters are provided in On-line Table 1.

Manual Segmentation

Manual segmentation was performed by a trained operator using ITK-SNAP 3.6 (www.itksnap.org).¹⁹ The intracranial space was outlined according to the guidelines provided by Nordenskjöld et al.²⁰ The segmented intracranial image was then used to segment the brain parenchyma by tracing the boundary between brain tissue and CSF.

Automated Brain Segmentation

CTSeg (Fig 1) adapts the unified segmentation algorithm¹⁷ from SPM12 and uses a CT template for the initial affine registration step (see Methods: Automated Brain Segmentation in the On-line Appendix for a detailed explanation of the CTSeg pipeline). CTSeg creates probabilistic and binarized segmentation maps of

Table 1: Comparison of automated TBV and TIV estimates with manual ground truth estimates^a

Parameter/Method	%Difference	Pearson's <i>r</i> (P Value)	ICC (P Value)	Bootstrap Mean ICC (95% CI)
TBV				
CTSeg probabilistic	-7.22±2.98	0.96 (<.001)	0.74 (<.001)	0.727 (0.724–0.730)
CTSeg binarized	1.58±3.46	0.95 (<.001)	0.94 (<.001)	0.937 (0.935–0.939)
TIV				
CTSeg-probabilistic	-12.15±1.44	0.99 (<.001)	0.71 (<.001)	0.685 (0.680–0.689)
CTSeg binarized	-3.28±1.36	0.99 (<.001)	0.97 (<.001)	0.962 (0.961–0.963)
BET	-5.12±0.667	0.99 (<.001)	0.94 (<.001)	0.930 (0.928–0.932)

^a%Difference is reported as means.

the brain and the intracranial space. The binarized segmentation maps are obtained by thresholding the probabilistic maps using optimal thresholds (Optimal Threshold Selection in the On-line Appendix:).

Statistical Methods

The overlap between the automated and manual segmentation masks was measured using the Dice similarity index (DSI).²¹ TIV and TBV were obtained from the probabilistic maps, and the binary masks were obtained using CTSeg. For probabilistic maps, volumes were calculated by integrating the partial tissue volumes (tissue probability at the voxel × voxel volume) over all the voxels from the respective tissue maps. Volume estimates were calculated from binary masks by multiplying the number of masked voxels by the unit voxel volume.

Volumes estimated using CTSeg were compared with the manual estimates using scatterplots and the Pearson's correlation coefficient. Systematic bias was assessed using Bland-Altman analysis,²² and percentage difference was calculated as a percentage of the manual estimates. The absolute agreement between automated and manual volumes was evaluated using the intraclass correlation coefficient (ICC) computed using 2-way ANOVA²³ with fixed effects. The 95% confidence intervals of the ICC were computed using bootstrapping with 1000 iterations. The volumes were checked for normality using the Kolmogorov-Smirnov test.²⁴ The TIV estimates of CTSeg were also compared with the state-of-the-art FSL Brain Extraction Tool for CT (BET; http://bit.ly/CTBET_BASH).¹³

CTSeg-estimated volumes from the images of age-matched subjects with AD and controls were used to compare brain atrophy between patients with AD and controls. Subjects with AD and controls were age-matched by minimizing the age difference using the MatchIt package²⁵ in R (<https://www.rdocumentation.org/packages/MatchIt/versions/3.0.2/topics/matchit>).²⁶ Previous studies have demonstrated that sex has no significant effect on TBV as a percentage of TIV (%TBV)²⁷ because it is a normalized measure that accounts for the variability introduced by head size and sex.^{27,28} Therefore, subjects were not sex-matched because all our analyses were performed on %TBV. TBV versus TIV and %TBV versus age scatterplots were used to compare brain atrophy in patients with AD and controls. Linear regression models were used to determine the significance of age, sex, and AD diagnosis on %TBV. For the regression models, the Age × AD diagnosis interaction term was added to check whether the rate of brain volume loss was significantly different between patients with AD and controls. Additionally, we investigated the effect of TIV by modeling TBV, using TIV as a confounding factor in the linear models, as

recommended in recent studies.^{20,29} TIV and sex were added in addition to Age and AD diagnosis while modeling TBV. Results with $P < .05$ are considered significant for all statistical analyses. Statistical analyses were performed using Python 2.7 (<https://www.python.org/download/releases/2.7/>), R 3.4.3 (<http://www.r-project.org/>), and Matlab 8.6.0. (MathWorks, Natick, Massachusetts).

RESULTS

Segmentation

CTSeg successfully segmented all 20 images from the manual segmentation dataset. The optimal image-intensity threshold obtained using a random selection of 10 training images was 0.2 for the brain mask and 0.0006 for the intracranial mask. These thresholds were robust when applied to the test set (On-line Fig 1).

Binary masks from CTSeg agreed well with the manual segmentation masks (the DSI was 0.94 ± 0.008 for brain and 0.98 ± 0.002 for the intracranial masks). The gyri and sulci in the superior slices of the brain were well-captured by CTSeg (On-line Fig 2).

Brain Volumetry

Comparison between automated and manual volume estimates is presented in Table 1. The binarized TBV and TIV estimates showed excellent agreement with the manual estimates (ICCs = 0.94 and 0.97, respectively), whereas the probabilistic estimates showed lower agreement (ICCs = 0.74 and 0.71 for TBV and TIV, respectively). TIV estimated using the BET also showed excellent agreement with manual TIV (ICC = 0.94) but was lower than binarized TIV from CTSeg. Binarized CTSeg also had the lowest bias in terms of the percentage difference (Table 1), and in the Bland-Altman plots (Fig 2) for both TIV (mean difference of -0.04L for CTSeg binarized versus -0.05L for BET and -0.13 for CTSeg probabilistic) and TBV (mean difference of 0.02L for CTSeg binarized versus -0.08L for CTSeg probabilistic for TBV). The pattern of the linear fit in the Bland-Altman plots showed that error increases with average volume and, therefore, head size for both estimates of CTSeg. However, the rate of increase was higher for probabilistic estimates than binarized estimates of CTSeg. The BET TIV estimate showed the lowest dependence of error on the average volume but showed larger bias than the binarized CTSeg TIV. Because the binarized CTSeg estimates showed better agreement with manual estimates, proceeding evaluations were made using only the binarized CTSeg method.

Brain Volumetry in AD

CTSeg was applied to the AD dataset containing 152 images. CTSeg successfully segmented 135 images (58 with AD and 77

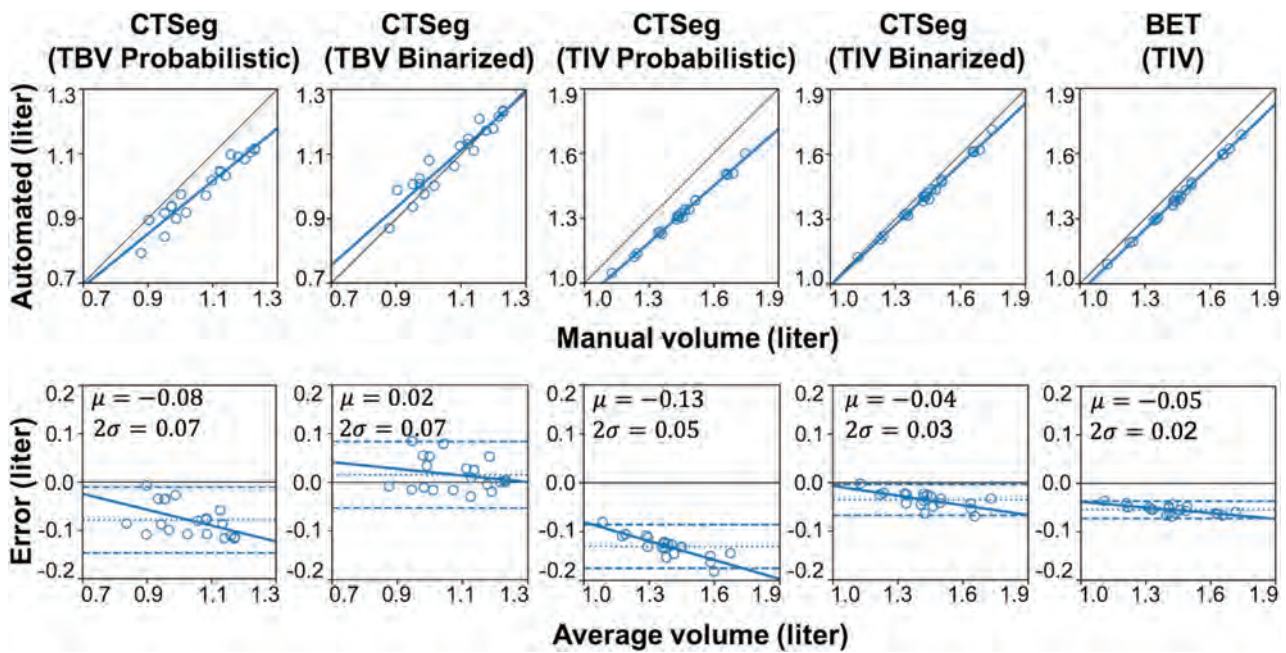


FIG 2. Scatterplots (*upper row*) of automated-versus-manual volume estimates and the linear fit between automated and manual volumes (*thick line*) and the line of equality (*thin line*). Bland-Altman plots (*lower row*) with automated-minus-manual volume differences on the y-axis and the average of automated and manual volumes on the x-axis. Mean difference ± 2 SDs is represented by *dotted* and *dashed horizontal lines*, respectively.

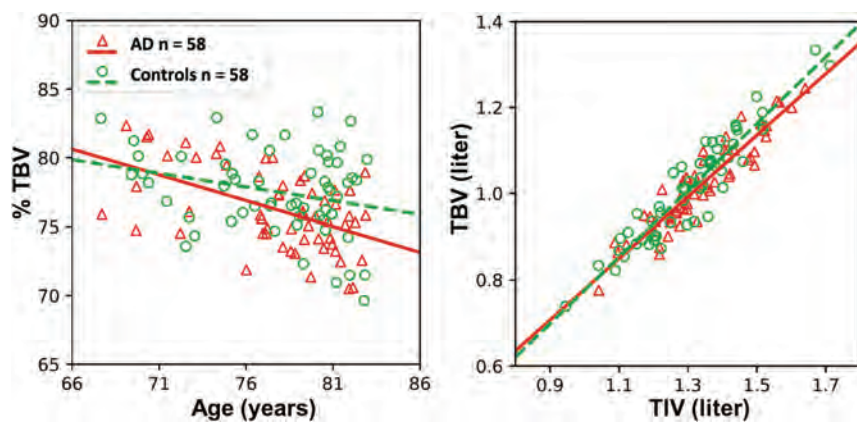


FIG 3. Scatterplot of %TBV (*left*) estimated using CTSeg versus age. Scatterplot of TBV versus TIV (*right*).

controls) of 152 images (88%). Reasons for CTSeg failures are discussed in the next section. After we excluded CTSeg failures, 58 control subjects were optimally age-matched to 58 subjects with AD (a total of $n = 116$ subjects). A paired t test confirmed no significant age difference ($P = .74$) between the 2 groups after age-matching. Group comparisons were performed on binarized volumes estimated from the age-matched subjects. TBV and %TBV computed for AD and controls are presented in Fig 3. Linear fit to %TBV indicated a higher loss with age in the AD group than in controls. We observed significantly lower mean %TBV ($P < .05$) in the AD group (76.24 ± 2.87) compared to the control group (77.52 ± 3.05). A paired t test among %TBVs of the matched subjects also showed a significant difference ($P < .05$) between the two groups. The linear fit in the

main effects model.

Segmentation Failures in the AD Dataset

CTSeg failed to produce acceptable segmentations for 4 of 62 AD images and 13 of 90 control images. Failures in the segmentation included segmentations of nonbrain regions like eyes as brain tissue or segmentation maps that did not resemble brain or intracranial space. On-line Table 3 summarizes the failure rate of CTSeg for different scanners. The overall failure rate was $< 15\%$ across all the scanners.

DISCUSSION

TBV is an important measure for assessing brain atrophy in AD and other neurodegenerative diseases. Although CT is widely

TBV-versus-TIV plot showed that the slope is lower for AD, suggesting a lower TBV-to-TIV ratio in subjects with AD. The results of the linear regression analysis are presented in On-line Table 2. Both age ($P < .001$) and AD diagnosis ($P < .05$) had a significant effect on % TBV. The Age \times AD diagnosis term was insignificant as an interaction term in the linear model. Similar results were observed when TBV was modeled using sex and TIV as additional covariates. Age and AD diagnosis were significant when these variables were modeled as main effects. TIV had a significant contribution in all regression models. Results remained the same when sex was removed from the

used in the clinical setting, segmentation methods to estimate TBV from head CT images are not available. We presented CTSeg, an automated head CT segmentation method, and validated the method by comparing it with manual segmentation.

TBV and TIV from binary CTSeg masks showed better agreement with manual estimates than the TBV and TIV estimates from probabilistic masks. This outcome was expected because the MR imaging–based default tissue probabilistic atlas map (TPM; <https://www.fil.ion.ucl.ac.uk/spm/toolbox/TPM/>) that we used did not model some of the anatomy present in CT images, and binarizing the masks by thresholding mitigated these errors. Additionally, the systematic bias in the TIV estimate using the binary masks was better than TIV estimated using the BET–based method by Muschelli et al.¹³

The utility of CTSeg was demonstrated in a cross-sectional dataset containing AD and control groups. We found that CTSeg-estimated volumes had a significant %TBV ($P < .05$) difference between the AD and control groups in a linear regression model with age, sex, and AD diagnosis as covariates. The sex of the subjects had no significant effect on the %TBV. This finding is in agreement with previous findings using MR images that used TIV to normalize global brain volumes.^{27,28} The average %TBV estimated from AD images was lower than that for matched controls. The statistical insignificance of Age \times AD diagnosis interaction on %TBV can be attributed to the cross-sectional nature of our dataset. We expect that significant TBV group differences can be achieved if longitudinal head CT images of the same subjects are tracked. Furthermore, some of the %TBV variability may be due to not accounting for the duration from the actual onset of AD with respect to the time of the CT acquisition. Another factor that may have contributed to the %TBV is that our controls may have atrophy due to undiagnosed disorders. We expect to see higher group differences in TBV if ADs are compared with disorder free healthy controls. Additionally, when TBV is modeled with TIV as a confounding variable, we observed similar results compared with %TBV. TIV was a significant confounding variable in all the models. Sex was insignificant in all the models, suggesting that correction for TIV removes the structural differences between AD men and women; this finding agrees with previous ones using MR imaging–estimated volumes.²⁹

Unlike MR imaging, the intensity of CT images is standardized and is a measure of radiation attenuation of the tissue. Therefore, we do not think that the scanner variability significantly affected our method. The standardized intensity in CT is, in fact, an advantage and makes the comparison of CT images across scanners easier, compared with MR images. Additionally, we expect the optimal thresholds of CTSeg to be widely applicable because SPM models the tissue intensities separately for each image. We confirmed the optimal threshold using two different approaches: random search and leave-one-out cross-validation. The high Dice similarity index in both approaches demonstrated the robustness of the optimal threshold. However, further validation on a larger dataset is required to verify the robustness of the threshold at different noise levels of CT images.

In CTSeg, we used a standard MR image–based TPM specific to an age range of 18–90 years for the segmentation.³⁰ The CT

template used for the initial registration was developed for an age range of 46–79 years.³¹ Although the age of the subjects used for this study was 67–89 years, we achieved good segmentation accuracy using the standard TPM and the CT template. However, if age-appropriate CT-based TPMs are used, we expect that segmentation accuracy would further improve. The TPM and the CT templates were created using images without brain abnormalities. Therefore, CTSeg assumes that the CT images to be segmented have brains that are free of large structural abnormalities like glioma, stroke, operations, and image artifacts due to beam-hardening and implants. However, CTSeg can be extended for applications for abnormal brain, like identifying lesions.³²

CTSeg marginally overestimated TBV due to the misclassification of dura as brain in the superior slices of the image. This overestimation can be attributed to the low contrast-to-noise ratio among the soft tissues of CT images. Misclassification of the dura is a known problem even in the segmentation of T1-weighted MR images.³³ TIV and TBV estimates from all automated methods tested in this study exhibited a linear dependence of error with head size. Binarizing the probabilistic maps using an optimal threshold slightly reduced this linear dependence to some extent, and this phenomenon can be attributed to several reasons: one reason may be the partial volume effect, in which a single voxel represents ≥ 2 tissues due to the finite spatial resolution of the image.³⁴ The number of voxels at tissue boundaries increases with head size, thereby increasing the error in volume estimation due to the partial volume effect. The linear dependence of error and head size can also be attributed to errors in spatial registration and the allometric effect of the tissue priors. In the case of an intracranial mask, the optimal threshold was very low due to the influence of the high bone intensity (compared with CSF) on the partial volume effect for voxels near the bone-CSF interface.

We computed optimal thresholds for CT images with 5-mm image section thickness, which is the clinical standard for CT images. Because the partial volume effect increases with section thickness,³⁵ thresholds may need to be derived independently for images with different section thicknesses. However, CT images reconstructed with smaller section thicknesses have a lower contrast-to-noise, which can lead to larger errors in the segmentation of brain tissue using CTSeg. Therefore, care should be taken when applying CTSeg to high-resolution images. On close visual inspection, we noted that some brain-CSF boundary regions were misclassified, especially in the left and right regions of the frontal lobe where the brain is closer to the skull and in regions between the brain hemispheres where the dura is present (On-line Fig 2). The misclassifications in intracranial maps (On-line Fig 3) were observed at the boundaries of the intracranial space in the superior and inferior slices, resulting in lower TIV estimates compared with manual segmentation. We also note that the binarized segmentation misclassified some parts of the eyes as the intracranial volume. This shortcoming can be corrected by registering a standard intracranial mask onto the binary intracranial mask obtained using CTSeg and excluding the voxels classified as TIV that are outside the registered standard intracranial mask.³⁶

CONCLUSIONS

We present CTseg to automatically estimate TBV and TIV from nonenhanced head CT images acquired for diagnostic purposes that were originally intended for visual evaluations by radiologists. We show that CTseg can accurately estimate TBV and TIV. Application of CTseg on CT images from subjects with AD and controls provides evidence that CTseg can be used for detection and tracking of global brain atrophy in neurodegenerative diseases. AD does not have symptoms until the mild cognitive impairment stage, which occurs several years after the onset, and CTseg may be used to track brain atrophy in these patients. In addition, CTseg can be applied to clinical CT archives to develop normative brain volumes and to research studies involving neurodegenerative diseases that show global brain volume loss.

ACKNOWLEDGMENTS

We thank the Geisinger Health System Foundation for the financial support.

Disclosures: Stefi A. Baum—UNRELATED: Board Membership: Only in astrophysics, my primary research field; no money paid; Consultancy: only in astrophysics, my primary research field; money paid via the National Aeronautics and Space Administration. Employment: University of Manitoba. Comments: I am a professor of Physics and Astronomy and Dean of Science at the University of Manitoba; Grants/Grants Pending: only in Canada in my primary field of research, Astrophysics from the Natural Sciences and Engineering Research Council of Canada.* Maya Lichtenstein—UNRELATED: Grants/Grants Pending: Biohaven Pharmaceuticals/Alzheimer's Disease Cooperative Study, Comments: Site Principal Investigator for the T2 Protect: Phase 2 Randomized Double Blind Placebo-Controlled Trial to Evaluate the Efficacy and Safety of BHV-4157 in Patients with Mild to Moderate Alzheimer's Disease.* *Money paid to the institution.

REFERENCES

1. Smeets D, Ribbens A, Sima DM, et al. **Reliable measurements of brain atrophy in individual patients with multiple sclerosis.** *Brain Behav* 2016;6:e00518–12 CrossRef Medline
2. Giorgio A, De Stefano N. **Clinical use of brain volumetry.** *J Magn Reson Imaging* 2013;37:1–14 CrossRef Medline
3. Li X, Morgan PS, Ashburner J, et al. **The first step for neuroimaging data analysis: DICOM to NIFTI conversion.** *J Neurosci Methods* 2016;264:47–56 CrossRef Medline
4. Manniesing R, Oei MT, Oostveen LJ, et al. **White matter and gray matter segmentation in 4D computed tomography.** *Sci Rep* 2017;7:119 CrossRef Medline
5. Mandell JG, Langelan JW, Webb AG, et al. **Volumetric brain analysis in neurosurgery, Part 1: particle filter segmentation of brain and cerebrospinal fluid growth dynamics from MRI and CT images.** *J Neurosurg Pediatr* 2015;15:113–24 CrossRef Medline
6. Chen YB, Liao J, Xie R, et al. **Discrimination of metastatic from hyperplastic pelvic lymph nodes in patients with cervical cancer by diffusion-weighted magnetic resonance imaging.** *Abdom Imaging* 2011;36:102–09 CrossRef Medline
7. Liu J, Huang S, Ihar V, et al. **Automatic model-guided segmentation of the human brain ventricular system from CT images.** *Acad Radiol* 2010;17:718–26 CrossRef Medline
8. Ruttimann UE, Joyce EM, Rio DE, et al. **Fully automated segmentation of cerebrospinal fluid in computed tomography.** *Psychiatry Res* 1993;50:101–19 CrossRef Medline
9. Cherukuri V, Ssenyonga P, Warf BC, et al. **Learning based segmentation of CT brain images: application to postoperative hydrocephalic scans.** *IEEE Trans Biomed Eng* 2018;65:1871–84 CrossRef Medline
10. Gupta V, Ambrosius W, Qian G, et al. **Automatic segmentation of cerebrospinal fluid, white and gray matter in unenhanced computed tomography images.** *Acad Radiol* 2010;17:1350–58 CrossRef Medline
11. Kemmling A, Wersching H, Berger K, et al. **Decomposing the Hounsfield unit: probabilistic segmentation of brain tissue in computed tomography.** *Clin Neuroradiol* 2012;22:79–91 CrossRef Medline
12. Imabayashi E, Matsuda H, Tabira T, et al; Japanese Alzheimer's Disease Neuroimaging Initiative. **Comparison between brain CT and MRI for voxel-based morphometry of Alzheimer's disease.** *Brain Behav* 2013;3:487–93 CrossRef Medline
13. Muschelli J, Ullman NL, Mould WA, et al. **Validated automatic brain extraction of head CT images.** *Neuroimage* 2015;114:379–85 CrossRef Medline
14. Aguilar C, Edholm K, Simmons A, et al. **Automated CT-based segmentation and quantification of total intracranial volume.** *Eur Radiol* 2015;25:3151–60 CrossRef Medline
15. Jenkins R, Fox NC, Rossor AM, et al. **Intracranial volume and Alzheimer disease.** *Arch Neurol* 2000;57:220–24 CrossRef Medline
16. Irimia A, Maher AS, Rostovsky KA, et al. **Brain segmentation from computed tomography of healthy aging and geriatric concussion at variable spatial resolutions.** *Front Neuroinform* 2019;13:9 CrossRef Medline
17. Ashburner J, Friston KJ. **Unified segmentation.** *Neuroimage* 2005;26:839–51 CrossRef Medline
18. Centers for Disease Control and Prevention. **International Classification of Diseases, Ninth Revision (ICD-9).** National Center for Health Statistics. <https://www.cdc.gov/nchs/icd/icd9.htm>. Accessed November 8, 2019
19. Yushkevich PA, Piven J, Hazlett HC, et al. **User-guided 3D active contour segmentation of anatomical structures: significantly improved efficiency and reliability.** *Neuroimage* 2006;31:1116–28 CrossRef Medline
20. Nordenskjöld R, Malmberg F, Larsson EM, et al. **Intracranial volume estimated with commonly used methods could introduce bias in studies including brain volume measurements.** *Neuroimage* 2013;83:355–60 CrossRef Medline
21. Dice LR. **Measures of the amount of ecologic association between species.** *Ecology* 1945;26:297–302 CrossRef
22. Bland JM, Altman D. **Statistical methods for assessing agreement between two methods of clinical measurement.** *Lancet* 1986;1:307–10
23. McGraw KO, Wong SP. **Forming inferences about some intraclass correlation coefficients.** *Psychological Methods* 1996;1:30–46 CrossRef
24. Massey FJ. **The Kolmogorov-Smirnov test for goodness of fit.** *J Am Stat Assoc* 1951;46:68–78 CrossRef
25. Ho DE, Imai K, King G, et al. **MatchIt: nonparametric preprocessing for parametric causal inference.** <https://www.rdocumentation.org/packages/MatchIt/versions/3.0.2/topics/matchit>. Accessed 20 Jan, 2020
26. Core Team R. **R: A Language and Environment for Statistical Computing.** Vienna: R Foundation for Statistical Computing; 2014
27. Smith CD, Chebrolu H, Wekstein DR, et al. **Age and gender effects on human brain anatomy: a voxel-based morphometric study in healthy elderly.** *Neurobiol Aging* 2007;28:1075–87 CrossRef Medline
28. Kruggel F. **MRI-based volumetry of head compartments: normative values of healthy adults.** *Neuroimage* 2006;30:1–11 CrossRef Medline
29. Voevodskaya O, Simmons A, Nordenskjöld R, et al; Alzheimer's Disease Neuroimaging Initiative. **The effects of intracranial volume adjustment approaches on multiple regional MRI volumes in healthy aging and Alzheimer's disease.** *Front Aging Neurosci* 2014;6:264 CrossRef
30. Mazziotta J, Toga A, Evans A, et al. **A probabilistic atlas and reference system for the human brain: International Consortium for Brain Mapping (ICBM).** *Philos Trans R Soc Lond, B Biol Sci* 2001;356:1293–322 CrossRef Medline

31. Rorden C, Bonilha L, Fridriksson J, et al. **Age-specific CT and MRI templates for spatial normalization.** *Neuroimage* 2012;61:957–65 CrossRef Medline
32. Cabezas M, Oliver A, Lladó X, et al. **A review of atlas-based segmentation for magnetic resonance brain images.** *Comput Methods Programs Biomed* 2011;104:e158–77 CrossRef Medline
33. Viviani R, Pracht ED, Brenner D, et al. **Multimodal MEMPRAGE, FLAIR, and R2* segmentation to resolve dura and vessels from cortical gray matter.** *Front Neurosci* 2017;11:258 CrossRef Medline
34. Tohka J, Zijdenbos A, Evans A. **Fast and robust parameter estimation for statistical partial volume models in brain MRI.** *Neuroimage* 2004;23:84–97 CrossRef Medline
35. Souza A, Udupa JK, Saha PK. **Volume rendering in the presence of partial volume effects.** *IEEE Trans Med Imaging* 2005;24:223–35 CrossRef Medline
36. Malone IB, Leung KK, Clegg S, et al. **Accurate automatic estimation of total intracranial volume: a nuisance variable with less nuisance.** *Neuroimage* 2015;104:366–72 CrossRef Medline

Metal Artifact Reduction in Head CT Performed for Patients with Deep Brain Stimulation Devices: Effectiveness of a Single-Energy Metal Artifact Reduction Algorithm

Y. Nagayama, S. Tanoue, S. Oda, D. Sakabe, T. Emoto, M. Kidoh, H. Uetani, A. Sasao, T. Nakaura, O. Ikeda, K. Yamada, and Y. Yamashita

ABSTRACT

BACKGROUND AND PURPOSE: Deep brain stimulation electrodes induce massive artifacts on CT images, deteriorating the diagnostic value of examinations. We aimed to investigate the usefulness and potential limitations of a single-energy metal artifact reduction algorithm in head CT performed in patients with implanted deep brain stimulation devices.

MATERIALS AND METHODS: Thirty-four patients with deep brain stimulation (bilateral, $n = 28$) who underwent head CT on a 320-detector row scanner and whose images were reconstructed with and without single-energy metal artifact reduction at the examinations were retrospectively included. The severity of artifacts around electrodes was assessed objectively using SDs and an artifact index. Two radiologists subjectively evaluated the severity of artifacts from electrodes, the visibility of electrode localization and surrounding structures, and overall diagnostic confidence on 4-point scales. Background image quality (GM-WM contrast and image noise) was subjectively and objectively assessed. The presence and location of artifacts newly produced by single-energy metal artifact reduction were analyzed.

RESULTS: Single-energy metal artifact reduction provided lower objective and subjective metal artifacts and improved visualization of electrode localization and surrounding structures and diagnostic confidence compared with non-single-energy metal artifact reduction images, with statistical significance (all, $P < .01$). No significant differences were observed in GM-WM contrast and image noise (all, $P \geq .11$). The new artifacts from single-energy metal artifact reduction were prominently observed in patients with bilateral deep brain stimulation at high convexity, possibly induced by deep brain stimulation leads placed under the parietal scalp.

CONCLUSIONS: Single-energy metal artifact reduction substantially reduces the metal artifacts from deep brain stimulation electrodes and improves the visibility of intracranial structures without affecting background image quality. However, non-single-energy metal artifact reduction images should be simultaneously reviewed to accurately assess the entire intracranial area, particularly in patients with bilateral deep brain stimulation.

ABBREVIATIONS: DBS = deep brain stimulation; MAR = metal artifact reduction; SEMAR = single-energy metal artifact reduction

Deep brain stimulation (DBS) electrode implantation has been widely performed as an established surgical procedure for the treatment of various movement disorders such as Parkinson disease, medically intractable essential tremor, and dystonia.¹ DBS has also been increasingly used for epilepsy, neuropathic pain, and psychiatric disorders.² The main targets of

DBS are the subthalamic nucleus, globus pallidus pars interna, and ventral intermediate nucleus of the thalamus.^{1,2} CT is fast, easily accessible, and less expensive compared with MR imaging and is often used for evaluating the contact location of electrodes, surgical complications, and other intracranial abnormalities not related to a surgical procedure in patients implanted with DBS devices. However, metal artifacts induced by the electrodes usually hamper the visualization of implants and the surrounding intracranial structures, thereby increasing the potential risk of missing relevant findings and deteriorating the diagnostic utility of the examination.³

Metal artifacts are mainly introduced by 2 different physical phenomena: photon starvation as a consequence of a complete x-ray photon absorption and beam-hardening caused by the preferential absorption of low-energy photons.⁴ The degree of x-ray photon absorption and the resulting physical effects on CT

Received August 26, 2019; accepted after revision November 15.

From the Department of Diagnostic Radiology (Y.N., S.O., M.K., H.U., A.S., T.N., O.I., Y.Y.), Graduate School of Medical Sciences, and Departments of Neurosurgery (K.Y.) and Diagnostic Radiology (S.T.), Graduate School of Life Sciences, Kumamoto University, Kumamoto, Japan; and Department of Central Radiology (D.S., T.E.), Kumamoto University Hospital, Kumamoto, Japan.

Please address correspondence to Yasunori Nagayama, MD, PhD, Department of Diagnostic Radiology, Graduate School of Medical Sciences, Kumamoto University, 1-1-1, Honjo, Chuo-ku, Kumamoto 860-8556, Japan; e-mail: y.nagayama1980@gmail.com

<http://dx.doi.org/10.3174/ajnr.A6375>

Table 1: Patient and device characteristics

	Mean \pm SD or No. (%)
Age (yr)	68.0 \pm 10.3
Male/female ratio	10 (29.4):24 (70.6)
Underlying disease	
Parkinson disease	21 (61.8)
Essential tremor	6 (17.6)
Dyskinesia	5 (14.7)
Others	2 (5.9)
Unilateral/bilateral DBS	6 (17.6)/28 (82.4)
DBS lead model	
Model 3387/3389 (Medtronic)	53 (85.5)/9 (14.5)
Targets of DBS	
STN/GPi/Vim	42 (67.7)/11 (17.7)/9 (14.5)

Note:—GPi indicates globus pallidus internal; STN, subthalamic nucleus; Vim, ventral intermediate nucleus of thalamus.

images depend on the composition, size, and the shape of the metallic hardware.⁵⁻⁷ Small implants made of metal having a relatively low atomic number, such as a surgical clip made of titanium (atomic number 22), may cause minor beam-hardening.⁶⁻⁸ In contrast, hardware made of metals having a high atomic number, such as DBS electrodes made of platinum (atomic number 78) and iridium (atomic number 77), usually cause severe bright and dark streak artifacts due to photon starvation, deteriorating the image quality and diagnostic values of the CT examination.^{6,7}

Several techniques, including increased tube voltage, tube current, and application of high kiloelectron volt virtual monoenergetic imaging from dual-energy CT, can aid in the reduction of metal artifacts.^{6,7} However, these approaches have limited value for handling photon starvation induced by large or high atomic number metallic implants.^{6,9,10} As an alternative approach, a single-energy metal artifact reduction (SEMAR) algorithm, a raw data-based metal artifact reduction (MAR) algorithm used in conventional single-energy CT, has been recently developed.¹¹ This algorithm removes severe metal artifacts induced by photon starvation using multiple steps of data segmentation and interpolation along with repeat forward and back projections in the projection and image data domains. Thus far, a few studies have shown that SEMAR can substantially improve the image quality by reducing the metal artifacts in several clinical conditions.¹²⁻¹⁵ However, no prior investigations have evaluated the added value and possible limitations of using the SEMAR algorithm for head CT performed on the subgroup of patients implanted with DBS devices, in which strong metal artifacts have been observed.

This study aimed to investigate the impact of the SEMAR algorithm on the subjective and objective image quality of head CT performed in patients implanted with DBS devices.

MATERIALS AND METHODS

This retrospective study was approved by the institutional review board (Kumamoto University), and the requirement for written informed consent was waived.

Patients

Using our radiology data base, we retrospectively screened patients for inclusion among those implanted with DBS devices

who underwent noncontrast head CT between January 2016 and December 2018. Our inclusion criteria were the following: 1) older than 18 years of age; 2) use of a standardized image-acquisition protocol on a 320-detector row multidetector CT system, as detailed later; and 3) absence of other metallic materials possibly affecting the artifact analysis. In total, 34 patients (10 men, 24 women; mean age, 68.0 \pm 10.3 years) who fulfilled the above criteria were analyzed. Clinical indications for head CT were the evaluation of contact locations and surgical complications ($n = 24$); suspicion of cerebrovascular disease unlikely related to surgical procedures ($n = 7$); head trauma ($n = 1$); and follow-up of known cavernous hemangioma ($n = 1$) or pituitary tumor ($n = 1$). Among the included patients, 28 were implanted with bilateral DBS devices and 6 were implanted with unilateral DBS devices; thus, a total of 62 DBS electrodes were evaluated. Detailed patient demographics are summarized in Table 1.

DBS Implantation Procedure

All patients underwent a standard DBS implantation procedure in accordance with our institution's good clinical practice. In brief, DBS leads (Model-3387 for subthalamic nucleus-DBS and globus pallidus pars interna-DBS or Model-3389 for the ventral intermediate nucleus of the thalamus-DBS, both 40-cm long; Medtronic; Minneapolis, Minnesota), composed of iridium alloy and containing 4 platinum-iridium electrodes near the tip, were placed within the target positions through burr-holes in the skull. After the operator ensured that the electrodes were correctly positioned to control movement symptoms, the excess extracranial DBS leads were looped under the scalp around the burr-holes. The extracranial DBS lead and internal pulse generator subcutaneously implanted in the subclavian portion of the chest were connected with the extension wire running under the skin from the chest to the neck and head (Fig 1, left).

Image Acquisition

A 320-detector row multidetector CT system (Aquilion ONE, VISION Edition; Canon Medical Systems, Otawara, Japan) was used for scanning. Patients were scanned in the supine position with the following parameters: tube voltage, 120 kV(peak); tube current, 260 mA (without automated modulation); rotation time, 1.0 seconds; pitch factor, 0.637; detector collimation, 80 \times 0.5 mm. For each patient, 2 sets of axial images with 5-mm slices were reconstructed: one using the iterative reconstruction technique (adaptive iterative dose reconstruction [AIDR] 3D; Canon Medical Systems) at the noise-reduction level of "weak," referred to as non-SEMAR images, and the second using the AIDR 3D (weak) plus the SEMAR algorithm, referred to as SEMAR images. Both image series were reconstructed when clinical CT was performed as part of the original head CT examination.

Quantitative Image Analysis

Quantitative image analyses were performed in consensus by 2 board-certified radiologists having 11 and 14 years of experience in neuroimaging. In this session, all images were reviewed together by both the radiologists. At the section level exhibiting visually the most pronounced artifacts from electrodes, 4 circular

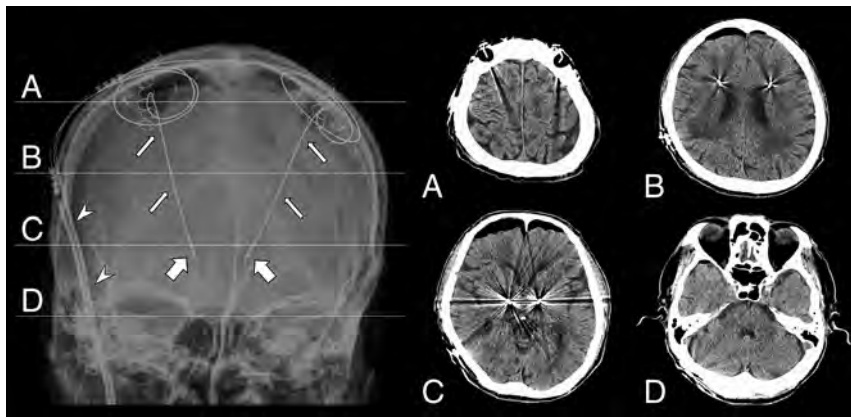


FIG 1. Left, postoperative radiographic image of a 67-year-old man implanted with a bilateral subthalamic nucleus-DBS lead. The DBS system comprises leads (small arrows), electrodes located at lead tips (large arrows), and subcutaneous extension cables (arrowheads) connecting leads to the pulse generator subcutaneously implanted in the right chest wall (not shown). The excess extracranial part of DBS leads was looped under the parietal scalp. The horizontal lines show the section levels of high convexity (A), corona radiata (B), basal ganglia (C), and posterior fossa (D). Right, axial non-SEMAR CT images at the section levels corresponding to the lines drawn in the left radiographic image (A–D), where the presence and degree of artifacts created by SEMAR reconstruction were separately scored.

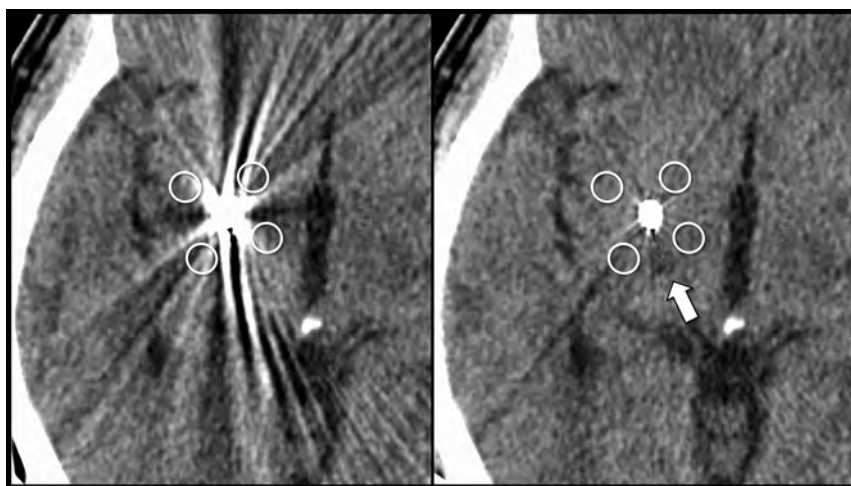


FIG 2. Axial postoperative CT images of a 55-year-old man with dystonia secondary to right thalamic hemorrhage treated by unilateral globus pallidus pars interna-DBS. To quantify the artifact severity, we placed 4 ROIs around the electrodes on non-SEMAR (left) and SEMAR (right) images. The ROI setting was consistent between both images. Compared with non-SEMAR images, SEMAR images substantially reduce artifacts from electrodes and clearly depict the old hemorragic changes in the right thalamus (arrow).

ROIs of approximately 20 mm² were drawn around each electrode (Fig 2).¹³ Additionally, ROIs were placed on the cerebral white matter (approximately 50 mm²) and adjacent cortical gray matter (approximately 10 mm²) on the frontal lobe at the section level not or least affected by the metal artifacts,¹⁰ while the visible artifacts, focal lesions, and adjacent structures were excluded from the ROIs. The mean and SD of the CT attenuation in each ROI were recorded. The averaged SD of the 4 ROIs placed around each DBS electrode was considered an index of the metal artifacts.¹³ For minimizing the effect of background image noise on the metal artifact quantification, we also calculated the artifact index (AI) as follows:^{12,16}

$$AI = \sqrt{[(SD \text{ around the DBS Electrodes})^2 - (\text{Background Image Noise})^2]}.$$

In this study, the SD at the cerebral WM on the frontal lobe was defined as the background image noise in accordance with the literature.¹⁰ The GM-WM contrast was calculated as the difference between the CT attenuations of the GM and WM. This value was divided by the background image noise to calculate the contrast-to-noise ratio. The GM-WM contrast and contrast-to-noise ratio were not measured for the area affected by artifacts because the presence of dark and bright artifacts could make the CT attenuation unreliable for representing brain tissue contrast. The size and location of each ROI were kept constant for non-SEMAR and SEMAR images using the copy and paste function, and quantifications were performed twice to retain data consistency using the averaged values for the analysis. The mean and SD of each quantitative value among 34 patients were calculated for non-SEMAR and SEMAR images.

Qualitative Image Analysis

Two board-certified radiologists having 8 and 11 years of experience who were blinded to the reconstruction algorithms and patient information independently evaluated the non-SEMAR and SEMAR image quality in random order using 4-point scales. Scoring was performed on images without any features to help readers identify the SEMAR and non-SEMAR images. The window level and width were set at 35 and 80 HU, respectively. At the section levels with the most severe artifacts, the severity of metal artifacts from DBS electrodes was assessed as 1 = severe (unacceptable); 2 = moderate (acceptable only under limited conditions); 3 = mild (mostly acceptable); 4 = minimal/absent. The visibility of the electrode localization and intracranial anatomic landmarks (basal ganglia, thalamus, cortico-medullary junction, lateral ventricle, third ventricle, and Sylvian fissure) were scored as 1 = no visualization; 2 = poor (only partially visible); 3 = moderate (mostly visible); and 4 = good (completely visible). At the region not or minimally affected by the artifacts, the background image quality was assessed on the basis of the image noise and GM-WM contrast (1 = undiagnostic; 2 = suboptimal; 3 = average; and 4 = excellent). Then, the overall

diagnostic confidence was graded as 1 = undiagnostic and 2 = diagnostic only under limited conditions; 3 = mostly diagnostic; and 4 = completely diagnostic. Interreader disagreement was resolved by consensus during a subsequent joint reading to determine the final score. The mean and SD of each score obtained from 34 patients were calculated for SEMAR and non-SEMAR images.

Assessment of New Artifacts Induced by SEMAR

Subsequent to the above blinded qualitative assessments, readers were asked to simultaneously review the SEMAR and non-SEMAR images and to determine the presence and degree of new artifacts developed by the SEMAR algorithm on a 4-point scale (1 = severe, unacceptable; 2 = moderate, partially impaired diagnostic confidence; 3 = mild, mostly acceptable; and 4 = absent). In this session, readers were informed about which image was reconstructed with or without SEMAR. The scoring was performed separately for each section level of high convexity, corona radiata, basal ganglia, and posterior fossa. Figure 1 shows a typical cranial radiographic image of patients implanted with bilateral DBS devices (left) and corresponding axial non-SEMAR images at the section levels for the evaluation of a new artifacts (right). Interreader disagreement was resolved by consensus during a joint reading to determine the final score. The mean and SD values of each final score among 34 patients were calculated for SEMAR and non-SEMAR images.

Table 2: Quantitative analysis^a

	Non-SEMAR	SEMAR	P Value
Severity of metallic artifacts			
SD around DBS electrodes (HU)	28.3 ± 9.1	9.8 ± 3.2	<.01
Artifact index (HU)	28.0 ± 9.2	9.0 ± 3.5	<.01
Background image quality			
GM-WM contrast (HU)	11.7 ± 2.7	11.6 ± 2.4	.35
Image noise (HU)	3.8 ± 0.7	3.7 ± 0.7	.17
CNR	3.2 ± 1.0	3.2 ± 0.8	.65

Note:—CNR indicates contrast-to-noise ratio; HU, Hounsfield unit.

^aData are means.

Table 3: Qualitative image analysis^a

	Non-SEMAR	SEMAR	P Value	κ Value	
				Non-SEMAR	SEMAR
The severity of metallic artifacts	1.2 ± 0.4	2.9 ± 0.2	<.01	0.53 (5)	0.65 (1)
Visibility of structures					
Electrode localization	1.5 ± 0.6	3.5 ± 0.5	<.01	0.62 (8)	0.53 (8)
Basal ganglia	1.2 ± 0.4	3.0 ± 0.4	<.01	0.57 (5)	0.61 (5)
Thalamus	1.1 ± 0.3	2.8 ± 0.5	<.01	0.63 (2)	0.66 (5)
Cortico-medullary junction	1.8 ± 0.3	3.4 ± 0.5	<.01	0.51 (7)	0.72 (5)
Sylvian fissure	2.1 ± 0.7	3.7 ± 0.5	<.01	0.58 (8)	0.58 (6)
Lateral ventricle	2.0 ± 0.5	3.8 ± 0.4	<.01	0.70 (4)	0.53 (9)
Third ventricle	1.6 ± 0.5	3.2 ± 0.7	<.01	0.56 (7)	0.58 (6)
Background image quality					
GM-WM contrast	3.2 ± 0.6	3.3 ± 0.6	.11	0.60 (8)	0.68 (7)
Image noise	3.2 ± 0.4	3.2 ± 0.4	.32	0.61 (4)	0.53 (4)
Overall diagnostic confidence	1.4 ± 0.5	3.1 ± 0.4	<.01	0.52 (8)	0.56 (4)

^aData are means. Parentheses show the number of cases for which the subjective score before consensus reading was disputed by both readers. Scale for subjective score: 1 = undiagnostic, 2 = suboptimal, 3 = acceptable, 4 = fully diagnostic.

Statistical Analysis

Statistical analyses were performed using a statistical software package (R statistical and computing software, Version 3.2.2; www.r-project.org/). All numeric values are expressed as mean ± SD, whereas categorical variables are expressed as proportions (percentage). The quantitative measurements between the SEMAR and non-SEMAR images were compared using the paired *t* test after the normality of the distribution was confirmed using the Kolmogorov-Smirnov test. The subjective scores were compared using the Wilcoxon signed rank test. The interobserver agreement was assessed with the κ values (≤0.20 = poor, 0.21–0.40 = fair, 0.41–0.60 = moderate, 0.61–0.80 = substantial, and 0.81–1.00 = perfect). *P* < .05 was considered significant.

RESULTS

Quantitative Analysis

Table 2 summarizes the results of quantitative image analysis. The mean and SD around DBS electrodes and artifact index values for SEMAR images were significantly lower than those for non-SEMAR images (*P* < .01). For the brain segments not affected by metal artifacts, no significant differences in GM-WM contrast, image noise, and contrast-to-noise ratio were observed between both images (*P* = .17–.65).

Qualitative Analysis

Table 3 shows the qualitative image-analysis results. SEMAR images provided significantly fewer metal artifacts and improved visibility of electrode localization and surrounding anatomic structures compared with non-SEMAR images (*P* < .01). Subjective scores for GM-WM contrast (*P* = .11) and image noise (*P* = .32) at the region not affected by metal artifacts were not significantly different between SEMAR and non-SEMAR images. The overall diagnostic confidence was significantly higher in SEMAR compared with non-SEMAR images (*P* < .01). Interobserver agreement was moderate to substantial (κ = 0.51–0.72) for all evaluation criteria. Before the consensus reading, the score disagreement between readers in the visibility of structures, background of image quality, and overall diagnostic confidence ranged from 2/34 to 8/34 cases (5.9%–23.5%) and 1/34 to 9/34 cases (2.9%–26.5%) of non-SEMAR and SEMAR image series, respectively.

Table 4: New artifacts induced by SEMAR^a

Section Levels	All Patients	Subgroup Analysis		P Value
		Unilateral DBS	Bilateral DBS	
High convexity	2.7 ± 0.8	3.7 ± 0.5	2.5 ± 0.6	<.01
Corona radiata	3.9 ± 0.3	4.0 ± 0	3.9 ± 0.4	.30
Basal ganglia	3.9 ± 0.2	4.0 ± 0	3.9 ± 0.3	.49
Posterior fossa	3.7 ± 0.6	4.0 ± 0	3.7 ± 0.6	.15

^aData are means. Scale for subjective score: 1 = severe, 2 = moderate, 3 = mild, 4 = absent.

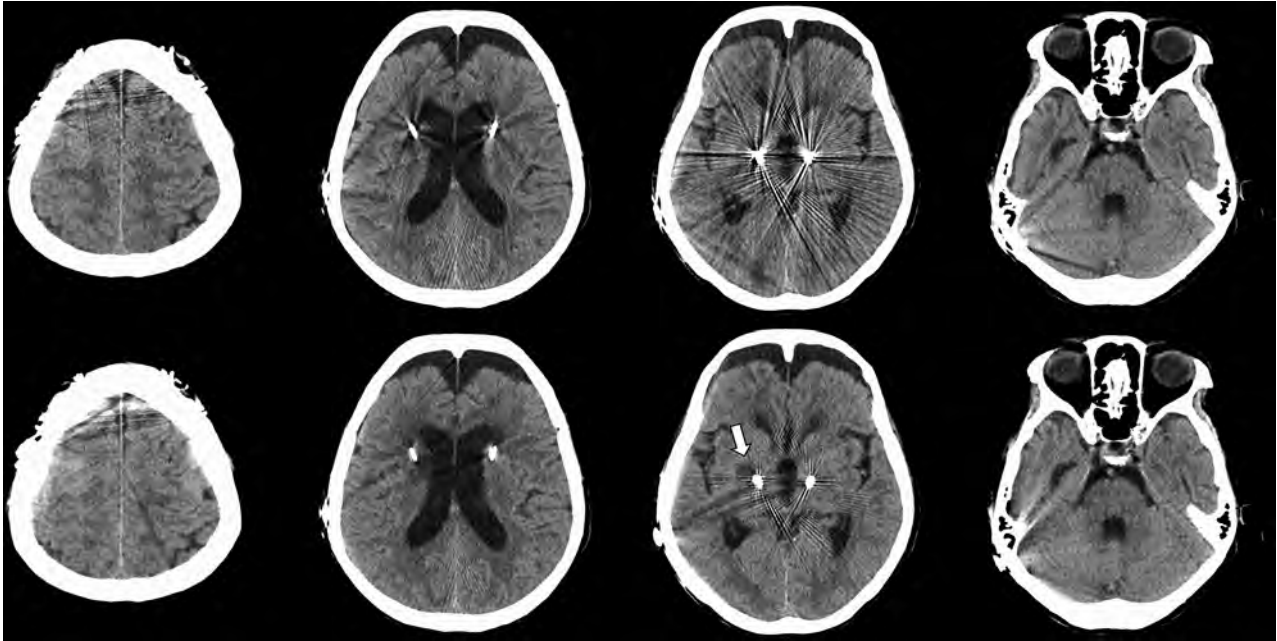


FIG 3. Axial CT images of a 71-year-old woman with Parkinson disease treated with bilateral subthalamic nucleus-DBS. Compared with non-SEMAR images (*upper row*), SEMAR images (*lower row*) substantially reduce artifacts from intracranial leads and electrodes, without compromising the brain tissue contrast. Note that the low-attenuation area of old cerebral hemorrhage around the right DBS lead is clearly visible only in SEMAR images. However, new artifacts possibly induced by looped DBS leads under the parietal scalp are observed in the SEMAR image at the section level of high convexity.

New Artifacts Induced by the SEMAR Algorithm

During simultaneous comparisons, new artifacts created by SEMAR, such as smudged fuzzy high-attenuation areas were prominently observed at the section level of higher convexity in patients implanted with bilateral DBS devices, whereas they were scanty observed at other section levels and in patients implanted with unilateral DBS devices (Table 4). These new artifacts were mainly derived from looped DBS leads placed under the parietal scalp, degrading the depiction of some intracranial structures such as the sulcus and cortico-medullary junction that could be more clearly visualized in non-SEMAR images (Fig 3). Interobserver agreement for assessing new artifacts was moderate to substantial ($\kappa = 0.52$ – 0.67).

DISCUSSION

This study demonstrates that SEMAR could improve the visibility of numerous intracranial anatomic landmarks and the diagnostic confidence of head CT for patients with DBS by reducing the metal artifacts from electrodes. Additionally, we confirmed that subjective and objective background image quality (ie, GM-WM

contrast and image noise) was identical between SEMAR and non-SEMAR images. In contrast, despite the substantial improvement in the overall diagnostic confidence, the SEMAR algorithm was found to potentially introduce new artifacts, particularly at the area with higher convexity in patients with bilateral DBS.

The usefulness of SEMAR has been noted for patients with several types of metallic implants,^{12–15,17} while only 2 studies have addressed its feasibility for cranial CT.^{14,15} Pan et al¹⁴ demonstrated that SEMAR could reduce the artifacts from neurosurgical clips or endovascular coils without affecting the quantitative perfusion parameters compared with non-SEMAR images. Katsura et al¹⁵ also revealed that SEMAR substantially reduced the artifacts from platinum endovascular coils while preserving the arterial iodine contrast by analyzing 20 patients who underwent postinterventional cerebral CT angiography. Despite these suggestive findings, no prior study has applied the SEMAR for non-contrast head CT performed for patients with DBS. Given that the physical effects causing metal artifacts are primarily dependent on the geometry and composition of the metallic devices,^{5–7} the effects of MAR algorithms on the image quality should be analyzed for individual clinical situations. In this context, our study

revealed that SEMAR could be an effective and suitable technique for evaluating intracranial abnormalities around the DBS electrodes, providing the evidence for an additional clinical applicability of this algorithm. As shown in Figs 2 and 3, some findings hidden under severe streaks in non-SEMAR images could be clearly depicted after SEMAR application, possibly yielding improved diagnostic values and optimal patient management while eliminating the necessity for additional MR imaging.

The reconstruction of higher kiloelectron volt virtual monoenergetic imaging from dual-energy CT is another established technique to reduce metal artifacts.^{6,7} This approach is beneficial for suppressing beam-hardening induced by small and low atomic number metals but requires specific dual-energy CT scanners that are less available than the conventional single-energy CT and may be insufficient for removing bright and dark streaks caused by photon starvation from metals with a large mass or higher atomic number such as DBS electrodes.^{6,9,10,17,18} Furthermore, increasing the x-ray energy decreases the soft-tissue contrast (eg, GM-WM contrast) in head CT images due to the reduced photoelectric effect.^{10,19-22} Such a deterioration of low-contrast resolution may obscure relevant anatomic structures and certain intracranial abnormalities.²¹ In contrast, the SEMAR algorithm was primarily developed to mitigate the photon starvation induced by metals on conventional single-energy CT, and it only works on pixels segmented as metal on the original image data based on the attenuation threshold. In line with a few reports showing that the iodine contrast enhancement could be preserved in SEMAR images,^{15,17} we also confirmed that SEMAR could maintain the more subtle attenuation difference of GM-WM contrast (approximately 10 HU) while drastically reducing metal artifacts. The other important advantage of SEMAR relative to the dual-energy CT technique is that artifact reduction can be retrospectively achieved without prospective patient selection, optimizing scan parameters before image acquisition and increasing the radiation dose.

Other than SEMAR, dedicated MAR algorithms have been developed and investigated for patients with DBS.^{10,23} Aissa et al²³ demonstrated that Iterative Metal Artifact Reduction (iMAR; Siemens, Erlangen, Germany) could reduce metal artifacts near DBS electrodes compared with the filtered back-projection algorithm by analyzing 17 patients who underwent head CT after DBS implantation. Furthermore, Große Hokamp et al¹⁰ revealed that O-MAR (Philips Healthcare, Best, the Netherlands) could effectively reduce the artifacts from DBS electrodes compared with the conventional iterative reconstruction or high-kiloelectron volt virtual monoenergetic imaging. Our results were mostly concordant with these preliminary findings despite the substantial differences in imaging properties of each MAR algorithm.^{9,18,24,25}

Previous studies have demonstrated that “new artifacts” could be generated around metallic devices by applying MAR algorithms.^{5,9,18,24} However, their effect on the image quality has not been assessed in SEMAR images in patients implanted with DBS devices.^{10,23} New artifacts from SEMAR were prominently observed in the slices with high convexity levels in patients with bilateral DBS, whereas they were scantily observed at the other section levels and in patients with unilateral DBS. The potential

explanation of this observation is that the image data at high convexity include multiple thin metal fragments (ie, looped excess DBS leads placed under the parietal scalp) in-plane.²⁶ Because SEMAR uses a Hounsfield unit threshold for metal segmentation, these conditions might cause a missed metal segmentation and inaccurate interpolation due to metal-induced scattering, partial volume, and beam-hardening artifacts, particularly in patients with bilateral DBS, thus, introducing new artifacts in final SEMAR images.^{5,6} Although these artifacts could affect only limited anatomic areas and overall diagnostic confidence was substantially improved on SEMAR images, non-SEMAR images should be simultaneously reviewed to avoid misinterpretation.

The past several years have seen an increase in the use of artificial intelligence, such as deep learning in medical imaging, and its feasibility has been exploited for mitigating CT metal artifacts.^{27,28} For instance, convolutional neural networks have been applied to correct the sinogram data corrupted by metals. Preliminary results have suggested that such a deep learning-based MAR approach outperforms existing MAR algorithms in terms of metal artifact suppression and preservation of the boundary between the implanted metal and surrounding tissue, which is usually difficult to correctly recover in commercially available MAR.^{27,28} Validating deep learning based MAR algorithms clinical utility and comparison with existing MAR algorithms for DBS settings may be interesting research subjects in the future.

This study has several limitations. First, this is a retrospective single-center study that includes a relatively small number of patients with DBS. Although our sample size was larger than that of recent studies focusing on MAR in head CT,^{10,15,23} further studies are required to confirm our results. Second, we could not compare the diagnostic performance of SEMAR and non-SEMAR images because of the lack of a sufficient reference standard in most cases. We focused on evaluating subjective and objective image quality to reveal the potential values and limitations of SEMAR as a standard-of-care head CT for DBS settings. Further investigations should be performed to clarify whether the additive use of SEMAR could improve the diagnostic accuracy, patient management, and clinical consequences. Third, in qualitative analysis, the interrater agreement for some variables was relatively limited, possibly due to the inherent nature of subjective assessment. Nevertheless, subsequently performed consensus reading could mitigate the individual assessment bias and make our results generalizable. Last, our results were limited to images obtained with vendor-specific algorithms and our standard-of-care 320-detector row CT protocol and may not be directly transposable to images obtained with other MAR algorithms and different acquisition protocols.^{9,18,24} Because we could not directly compare the performance of SEMAR with that of different MAR techniques, further investigations are warranted to clarify the most effective MAR for handling the artifacts from DBS devices, particularly for institutions equipped with multiple CT scanners.

CONCLUSIONS

The application of the SEMAR algorithm in patients implanted with DBS devices substantially reduces metal artifacts from

electrodes and improves visualization of numerous anatomic landmarks and the diagnostic confidence of head CT. Given that the new artifacts could be introduced by SEMAR, particularly at the high-convexity levels in patients with bilateral DBS, the combined review of SEMAR and non-SEMAR images might be recommended for more accurate image interpretation.

REFERENCES

1. Fasano A, Lozano AM. **Deep brain stimulation for movement disorders: 2015 and beyond.** *Curr Opin Neurol* 2015;28:423–36 CrossRef Medline
2. Holtzheimer PE, Mayberg HS. **Deep brain stimulation for psychiatric disorders.** *Annu Rev Neurosci* 2011;34:289–307 CrossRef Medline
3. Sitz A, Hoevels M, Hellerbach A, et al. **Determining the orientation angle of directional leads for deep brain stimulation using computed tomography and digital x-ray imaging: a phantom study.** *Med Phys* 2017;44:4463–73 CrossRef Medline
4. Barrett JF, Keat N. **Artifacts in CT: recognition and avoidance.** *Radiographics* 2004;24:1679–91 CrossRef Medline
5. Han SC, Chung YE, Lee YH, et al. **Metal artifact reduction software used with abdominopelvic dual-energy CT of patients with metal hip prostheses: assessment of image quality and clinical feasibility.** *AJR Am J Roentgenol* 2014;203:788–95 CrossRef Medline
6. Katsura M, Sato J, Akahane M, et al. **Current and novel techniques for metal artifact reduction at CT: practical guide for radiologists.** *Radiographics* 2018;38:450–61 CrossRef Medline
7. Gjestebly L, de Man BD, Jin Y, et al. **Metal artifact reduction in CT: where are we after four decades?** *IEEE Access* 2016;4:5826–49. <https://ieeexplore.ieee.org/document/7565564>. Accessed April 3, 2019
8. Nagayama Y, Nakaura T, Tsuji A, et al. **Cerebral bone subtraction CT angiography using 80 kVp and sinogram-affirmed iterative reconstruction: contrast medium and radiation dose reduction with improvement of image quality.** *Neuroradiology* 2017;59:127–34 CrossRef Medline
9. Andersson KM, Norrman E, Geijer H, et al. **Visual grading evaluation of commercially available metal artefact reduction techniques in hip prosthesis computed tomography.** *Br J Radiol* 2016;89:20150993 CrossRef Medline
10. Große Hokamp N, Hellerbach A, Gierich A, et al. **Reduction of artifacts caused by deep brain stimulating electrodes in cranial computed tomography imaging by means of virtual monoenergetic images, metal artifact reduction algorithms, and their combination.** *Invest Radiol* 2018;53:424–31 CrossRef Medline
11. Chang YB, Xu D, Zamyatin AA. **Metal artifact reduction algorithm for single energy and dual-energy CT scans.** In: *Proceedings of the 2012 IEEE Nuclear Science Symposium and Medical Imaging Conference Record (NSS/MIC)*, Anaheim, California. October 27 to November 3, 2012:3426–29
12. Yasaka K, Kamiya K, Irie R, et al. **Metal artefact reduction for patients with metallic dental fillings in helical neck computed tomography: comparison of adaptive iterative dose reduction 3D (AIDR 3D), forward-projected model-based iterative reconstruction solution (FIRST) and AIDR 3D with single-energy metal artefact reduction (SEMAR).** *Dentomaxillofac Radiol* 2016;45:20160114 CrossRef Medline
13. Kidoh M, Utsunomiya D, Ikeda O, et al. **Reduction of metallic coil artefacts in computed tomography body imaging: effects of a new single-energy metal artefact reduction algorithm.** *Eur Radiol* 2016;26:1378–86 CrossRef Medline
14. Pan YN, Chen G, Li AJ, et al. **Reduction of metallic artifacts of the post-treatment intracranial aneurysms: effects of single energy metal artifact reduction algorithm.** *Clin Neuroradiol* 2019;29:277–84 CrossRef
15. Katsura M, Sato J, Akahane M, et al. **Single-energy metal artifact reduction technique for reducing metallic coil artifacts on post-interventional cerebral CT and CT angiography.** *Neuroradiology* 2018;60:1141–50 CrossRef Medline
16. Dong Y, Shi AJ, Wu JL, et al. **Metal artifact reduction using virtual monochromatic images for patients with pedicle screws implants on CT.** *Eur Spine J* 2016;25:1754–63 CrossRef Medline
17. Kidoh M, Utsunomiya D, Oda S, et al. **CT venography after knee replacement surgery: comparison of dual-energy CT-based monochromatic imaging and single-energy metal artifact reduction techniques on a 320-row CT scanner.** *Acta Radiol Open* 2017;6:2058460117693463 CrossRef Medline
18. Andersson KM, Nowik P, Persliden J, et al. **Metal artefact reduction in CT imaging of hip prostheses—an evaluation of commercial techniques provided by four vendors.** *Br J Radiol* 2015;88:20140473 CrossRef Medline
19. Pomerantz SR, Kamalian S, Zhang D, et al. **Virtual monochromatic reconstruction of dual-energy unenhanced head CT at 65-75 keV maximizes image quality compared with conventional polychromatic CT.** *Radiology* 2013;266:318–25 CrossRef Medline
20. Zhao XM, Wang M, Wu RZ, et al. **Dual-layer spectral detector CT monoenergetic reconstruction improves image quality of non-contrast cerebral CT as compared with conventional single energy CT.** *Eur J Radiol* 2018;103:131–38 CrossRef Medline
21. Lennartz S, Laukamp KR, Neuhaus V, et al. **Dual-layer detector CT of the head: initial experience in visualization of intracranial hemorrhage and hypodense brain lesions using virtual monoenergetic images.** *Eur J Radiol* 2018;108:177–83 CrossRef Medline
22. Nagayama Y, Nakaura T, Tsuji A, et al. **Radiation dose reduction using 100-kVp and a sinogram-affirmed iterative reconstruction algorithm in adolescent head CT: impact on grey-white matter contrast and image noise.** *Eur Radiol* 2017;27:2717–25 CrossRef Medline
23. Aissa J, Boos J, Schleich C, et al. **Metal artifact reduction in computed tomography after deep brain stimulation electrode placement using iterative reconstructions.** *Invest Radiol* 2017;52:18–22 CrossRef Medline
24. Bolstad K, Flatabo S, Aadnevik D, et al. **Metal artifact reduction in CT, a phantom study: subjective and objective evaluation of four commercial metal artifact reduction algorithms when used on three different orthopedic metal implants.** *Acta Radiol* 2018;59:1110–18 CrossRef Medline
25. Chou R, Li JH, Ying LK, et al. **Quantitative assessment of three vendor's metal artifact reduction techniques for CT imaging using a customized phantom.** *Comput Assist Surg (Abingdon)* 2019;24:34–42 CrossRef Medline
26. Golestanirad L, Kirsch J, Bonmassar G, et al. **RF-induced heating in tissue near bilateral DBS implants during MRI at 1.5T and 3T: the role of surgical lead management.** *Neuroimage* 2019;184:566–76 CrossRef Medline
27. Ghani MU, Karl WC. **Deep learning based sinogram correction for metal artifact reduction.** *Electronic Imaging* 2018;2018:4721–28 CrossRef
28. Zhang Y, Yu H. **Convolutional neural network-based metal artifact reduction in x-ray computed tomography.** *IEEE Trans Med Imaging* 2018;37:1370–81 CrossRef Medline

Spiral T1 Spin-Echo for Routine Postcontrast Brain MRI Exams: A Multicenter Multireader Clinical Evaluation

M.B. Ooi, Z. Li, R.K. Robison, D. Wang, A.G. Anderson III, N.R. Zwart, A. Bakhru, S. Nagaraj, T. Mathews, S. Hey, J.J. Koonen, I.E. Dimitrov, H.T. Friel, Q. Lu, M. Obara, I. Saha, H. Wang, Y. Wang, Y. Zhao, M. Temkit, H.H. Hu, T.L. Chenevert, O. Togao, J.A. Tkach, U.D. Nagaraj, M.C. Pinho, R.K. Gupta, J.E. Small, M.M. Kunst, J.P. Karis, J.B. Andre, J.H. Miller, N.K. Pinter, and J.G. Pipe



ABSTRACT

BACKGROUND AND PURPOSE: Spiral MR imaging has several advantages compared with Cartesian MR imaging that can be leveraged for added clinical value. A multicenter multireader study was designed to compare spiral with standard-of-care Cartesian postcontrast structural brain MR imaging on the basis of relative performance in 10 metrics of image quality, artifact prevalence, and diagnostic benefit.

MATERIALS AND METHODS: Seven clinical sites acquired 88 total subjects. For each subject, sites acquired 2 postcontrast MR imaging scans: a spiral 2D T1 spin-echo, and 1 of 4 routine Cartesian 2D T1 spin-echo/TSE scans (fully sampled spin-echo at 3T, 1.5T, partial Fourier, TSE). The spiral acquisition matched the Cartesian scan for scan time, geometry, and contrast. Nine neuroradiologists independently reviewed each subject, with the matching pair of spiral and Cartesian scans compared side-by-side, and scored on 10 image-quality metrics (5-point Likert scale) focused on intracranial assessment. The Wilcoxon signed rank test evaluated relative performance of spiral versus Cartesian, while the Kruskal-Wallis test assessed interprotocol differences.

RESULTS: Spiral was superior to Cartesian in 7 of 10 metrics (flow artifact mitigation, SNR, GM/WM contrast, image sharpness, lesion conspicuity, preference for diagnosing abnormal enhancement, and overall intracranial image quality), comparable in 1 of 10 metrics (motion artifacts), and inferior in 2 of 10 metrics (susceptibility artifacts, overall extracranial image quality) related to magnetic susceptibility ($P < .05$). Interprotocol comparison confirmed relatively higher SNR and GM/WM contrast for partial Fourier and TSE protocol groups, respectively ($P < .05$).

CONCLUSIONS: Spiral 2D T1 spin-echo for routine structural brain MR imaging is feasible in the clinic with conventional scanners and was preferred by neuroradiologists for overall postcontrast intracranial evaluation.

ABBREVIATIONS: Cart = Cartesian; IQ = image quality; NA = not applicable; SE = spin-echo; TSE = turbo spin-echo

Structural T1-weighted sequences are a fundamental component of routine postcontrast brain MR imaging examinations. These contrast-enhanced images are used for the diagnostic detection and evaluation of abnormal enhancement, including tumors, infections, and inflammatory diseases. Cartesian 2D T1 spin-echo (SE) is widely used as the standard-of-care, though it is relatively slow due to its single phase-encode per shot k -space

coverage, and is not compatible with parallel imaging due to strong free-induction decay artifacts from the refocusing radio-frequency pulse. Two routine speed-up options include Cartesian 2D T1-SE with partial-Fourier k -space coverage, but at the cost of reduced SNR; alternatively, Cartesian 2D T1 turbo spin-echo

Received October 21, 2019; accepted after revision December 10.

From Philips Healthcare (M.B.O., I.E.D., H.T.F., Q.L., H.W., Y.W., Y.Z.), Gainesville, Florida; Barrow Neurological Institute (Z.L., A.G.A., N.R.Z., J.P.K.), Phoenix, Arizona; Mayo Clinic (D.W., J.G.P.), Rochester, Minnesota; Phoenix Children's Hospital (R.K.R., M.T., H.H.H., J.H.M.), Phoenix, Arizona; DENT Neurologic Institute (N.K.P.), Buffalo, New York; Philips Healthcare (A.B., S.N., T.M.), Bangalore, India; Philips Healthcare, (S.H., J.J.K.), Best, the Netherlands; Philips Healthcare (M.O.), Tokyo, Japan; Philips Healthcare (I.S.), Gurgaon, India; University of Michigan (T.L.C.), Ann Arbor, Michigan; Kyushu University Hospital (O.T.), Kyushu, Japan; Cincinnati Children's Hospital (J.A.T., U.D.N.), Cincinnati, Ohio; University of Texas Southwestern Medical Center (M.C.P.), Dallas, Texas; Fortis Memorial Research Institute (R.K.G.), Gurgaon, India; Lahey Hospital and Medical Center (J.E.S., M.M.K.), Burlington, Massachusetts; and University of Washington (J.B.A.), Seattle, Washington.

Paper previously presented, in part, as an oral scientific presentation at: Annual Meeting of the Radiological Society of North America, December 1–6, 2019; Chicago, Illinois; and an oral scientific presentation at: Annual Meeting of the International Society of Magnetic Resonance in Medicine, June 16–21, 2018; Paris, France.

This work is funded, in part, by Philips Healthcare (Z.L., R.K.R., D.W., A.G.A., N.R.Z., J.G.P.).

Please address correspondence to Melvyn B. Ooi, PhD, Barrow Neurological Institute, Keller Center, 350 W Thomas Rd, Phoenix, AZ 85013; e-mail: melvyn.ooi@philips.com

 Indicates article with supplemental on-line table.

 Indicates article with supplemental on-line photos.

<http://dx.doi.org/10.3174/ajnr.A6409>

(TSE) uses an echo-train to cover multiple k -space lines per shot, but at the cost of reduced T1 contrast. A challenge common to all Cartesian methods is flow artifacts originating from CSF/blood flow, which manifest in images as a classic coherent ringing in the phase-encoding direction. These artifacts can obscure lesions and lower overall diagnostic confidence. Flow artifacts are further exacerbated in contrast-enhanced scans due to the hyperintense vascular signal.

Spiral MR imaging, a non-Cartesian technique that uses a spiral k -space trajectory,^{1,2} provides several advantages over routine Cartesian MR imaging. A primary benefit is scan efficiency due to the longer acquisition duration (τ) per shot, which enables a concurrent decrease in scan time and/or an increase in SNR.³ Spirals are also more robust to artifacts such as flow, foldover aliasing, geometric distortions, and Gibbs ringing; this is due to the spiral trajectory's inherently reduced gradient moments,⁴ center of k -space oversampling, nondedicated phase-encoding direction, and incoherent dispersion of unwanted signal changes between spiral arms.⁵ Our spiral implementation is Dixon-based by design,⁶ therefore, the generation of separate water and fat images is another intrinsic benefit. Spiral MR imaging has demonstrated unique advantages across a wide range of applications, including diffusion,⁷ perfusion,⁸ fMRI,⁹ and real-time speech.¹⁰ These and previous studies were predominantly performed in research settings, on healthy volunteers, required specialized hardware/reconstruction approaches that are not practical in a high-throughput clinical environment, and/or otherwise described functional (rather than structural) applications with lower image-resolution requirements. Despite its benefits, spiral MR imaging has therefore not gained widespread clinical adoption due to its greater demand on system fidelity (eg, B_0 homogeneity, gradient accuracy/precision) and reconstruction complexity.

We present here a multicenter clinical evaluation of spiral MR imaging as an alternative to Cartesian MR imaging for routine structural brain examinations, based on previous sequence optimization efforts and earlier clinical feasibility results.¹¹⁻¹³ Spiral 2D T1-SE is compared with Cartesian 2D T1-SE/TSE protocols that are representative of standard-of-care postcontrast brain MR imaging. A multireader study assessed relative performance based on 10 metrics of image quality, artifact prevalence, and diagnostic benefit.

MATERIALS AND METHODS

Industrial Support

The spiral pulse sequence and reconstruction algorithm is a collaborative "work-in-progress," developed by the Barrow Neurological Institute and Mayo Clinic (Z.L., D.W., N.R.Z., R.K.R., A.G.A., M.B.O., J.G.P.) and funded, in part, by Philips Healthcare.

Patient Population

This prospective multicenter study was approved by the institutional review board at each site and was Health Insurance Portability and Accountability Act-compliant. Subjects were scanned at 7 clinical sites from April 2018 to November 2018, and informed consent was obtained from each subject (4 sites) or waived (3 sites) as a minimum-risk study to add the

proposed sequence at the end of a routine brain MR imaging examination.

Patients undergoing clinically indicated postcontrast routine brain MR imaging examinations were eligible for study inclusion. One hundred subjects were initially imaged. Of these, 12 subjects were excluded due to technical factors, protocol deviations that invalidated scan comparisons, and severe bulk motion. Thus, 88 subjects met the inclusion criteria (54 women, 34 men; mean age, 45 ± 22 years) and were subsequently analyzed.

Imaging Methods

The study was performed on five 3T and three 1.5T MR imaging scanners (Ingenia; Philips Healthcare, Best, the Netherlands) with a standard hardware configuration, using a 15- or 32-channel head coil as per the routine of each site. The spiral 2D T1-SE (spiral-SE) sequence consisted of conventional 90° - 180° radiofrequency pulses, followed by a fully sampled spiral-out readout¹⁴ with acquisition duration $\tau \sim 12/22$ ms for 3T/1.5T. Crusher gradients around the 180° refocusing radiofrequency pulse provided additional flow signal suppression and black-blood contrast.¹¹ The spiral implementation is Dixon-based by design, with samples acquired at 2 or 3 unique TEs to encode chemical-shift information, in order to account for the different blurring properties of water/fat. On-line reconstruction (~ 1 second/slice) was performed using a conjugate gradient algorithm for joint off-resonance deblurring and Dixon-based water/fat separation,⁶ resulting in the intrinsic generation of separate water and fat (along with in-phase, out-of-phase) image series. A B_0 prescan (~ 30 seconds) was acquired before the spiral scan for use in reconstruction.

Spiral-SE was evaluated against 4 different Cartesian 2D T1-SE (Cart-SE) based protocols, which reflected the standard-of-care of each site. These 4 protocol comparison groups (G1-G4) were G1, fully sampled Cart-SE at 3T, and G2, at 1.5T; alternatively, as speed-up options, sites used G3, Cart-SE with half scan for partial k -space coverage, and G4, Cartesian 2D T1-TSE with an echo-train to cover multiple k -space lines per shot. Spiral-SE protocols were designed to match each group of G1-G4 for scan time, geometry, and contrast-related parameters as closely as possible, given the constraints of each sequence. Typical parameters for the matching pairs of spiral-versus-Cartesian scans in G1-G4 are shown in the On-line Table.

For each subject, one of the G1-G4 protocols was acquired, resulting in a matching pair of postcontrast spiral-versus-Cartesian scans for subsequent evaluation. The pair of scans was alternately acquired in forward/reverse order (i.e. spiral followed by Cartesian, or Cartesian followed by spiral) to minimize bias related to delayed enhancement, and added to the end of the routine brain examination to minimize disruption to the clinical routine.

Radiologic Assessment

Nine neuroradiologists, representing the participating sites, each performed an independent review of all 88 subjects. For each subject, the matching pair of spiral and Cartesian scans was compared side-by-side and scored relative to one another on 10 image quality (IQ) metrics (M1-M10): M1, flow artifact

mitigation; M2, subjective SNR; M3, GM/WM contrast; M4, image sharpness or delineation of brain structures; M5, individual lesion conspicuity, marked not applicable (NA) if no visible lesions; M6, diagnostic preference for detecting abnormal enhancement, which is the clinical use case of the sequence, in which only diagnostically relevant differences should be considered; M7, overall IQ, intracranial compartment only; M8, motion artifact mitigation; M9, susceptibility artifact mitigation; and M10, overall IQ, extracranial compartment only.

M1–M9 were evaluated in the intracranial compartment only, defined as the brain parenchyma, meninges, and blood vessels. M10 was evaluated in the extracranial compartment only, defined as the skull base and below, as well as the nasal cavity, paranasal sinuses, temporal bone, and orbits. This evaluation was performed to align with the primary clinical use case of the T1-SE/TSE protocol for intracranial compartment evaluation, while providing a summary metric for extracranial compartment assessment. Each metric was scored on an ordinal 5-point Likert scale: 1 = Cartesian is much better; 2 = Cartesian is better; 3 = Cartesian is comparable with spiral; 4 = spiral is better; 5 = spiral is much better. Cartesian and spiral scans were anonymized as “method A” and “method B,” though for the spiral scans, both water-only and water+fat Dixon image series were provided for review.

Statistical Analysis

Statistical analysis was performed in R statistical and computing software (Version 3.5.1; <http://www.r-project.org/>), and data preparation/plotting, in Python (Version 3.6.7; <https://www.python.org/downloads/release/python-367/>), with the consultation of a biostatistician (M.T.). Nonparametric statistics were used due to the ordinal scoring data. The one-sample Wilcoxon signed rank test was used to evaluate the relative performance of spiral versus Cartesian. Here, we tested the null hypothesis $H_0: \Delta = 3$ versus $H_1: \Delta \neq 3$, where Δ is the median score over the subject population for a given IQ metric; because a score of 3 = Cartesian is comparable with spiral, null hypothesis rejection H_1 suggests that the scoring distribution is not symmetric about 3 but is in favor of either spiral ($\Delta > 3$) or Cartesian ($\Delta < 3$). The Kruskal-Wallis test was used to assess intergroup similarity (H_0) or difference (H_1) between the distributions of G1–G4, followed by post hoc analysis with the Dunn test for multiple pair-wise comparisons to determine the relative performances within G1–G4. Wilcoxon and Kruskal-Wallis tests were evaluated for each IQ metric M1–M10 using the populations over all subjects ($n = 88$) and also separated by protocol group (G1–G4, $n = 42, 20, 13, 13$, respectively). The median reviewer score was used for a given subject. A P value $< .05$ was chosen for statistical significance (H_1). To control for increased type I error incurred by multiple tests, we adjusted all P values for false discovery rate using the Benjamini-Hochberg procedure. Inter-reviewer agreement was assessed by the κ statistic.

RESULTS

Figures 1–4 show images representative of the multireader scoring results for all 10 metrics. Most images are from G1, which is

the most direct comparison of fully-sampled single phase-encoded spiral versus Cartesian and the largest sample size; images from other protocol groups are shown when appropriate. On-line Figures 1–4 contain histograms of all scores for each of M1–M10. Images in Figs 1–4 were selected to reflect the histogram trends in On-line Figs 1–4, respectively, and provide complementary information when viewed together as described below.

Figure 1 and On-line Fig 1 illustrate flow artifact mitigation (M1). The most prominent flow artifacts, either due to CSF or blood flow, are often observed in the posterior cranial fossa (Fig 1). These artifacts severely corrupt Cartesian images (bottom row), manifesting as coherent ringing artifacts in the left-right phase-encoding direction, most commonly around the brain stem, transverse sinuses, sagittal sinuses, carotid arteries, and their branches. Matching spirals (top row) demonstrate significant/consistent flow artifact reduction in these areas. This benefit also extends to the middle cranial fossa (On-line Fig 1A). On-line Fig 1B provides a histogram of all M1 scores and is described in more detail in the legend.

Figure 2 and On-line Fig 2 summarize metrics related to general image attributes: subjective SNR (M2), GM/WM contrast (M3), and image sharpness (M4). Histogram distributions (On-line Fig 2) are right-skewed and qualitatively favorable for spiral across all 3 metrics. Subjective SNR (On-line Fig 2A) shows an elevated bar for G3 with a score of 5, corresponding to a higher relative benefit for spiral-versus-Cartesian SE with half scan, compared with protocols G1, G2, G4. Similarly, GM/WM contrast (On-line Fig 2B) shows an elevated bar for G4 with a score of 5, corresponding to a higher relative benefit for spiral-versus-Cartesian TSE, compared with protocols G1, G2, G3. Figure 2 highlights these benefits for protocol groups G1 (fully-sampled reference), G3 (elevated SNR), and G4 (elevated contrast).

Figure 3 and On-line Fig 3 demonstrate spiral improvement for clinically related metrics: individual lesion conspicuity (M5) and diagnostic preference for detecting abnormal enhancement (M6), together with a summary score for overall intracranial IQ (M7). Histograms (On-line Fig 3) show right-skewness in favor of spiral across all 3 metrics. Figure 3 highlights the increased diagnostic confidence for spiral in areas with pathologies, including areas with superior suppression of strong flow-ringing artifacts (column 1), removal of more subtle vascular artifacts that may otherwise be confounded with enhancing lesions (columns 2 and 3), and improved lesion visualization due to overall higher SNR (columns 4–6).

Figure 4 and On-line Fig 4 show metrics for motion artifacts (M8), susceptibility artifacts (M9), and overall extracranial IQ (M10). Histograms (On-line Fig 4) show spiral performed comparable with (M8) or poorer than Cartesian (M9, M10). Figure 4A shows increased susceptibility artifacts for spiral around areas of artificially/naturally occurring magnetic susceptibility, which can manifest as signal loss and residual blurring. Similar susceptibility artifacts are observed in the extracranial space for spiral, as reflected in the M10 scores in favor of Cartesian (On-line Fig 4C). Further inspection of On-line Fig 4C shows that ~15% of all cases were given a score of 4, predominantly by 2 reviewers (orange, green). These 2 reviewers commented that despite the

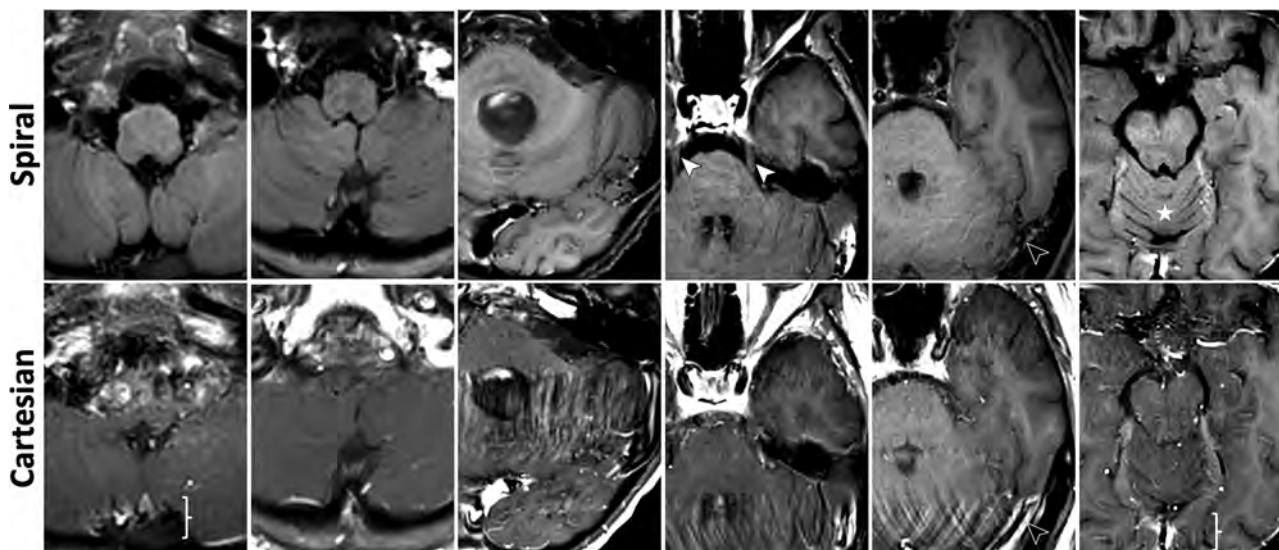


FIG 1. Images illustrating metrics: flow artifact mitigation (M1). See On-line Fig 1 for corresponding histogram of scores. Spirals demonstrate significant and consistent flow artifact mitigation in the inferior slices. All images are taken from G1. *Columns 1–2*, Strong flow artifacts around the brain stem and sagittal sinus (*brace*) in Cartesian are effectively suppressed in spirals, where the previously obscured brain stem and cerebellum are now clearly visualized. *Column 3–5*, Cartesians exhibit severe flow-ringing artifacts in the phase-encoding direction (*left-right*) originating from the transverse sinuses and carotid arteries. Spirals produce significantly cleaner images, making visible the cerebellum, anterior temporal lobe, and trigeminal nerves (*white arrows*); residual flow artifacts in spiral manifest as faint circular ripples emanating from the flow source (*black arrows*). *Column 6*, Flow signal in the branches of the carotid, vertebral arteries, and the straight sinus (*brace*) is well-suppressed in spiral, providing finer structural details of the frontal basal area and cerebellum (*star*). In Figs 1–4, all spiral images are water-only for brevity.

generally better extracranial IQ of Cartesian, spiral was preferred on a case-by-case basis due to its intrinsic Dixon capability. Figure 4B highlights this advantage, in which spiral water-only images are beneficial for delineating pathologies in/around fat tissue.

Figure 5 summarizes the statistical analysis. The Wilcoxon signed rank test showed that spiral performs better than Cartesian (green) in 7/10 metrics, M1–M7, across all protocol groups; spiral is comparable with Cartesian (blue) in 1/10 metric, M8, across all protocol groups; spiral performs poorer than Cartesian (red) in 2/10 metrics, M9–M10, across all protocol groups, with the exception of M9, G4 (blue). The Kruskal-Wallis with Dunn post hoc analysis provides statistical confirmation of the interprotocol trends observed in the histograms. M2, G3 showed relatively better performance than all other protocols, consistent with the elevated bar in On-line Fig 2A. Similarly, M3, G4 performed better relative to all other protocols, matching the elevated bar in On-line Fig 2B. Inter-reviewer agreement scores based on the original 5-point scale (κ_{5cat}) are “slight” to “fair.” To further investigate inter-reviewer agreement, all scores were aggregated to a 3-point scale, as either Cartesian is much better or better (scores = 1, 2, respectively), Cartesian is comparable with spiral (score = 3, unchanged), or spiral is better or much better (scores = 4, 5, respectively). Inter-reviewer agreement scores based on this 3-point scale (κ_{3cat}) improved to “moderate” or “substantial” for some metrics, suggesting that a source of inter-reviewer difference is due to assessing “better” versus “much better” conditions rather than an entirely different preference between spiral or Cartesian. The Wilcoxon signed rank test was repeated with scores based on the 3-point scale

(On-line Figure 5), which did not change the overall conclusions of Figure 5.

DISCUSSION

This multicenter clinical evaluation of spiral MR imaging was conducted at sites that represent a variety of MR imaging expert levels, from luminary research institutions to hospitals with limited research support. Furthermore, spiral acquisition and reconstruction were performed on both 3T and 1.5T scanners with standard hardware configurations. To the best of our knowledge, this multicenter study is the first of its scale and kind to demonstrate the clinical feasibility of spiral MR imaging for routine structural imaging.

Spirals were superior to standard-of-care Cartesian in 7 of 10 assessed metrics. From M1 to M5, the strongest consensus benefit of spiral was flow artifact mitigation, followed by subjective SNR and GM/WM contrast. These cumulative benefits enabled clearer visualization of brain structures and lesions, resulting in better scores in M6–M7 for overall diagnostic preference and intracranial image quality, respectively. The most prominent areas of benefit included the middle cranial fossa, deep gray matter, and posterior cranial fossa. In the middle cranial fossa, reduced flow artifacts around the carotid arteries, in particular, increased diagnostic confidence for temporal lobe pathologies. In deep gray matter, increased SNR, contrast, and lack of flow from the third ventricle and small vessels improved demarcation of the basal ganglia and adjacent white matter tracts. In the posterior cranial fossa, significant flow artifact mitigation from the vertebrobasilar arteries, venous sinuses, fourth ventricle, and foramen magnum dramatically improved image quality of the brain stem, cerebellum, and cranial nerves. Improved anatomic visualization

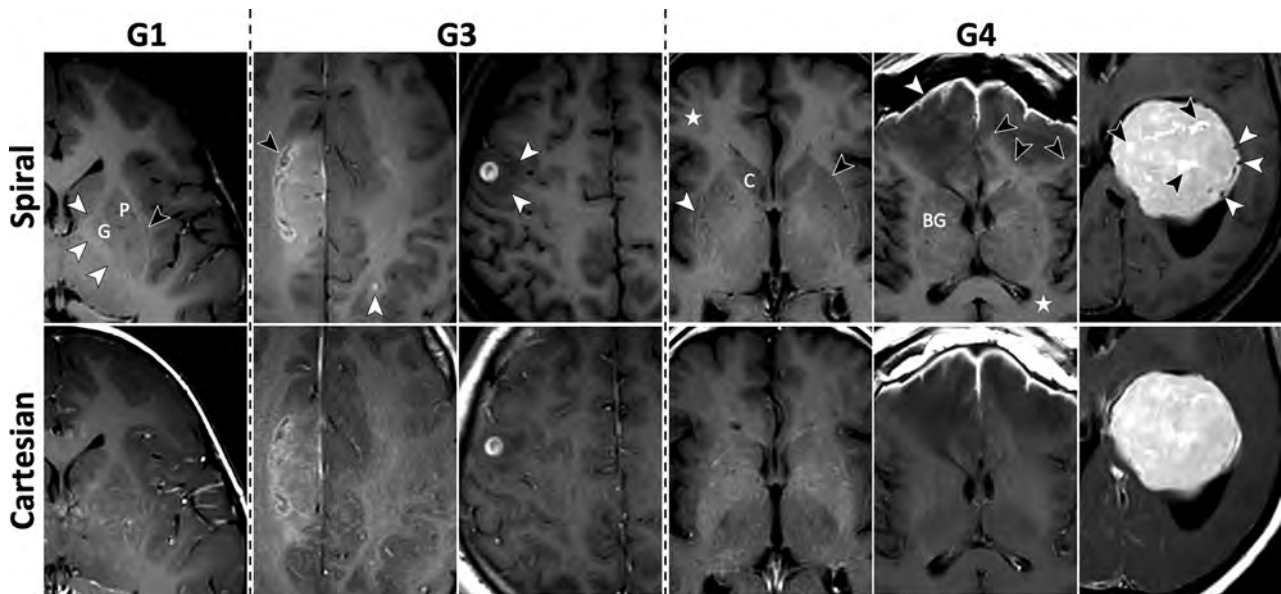


FIG 2. Images for metrics: subjective SNR (M2), GM/WM contrast (M3), and image sharpness (M4). See On-line Fig 2 for corresponding histograms of scores. *Column 1*, Spiral has higher SNR and GM/WM contrast as demonstrated by the sharper demarcation of the putamen (P) and globus pallidus (G) from surrounding WM tracts. The internal capsule, claustrum, external capsule, and extreme capsule are clearly distinguishable on spiral (*white and black arrows*), with sharper margins and higher contrast compared with Cartesian. The cortex and subcortical WM show higher contrast as well. *Column 2*, Grade II *isocitrate dehydrogenase (IDH)* mutant astrocytoma following radiation therapy is seen in the right hemisphere, showing a more detailed appearance on the spiral (*black arrow*). The higher spiral SNR also enables confident detection of an enhancing metastasis in the left parietal lobe (*white arrow*); this lesion is only faintly visible on the Cartesian. *Column 3*, Spiral shows better defined borders of the vasogenic edema (*white arrows*) surrounding the contrast-enhancing metastasis. The overall appearance of the lesion is the same on the 2 sequences. *Column 4*, Spiral demonstrates higher GM/WM contrast, particularly conspicuous by comparing details of the basal ganglia and delineation of the caudate head (C), lateral borders of the anterior putamen (*black arrow*), and claustrum (*white arrow*). The cerebral cortex and subcortical WM are better distinguished (*star*). *Column 5*, Meningitis (*white arrow*) and early cerebritis. The extent of the vasogenic edema is easier to assess on spiral due to the higher contrast and sharper boundary with the WM (*black arrows*). The contrast between WM and deep GM structures (BG) and the cortex (*star*) is again higher with spiral. *Column 6*, Spiral GM/WM contrast is generally higher, while Cartesian has less distinguishable GM/WM boundaries. Internal structure of the intraventricular meningioma shows more details, evident by smaller areas of increased enhancement (*black arrows*) and vascular structures (*white arrows*) due to spiral flow compensation.

benefits brain imaging in general and, specifically, applications requiring precise anatomic localization such as presurgical planning and image-based morphology. Also, pathologies adjacent to fat tissue were better depicted, exploiting the intrinsic Dixon, suggesting potential utility in head and neck imaging.

The higher scan efficiency of spirals can be leveraged for faster scans and/or increased SNR. In this study, spirals were scan time-matched to Cartesian, resulting in an SNR benefit (M2). With protocol G1 as an example, spirals achieved ~150% higher SNR versus Cartesian. If speed is prioritized, a fully-sampled spiral is approximately 4 times faster (scan time = 54 seconds) with ~75% SNR versus Cartesian. If it is SNR-matched, spiral is approximately 2.3 times faster (scan time = 94 seconds). Two current speed-up options for routine Cart-SE-based protocols come with trade-offs: reduced SNR due to partial *k*-space coverage (G3) and reduced GM/WM contrast due to the longer echo-train (G4). In both cases, a fully sampled, scan time-matched spiral was acquired without these trade-offs. Interprotocol histogram and Kruskal-Wallis analysis confirm this advantage, with spirals in G3 and G4 demonstrating relatively higher scores for subjective SNR (M2) and GM/WM contrast (M3), respectively, compared with the other protocols. Spirals prioritizing speed may benefit fast screening, and emergency department protocols.

Vascular applications are an area where the scan efficiency, flow suppression, and intrinsic Dixon of the spiral may be leveraged for added clinical value. Vessel wall imaging using current 2D techniques is slow due to high spatial resolution and requires CSF/blood signal suppression and fat suppression for vessels near the scalp—attributes that have been addressed with the proposed spiral 2D T1-SE. Flow suppression also benefits tumor imaging by separating vascular components in tissue, enabling more precise tumor-size assessment and differentiation of thrombosed/flowing components in vascular tumors. Promising early results have also been demonstrated with spiral TOF-MRA.¹⁵ For structural T1-weighted sequences, many protocols prefer 3D over 2D scans; a high-resolution isotropic spiral 3D sequence, with the detailed advantages, will be a competitive alternative to current Cartesian 3D sequences and could eliminate the need for additional fat-suppressed scans as demonstrated for orbit examinations.¹⁶

Spirals were comparable with Cartesian in 1 of 10 metrics, motion artifacts. The spiral *k*-space trajectory itself is less sensitive to motion.^{5,9,10} However, a confounding factor is spatial misregistration between the B_0 prescan and the spiral scan due to bulk head motion, which would result in residual blurring. Further study is required to separate these effects, which may also be mitigated with concurrent motion-tracking/ B_0 mapping¹⁷ or self- B_0 techniques.¹⁸

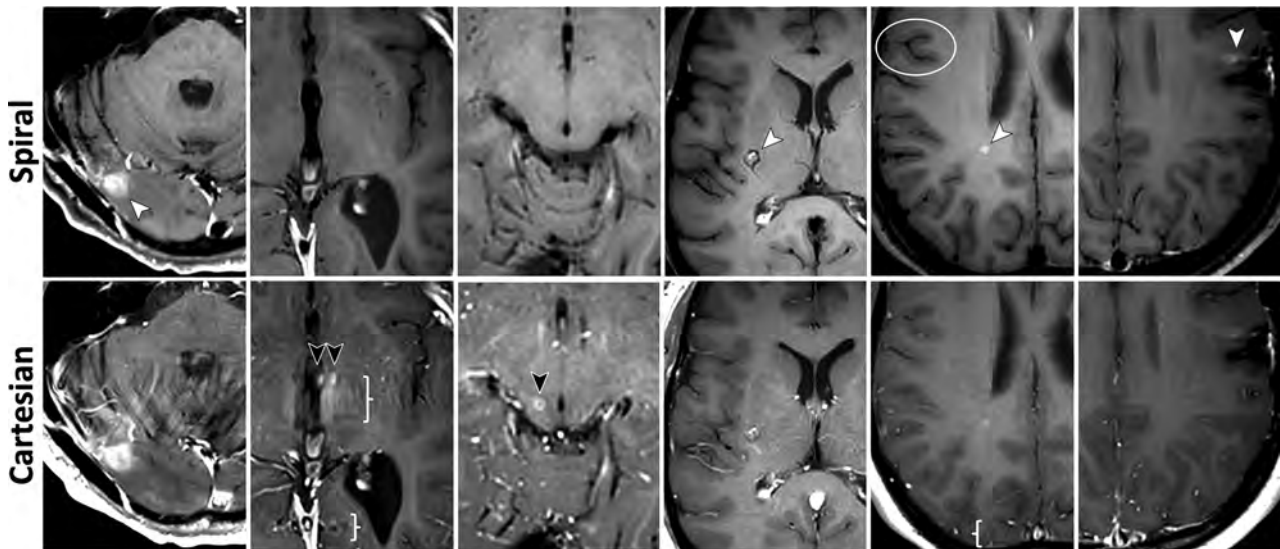


FIG 3. Images for metrics: individual lesion conspicuity (M5), diagnostic preference for detecting abnormal enhancement (M6), and overall intracranial IQ (M7). See On-line Fig 3 for corresponding histograms of scores. All images are taken from G1. *Column 1*, Enhancing lesion (*white arrow*) and surrounding area are better evaluated due to spiral flow artifact reduction. *Columns 2 and 3*, Misleading hyperintense vascular artifacts (*black arrows*) are removed in spiral, along with flow-ringing artifacts (*braces*). *Column 4*, Cavernous hemangioma in the right basal ganglia (*white arrow*). The peripheral vascular component is well-separated from the central, contrast-enhancing part by spiral flow suppression. *Column 5*, An enhancing demyelinating lesion (*white arrow*) is better depicted on spiral. The spiral was acquired before the Cartesian in this case; thus, the difference is not a result of delayed enhancement. Better delineation of the cortex and higher GM/WM contrast are seen again (*circle*), along with removal of flow ringing (*brace*). *Column 6*, Postsurgical residual enhancement (*white arrow*) has higher signal and better delineation in spiral, which increases diagnostic confidence.

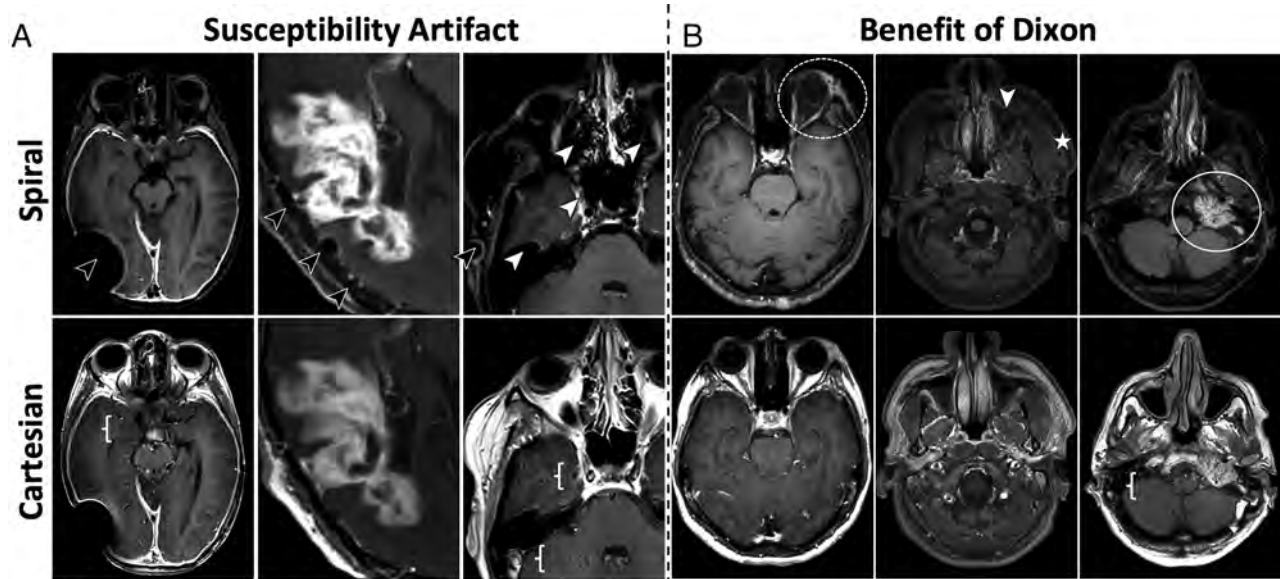


FIG 4. Images for metrics: motion artifacts (M8), susceptibility artifacts (M9), and overall extracranial IQ (M10). See On-line Fig 4 for corresponding histograms of scores. *A*, More pronounced susceptibility artifacts in spirals, appearing as signal voids and residual blurring. These occur in areas where the B_0 field changes rapidly, such as around metallic implants, surgical clips, and resections (*black arrows*), as well as air/tissue interfaces in the nasal cavity and sinuses (*white arrows*). Spiral benefits can be seen in the more detailed internal structure of the enhancing area and flow artifact suppression (*braces*). *B*, Extracranial examples that benefit from the intrinsic Dixon water/fat separation of the spiral. *Column 4*, Spiral shows increased conspicuity of left periorbital inflammatory stranding (*dashed circle*). *Column 5*, Sinus and soft-tissue pathology, where spiral increases the visibility of asymmetric inflammatory stranding in the left masticator space (*star*), though susceptibility artifacts limit visualization of the left maxillary sinus retention cyst (*white arrow*), while the right maxillary sinus fluid is seen with both techniques. *Column 6*, Left glomus jugulare tumor (*white circle*), where spiral highlights the enhancing tumor and separates it from the adjacent fat, while also mitigating posterior fossa flow artifacts (*brace*).

		Wilcoxon Signed-Rank Test and Kruskal-Wallis Test Per Protocol Comparison Group				Inter-Reviewer Agreement		
		All	G1	G2	G3	G4	κ_{5cat}	κ_{3cat}
Scoring Metrics	M1. Flow artifact		>G2,G4		>G2,G4		0.28	0.73
	M2. Subjective SNR				>G1,G2,G4		0.23	0.49
	M3. GM/WM contrast					>G1,G2,G3	0.10	0.30
	M4. Image sharpness				>G2		0.09	0.15
	M5. Lesion conspicuity						0.20	0.29
	M6. Diagnostic pref. – IC		>G2		>G1,G2	>G2	0.20	0.48
	M7. Overall IQ – IC						0.26	0.53
	M8. Motion artifact					>G1,G2	0.25	0.20
	M9. Susceptibility artifact						0.08	0.10
	M10. Overall IQ – EC						0.04	0.12

FIG 5. Statistical test results for all assessed metrics (rows: M1–M10), over all protocol groups (columns: All = all cases, G1–G4). Colors denote Wilcoxon signed rank test results: Green indicates that spiral is better than Cartesian (P value $< .05$; $\Delta > 3$); blue, spiral is comparable with Cartesian (P value $> .05$); and red, Cartesian is better than spiral (P value $< .05$; $\Delta < 3$). Text within colored cells summarizes Kruskal-Wallis and Dunn test results for interprotocol comparisons. If a row contains text, Kruskal-Wallis resulted in a difference in relative performances between G1–G4 (P value $< .05$); otherwise there was no significant difference between protocols. The text itself summarizes Dunn multiple pair-wise comparison results. For example, for M2, there was a significant difference between G1–G4, where G3 scores were relatively higher than G1, G2, G4. Similarly for M3, G4 scores were relatively higher than G1, G2, G3. Noncolored cells in M5 are groups with insufficient samples ($n \leq 5$) because subjects without lesions were excluded (marked NA). Inter-reviewer agreement is reported for κ_{5cat} and κ_{3cat} . IC indicates intracranial compartment; EC, extracranial compartment; pref, preference; κ_{5cat} , κ statistic for 5-point scale; κ_{3cat} , κ statistic for 3-point scale.

Spiral performed poorer than Cartesian in 2 of 10 metrics, both related to magnetic susceptibility in areas where the B_0 map changes rapidly or is not well-defined. Signal voids and residual blurring can occur in these areas; while these susceptibility artifacts were readily recognizable and did not mimic pathology, diagnostic confidence in artifactual regions may be reduced. Imaging in areas of large magnetic susceptibility is a technical challenge for spiral due to its longer acquisition duration τ , which increases the sensitivity of the technique to off-resonances. Shortening τ ,¹⁰ especially when imaging near metal implants, is one solution, though at the cost of scan efficiency. For maintaining a longer τ while mitigating susceptibility artifacts, solutions include improved system characterization^{7,19} and alternative deblurring/autofocusing algorithms.²⁰

There were several limitations to our study. While the reviewers were blinded to the spiral and Cartesian scan names for scoring, the images themselves contained potentially distinguishable characteristics such as flow artifacts that manifested as swirls in spiral-versus-ringing in Cartesian due to their inherently different k -space trajectories. Such features could make each method identifiable to a trained neuroradiologist. Furthermore, spiral images included additional features such as Dixon (water/fat separation) and crusher gradients (flow signal suppression), which could represent a source of sequence identification and/or potential bias.

Regarding Dixon, we elected to distinguish this as an intrinsic benefit of our spiral design and so provided both spiral water-only and water+fat Dixon image series for review. An alternative approach would be acquisition of Cartesian Dixon with matching Dixon image series. However, this approach would have required changing the standard-of-care for the Cartesian approach, and the

added duration would have been impractical for the clinical workflows in this multicenter study. For example, a protocol G1 Cartesian scan time of 3:35 minutes would have doubled to 7 minutes with 2-TE Dixon; paired with a spiral scan time matched to 7 minutes, the result is an additional 14 minutes per subject.

Regarding crusher gradients, this option is not commercially available with the vendor's Cart-SE. The spiral-SE uses a spiral-out readout, which enables the insertion of crusher gradients with a minimum increase in TE. On the other hand, insertion of crusher gradients into the Cart-SE would further increase TE (and TR), resulting in reduced SNR and GM/WM contrast. To avoid these trade-offs and to compare with standard-of-care, we therefore did not add crusher gradients to the Cart-SE.

To control for these differences, this study was therefore designed to achieve a fair comparison between spiral and Cartesian protocols by closely matching scan time, geometry (FOV, voxel volume), and contrast-related parameters (TR, TE, flip angle). Standard-of-care Cart-SE/TSE parameters were used as a fixed reference. Spiral SE protocols were then optimized, given these parameter constraints, including the addition of Dixon and crusher gradients within the same scan time, and so forth. Such parameter matching was performed across all protocols and scanners in this multicenter evaluation.

CONCLUSIONS

Spiral 2D T1-SE for routine structural brain MR imaging is feasible in a clinical population, can be performed at both 3T/1.5T with conventional scanner hardware, and provides several added-value benefits compared with standard-of-care Cartesian 2D T1-SE/TSE. Spiral was superior to Cartesian in 7 of 10 assessed metrics—with strong consensus benefits to flow artifact mitigation,

subjective SNR, and GM/WM contrast—and was preferred by neuroradiologists for overall postcontrast intracranial evaluation (M6, M7). Spiral was comparable with Cartesian in 1 of 10 metrics and inferior in 2 of 10 metrics, most notably related to magnetic susceptibility. Ongoing methods development aims to improve the robustness of spiral MR imaging in these areas, while also exploring new clinical applications.

ACKNOWLEDGMENTS

We thank the following MR imaging technologists for preliminary sequence testing to support protocol optimization: Michael McGranor, Amber Pokorney, Aaron Coover, Efrem Acosta, Soorena Rejaey, Stacey Sullivan Richard, and Noah Briller. We also thank Philips Healthcare for technical support and helpful discussions: Jan Groen, Miha Fuderer, Ad Moerland, Gerald van Ensbergen, Wim Prins, Johan van den Brink, Ashwin Krishnakumar, Kim van de Ven, Liesbeth Geerts-Ossevoort, Patrick Gross, Elizabeth Moore, Jonathan Chia, Marc Van Cauteren, Peter Martin, and Paul Folkers.

Disclosures: Melvyn B. Ooi—*RELATED: Grant: Philips Healthcare, Comments: This work was funded, in part, by Philips Healthcare, paid to Barrow Neurological Institute and Mayo Clinic**; *UNRELATED: Employment: Philips Healthcare.* Zhiqiang Li—*RELATED: Grant: Philips Healthcare, Comments: grant and research support.* Ryan K. Robison—RELATED: Grant: Philips Healthcare, Comments: Grant funding from Philips Healthcare related to this work occurred at my previous institution and was prior to the data acquisition, analysis, and manuscript revision specific to this submission.* Dinghui Wang—RELATED: Grant: Philips Healthcare, Comments: Research support from Philips Healthcare.* Ashley G. Anderson—RELATED: Grant: Philips Healthcare, Comments: This work was supported by a grant from Philips Healthcare*; *Support for Travel to Meetings for the Study or Other Purposes: Philips Healthcare, Comments: I participated in several conferences, and my travel was funded by grants from Philips Healthcare**; *UNRELATED: Employment: Philips Healthcare, Hyperfine Research, Inc. Stock/Stock Options: Philips Healthcare, Hyperfine Research, Inc, Comments: I was employed by Philips Healthcare for some of the time during preparation of this article. At the time of submission, I am an employee of another medical imaging company, Hyperfine Research, Inc. As part of my regular compensation, I have received stock options and participated in employee stock purchase programs.* Silke Hey—*UNRELATED: Employment: Philips Healthcare Netherlands.* Jos Koonen—*RELATED: Grant: Eureka, Comments: Eureka Cluster Program ITEA, project STARLIT (16016)* Nandor K. Pinter—UNRELATED: Payment for Lectures Including Service on Speakers Bureaus: Philips Healthcare.* James G. Pipe—*RELATED: Grant: Philips Healthcare.* Ivan Dimitrov—UNRELATED: Employment: Philips Healthcare.* Quin Lu—*UNRELATED: Employment: Philips Healthcare; Stock/Stock Options: Philips Healthcare.* Yansong Zhao—*UNRELATED: Employment: Philips Healthcare.* Hui Wang—*UNRELATED: Employment: Philips Healthcare.* Nicholas R. Zwart—*RELATED: Grant: Philips Healthcare*; Support for Travel to Meetings for the Study or Other Purposes: Philips Healthcare.* Yi Wang—UNRELATED: Employment: Philips Healthcare.* Jalal B. Andre—*UNRELATED: Grants/Grants Pending: Philips Healthcare, Comments: research grant.* Thomas L. Chenevert—UNRELATED: Patents (Planned, Pending or Issued): Patent unrelated to this work was licensed to Philips Healthcare, Comments: no money paid.* Makoto Obara—*OTHER RELATIONSHIPS: I am a Philips Japan employee. *Money paid to institution.**

REFERENCES

- Ahn CB, Kim JH, Cho ZH. **High-speed spiral-scan echo planar NMR imaging-I.** *IEEE Trans Med Imaging* 1986;5:2–7 CrossRef Medline
- Meyer CH, Hu BS, Nishimura DG, et al. **Fast spiral coronary artery imaging.** *Magn Reson Med* 1992;28:202–13 CrossRef Medline
- Pipe JG, Robison RK. **Simplified signal equations for spoiled gradient echo MRI.** In: *Proceedings of the Annual Meeting of the International Society of Magnetic Resonance in Medicine*, Stockholm, Sweden. May 1–7, 2010
- Nishimura DG, Irarrazabal P, Meyer CH. **A velocity k-space analysis of flow effects in echo-planar and spiral imaging.** *Magn Reson Med* 1995;33:549–56 CrossRef Medline
- Pipe JG, Ahunbay E, Menon P. **Effects of interleaved order for spiral MRI of dynamic processes.** *Magn Reson Med* 1999;41:417–22 CrossRef Medline
- Wang D, Zwart NR, Pipe JG. **Joint water-fat separation and deblurring for spiral imaging.** *Magn Reson Med* 2018;79:3218–28 CrossRef Medline
- Wilm BJ, Barmet C, Gross S, et al. **Single-shot spiral imaging enabled by an expanded encoding model: demonstration in diffusion MRI.** *Magn Reson Med* 2017;77:83–91 CrossRef Medline
- Li Z, Schar M, Wang D, et al. **Arterial spin labeled perfusion imaging using three-dimensional turbo spin echo with a distributed spiral-in/out trajectory.** *Magn Reson Med* 2016;75:266–73 CrossRef Medline
- Glover GH. **Spiral imaging in fMRI.** *Neuroimage* 2012;62:706–12 CrossRef Medline
- Lingala SG, Sutton BP, Miquel ME, et al. **Recommendations for real-time speech MRI.** *J Magn Reson Imaging* 2016;43:28–44 CrossRef Medline
- Li Z, Hu HH, Miller JH, et al. **A spiral spin-echo MR imaging technique for improved flow artifact suppression in T1-weighted post-contrast brain imaging: a comparison with Cartesian turbo spin-echo.** *AJNR Am J Neuroradiol* 2016;37:642–47 CrossRef Medline
- Ooi MB, Li Z, Wang D, et al. **Benefits and challenges of spiral MRI in routine clinical brain imaging: early results.** In: *Proceedings of the Annual Meeting of the International Society of Magnetic Resonance in Medicine*; Paris, France. June 16–21, 2018
- Ooi MB, Li Z, Robison RK, et al. **Spiral T1-SE for routine post-contrast brain MRI: multi-center/reader study results.** In: *Proceedings of the Annual Meeting of the Radiological Society of North America*, Chicago, Illinois. December 1–6, 2019
- Pipe JG, Zwart NR. **Spiral trajectory design: a flexible numerical algorithm and base analytical equations.** *Magn Reson Med* 2014;71:278–85 CrossRef Medline
- Wang D, Ooi MB, Zwart NR, et al. **Spiral time of flight with sliding slice localized quadratic encoding.** In: *Proceedings of the Annual Meeting and Exhibition of the International Society of Magnetic Resonance in Medicine*, Montreal, Quebec, Canada. May 11–16, 2019
- Friel H, McGranor M, Ooi MB, et al. **Clinical application of spiral 3D TFE-IR for postcontrast brain.** In: *Proceedings of the Annual Meeting of the American Society of Neuroradiology*, Vancouver, British Columbia, Canada. June 2–7, 2018
- Aranovitch A, Vionnet L, Gross S, et al. **High-resolution T2*-weighted imaging of subcortical brain enhanced by motion and field compensation.** In: *Proceedings of the Annual Meeting of the International Society of Magnetic Resonance in Medicine*. Paris, France. June 16–21, 2018
- Liu C, Bammer R, Kim DH, et al. **Self-navigated interleaved spiral (SNAILS): application to high-resolution diffusion tensor imaging.** *Magn Reson Med* 2004;52:1388–96 CrossRef Medline
- Robison RK, Li Z, Wang D, et al. **Correction of B0 eddy current effects in spiral MRI.** *Magn Reson Med* 2019;81:2501–13 CrossRef Medline
- Man LC, Pauly JM, Macovski A. **Improved automatic off-resonance correction without a field map in spiral imaging.** *Magn Reson Med* 1997;37:906–13 CrossRef Medline

MR Diffusional Kurtosis Imaging–Based Assessment of Brain Microstructural Changes in Patients with Moyamoya Disease before and after Revascularization

P.-G. Qiao, X. Cheng, G.-J. Li, P. Song, C. Han, and Z.-H. Yang



ABSTRACT

BACKGROUND AND PURPOSE: Conventional imaging examinations are insufficient to accurately assess brain damage in patients with Moyamoya disease. Our aim was to observe brain microstructural changes in patients with Moyamoya disease by diffusional kurtosis imaging and provide support data for application of this technique in individualized assessment of disease severity and surgical outcome among patients with Moyamoya disease.

MATERIALS AND METHODS: A total of 64 patients with Moyamoya disease and 15 healthy volunteers underwent diffusional kurtosis imaging, and a second scanning was offered to surgical patients 3–4 months after revascularization. The diffusional kurtosis imaging parameter maps were obtained for mean kurtosis, axial kurtosis, radial kurtosis, fractional anisotropy, mean diffusivity, axial diffusivity, and radial diffusivity. The parameter values were measured in sensory pathway–related regions for all subjects. Differences in diffusional kurtosis imaging parameters of these brain regions were examined for healthy volunteers, patients without acroparesthesia, and asymptomatic and symptomatic sides of patients with acroparesthesia. Changes in diffusional kurtosis imaging parameters of patients with Moyamoya disease before and after revascularization were compared.

RESULTS: Compared with healthy volunteers, patients with Moyamoya disease showed decreased mean kurtosis, axial kurtosis, radial kurtosis, and fractional anisotropy in the corona radiata. Similarly, mean kurtosis, radial kurtosis, and fractional anisotropy decreased in the posterior limb of the internal capsule, whereas axial kurtosis decreased and radial kurtosis increased in the thalamus of patients with Moyamoya disease compared with healthy volunteers. Compared with the asymptomatic contralateral hemisphere, the symptomatic group showed increased mean kurtosis in the contralateral primary somatosensory cortex, increased fractional anisotropy in the contralateral corona radiata and posterior limb of the internal capsule, and decreased axial kurtosis in the contralateral thalamus. Among patients with Moyamoya disease with acroparesthesia, mean kurtosis decreased in the primary somatosensory cortex on the operated side following revascularization.

CONCLUSIONS: The diffusional kurtosis imaging technique is applicable to patients with Moyamoya disease for detecting brain microstructural changes in white and gray matter before and after revascularization; this feature is useful in the assessment of disease severity and surgical outcome.

ABBREVIATIONS: AD = axial diffusivity; AK = axial kurtosis; DKI = diffusional kurtosis imaging; EDAS = encephaloduroarteriosynangiosis; FA = fractional anisotropy; MD = mean diffusivity; MK = mean kurtosis; MMD = Moyamoya disease; RK = radial kurtosis; RD = radial diffusivity; SI = primary somatosensory cortex; TTP = time-to-peak

Moyamoya disease (MMD) is a chronic occlusive cerebrovascular disease characterized by stenosis and occlusion of the terminal portion of the bilateral internal carotid arteries

associated with the formation of an abnormal vascular network at the cerebral basal ganglia.¹ On the basis of angiographic manifestations, Suzuki and Takaku² classified the development of MMD into 6 stages. Currently, Suzuki staging is the primary criterion for clinical assessment of disease severity in patients with MMD. However, the natural course and prognostic factors of MMD are

Received February 12, 2019; accepted after revision December 10.

From the Department of Radiology (P.-G.Q., X.C., Z.-H.Y.), Beijing Friendship Hospital, Capital Medical University, Beijing, China; Departments of Radiology (P.-G.Q., G.-J.L.) and Neurosurgery (G.-J.L., C.H.), Affiliated Hospital of Academy of Military Medical Sciences, Beijing, China; Department of Radiology (P.S.), Liaocheng People's Hospital, Liaocheng, China; and Beijing Universal Medical Imaging Diagnostic Center (G.-J.L.), Beijing, China.

P.-G. Qiao and X. Cheng contributed equally to this work.

This work was supported by grants from the National Natural Science Foundation of China (No. 81701663).

Please address correspondence to Zheng-Han Yang, MD, Department of Radiology, Beijing Friendship Hospital, Capital Medical University, 95 YongAn Rd, Beijing, 100050, P.R. China; e-mail: cjr.yangzhenghan@vip.163.com

Indicates open access to non-subscribers at www.ajnr.org

<http://dx.doi.org/10.3174/ajnr.A6392>

still unclear, and its clinical manifestations vary among patients. Even patients in the same Suzuki stage may manifest different clinical features.³ In addition, the detection rate of asymptomatic MMD has been growing year by year, which further perplexes MMD treatment.⁴ In a multicenter study conducted in Japan, 75% of the affected hemispheres in asymptomatic patients with MMD were classified into Suzuki stages III–IV, and ~45% of the affected hemispheres had decreased cerebral vascular reactivity or cerebral blood flow, whereas 20.8% of the affected hemispheres had cerebral infarction lesions.⁵ Patients with MMD may have different clinical manifestations in long-term chronic ischemic conditions even if the Suzuki stage is identical and no changes in brain parenchyma are detected by conventional MR imaging.⁶ Therefore, conventional imaging examinations are insufficient to accurately assess brain damage in patients with MMD.

DWI-based DTI and diffusional kurtosis imaging (DKI) can illustrate fine changes in the microstructure of the central nervous system and quantitatively assess the damage to brain tissue. On the basis of a Gaussian distribution model, DTI can reflect microstructural changes in cerebral white matter and detect its integrity because DTI parameter changes are sensitive indicators for structural changes in axons, myelin, and organelles.^{7–9} This technique can be used to detect changes in early ischemic damage for patients with MMD,¹⁰ among whom such early damage may be associated with neurologic impairment.¹¹ However, DTI is not sensitive to changes in cerebral gray matter due to the distribution and diffusion isotropy. On the basis of a non-Gaussian distribution model, DKI can sensitively reflect microstructural changes in gray matter areas, neurodegenerative diseases, tumor microenvironment, and posttraumatic brain tissue.^{7,12–14} The use of DKI enables the detection of more extensive brain damage in patients with MMD, especially early damage to the intersection of white matter fibers.⁸

Despite early detection of white matter microstructural damage in patients with MMD by DTI and DKI, the association between such damage and neurologic impairment in these patients remains unclear. While a handful of studies have suggested an association between this damage and cognitive impairment, its relationship with MMD and other common sensory, motor, verbal, and visual impairments is yet to be reported. In addition, there is a dearth of studies on early damage to white matter and patient prognosis, as well as the associated changes following revascularization. Moreover, DKI allows detection of gray matter microstructural changes, yet such changes have received far less investigation in patients with MMD.

In this study, we used DKI to detect microstructural changes in sensory pathway–related regions of brain tissue among patients with MMD with acroparesthesia and clarified whether such changes would improve in these patients following revascularization. The results could provide support for the application of DKI in individualized assessment of disease severity and surgical outcome among patients with MMD.

MATERIALS AND METHODS

Subjects

Sixty-four patients with MMD (27 men and 37 women) were recruited from July 2015 to April 2016. The patients had a median age of 35 years (range, 16–45 years). Thirty-three patients

presented with unilateral paroxysmal numbness or hypoesthesia, 15 of whom underwent encephaloduroarteriosynangiosis (EDAS). Acroparesthesia was absent in the remaining 31 patients, 14 of whom underwent EDAS.

The inclusion criteria were as follows: 1) The patient was diagnosed and staged by digital subtraction angiography; 2) the patient remained in a stable condition, had no cerebral hemorrhage before scanning, presented with no cerebral infarction in the bilateral primary somatosensory cortex (SI) by conventional MR imaging, and cooperated with the examination; 3) the patient reported no other neurologic or psychiatric diseases; and 4) the patient was right-handed.

In addition, 15 healthy age- and sex-matched volunteers were selected. All subjects were provided with details of the examination and the necessary precautions. Signed informed consent was obtained from each subject before the examination. The ethics committee of the Affiliated Hospital of Academy of Military Medical Sciences approved the study.

MR Imaging

The MR imaging was performed on a 3T Skyra MR imager (Siemens, Erlangen, Germany) using a 32-channel standard head coil. All subjects underwent DKI, whereas patients with MMD also underwent contrast-enhanced DSC MR imaging. MR imaging was performed for all patients within 1 week before and after digital subtraction angiography, and a second MR imaging was offered to 29 surgical patients 3–4 months following EDAS.

DKI scans were acquired by axial echo-planar imaging using the following parameters: TR = 5600 ms; TE = 92 ms; FOV = 228 mm; matrix = 384 × 384 mm²; section thickness = 3 mm; b-value = 0, 1000, and 2000 s/mm²; direction of diffusion-sensitive gradient field applied = 30; and scanning time = 7 minutes 2 seconds.

DSC-MR imaging was performed by echo-planar imaging using the following parameters: TR = 1870 ms; TE = 30 ms; FOV = 220 mm; matrix = 128 × 128 mm²; section thickness = 4 mm; section spacing = 1.2 mm; section number = 24; and acquisition time phase = 60 seconds. After the start of the scan, a high-pressure syringe was used to inject a gadolinium-based contrast agent (0.2 mL/kg; gadopentetate dimeglumine, Magnevist; Bayer HealthCare Pharmaceuticals, Wayne, New Jersey) at the rate of 4–5 mL/s in the sixth time phase.

DKI Analysis

Data were exported from the workstation and converted to the NIfTI1 data format using “dcm2nii” in MRICron (Version 6; <https://www.nitrc.org/projects/mricron/>). The converted data were imported into the Diffusional Kurtosis Estimator (Version 2.5.1; Medical University of South Carolina Center for Biomedical Imaging, Charleston, South Carolina) for preprocessing, namely spatial smoothing (full width at half maximum = 3.75), median filtering, linear trend removal, and denoise processing.

Seven DKI parameters were extracted (Fig 1): mean kurtosis (MK), axial kurtosis (AK), radial kurtosis (RK), fractional anisotropy (FA), mean diffusivity (MD), axial diffusivity (AD), and radial diffusivity (RD). The parameter values were

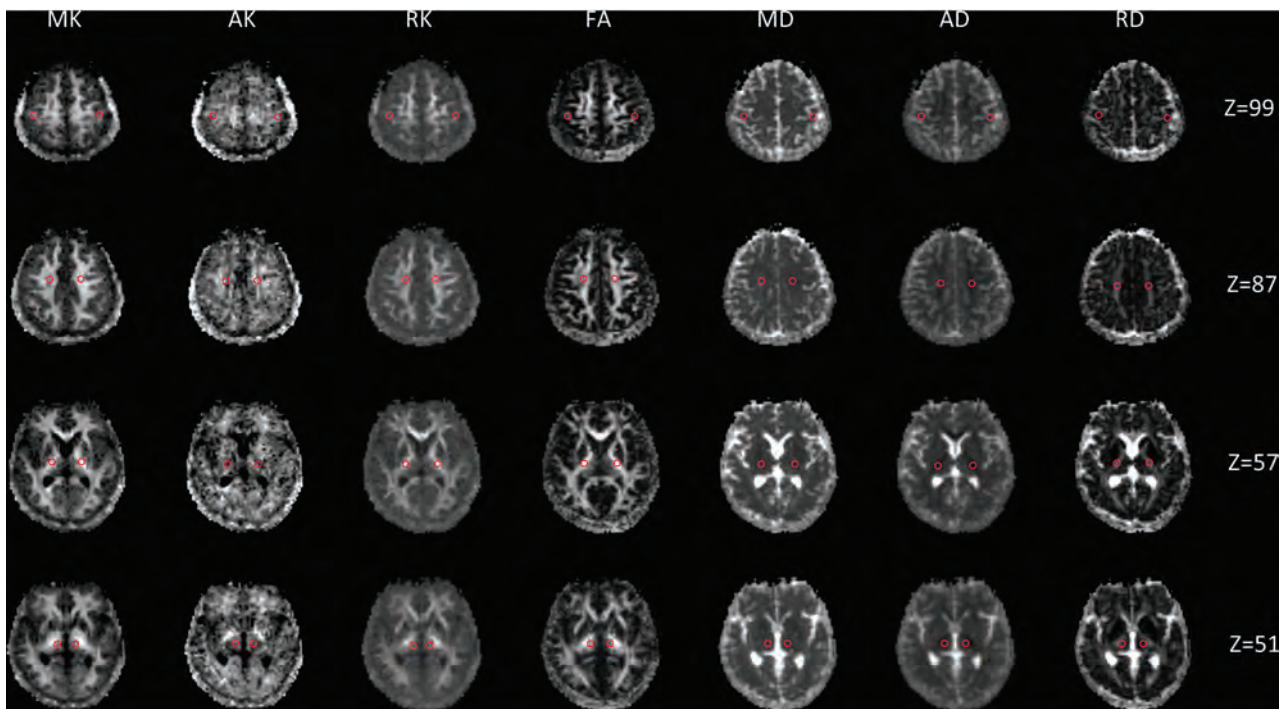


FIG 1. DKI parameter maps of patients with MMD. From left to right: MK, AK, RK, FA, MD, AD, and RD. Selection of ROIs in the bilateral primary SI, corona radiata, posterior limb of the internal capsule, and thalamus is shown in red circles.

measured in the bilateral SI, corona radiata, posterior limb of the internal capsule, and thalamus of all subjects using the ROI method by a radiologist who had >10 years of experience in neuroimaging. Three circular ROIs (5 mm in diameter) were selected at random from different layers of each brain region. The ROIs were not selected from the infarct region. Finally, the mean of the ROIs was taken as the quantitative DKI parameter value in each region.

DSC-MR Image Analysis

The DSC-MR images were imported into the syngo via 20 postprocessing workstation (Siemens). Four hemodynamic parameter maps were obtained using the arterial input function model: relative cerebral blood volume, relative cerebral blood flow, relative mean transit time, and time-to-peak (TTP). In clinical practice, we found that TTP is more sensitive than the other 3 parameters in detecting hemodynamic impairment in patients with Moyamoya disease and their hemodynamic improvement after vascular reconstruction. In a study by Wityk et al,¹⁵ TTP was also used to evaluate hemodynamic changes in patients with Moyamoya disease after vascular reconstruction. Therefore, we selected TTP to evaluate hemodynamic changes in patients with Moyamoya disease. The TTP was measured in the middle cerebral artery supply area surrounding the bilateral central sulcus (M), bilateral corona radiata (C), bilateral basal ganglia (B), bilateral thalamus (T), and bilateral cerebellar hemisphere. The difference in TTP between each region and the ipsilateral cerebellar hemisphere (ie, ΔTTP_M , ΔTTP_C , ΔTTP_B , and ΔTTP_T) represents the quantitative parameter of blood perfusion in the bilateral SI, corona radiata, basal ganglia, and thalamus.

Statistical Analysis

A preliminary comparison revealed no obvious differences in DKI parameters of the bilateral SI, corona radiata, posterior limb of the internal capsule, and thalamus among healthy volunteers. Hence, data from the left and right sides of healthy volunteers were combined to compose the control group. In addition, data from the left and right sides of patients with MMD without acroparesthesia were combined to form the group without acroparesthesia, and data from the symptomatic and asymptomatic sides of patients with unilateral acroparesthesia were combined to form the symptomatic and asymptomatic groups, respectively.

All statistical analyses were performed using SAS (Version 9.3; SAS Institute, Cary, North Carolina). The Kruskal-Wallis test was used to determine differences in DKI parameters among the 4 groups. The paired-samples *t* test or signed rank test was used to compare DKI parameters between the symptomatic and asymptomatic groups of patients with MMD with acroparesthesia, as well as to compare DKI parameters and ΔTTP on the operated side of surgical patients before and 3–4 months after EDAS. A *P* value < .05 was considered statistically significant.

RESULTS

Differences in DKI Parameters of Sensory Pathway–Related Brain Regions in Patients with MMD

Comparison of DKI parameters among the 4 groups revealed no significant changes in the SI of patients with MMD compared with healthy volunteers (Fig 2). However, patients with MMD had decreased MK, AK, RK, and FA values and increased MD, AD, and RD values in the corona radiata (Fig 3). In addition, the MK, RK, and FA decreased, whereas the MD and RD values increased in the posterior limb of the internal capsule among

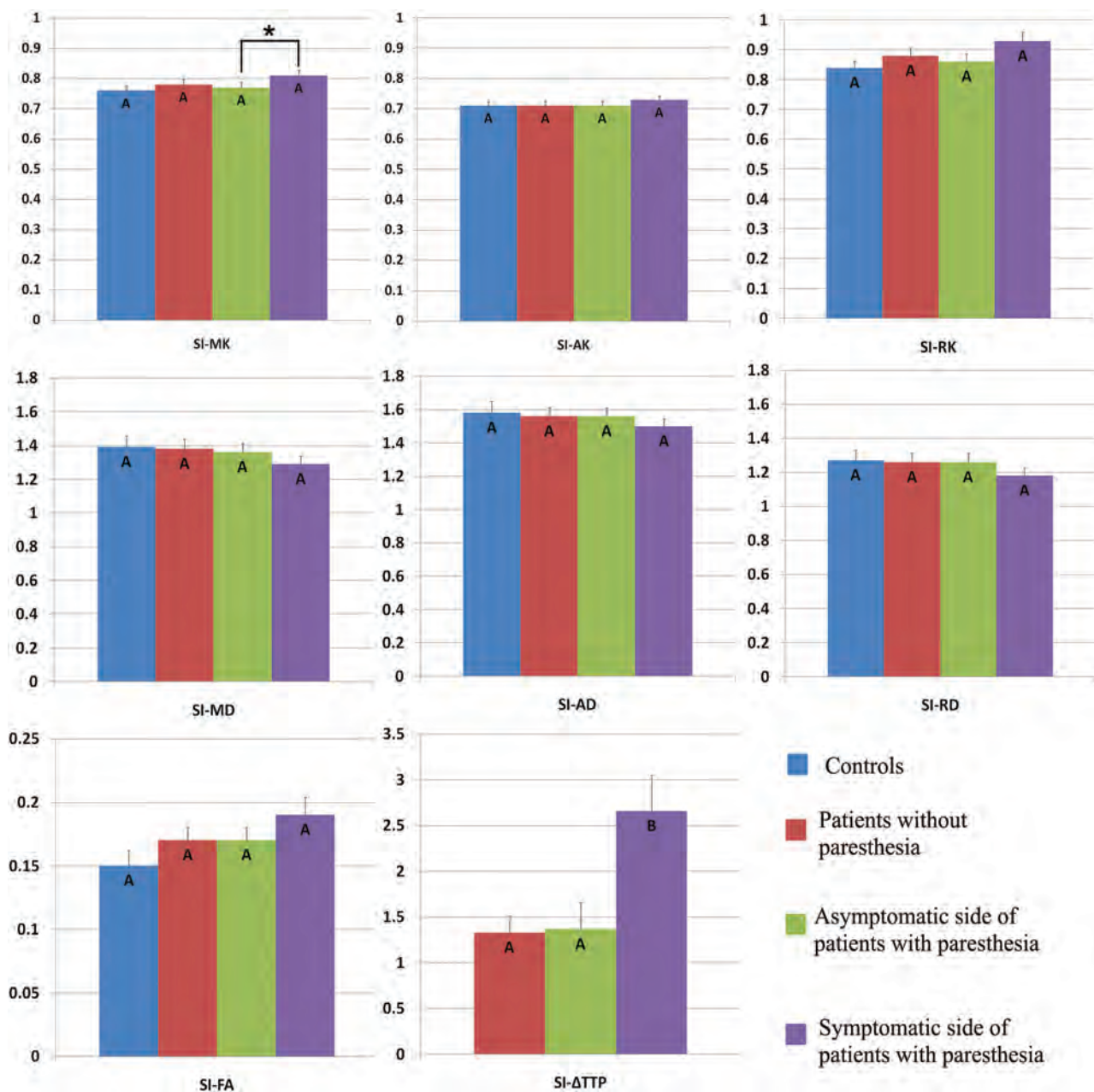


FIG 2. Comparison of DKI parameters in the contralateral SI among healthy volunteers (controls), patients with MMD without acroparesthesia, the asymptomatic side of patients with MMD with acroparesthesia, and the symptomatic side of patients with MMD with acroparesthesia. Group means were compared using the Kruskal-Wallis test. Different letters on the column indicate a significant difference by pair-wise comparison ($P < .05$). The asterisk represents a significant difference between the symptomatic and asymptomatic sides of patients with acroparesthesia by self-paired comparison (signed rank test, $P < .05$). Error bars represent standard errors.

patients with MMD (Fig 4). Decreased AK and increased RK, AD, and RD values were noted in the thalami of patients with MMD (Fig 5).

Self-paired comparison of patients with MMD with acroparesthesia revealed that compared with parameter values of the asymptomatic contralateral hemisphere, the MK value was increased and the Δ TTP was prolonged in the symptomatic contralateral SI (Fig 2). In addition, increased FA values and prolonged Δ TTP were observed in the symptomatic contralateral corona radiata (Fig 3) and posterior limb of the internal capsule (Fig 4). The AK decreased whereas the MD and AD values

increased in the symptomatic contralateral thalamus, but no significant change was found in the Δ TTP (Fig 5).

Changes in DKI Parameters of Sensory Pathway–Related Brain Regions in Patients with MMD following EDAS

Among the 15 surgical patients with acroparesthesia, limb symptoms disappeared in 9 patients and were markedly mitigated in the other 6 patients 3–4 months after EDAS. Compared with before the operation, the Δ TTP was shortened and the MK value decreased, whereas the MD, AD, and RD values increased in the SI of the operated side (Table 1).

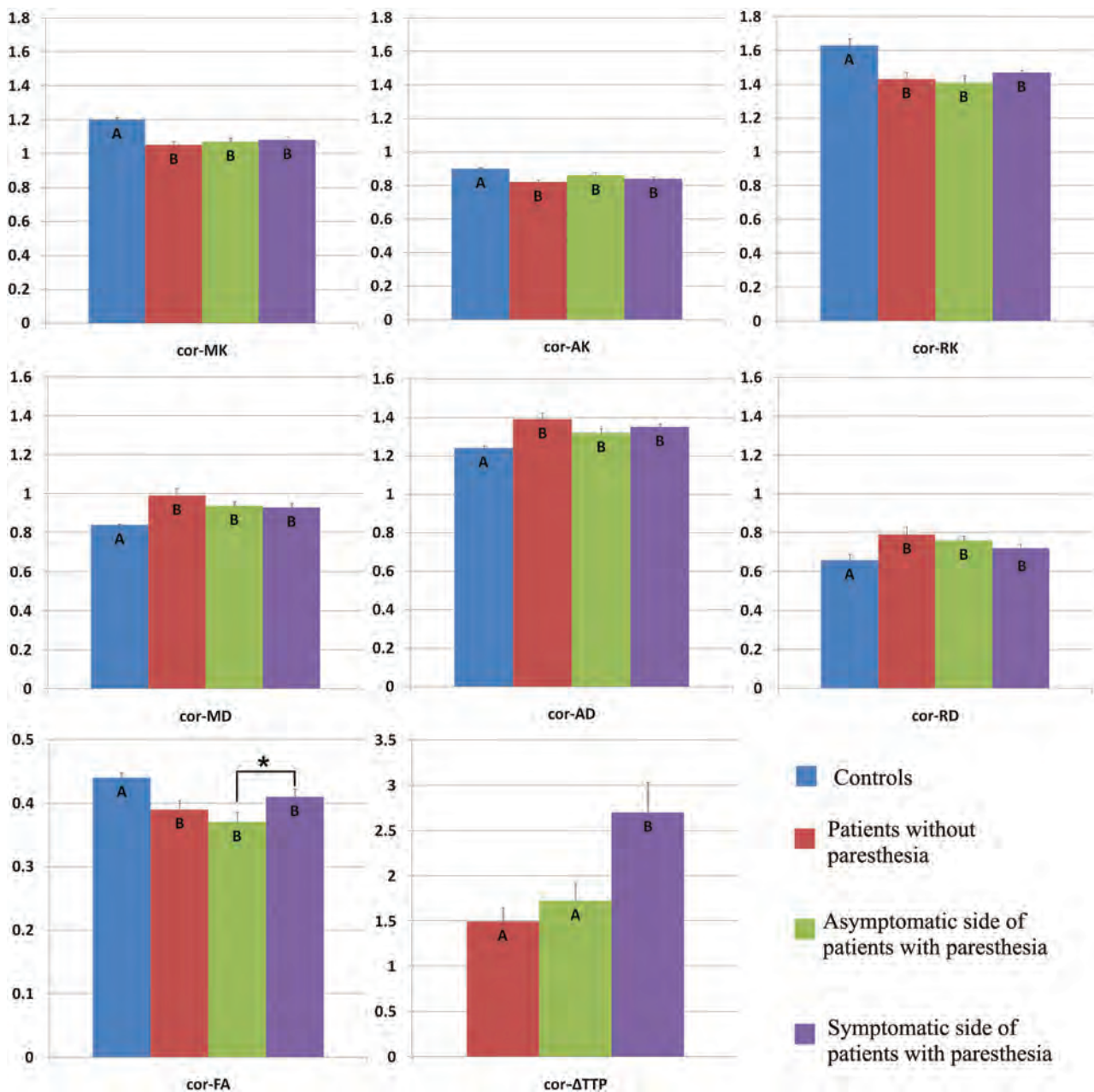


FIG 3. Comparison of DKI parameters in the contralateral corona radiata among healthy volunteers (controls), patients with MMD without acroparesthesia, the asymptomatic side of patients with MMD with acroparesthesia, and the symptomatic side of patients with MMD with acroparesthesia. Group means were compared using the Kruskal-Wallis test. Different letters on the column indicate a significant difference by pair-wise comparison ($P < .05$). The asterisk represents a significant difference between the symptomatic and asymptomatic sides of patients with acroparesthesia by self-paired comparison (signed rank test, $P < .05$). Error bars represent standard errors. Cor indicates coronal radiata.

However, no significant changes in DKI parameters were observed in the corona radiata, posterior limb of the internal capsule, or thalamus on the operated side.

The preoperative symptoms of the 14 surgical patients without acroparesthesia were dizziness, headache, blurred vision, or inarticulateness. These symptoms were mitigated or disappeared 3–4 months after EDAS. Compared with before the operation, the Δ TTP was shortened and the MK decreased in the SI on the operated side (Table 2), whereas the Δ TTP was shortened, the FA decreased, and the RD increased in the corona radiata on the operated side (Table 3). The DKI parameters did not change

significantly in the posterior limb of the internal capsule or thalamus before and after the operation.

DISCUSSION

This study shows that DKI can detect microstructural changes in brain tissue among patients with MMD before the detection of brain parenchymal changes by conventional MR imaging. The white matter microstructure may change in patients with MMD during long-term chronic ischemia, even in those with normal-appearing white matter.⁶ On the basis of DTI, Jeong et al¹⁰ found

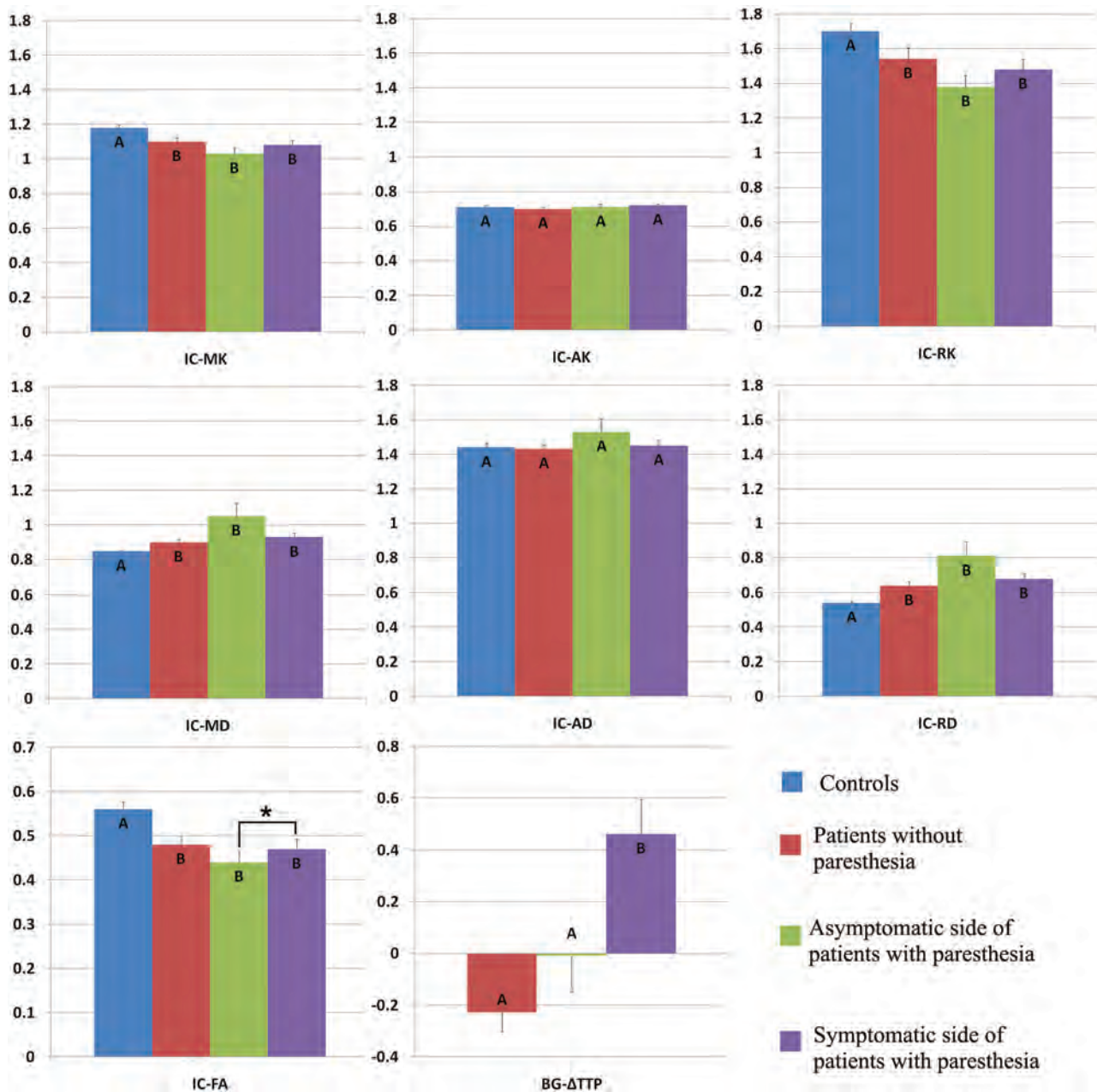


FIG 4. Comparison of DKI parameters in the contralateral posterior limb of the internal capsule among healthy volunteers (controls), patients with MMD without acroparesthesia, the asymptomatic side of patients with MMD with acroparesthesia, and the symptomatic side of patients with MMD with acroparesthesia. Group means were compared using the Kruskal-Wallis test. Different letters on the column indicate significant differences by pair-wise comparison ($P < .05$). The *asterisk* represents a significant difference between the symptomatic and asymptomatic sides of patients with acroparesthesia by self-paired comparison (signed rank test, $P < .05$). Error bars represent standard errors. IC indicates internal capsule.

a decrease in the FA values but an increase in the ADC values in the bilateral corona radiata of patients with MMD. Using DKI, Kazumata et al¹⁶ found that the MK value decreased in the white matter on the right forehead; the white matter in the occipital subcortex; and the frontoparietal white matter in the superior longitudinal fasciculus branches, corona radiata, corpus callosum, and bilateral thalamus of patients with MMD. However, these 2 studies did not report microstructural changes in relevant brain regions among patients with MMD with specific clinical symptoms. In other words, the changes observed in the white matter

of patients with MMD may occur commonly in long-term chronic ischemic conditions. Therefore, such changes cannot explain the diversity of clinical symptoms in patients with MMD.

Here, we observed the changes in DKI parameters of sensory pathway-related brain regions among patients with MMD with unilateral acroparesthesia. Compared with healthy volunteers, the patients with MMD presented similar changes in sensory pathway-related white matter regions, including the posterior limb of the internal capsule and corona radiata. This result is in agreement with the observations of Jeong et al¹⁰ and

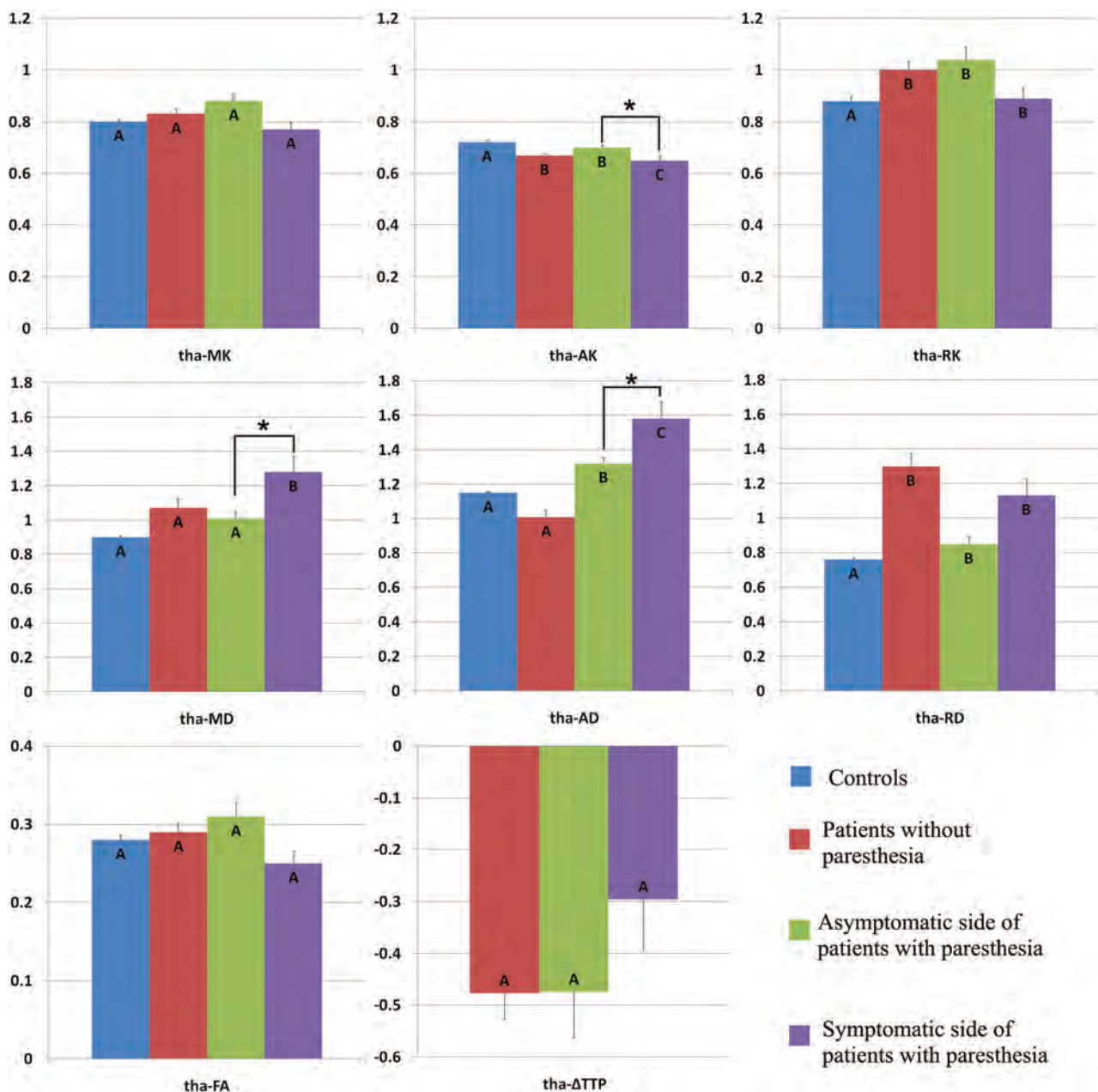


FIG 5. Comparison of DKI parameters in the contralateral thalamus among healthy volunteers (controls), patients with MMD without acroparesthesia, the asymptomatic side of patients with MMD with acroparesthesia, and the symptomatic side of patients with MMD with acroparesthesia. Group means were compared using the Kruskal-Wallis test. Different letters on the column indicate a significant difference by pairwise comparison ($P < .05$). The asterisk represents a significant difference between the symptomatic and asymptomatic sides of patients with acroparesthesia by self-paired comparison (signed rank test, $P < .05$). Error bars represent standard errors. Tha indicates thalamus.

Kazumata et al.¹⁶ Among the DKI parameters reflecting white matter changes, a decrease of RK is associated with demyelination, whereas a change of AK reflects axonal degeneration.¹⁷ An increase of RD is linked to myelin degeneration or increased extracellular fluid around the ventricle,¹⁸ and an increase of AD is related to axonal degeneration.¹⁹ Therefore, dynamic changes in DKI parameters of the white matter among patients with MMD represent degenerative changes in brain tissue during long-term chronic ischemia.

On the basis of paired comparison of sensory pathway-related brain regions between the symptomatic and asymptomatic

groups of patients with MMD with acroparesthesia, we observed increased MK values in the contralateral SI, increased FA in the contralateral corona radiata, increased FA values in the contralateral posterior limb of the internal capsule, and increased TTP in the corresponding region of the symptomatic contralateral hemisphere. In an ischemic state, the increase of MK may represent acute brain damage related to axon beading, microglia upregulation, or other microstructural changes.²⁰⁻²² The increase of FA in white matter can occur in the case of insufficient brain perfusion (but not infarction).^{23,24} This change of FA, which also represents acute brain damage, may be related to cytotoxic

Table 1: Comparison of DKI parameters in the primary somatosensory cortex of the operated side in patients with MMD with unilateral acroparesthesia before and after encephaloduroarteriosynangiosis^a

DKI Parameter	Primary Somatosensory Cortex		Statistic	P
	Before EDAS	After EDAS		
MK	0.80 ± 0.09	0.75 ± 0.09	t = -2.5012	0.02
AK	0.72 ± 0.07	0.68 ± 0.07	t = -2.1028	0.06
RK	0.91 ± 0.15	0.86 ± 0.16	t = -1.6657	0.12
FA	0.18 ± 0.07	0.18 ± 0.11	S = -15.5	0.30
MD	1.32 ± 0.23	1.49 ± 0.35	t = 2.5373	0.02
AD	1.53 ± 0.20	1.68 ± 0.33	t = 2.4626	0.03
RD	1.22 ± 0.24	1.38 ± 0.36	t = 2.4966	0.02
ΔTTP (sec)	2.55 ± 2.14	1.07 ± 0.92	S = 46	0.007

Note:—S indicates the Rank Statistic of signed rank sum test.

^a EDAS; n = 15, $\bar{x} \pm s$. Statistical analysis was performed by a self-paired t test or signed rank sum test.

Table 2: Comparison of DKI parameters in the primary somatosensory cortex of the operated side in patients with MMD without acroparesthesia before and after encephaloduroarteriosynangiosis^a

DKI Parameter	Primary Somatosensory Cortex		Statistic	P
	Before EDAS	After EDAS		
MK	0.81 ± 0.11	0.75 ± 0.11	t = -2.3113	0.04
AK	0.73 ± 0.10	0.70 ± 0.09	t = -1.1748	0.26
RK	0.92 ± 0.17	0.83 ± 0.19	t = -2.1186	0.05
FA	0.18 ± 0.07	0.15 ± 0.07	t = -2.009	0.06
MD	1.31 ± 0.30	1.43 ± 0.40	S = 18	0.32
AD	1.50 ± 0.29	1.61 ± 0.39	S = 18.5	0.36
RD	1.17 ± 0.29	1.33 ± 0.41	S = 22.5	0.21
ΔTTP (sec)	2.67 ± 1.52	0.93 ± 0.76	S = -51.5	<0.001

Note:—S indicates the Rank Statistic of signed rank sum test.

^a EDAS; n = 14, $\bar{x} \pm s$. Statistical analysis was performed by a self-paired t test or signed rank sum test.

Table 3: Comparison of DKI parameters in the corona radiata of the operated side in patients with MMD without acroparesthesia before and after encephaloduroarteriosynangiosis^a

DKI Parameter	Corona Radiata		Statistic	P
	Before EDAS	After EDAS		
MK	1.11 ± 0.09	1.06 ± 0.12	t = -1.41963	0.17
AK	0.84 ± 0.06	0.83 ± 0.05	t = -1.20239	0.25
RK	1.54 ± 0.25	1.37 ± 0.21	t = -1.97407	0.07
FA	0.42 ± 0.09	0.35 ± 0.07	S = -39	0.04
MD	0.91 ± 0.08	0.95 ± 0.09	S = 31	0.08
AD	1.35 ± 0.11	1.30 ± 0.09	t = 1.7969	0.09
RD	0.70 ± 0.11	0.77 ± 0.10	S = 43	0.04
ΔTTP (s)	2.13 ± 1.29	1.73 ± 1.23	S = 48	0.02

Note:—S indicates the Rank Statistic of signed rank sum test.

^a EDAS; n = 14, $\bar{x} \pm s$. Statistical analysis was performed by a self-paired t test or signed rank sum test.

edema without a significant change in structural coherence.²⁵ All such brain damage may be the main cause of the clinical symptoms in patients with MMD. Among the patients with MMD undergoing revascularization, the ΔTTP was shortened and the MK value was decreased in the SI on the operated side. In addition, the ΔTTP was shortened, and the FA value decreased in the corona radiata on the operated side. All these postoperative changes were associated with improved clinical symptoms in the surgical patients. These results suggest that the observed changes in the SI and white matter regions are reversible along with the improvement of cerebral blood perfusion.

This study was the first to investigate changes in DKI parameters of sensory pathway-related brain regions among patients with MMD with acroparesthesia. In the case of long-term chronic ischemia, the microstructure of brain tissue may be altered and the DKI parameters likely undergo changes (a decrease in kurtosis, a decrease in FA, and an increase in diffusivity) in patients with MMD. When the hemodynamic state is stable, these parameters are also in a relatively stable or pseudonormal state; on further hemodynamic damage, some acute or specific changes may occur in the microstructure of the brain, causing DKI parameter changes (an increase in the MK of the gray matter and an increase in the FA of the white matter). These changes would return to a pseudonormal state during hemodynamic improvement after revascularization.

During the follow-up of MMD, DSC-MR imaging is an important technique for the assessment of cerebral blood perfusion; however, there is no clear standard to assess the severity of the disease. Our results indicate that DKI enables timely detection of changes in brain tissue microstructure of patients with MMD with reduced cerebral blood perfusion, which is helpful to assess the disease severity and the surgical outcome.

Our study has some limitations. First, the patients had re-examination results for only 3–4 months after the operation and lacked a long-term follow-up record. Because indirect revascularization was used as the surgical approach for all patients, a longer follow-up period could facilitate the study of changes in DKI parameters

during hemodynamic improvement. Second, due to the small sample size, especially of postoperative samples, it was impossible to effectively determine changes in DKI parameters for patients with different symptom improvements after the operation. Third, functional imaging techniques that can quantitatively reflect cerebral blood flow changes, such as PET and SPECT, were not used for the hemodynamic assessment.

CONCLUSIONS

The DKI technique can detect microstructural changes in the cerebral white and gray matter of patients with MMD before and after revascularization in a timely manner. It is a sensitive

method for use in the follow-up of patients with MMD, which supports the assessment of disease severity and surgical outcome.

Disclosures: Peng-Gang Qiao—RELATED: Grant: National Natural Science Foundation of China, Comments: grant No. 81701663. Money paid to the institution.

REFERENCES

1. Research Committee on the Pathology and Treatment of Spontaneous Occlusion of the Circle of Willis, Health Labour Sciences Research Grant for Research on Measures for Intractable Diseases. **Guidelines for diagnosis and treatment of moyamoya disease (spontaneous occlusion of the circle of Willis).** *Neurol Med Chir (Tokyo)* 2012; 52:245–66 CrossRef Medline
2. Suzuki J, Takaku A. **Cerebrovascular “moyamoya” disease: disease showing abnormal net-like vessels in base of brain.** *Arch Neurol* 1969;20:288–99 CrossRef Medline
3. Hervé D, Kossorotoff M, Bresson D, et al. **French clinical practice guidelines for Moyamoya angiopathy.** *Rev Neurol (Paris)* 2018;174: 292–303 CrossRef Medline
4. Ikeda K, Iwasaki Y, Kashihara H, et al. **Adult moyamoya disease in the asymptomatic Japanese population.** *J Clin Neurosci* 2006;13: 334–38 CrossRef Medline
5. Kuroda S, Hashimoto N, Yoshimoto T, et al; Research Committee on Moyamoya Disease in Japan. **Radiological findings, clinical course, and outcome in asymptomatic moyamoya disease: results of multicenter survey in Japan.** *Stroke* 2007;38:1430–35 CrossRef Medline
6. Hara S, Hori M, Murata S, et al. **Microstructural damage in normal-appearing brain parenchyma and neurocognitive dysfunction in adult Moyamoya disease.** *Stroke* 2018;49:2504–07 CrossRef Medline
7. Farrell JA, Zhang J, Jones MV, et al. **Q-space and conventional diffusion imaging of axon and myelin damage in the rat spinal cord after axotomy.** *Magn Reson Med* 2010;63:1323–35 CrossRef Medline
8. Jiang Q, Qu C, Chopp M, et al. **MRI evaluation of axonal reorganization after bone marrow stromal cell treatment of traumatic brain injury.** *NMR Biomed* 2011;24:1119–28 CrossRef Medline
9. Takagi T, Nakamura M, Yamada M, et al. **Visualization of peripheral nerve degeneration and regeneration: monitoring with diffusion tensor tractography.** *Neuroimage* 2009;44:884–92 CrossRef Medline
10. Jeong H, Kim J, Choi HS, et al. **Changes in integrity of normal-appearing white matter in patients with moyamoya disease: a diffusion tensor imaging study.** *AJNR Am J Neuroradiol* 2011;32:1893–98 CrossRef Medline
11. Bandettini PA, Wong EC, Hinks RS, et al. **Time course EPI of human brain function during task activation.** *Magn Reson Med* 1992;25:390–97 CrossRef Medline
12. Raab P, Hattingen E, Franz K, et al. **Cerebral gliomas: diffusional kurtosis imaging analysis of microstructural differences.** *Radiology* 2010;254:876–81 CrossRef Medline
13. Jensen JH, Falangola MF, Hu C, et al. **Preliminary observations of increased diffusional kurtosis in human brain following recent cerebral infarction.** *NMR Biomed* 2011;24:452–57 CrossRef Medline
14. Hui ES, Fieremans E, Jensen JH, et al. **Stroke assessment with diffusional kurtosis imaging.** *Stroke* 2012;43:2968–73 CrossRef Medline
15. Wityk RJ, Hillis A, Beauchamp N, et al. **Perfusion-weighted magnetic resonance imaging in adult moyamoya syndrome: characteristic patterns and change after surgical intervention: case report.** *Neurosurgery* 2002;51:1499–505 Medline
16. Kazumata K, Tha KK, Narita H, et al. **Characteristics of diffusional kurtosis in chronic ischemia of adult moyamoya disease: comparing diffusional kurtosis and diffusion tensor imaging.** *AJNR Am J Neuroradiol* 2016;37:1432–39 CrossRef Medline
17. Cheung MM, Hui ES, Chan KC, et al. **Does diffusion kurtosis imaging lead to better neural tissue characterization? A rodent brain maturation study.** *Neuroimage* 2009;45:386–92 CrossRef Medline
18. Cechetti F, Pagnussat AS, Worm PV, et al. **Chronic brain hypoperfusion causes early glial activation and neuronal death, and subsequent long-term memory impairment.** *Brain Res Bull* 2012;87:109–16 CrossRef Medline
19. Kazumata K, Tha KK, Narita H, et al. **Chronic ischemia alters brain microstructural integrity and cognitive performance in adult Moyamoya disease.** *Stroke* 2015;46:354–60 CrossRef Medline
20. Weber RA, Hui ES, Jensen JH, et al. **Diffusional kurtosis and diffusion tensor imaging reveal different time-sensitive stroke-induced microstructural changes.** *Stroke* 2015;46:545–50 CrossRef Medline
21. Zhu LH, Zhang ZP, Wang FN, et al. **Diffusion kurtosis imaging of microstructural changes in brain tissue affected by acute ischemic stroke in different locations.** *Neural Regen Res* 2019;14:272–79 CrossRef Medline
22. Guo YL, Zhang ZP, Zhang GS, et al. **Evaluation of mean diffusion and kurtosis MRI mismatch in subacute ischemic stroke: comparison with NIHSS score.** *Brain Res* 2016;1644:231–39 CrossRef Medline
23. Nael K, Trouard TP, Lafleur SR, et al. **White matter ischemic changes in hyperacute ischemic stroke: voxel-based analysis using diffusion tensor imaging and MR perfusion.** *Stroke* 2015;46:413–18 CrossRef Medline
24. Carano RA, Li F, Irie K, et al. **Multispectral analysis of the temporal evolution of cerebral ischemia in the rat brain.** *J Magn Reson Imaging* 2000;12:842–58 CrossRef Medline
25. Yang Q, Tress BM, Barber PA, et al. **Serial study of apparent diffusion coefficient and anisotropy in patients with acute stroke.** *Stroke* 1999;30:2382–90 CrossRef Medline

Effects of Susceptibility Artifacts on Perfusion MRI in Patients with Primary Brain Tumor: A Comparison of Arterial Spin-Labeling versus DSC

H. Maral, E. Ertekin, Ö. Tunçyürek, and Y. Özsunar

ABSTRACT

BACKGROUND AND PURPOSE: Our aim was to investigate the effects of intratumoral hemorrhage, calcification, and postoperative changes on the sensitivity of arterial spin-labeling and DSC perfusion MR imaging in patients with primary brain tumors.

MATERIALS AND METHODS: Eighty-six brain tumor lesions were examined with single-phase and multiphase arterial spin-labeling and DSC perfusion MR imaging. The lesions that had no intratumoral bleeding/calcifications and history of surgery were assigned to group 1 ($n = 38$), and the lesions that had these were assigned to group 2 ($n = 48$). The relative regional cerebral blood flow was calculated in both perfusion methods, and relative regional cerebral blood volume was calculated in DSC. Imaging results were correlated with histopathology or follow-up.

RESULTS: In the quantitative evaluation, the sensitivity and specificity of relative regional cerebral blood flow in multiphase arterial spin-labeling perfusion were 94.4% and 80% in group 1 and 78.3% and 88% in group 2, respectively. The sensitivity and specificity of relative regional cerebral blood flow in DSC perfusion were 88.9% and 75% in group 1 and 78.3% and 84% in group 2, respectively. The sensitivity and specificity of relative regional cerebral blood volume in DSC perfusion were 66.7% and 100% in group 1 and 69.6% and 96% in group 2, respectively. In the qualitative evaluation, the sensitivities for single-phase and multiphase arterial spin-labeling were 48.2% and 79.3%, respectively, with 100% specificity for both.

CONCLUSIONS: The sensitivity and specificity of multiphase arterial spin-labeling were similar to those of DSC perfusion irrespective of bleeding and calcification in primary brain tumors. Thus, we suggest that noncontrast multiphase arterial spin-labeling can be used instead of DSC perfusion MR imaging in the diagnosis and follow-up of intracranial tumors.

ABBREVIATIONS: ASL = arterial spin-labeling; mpASL = multiphase ASL; PI = perfusion imaging; rCBF = relative CBF; ROC = receiver operating characteristic; rrCBF = relative regional CBF; rrCBV = relative regional CBV; spASL = single-phase ASL

Perfusion MR imaging is a technique that provides information on angiogenesis at the microscopic level.¹ DSC MR imaging is a widely used and generally accepted MR imaging perfusion method for brain tumor diagnosis and staging.²⁻⁴ Arterial spin-labeling (ASL) is a promising perfusion MR imaging method, which is repeatable, low-cost, and noninvasive and does not require the administration of exogenous contrast.⁵

Brain tumors are often heterogeneous lesions and may include bleeding and calcification.⁶ In addition, bleeding residues such as hemosiderin are frequently seen in patients postoperatively.^{2,7} It is

known that the content of hemorrhage residues and calcium disturb the inhomogeneity of the magnetic field, reducing the sensitivity of perfusion by causing susceptibility artifacts.⁸ Some studies have reported that DSC perfusion imaging (PI) is more commonly affected by susceptibility artifacts compared with ASL-PI.⁹⁻¹¹ However, there are no large case series studies investigating this issue systematically. The primary purpose of our study was to investigate how these artifacts affect the sensitivity of both perfusion techniques in distinguishing malignant from benign brain tumors. The second aim was to compare the sensitivity of single- and multiphase ASL (spASL and mpASL) methods in distinguishing malignant from benign brain tumors. In addition, we compared the relative regional CBV (rrCBV) and relative regional CBF (rrCBF) values used in the literature to determine which method was more useful.

MATERIALS AND METHODS

Approval of the local ethics committee was obtained for the study.

Received June 21, 2019; accepted after revision November 25.

From the Department of Radiology (H.M.), Dr. Siyami Ersek Thoracic and Cardiovascular Surgery Training and Research Hospital, Istanbul, Turkey; Department of Radiology (E.E., Ö.T., Y.Ö.), Aydın Adnan Menderes University Faculty of Medicine, Aydın, Turkey; and Department of Radiology (Ö.T.), Near East University Faculty of Medicine, Nicosia, Cyprus.

Please address correspondence to Hakan Maral, Dr. Siyami Ersek Thoracic and Cardiovascular Surgery Training and Research Hospital, Department of Radiology, 13 Tibbiye Street, Üsküdar/Istanbul 34668, Turkey; e-mail: hknmaral@gmail.com <http://dx.doi.org/10.3174/ajnr.A6384>

Table 1: Perfusion MR imaging parameters

Sequence Parameters	spASL	mpASL	DSC
Acquired orientation	Axial	Axial	Axial
TR (ms)	4000	250	1800
TE (ms)	25	20	40
Flip angle	70°	35°	75°
FOV (mm ²)	240	240	224
Matrix (pixel)	68 × 68	68 × 68	88 × 88
Thickness/gap (mm)	6/0.6	6/0.6	5/0
Pulse delay times (ms)	1200	300, 550, 800, 1050, 1300, 1550, 1800, 2050	—
Label thickness/gap (mm)	100/20	130/20	—
Acquisition time	4 min 8 sec	4 min 8 sec	1 min 40 sec

Note:—indicates “no labelling” and “no pulse delay time”; DSC, dynamic susceptibility contrast; FOV, field-of-view; mpASL, multi phase arterial spin-labeling; spASL, single phase arterial spin-labeling; TE, echo time; TR, repetition time.

Patient Selection

Records of all lesions were retrospectively reviewed for patients who were diagnosed with an intracranial mass and who had undergone perfusion MR imaging at Adnan Menderes University, Department of Radiology, with both ASL-PI and DSC-PI methods between January 2011 and February 2017. In total, we investigated 133 patients. A total of 54 lesions were excluded from the study, consisting of 7 lesions with an extra-axial mass, 8 lesions that were thought to be benign but were lost to follow-up, 5 lesions in patients who died of nontumor causes, 9 lesions without primary brain tumor, and 25 lesions with unverified diagnosis. A total of 86 lesions from 79 patients were included in the study.

The diagnosis of the lesions was confirmed either histopathologically or by performing follow-up MR imaging for at least 11 months. In the follow-up period, the lesions were considered benign when they did not appear different in terms of size, appearance, and enhancement compared with the previous images. The lesions were considered malignant when progression was observed in the images during the follow-up period. Samples for histopathologic examination were obtained by an operation or stereotactic biopsy.

The grading of tumors was performed on the basis of the pathologic criteria of the World Health Organization (2016) (grades I, II, III, IV). Grade I and II tumors were considered low-grade (benign), whereas grade III and IV tumors were considered high-grade (malignant).

Imaging Protocol

MR imaging was performed at 1.5T (Achieva; Philips Healthcare, Best, the Netherlands). T1-weighted axial, T2-weighted axial, FLAIR axial, and T2-weighted sagittal MR images were obtained during conventional brain MR imaging. The T2* sequence was used to determine intralesional bleeding or calcifications. The separation of calcium and blood from each other cannot be done using only the T2* sequence. We did not make such a distinction. The ASL perfusion sequence was performed before administering the MR imaging contrast agent. The pulsed ASL technique was used for spASL and mpASL. Afterward, a DSC sequence was performed using an automatic injector. Gadoterate meglumine was administered as the contrast agent via the antecubital vein at a dose of 0.1 mmol/kg (1 mmol = 0.5 mL) using an 18-ga IV catheter at a rate of 10 mL/s automatically (Spectris Solaris EP MR Injection System; MedRad, Indianola, Pennsylvania). This was followed by 20 mL of physiologic saline solution injection at almost the same rate. Parameters of the conventional brain MR imaging sequence

were the following: T1-weighted, matrix = 212 × 168 (T2-weighted = 232 × 168); FOV = 210 mm; TR = 460 ms (T2-weighted = 5700 ms); TE = 10 ms (T2-weighted = 110 ms); flip angle = 69° (T2-weighted = 90°); thickness = 5 mm with 1-mm interslice gaps; number of slices = 23; acquisition time = 90 seconds.

Multiphase ASL was capable of multisection image acquisition at multiple TI (inversion time) points and was based on the pulsed ASL technique. Image acquisition was performed at 8 TIs. For the mpASL for the first section, the minimum TI was 300 ms and subsequent TIs were increased by 250 ms, label thickness was 130 mm, and label gap was 20 mm. A total of 2880 images, including 1440 labeled and 1440 control images, were obtained. For the spASL, the pulse delay time was 1200 ms, label thickness was 100 mm, and label gap was 20 mm. In both spASL and mpASL, the labeling slab was positioned at the level of upper cervical region. Other features of the perfusion sequences are shown in the Table 1.

Data Processing

Image analysis was performed in an imaging workspace (Extended MR WorkSpace, Version 2.6.3.5; Philips Healthcare) with the special application tools, namely “neuro perfusion” and “Image Algebra” for DSC-PI and ASL-PI, respectively. DSC and ASL perfusion maps were evaluated by 2 radiologists with 4 and 20 years of neuroradiology experience (H.M. and Y.Ö.). Images were first evaluated by a radiologist (H.M.) with 4 years of neuroradiology experience. In cases where the first radiologist (H. M.) doubts, both radiologists evaluated the images together and arrived at the final decision. In addition, in the quantitative evaluation, the inter-rater agreement was evaluated using measurements from the ASL and DSC maps in another session. The same cutoff values were used in terms of benign-malignant distinction for a more objective evaluation. For the quantitative analysis, the lesions that had not previously undergone an operation and had no bleeding or calcification within the mass were classified as group 1. The lesions that had previous surgical treatment or had bleeding and/or calcifications within the mass were classified as group 2. In another session, lesions with both single- and multiphase ASL examinations were assessed by a qualitative analysis for malignancy detection.

Evaluation of ASL Perfusion

In the ASL data processing, subtraction images of the labeled and control images were obtained. The technique of generating

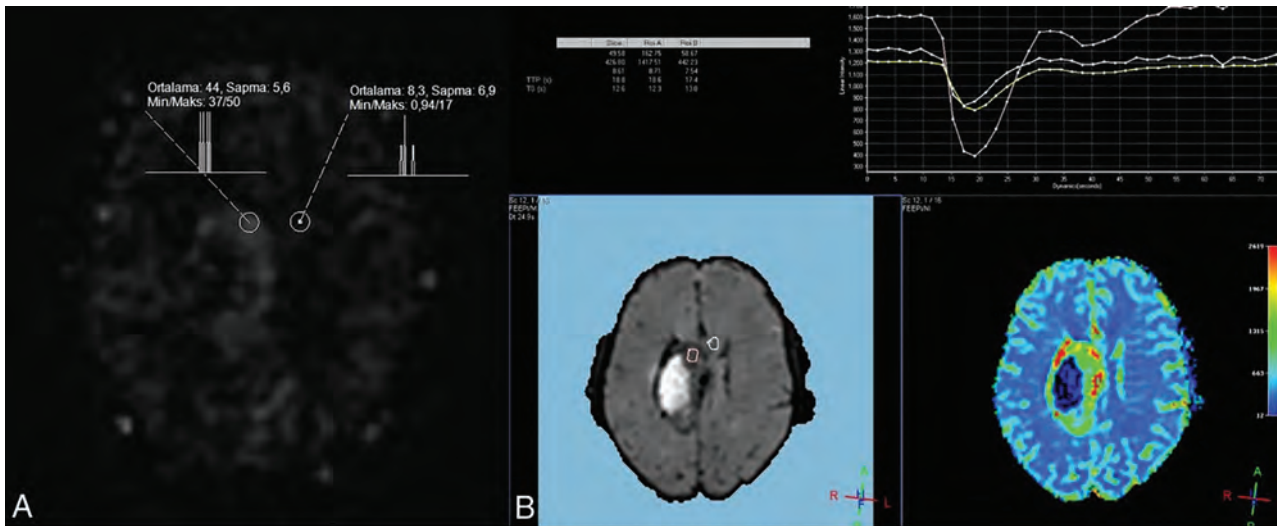


FIG 1. ROIs were located in the tumor and white matter of the contralateral hemisphere, and the measurements are seen on mpASL (A) and DSC (B) perfusion maps.

pulsed single- and multiphase ASL perfusion maps is described elsewhere.¹¹⁻¹⁴ Typically, the spASL measurements were obtained at a single TI between labeling and image acquisition. In the mpASL mapping, for the first slice, minimum inversion time was 300 ms, and subsequent inversion times were increased by 250 ms, and 48 subtraction images of the labeled and control images were obtained. The tumors were evaluated in the image in which delineation was best observed.

For the quantitative analysis in mpASL, a manually drawn elliptic ROI was placed on the solid and brightest portion of tumor seen in the subtraction images, which was assumed to have a high rate of perfusion. On average, 3 ROIs were placed on the basis of the lesion size, and the highest rCBF values were chosen. To normalize the values obtained, we drew an ROI of a size equal to the white matter in the contralateral hemisphere, which was the mirror symmetry of the tumor localization. A large ROI from the contralateral centrum semiovale was placed for patients in whom the ROI in the contralateral white matter could be small or problematic. The value of the maximum relative CBF (rCBF) of the tumor divided by the rCBF of the contralateral normal WM provided the value of the rrCBF (Fig 1). We used conventional sequences to place the ROI on the solid part of the tumor on the perfusion map. In particular, we used the T2-weighted images.

In the qualitative evaluation, the scoring was performed on a scale from 0 to 3. A zero score indicated that the lesion was hypointense compared with the white matter. A score of 1 indicated an isointense lesion compared with the white matter, and a score of 2 indicated a hyperintense lesion compared with the white matter. A score of 3 indicated that the lesion was remarkably hyperintense. The lesions with scores of 0 and 1 were considered benign, whereas the lesions with scores of 2 and 3 were considered malignant.

Evaluation of DSC Perfusion

For the quantitative evaluation, the arterial input function was determined after selecting the anterior cerebral artery or the middle cerebral artery on draft images to create DSC perfusion maps,

marking the contrast plateau on signal intensity–time curves, and finally creating the color maps. The contrast agent (gadolinium) that is extravasated due to the impaired blood-brain barrier causes permanent signal loss on T2-weighted sequences due to residual effect. Permanent signal loss influences first-passage images and subsequent recirculated images.¹⁵ To prevent the occurrence of leaking artifacts, software and correction algorithms were used (Extended MR WorkSpace, Version 2.6.3.5). The lesion was detected on the color DSC perfusion map, and relative regional CBF and CBV values were calculated by repeating the above-mentioned procedures with the ASL technique (Fig 1).

Statistical Analysis

The SPSS 23.0 program (IBM, Armonk, New York) was used for the statistical analyses. Receiver operating characteristic (ROC) curve analysis was used for determining the respective cutoff values. Comparison of ROC curves was performed by MedCalc, Version 18.11.0 (MedCalc Software, Mariakerke, Belgium). Normality tests were used for determining the distribution of continuous data (Kolmogorov-Smirnov), and nonparametric tests were used. The correlation between the perfusion parameters was assessed using the Spearman correlation analysis. The κ test was used for interrater agreement. $P < .05$ was considered significant.

RESULTS

A total of 86 lesions in 79 patients were evaluated. Of the included lesions, 48 (55.8%) were in men and 38 (44.2%) were in women, with a mean age of 48.9 ± 18.6 years. The diagnosis was made histopathologically in 38 (44.2%) lesions. The remaining 48 (55.8%) lesions were diagnosed during the follow-up period. Of the lesions in which the diagnosis was made histopathologically, 14 were glioblastomas, 7 were diffuse astrocytomas, 7 were anaplastic astrocytomas, 2 were WHO grade II oligodendrogliomas, 2 were anaplastic oligodendrogliomas, 2 were gliosarcomas, 2

Table 2: Histopathologic and follow-up diagnosis

	No.	Percentage
Histopathologic diagnosis	38	44.2
Benign lesions	13	15.1
Diffuse astrocytoma	7	8.1
WHO grade II oligodendroglioma	2	2.3
DNET	2	2.3
Cerebellar astrocytoma	1	1.2
Ganglioglioma	1	1.2
Malignant lesions	25	29.1
Glioblastoma	14	16.3
Anaplastic astrocytoma	7	8.1
Anaplastic oligodendroglioma	2	2.3
Gliosarcoma	2	2.3
Follow-up diagnosis	48	55.8
Benign lesions	32	37.2
Malignant lesions	16	18.6
Total	86	100

Note:—DNET indicate dysembryoplastic neuroepithelial tumors.

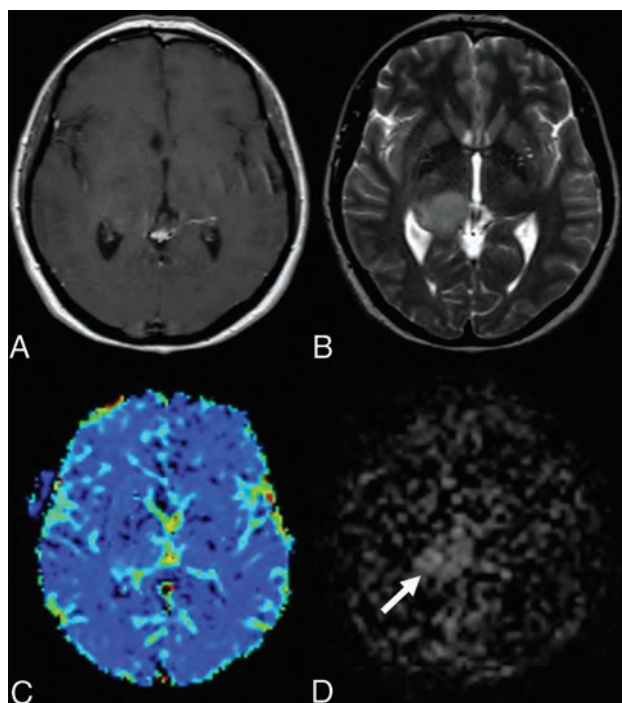


FIG 2. Anaplastic astrocytoma in a 44-year-old female patient. There is a mass in the T2-weighted (B) sequence showing a signal increase in the right thalamus. Also, there is a slight expansion in both T2-weighted (B) and the postcontrast T1-weighted (A) sequences. There is no significant enhancement in the postcontrast T1-weighted (A) MR image. There are no significant increases in perfusion in the mass localization derived from the DSC (C) perfusion color map (DSC rrCBF = 1). In the mpASL perfusion map (D), the perfusion increase in the mass localization can be seen clearly (ASL rrCBF = 3.3) (arrow).

were dysembryoplastic neuroepithelial tumors, 1 was a cerebellar astrocytoma, and 1 was a ganglioglioma (Table 2).

In 48 lesions, the diagnosis was made by follow-up imaging (32 benign lesions, 16 malignant lesions). Sixteen lesions were diagnosed as malignant due to an increase in the lesion size and/or increased enhancement/perfusion during follow-up (Table 2). The mean follow-up period was 20.18 months (range, 11–60 months).

There were 38 lesions in group 1 (patients underwent no previous operations and had no findings of intratumoral hemorrhage/calcification) (Fig 2). Lesions with intratumoral hemorrhages and/or calcifications and lesions having undergone an operation previously for brain tumors (48 cases total) were recorded as group 2 (Fig 3).

The mean rrCBF and rrCBV values were approximately 2.3–2.7 times higher in the lesions with malignant primary tumors compared with the lesions with benign primary tumors, using the combination of histopathology or 11-month stability. There was a significant difference between the malignant and benign groups in terms of the both rrCBF and rrCBV values ($P < .001$ for both values and technique) (Table 3).

In the ROC analysis performed for evaluating the perfusion characteristics, the areas under the curve for rrCBF in the mpASL and DSC were found to be 0.879 and 0.886, respectively (Fig 4). On the basis of equal misclassification rates, cutoff values of 1.4 and 1.5, respectively, for the mpASL rrCBF and DSC rrCBF ratios, were the best in discriminating benign from malignant tumors (Table 3). For the quantitative evaluation, rrCBV measurements were also performed with the DSC-PI. In the ROC analysis, the area under the curve for perfusion evaluation of the rrCBV was calculated to be 0.902 (Fig 4). A cutoff value of 2.2 was accepted for the rrCBV value in DSC-PI (Table 3). No statistically significant difference was found in the comparison of ROC curves in group 1, in group 2, and in all lesions (P values between .214 and .821).

The interrater agreement was good for ASL map ($\kappa = 0.766$) and very good for CBF and CBV on the DSC map ($\kappa = 0.907$ and $\kappa = 0.923$, respectively). The correlation analyses among the perfusion parameters revealed a strong correlation between the mpASL rrCBF and the DSC rrCBF ($r = 713, P < .001$). There was also a strong correlation between the mpASL rrCBF and the DSC rrCBV ($r = 675, P < .001$). Furthermore, there was a very strong correlation between the DSC rrCBF and the DSC rrCBV ($r = 907, P < .001$).

There were 55 lesions (26 benign and 29 malignant lesions) that had undergone both single and multiphase ASL-PI. In the qualitative evaluation of the mpASL-PI map, 23 of 29 malignant lesions were diagnosed correctly and all 26 benign lesions were diagnosed correctly (mpASL-PI, sensitivity = 79.3%, specificity = 100%). On the qualitative evaluation of the spASL-PI map, 14 of 29 malignant lesions were diagnosed correctly and all 26 benign lesions were diagnosed correctly (spASL-PI: sensitivity = 48.2%, specificity = 100%). Although there was a perfusion increase in the mpASL in 9 malignant cases, there was no increase in perfusion was observed in the spASL imaging (Fig 5).

DISCUSSION

In our study, we found that the rrCBF values in both mpASL and DSC perfusion MR imaging were more sensitive than the rrCBV values in DSC perfusion MR imaging in identifying the tumor tissue in the lesions with susceptibility artifacts due to bleeding and/or calcifications. When the mpASL and DSC perfusion MR imaging were compared, the sensitivity and accuracy of ASL perfusion was higher but the difference was not statistically significant. These findings are consistent with the literature. Previously, the

superiority of mpASL to spASL was shown in healthy patients.^{16,17} In our study, we also showed that mpASL was significantly superior in patients with primary brain tumors.

In the literature, there are many studies comparing the functional and conventional MR imaging techniques, showing that rrCBV is the most sensitive marker in differentiating benign from malignant lesions and in evaluating whether a brain tumor is recurrent or residual.^{14,18-21} However, most of these studies did not use ASL-PI.^{3,4} In most studies using ASL-PI, only spASL was evaluated,¹⁸⁻²⁰ and some studies reported that spASL had a higher

sensitivity.¹⁴ Ozsunar et al¹⁴ showed that the sensitivity of ASL was high (94%), but its specificity was low (50%) in a study comparing spASL with DSC-PI in distinguishing tumor recurrence from radiation necrosis. Cebeci et al²¹ conducted a study and compared mpASL and DSC perfusion techniques, reporting that the specificity of ASL was higher than that obtained in DSC perfusion (92.3% versus 76.9%). When ASL and DSC perfusion were used in combination, all malignant lesions were diagnosed accurately. In our study, we found that the rrCBF value derived from mpASL perfusion had a higher sensitivity and accuracy compared with the DSC

perfusion parameters, rrCBF and rrCBV, in discriminating benign and malignant tumors. However, this difference was not statistically significant. Although the specificity of rrCBF values in DSC perfusion was slightly lower, the sensitivity and accuracy rates were higher than those of rrCBV.

In the literature, it has been reported that intratumoral calcifications and/or bleeding or postoperative changes cause susceptibility artifacts more commonly in DSC compared with ASL.⁹⁻¹¹ In pathologies in which the blood-brain barrier is severely impaired (such as in glioblastomas and meningiomas), the leakage of the contrast medium into the extravascular area is one of the reasons for incorrect calculations in DSC-PI.²² However, the studies in this field are limited and not systematic. In the current study, which examined 2 groups of lesions (with native tumors and with tumors that might contain artifacts), we found that susceptibility artifacts resulted in a decrease in the diagnostic sensitivity in both the mpASL-PI and DSC-PI methods at similar rates (in group 2, both ASL and DSC sensitivity was 80%). This situation may be related

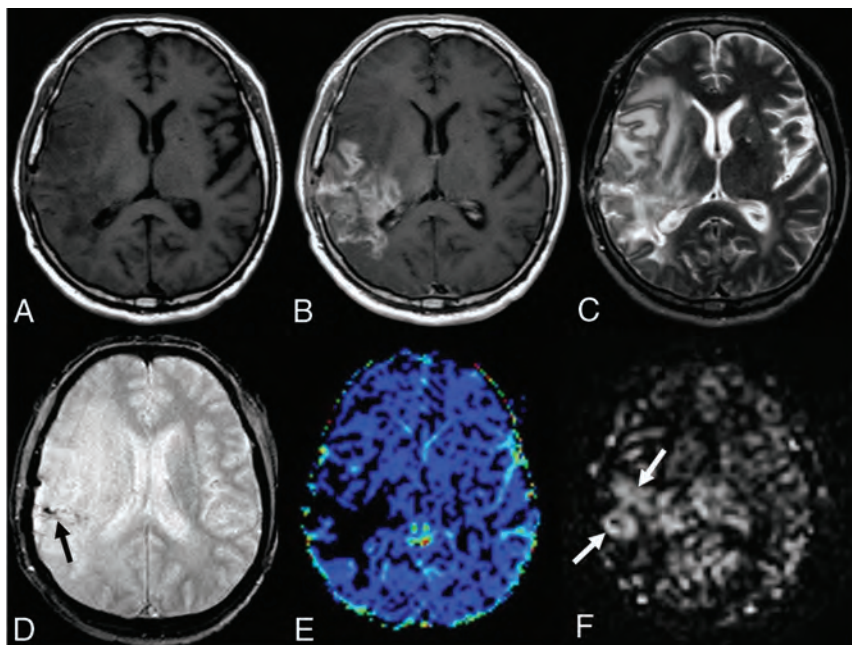


FIG 3. A 49-year-old male patient who underwent an operation and received chemoradiotherapy due to a glioblastoma in the temporoparietal region 1 year ago. T1-weighted (A) and T2-weighted (C) MR images show postoperative changes and alterations in the signal intensities in the right temporoparietal region. The postcontrast image (B) shows wide-scale enhancement in the site of the operation. The T2*-weighted image (D) shows hypointensities secondary to old bleeding residues (black arrow). The DSC perfusion map (E) shows a large perfusion signal loss caused by leakage artifacts in the contrasted areas (DSC rrCBF = 1.3). In the mpASL perfusion map (F), there is a significant increase in perfusion at the site of the operation (white arrows) (ASL rrCBF = 3.5). The patient was diagnosed with a recurrent glioblastoma after the second operation.

Table 3: Perfusion parameters of benign and malignant tumors on the quantitative evaluation

	Benign Tumors Mean (± SD)	Malignant Tumors Mean (± SD)	P ^a	Sensitivity (%)	Specificity (%)	Accuracy (%)
All lesions (n = 86) ^b						
mpASL rrCBF	1.19 (0.59)	2.84 (1.44)	<.001	85.4	84.4	84.9
DSC rrCBF	1.19 (0.69)	2.93 (1.57)	<.001	82.9	80.0	81.45
DSC rrCBV	1.20 (0.62)	3.07 (1.43)	<.001	68.3	97.8	83.05
Group 1 (n = 38) ^c						
mpASL rrCBF	1.24 (0.47)	3.06 (1.45)	<.001	94.4	80.0	87.2
DSC rrCBF	1.33 (0.83)	3.13 (1.80)	<.001	88.9	75.0	81.95
DSC rrCBV	1.32 (0.67)	3.22 (1.43)	<.001	66.7	100	83.35
Group 2 (n = 48) ^d						
mpASL rrCBF	1.16 (0.68)	2.67 (1.45)	<.001	78.3	88.0	83.15
DSC rrCBF	1.08 (0.54)	2.77 (1.39)	<.001	78.3	84.0	81.15
DSC rrCBV	1.10 (0.58)	2.96 (1.45)	<.001	69.6	96.0	82.8

^a Mann-Whitney U test.

^b Benign (n = 45), malignant (n = 41).

^c Benign (n = 20), malignant (n = 18).

^d Benign (n = 25), malignant (n = 23).

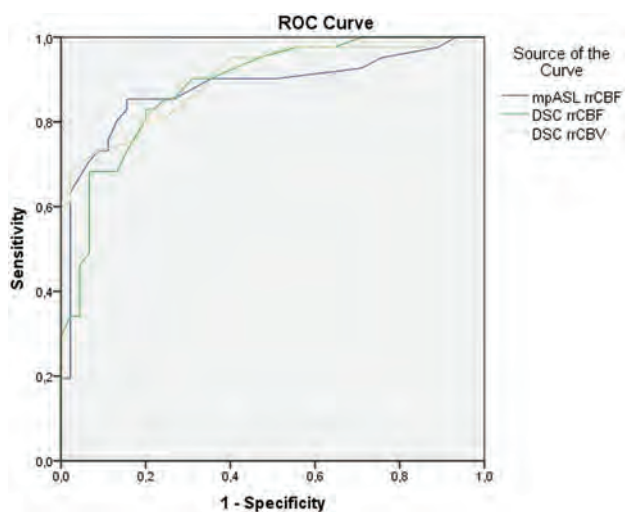


FIG 4. The ROC analysis curve. The blue line shows mpASL perfusion, and the green and the brown lines represent the DSC perfusion MR imaging technique for rrCBF and rrCBV, respectively.

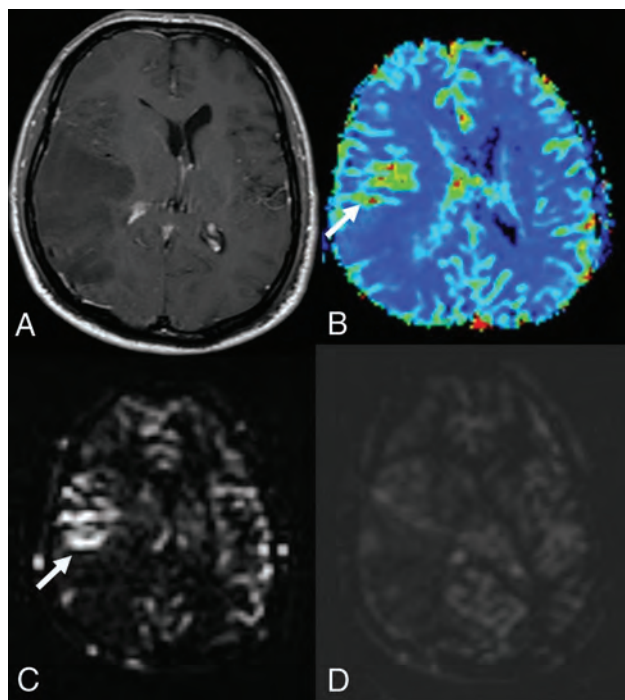


FIG 5. Anaplastic astrocytoma in a 41-year-old male patient. Post-contrast T1-weighted (A) image shows a wide nonenhancing mass lesion in the right temporoparietal region. There was no diffusion restriction (not shown here). The DSC (B) and mpASL (C) maps show significantly hyperperfused areas within the mass (arrows) (DSC rrCBF = 2.3, ASL rrCBF = 4.6). The spASL (D) map shows no increases in perfusion. It is also remarkable that the signal-to-noise ratio of spASL is lower than that of mpASL.

to the mpASL technique we use. However, the specificity was higher in group 2 (82.6% and 78.3% in group 1, 88.5% and 84.6% in group 2, respectively for mpASL and DSC). Signal loss due to hypoperfusion, microhemorrhages, and old bleeding residues secondary to an operation and radiation therapy may explain the lower false-positive values in group 2.²³

The recent 2016 World Health Organization classification has also shown us that genetic and molecular typing is crucial to progression in brain tumors.⁶ The minimum follow-up period in our study was 11 months. In some studies in the literature, the follow-up period was between 6 months and 2 years.⁵ Some previous studies that used a 6-month follow-up period were conducted before the relationship between some molecular markers and tumor prognosis was known.⁵

The disadvantages of the ASL perfusion technique are that only CBF mapping can be performed and CBF values can be measured. DSC perfusion can provide other parameters as well. Not obtaining other parameters, primarily the CBV, is an important limitation of the ASL technique. Although there are studies of the measurement of CBV by the ASL technique, the evaluation of ASL with CBV has not yet been used in clinical practice.²⁴ Moreover, geometric resolution of ASL perfusion maps obtained without contrast agent administration is lower than in the DSC perfusion maps, and low SNR is the other disadvantage of the ASL-PI. This problem may be overcome by the 3D pseudocontinuous method. The problem is less for examinations with high magnetic field strength. In our study, we used the pulsed ASL method on a 1.5T device. The ASL technique needs multiple repetitions for higher SNR, which causes longer imaging times. ASL image acquisition at multiple sections at multiple time points was also an advantage of this study.

There are many options in using the ASL technique, namely the single-phase and multiphase, pulsed, and continuous or pseudocontinuous methods.²³ There is no consensus on the clinical usefulness and diagnostic sensitivity of these methods in the literature. The spASL measurements are conducted at a single TI between labeling and image acquisition. The effects of the arterial arrival time or arterial transit time on CBF estimation make it difficult to get the best enhancement of the signal and evaluation. This problem can cause misinterpretation and errors in interpreting the qualitative and quantitative analyses of perfusion characteristics. Performing multiple ASL acquisitions at various TIs between the labeling and image acquisition can be used for solving this transit time problem. In our study, 63 lesions were qualitatively evaluated with multiphase and single-phase ASL techniques. In the qualitative evaluation with the mpASL-PI, while 27 of 34 malignant lesions were diagnosed correctly (sensitivity = 79.4%), only 17 malignant lesions were diagnosed correctly on the spASL-PI (sensitivity = 50%). As far as we know, there are no available studies comparing these 3 ASL methods in patients with brain tumors. However, in some studies, it has been shown that mpASL can give better SNR and more accurate CBF values in healthy subjects.^{16,17} We used the pulsed ASL at 1.5T in our study. However, these studies use the pseudocontinuous ASL at 3T.^{16,17} Therefore, it is not possible to make a complete comparison between the results of pseudocontinuous ASL and pulsed ASL studies. On the basis of our findings and the data in the literature, we concluded that it would be more appropriate to use mpASL instead of spASL in terms of diagnostic reliability in the evaluation of patients with intracranial tumors.

Limitations of our study are the retrospective nature of the study design and the lack of availability of histopathologic diagnoses in all lesions. The use of a 1.5T device in the study might

have an unfavorable effect on sensitivity. Optimum pulse-labeling duration differs in different age groups, and this might affect the signal. mpASL can be used to overcome this potential pitfall. Vendors suggest the use of low-resolution mpASL to choose the optimum higher resolution spASL. We used this method as suggested at the beginning, but unfortunately, we could not apply it to all patients because we had a large number of patients and heavy workload. Therefore, we preferred to evaluate the 2 ASL methods separately in our study. This is one of the limitations of our methodology.

CONCLUSIONS

The sensitivity and specificity of mpASL are similar to those of DSC perfusion, irrespective of bleeding and calcification in primary brain tumors. Other advantages of ASL include it being a contrast-free method, repeatable, and less costly. Therefore, we believe that noncontrast multiphase ASL can be used instead of DSC MR perfusion in the diagnosis and follow-up of primary intracranial tumors.

REFERENCES

- Kimura M, da Cruz LC Jr. **Multiparametric MR imaging in the assessment of brain tumors.** *Magn Reson Imaging Clin N Am* 2016;24:87–122 CrossRef Medline
- Heo YJ, Kim HS, Park JE, et al. **Uninterpretable dynamic susceptibility contrast-enhanced perfusion MR images in patients with post-treatment glioblastomas: cross-validation of alternative imaging options.** *PLoS One* 2015;10:e0136380 CrossRef Medline
- Law M, Yang S, Wang H, et al. **Glioma grading: sensitivity, specificity, and predictive values of perfusion MR imaging and proton MR spectroscopic imaging compared with conventional MR imaging.** *AJNR Am J Neuroradiol* 2003;24:1989–98 Medline
- Knopp EA, Cha S, Johnson G, et al. **Glial neoplasms: dynamic contrast-enhanced T2*-weighted MR imaging.** *Radiology* 1999;211:791–98 CrossRef Medline
- Ata ES, Turgut M, Eraslan C, et al. **Comparison between dynamic susceptibility contrast magnetic resonance imaging and arterial spin labeling techniques in distinguishing malignant from benign brain tumors.** *Eur J Radiol* 2016;85:1545–53 CrossRef Medline
- Louis DN, Perry A, Reifenberger G, et al. **The 2016 World Health Organization Classification of Tumors of the Central Nervous System: a summary.** *Acta Neuropathol* 2016;131:803–20 CrossRef Medline
- Hu LS, Baxter LC, Smith KA, et al. **Relative cerebral blood volume values to differentiate high-grade glioma recurrence from posttreatment radiation effect: direct correlation between image-guided tissue histopathology and localized dynamic susceptibility-weighted contrast-enhanced perfusion MR imaging measurements.** *AJNR Am J Neuroradiol* 2009;30:552–58 CrossRef Medline
- Aksoy FG, Lev MH. **Dynamic contrast-enhanced brain perfusion imaging: technique and clinical applications.** *Semin Ultrasound CT MR* 2000;21:462–77 CrossRef Medline
- Lev MH, Ozsunar Y, Henson JW, et al. **Glial tumor grading and outcome prediction using dynamic spin-echo MR susceptibility mapping compared with conventional contrast-enhanced MR: confounding effect of elevated rCBV of oligodendrogliomas [corrected].** *AJNR Am J Neuroradiol* 2004;25:214–21 Medline
- Xu Q, Liu Q, Ge H, et al. **Tumor recurrence versus treatment effects in glioma: a comparative study of three-dimensional pseudo-continuous arterial spin labeling and dynamic susceptibility contrast imaging.** *Medicine (Baltimore)* 2017;96:e9332 CrossRef Medline
- Kimura H, Takeuchi H, Koshimoto Y, et al. **Perfusion imaging of meningioma by using continuous arterial spin-labeling: comparison with dynamic susceptibility-weighted contrast-enhanced MR images and histopathologic features.** *AJNR Am J Neuroradiol* 2006;27:85–93 Medline
- Warmuth C, Gunther M, Zimmer C. **Quantification of blood flow in brain tumors: comparison of arterial spin labeling and dynamic susceptibility-weighted contrast-enhanced MR imaging.** *Radiology* 2003;228:523–32 CrossRef Medline
- Weber MA, Thilmann C, Lichy MP, et al. **Assessment of irradiated brain metastases by means of arterial spin-labeling and dynamic susceptibility-weighted contrast-enhanced perfusion MRI: initial results.** *Invest Radiol* 2004;39:277–87 CrossRef Medline
- Ozsunar Y, Mullins ME, Kwong K, et al. **Glioma recurrence versus radiation necrosis? A pilot comparison of arterial spin-labeled, dynamic susceptibility contrast enhanced MRI, and FDG-PET imaging.** *Acad Radiol* 2010;17:282–90 CrossRef Medline
- Asllani I, Borogovac A, Brown TR. **Regression algorithm correcting for partial volume effects in arterial spin-labeling MRI.** *Magn Reson Med* 2008;60:1362–71 CrossRef Medline
- Fazlollahi A, Bourgeat P, Liang X, et al. **Reproducibility of multiphase pseudo-continuous arterial spin labeling and the effect of post-processing analysis methods.** *Neuroimage* 2015;117:191–201 CrossRef Medline
- Wu B, Lou X, Wu X, et al. **Intra- and interscanner reliability and reproducibility of 3D whole-brain pseudo-continuous arterial spin-labeling MR perfusion at 3T.** *J Magn Reson Imaging* 2014;39:402–09 CrossRef Medline
- Ma H, Wang Z, Xu K, et al. **Three-dimensional arterial spin labeling imaging and dynamic susceptibility contrast perfusion-weighted imaging value in diagnosing glioma grade prior to surgery.** *Exp Ther Med* 2017;13:2691–98 CrossRef Medline
- Choi YJ, Kim HS, Jahng GH, et al. **Pseudoprogression in patients with glioblastoma: added value of arterial spin labeling to dynamic susceptibility contrast perfusion MR imaging.** *Acta Radiol* 2013;54:448–54 CrossRef Medline
- Seeger A, Braun C, Skardelly M, et al. **Comparison of three different MR perfusion techniques and MR spectroscopy for multiparametric assessment in distinguishing recurrent high-grade gliomas from stable disease.** *Acad Radiol* 2013;20:1557–65 CrossRef Medline
- Cebeci H, Aydin O, Ozturk-Isik E, et al. **Assessment of perfusion in glial tumors with arterial spin labeling: comparison with dynamic susceptibility contrast method.** *Eur J Radiol* 2014;83:1914–19 CrossRef Medline
- Boxerman JL, Schmainda KM, Weisskoff RM. **Relative cerebral blood volume maps corrected for contrast agent extravasation significantly correlate with glioma tumor grade, whereas uncorrected maps do not.** *AJNR Am J Neuroradiol* 2006;27:859–67 Medline
- Pollock JM, Tan H, Kraft RA, et al. **Arterial spin-labeled MR perfusion imaging: clinical applications.** *Magn Reson Imaging Clin N Am* 2009;17:315–38 CrossRef Medline
- Yan L, Li C, Kilroy E, et al. **Quantification of arterial cerebral blood volume using multiphase-balanced SSFP-based ASL.** *Magn Reson Med* 2012;68:130–39 CrossRef Medline

How Do Physicians Approach Intravenous Alteplase Treatment in Patients with Acute Ischemic Stroke Who Are Eligible for Intravenous Alteplase and Endovascular Therapy? Insights from UNMASK-EVT

J.M. Ospel, N. Kashani, U. Fischer, B.K. Menon, M. Almekhlafi, A.T. Wilson, M.M. Foss, G. Saposnik, M. Goyal, and M.D. Hill



ABSTRACT

BACKGROUND AND PURPOSE: With increasing use of endovascular therapy, physicians' attitudes toward intravenous alteplase in endovascular therapy–eligible patients may be changing. We explored current intravenous alteplase treatment practices of physicians in endovascular therapy– and alteplase-eligible patients with acute stroke using prespecified case scenarios and compared how their current local treatment practices differ compared with an assumed ideal environment.

MATERIALS AND METHODS: In an international multidisciplinary survey, 607 physicians involved in acute stroke care were randomly assigned 10 of 22 case scenarios, among them 14 with guideline-based alteplase recommendations (9 with level 1A and 5 with level 2B recommendation) and were asked how they would treat the patient: A) under their current local resources, and B) under assumed ideal conditions. Answer options were the following: 1) anticoagulation/antiplatelet therapy, 2) endovascular therapy, 3) endovascular therapy plus intravenous alteplase, and 4) intravenous alteplase. Decision rates were calculated, and multivariable regression analysis was performed to determine variables associated with the decision to abandon intravenous alteplase.

RESULTS: In cases with guideline recommendations for alteplase, physicians favored alteplase in 82.0% under current local resources and in 79.3% under assumed ideal conditions ($P < .001$). Under assumed ideal conditions, interventional neuroradiologists would refrain from intravenous alteplase most often (6.28%, OR = 2.40; 95% CI, 1.01–5.71). When physicians' current and ideal decisions differed, most would like to add endovascular therapy to intravenous alteplase in an ideal setting (196/3861 responses, 5.1%).

CONCLUSIONS: In patients eligible for endovascular therapy and intravenous alteplase, we observed a slightly lower decision rate in favor of intravenous alteplase under assumed ideal conditions compared with the decision rate under current local resources.

ABBREVIATIONS: EVT = endovascular therapy; LVO = large-vessel occlusion

Since 2015, endovascular therapy (EVT) and intravenous alteplase as a combined treatment have been standard of care in patients with acute ischemic stroke with large-vessel occlusion

(LVO) eligible for intravenous alteplase.¹ When the 5 major EVT trials were conducted, intravenous alteplase was the only approved treatment for acute ischemic stroke.² Hence, the only acceptable trial design from an ethical standpoint was to test EVT in combination with intravenous alteplase against standard medical treatment.

A new question now arises: Does intravenous alteplase provide additional value in the setting of acute ischemic stroke due to LVO when EVT is going to be performed anyway? This question will be answered by 3 ongoing randomized controlled trials (Bridging Thrombolysis Versus Direct Mechanical Thrombectomy in Acute Ischemic Stroke [SWIFT-DIRECT], NCT03192332; Intravenous Treatment followed by Intra-Arterial Treatment versus Direct Intra-Arterial Treatment for Acute Ischaemic Stroke Caused by a Proximal Intracranial Occlusion [MR CLEAN NO IV], ISRCTN80619088; and Direct Intra-Arterial Thrombectomy in Order to Revascularize AIS Patients With Large Vessel Occlusion Efficiently in Chinese Tertiary Hospitals [DIRECT-

Received September 23, 2019; accepted after revision December 11.

From the Departments of Clinical Neurosciences (J.M.O., B.K.M., M.A., A.T.W., M.M.F., M.G., M.D.H.) and Radiology (N.K., B.K.M., M.A., M.G., M.D.H.), University of Calgary, Calgary, Alberta, Canada; Division of Neuroradiology (J.M.O.), Clinic of Radiology and Nuclear Medicine, University Hospital Basel, University of Basel, Basel, Switzerland; University Hospital Bern (U.F.), Inselspital, University of Bern, Bern, Switzerland; and Division of Neurology (G.S.), Department of Medicine, St. Michael's Hospital, University of Toronto, Toronto, Ontario, Canada.

The study was funded by Stryker Inc through an unrestricted research grant to the University of Calgary. Stryker was not involved in the design, execution, analysis, and interpretation or reporting of the results.

Please address correspondence to Johanna M. Ospel, MD, Department of Clinical Neurosciences, Foothills Medical Centre, 1403 29th St NW, Calgary, AB, T2N2T9, Canada; e-mail: johannaospel@gmail.com; @johanna_ospel



Indicates article with supplemental on-line tables.

<http://dx.doi.org/10.3174/ajnr.A6396>

MT], (NCT03469206). Current understanding suggests that there is likely modest incremental benefit only and that the benefit may mainly accrue to those who reperfuse before the planned EVT procedure. Early reperfusion in the setting of proximal LVO occurs only in relatively few patients: In the Identifying New Approaches to Optimize Thrombus Characterization for Predicting Early Recanalization and Reperfusion With IV Alteplase and Other Treatments Using Serial CT Angiography (INTERRSeCT) study, 10% of distal ICAs and 21% of proximal M1s recanalized on follow-up CTA.³ In the Tenecteplase Versus Alteplase Before Endovascular Therapy for Ischemic Stroke (EXTEND-IA TNK) study, recanalization before EVT in proximal vessel occlusion was 10% with alteplase and 20% with tenecteplase during the time of transfer to the EVT hospital.⁴ The proportion may be lower if the time to EVT is fast. In the Endovascular Treatment for Small Core and Anterior Circulation Proximal Occlusion With Emphasis on Minimizing CT to Recanalization Times (ESCAPE) Trial, for instance, in which a large majority of patients were treated directly at the EVT center with very fast intravenous alteplase-to-EVT times, early recanalization was observed in only 5% of patients.⁵

In patients with drip-and-ship, however, when the time to EVT is longer, recanalization rates with alteplase might be higher. There is also evidence that intravenous alteplase before EVT might improve patient outcomes by reducing downstream microvascular thrombosis.⁶ Furthermore, complete recanalization with EVT is not guaranteed, and alteplase is most likely beneficial in cases with incomplete or failed recanalization. Current guidelines support providing both treatments concurrently when both are clinically appropriate.

However, clinical practice often does not match published evidence and guideline recommendations. How do physicians around the world currently approach intravenous alteplase treatment in the acute stroke setting in their clinical routine? This study aimed to explore real-life intravenous alteplase treatment practices of physicians across different countries and specialties using prespecified case scenarios.

MATERIALS AND METHODS

Survey Design

An international cross-sectional Web-based survey (UNMASK-EVT) was conducted among stroke physicians to explore their current treatment practices in acute ischemic stroke.⁷ Participants were assigned to 10 of 22 case scenarios and asked how they would treat the patient in the given scenario: A) under their current local resources, and B) under assumed ideal conditions, with no resource restraints of any kind. In this context, current local resources could reflect monetary and infrastructural limitations (lacking access to endovascular treatment facilities), staff resources (lacking availability of technicians/nurses), and local/institutional policies (such as hospital-specific rules regarding very old patients, and so forth). Answer options were the following: 1) anticoagulation/antiplatelet therapy, 2) EVT, 3) EVT plus intravenous alteplase, and 4) intravenous alteplase. Response data were obtained from November 26, 2017, to March 27, 2018. The study was approved by the local ethics board of the University of Calgary.

Table 1: Participants' demographic baseline characteristics (n = 607)

Demographics	
Specialty (No.) (%)	
Neurology	326 (53.7)
Interventional neuroradiology	173 (28.5)
Neurosurgery	81 (13.3)
Others	27 (4.2)
Hospital setting (No.) (%)	
Academic	551 (90.8)
Nonacademic	56 (9.2)
Age (median) (IQR) (yr)	44 (39–50)
Experience (median) (IQR) (yr)	13 (8–20)
Annual personal stroke volume (median) (IQR)	100 (50–250)
Annual personal EVT volume (median) (IQR)	30 (15–50)
Annual center tPA volume (median) (IQR)	100 (50–170)
Annual center EVT volume median (IQR)	65 (30–120)

Note.—IQR indicates interquartile range; yr, years.

Survey Participants

We invited 1330 stroke physicians (neurologists, interventional neuroradiologists, endovascular neurosurgeons, and other physicians, mostly internists and geriatricians, directly involved in acute stroke care) from 38 countries to participate in the survey. No restrictions regarding hospital setting, case volume, or experience levels were applied. Before answering the case scenarios, participants provided personal data (age, sex, years of experience in stroke treatment, estimated number of stroke patients treated per year, number of thrombectomies performed per year, geographic region, subspecialty, and hospital setting).

Clinical Case Scenarios

Twenty-two case scenarios were designed with different guideline recommendations for intravenous alteplase (9 with level 1A and 5 with level 2B recommendations, 2 without recommendations, and 6 with contraindications for intravenous alteplase) and EVT (8 with level 1A and 11 with level 2B recommendations, and 3 without recommendations for EVT).⁸ In the following analysis, only those 14 scenarios were included in which intravenous alteplase is recommended according to current American Heart Association/American Stroke Association guidelines (9 with level 1A and 5 with level 2B recommendations). Of note, the survey participants were presented with only the case vignettes; the evidence levels for EVT and alteplase treatment were not provided to them. For detailed descriptions of the case scenarios and corresponding evidence levels see On-line Table 1.

Statistical Analysis

Survey data were analyzed using descriptive statistics. Differences between categorical variables were assessed with the χ^2 test. Multivariable logistic regression with responses clustered within the respondent was used to estimate the association between patient and physician baseline characteristics and the decision to abandon intravenous alteplase when switching from current local resources to assumed ideal conditions. Models included patient and physician baseline characteristics, namely physician age and practice experience in years; personal annual EVT and stroke treatment volume; annual center intravenous alteplase and EVT volume; geographic region; specialty and hospital setting; presentation time; baseline ASPECTS; time since symptom onset; patient age; site of occlusion; and baseline functional status. Continuous variables were converted into deciles.

Table 2: Current and ideal decision rates in favor of intravenous alteplase overall and by evidence level^a

	EVT Level 1A	EVT Level 2B	EVT NG	Total
tPA level 1A				
Current	85.1 (1408)	85.0 (703)	–	85.0 (2111)
Ideal	82.1 (1359)	83.0 (687)	–	82.4 (2046)
tPA level 2B				
Current	77.5 (214)	84.3 (697)	52.0 (143)	76.5 (1054)
Ideal	75.0 (207)	80.5 (666)	52.0 (143)	73.7 (1016)
Total				
Current	84.0 (1622)	84.6 (1400)	52.0 (143)	82.0 (3165)
Ideal	81.1 (1566)	81.8 (1353)	52.0 (143)	79.3 (3062)

Note:—NG indicates no guideline coverage; –, no responses in this category.

^aCase scenarios with guideline-based alteplase recommendation only. Data are (%) (No.).

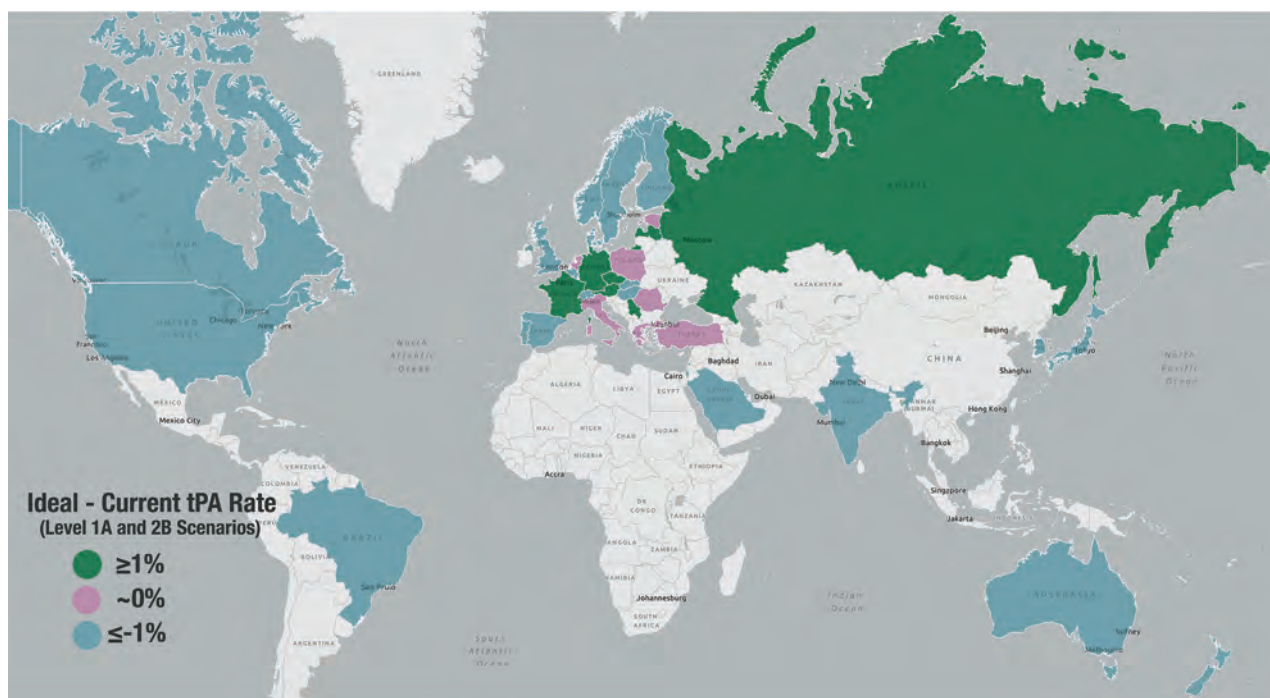


FIG 1. Resources gap (ideal minus current intravenous alteplase rates) in different countries. In green countries, the resources gap was positive ($>1\%$)—ie, physicians would want to treat more patients with intravenous alteplase in an ideal environment than they currently do under their current local resources. Pink countries are those with no resources gap—ie, the intravenous alteplase treatment decision under assumed ideal conditions matched the one under current local resources. In blue countries, the resources gap was negative—ie, physicians are currently treating more patients with intravenous alteplase than they would like to in an ideal environment.

All tests were 2-sided, and conventional levels of significance ($\alpha = .05$) were used for interpretation. Data analyses were performed in STATA 15.1 (StataCorp, College Station, Texas). Figures were created with Power BI desktop 2016 and the Mapbox Visual Plugin (Microsoft, Redmond, Washington).

RESULTS

Response Rate and Participants' Demographic Characteristics

A total of 607 physicians of different subspecialties from 38 countries completed the survey (response rate, 45.6%). Table 1 provides an overview about participants' demographic baseline characteristics. A total of 6070 responses were obtained for the 22 case scenarios, among them 3861 for the 14 scenarios with the guideline-based alteplase recommendation. Only the latter ones were included in the following analysis. The number of responses, evidence level, and

alteplase decision rates for each single case scenario can be found in the On-line Table 2.

Current and Ideal Decision Rates in Favor of Intravenous Alteplase

Table 2 shows the overall and evidence level-specific intravenous alteplase decision rates under current local resources and assumed ideal conditions. Overall, slightly fewer physicians would treat with intravenous alteplase under assumed ideal conditions (79.3%) compared with their decision under current local resources (82.0%; risk difference, 2.7%; $P < .001$; Table 2). This decision held true for neurologists, who constituted the largest group among all specialties, as well (85.7 versus 87.7%, $P < .001$). Only in case scenarios with level 2B evidence for intravenous alteplase and without guideline-based EVT recommendations would

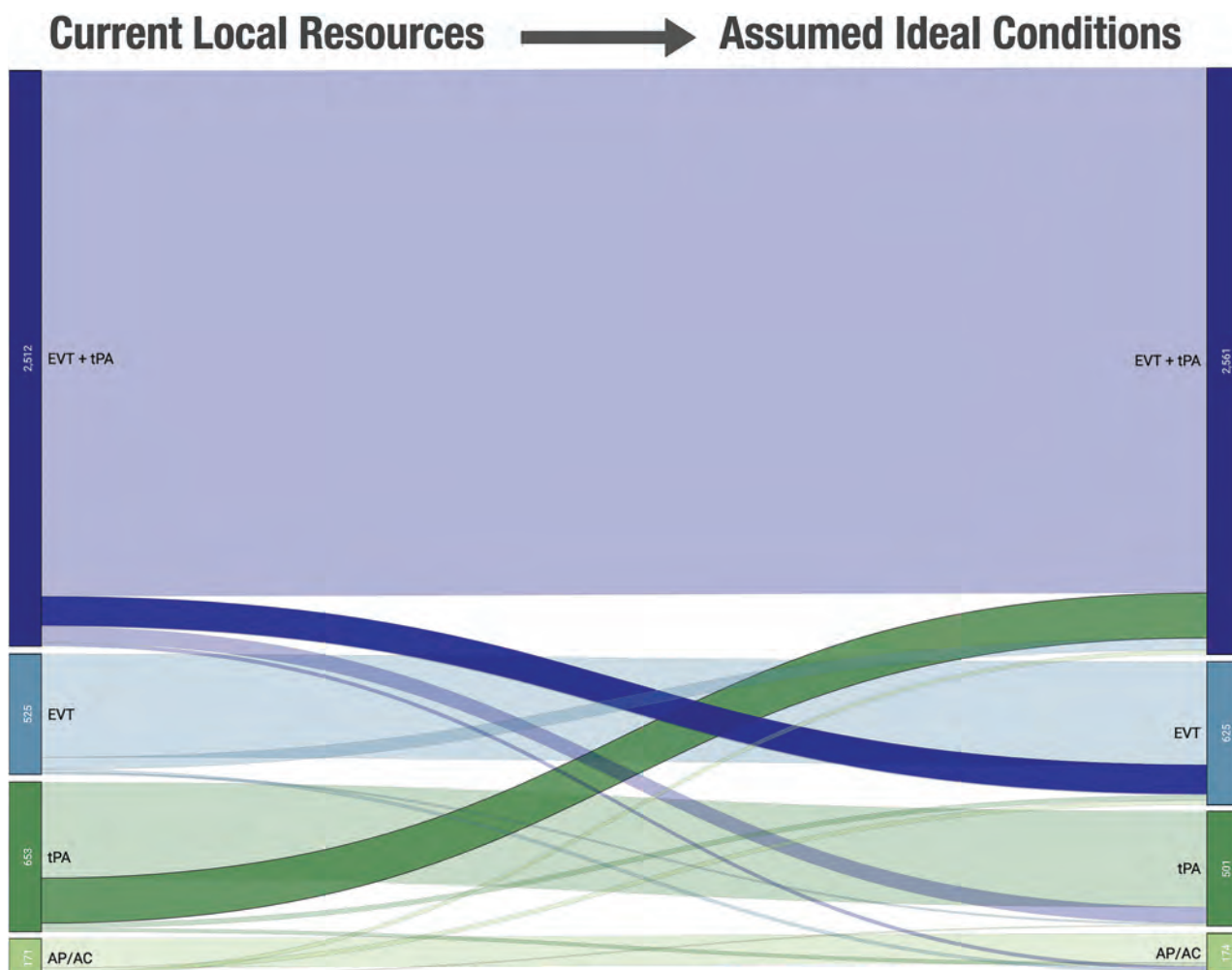


FIG 2. Changes in decision-making from current local resources (*left*) to assumed ideal conditions (*right*). The width of the streams is proportional to the number of changes. tPA, intravenous alteplase; AP/AC, antiplatelet or anticoagulation therapy.

participants proceed equally often with EVT under assumed ideal conditions and current local resources (52.0%, Table 2). Fig 1 illustrates the resources gap (ideal minus current intravenous alteplase decision rates) by country. In most countries, current intravenous alteplase decision rates are higher than the ideal rates.

Changes in Treatment Decision from Current Local Resources to Assumed Ideal Conditions

Fig 2 illustrates how physicians' decision-making changed between current local resources and assumed ideal conditions. Overall, patients in most case scenarios would have received the same treatment under current local resources and assumed ideal conditions. Among those physicians who changed their treatment approach under assumed ideal conditions, most of them would have liked to add EVT to intravenous alteplase (dark green stream in Fig 2; 196/3861 responses, 5.1%). The second-largest change occurred from alteplase plus EVT to EVT alone (dark blue stream in Fig 2; 133/3861 responses, 3.4%). Overall, alteplase would have been added in 84/3861 (2.2%) scenarios under assumed ideal conditions, while it would have been removed in 187/3861 (4.8%) scenarios.

Physician and Patient Characteristics Associated with the Decision to Abandon Intravenous Alteplase under Assumed Ideal Conditions

Multivariable logistic regression analysis revealed that of all physician characteristics, only the specialty of interventional neuroradiology was significantly associated with the decision to abandon intravenous alteplase (OR = 2.40; 95% CI, 1.01–5.71; reference category neurology) when switching from current local resources to assumed ideal conditions. Fig 3 shows the percentage of physicians who would drop and add intravenous alteplase when switching from current local resources to assumed ideal conditions. In an ideal environment, all specialties would drop intravenous alteplase more often than they would add it, and this choice was most pronounced in interventional neuroradiologists and neurosurgeons. Other physician factors (age, practice experience in years, personal annual EVT and stroke treatment volume, annual center intravenous alteplase and EVT volume, geographic region, hospital setting) and patient factors (presentation time, baseline ASPECTS, time since symptom onset, patient age, site of occlusion, baseline functional status) were not significantly associated with the decision to abandon intravenous alteplase.

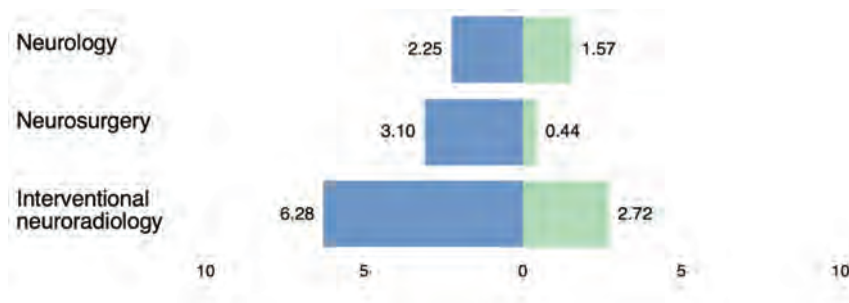


FIG 3. Percentage of physicians who would drop intravenous alteplase (blue bars) and add intravenous alteplase (green bars) by specialty.

DISCUSSION

In this multidisciplinary survey, we evaluated how physicians around the world approach intravenous alteplase treatment in patients eligible for EVT and alteplase treatment and how they would like to change their treatment practice when assuming ideal conditions (ie, in the absence of any external limitations). We found slightly lower reported intravenous alteplase decision rates under assumed ideal conditions compared with decision rates under current local resources (2.7% risk difference, Table 2). This finding mostly held true within individual countries as well (Fig 1). We suspect that under ideal conditions, EVT would be more readily available and that this reduction in reported alteplase treatment rates shows physicians' demands for a single method of reperfusion that has a high success rate. This behavior may reflect binary thinking: One solution is preferred when, in fact, the 2 treatments may be synergistic. While intravenous alteplase has been proven to be an effective treatment in acute ischemic stroke, and although recanalization rates for LVO are lower than for distal occlusions (5–10%),^{9,10} concurrent administration of alteplase and the use of EVT afford the possibility of early recanalization, even in patients with LVO.¹⁰ Furthermore, medical thrombolysis may facilitate EVT¹¹ through a reduction in a thrombus-endothelial interaction, leading to more effective first-pass reperfusion and by causing thrombolysis of distal emboli (whether such emboli are iatrogenic or due to the original stroke event).^{6,12} Indeed, our results show that among those physicians who changed their treatment decision when switching from current local resources to assumed ideal conditions, most of them would opt for a combined approach and add EVT to intravenous alteplase (Fig 2). This increase in EVT rates probably occurred because access to EVT is currently limited in many hospital settings.

In contrast, there are potential negative attributes of treatment with alteplase. The efficacy of both EVT and medical thrombolysis with alteplase is highly time-dependent, and difficulties in determining intravenous alteplase eligibility and initial transfer to a primary stroke center for its administration can substantially delay EVT, thereby reducing EVT efficacy and ultimately worsening patient outcome.^{13–16} Moreover, the absolute rate of major hemorrhage is slightly higher when alteplase is used, though it is not statistically significant.^{17,18} Both EVT and intravenous alteplase may cause thrombus fragmentation and distal embolization, but when alteplase is used primarily, it may convert a relatively

straightforward M1 embolectomy into a more difficult procedure, involving ≥ 2 middle cerebral artery branch occlusions. This feature potentially increases treatment costs without improving outcomes.¹⁹ These considerations could potentially explain why ideal alteplase rates were significantly lower (both in the overall group of participants as well as among neurologists, who constituted the largest specialty subgroup) than ideal rates, despite formal evidence for alteplase treatment. The difference was statistically

significant but small and of unclear clinical significance. However, depending on the results of MR CLEAN NO IV, DIRECT-MT, and SWIFT-DIRECT, this gap might grow further in the future. The specialty of interventional neuroradiology reported a significantly increased probability of dropping intravenous alteplase when switching from current local resources to assumed ideal conditions. This is likely due to treatment familiarity, but it could also potentially reflect a bias of binary thinking in treatment decision-making. The differences between current and ideal intravenous alteplase treatment rates in different countries, and particularly between North America and Europe (Fig 1), are most likely multifactorial and related to infrastructure and local policies. While the North American and European guidelines mostly agree in their alteplase and EVT treatment recommendations, local/institutional policies might differ across countries. Because neurologists were the largest group in almost all countries, physician specialty is probably not the main reason for these discrepancies. The exact reasons for the observed differences can, however, not be determined in this study and should be made subject to further research. Particularly in developing countries, many of which were not captured in this survey, access to EVT is still lacking and intravenous alteplase remains the mainstay of acute stroke therapy.

Our study has several limitations that deserve comment. The overall response rate of this survey was modest at 45.6%. Although the difference between current and ideal intravenous alteplase decision rates was statistically significant, the overall difference was small and the clinical significance of these discrepancies remains to be clarified. Enrollment was based on institutional networks and cooperations, potentially leading to a selection bias. Neurosurgeons and interventional neuroradiologists, who made up 42% of the participants, do not decide about alteplase treatment in most practice settings. We tried to design case scenarios that reflect clinical routine as realistically as possible, but a case-based survey cannot fully capture real-life decision-making. We did not obtain any information about the specific nature of external limitations that cause the resource gaps observed in our study. Furthermore, it is possible that lack of access to EVT in participants' current local setting, as is the case in many countries that were represented in this survey, also influences their treatment decisions under assumed ideal conditions: Physicians who do not have access to EVT might not be familiar with this treatment and might, thus, not feel comfortable offering it even if

they could. Last, the results of this survey are a snapshot in time, whereas clinical decision-making is a dynamic construct; it is possible, for instance, that more liberal EVT treatment practices in the future will cause further reactive changes in intravenous alteplase treatment practice. Despite its limitations, this study helps to explore how intravenous alteplase treatment in patients with acute ischemic stroke is currently approached across a broad international, multidisciplinary spectrum and provides a helpful context for the 3 ongoing randomized trials.

CONCLUSIONS

Participants of this survey stated that they would treat slightly more patients with intravenous alteplase in their current local setting than they would in an ideal environment. These differences, though statistically significant, were, however, small, and their clinical significance remains unclear at the moment. Physicians who changed their decisions under assumed ideal conditions mostly wanted to add EVT in addition to intravenous alteplase.

ACKNOWLEDGMENTS

The authors are most grateful to all physicians participating in the study.

Disclosures: Johanna M. Ospel—*RELATED: Grant:* Julia Bangerer—Rhyner Foundation, University of Basel Forschungsfonds, Freiwillige Akademische Gesellschaft Basel, *Comments:* research scholarship. Nima Kashani—*UNRELATED: Employment:* Calgary University. Urs Fischer—*UNRELATED: Consultancy:* Medtronic, Stryker, CSL Behring*; *Grants/Grants Pending:* Medtronic, *Comments:* SWIFT DIRECT trial.* Bijoy K. Menon—*OTHER RELATIONSHIPS:* I hold a patent on systems of triage in acute stroke and stock in Circle Neurovascular Imaging. Mona M. Foss—*RELATED: Consulting Fee or Honorarium:* University of Calgary, *Comments:* honorarium for statistical consulting. Gustavo Saposnik—*RELATED: Support for Travel to Meetings for the Study or Other Purposes:* University of Calgary; *UNRELATED: Consultancy:* Roche, Servier, Celgene; *Employment:* St. Michael's Hospital; *Grants/Grants Pending:* Roche, Servier; *Payment for Lectures Including Service on Speakers Bureaus:* Celgene, Servier; *Travel/Accommodations/Meeting Expenses Unrelated to Activities Listed:* Roche, *Comments:* to attend ECTRIMS 2019. Mayank Goyal—*RELATED: Grant:* Stryker, *Comments:* unrestricted research grant for conduction of UNMASK EVT*; *UNRELATED: Consultancy:* Medtronic, Stryker, Mentic, Micro-Vention, *Comments:* consulting regarding acute stroke intervention and products; *Patents (Planned, Pending or Issued):* GE Healthcare, *Comments:* licensing agreement for systems of acute stroke diagnosis. Michael D. Hill—*RELATED: Grant:* Stryker, *Comments:* grant to the University of Calgary for the UNMASK-EVT project*; *UNRELATED: Board Membership:* Coalition for National Science Funding Canadian Neuroscience Federation (CNSF) and Canadian Stroke Consortium (CSC), *Comments:* not-for-profit boards in stroke and neurology; *Consultancy:* Merck, *Comments:* paid consultancy for adjudicating clinical trial outcome events; *Grants/Grants Pending:* multiple sources, *Comments:* multiple grants from both industry and public sources for clinical trials*; *Patents (Planned, Pending or Issued):* patent on stroke care, *Comments:* patent granted. No money paid; *Stock/Stock Options:* Calgary Scientific Inc (CSI), *Comments:* stock owner in CSI, imaging and computer-rendering company. Mohammed Almekhlafi—*RELATED: Grant:* Stryker. *Money paid to the institution.

REFERENCES

- Goyal M, Menon BK, van Zwam WH, et al; HERMES Collaborators. **Endovascular thrombectomy after large-vessel ischaemic stroke: a meta-analysis of individual patient data from five randomised trials.** *Lancet* 2016;387:1723–31 CrossRef Medline
- Campbell BC, Meretoja A, Donnan GA, et al. **Twenty-year history of the evolution of stroke thrombolysis with intravenous alteplase to reduce long-term disability.** *Stroke* 2015;46:2341–46 CrossRef Medline
- Menon BK, Al-Ajlan FS, Najm M, et al; INTERRSeCT Study Investigators. **Association of clinical, imaging, and thrombus characteristics with recanalization of visible intracranial occlusion in patients with acute ischemic stroke.** *JAMA* 2018;320:1017–26 CrossRef Medline
- Campbell BC, Mitchell PJ, Churilov L, et al; EXTEND-IA TNK Investigators. **Tenecteplase versus alteplase before thrombectomy for ischemic stroke.** *N Engl J Med* 2018;378:1573–82 CrossRef Medline
- Goyal M, Demchuk AM, Menon BK, et al; ESCAPE Trial Investigators. **Randomized assessment of rapid endovascular treatment of ischemic stroke.** *N Engl J Med* 2015;372:1019–30 CrossRef Medline
- Desilles JP, Loyau S, Syvannarath V, et al. **Alteplase reduces downstream microvascular thrombosis and improves the benefit of large artery recanalization in stroke.** *Stroke* 2015;46:3241–48 CrossRef Medline
- Saposnik GM, Kashani N, Wilson AT, et al. **Factors associated with the decision-making on endovascular thrombectomy for the management of acute ischemic stroke.** *Stroke* 2019;50:2441–47 CrossRef Medline
- Powers WJ, Rabinstein AA, Ackerson T, et al; American Heart Association Stroke Council. **2018 Guidelines for the Early Management of Patients with Acute Ischemic Stroke: A Guideline for Healthcare Professionals from the American Heart Association/American Stroke Association.** *Stroke* 2018;49:e46–110 CrossRef Medline
- Mueller L, Pult F, Meisterernst J, et al. **Impact of intravenous thrombolysis on recanalization rates in patients with stroke treated with bridging therapy.** *Eur J Neurol* 2017;24:1016–21 CrossRef Medline
- Seners P, Turc G, Maier B, et al. **Incidence and predictors of early recanalization after intravenous thrombolysis: a systematic review and meta-analysis.** *Stroke* 2016;47:2409–12 CrossRef Medline
- Guedin P, Larcher A, Decroix JP, et al. **Prior IV thrombolysis facilitates mechanical thrombectomy in acute ischemic stroke.** *J Stroke Cerebrovasc Dis* 2015;24:952–57 CrossRef Medline
- Davalos A, Pereira VM, Chapot R, et al; Solitaire Group. **Retrospective multicenter study of Solitaire FR for revascularization in the treatment of acute ischemic stroke.** *Stroke* 2012;43:2699–705 CrossRef Medline
- Choi PM, Desai JA, Kashyap D, et al. **Are all stroke patients eligible for fast alteplase treatment? An analysis of unavoidable delays.** *Acad Emerg Med* 2016;23:393–99 CrossRef Medline
- Dhaliwal J, Ferrigno B, Abiola O, et al. **Hospital-based intervention to reduce tPA administration time.** *Interdisciplinary Neurosurgery* 2019;15:15–18. CrossRef
- Kamal N, Sheng S, Xian Y, et al. **Delays in door-to-needle times and their impact on treatment time and outcomes in Get with the Guidelines-Stroke.** *Stroke* 2017;48:946–54 CrossRef Medline
- Mohamad NF, Hastrup S, Rasmussen M, et al. **Bypassing primary stroke centre reduces delay and improves outcomes for patients with large vessel occlusion.** *Eur Stroke J* 2016;1:85–92 CrossRef Medline
- Wardlaw JM, Murray V, Berge E, et al. **Thrombolysis for acute ischaemic stroke.** *Cochrane Database Syst Rev* 2014;7:CD000213 CrossRef
- Yaghi S, Eisenberger A, Willey JZ. **Symptomatic intracerebral hemorrhage in acute ischemic stroke after thrombolysis with intravenous recombinant tissue plasminogen activator: a review of natural history and treatment.** *JAMA Neurol* 2014;71:1181–85 CrossRef Medline
- Rai AT, Boo S, Buseman C, et al. **Intravenous thrombolysis before endovascular therapy for large vessel strokes can lead to significantly higher hospital costs without improving outcomes.** *J Neurointerv Surg* 2018;10:17–21 CrossRef Medline

Impact of Aortic Arch Anatomy on Technical Performance and Clinical Outcomes in Patients with Acute Ischemic Stroke

J.A. Knox, M.D. Alexander, D.B. McCoy, D.C. Murph, P.J. Hinckley, J.C. Ch'ang, C.F. Dowd, V.V. Halbach, R.T. Higashida, M.R. Amans, S.W. Hetts, and D.L. Cooke



ABSTRACT

BACKGROUND AND PURPOSE: Arterial access is a technical consideration of mechanical thrombectomy that may affect procedural time, but few studies exist detailing the relationship of anatomy to procedural times and patient outcomes. We sought to investigate the respective impact of aortic arch and carotid artery anatomy on endovascular procedural times in patients with large-vessel occlusion.

MATERIALS AND METHODS: We retrospectively reviewed imaging and medical records of 207 patients from 2 academic institutions who underwent mechanical thrombectomy for anterior circulation large-vessel occlusion from January 2015 to July 2018. Preintervention CTAs were assessed to measure features of the aortic arch and ipsilateral great vessel anatomy. These included the cranial-to-caudal distance from the origin of the innominate artery to the top of the aortic arch and the takeoff angle of the respective great vessel from the arch. mRS scores were calculated from rehabilitation and other outpatient documentation. We performed bootstrap, stepwise regressions to model groin puncture to reperfusion time and binary mRS outcomes (good outcome, $mRS \leq 2$).

RESULTS: From our linear regression for groin puncture to reperfusion time, we found a significant association of the great vessel takeoff angle ($P = .002$) and caudal distance from the origin of the innominate artery to the top of the aortic arch ($P = .05$). Regression analysis for the binary mRS revealed a significant association with groin puncture to reperfusion time ($P < .001$).

CONCLUSIONS: These results demonstrate that patients with larger takeoff angles and extreme aortic arches have an association with longer procedural times as approached from transfemoral access routes.

ABBREVIATIONS: CCA = common carotid artery; CCIA = the cranial-to-caudal distance from the origin of the innominate artery to the top of the aortic arch; GPRT = groin puncture to reperfusion time; HTN = hypertension; LVO = large-vessel occlusion

Ischemic stroke is the fifth leading cause of death and the leading cause of long-term disability in the United States.¹ Recent studies have established mechanical thrombectomy as the criterion standard of care for large-vessel occlusion over tPA alone.²⁻⁵ These and other studies have demonstrated that reduced time between the onset of symptoms and reperfusion leads to better clinical outcomes.^{6,7} That time interval comprises prehospital

and in-house elements, but physicians can largely affect only the latter. The interplay of minimizing the time from a patient's symptom onset to reperfusion with the degree of reperfusion itself is at the core of current practice for the treatment of large-vessel occlusion (LVO).

While challenging arterial anatomy can lead to longer procedural times, scant literature exists detailing the impact of arch and carotid anatomy on procedural times. Ribo et al⁸ demonstrated that patients with difficult access have lower rates of recanalization and that carotid artery tortuosity can contribute to difficult access, but the aortic arch and carotid anatomy were not measured in this analysis. Kaymaz et al⁹ found a significant correlation between internal carotid access time and vessel anatomy, specifically the takeoff angle of the left common carotid artery (CCA)/innominate artery and CCA tortuosity. While these studies demonstrate that carotid tortuosity may extend the time to reperfusion, the impact of aortic arch anatomy on operative times has not been demonstrated. Additionally, no studies have looked

Received July 14, 2019; accepted after revision December 11.

From the Departments of Radiology (J.A.K., D.B.M., D.C.M., P.J.H., C.F.D., V.V.H., R.T.H., M.R.A., S.W.H., D.L.C.) and Neurology (J.C.C.), University of California, San Francisco, San Francisco, California; and Department of Radiology (M.D.A.), University of Utah, Salt Lake City, Utah.

This publication was supported by the National Center for Advancing Translational Sciences, National Institutes of Health, through the University of California, San Francisco—Clinical & Translational Science Institute grant No. TL1 TR001871.

Please address correspondence to Joseph A. Knox, BA, University of California, San Francisco, Department of Radiology, 513 Parnassus Ave, Suite S-245, San Francisco, CA 94143; e-mail: joseph.knox@ucsf.edu

Indicates open access to non-subscribers at www.ajnr.org

<http://dx.doi.org/10.3174/ajnr.A6422>

Table 1: Demographic variables

Variable	Mean or %
Age (yr)	69.4 (range, 21–98)
Sex (male)	45.4%
Side (left)	54.6%
Ethnicity	
White	56.9%
Asian	21.6%
Hispanic	13.7%
African American	7.4%
Pacific Islander	0.5%
Hypertension	68.1%
Hyperlipidemia	44.4%
Diabetes mellitus	24.2%
Coronary/peripheral artery disease	24.2%
Atrial fibrillation	44.9%
Prior stroke	14.0%

at the impact of the aortic arch and carotid artery tortuosity on clinical outcomes in LVO.

The purpose of this study was to investigate the respective impact of the aortic arch and carotid artery anatomy on endovascular procedural times in patients with LVO and to build a multi-variable model that may be prospectively applied to better direct arterial access approaches during LVO intervention.

MATERIALS AND METHODS

Patient Selection

This study was institutional review board–approved at both the University of California San Francisco and the University of Utah, and no informed consent was required. A total of 207 consecutive patients who underwent mechanical thrombectomy for anterior circulation LVO from January 2015 to July 2018 were included in this study. We had patient cohorts from 3 separate sites at 3 separate academic centers, which are staffed by fellowship-trained neurointerventional surgeons. We excluded patients who had an aborted endovascular intervention and acute ischemic stroke in the posterior circulation. Reasons for aborted interventions ranged from collateral filling seen during the intervention to rapid patient decompensation.

Patient and procedural data were collected retrospectively from the electronic medical record. Data points collected included the following: demographics (age at time of thrombectomy, sex, ethnicity), medical history (eg, hypertension [HTN], hyperlipidemia, diabetes mellitus, coronary artery disease/peripheral artery disease, atrial fibrillation, prior stroke), acute ischemic stroke episode details (eg, baseline mRS and NIHSS, last seen healthy to endovascular procedure start time, clot side, clot location, ASPECTS), and procedural intervention details (eg, exchange wire used, Simmons catheter use, stent placement, angioplasty, procedural time). Ethnicity data was collected due to the well-established differences in stroke rates amongst our studied ethnic groups. See Table 1 for basic demographic information on our study cohort.

Our primary outcome measures included groin puncture to reperfusion time (GPRT) and mRS, which were recorded from the medical record at discharge, 30 days, and 90 days.¹⁰

Procedure

Surgical procedures were performed by 9 different neurointerventional surgeons, each having at least 5 years of experience in endovascular stroke treatment at quaternary centers. All procedures were performed with the patient under moderate sedation or monitored anesthesia care, with general endotracheal anesthesia used only when necessary. Case selection was as prescribed by the 2015 and later 2018 American Heart Association/American Stroke Association guidelines. Equipment choice and technical details were case-specific as directed by the attending interventionalist at each site. Each procedure was performed according to the purview of the attending surgeon, the details of which were dictated by the clinical condition, though a stent retriever in tandem with catheter aspiration was the most frequently used thrombectomy technique.

Anatomic Measurement Protocol

CTA images were independently reviewed by 3 board-certified neuroradiologists and 1 trained medical student. Preprocedural CTA images were reviewed in the axial, coronal, and sagittal planes to generate anatomic metrics. Imaging analyses for the parameters of the aortic arch and carotid artery were similar to those described in the literature.^{9,11} Carotid and aortic length and angulation were directly calculated in the sagittal and coronal planes. Carotid and aortic length were defined as the curvilinear distance between the vessel origin and end. We limited our measurements to those that could be quickly generated from a CTA, including aortic arch variables (aortic arch types 1–3, medial-to-lateral span, anterior-to-posterior span, and the cranial-to-caudal distance from the origin of the innominate artery to the top of the aortic arch [CCIA]) and carotid artery variables (CCA/innominate takeoff angle, medial-to-lateral span of the CCA, and anterior-to-posterior span of the CCA). For anatomic spans, measurements were made with the caliper extending from the specific dimensional extreme at the margin of the target vessel to the edge of the film as a reference, allowing measurement across multiple cuts. For the takeoff angle, the angle between vessels was defined as the angle of the vessel off the aortic arch in reference to a straight line down the curve of the spine. For right-sided strokes, the innominate angle was calculated, and for left-sided strokes, the CCA angle was calculated. For arch type (I, II, or III), classifications were made as previously described.¹² Figure 1 gives detailed examples of these measurements and calculations.

Statistical Analysis

Statistical analyses were performed in R, Version 3.5 (<http://www.r-project.org/>).¹³ Before regression analysis, univariate analysis (logistic for mRS binary outcome and linear for reperfusion time) was used to determine which variables were independently associated with each outcome. The variables with *P* values < .1 were included in subsequent stepwise regression modeling. Because the most recent mRS score was limited (90-day follow-up), a composite variable was created, representing the most recent mRS score available for each patient. A binary mRS variable was created using the most recent mRS postprocedural metric, which stratified patients into either those with an mRS score of ≤2 or those with an mRS score of >2.

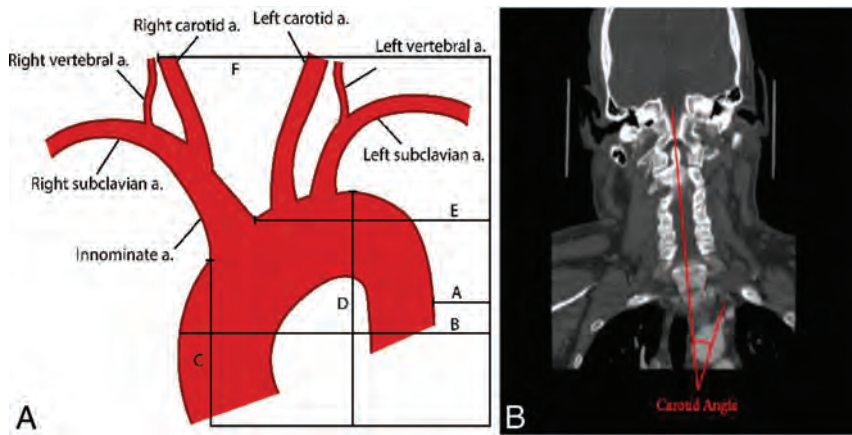


FIG 1. A, Diagram showing the calculation of sample measurements. B minus A represents the medial-to-lateral span of the aorta. E minus F represents the medial-to-lateral span of the right carotid artery. D minus C represents the cranial-to-caudal span of the aortic arch. B, Sample takeoff angle measurement of the left CCA on CTA with the angle of the spine as a reference. a. indicates artery.

Table 2: Results of groin puncture to reperfusion bootstrap while controlling for site^a

Variable	Estimate	Standard Error	P Value
Simmons (none)	13.74	8.01	.09
Tandem (none)	25.65 ^b	8.0 ^b	.02 ^b
Takeoff angle [10 degrees]	5.29 ^b	1.70 ^b	.002 ^b
Aorta cranial-caudal [5 mm]	2.98 ^b	1.48 ^b	.05 ^b
Left side (right)	2.32	5.01	.64
Site 2 (site 1)	2.48	6.42	.70
Site 3 (site 1)	-12.16	6.38	.06

^a Categorical values are indicated by parentheses with the baseline comparison within the parentheses. For continuous variables, units are shown in brackets.

^b Significant associations.

For both the GPRT outcome and the mRS outcome variable, a bootstrapped, stepwise linear regression model was used to model predictor variables. To determine the predictive validity of each model, we split the 207 observations into a training group (70%, 145 observations) and testing data (30%, 62 observations). Mean squared error as a percentage of the GPRT range and accuracy to classify binarized mRS change was used to determine the predictability of the 2 outcomes. One final model was determined for each outcome on the basis of the frequency of the variables used in the bootstrap and the reliability of the coefficients. In addition, the effect of a triple interaction of the takeoff angle, HTN and age on the GPRT was modeled. The GPRT was thought to be modulated by HTN and age on the basis of clinical experience from neurointerventionalists.

RESULTS

Anatomic Measurements

All except 7 patients (3.3%) had a complete series of images allowing accurate measurement of all anatomic variables. The most common reason for measurements not being obtained was the inferior aspect of images not including the aortic arch. The mean cranial-caudal span of the aorta was 10.9 ± 8.9 mm. The mean medial-lateral span and anterior-posterior span

of the aorta were 61.6 ± 15.5 mm and 101.0 ± 17 mm, respectively. The mean medial-lateral span of the carotid arteries on the affected side were 36.5 ± 12.4 mm and 28.2 ± 14.4 mm, respectively. The mean takeoff angle of either the innominate artery or carotid artery on the affected side was $20.3^\circ \pm 16.6^\circ$.

Procedural Outcomes

The mean GPRT was 55.6 ± 35.2 minutes with an interquartile range of 30–68 minutes. TICI 2b–3 recanalization was achieved in 159 cases (76.8%), while 12 cases resulted in TICI 0. One hundred nineteen clots were in M1 (57.5%), 48 (23.2%) were in the ICA, 39 (18.8%) were in M2, and 1 case (0.5%) was in the CCA. Tandem lesions occurred in 21 cases

(10.1%). Stents or percutaneous transluminal angioplasty was used in 14 (6.8%) and 21 (10.1%) cases, respectively. A Simmons catheter or an exchange wire was used in 24 (11.6%) and 48 (23.2%) cases, respectively. Last seen healthy to groin puncture time and last seen healthy to reperfusion time were found to be highly correlated (Pearson = 0.99); therefore, last seen healthy to reperfusion time was removed from downstream analysis.

For GPRT, the takeoff angle was the strongest and most consistent predictor, being included in 93.9% of the bootstrap models with coefficients being 100% positive. Table 2 outlines the results of the final model determined by bootstrap, stepwise regression modeling for the GPRT. The variables included in the final model were Simmons catheter use, tandem lesions, takeoff angle, cranial-to-caudal span of the aortic arch, side, and site. Variables that showed individual statistical significance with the GPRT were tandem lesions (tandem lesions resulted in a 25 minute 39 second increase in the GPRT, $P = 0.02$), takeoff angle (a 10° angle increase corresponding to a 5 minute 17 second increase in the GPRT, $P = .002$), and CCIA (a 5-mm increase in the CCIA span corresponded to a 2 minute 59 second increase in GPRT, $P = .05$). Site 3 compared with site 1 showed a borderline significant decrease in reperfusion times (-12 minute 36 second, $P = .06$). When we applied this model to the test set, the mean squared error was 34 and represents the mean error in minutes. Therefore, our model is accurate within 34 minutes in predicting reperfusion times.

Due to a limited sample size, we were able to find only a borderline significant triple interaction for hypertension, age, and the takeoff angle on the GPRT modeling, though this trending effect is apparent and shown in Fig 2. This interaction modeling demonstrates a shift in the association between the takeoff angle and GPRT as age increases in patients without hypertension ($P = .22$), which is absent in patients with hypertension (Fig 2). For example, in patients without hypertension, we found that a 1-SD increase of the takeoff angle was associated with a 16 minute 46 second increase in the groin puncture to reperfusion time, whereas for patients with hypertension, a 1-SD increase in

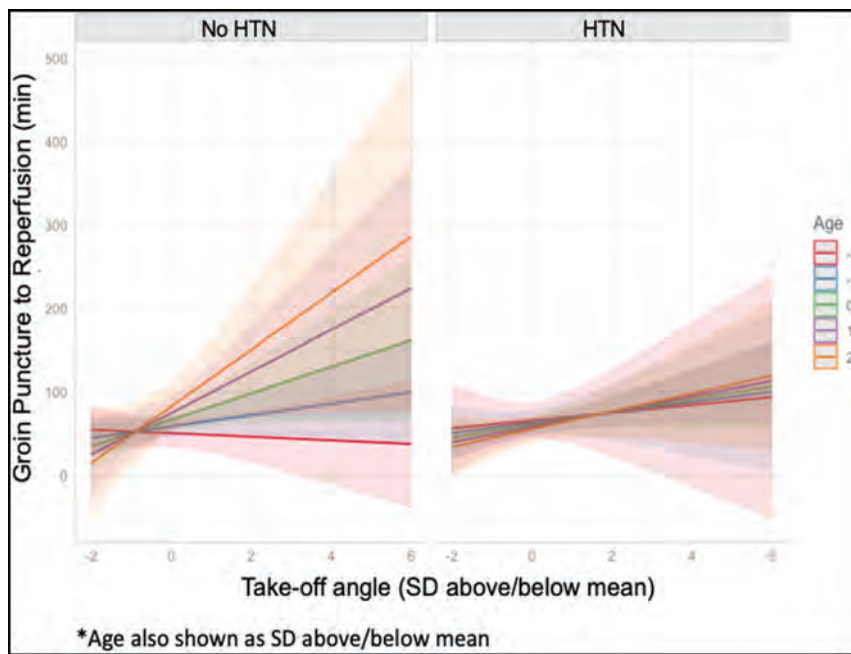


FIG 2. Results of interaction modeling for groin puncture to reperfusion. Associations between the takeoff angle (x-axis) and GPRT in minutes (y-axis) are shown in patients with and without hypertension. Data are standardized to units of the SD from the mean of both age and the takeoff angle. Age is plotted by SDs from the mean from -2 to $+2$ SDs of age.

Table 3: Results of bootstrap, stepwise logistic regression for binary mRS, controlling for mRS time point^a

Variable	OR	Lower CI	Upper CI	P Value
mRS: 30 days (discharge)	0.16 ^b	0.04 ^b	0.54 ^b	.004 ^b
mRS: 90 days (discharge)	0.13 ^b	0.04 ^b	0.40 ^b	<.001 ^b
mRS preprocedure [mRS score]	3.59 ^b	2.16 ^b	6.53 ^b	<.001 ^b
Exchange wire (none)	2.98	1.02	9.26	.05
ASPECTS [ASPECTS]	0.77	0.59	1.00	.05
HTN (none)	3.08 ^b	1.08 ^b	9.30 ^b	.04 ^b
Arch II (I)	0.57	0.19	1.65	.30
Arch III (I)	1.16 ^b	0.26	5.18	.85
Site 2 (I)	1.63	0.54	5.05	.39
Site 3 (I)	0.79	0.24	2.65	.70
LSNRT [60 min]	1.07	0.99	1.17	.09
GPRT [15 min]	1.93 ^b	1.52 ^b	2.55 ^b	<.001 ^b
Age [yr]	0.99	0.95	1.02	.47
Aorta medial-lateral [mm]	1.00	0.97	1.02	.82
Carotid anterior-posterior [min]	1.02	0.99	1.05	.16
Side L (R)	0.46	0.18	1.09	.09

Note:—LSNRT indicates last seen healthy to reperfusion time; L, left; R, right.

^aCategoric values are indicated by parentheses with the baseline comparison within the parentheses. For continuous variables, units are shown in brackets.

^bSignificant associations.

the takeoff angle was associated with a 9 minute 13 second increase in the groin puncture to reperfusion time, all while holding age at a mean value.

Clinical Outcomes

The mean last seen healthy to reperfusion time was 434.5 ± 321 minutes, with an interquartile range of 230–509 minutes. The mean preprocedural and postprocedural NIHSS scores were 16.8 ± 6.6 and 10.6 ± 9.1 , respectively, with 131 (63.3%) patients having a recorded postprocedural NIHSS. Two-hundred patients

(96.6%) had a recorded preprocedural mRS, and 187 patients (90.3%) had an mRS score recorded at discharge. Only 103 (49.8%) and 97 (46.9%) patients had 30-day mRS scores and 90-day mRS scores, respectively. One hundred twenty-five patients (60.3%) had either a 30-day or 90-day mRS score available. When patients were dichotomized into $mRS \leq 2$ or > 2 by the most recent score, 73.8% were in the higher mRS group, indicating a poor outcome.

Table 3 summarizes the results of the final model determined by bootstrap, stepwise logistic regression for binary mRS outcomes. Statistically significant independent predictors of more severe disability ($mRS > 2$) included the mRS type (compared with the mRS score recorded at discharge, mRS at 30 days had a reduced risk of severe mRS score, OR = 0.16, $P = .004$, and similarly for mRS recorded at 90 days, OR = 0.13, $P < .001$), preprocedural mRS (a 1-unit increase in the preprocedural mRS was associated with a 359% higher odds of a severe postsurgical score, $P = <.001$), hypertension (having hypertension increased the odds of a severe mRS score by 3.08-fold, $P = .04$), and GPRT (a 15-minute increase in the GPRT resulted in a 1.93-times increase of a severe mRS score, $P = <.001$). A borderline significant variable was the use of an exchange wire (2.98-time increase in a severe mRS score, $P = .05$), and a 1-unit increase in the ASPECTS was associated with reduced risk (OR = 0.77, $P = .05$). When applying this model to the test set, we found an accuracy of 80.63.

DISCUSSION

Patient demographic data, outcomes, and procedural results in our cohort were comparable with the populations and results of large-scale mechanical thrombectomy studies.^{5,14} Notably, our cohort had higher rates of atrial fibrillation at 45%. In addition, despite the higher last seen healthy to reperfusion time of our cohort compared with other studies, our outcome data are similar, with 73% of patients in the $mRS > 2$ group for the most recent mRS score. The longer last seen healthy to reperfusion time is likely because we did not include a temporal cutoff from stroke onset to presentation as previous studies did.

From the measured anatomic variables, we found that the takeoff angle and CCIA were significant independent predictors of procedural time. Although the CCIA has never been specifically shown to have an influence on procedural times in mechanical thrombectomy, unfavorable arch types (type II or III) have been associated with more ischemic events and longer procedural times in patients undergoing carotid stent placement.¹⁵⁻¹⁸ However, most of these studies found subjective associations primarily with arch type or, in 1 study, a composite “B.A.D. score” based on bovine variation, aortic arch type, and ICA dolichoarteriopathy.¹⁸ The 1 study to directly measure angulation did not use groin puncture to reperfusion time or clinical status as outcome measures but rather fluoroscopy time.¹⁹ In addition, all of these studies were from a single institution, with only 1 study including both procedural time measures and clinical outcomes. While we did not find arch type itself to be predictive of procedural time as in prior studies, the CCIA can be seen as a linear variable transformation of the ordinal variable arch type.¹² Among the 2 anatomic predictors of procedural time, the takeoff angle was more statistically significant and had a larger range of values. One prior study on mechanical thrombectomy found the takeoff angle of the CCA and the innominate artery as well as the tortuosity of the CCA to have the most significant influence in internal carotid artery access time, in agreement with our results.⁹ Collectively, these results confirm the notion that the takeoff angle of the innominate artery or left CCA is the first and possibly most difficult hurdle in ICA access from a femoral approach. Notably, our study examined overall procedural time and included a multivariate analysis compared with examination of internal carotid access time by univariate analysis of the prior study. The anatomic factors that we examined were chosen on the basis of calculations that could be standardized and quickly performed on preprocedural CTAs; thus, tortuosity was not included as a variable due to its more involved measurement criteria.⁹ The measurement of the takeoff angle in reference to the spine can likely be accomplished in <30 seconds by an experienced user, emphasizing the relative brevity of selected measurements in an emergency LVO.

When examining the effects of age and hypertension on the takeoff angle and procedural times through triple-interaction modeling, we found age to be a modifier of the effect of the takeoff angle on procedural times in patients without hypertension. The tortuosity of the carotid arteries seen in older patients appears to be influenced by long-standing hypertension and atherosclerosis.²⁰⁻²² Older patients without hypertension appear to be the most difficult cohort to access from our analysis, suggesting another etiology to the apparent tortuosity in the patient population, such as atherosclerosis. Thus, the presence or absence of HTN as a function of age conveys properties about the rigidity of the vessel wall, a dimension we have less success in capturing through conventional imaging alone.²³ Overall, our results suggest that an operator with a few pieces of information such as the takeoff angle, HTN status, and age may be able to make better judgments around a case with the ultimate goal of shrinking time to reperfusion.²⁴

From our clinical outcome analysis, we found that faster procedural times and last seen healthy to reperfusion times were associated with better outcomes, in agreement with prior

studies.^{25,26} Procedural times did significantly vary by site, but this was controlled for in our logistic regression. We did not find last seen healthy to reperfusion time to be significantly associated with more severe disability; however, it trended toward significance. This trend is likely due to the subjective nature of this variable, in addition to limitations of data collection from our county hospital site. We also did not find the ASPECTS to be a significant predictor of more severe disability, but this finding was likely due to the relative distribution of our ASPECTS with >90% being ≥ 6 .

On the basis of the results, operators may consider the use of a Simmons catheter at case start for instances with a carotid takeoff angle of $>10^\circ$ and/or an innominate origin of 5 mm caudal to the aortic apex. Furthermore, if a Simmons catheter is ineffective after 10 minutes of effort, operators should consider an alternative access approach (eg, carotid or radial), depending on their level of comfort and the particular clinical scenario. If a transcervical approach is used, general anesthesia is recommended; thus, mean arterial pressures must be maintained during induction and throughout the anesthesia period. In these cases, at our institution, arterial closure is performed by vascular or neurologic surgery, though other methods (eg, manual compression, closure device) have been described. The authors have no experience with transradial approaches for stroke, though we are aware of series describing success in both the anterior and posterior circulations.^{27,28} Prospective study of patients with anatomy that may prove more difficult to access via a transfemoral route using such alternative methods would benefit the community.

The retrospective nature of this study is a limitation. In addition, a certain amount of error should be taken into account for the measurement of takeoff angles, because this is the most subjective of our anatomic variables. For our clinical outcome analysis, we did not have access to longitudinal outcome data for half of our patients and thus had to create a composite mRS score for all patients. We did control for the time point in our logistic regression analysis to try to overcome this limitation. Finally, because this was a multi-institutional study, there were likely unstudied technical differences among institutions.

CONCLUSIONS

There was a strong association between larger takeoff angles and higher aortic arches and longer procedural times, especially in older patients without hypertension. This study presents a unique, comprehensive analysis of objective measurements of aortic arch anatomic factors, examining their effect on both procedural times and clinical outcomes. A nonfemoral access method such as direct carotid puncture should be considered when one is presented with these difficult patient and anatomic factors, to minimize procedural duration.

ACKNOWLEDGMENTS

We would like to thank Jacquelyn Withers for helping design our figures.

Disclosures: Joseph A. Knox—RELATED: Grant: National Institutes of Health TL1 TR001871, Comments: I received a National Institutes of Health TL1 research grant to perform yearlong research at the University of California,

San Francisco, where I attend the medical school. This research was supported by that grant. Christopher F. Dowd—UNRELATED: Other: Microvention, Comments: Chief Adjudicator for the FRED Flow Diverter Clinical Trial.* Matthew R. Amans—UNRELATED: Consultancy: Medtronic, Comments: Pipeline proctor; Grants/Grants Pending: National Institutes of Health, Comments: National Institutes of Health R21DC016087. *Money paid to the institution.

REFERENCES

1. Benjamin EJ, Blaha MJ, Chiuve SE, et al; American Heart Association Statistics Committee and Stroke Statistics Subcommittee. **Heart Disease and Stroke Statistics: 2017 Update—A Report from the American Heart Association.** *Circulation* 2017;135:e146–603 CrossRef Medline
2. Saver JL, Goyal M, Bonafe A, et al; SWIFT PRIME Investigators. **Stent-retriever thrombectomy after intravenous t-PA vs. t-PA alone in stroke.** *N Engl J Med* 2015;372:2285–95 CrossRef Medline
3. Goyal M, Demchuk AM, Menon BK, et al; ESCAPE Trial Investigators. **Randomized assessment of rapid endovascular treatment of ischemic stroke.** *N Engl J Med* 2015;372:1019–30 CrossRef Medline
4. Campbell BC, Mitchell PJ, Kleinig TJ, et al. **Endovascular therapy for ischemic stroke with perfusion-imaging selection.** *N Engl J Med* 2015;372:1009–18 CrossRef Medline
5. Berkhemer OA, Fransen PS, Beumer D, et al; MR CLEAN Investigators. **A randomized trial of intraarterial treatment for acute ischemic stroke.** *N Engl J Med* 2015;372:11–20 CrossRef Medline
6. Hassan AE, Chaudhry SA, Miley JT, et al. **Microcatheter to recanalization (procedure time) predicts outcomes in endovascular treatment in patients with acute ischemic stroke: when do we stop?** *AJNR Am J Neuroradiol* 2013;34:354–59 CrossRef Medline
7. Spiotta AM, Vargas J, Turner R, et al. **The golden hour of stroke intervention: effect of thrombectomy procedural time in acute ischemic stroke on outcome.** *J Neurointerv Surg* 2014;6:511–16 CrossRef Medline
8. Ribo M, Flores A, Rubiera M, et al. **Difficult catheter access to the occluded vessel during endovascular treatment of acute ischemic stroke is associated with worse clinical outcome.** *J Neurointerv Surg* 2013;5(Suppl 1):170–73 CrossRef Medline
9. Kaymaz Z, Nikoubashman O, Brockmann M, et al. **Influence of carotid tortuosity on internal carotid artery access time in the treatment of acute ischemic stroke.** *Interv Neuroradiol* 2017;23:583–88 CrossRef
10. Banks JL, Marotta CA. **Outcomes validity and reliability of the Modified Rankin Scale: implications for stroke clinical trials: a literature review and synthesis.** *Stroke* 2007;38:1091–96 CrossRef Medline
11. Boufi M, Guivier-Curien C, Loundou AD, et al. **Morphological analysis of healthy aortic arch.** *Eur J Vasc Endovasc Surg* 2017;53:663–70 CrossRef Medline
12. Lin SC, Trocciola SM, Rhee J, et al. **Analysis of anatomic factors and age in patients undergoing carotid angioplasty and stenting.** *Ann Vasc Surg* 2005;19:798–804 Medline
13. R Foundation for Statistical Computing. **R: A Language and Environment for Statistical Computing.** 2018. <https://www.R-project.org>. Accessed January 31, 2019
14. Campbell BC, Mitchell PJ, Kleinig TJ, et al; EXTEND-IA Investigators. **Endovascular therapy for ischemic stroke with perfusion-imaging selection.** *N Engl J Med* 2015;372:1009–18 CrossRef Medline
15. Dumont TM, Mokin M, Wach MM, et al. **Understanding risk factors for perioperative ischemic events with carotid stenting: is patient age over 80 years or is unfavorable arch anatomy to blame?** *J Neurointerv Surg* 2014;6:219–24 CrossRef Medline
16. Burzotta F, Nerla R, Pirozzolo G, et al. **Clinical and procedural impact of aortic arch anatomic variants in carotid stenting procedures.** *Catheter Cardiovasc Interv* 2015;86:480–89 CrossRef Medline
17. Müller MD, Ahlhelm FJ, Von Hessling A, et al. **Vascular anatomy predicts the risk of cerebral ischemia in patients randomized to carotid stenting versus endarterectomy.** *Stroke* 2017;48:1285–92 CrossRef Medline
18. Snelling BM, Sur S, Shah SS, et al. **Unfavorable vascular anatomy is associated with increased revascularization time and worse outcome in anterior circulation thrombectomy.** *World Neurosurg* 2018;120:e976–83 CrossRef Medline
19. Madhwal S, Rajagopal V, Bhatt DL, et al. **Predictors of difficult carotid stenting as determined by aortic arch angiography.** *J Invasive Cardiol* 2008;20:200–04 Medline
20. Pancera P, Ribul M, Presciuttini B, et al. **Prevalence of carotid artery kinking in 590 consecutive subjects evaluated by Echocolor-doppler: is there a correlation with arterial hypertension?** *J Intern Med* 2000;248:7–12 CrossRef
21. Del Corso L, Moruzzo D, Conte B, et al. **Tortuosity, kinking, and coiling of the carotid artery: expression of atherosclerosis or aging?** *Angiology* 1998;49:361–71 CrossRef Medline
22. Han HC. **Twisted blood vessels: symptoms, etiology and biomechanical mechanisms.** *J Vasc Res* 2012;49:185–87 CrossRef Medline
23. Messas E, Pernot M, Couade M. **Arterial wall elasticity: state of the art and future prospects.** *Diagn Interv Imaging* 2013;94:561–69 CrossRef Medline
24. Bourcier R, Goyal M, Liebeskind DS, et al; HERMES Trialists Collaboration. **Association of time from stroke onset to groin puncture with quality of reperfusion after mechanical thrombectomy: a meta-analysis of individual patient data from 7 randomized clinical trials.** *JAMA Neurol* 2019;76:405–11 CrossRef Medline
25. Schmitz ML, Yeatts SD, Tomsick TA, et al. **Recanalization and angiographic reperfusion are both associated with a favorable clinical outcome in the IMS III trial.** *Interv Neurol* 2016;5:118–12 CrossRef Medline
26. Mulder M, Jansen IG, Goldhoorn RJ, et al. **Time to endovascular treatment and outcome in acute ischemic stroke: MR CLEAN Registry results.** *Circulation* 2018;138:232–40 CrossRef Medline
27. Chen SH, Snelling BM, Sur S, et al. **Transradial versus transfemoral access for anterior circulation mechanical thrombectomy: comparison of technical and clinical outcomes.** *J Neurointerv Surg* 2019;11:874–78 CrossRef Medline
28. Maud A, Khatri R, Chaudhry MRA, et al. **Transradial access results in faster skin puncture to reperfusion time than transfemoral access in posterior circulation mechanical thrombectomy.** *J Vasc Interv Neurol* 2019;10:53–57 Medline

DWI-Based Algorithm to Predict Disability in Patients Treated with Thrombectomy for Acute Stroke

H. Raoult, M.V. Lassalle, B. Parat, C. Rousseau, F. Eugène, S. Vannier, S. Evain, A. Le Bras, T. Ronziere, J.C. Ferre, J.Y. Gauvrit, and B. Laviolle



ABSTRACT

BACKGROUND AND PURPOSE: The reasons for poor clinical outcome after thrombectomy for acute stroke, concerning around half of all patients, are misunderstood. We developed a hierarchic algorithm based on DWI to better identify patients at high risk of disability.

MATERIALS AND METHODS: Our single-center, retrospective study included consecutive patients with acute ischemic stroke who underwent thrombectomy for large anterior artery occlusion and underwent pretreatment DWI. The primary outcome was the mRS at 3 months after stroke onset. Multivariable regression was used to identify independent clinical and imaging predictors of poor prognosis (mRS > 2) at 3 months, and a hierarchic algorithm predictive of disability was developed.

RESULTS: A total of 149 patients were analyzed. In decreasing importance, DWI lesion volume of >80 mL, baseline NIHSS score of >14, age older than 75 years, and time from stroke onset to groin puncture of >4 hours were independent predictors of poor prognosis. The predictive hierarchic algorithm developed from the multivariate analysis predicted the risk of disability at 3 months for up to 100% of patients with a high predictive value. The area under the receiver operating characteristic curve was 0.87.

CONCLUSIONS: The DWI-based hierarchic algorithm we developed is highly predictive of disability at 3 months after thrombectomy and is easy to use in routine practice.

Stroke is one of the leading causes of mortality and disability worldwide.¹ In recent years, multiple randomized controlled trials have shown that endovascular treatment improves functional outcome in patients with a proximal occlusion of the anterior circulation,² with an efficacy unmatched by any previous therapy for stroke management, given a number needed to treat of <3 to achieve improved functional outcome. Endovascular treatment with or without intravenous alteplase yields a high recanalization rate of up to 90%^{2,3} and is therefore a validated, effective, and safe treatment now recommended for these patients.^{4,5} Current stroke guidelines are based on data from these randomized controlled trials including highly selected patients. Their encouraging results led to more widespread use of endovascular treatment; therefore, broader criteria than

those recommended are now used in current practice to treat, for example, elderly patients,⁶ patients with minimal stroke symptoms,⁷ or patients in late time windows up to 24 hours after stroke onset.⁸ On the other hand, the Highly Effective Reperfusion using Multiple Endovascular Devices (HERMES) meta-analysis of the main trials also highlighted that half of all patients have poor clinical outcomes despite successful technical recanalization.²

Because the reasons for poor clinical outcome after thrombectomy are not clearly understood⁹ and given that in clinical practice, patients are often of advanced age and present with high stroke severity or a large ischemic volume, patient selection for thrombectomy warrants improvement. Multiple individual poor prognostic factors may be involved simultaneously.⁹ Several prognostic tools have, therefore, been proposed,¹⁰⁻¹³ based on clinical and radiologic pretreatment criteria to predict the risk of disability after thrombectomy: Mainly advanced age, a high baseline NIHSS score, and a low baseline ASPECTS on noncontrast CT have been identified as reliable predictors of prognosis. However, these studies were conducted before the latest trials and were mainly based on CT but rarely on MR imaging to triage patients. Yet DWI was shown to be more accurate than noncontrast CT¹⁴ for estimating the ischemic core and was more accurate than perfusion CT for predicting final infarct volume.¹⁵ These findings suggest that DWI would be a better imaging

Received August 6, 2019; accepted after revision November 14.

From the Departments of Neuroradiology (H.R., B.P., F.E., J.C.F., J.Y.G.), Neurology (M.V.L., S.V., T.R.), and Clinical Pharmacology (C.R., B.L.), Institut National de la Santé et de la Recherche Médicale, Centre d'Investigation Clinique de Rennes, Centre Hospitalier Universitaire Rennes, Rennes, France; and Departments of Neurology (S.E.) and Radiology (A.L.B.), Centre Hospitalier Universitaire Bretagne Atlantique, Vannes, France.

Please address correspondence to Héléne Raoult, MD, PhD, Neuroradiologie, CHU Pontchaillou, 2 Rue Henri Le Guilloux, 35033 Rennes, France; e-mail: helene.raoult@chu-rennes.fr



Indicates article with supplemental on-line photo.

<http://dx.doi.org/10.3174/ajnr.A6379>

parameter than CT for predicting futile outcomes. A recent meta-analysis from the HERMES group¹⁶ showed that core infarct volume correlated with 3-month clinical outcome and that patients selected by MR imaging, though accounting for only 18% of cases, had superior outcomes relative to patients selected by CT and CT perfusion estimates of core infarction. The recent THrombectomie des Artères Cerebrales (THRACE) trial used DWI for pretreatment imaging in 70% of patients, identifying DWI volume as an independent factor predictive of poor outcome and showing the benefit of thrombectomy decreasing with an increase in lesion volume.¹⁷

The purpose of our study was to develop a hierarchic algorithm based on MR imaging and clinical data to better identify patients who may not benefit from thrombectomy, given the risk of disability.

MATERIALS AND METHODS

Study Design and Patients

This was a retrospective, observational study including all consecutive patients admitted directly to Rennes University Hospital or referred from 3 other general hospitals (Vannes, Saint-Brieuc and Saint-Malo hospitals) between January 2015 and May 2017. The local ethics review board found the research to conform to generally accepted scientific principles and ethical standards (committee decision No. 17.71, December 18, 2017). According to French legislation, no informed consent was required in view of the observational and retrospective nature of this study, and all patients were informed of its purpose and the procedures involved and of their right to refuse use of their data.

Inclusion criteria were the following: patients 18 years of age or older, presenting with acute ischemic stroke with proximal arterial occlusion of the anterior circulation confirmed on 1.5 or 3T MR imaging, admitted to our center within 6 hours of symptom onset, and undergoing endovascular treatment with or without intravenous alteplase. Exclusion criteria were the following: posterior circulation stroke on MR imaging, prestroke mRS > 2, and no available prethrombectomy MR imaging or modified mRS at 3 months after stroke onset (accepted limit, 120 days).

Intravenous thrombolysis was performed within 4.5 hours of stroke onset by intravenous administration of 0.9 mg/kg of alteplase (maximum, 90 mg) with an initial bolus of 10% of the total dose followed by an infusion of the remaining dose during 60 minutes. Endovascular thrombectomy was performed by neurointerventionalists with >5 years' experience. At the beginning of the procedure, an intravenous heparin bolus (1500–2000 IU) was administered to patients who did not receive intravenous alteplase. With the patient under conscious sedation or general anesthesia (as determined by the medical team), endovascular treatment was performed using a coaxial (6F or 8F guiding catheter) or triaxial system (long introducer sheath or 8F guiding catheter with an intermediate aspiration catheter) and a combined approach with a microcatheter-delivered stent retriever and manual aspiration during stent retrieval (up to 5 passes if necessary).

Clinical and Imaging Data Collection

The following data were collected at baseline: demographic characteristics (age and sex); history of treated diabetes mellitus,

hypertension and/or atrial fibrillation, and history of ischemic stroke and transient ischemic attack; blood glucose level; systolic blood pressure; and NIHSS range of 0–42, with higher scores indicating more severe neurologic deficits.

The ischemic infarct lesion volume on pretreatment MR imaging was calculated from the ADC of DWI using a semiautomatic segmentation method with an AW Server 3.2 (2106; GE Healthcare, Milwaukee, Wisconsin). The ASPECTS (DWI-ASPECTS) was determined by a senior neuroradiologist (with >5 years' experience). Intracranial occlusion location and infarct side were indicated on MR imaging. We also collected stroke treatment details: intravenous alteplase administration, time from stroke onset to groin puncture, anesthesia type (general anesthesia or conscious sedation), and post-thrombectomy angiographic results according to the TICI grading system, with a score of 2b or 3 corresponding to reperfusion of at least 50% of the affected arterial territory. Symptomatic intracranial hemorrhage at 24 hours was defined as bleeding visible on CT plus an increase in the NIHSS score of at least 4 points.³

Statistical Analysis

Statistical analysis was performed using SAS software 9.4 (SAS Institute, Cary, North Carolina). For continuous variables, the mean \pm SD is reported, and for categorical variables, the number of patients in each category and the corresponding percentage are given. Patients were divided into 2 groups according to the mRS at 3 months (poor prognosis, mRS > 2; and good prognosis, mRS \leq 2). The characteristics of the 2 groups were compared using the Student *t* test or Wilcoxon rank sum test when appropriate for continuous variables, and the χ^2 or Fisher exact test when appropriate for categorical variables. To identify risk factors independently associated with poor prognosis, we entered variables found to be significantly different ($P < .20$) between the 2 groups into a forward stepwise logistic regression model. Each variable used in this logistic regression analysis was binary. Cutoff values were those with the best sensitivity and specificity found on the receiver operating characteristic curves for each variable. A predictive hierarchic algorithm showing the likelihood of poor prognosis at 3 months was also constructed using the variables in the logistic model at the $P < .01$ level. For all analyses, $P < .05$ was considered statistically significant.

RESULTS

During the study period, 289 patients underwent endovascular treatment for acute anterior circulation stroke secondary to large intracranial arterial occlusion, and finally a total of 149 patients were included in the analysis (Fig 1).

Population Characteristics

Table 1 shows baseline characteristics in the 2 groups. A total of 80 patients (53.7%; 95% CI, 45.3%–61.9%) had a poor prognosis at 3 months (20 with mRS = 3, seventeen with mRS = 4, five with mRS = 5, and 38 with mRS = 6). Compared with patients with good prognoses, patients with poor prognoses at 3 months were older; had a more frequent history of hypertension and atrial fibrillation; and had higher blood glucose levels, a higher NIHSS score at baseline, a higher DWI lesion volume and DWI-

ASPECTS, and more terminal internal carotid artery occlusions. Stroke treatment details showed that compared with patients with good prognoses, patients with poor prognoses at 3 months were less often treated with intravenous alteplase, had general anesthesia more often, and had a longer time from stroke onset to groin puncture and a higher rate of recanalization failure. Successful recanalization (as assessed by a TICCI score of 2b or 3) was achieved in 122 patients (81.9%; 95% CI, 74.7%–87.7%). Symptomatic intracranial hemorrhage was observed in 5 patients (4.3%) of a total 117 patients with available data.

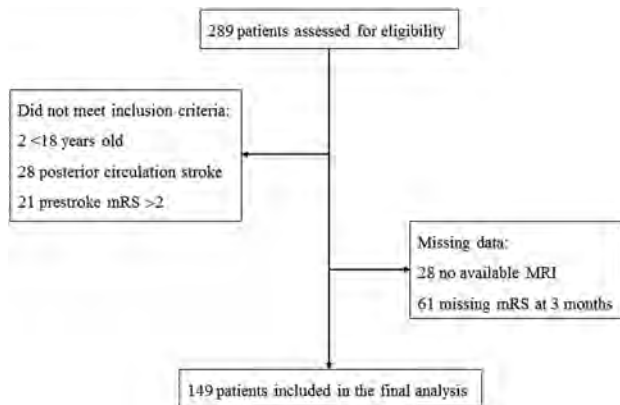


FIG 1. Flow chart.

Prognostic Factors

Multivariate logistic regression analysis identified 4 independent risk factors of poor prognosis at 3 months, which were in decreasing importance: DWI lesion volume >80 mL, baseline NIHSS score >14, age older than 75 years, and time from stroke onset to groin puncture of > 4 hours (Table 2). The predictive quality of the logistic model was high, as illustrated by an area under the receiver operating characteristic curve of 0.87 with a 95% CI, 0.81–0.93 (Fig 2). DWI volume of 80 mL had the best sensitivity and specificity with an area under the receiver operating characteristics curve of 0.71 (a patient with a DWI lesion of >80 mL had 96.8% of risk of poor outcome, and a patient with a DWI lesion of ≤80 mL had a 61.8% of chance of good outcome). For DWI-ASPECTS, the area under the receiver operating characteristics curve was 0.73, and a patient with a score of <5 had 84.8% of risk of poor outcome, whereas a patient with an ASPECTS of ≥5 had a 60.2% of chance of good outcome. A close relationship was observed between DWI-ASPECTS and DWI lesion volume with a correlation coefficient of 0.87 (plot in On-line Figure). Only DWI volume was a significant predictor with a relative difference in means between the good and poor prognosis groups of 61% (31% for DWI-ASPECTS).

We developed a hierarchic algorithm, with the variables entered in the model at the $P < .01$ level showing the proportion of poor prognoses at 3 months predicted with the model and the corresponding number of patients with poor prognoses observed in our population (Fig 3). The percentage of poor prognoses was

Table 1: Characteristics of the study population^a

Variable	Total (n = 149)	Good Prognosis: mRS at 3 Months ≤ 2 (n = 69)	Poor Prognosis: mRS at 3 Months > 2 (n = 80)	P Value
Age (yr)	68.7 ± 14.3	65.8 ± 15.1	71.2 ± 13.2	.022
Sex ratio (female/male)	71:78	32:37	39:41	.772
Diabetes mellitus	15 (10.1%)	4 (5.8%)	11 (13.8%)	.108
Arterial hypertension	88 (59.1%)	33 (47.8%)	55 (68.8%)	.010
Atrial fibrillation	37 (24.8%)	10 (14.5%)	27 (33.8%)	.007
History of stroke or transient ischemic attack	25 (16.8%)	8 (11.6%)	17 (21.3%)	.116
Prestroke mRS				.670
0	137 (91.9%)	65 (94.2%)	72 (90.0%)	
1	10 (6.7%)	3 (4.3%)	7 (8.8%)	
2	2 (1.3%)	1 (1.4%)	1 (1.3%)	
Systolic blood pressure (mm Hg)	153.4 ± 27.6	155.7 ± 28.3	151.3 ± 27.0	.372
Blood glucose level (mmol/L)	6.9 ± 2.2	6.3 ± 1.3	7.4 ± 2.6	.001
Baseline NIHSS score	16.3 ± 5.4	13.8 ± 5.6	18.5 ± 4.2	< .001
DWI-ASPECTS	5.9 ± 2.7	7.1 ± 2.1	4.9 ± 2.7	< .001
DWI volume (mL)	53.3 ± 64.8	23.8 ± 18.7	81.1 ± 79.2	< .001
Occlusion location				< .001
M1	95 (63.8%)	45 (65.2%)	50 (62.5%)	
M2	21 (14.1%)	18 (26.1%)	3 (3.8%)	
Terminal ICA	33 (22.1%)	6 (8.7%)	27 (33.8%)	
Intravenous alteplase	115 (77.2%)	60 (87.0%)	55 (68.8%)	.008
Stroke side				.304
Left	65 (43.6%)	27 (39.1%)	38 (47.5%)	
Right	84 (56.4%)	42 (60.9%)	42 (52.5%)	
Time from stroke onset to groin puncture (hr)	3.9 ± 1.3	3.6 ± 1.2	4.2 ± 1.3	.002
Recanalization score				.019
TICCI 2b/3	122 (81.9%)	62 (89.9%)	60 (75.0%)	
TICCI 0/1/2a	27 (18.1%)	7 (10.1%)	20 (25.0%)	
Anesthesia				.032
Conscious sedation	68 (45.6%)	38 (55.1%)	30 (37.5%)	
General anesthesia	81 (54.4%)	31 (44.9%)	50 (62.5%)	

^a Quantitative variables are expressed as means; qualitative variables are expressed as numbers (corresponding percentage).

51.4% for the entire population. The model predicted up to 100% poor prognosis in patients who had a DWI lesion volume of >80 mL and age older than 75 years, or DWI lesion volume of >80 mL and time to groin puncture of >4 hours. A baseline NIHSS score of >14 provided additional information when the DWI lesion volume was \leq 80 mL, increasing prediction of poor

prognosis from 19.1% to 56.3%. When age older than 75 years and time from stroke onset to groin puncture of >4 hours were added, it allowed prediction of 100% of poor prognosis cases.

DISCUSSION

Our study identified prethrombectomy DWI lesion volume as a crucial predictor of disability at 3 months. DWI lesion volume of >80 mL, baseline NIHSS score of >14, age older than 75 years, and time from stroke onset to groin puncture of >4 hours were 4 identified independent risk factors of decreasing importance associated with poor prognosis at 3 months after thrombectomy. On this basis, we developed a hierarchic predictive algorithm for the likelihood of disability with a high predictive value (area under the curve, 0.87). The importance of using this type of prediction tool in clinical practice was illustrated by the 53.7% of patients with disability we observed, in full agreement with literature data (54.0% in HERMES meta-analysis²).

We present a novel tool combining DWI with clinical data for predicting the risk of disability after thrombectomy. Most published prognostic clinical decision tools for identifying patients who may or may not benefit from intra-arterial treatment involved CT^{10,12} and showed that a low CT-ASPECTS (\leq 7¹³ or \leq 5¹⁸) was associated with worse outcome. However, DWI proved to be more accurate than CT for predicting poor outcome because area under the curve scores for DWI-ASPECTS and lesion volume were higher (0.70) than those of noncontrast or postcontrast CT (0.55)¹⁴ and more accurate than perfusion CT for predicting good outcome (area under the curve, 0.58).^{19,20} Then studies increasingly focused on MR imaging to select patients.^{3,21-24} Then, an ancillary study of the THRACE trial reported that lesion volume was an independent predictor of disability because the number of patients needed to treat to achieve functional independence increased with lesion volume (10 patients for a volume of 80 mL, 15 for 135 mL), but no treatment-

Table 2: Variables independently associated with poor prognosis identified in logistic regression analysis

Variables	Odds Ratio (95% CI)	P Value
DWI lesion volume >80 mL	37.47 (4.62–303.63)	.0007
NIHSS score >14	5.84 (2.20–15.52)	.0004
Age older than 75 yr	6.15 (2.35–16.11)	.0002
Time from stroke onset to groin puncture (hr)	2.55 (1.02–6.39)	.0456

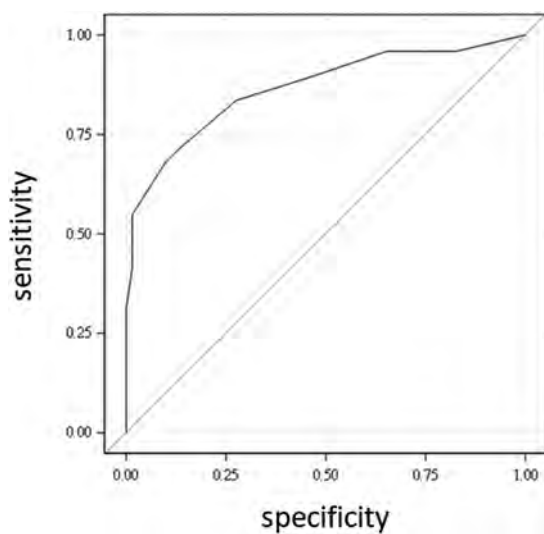


FIG 2. Receiver operating characteristic curve of the logistic model for prediction of poor prognosis: area under curve = 0.87.

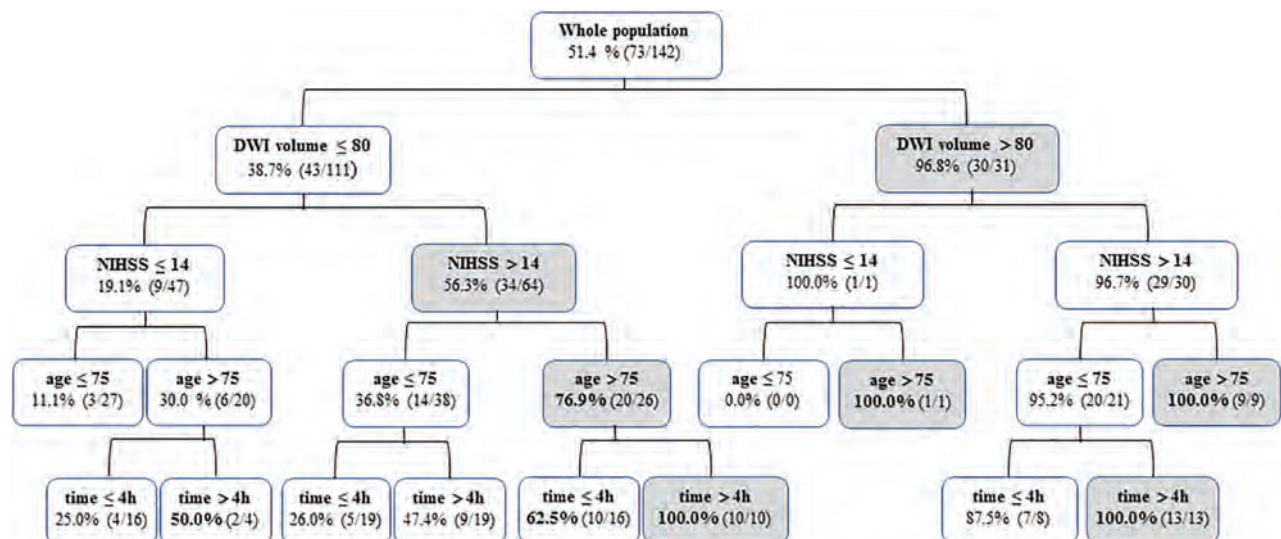


FIG 3. Hierarchic algorithm based on the 4 independent variables from the multivariate analysis for predicting poor prognosis at 3 months after thrombectomy. The algorithm shows the percentage of poor prognoses (mRS > 2 at 3 months) predicted with the model and the corresponding number of cases observed in our population.

by-dichotomized volume interaction for functional independence was observed.¹⁷

Our statistical method extracted cutoff values from receiver operating characteristic curves and identified a volume of 80 mL as having the best sensitivity and specificity for predicting poor outcome. The DWI-ASPECTS was not identified in the multivariate analysis due to the close association with DWI lesion volume, but a threshold of <5 was identified from the receiver operating characteristic curve after univariate analysis as predicting poor outcome. Both of these threshold values are in line with the latest Society of Neurointerventional Surgery guidelines, considering thrombectomy for class I level of evidence A indications in patients with anterior circulation acute stroke within 6 hours and either MR imaging DWI-ASPECTS of ≥ 6 or a small DWI lesion of <50 – 70 mL.²⁵ There is controversy in the literature about treating patients with large infarct core volumes. Recent studies showed up to 25%²¹ to 34%²² good outcomes in patients with a DWI-ASPECTS of ≤ 5 , particularly in young patients.²³ Our study corroborates the benefit of thrombectomy, given the 15.2% chance of good outcome in patients with a DWI-ASPECTS of ≤ 5 . However, a patient with a DWI lesion of >80 mL has only a 3.2% chance of good outcome, suggesting that this variable is more efficient than DWI-ASPECTS for triage decisions.

We identified older age and a high baseline NIHSS score as the strongest predictive variables after DWI lesion volume. Most studies have illustrated the important role of both these predictors of poor outcome at 3 months.^{10–12,14,17,26,27} We considered an age threshold of older than 75 years as predictive of disability, which is in accordance with literature data that identified an age between 65 and 80 years.^{10,13,28} The previously published baseline NIHSS threshold is variable from >10 ²⁸ to >20 ,^{27,28} which is also in accordance with our results (>14). Time delay from stroke onset to groin puncture was identified as the least significant predictor of poor outcome, ranking fourth in our model, but it allowed predicting 100% of poor outcomes for patients with a DWI lesion volume of >80 mL and age 75 years or younger, or for patients with DWI lesion volume of ≤ 80 mL, an NIHSS score of >14 , and age older than 75 years. The literature is contradictory as to the prognostic value of a longer time to thrombectomy. It was shown to be a poor prognostic factor^{26,27} by some authors, while others highlighted its modest¹⁰ or insignificant association^{12,29} with prognosis. This difference questions the decision not to treat patients due to a longer time from stroke onset, especially with lesion volume of ≤ 80 mL and/or age 75 years or younger, especially in patients who need to be transferred to an intervention center,³⁰ or for patients beyond a common therapeutic window⁸ or with an unknown stroke onset time.²⁹

Our hierarchic algorithm did not retain as significant certain variables such as systolic blood pressure or history of ischemic stroke or diabetes mellitus, which were identified in previous studies but with different population characteristics.¹⁰ For example, our patients had a shorter time to groin puncture (234 versus 260 minutes¹⁰) and a higher percentage of effective recanalization (82% versus 59%). This high successful recanalization rate of 75% for the patient group with poor outcome may also explain why this variable did not emerge as a significant prognostic factor. Last, collaterals were not evaluated in our MR imaging-based

algorithm due to a lack of well-validated scales. Yet collaterals are a compensatory phenomenon, and their absence is presumed to be associated with larger core infarct volumes and poor prognosis.³¹

The proposed hierarchic algorithm is based on the DWI lesion volume and 3 clinical predictors with cutoff values and is very easy to use in clinical practice to predict the lack of clinical benefit of thrombectomy. Its predictive value is higher than in most previous scores proposed, with an area under the curve of 0.87, and 0.75 for the HIAT2 score¹³ and 0.79 for the Pittsburgh Response to Endovascular Therapy score.¹² Again, this superior result may be explained by the use of MR imaging instead of CT, given that MR imaging is the most accurate and validated method for assessing acute stroke lesions. Other factors such as the use of newer thrombectomy devices and earlier time to recanalization may also explain this higher predictive value. The limitations of our study lie in its retrospective nature and relatively small sample size, especially for subgroups of patients combining >2 risk factors. Additionally, 61 patients were excluded due to missing 3-month mRS scores. Last, in the patient subgroup with DWI volumes of >80 mL, the addition of the NIHSS score, age, and time to groin puncture adds very little predictive value to the algorithm (96% compared with 100%). Further validation cohort studies are also needed to confirm the high predictive value.

CONCLUSIONS

Our study involved development of a hierarchic algorithm based on DWI lesion volume, age, baseline NIHSS score, and time to puncture for predicting disability at 3 months after thrombectomy with a high predictive value. This algorithm could help to design a clinical decision-making tool for better identification of patients for whom thrombectomy would be futile.

Disclosures: François Eugène—UNRELATED: Consultancy; BIOMODEX SAS. Sarah Evain—UNRELATED: Payment for development of educational presentations; CHEM, Comments: Private educational group for paramedical et medical formation; Travel/accommodations/meeting expenses unrelated to activities listed; SLICE group, Comments: SLICE meeting travel, accommodation, meeting. Thomas Ronziere—RELATED: Support for Travel to Meetings for the Study or Other Purposes: Shire, Genzyme.

REFERENCES

1. Lopez AD, Mathers CD, Ezzati M, et al. **Global and regional burden of disease and risk factors, 2001: systematic analysis of population health data.** *Lancet* 2006;367:1747–57 CrossRef Medline
2. Goyal M, Menon BK, van Zwam WH, et al. **Endovascular thrombectomy after large-vessel ischaemic stroke: a meta-analysis of individual patient data from five randomised trials.** *Lancet* 2016;387:1723–31 CrossRef Medline
3. Bracadar S, Ducrocq X, Mas JL, et al. **Mechanical thrombectomy after intravenous alteplase versus alteplase alone after stroke (THRACE): a randomised controlled trial.** *Lancet Neurol* 2016;15:1138–47 CrossRef Medline
4. Powers WJ, Rabinstein AA, Ackerson T, et al. **2018 Guidelines for the Early Management of Patients with Acute Ischemic Stroke: A Guideline for Healthcare Professionals From the American Heart Association/American Stroke Association.** *Stroke*. 2018;49:e46–e110 CrossRef Medline
5. Wahlgren N, Moreira T, Michel P, et al. **Mechanical thrombectomy in acute ischemic stroke: Consensus statement by ESO-Karolinska**

- Stroke Update 2014/2015, supported by ESO, ESMINT, ESNR and EAN.** *Int J Stroke* 2016;11:134–47 CrossRef Medline
6. Alawieh A, Zaraket F, Alawieh MB, et al. **Using machine learning to optimize selection of elderly patients for endovascular thrombectomy.** *J Neurointerv Surg* 2019;11:847–51 CrossRef Medline
 7. Haussen DC, Lima FO, Bousslama M, et al. **Thrombectomy versus medical management for large vessel occlusion strokes with minimal symptoms: an analysis from STOPStroke and GESTOR cohorts.** *J Neurointerv Surg* 2018;10:325–29 CrossRef Medline
 8. Nogueira RG, Jadhav AP, Haussen DC, et al. **Thrombectomy 6 to 24 hours after stroke with a mismatch between deficit and infarct.** *N Engl J Med* 2018;378:11–21 CrossRef Medline
 9. Nie X, Pu Y, Zhang Z, et al. **Futile recanalization after endovascular therapy in acute ischemic stroke.** *Biomed Res Int* 2018;2018:879548 CrossRef Medline
 10. Venema E, Mulder M, Roozenbeek B, et al. **Selection of patients for intra-arterial treatment for acute ischaemic stroke: development and validation of a clinical decision tool in two randomised trials.** *BMJ* 2017;357:j1710 CrossRef Medline
 11. Hallevi H, Barreto AD, Liebeskind DS, et al. **Identifying patients at high risk for poor outcome after intra-arterial therapy for acute ischemic stroke.** *Stroke* 2009;40:1780–85 CrossRef Medline
 12. Rangaraju S, Aghaebrahim A, Streib C, et al. **Pittsburgh Response to Endovascular therapy (PRE) score: optimizing patient selection for endovascular therapy for large vessel occlusion strokes.** *J Neurointerv Surg* 2015;7:783–88 CrossRef Medline
 13. Sarraj A, Albright K, Barreto AD, et al. **Optimizing prediction scores for poor outcome after intra-arterial therapy in anterior circulation acute ischemic stroke.** *Stroke* 2013;44:3324–30 CrossRef Medline
 14. Han M, Choi JW, Rim NJ, et al. **Cerebral infarct volume measurements to improve patient selection for endovascular treatment.** *Medicine (Baltimore)* 2016;95:e4702 CrossRef Medline
 15. Huisa BN, Neil WP, Schrader R, et al. **Clinical use of computed tomographic perfusion for the diagnosis and prediction of lesion growth in acute ischemic stroke.** *J Stroke Cerebrovasc Dis* 2014; 23:114–22 CrossRef Medline
 16. Campbell BC, Majoie C, Albers GW, et al. **Penumbra imaging and functional outcome in patients with anterior circulation ischaemic stroke treated with endovascular thrombectomy versus medical therapy: a meta-analysis of individual patient-level data.** *Lancet Neurol* 2019;18:46–55 CrossRef Medline
 17. Xie Y, Oppenheim C, Guillemin F, et al. **Pretreatment lesion volume impacts clinical outcome and thrombectomy efficacy: pretreatment lesion volume and stroke outcome.** *Ann Neurol* 2018;83: 178–85 CrossRef Medline
 18. Kawiorski MM, Martínez-Sánchez P, García-Pastor A, et al. **Alberta Stroke Program Early CT Score applied to CT angiography source images is a strong predictor of futile recanalization in acute ischemic stroke.** *Neuroradiology* 2016;58:487–93 CrossRef Medline
 19. Naylor J, Churilov L, Chen Z, et al. **Reliability, reproducibility and prognostic accuracy of the Alberta Stroke Program Early CT Score on CT perfusion and non-contrast CT in hyperacute stroke.** *Cerebrovasc Dis* 2017;44:195–202 CrossRef Medline
 20. Raza SA, Barreira CM, Rodrigues GM, et al. **Prognostic importance of CT ASPECTS and CT perfusion measures of infarction in anterior emergent large vessel occlusions.** *J Neurointerv Surg* 2019;11: 670–74 CrossRef Medline
 21. Panni P, Gory B, Xie Y, et al. **Acute stroke with large ischemic core treated by thrombectomy: predictors of good outcome and mortality.** *Stroke* 2019;50:1164–71 CrossRef Medline
 22. Manceau PF, Soize S, Gawlitza M, et al. **Is there a benefit of mechanical thrombectomy in patients with large stroke (DWI-ASPECTS ≤ 5)?** *Eur J Neurol* 2018;25:105–10 CrossRef Medline
 23. Daniere F, Lobotesis K, Machi P, et al. **Patient selection for stroke endovascular therapy: DWI-ASPECTS thresholds should vary among age groups—insights from the RECAST study.** *AJNR Am J Neuroradiol* 2015;36:32–39 CrossRef Medline
 24. Leslie-Mazwi TM, Hirsch JA, Falcone GJ, et al. **Endovascular stroke treatment outcomes after patient selection based on magnetic resonance imaging and clinical criteria.** *JAMA Neurol* 2016;73:43–49 CrossRef Medline
 25. Mokin M, Ansari SA, McTaggart RA, et al. **Indications for thrombectomy in acute ischemic stroke from Emergent Large Vessel Occlusion (ELVO): report of the SNIS Standards and Guidelines Committee.** *J Neurointerv Surg* 2019;11:215–20 CrossRef Medline
 26. Hussein HM, Saleem MA, Qureshi AI. **Rates and predictors of futile recanalization in patients undergoing endovascular treatment in a multicenter clinical trial.** *Neuroradiology* 2018;60:557–63 CrossRef Medline
 27. Shi Z-S, Liebeskind DS, Xiang B, et al. **Predictors of functional dependence despite successful revascularization in large-vessel occlusion strokes.** *Stroke* 2014;45:1977–84 CrossRef Medline
 28. Hussein HM, Georgiadis AL, Vazquez G, et al. **Occurrence and predictors of futile recanalization following endovascular treatment among patients with acute ischemic stroke: a multicenter study.** *AJNR Am J Neuroradiol* 2010;31:454–58 CrossRef Medline
 29. Nagel S, Herweh C, Pfaff JA, et al. **Simplified selection criteria for patients with longer or unknown time to treatment predict good outcome after mechanical thrombectomy.** *J Neurointerv Surg* 2019; 11:559–62 CrossRef Medline
 30. Sablot D, Dumitrana A, Leibinger F, et al. **Futile inter-hospital transfer for mechanical thrombectomy in a semi-rural context: analysis of a 6-year prospective registry.** *J Neurointerv Surg* 2019;11:539–44 CrossRef Medline
 31. Renú A, Laredo C, Montejo C, et al. **Greater infarct growth limiting effect of mechanical thrombectomy in stroke patients with poor collaterals.** *J Neurointerv Surg* 2019;11:989–93 CrossRef Medline

Endovascular Treatment Decisions in Patients with M2 Segment MCA Occlusions

 M. Almekhlafi,  J.M. Ospel,  G. Saposnik,  N. Kashani,  A. Demchuk,  M.D. Hill,  M. Goyal, and  B.K. Menon



ABSTRACT

BACKGROUND AND PURPOSE: Endovascular therapy in acute ischemic stroke is rapidly evolving. We explored physicians' treatment attitudes and practice in patients with acute ischemic stroke due to M2 occlusion, given the absence of Level-1 guidelines.

MATERIALS AND METHODS: We conducted an international multidisciplinary survey among physicians involved in acute stroke care. Respondents were presented with 10 of 22 case scenarios (4 with proximal M2 occlusions and 1 with a small-branch M2 occlusion) and asked about their treatment approach under A) current local resources, and B) assumed ideal conditions (no monetary or infrastructural restraints). Overall treatment decisions were evaluated; subgroup analyses by physician and patient baseline characteristics were performed.

RESULTS: A total of 607 physicians participated. Most of the respondents decided in favor of endovascular therapy in M2 occlusions, both under current local resources and assumed ideal conditions (65.4% versus 69.6%; $P = .017$). Under current local resources, older patient age ($P < .001$), longer time since symptom onset ($P < .001$), high center endovascular therapy volume ($P < .001$), high personal endovascular therapy volume ($P = .005$), and neurosurgeons ($P < .001$) were more likely to favor endovascular therapy. European respondents were less likely to favor endovascular therapy ($P = .001$). Under assumed ideal conditions, older patient age ($P < .001$), longer time since symptom onset ($P < .001$), high center endovascular therapy volume ($P = .041$), high personal endovascular therapy volume ($P = .002$), and Asian respondents were more likely to favor endovascular therapy ($P = .037$). Respondents with more experience ($P = .048$) and high annual stroke thrombolysis treatment volume ($P = .001$) were less likely to favor endovascular therapy.

CONCLUSIONS: Patients with M2 occlusions are considered appropriate candidates for endovascular therapy by most respondents in this survey, especially by those performing endovascular therapy more often and those practicing in high-volume centers.

ABBREVIATIONS: EVT = endovascular therapy; IQR = interquartile range

Acute ischemic stroke due to large arterial occlusions is a disabling condition with devastating consequences, unless timely reperfusion is achieved.¹⁻³ Strokes caused by M2 segment MCA occlusions can present with severe symptoms and lead to large infarct volumes, with substantial morbidity and mortality.⁴ Recent endovascular stroke trials focused on patients likely to attain the greatest benefit from endovascular therapy (EVT). These trials mainly included patients with proximal (terminal

internal carotid "ICA" and proximal middle cerebral artery "M1") occlusions.⁵ Accordingly, current guidelines state that the benefit of EVT is uncertain in patients with M2 segment MCA occlusions; however, many operators believe that EVT is appropriate in these patients.⁶

Since the publication of the recent EVT trials^{5,7} in 2015, many studies have been published that report the safety and efficacy of EVT in patients with M2 segment MCA occlusions, including a patient-level meta-analysis from the Highly Effective Reperfusion evaluated in Multiple Endovascular Stroke trials Collaboration.^{4,7-11} Many operators now routinely perform EVT in patients with

Received September 27, 2019; accepted after revision December 9.

From the Department of Clinical Neurosciences (M.A., J.M.O., A.D., M.D.H., M.G., B.K.M.), Hotchkiss Brain Institute; and Departments of Radiology (M.A., N.K., A.D., M.D.H., M.G., B.K.M.) and Community Health Sciences (M.A., M.D.H., B.K.M.), University of Calgary, Calgary, Alberta, Canada; Department of Radiology (J.M.O.), University Hospital Basel, University Basel, Basel, Switzerland; and Stroke Outcomes and Decision Neuroscience Research Unit (G.S.), Department of Medicine, and Li Ka Shing Knowledge Institute (G.S.), St. Michael's Hospital, University of Toronto, Toronto, Ontario, Canada

This study was supported by an unrestricted research grant from Stryker Inc. to the University of Calgary. The company was neither involved in the design and execution of the trial nor in the analysis and interpretation of its results.

Please address correspondence to Bijoy K. Menon, MD, Departments of Clinical Neurosciences, Radiology and Community Health Sciences, Foothills Medical Centre, University of Calgary, 1403 29th St. NW, Calgary, Alberta, T2N2T9, Canada; e-mail: docbijoymenon@gmail.com; @AlmekhlafiMa; @johanna_ospel; @NimaKashani; @bijoymenon; @mayank_G0

 Indicates article with supplemental on-line table.

<http://dx.doi.org/10.3174/ajnr.A6397>

EVT decision rates for M2 segment MCA occlusion case scenarios

Case Vignette	EVT		
	Evidence Level	Rate under Current Local Resources (%)	Rate under Assumed Ideal Conditions (%)
An 88-year-old, right-handed man has arrived at your hospital at 10:00 AM with right hemiparesis and aphasia; symptom onset was 3 hours ago; his stroke severity measured by NIHSS is 14; ASPECTS on noncontrast CT is 7; baseline CTA reveals a proximal left M2 segment MCA occlusion	2B	81.6	85.9
A 45-year-old, left-handed man has arrived at your hospital at 1:00 PM with left hemiparesis and visual field defect; he was last seen as normal 12 hours ago; his stroke severity measured by NIHSS is 15; ASPECTS on noncontrast CT is 8; baseline CTA shows a proximal right M2 segment MCA occlusion	2B	68.7	75.3
A 94-year-old, left-handed woman has arrived at your hospital at 2:00 AM with right hemiparesis and aphasia; symptom onset was 3.5 hours ago; her stroke severity measured by NIHSS is 12; ASPECTS on noncontrast CT is 7; the baseline CTA shows a proximal left M2 segment MCA occlusion	2B	60.3%	67.2%
An 85-year-old, right-handed woman has arrived at your hospital at 11:00 PM with left hemiparesis; symptoms are 3 hours from onset; her stroke severity as measured by NIHSS is 9; ASPECTS on noncontrast CT is 6; baseline CTA shows a proximal right M2 segment MCA occlusion; she has a history of mild cognitive impairment	2B	62.3	63.4
A 56-year-old, right-handed man has arrived at your hospital at 3:00 PM with global aphasia; symptoms are 3 hours from onset; his stroke severity measured by NIHSS is 8; ASPECTS on noncontrast CT is 9; baseline CTA reveals a small-branch left M2 segment MCA occlusion	2B	53.8	56.4

ischemic stroke and with M2 segment MCA occlusions. However, EVT decision-making in these patients is variable due to a lack of clear guideline-based treatment recommendations. Until now, little was known about how physicians make treatment decisions with regard to EVT in patients with acute ischemic stroke and with M2 segment MCA occlusions and what factors guide this process. By using a worldwide survey, this study aims to explore how physicians from different subspecialties manage patients with acute ischemic stroke due to M2 segment MCA occlusions.

MATERIALS AND METHODS

Survey Design

An international cross-sectional Web-based survey (UNMASK-EVT) among stroke physicians and neurointerventionalists was conducted to understand the current treatment practice and decision-making with regard to using EVT in patients with acute ischemic stroke.¹² Respondents were randomly assigned 10 of a pool of 22 ischemic stroke case scenarios (5 with ICA occlusion, 12 with M1 segment MCA occlusion, 5 with M2 segment MCA occlusion [4 proximal and 1 small-branch M2 segment MCA occlusion]). Respondents were then asked how they would treat the patient in the given scenario under local current resources and under assumed ideal conditions (ie, without monetary or infrastructural limitations). Response data were obtained from November 26, 2017, to March 27, 2018. Further details of the study have been published elsewhere (see the Table for all case vignettes).¹²

Survey Respondents

A total of 1330 stroke physicians (neurologists, interventional neuroradiologists, neurosurgeons, internists, geriatricians, and

other physicians directly involved in acute stroke care) from 38 countries around the world were invited to participate in the survey by e-mail. No restrictions were applied with regard to years of experience or academic versus nonacademic background. Before accessing the case scenarios, the responding physicians provided personal and practice data, namely, age, sex, years of experience in stroke treatment, personal and center-specific estimated number of annual patients with stroke treated, geographic region, subspecialty, and hospital setting.

Statistical Analysis

Data are described by using standard descriptive statistics. Subgroup analyses used the χ^2 test for differences in proportions and the nonparametric Wilcoxon rank sum test for differences in continuous data. Multivariable logistic regression with backward elimination was used to determine variables associated with an EVT decision among the 5 case scenarios with M2 segment MCA occlusions. All the models were adjusted for baseline ASPECTS, time from symptom onset to imaging, and patient age. Sensitivity analyses used mixed-effects logistic regression with “respondent” as a random-effects variable to account for hierarchical clustering of data within respondents. Two-sided $P < .05$ was considered statistically significant. All analyses were performed by using Stata version 15.1 (StatCorp, College Station, Texas).

RESULTS

Overall, 607 physicians (45.6%) responded to the survey request. Across the 22 survey scenarios, 75.6% of the physicians favored

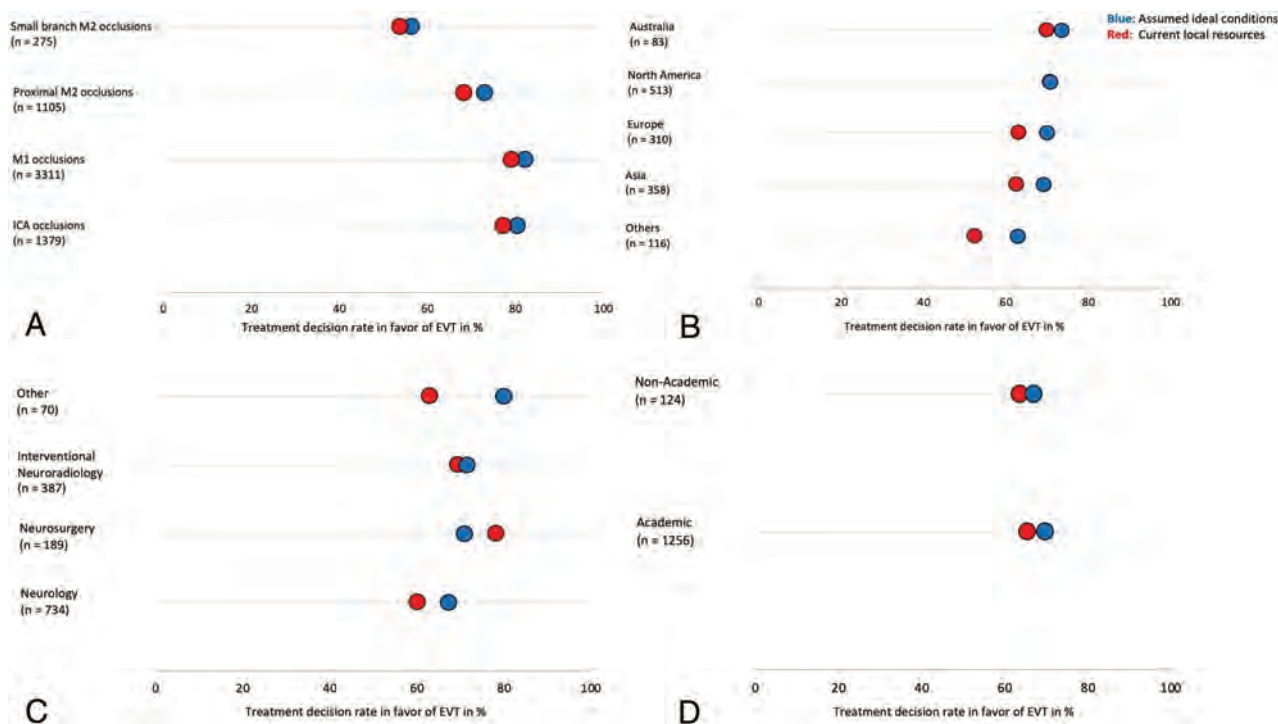


FIG 1. Decision rates in favor of EVT for different occlusion locations (A), decision rates in favor of EVT in M2 segment MCA occlusions for different geographic regions (B), for different specialties (C), and hospital settings (D). Blue dots illustrate decision rates under assumed ideal conditions and red dots decision rates under current local resources. Decision rates under current resources and assuming ideal conditions in North America in (B) were identical. Decision rates under current resources for neurosurgeons were lower than under assumed ideal conditions (C).

using EVT (responses, 4586/6070) with current resources and 79.0% under assumed ideal conditions (responses, 4793/6070). The EVT decision rate for M2 segment MCA occlusions was also high, given the current resources (65.4%) and when assuming ideal conditions (69.6%) ($P = .017$). Even in the scenario that describes a patient with a small-branch M2 segment MCA occlusion eligible for IV tPA, more than half of the respondents favored an EVT approach (53.8% under current resources and 56.4% when assuming ideal conditions). However, these responses were lower than those for more proximal occlusions (ICA–M1 segment MCA, 78.6% and 81.7% under current resources and assumed ideal conditions, respectively; $P < .001$ for difference in proportions) (Fig 1A). An overview of EVT decision rates under current resources and assumed ideal conditions for the 5 M2 segment MCA occlusion scenarios is provided in the Table. EVT decision rates under current resources and assumed ideal conditions across all countries for the 5 M2 segment MCA occlusion scenarios are shown in Fig 2.

Responses under Current Local Resources

The EVT decision for M2 segment MCA occlusions differed significantly between regions under current local resources ($P < .001$) (Fig 1B). Respondents from North America decided most often in favor of EVT (70.8%), whereas those from “other regions” ranked lowest (52.6%). The EVT decision also differed significantly across different specialties, with neurosurgeons ranking highest (78.3%) and neurologists ranking lowest (60.1%) ($P < .001$) (Fig 1C). The EVT

decision between academic centers (65.5%) and nonacademic centers (63.7%) did not differ significantly ($P = .119$) (Fig 1D).

Respondents who favored EVT for M2 segment MCA occlusions under current local resources performed significantly more endovascular procedures per year (median, 30 procedures; [interquartile range {IQR}, 30] versus 20 procedures [IQR, 30]; $P < .001$) and worked in centers with a significantly higher annual EVT volume (median, 80 cases annually [IQR, 100] versus 40 [IQR, 70]; $P < .001$) and annual IV tPA volume (median, 100 cases annually [IQR, 125] versus 80 [IQR, 110]; $P < .001$) than those who refrained from using EVT. Survey respondents were younger (median age, 43 years [IQR, 12 years] versus 45 years [IQR, 13 years]; $P < .001$) and had fewer years of practice experience (median, 12 years [IQR, 13 years] versus 14.5 years [IQR, 13 years]; $P = .009$) than their peers who refrained from EVT.

Multivariable Analyses

In the multivariable analysis (On-line Table), the odds for choosing EVT for patients with M2 segment MCA occlusion were higher with increasing patient age (per decile increase in age, OR 1.02 [95% CI, 1.01–1.02]; $P < .001$), time from symptom onset (per hour, OR 1.09 [95% CI, 1.04–1.14]; $P < .001$), if respondents had a neurosurgical background (versus neurologists, OR 2.60 [95% CI, 1.71–3.94]; $P < .001$), if the respondent’s center had higher annual EVT case volume (per decile increase in case volume, OR 1.21 [95% CI, 1.13–1.28]; $P < .001$), if the respondents performed more EVT cases per year (per decile increase in case volume, OR 1.08 [95% CI,

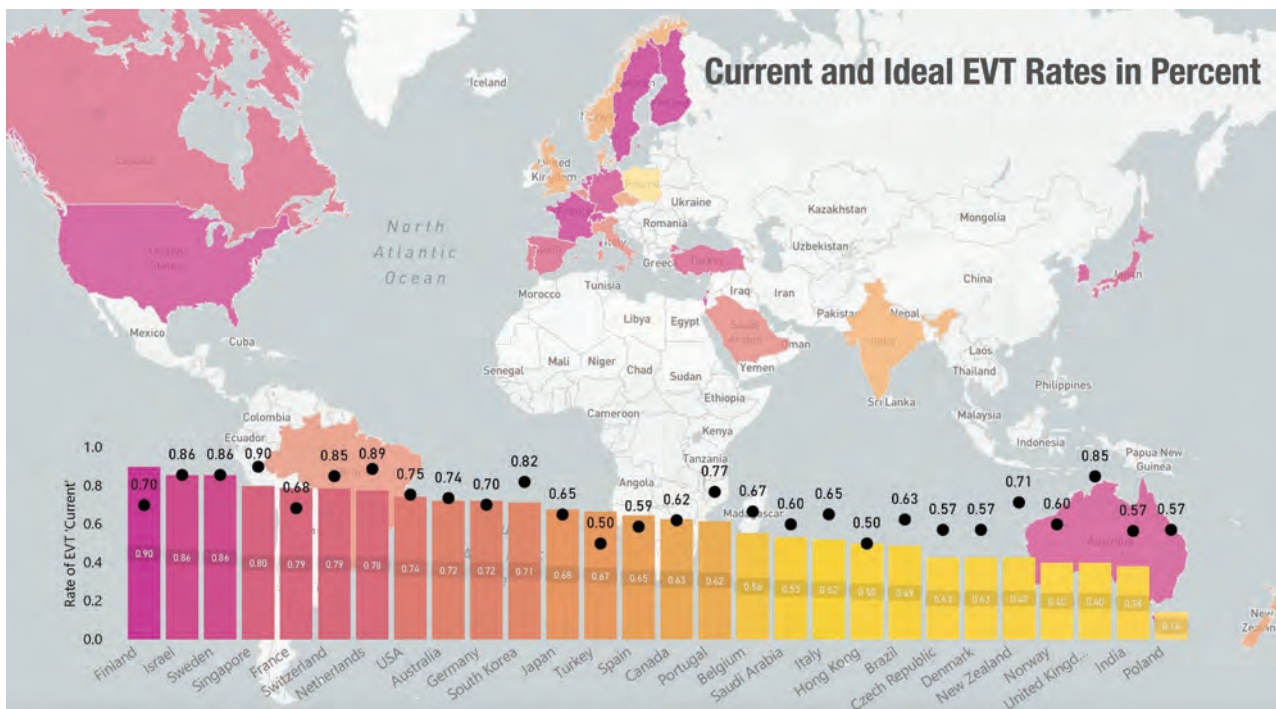


FIG 2. Decision rates in favor of EVT in patients with M2 segment MCA occlusions by survey respondents across the globe, stratified by country, under current resources (bars), and assumed ideal conditions (black dots).

1.02–1.15]; $P = .005$). Respondents from Europe were less likely to offer EVT (OR 0.68 [95% CI, 0.49–0.94]; $P = .001$) when compared with the respondents from North America.

Responses under Assumed Ideal Conditions

The EVT decision for M2 segment MCA occlusions did not differ significantly between regions under assumed ideal conditions ($P = .486$) (Fig 1B). Respondents from Australia decided most often in favor of EVT (73.5%), whereas those from “other regions” ranked lowest (62.9%). The EVT decision did not differ significantly across different specialties with “other specialties” ranking highest (80.0%) and neurologists lowest (67.3%) ($P = .099$) (Fig 1C). The EVT decision between academic centers (69.9%) and nonacademic centers (66.9%) did not differ significantly ($P = .812$) (Fig 1D).

Respondents who favored using EVT for M2 segment MCA occlusions under assumed ideal conditions performed significantly more endovascular procedures per year (median, 30 [IQR, 35] versus 24 [IQR, 28]; $P < .001$) and worked in centers with a significantly higher annual EVT volume (median, 75 cases annually [IQR, 97] versus 50 [IQR, 80]; $P < .001$) than those respondents who declined EVT. Survey respondents were younger (median age, 43 years [IQR, 11 years] versus 46 years [IQR, 13 years]; $P < .001$) and had fewer years of practice experience (median, 12 years [IQR, 11 years] versus 15 years [IQR, 13 years]; $P < .001$) than their peers who refrained from using EVT.

Multivariable Analyses

In the multivariable analyses (On-line Table), the odds for choosing EVT were higher with increasing patient age (per decile increase in age, OR 1.02 [95% CI, 1.01–1.03]; $P < .001$), time

from symptom onset (per hour, OR 1.12 [95% CI, 1.07–1.18]; $P < .001$), for respondents practicing in Asia (versus North America, OR 1.55 [95% CI, 1.08–2.22]; $P = .037$), if the respondent’s center had higher annual EVT case volume (per decile increase in case volume, OR 1.07 [95% CI, 1.00–1.13]; $P = .041$), if the respondents performed more EVT cases per year (per decile increase in case volume, OR 1.09 [95% CI, 1.03–1.16]; $P = .002$) were associated with higher odds of EVT use under assumed ideal conditions. The respondent’s years of experience (per decile increase, OR 0.91 [95% CI, 0.83–1.00]; $P = .048$) and personal annual stroke thrombolysis cases (per 10 case increase, OR 0.93 [95% CI, 0.89–0.97]; $P = .001$) were associated with lower odds to proceed with EVT in patients with M2 segment MCA occlusion. The results were similar in sensitivity analyses when using mixed-effects modeling that accounted for clustering of response data within survey respondents (results not shown).

DISCUSSION

EVT decision-making for patients with an acute ischemic stroke and M2 segment MCA occlusions has been subject to debate because these patients were generally excluded from the largest EVT trials. In our study, most of the physicians who participated in this survey reported that they favored EVT in patients with acute ischemic stroke with M2 segment MCA occlusion. This reflects confidence in EVT as a safe and effective treatment option, even beyond large-vessel occlusions. The small but significant gap between current and ideal treatment decisions indicates that, although the respondents believed that EVT should be performed, their environment did not yet allow them to do so. This might change in the future as more evidence for safety and

efficacy of EVT in M2 segment MCA occlusions becomes available.^{4,7-11}

Survey respondents were more likely to predict that they would treat patients with ICA-M1 segment MCA occlusions with EVT than patients with M2 segment MCA occlusions. This most likely reflects current guidelines, which assign Class-1 Level-A evidence for EVT only in proximal (ICA-M1 segment MCA) occlusions.⁶ Analyses of the influence of baseline characteristics on physicians' decision to offer EVT to patients with M2 segment MCA occlusions revealed that the time from symptom onset to treatment, the baseline NIHSS, and the baseline ASPECTS were significant. This confirms that clinical and imaging baseline characteristics play an important role in clinical decision-making; the same variables that determine EVT eligibility in proximal-vessel occlusions⁶ are the variables that physicians rely on for decision-making in patients with M2 segment MCA occlusions.

Neither current nor ideal treatment decisions differed between academic and nonacademic centers in this survey. Physicians' treatment decisions, therefore, do not seem to be influenced by their institution's academic profile. Physicians who favor EVT under current local resources and under assumed ideal conditions worked in high EVT volume centers and performed significantly more EVT cases per year than those refraining from EVT. This reflects that experience with endovascular treatment makes physicians more comfortable offering EVT to their patients with M2 segment MCA occlusions. Interestingly, physicians who opt to use EVT in patients with M2 segment MCA occlusions were younger and had been in practice for fewer years than those who decided against using EVT. It is possible that these younger physicians were trained during the advent of stent retrievers and small distal aspiration catheters, techniques that make recanalization of M2 segment MCA occlusions safely achievable.

Significant differences were observed in reported EVT treatment decisions among the different geographic regions under current local resources but not under assumed ideal conditions (Fig 1B). Regions where physicians most preferred using EVT also showed the smallest gap between current and ideal treatment decisions, whereas regions with the lowest preference for using EVT showed the largest discrepancy between current and ideal decision rates. Respondents from Europe were less likely to offer EVT compared with the respondents from North America.

This could relate to access to EVT, differences in practice parameters and health care systems, differences in guidelines, and how practitioners implement these guidelines in their practice. Similarly, treatment decisions among different subspecialties under current local resources differed significantly but not under assumed ideal conditions (Fig 1C). These observations could point toward external factors (eg, insufficient access to treatment facilities, monetary and health policy-related limitations) as a possible cause for low EVT decision rates in some regions. For example, alteplase utilization remains <1% in many developing countries.¹³ This may motivate the use of EVT in regions where patients or local jurisdictions are unable to afford alteplase.¹⁴ The gap between current and ideal practices in such regions may also reflect the limited resources of publicly funded hospitals or the patients' means in areas with mostly private hospitals. This could

promote the use of manual aspiration at the clot interface as the primary and economically efficient EVT technique in local practices.¹³ In some other countries in Africa, Asia, and Europe, EVT is either not available or not offered around the clock.¹⁵ Such limitations with the subsequent impact on the access to EVT-capable facilities and devices are all important determinants of the decision for or against using EVT.

Although this study clearly shows that M2 segment MCA occlusions are considered an appropriate target for EVT across all countries and specialties, there was substantial variability in decision-making among physicians. This is not surprising because no randomized controlled trials demonstrated EVT efficacy in M2 segment MCA occlusions. To the best of our knowledge, there currently are no plans for such a trial. The main reason for this is the lack of clinical equipoise. Most physicians consider EVT the superior treatment for patients with all endovascular accessible occlusions, including the M2 segment; hence, only a few are willing to randomize patients with distal accessible occlusions.

Any future trial that seeks to enroll patients with M2 segment MCA occlusions, therefore, will need to take into account the lack of equipoise and the potential for bias in trial enrollment (patients with unfavorable risk profiles who are unlikely to benefit from EVT are more likely to get enrolled). Evidence from high-quality patient-level meta-analysis such as from the Highly Effective Reperfusion evaluated in Multiple Endovascular Stroke trials Collaboration⁷ and from cohort studies that enrolled patients with M2 segment MCA occlusions who have not been offered EVT such as the Identifying New Approaches to Optimize Thrombus Characterization for Predicting Early Recanalization and Reperfusion With IV Alteplase and Other Treatments Using Serial CT Angiography (INTERSeCT) study,¹⁶ and numerous other nonrandomized studies^{4,8-11} may show the best available data for efficacy of EVT in such occlusions. In this situation, professional organizations and guideline committees may consider revising the endovascular treatment recommendations for M2 segment MCA occlusions despite the lack of Level-1A evidence. This will stimulate further improvement in the design of devices and aspiration catheters specifically tailored for distal vessels.

Limitations

Our study had several limitations. First, the survey respondents were contacted by using a purposive sampling strategy that relied on personal contacts with local principal investigators. The absence of a comprehensive international register of stroke physicians and neurointerventionalists means that it is not certain that the respondents were representative of their region or country. Although the overall survey completion rate was high, the number of responses for some countries and specialties was relatively low and, therefore, might not be fully representative of practices within that country or that specialty. Finally, physician decisions made in this survey were based on hypothetical scenarios and may not reflect decisions that may be taken in real life or for patients with different clinical or imaging parameters. Our survey does not account for some anatomic factors, for example, the diameter of the affected M2 artery, that may impact treatment decisions. Despite these limitations, our study provides valuable

insights into current treatment approaches in patients with M2 segment MCA occlusions across different settings, regions, and specialties.

CONCLUSIONS

In the present study, EVT was considered the most likely selected treatment for patients with M2 segment MCA occlusions by practicing physicians.

ACKNOWLEDGMENTS

The authors thank the participants of this survey.

Disclosures: Johanna M. Ospel—*RELATED: Grant:* Julia Bangerer Rhyner Foundation, University of Basel Forschungsfonds, Freiwillige Akademische Gesellschaft Basel, *Comments:* Research scholarship. Gustavo Saposnik—*RELATED: Support for Travel to Meetings for the Study or Other Purposes:* University of Calgary; *UNRELATED: Consultancy:* Roche, Servier, Celgene; *Grants/Grants Pending:* Roche, Servier*; *Payment for Lectures Including Service on Speakers Bureaus:* Celgene, Servier; *Travel/Accommodations/Meeting Expenses Unrelated to Activities Listed:* Roche, *Comments:* Attendo to Ectrims 2019. Nima Kashani—*UNRELATED: Employment:* Calgary University. Andrew Demchuk—*RELATED: Consulting fee or honorarium:* Medtronic, *Comments:* CME events; *UNRELATED: Patents (Planned, Pending or Issued):* Circle NVI; *Stock/stock options:* Circle NVI. Michael D. Hill—*RELATED: Grant:* Stryker, *Comments:* Grant to the University of Calgary for the UNMASK-EVT project*; *UNRELATED: Board Membership:* CNSF board, CSC board, *Comments:* Not for profit boards in stroke and neurology; *Consultancy:* Merck, *Comments:* Paid consultancy for adjudicating clinical trial outcome events in clinical trials; *Grants/Grants Pending:* Multiple sources (public, industry), *Comments:* Multiple grants from both industry and public sources for clinical trials*; *Patents (Planned, Pending or Issued):* Patent in stroke care granted, *Comments:* Patent granted, no money paid; *Stock/Stock Options:* Calgary Scientific, *Comments:* Stock owner in CSI, imaging and computer rendering company.* Mayank Goyal—*RELATED: Grant:* Stryker, *Comments:* Unrestricted research grant towards this study*; *UNRELATED: Consultancy:* Medtronic, Stryker, Mentice, Microvention; *Patents (Planned, Pending or Issued):* GE Healthcare, *Comments:* Licensing agreement for systems of acute stroke diagnosis. Bijoy K. Menon—*Other Relationships:* Holds a patent on systems of triage in acute stroke, holds stock in Circle Neurovascular Inc. *Money paid to institution.

REFERENCES

1. Hartmann A, Rundek T, Mast H, et al. **Mortality and causes of death after first ischemic stroke: the Northern Manhattan Stroke Study.** *Neurology* 2001;57:2000–05 CrossRef Medline
2. Koton S, Tanne D, Green MS, et al. **Mortality and predictors of death 1 month and 3 years after first-ever ischemic stroke: data from the first National Acute Stroke Israeli Survey (NASIS 2004).** *Neuroepidemiology* 2010;34:90–96 CrossRef Medline
3. Paolucci S, Antonucci G, Grasso MG, et al. **Functional outcome of ischemic and hemorrhagic stroke patients after inpatient**

- rehabilitation: a matched comparison.** *Stroke* 2003;34:2861–65 CrossRef Medline
4. Rai AT, Domico JR, Buseman C, et al. **A population-based incidence of M2 strokes indicates potential expansion of large vessel occlusions amenable to endovascular therapy.** *J Neurointerv Surg* 2018;10:510–15 CrossRef Medline
 5. Menon BK, Hill MD, Goyal M. **Response by Menon to letter regarding article, “Analysis of workflow and time to treatment on thrombectomy outcome in the Endovascular Treatment for Small Core and Proximal Occlusion Ischemic Stroke (ESCAPE) randomized controlled trial.”** *Circulation* 2016;134:e406–07 CrossRef Medline
 6. Powers WJ, Rabinstein AA, Ackerson T, et al. **2018 guidelines for the early management of patients with acute ischemic stroke: a guideline for healthcare professionals from the American Heart Association/American Stroke Association.** *Stroke* 2018;49:e46–10 CrossRef Medline
 7. Menon BK, Hill MD, Davalos A, et al. **Efficacy of endovascular thrombectomy in patients with M2 segment middle cerebral artery occlusions: meta-analysis of data from the HERMES Collaboration.** *J Neurointerv Surg* 2019;11:1065–69 CrossRef
 8. Dorn F, Lockau H, Stetefeld H, et al. **Mechanical thrombectomy of M2-occlusion.** *J Stroke Cerebrovasc Dis* 2015;24:1465–70 CrossRef Medline
 9. Grossberg JA, Rebello LC, Haussen DC, et al. **Beyond large vessel occlusion strokes: distal occlusion thrombectomy.** *Stroke* 2018;49:1662–68 CrossRef Medline
 10. Coutinho JM, Liebeskind DS, Slater LA, et al. **Mechanical thrombectomy for isolated M2 occlusions: a post hoc analysis of the STAR, SWIFT, and SWIFT PRIME studies.** *AJNR Am J Neuroradiol* 2016;37:667–72 CrossRef Medline
 11. Sheth SA, Yoo B, Saver JL, et al. **M2 occlusions as targets for endovascular therapy: comprehensive analysis of diffusion/perfusion MRI, angiography, and clinical outcomes.** *J Neurointerv Surg* 2015;7:478–83 CrossRef Medline
 12. Saposnik G, Menon BK, Kashani N, et al. **Factors associated with the decision-making on endovascular thrombectomy for the management of acute ischemic stroke.** *Stroke* 2019;50:2441–47 CrossRef
 13. Roa JA, Martins SCO, Mont’Alverne FJ. **Stroke care and mechanical thrombectomy in developing countries.** In: Samaniego E, Hasan D, eds. *Acute Stroke Management in the Era of Thrombectomy.* Cham: Springer-Verlag; 2019;203–20
 14. Pandian JD, Sethi V, Dhillon R, et al. **Is intravenous thrombolysis feasible in a developing country?** *Cerebrovasc Dis* 2005;20:134–36 CrossRef Medline
 15. Stevens E, Emmett E, Wang Y, et al. *The Burden of Stroke in Europe.* London: Stroke Alliance for Europe; 2017
 16. Menon BK, Al-Ajlan FS, Najm M, et al. **Association of clinical, imaging, and thrombus characteristics with recanalization of visible intracranial occlusion in patients with acute ischemic stroke.** *JAMA* 2018;320:1017–26 CrossRef Medline

Delayed Leukoencephalopathy: A Rare Complication after Coiling of Cerebral Aneurysms

A. Ikemura, T. Ishibashi, K. Otani, I. Yuki, T. Kodama, I. Kan, N. Kato, and Y. Murayama



ABSTRACT

BACKGROUND AND PURPOSE: Delayed leukoencephalopathy is a rare complication that occurs after endovascular coiling of cerebral aneurysms. We aimed to describe a clinical picture of delayed leukoencephalopathy and explore potential associations with procedural characteristics.

MATERIALS AND METHODS: We considered endovascular coiling procedures for cerebral aneurysms performed between January 2006 and December 2017 in our institution with follow-up MRIs. We used logistic regression models to estimate the ORs of delayed leukoencephalopathy for each procedural characteristic.

RESULTS: We reviewed 1754 endovascular coiling procedures of 1594 aneurysms. Sixteen of 1722 (0.9%) procedures demonstrated delayed leukoencephalopathy on follow-up FLAIR MR imaging examinations after a median period of 71.5 days (interquartile range, 30–101 days) in the form of high-signal changes in the white matter at locations remote from the coil mass. Seven patients had headaches or hemiparesis, and 9 patients were asymptomatic. All imaging-associated changes improved subsequently. We found indications suggesting an association between delayed leukoencephalopathy and the number of microcatheters used per procedure ($P = .009$), along with indications suggesting that these procedures required larger median volumes of contrast medium (225 versus 175 mL, OR = 5.5, $P = .008$) as well as a longer median fluoroscopy duration (123.6 versus 99.3 minutes, OR = 3.0, $P = .06$). Our data did not suggest that delayed leukoencephalopathy was associated with the number of coils ($P = .57$), microguidewires ($P = .35$), and guiding systems ($P = .57$).

CONCLUSIONS: Delayed leukoencephalopathy after coiling of cerebral aneurysms may have multiple etiologies such as foreign body emboli, contrast-induced encephalopathy, or hypersensitivity reaction to foreign bodies.

ABBREVIATION: DL = delayed leukoencephalopathy

Endovascular coiling is an effective procedure for preventing rupture of cerebral aneurysms or treating ruptured aneurysms.^{1,2} However, a small percentage of patients experience complications,³ which include thromboembolic events (incidence rate of 4.7%–12.5%) and aneurysm rupture (incidence rate of 2.0%–8.8%),³ along with posterior reversible encephalopathy

syndrome^{4,5} and perianeurysmal edema, which may be indicative of symptomatic inflammatory reactions.^{6–8} Recently, delayed leukoencephalopathy (DL) has emerged as a new type of complication under several names, including delayed leukoencephalopathy,⁹ delayed enhancing lesions,¹⁰ and delayed multiple white matter lesions.¹¹ Its various suggested etiologies include granulation reaction caused by foreign body emboli from the hydrophilic coating of procedural devices,^{10,12–15} contrast-induced encephalopathy,^{16,17} and nickel¹¹ or bioactive polyglycolic/polylactic acid coil sensitivity.^{9,18} Despite an increasing number of reported cases, the overall clinical picture (natural history, incidence, onset time, symptoms, treatment, mortality, and morbidity) of DL remains unclear.

We aimed to define the clinical features of DL and investigate its possible associations with procedural characteristics in a retrospective study of cerebral aneurysms treated by endovascular coiling.

Received September 9, 2019; accepted after revision November 27.

From the Department of Neurosurgery (A.I., T.I., K.O., I.Y., T.K., I.K., N.K., Y.M.), Jikei University School of Medicine, Tokyo, Japan; Siemens Healthcare K.K. (K.O.), Tokyo, Japan; and Department of Neurological Surgery (I.Y.), University of California Irvine, Irvine, California.

Paper presented, in part, at: Annual Meeting of the Japan Neurosurgical Society, October 10–12, 2018, Sendai, Japan; and Annual Meeting of the Japanese Society for Neuroendovascular Therapy, November 22–24, 2018, Miyagi, Japan.

Please address correspondence to Ayako Ikemura, MD, PhD, Department of Neurosurgery, Jikei University School of Medicine, 3-25-8 Nishi-Shimbashi, Minato-ku, Tokyo 105-8461, Japan; e-mail: ayako.udgw613@gmail.com

Indicates article with supplemental on-line tables.

<http://dx.doi.org/10.3174/ajnr.A6386>

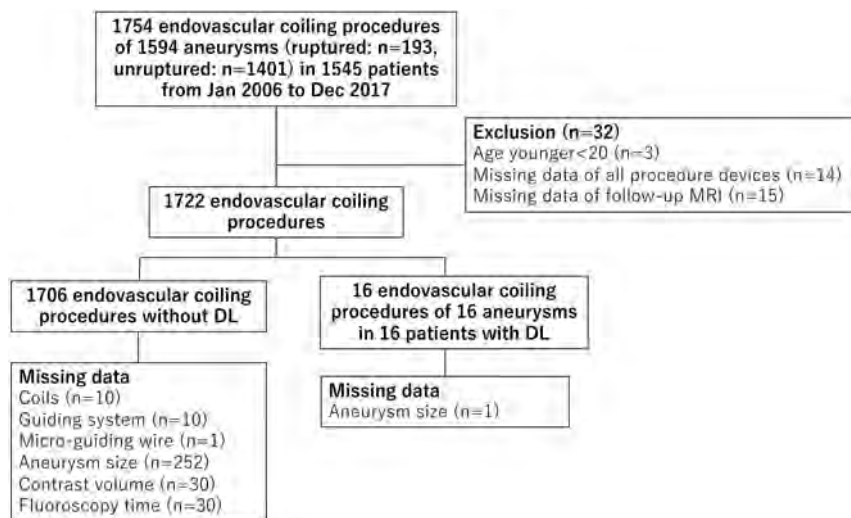


FIG 1. Flow diagram of procedure inclusion.

MATERIALS AND METHODS

Study Design and Participants

The internal review board of Jikei University Hospital approved this study (approval number 29–228 [8844]). All data related to the management of cerebral aneurysms were extracted from a comprehensive observational data base after approval of an internal review board. Each patient provided comprehensive written consent for the procedures and examinations. Specific informed consent for this study was waived because the data were obtained from routine examinations and treatments and analyzed retrospectively. At the request of the internal review board, we posted a notice of the study and gave patients an opportunity to refuse participation.

Patients with aneurysms (20 years of age or older) who underwent endovascular coiling and a follow-up MR imaging examination after 3, 6, and 12 months at our institution, between January 2006 and December 2017, were considered. For each procedure, patient age and sex, aneurysm location, largest diameter of the aneurysm, fluoroscopy time, and the type and volume of iodinated contrast medium, along with the type and number of devices used in the procedure, were extracted. Devices were defined as guiding systems (ie, guiding sheaths, guiding catheters, and median catheters), microcatheters (including balloon catheters), microguidewires, and coils. We did not consider whether the devices were used simultaneously. Furthermore, we did not consider stents and flow diverters in our analysis. Patients with DL were reviewed for their clinical history, which included MR imaging findings, neurologic findings, treatment of DL, final clinical outcome (minor morbidity, major morbidity, mortality), other procedural complications, allergy tests, time of onset of DL, and time of disappearance of DL.

Procedure

Endovascular coiling for all aneurysms was performed using digital subtraction angiography with a standard iodine contrast agent following our clinical routine.^{19,20} Patients received general anesthesia and systemic anticoagulation with heparin. The type and

number of devices were customized during each procedure. Double-catheter, balloon-assisted, or stent-assisted techniques were used to prevent coil herniation into the parent artery in cases of wide-neck aneurysms.

MR Imaging

Follow-up MR imaging examinations were performed using a 1.5T or 3T MR imaging system, routinely including DWI, FLAIR, T1WI, T2WI, and TOF-MRA to identify possible recanalization of the treated aneurysm or postprocedural complications. Contrast-enhanced MR imaging was added at 12 months after the procedure at the discretion of the attending physician.

We considered the following MR imaging outcomes associated with DL:

1. Broad high-signal changes on FLAIR images in the white matter at regions remotely located from the coil mass and observed at ≥ 2 weeks after the procedure, while the DWI findings remained normal. (These findings were not present immediately after the procedure.)
2. Decreases in size or the disappearance of high-signal changes on FLAIR images within a few months.

Statistical Analyses

Descriptive statistics were used to summarize the results. Distribution of each variable was assessed using normal quantile plots. DL proportions were calculated for each patient and procedural characteristic. We assessed the association of DL with the number of guiding systems, microguidewires, and microcatheters by classifying the procedures into 2 groups, using 1 device or >1 device. The number of bioactive polyglycolic/poly-lactic acid coils per procedure was classified as no such coil used and ≥ 1 such coil used. The association of DL with the variables of age, largest aneurysm diameter, contrast volume, fluoroscopy time, and number of coils was assessed by classifying them into 2 groups of smaller than or equal to or larger than the median of the variable. ORs for the occurrence of DL were estimated by logistic regression. The evidence of an association was assessed using the Fisher exact test. Commercial software was used for the analyses (STATA, Release 15; StataCorp, College Station, Texas).

RESULTS

Patient Demographics

Our institution performed 1754 endovascular coiling procedures for 1594 cerebral aneurysms (193 ruptured, 1401 unruptured) between January 2006 and December 2017. The flow diagram regarding the selection of the procedures is presented in Fig 1. Three patients (younger than 20 years of age), 14 procedures that did not have any data regarding procedure devices, and 15 procedures that did not include follow-up MR imaging examination were excluded. There were 1722 procedures in the final analysis.

Table 1: Patients with delayed leukoencephalopathy—aneurysm location, size, detection to disappearance intervals, postprocedural symptoms, treatment, and allergy test

No.	Location of Aneurysm	Largest Diameter of Aneurysm (mm)	Interval between Intervention and Detection of DL (days)	Interval between Intervention and Disappearance of DL (days)	Symptom	Treatment	Allergy Test
1	IC-SHA	NA	30	48	Weakness, aphasia	Free radical scavenger	NA
2	IC-SHA	8.4	28	–	Weakness	Steroid pulse, antihistamine	Pt, Zn, Mn
3	IC-SHA	3.8	88	188	None	Observation	NA
4	MCA	5.7	30	521	Weakness	Steroid pulse	All negative
5	IC-PcomA	5.1	93	360	Headache	Observation	All negative
6	IC-PcomA	5.1	28	224	None	Observation	Ir
7	ACA distal	5.6	103	269	None	Observation	NA
8	IC-ophthalmic	5.0	110	200	None	Observation	Zn, Sn, Cr
9	IC-ophthalmic	3.8	89	230	None	Observation	Zn
10	IC-PcomA	5.9	135	366	None	Observation	NA
11	IC-cavernous	17.0	55	–	Weakness	Steroid pulse	All negative
12	AcomA	7.9	30	229	Weakness, visual field loss	Steroid pulse	NA
13	AcomA	5.0	105	–	None	Observation	NA
14	IC-PcomA	9.4	48	360	None	Observation	NA
15	IC-SHA	5.8	16	87	Weakness, clumsy hand	Steroid agent, antihistamine	NA
16	IC-SHA	14.2	99	204	None	Observation	NA

Note:—NA indicates not available; IC, internal carotid; SHA, superior hypophysial artery; PcomA, posterior communicating artery; ACA, anterior cerebral artery; AcomA, anterior communicating artery; Pt, platinum; Zn, zinc; Mn, manganese; Ir, iridium; Sn, tin; Cr, chromium; –, imaging changes still slightly remaining at the end of the study.

The DL incidence was 0.9% (1706 procedures without DL and 16 with DL) during the study duration. Among the 16 aneurysms in the 16 procedures (16 patients) with DL, there were 1 ruptured and 15 unruptured aneurysms. Adjunctive to the endovascular coiling procedure, 1 aneurysm was treated using the stent-assisted technique; 1 with the balloon-assisted technique; and 14 with the double-catheter technique. DL patient demographics are presented in Table 1, and the associated details are listed in On-line Table 1.

Clinical Course

Fourteen patients with DL underwent endovascular treatment without intraprocedural complications and were neurologically intact without demonstrating abnormal MR imaging outcomes on the first day postsurgery. Among the 2 other patients with DL, one with an ICA-ophthalmic artery aneurysm demonstrated a worsening of visual acuity and evidence of central retinal artery occlusion. The patient was discharged 5 days after the procedure with mRS 1 (quarter blindness). The other presented with intraoperative aneurysm rupture; however, the coiling procedure could be completed after the rupture. The patient presented with a headache on the next day, and MR imaging revealed a minor subarachnoid hemorrhage. The patient was discharged after 8 days postsurgery without neurologic deficits.

DL symptoms or abnormal MR imaging findings were identified after a median period of 71.5 days (interquartile range, 30–101 days). Among the 16 patients with DL, there were 7 symptomatic and 9 asymptomatic patients. Among the symptomatic patients, 7 developed neurologic symptoms, 1 demonstrated continuous headache after discharge, and 6 developed motor weakness (1 with aphasia, 1 with visual field loss). These patients recovered from their symptoms after being treated with either

steroid therapy or free radical scavenger. The 9 asymptomatic patients recovered without medical intervention. There were no minor or major continuous morbidity or mortality. Among the 16 patients with DL, 7 underwent a skin patch test for metal hypersensitivity and 3 tested negative, while 4 tested positive (Table 1).

MR Imaging Findings

Follow-up of 4 of the 16 patients with DL included contrast-enhanced MR imaging. On the basis of abnormal MR imaging findings, all 16 patients were diagnosed with DL.

A follow-up MR imaging examination for each patient was continued until there was an improvement in the abnormal findings. High-signal changes on FLAIR images for 13 patients disappeared after a median period of 229 days (interquartile range, 200–360 days) after undergoing endovascular coiling. Minor levels of high-signal changes persisted in the remaining 3 patients; however, there was a noticeable decrease in the size of the high-signal region.

An illustrative case of a patient with DL whose follow-up included contrast-enhanced MR imaging is presented in Fig 2. DWI outcomes revealed no abnormal changes, but there were extensive high-signal changes on FLAIR images in a region that was primarily perfused by the vessel that underwent the endovascular procedure. Additionally, SWI outcomes demonstrated dot-shaped low signals in the regions with high-signal changes.

Procedural Characteristics

Procedural characteristics are summarized in Table 2 according to DL occurrence; and the associated DL odds ratios for each procedural characteristic, in Table 3. Details regarding the devices used during the procedures of patients with DL are listed in On-line Table 1, as well as the total number of devices by

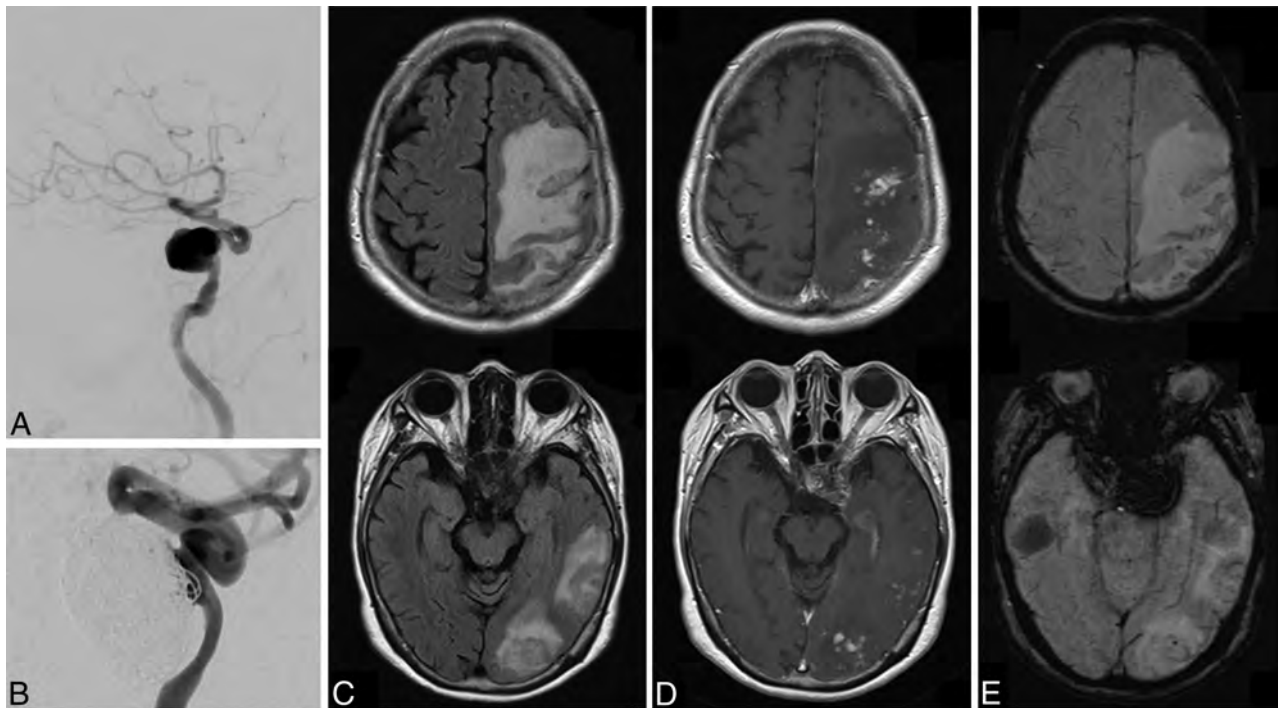


FIG 2. An illustrative case with left ICA aneurysm post-endovascular coiling (patient 11). The aneurysm size is >17 mm in maximum diameter (A), and endovascular coiling was successfully performed using the double-microcatheter technique (B). After 55 days, right weakness developed and broad high-signal change in the left parieto-occipital region is detected on a FLAIR image (C). In the same region, there is a scattered contrast effect (D) and low spotty regions in the SWI (E). The patient was hospitalized and treated with steroid pulse therapy, and the symptoms and image abnormality subsequently improved.

Table 2: Patient and procedure characteristics (per procedure) with and without DL^a

Characteristics	Without DL	With DL	All Patients
Female sex	71.3% (1217/1706)	81.3% (13/16)	71.4% (1230/1722)
Male sex	28.7% (489/1706)	18.8% (3/16)	28.6% (492/1722)
Age (yr)	59 (50–67)	59.5 (51–66.5)	59 (50–67)
Largest diameter of aneurysm (mm)	5.9 (4.7–8.0)	5.7 (5.0–8.4)	5.9 (4.8–8.0)
Fluoroscopy time (min)	99.3 (72.6–131.0)	123.6 (104.8–165.2)	99.5 (72.8–131.1)
Contrast volume (mL)	175 (150–220)	225 (195–240)	180 (150–220)
No. of coils	8 (6–13) (min 1–max 60)	10.5 (6–17) (min 2–max 36)	8 (6–13) (min 1–max 60)
No. of bioactive polyglycolic/poly-lactic acid coils	1 (0–3) (min 0–max 38)	0 (0–1) (min 0–max 9)	1 (0–3) (min 0–max 38)
No. of microcatheters (including balloon catheters)	2 (1–2) (min 1–max 10)	2 (2–2) (min 2–max 4)	2 (1–2) (min 1–max 10)
No. of microguidewires	2 (2–2) (min 1–max 7)	2 (1.5–2.5) (min 1–max 3)	2 (2–2) (min 1–max 7)
No. of guiding systems	1 (1–1.5) (min 1–max 3)	1 (1–1) (min 1–max 2)	1 (1–1) (min 1–max 3)

Note:—min indicates minimum; max, maximum.

^a Categorical variables are expressed in percentage and continuous variables in median and interquartile range.

manufacturer used in our hospital (On-line Table 2, guiding systems; On-line Table 3, microcatheters; On-line Table 4, microguidewires; and On-line Table 5, coils) for the procedures with and without DL. We used a Shuttle sheath (Cook, Bloomington, Indiana) in 2 of the 16 patients with DL, bioactive polyglycolic/poly-lactic acid coils in 6, and 2 microcatheters simultaneously via 1 guiding system in all patients with DL. Use of >180 mL of contrast medium was associated with higher DL odds (OR = 5.5; 95% CI, 1.6–19.5; $P = .008$) and use of >1 microcatheter ($P = .009$, Fisher exact test). Our results also suggested that median fluoroscopy time longer than 99.5 minutes was associated with higher DL odds (OR = 3.0; 95% CI, 1.0–9.5; $P = .06$). We

could not confirm an association of the use of bioactive polyglycolic/poly-lactic acid coils and higher odds of DL (OR = 0.4; 95% CI, 0.1–1.1; $P = .08$).

DISCUSSION

One of the strengths of our study is the large number of endovascular coiling procedures and patients with DL. We found that 0.9% of endovascular coiling procedures resulted in patients with DL and that their clinical course was typically benign.

The exact mechanism of DL remains uncertain; however, different hypotheses have been proposed. Some case reports

Table 3: Odds ratio of complications for each patient and procedure characteristic (per procedure) with and without DL^a

Characteristics	Without DL	With DL	OR (95% CI)	P Value
Female sex	71.3% (1217/1706)	81.3% (13/16)	Reference	
Male sex	28.7% (489/1706)	18.8% (3/16)	0.6 (0.2–2.0)	.39
Age (yr)				
59 or younger	50.6% (863/1706)	50.0% (8/16)	Reference	
Older than 59	49.4% (843/1706)	50.0% (8/16)	1.0 (0.4–2.7)	.96
Largest diameter of aneurysm				
≤5.9 mm	49.0% (713/1455)	53.3% (8/15)	Reference	
>5.9 mm	51.0% (742/1455)	46.7% (7/15)	0.8 (0.3–2.3)	.74
Fluoroscopy time				
≤99.5 min	50.3% (843/1676)	25.0% (4/16)	Reference	
>99.5 min	49.7% (833/1676)	75.0% (12/16)	3.0 (1.0–9.5)	.06
Contrast volume				
≤180 mL	56.2% (941/1676)	18.8% (3/16)	Reference	
>180 mL	43.9% (735/1676)	81.3% (13/16)	5.5 (1.6–19.5)	.008
No. of coils				
≤8	51.0% (865/1696)	43.8% (7/16)	Reference	
>8	49.0% (831/1696)	56.3% (9/16)	1.3 (0.5–3.6)	.57
No. of bioactive polyglycolic/polylactic acid coils				
0	39.9% (676/1696)	62.5% (10/16)	Reference	
≥1	60.1% (1020/1696)	37.5% (6/16)	0.4 (0.1–1.1)	.08
No. of microcatheters (including balloon catheters)				
1	27.0% (461/1706)	0% (0/16)		.009 (Fisher exact test)
>1	73.0% (1245/1706)	100% (16/16)		
No. of microguidewires				
1	16.2% (276/1705)	25.0% (4/16)	Reference	
>1	83.8% (1429/1705)	75.0% (12/16)	0.6 (0.2–1.8)	.35
No. of guiding systems				
1	75.0% (1272/1696)	81.3% (13/16)	Reference	
>1	25.0% (424/1696)	18.8% (3/16)	0.7 (0.2–2.4)	.57

^a Categorical variables are expressed in percentage and continuous variables in median and interquartile range.

indicated that DL may be a granulation reaction etiologically associated with foreign body emboli from the hydrophilic coating of the devices.^{10,12–14} Polymer coating embolism from intravascular devices has also been increasingly reported with regard to cardiovascular²¹ and endovascular therapy.^{22,23}

In a previous study analyzing a series of 3 cases with delayed enhancing lesions—each treated with the double microcatheter technique—Oh et al¹⁰ performed a benchtop evaluation of the inner lumen of microcatheters. They found material wearing off the catheter shafts after multiple in-and-out coil maneuvers and proposed that DL may be caused by the fragmentation of the inner wall of microcatheters and consecutive emboli. Shapiro et al¹² reported 5 patients who underwent coil-supported Pipeline Embolization Device (Covidien, Irvine, California) embolization or stent-supported endovascular coiling and presented with foreign body emboli after the procedure. Multiple catheters were used to treat most of the patients evaluated in our study because all endovascular coiling procedures involved stent or flow-diverter deliveries and all patients with DL were treated with multiple microcatheters. Therefore, our results also suggest that the hydrophilic coating of catheters may peel off and act as an embolic source due to the friction between the tight-fitting multiple catheters. The peeling off of the device coating may be associated with the complexity of these procedures, which may be reflected by a tendency of longer fluoroscopy duration in the procedures for patients with DL. In vitro experiments with multiple catheter

types and frequent replacement and repositioning are required for further investigation. We routinely used guiding systems with a fairly large inner lumen (up to 8F), but choosing even larger catheters may further lower the friction between devices.

The neurotoxicity of iodinated contrast medium, along with the disruption of the blood-brain barrier and leakage into the brain tissue, has previously been reported to be associated with contrast encephalopathy.^{16,17,24} Contrast-induced encephalopathy typically follows coronary angiography and intracranial endovascular treatment and is characterized on plain CT as leakage of contrast medium.^{25–27} Transient cortical blindness is a commonly reported complication due to contrast-induced encephalopathy and is considered to be associated with high doses of contrast agents.^{26,28} Our study estimated that the odds for experiencing DL were higher for larger volumes of contrast agent (>180 mL). The patients in our study did not undergo CT examinations; however, 1 patient with DL had high-signal changes on FLAIR images in the hemisphere opposite the treated vessel, and it is possible that the contrast medium may have been translocated to this location. These results support a hypothesis that using a higher dose of contrast medium than the patient can metabolize may be associated with DL.¹⁷

Nickel allergy or hypersensitivity to polyglycolic/polylactic acid coils is reported to potentially cause DL.^{9,29} In our study, only 7 patients with DL received patch tests for metal hypersensitivity, and none of these 7 patients had metal allergies associated

with nickel. We used polyglycolic/polylactic acid coils for only 6 of the 16 patients with DL. However, a hypersensitivity reaction to any foreign body used during the invasive procedures continues to be a possible etiology of DL.

It is our understanding that DL may be caused by various factors: foreign body emboli-associated granulation reaction, contrast-induced encephalopathy, or a hypersensitivity reaction to foreign bodies leading to identical image findings. We also cannot exclude interactions and associations between factors such as contrast-induced permeability and the retention of shaved-off catheter coating and the subsequent development of foreign body emboli.

Our study has several limitations. It was a single-center retrospective investigation using data collected from clinical routine procedures. The procedures included stents or flow diverters but not Woven EndoBridge devices (WEB; Sequent Medical, Aliso Viejo, California). There were only a few cases of DL despite the cases being relatively numerous compared with previous studies. None of our patients with DL had posterior circulation aneurysms, which may be related to sample size bias because DL has also been previously reported in such patients.¹¹ The number of cases of DL was too few to apply a multivariate logistic regression, and we could not investigate confounding of the procedural characteristics. Pathology tests were not performed. Only a few patients with DL underwent contrast-enhanced MR imaging, and none underwent CT. Our analysis could not distinguish between the simultaneous and consecutive use of microcatheters. We could not investigate associations of specific devices with DL because different types of guiding systems, microcatheters, microguidewires, and coils and their combinations were customized during each procedure, which resulted in unique combinations in almost every procedure.

CONCLUSIONS

DL is a rare complication following endovascular coiling of cerebral aneurysms. We believe that it may be associated with several etiologies, including foreign body emboli related to complicated procedures or contrast-induced encephalopathy or hypersensitivity reaction to foreign bodies. Although the clinical course of DL is mostly benign, clinicians need to be aware of the potential causes of DL.

ACKNOWLEDGMENTS

The authors wish to thank Ms Rie Sakima for clinical data preparation and the study team and all the study participants.

Disclosures: Katherine Otani—UNRELATED: Full-time employee of Siemens Healthcare K.K. Katherine Otani supported this study as a biostatistician. Yuichi Murayama—UNRELATED: Consultancy: Stryker, Kaneka Medix; Grants/Grants Pending: Stryker, Siemens K.K., Japan. Comments: research grant*; Payment for Lectures Including Service on Speakers Bureaus: Stryker, Cerenovus, Kaneka Medix; Royalties: Stryker.* *Money paid to the institution.

REFERENCES

1. Guglielmi G, Vinuela F, Sepetka I, et al. **Electrothrombosis of saccular aneurysms via endovascular approach, Part 1: electrochemical basis, technique, and experimental results.** *J Neurosurg* 1991;75:1-7 CrossRef Medline
2. Guglielmi G, Vinuela F, Dion J, et al. **Electrothrombosis of saccular aneurysms via endovascular approach, Part 2: preliminary clinical experience.** *J Neurosurg* 1991;75:8-14 CrossRef Medline
3. Orru E, Roccatagliata L, Cester G, et al. **Complications of endovascular treatment of cerebral aneurysms.** *Eur J Radiol* 2013;82:1653-58 CrossRef Medline
4. Bartyński WS. **Posterior reversible encephalopathy syndrome, Part 1: fundamental imaging and clinical features.** *AJNR Am J Neuroradiol* 2008;29:1036-42 CrossRef Medline
5. Bartyński WS. **Posterior reversible encephalopathy syndrome, Part 2: controversies surrounding pathophysiology of vasogenic edema.** *AJNR Am J Neuroradiol* 2008;29:1043-49 CrossRef Medline
6. Craven I, Patel UJ, Gibson A, et al. **Symptomatic perianeurysmal edema following bare platinum embolization of a small unruptured cerebral aneurysm.** *AJNR Am J Neuroradiol* 2009;30:1998-2000 CrossRef Medline
7. Horie N, Kitagawa N, Morikawa M, et al. **Progressive perianeurysmal edema induced after endovascular coil embolization: report of three cases and review of the literature.** *J Neurosurg* 2007;106:916-20 CrossRef Medline
8. Fanning NF, Willinsky RA, ter Brugge KG. **Wall enhancement, edema, and hydrocephalus after endovascular coil occlusion of intradural cerebral aneurysms.** *J Neurosurg* 2008;108:1074-86 CrossRef Medline
9. Fukushima Y, Nakahara I. **Delayed leucoencephalopathy after coil embolisation of unruptured cerebral aneurysm.** *BMJ Case Rep* 2018;2018 CrossRef Medline
10. Oh SW, Shin NY, Lee HJ, et al. **Delayed enhancing lesions after coil embolization of aneurysms: clinical experience and benchtop analyses.** *J Neurointerv Surg* 2017;9:1243-47 CrossRef Medline
11. Park HS, Nakagawa I, Yokoyama S, et al. **Nickel-associated delayed multiple white matter lesions after stent-assisted coil embolization of intracranial unruptured aneurysm.** *BMJ Case Rep* 2017;2017 CrossRef Medline
12. Shapiro M, Ollenschleger MD, Baccin C, et al. **Foreign body emboli following cerebrovascular interventions: clinical, radiographic, and histopathologic features.** *AJNR Am J Neuroradiol* 2015;36:2121-26 CrossRef Medline
13. Shotar E, Law-Ye B, Baronnet-Chauvet F, et al. **Non-ischemic cerebral enhancing lesions secondary to endovascular aneurysm therapy: nickel allergy or foreign body reaction? Case series and review of the literature.** *Neuroradiology* 2016;58:877-85 CrossRef Medline
14. Fealey ME, Edwards WD, Giannini C, et al. **Complications of endovascular polymers associated with vascular introducer sheaths and metallic coils in 3 patients, with literature review.** *Am J Surg Pathol* 2008;32:1310-16 CrossRef Medline
15. Cruz JP, Marotta T, O'Kelly C, et al. **Enhancing brain lesions after endovascular treatment of aneurysms.** *AJNR Am J Neuroradiol* 2014;35:1954-58 CrossRef Medline
16. Nagamine Y, Hayashi T, Takechi Y, et al. **Contrast-induced encephalopathy after coil embolization of an unruptured internal carotid artery aneurysm.** *Intern Med* 2014;53:2133-38 CrossRef Medline
17. Leong S, Fanning NF. **Persistent neurological deficit from iodinated contrast encephalopathy following intracranial aneurysm coiling: a case report and review of the literature.** *Interv Neuroradiol* 2012;18:33-41 CrossRef Medline
18. Ulus S, Yakupoğlu A, Kararslan E, et al. **Reversible intracranial parenchymal changes in MRI after MCA aneurysm treatment with stent-assisted coiling technique; possible nickel allergy.** *Neuroradiology* 2012;54:897-99 CrossRef Medline
19. Murayama Y, Nien YL, Duckwiler G, et al. **Guglielmi detachable coil embolization of cerebral aneurysms: 11 years' experience.** *J Neurosurg* 2003;98:959-66 CrossRef Medline

20. Murayama Y, Vinuela F, Duckwiler GR, et al. **Embolization of incidental cerebral aneurysms by using the Guglielmi detachable coil system.** *J Neurosurg* 1999;90:207–14 CrossRef Medline
21. Chopra AM, Mehta M, Bismuth J, et al. **Polymer coating embolism from intravascular medical devices: a clinical literature review.** *Cardiovasc Pathol* 2017;30:45–54 CrossRef Medline
22. Ansari SA, Anderson RR, Caron MJ, et al. **Hydrophilic polymer embolic complication during diagnostic cerebral angiography presenting with delayed intracranial hemorrhage: case report and literature review.** *J Neurointerv Surg* 2019;11:80–83 CrossRef Medline
23. Mehta RI, Rai AT, Vos JA, et al. **Intrathrombus polymer coating deposition: a pilot study of 91 patients undergoing endovascular therapy for acute large vessel stroke, Part I: histologic frequency.** *J Neurointerv Surg* 2019;11:1191–96 CrossRef Medline
24. Okazaki H, Tanaka K, Shishido T, et al. **Disruption of the blood-brain barrier caused by nonionic contrast medium used for abdominal angiography: CT demonstration.** *J Comput Assist Tomogr* 1989;13:893–95 CrossRef Medline
25. Guimaraens L, Vivas E, Fonnegra A, et al. **Transient encephalopathy from angiographic contrast: a rare complication in neuro-interventional procedures.** *Cardiovasc Interv Radiol* 2010;33:383–88 CrossRef Medline
26. Zwicker JC, Sila CA. **MRI findings in a case of transient cortical blindness after cardiac catheterization.** *Catheter Cardiovasc Interv* 2002;57:47–49 CrossRef Medline
27. Dangas G, Monsein LH, Laureno R, et al. **Transient contrast encephalopathy after carotid artery stenting.** *J Endovasc Ther* 2001;8:111–13 CrossRef Medline
28. Niimi Y, Kupersmith MJ, Ahmad S, et al. **Cortical blindness, transient and otherwise, associated with detachable coil embolization of intracranial aneurysms.** *AJNR Am J Neuroradiol* 2008;29:603–07 CrossRef Medline
29. Park HS, Nakagawa I, Yokoyama S, et al. **Nickel-associated delayed multiple white matter lesions after stent-assisted coil embolization of intracranial unruptured aneurysm.** *J Neurointerv Surg* 2018;10:e1 CrossRef Medline

Intra-Arterial Verapamil Treatment in Oral Therapy–Refractory Reversible Cerebral Vasoconstriction Syndrome

J.M. Ospel, C.H. Wright, R. Jung, L.L.M. Vidal, S. Manjila, G. Singh, D.V. Heck, A. Ray, and K.A. Blackham



ABSTRACT

SUMMARY: Reversible vasoconstriction syndrome is a complex of clinical symptoms and angiographic findings, which, while having a mostly benign clinical course, has clinical and imaging overlap with more serious disorders such as vasculitis and aneurysmal SAH and itself includes a minority of patients with fulminant vasoconstriction resulting in severe intracranial complications. Endovascular options for patients with refractory reversible cerebral vasoconstriction syndrome include intra-arterial vasodilator infusion similar to therapy for patients with vasospasm after SAH. To date, only case reports and 1 small series have discussed the utility of intra-arterial vasodilators for the treatment of reversible cerebral vasoconstriction syndrome. We report an additional series of 11 medically refractory cases of presumed or proved reversible cerebral vasoconstriction syndrome successfully treated with intra-arterial verapamil infusion. Furthermore, we propose that the reversal of vasoconstriction, as seen on angiography, could fulfill a diagnostic criterion.

ABBREVIATIONS: IA = intra-arterial; RCVS = reversible cerebral vasoconstriction syndrome

Reversible cerebral vasoconstriction syndrome (RCVS) describes a constellation of clinical and angiographic findings that includes severe headache and reversible segmental vasoconstriction of the cerebral arteries, with or without neurologic deficits. Diagnosis is difficult and one of exclusion because the differential diagnosis for sudden severe headache includes both aneurysmal and nonaneurysmal subarachnoid hemorrhage. Moreover, the broad differential diagnosis of vasoconstriction of the cerebral vessels encompasses diverse entities such as primary angiitis of the CNS and atherosclerosis. Numerous inciting factors for RCVS have been described, but the list of triggers continues to grow.^{1,2} Treatment options include medical optimization of risk

factors, corticosteroids, and oral or intra-arterial calcium channel blockers.³ If left untreated, RCVS can lead to permanent neurologic disability and even death.^{4–6} Complications such as hemorrhage and stroke are well-documented.^{1,7} In the past decade, on the basis of the experience with treatment of patients with vasospasm secondary to SAH, an endovascular approach using the intra-arterial (IA) infusion of calcium channel blockers in patients with refractory RCVS has emerged, with case reports and a small series of promptly improved vessel caliber and also symptoms.^{8,9} The underlying hypothesis is that the vasoconstriction of RCVS is vasospasm as observed in SAH and that similar treatment approaches will similarly prevent the development of permanent neurologic deficits. In this case series, we present 11 patients with documented or presumed RCVS who presented with or progressed to clinically relevant vasoconstriction and in whom IA treatment with verapamil resulted in clinical and radiographic improvement. A detailed narrative description, including illustrative images, of 3 exemplary patients is provided.

MATERIALS AND METHODS

Since 2006, the authors have used intra-arterial verapamil as a treatment option in patients with suspected RCVS and clinical deterioration. Individual cases of patients with presumed RCVS who underwent cerebral angiography with intra-arterial administration of verapamil were retrospectively identified through a departmental angiography data base search from 2006–2016 at the University Hospital of Basel, Switzerland; 2006–2016 at

Received December 31, 2018; accepted after revision November 16, 2019.

From the Department of Radiology (J.M.O., K.A.B.), Section of Neuroradiology and Interventional Neuroradiology, Basel University Hospital, University of Basel, Basel, Switzerland; Departments of Neurological Surgery (C.H.W.), and Neurosurgery (A.R.), University Hospitals of Cleveland Case Medical Center, Cleveland, Ohio; Department of Diagnostic Radiology and Nuclear Medicine (L.L.M.V.), University of Maryland Medical Center, Baltimore, Maryland; Department of Neurology (R.J.), The Sandra and Malcolm Berman Brain & Spine Institute, Sinai Hospital of Baltimore, Llifebridge Health, Baltimore, Maryland; Department of Neurosurgery and Neurosciences (S.M.), McLaren Bay Region Hospital, Bay City, Michigan; Department of Radiology (G.S.), Section of Neuroradiology, Newark Beth Israel Medical Center, Newark, New Jersey; and Forsyth Radiological Associates (D.V.H.), Winston-Salem, North Carolina.

Please address correspondence to Johanna Maria Ospel, MD, Department of Radiology, Basel University Hospital, University of Basel, Petersgraben 4, 4051 Basel, Basel, Switzerland; e-mail: johannamaria.ospel@usb.ch; @johanna_ospel; @KBlackhamMD



Indicates article with supplemental on-line table.

<http://dx.doi.org/10.3174/ajnr.A6378>

Table 1: Diagnostic criteria for RCVS⁴

	Criteria
1	Unusual, acute severe headache of progressive or sudden onset, presenting with or without neurologic focal deficit and/or seizure
2	Benign CSF analysis (protein level, <80 mg/dL; leukocyte count, <10/mm ³ ; and normal glucose level)
3	Imaging studies demonstrating 2 different points of vessel narrowing in at least 2 different intracranial arteries
4	Imaging proving absence of intracranial aneurysm/vascular malformation or aneurysmal SAH
5	Reversibility of intracranial vessel narrowing on short-term follow-up evaluation (<12 months)

University Hospitals of Cleveland, Case Medical Center in Cleveland, Ohio; and 2006–2011 at Forsythe Medical Center in Winston-Salem, North Carolina, which identified patients undergoing intra-arterial verapamil infusion for any reason. Inclusion criteria are listed in Table 1 and are based on work by Calabrese, et al.⁴ We interpreted criterion number 5 to include acute reversibility demonstrated as a result of verapamil treatment. Patients treated for vasospasm in the setting of nonaneurysmal (perimesencephalic) subarachnoid hemorrhage were excluded. Institutional board review approval (University Hospitals of Cleveland and Forsythe Medical Center) and individuals' written consent (University Hospital of Basel) were obtained for this multicenter case series. All imaging, clinical records, laboratory results, and treatment and follow-up data were obtained from the electronic medical records and PACS of the hospitals and were reviewed by 2 experienced neurointerventionalists (K.A.B./A.R.) to verify inclusion.

Image Interpretation

Procedural information and angiographic results were also retrospectively evaluated by 2 experienced neurointerventionalists (K.A.B./A.R.) for confirmation of treatment indications and results. A semiquantitative classification of grade was performed by visually assessing the luminal narrowing compared with the best normal vessel caliber on either the same study or prior cerebral angiograms using the following categories: 1) mild: luminal narrowing of <30% of normal caliber; 2) moderate: between 30% and 60% of normal caliber; and 3) severe: luminal narrowing of >60% of normal caliber, similar to the stratification described by Jun et al.¹⁰ At least 1 segmental focus of at least moderate proximal vasoconstriction or any distal vasoconstriction would indicate the need for intra-arterial treatment. Confirmation of an adequate angiographic response to treatment was defined as a 10%–30% improvement in the most severely constricted vessel caliber.

DSA and IA Verapamil Therapy

Endovascular treatment was performed using a standard biplane angiographic technique starting with a diagnostic series of both internal carotid arteries and the dominant vertebral artery, with the patient under systemic heparinization. IA verapamil was administered proximally in the affected vascular territory. Verapamil was diluted in saline to a final concentration of 1 mg/mL and pulse-infused at a rate of 1 mL/min through the diagnostic catheter, meaning that 1 mL of verapamil was manually injected every minute through the side port of a 3-way valve connected to the diagnostic catheter and also to a continuous heparinized saline flush, allowing intermittent flush. The overall dosage was determined by the vasoconstriction degree and distribution; higher doses of verapamil were used in more extensive and more severe vasoconstrictions with a range of

5–20 mg per territory (maximum of 20 mg per vessel and 60-mg total dose per session) as described in the treatment of subarachnoid hemorrhage-induced vasospasm by Jun et al.¹⁰ and Keuskamp et al.¹¹ Due to prolonged procedural times because of the slow infusion rate, treatment was performed with monitored anesthesia care with continuous monitoring of systemic blood pressure, heart rate, respiratory frequency, and arterial oxygen saturation. Repeat images to demonstrate the absence of embolic complications were obtained immediately following injection, and images to demonstrate the vasodilatory response were obtained at a minimum of 10 minutes following the injection.¹² At the end of the procedure, the patients were admitted to intensive care for blood pressure support and monitoring per protocol for patients with SAH and vasospasm. Patients were monitored clinically and with daily transcranial Doppler sonography.

RESULTS

Eleven patients with presumed RCVS who underwent IA treatment with verapamil were identified (Table 2 and On-line Table). All patients met the 5 criteria for RCVS (Table 1); 4 patients had ambulatory imaging documentation of complete vasoconstriction resolution, and the remaining patients without ambulatory follow-up had reversibility of the vasoconstriction at the time of treatment. Nine of the identified patients were women, and 2 were men, with a mean age of 38.2 ± 13.1 years. Serologic vasculitis work-up including antinuclear antibodies, rheumatoid factor, soluble substance A and soluble substance B antibodies, perinuclear antineutrophil cytoplasmic antibodies, and antineutrophil cytoplasmic antibodies was negative in all 11 patients. Brain biopsy in patient 1 was negative for vasculitis. Except for 1 groin pseudoaneurysm successfully treated with thrombin injection, there were no complications reported from the angiographic procedures.

All patients retrospectively met the angiographic criteria for treatment, and all territories treated met the criteria for an angiographic response. One patient required balloon angioplasty in addition to intra-arterial verapamil for severe ICA stenosis (patient 3). One patient who developed heparin-induced thrombocytopenia required the use of argatroban, a direct thrombin inhibitor, during her procedures (patient 4). All patients improved neurologically immediately following intra-arterial verapamil infusion, and all continued to show neurologic improvement on discharge. Four patients received and were unresponsive to steroids before the diagnosis of RCVS was considered. Five patients returned to the angiography suite multiple times because of recurrent symptoms or elevated transcranial Doppler studies (mean middle cerebral artery velocity greater than 120 cm/sec or greater than 20 percent elevation of flow velocity above baseline).

Table 2: Patient baseline characteristics, admission, treatment, and discharge metrics

Case	Age (yr)/Sex	Length of Stay (Days)	NIHSS (Admission/Discharge)	IA Verapamil (No. of Cycles/Total Amount)	Follow-Up Interval (Weeks)	Follow-Up Imaging Results or Clinical Examination
1	43/F	19	16/1	5/120 mg	16	Resolution of vasoconstriction
2	43/F	17	0/0	1/30 mg	1	Near-complete resolution of vasoconstriction
3	25/M	14	2/0	2/40 mg, Balloon angioplasty	5	Resolution of vasoconstriction
4	43/F	15	4/2	2/55 mg	12	mRS 1, cognitive delay, NIHSS 0
5	35/F	11	2/0	1/20 mg	1	mRS 0
6	25/F	3	0/0	1/15 mg	—	Lost to follow-up
7	27/F	6	4/1	1/12.5 mg	1	Resolution of vasoconstriction
8	33/M	4	0/0	1/10 mg	—	Lost to follow-up
9	69/F	30	10/4	3/60 mg	52	Died from multiple myeloma complications
10	52/F	11	0/0	1/10 mg	6	Resolution of vasoconstriction
11	25/F	21	4/0	6/180 mg	—	Lost to follow-up

Note:— indicates that no clinical or imaging follow-up was available.

Case 1

A 43-year-old woman developed thunderclap headache when she was running on the treadmill and went to an outside hospital where she had work-up for SAH, including CT of the head and lumbar puncture, which had negative findings. After a week, she developed acute worsening of headache with nausea and vomiting, and CT of the head at an outside hospital showed a right frontal hematoma. She was admitted to an outside hospital. MR imaging studies after 4 days showed right frontal hemorrhage, which was unchanged, and an MRA showed right ICA/MCA occlusion. At the outside hospital, she was treated with nimodipine and levetiracetam (Keppra), high-dose steroids, diazepam (Valium), and morphine. Her main symptoms were headache, confusion, and hallucinations; she also developed left hemivisual field inattention.

She was ultimately transferred to our hospital. On admission, her NIHSS score was 16, and she was found to have left-sided weakness, left hemianopia, and left hemiattention. MR imaging on admission showed multiple diffusion-restricted lesions in the bilateral hemispheres; however, lesions were more pronounced in the right hemisphere, particularly in the right MCA territory. DSA confirmed right ICA terminus occlusion extending into the right M1 segment with reconstitution of distal MCA branches via leptomeningeal collaterals. Multifocal vasoconstriction was seen in the left anterior circulation and was most severe in the bilateral posterior circulation (Fig 1). IA verapamil was injected in both ICAs (left ICA, 20 mg; right ICA, 5 mg) and the right vertebral artery (10 mg), whereupon angiographic improvement was observed, particularly in the distal vessels (Fig 1), with the exception of the occluded right ICA/MCA. Because left-sided weakness and somnolence immediately improved, we presumed that the vasodilation led to improved leptomeningeal collateral flow to the right MCA territory. Oral verapamil was started and titrated to 240 mg daily. Due to elevated transcranial sonography velocities or recurrent somnolence, IA verapamil treatment was repeated 4 additional times on hospital days 2, 3, and 4 for a total amount of 120 mg. Steroids were discontinued after a vasculitis work-up, including a brain biopsy negative for vasculitis. Other additional medications (nimodipine, morphine, diazepam, levetiracetam) were also stopped. With sustained clinical and sonographic improvement finally obtained, discharge occurred on

day 19. The only residual symptom was a mild left neglect. Follow-up MRA at 4 months showed persistent occlusion of the right ICA terminus and right MCA, but complete resolution of vasoconstriction in the remaining intracranial circulation. At 5-year follow-up, a slight weakness of the lower extremities and left lower quadrantanopia was still present.

Case 2

A 43-year-old woman presented at an outside hospital with headache and altered mental status; hyponatremia was found on laboratory work-up. She had a diagnosis of multiple sclerosis treated with interferon β -1 as well as a history of substance abuse and depression. MR imaging showed FLAIR signal alterations in both occipital and parietal lobes, consistent with posterior reversible encephalopathy syndrome, bilateral scattered foci of diffusion restriction, and demyelination consistent with multiple sclerosis. She was treated with oral verapamil and steroids and transferred to our hospital where DSA was performed for worsening confusion. It showed severe focal and segmental vasoconstriction in both the anterior and posterior circulations. A total amount of 30 mg of IA verapamil was injected in both ICAs (10 mg, respectively) and the left vertebral artery (10 mg), which led to improvement of intracranial vessel caliber and improvement of symptoms. Follow-up CTA after 6 days showed only residual mild narrowing of the right distal M1 and proximal M2 branches. Encephalopathic symptoms resolved, steroid medication was stopped, and oral verapamil was continued. The patient was discharged to rehabilitation on day 17.

Case 3

A 25-year-old man presented with a partial right hemiparesis and intermittent aphasia following an episode of head trauma in the setting of a history of chronic binge drinking. The patient had known hypoparathyroidism, and on admission, he had elevated liver enzymes. He presented twice to an outside hospital, and ultimately CT and CTA were performed, which showed vasoconstriction. The patient was transferred to our hospital on day 10 post-trauma with motor weakness of the right leg, headache, and intermittent aphasia. MR imaging performed on hospital day 1

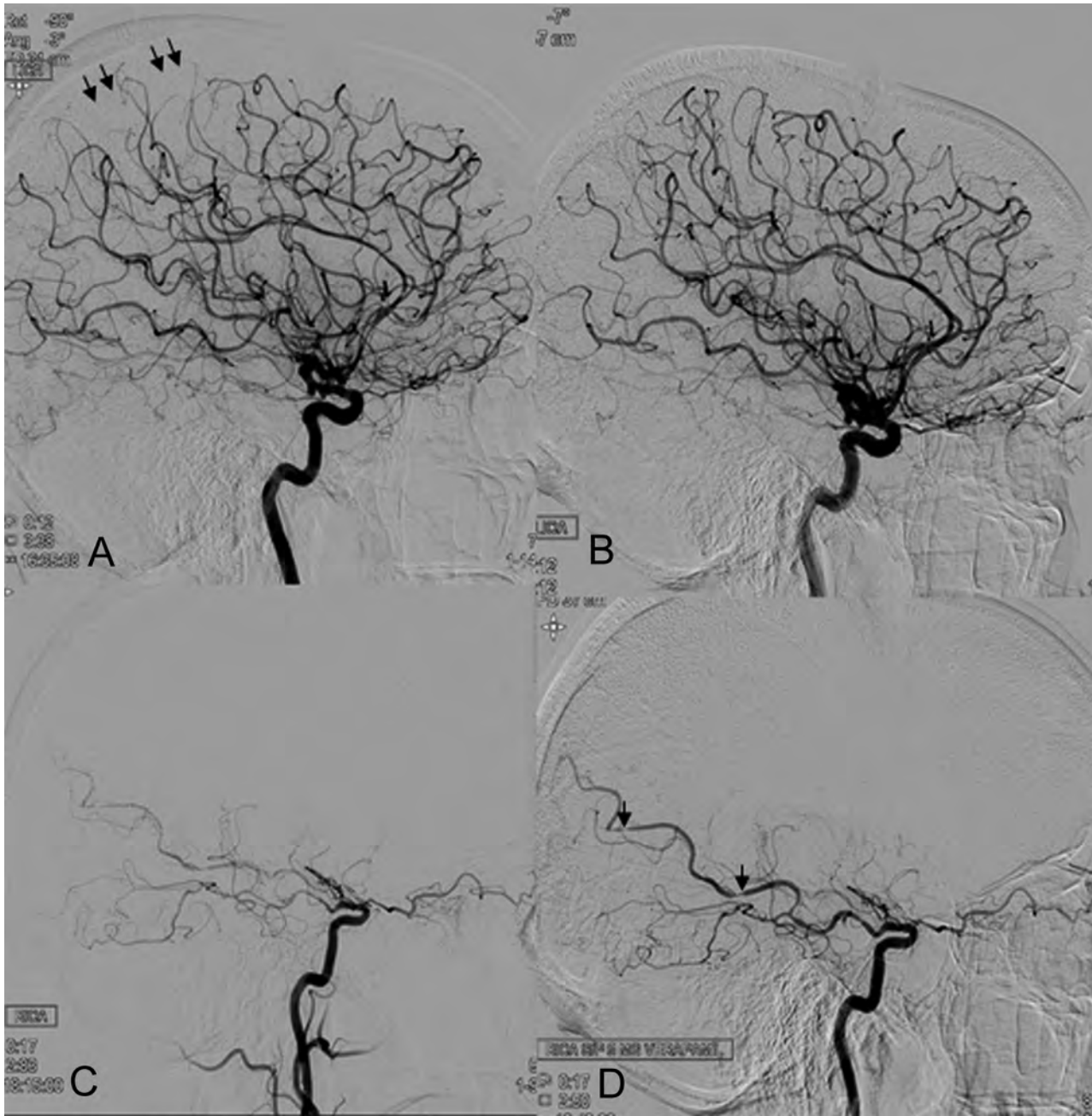


FIG 1. DSA of patient 1 illustrates, in the left anterior circulation, diffuse vasoconstriction in peripheral MCA branches before verapamil infusion (arrows in A), which resolves following IA verapamil injection (B). The lower row shows occlusion of the right internal carotid terminus and a filiform caliber of the posterior cerebral artery, which arises from the left posterior communicating artery (C). The caliber increases markedly following verapamil injection, with some residual focal narrowing (arrows in D).

showed acute ischemia in the left anterior cerebral artery territory, bilateral SAH, a small amount of intraventricular hemorrhage, and severe narrowing of both ICA and the basilar artery (Fig 2). Endovascular treatment was performed on hospital day 2 in the morning with IA verapamil injection in the left ICA and basilar artery (10 mg, respectively), with improvement in the basilar narrowing (Fig 2). Due to agitation and fluctuating clinical status including transient aphasia during the procedure, the patient was intubated and taken to MR imaging, where no new ischemic lesions were identified. The patient returned to the angiography suite for

uncomplicated angioplasty of the severe narrowing of the right ICA. Additionally, 10 mg in the right ICA and, again, 10 mg in the basilar artery were administered; overall, 40 mg of verapamil was administered. After extubation, the clinical symptoms improved, oral nimodipine was started at 180 mg per day, and the patient was placed in intensive care for 1 week. Oral nimodipine was discontinued on hospital day 12 due to resolution of symptoms. Twenty-four days had passed since the initial presentation, and discharge occurred on hospital day 14 to rehabilitation. Findings of an MRA at 5 weeks postdischarge were normal (Fig 2).

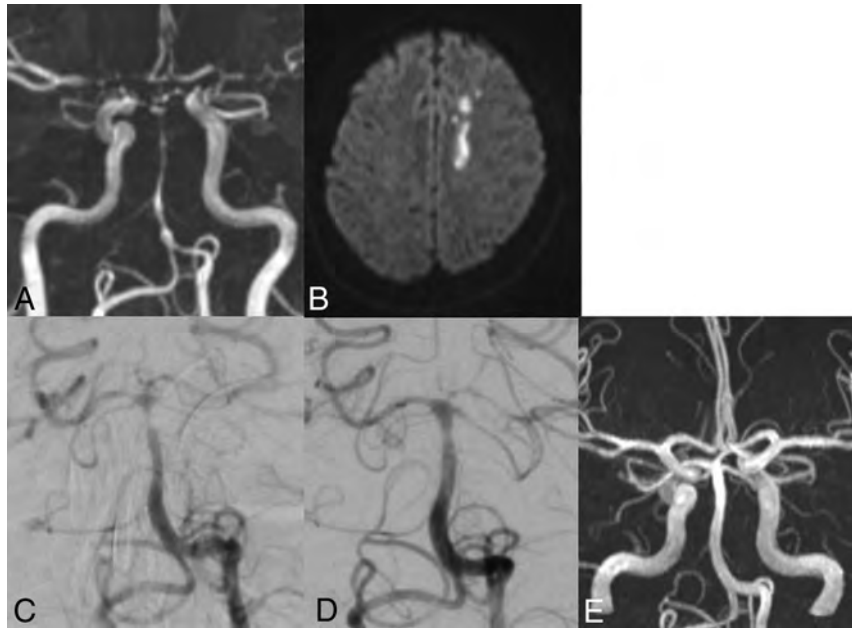


FIG 2. MRA of patient 3 on hospital day 1 shows severe vasoconstriction of the basilar artery as well as both ICA terminuses and M1 segments (A). Diffusion-weighted imaging reveals acute ischemia in the left anterior cerebral artery territory (B). Angiogram on hospital day 2 shows severe distal basilar occlusion (C). One hour after infusion of 10 mg of IA verapamil in the proximal left vertebral artery, the spasm is markedly reduced (D). Follow-up MRA, 5 weeks after discharge, demonstrates complete resolution of vasoconstriction (E).

DISCUSSION

In most cases, RCVS is a benign and self-limiting condition with spontaneous resolution; however, it can also be a complex clinico-radiologic challenge.⁴ Despite oral and intravenous calcium channel blockers,^{1,13-16} additional pathologic imaging features besides the typical “string of beads” appearance of vasoconstriction have been described in 12%–81% of patients.¹ Unfortunately, the diagnosis is often delayed, and the initial clinical treatment is variable if not disorganized due to inexperience with the condition and its overlap with other disorders such as aneurysmal or nonaneurysmal SAH and vasculitis. RCVS can be easily mistaken for primary angiitis of the central nervous system even on digital subtraction angiography. Treatment options include medical optimization of risk factors, corticosteroids and oral or intra-arterial calcium channel blockers. The course can be monitored clinically and by using transcranial Doppler and complete resolution of vasoconstriction within 3 months is the typical confirmation for the diagnosis of RCVS.

All of our patients ultimately underwent IA treatment with verapamil due to their refractory, progressive clinical course. Our female preponderance and age range (25–69 years) reflect the predisposition of the syndrome for women (sex ratios from 2:1 up to 10:1 have been reported^{2,7,17}) and the known predilection for young and middle-aged individuals, however, there are descriptions of RCVS in patients up to 76 years of age.^{2,7,18,19}

In all of our patients, at least 1 imaging complication was present (acute ischemia: 8 patients; intraparenchymal hemorrhage: 3 patients; cortical SAH: 4 patients; posterior reversible encephalopathy syndrome: 2 patients). In the medical literature, up to 39% of the patients with RCVS have been reported to

develop ischemic events,¹ and 12%–20% of patients were positive for intraparenchymal hemorrhage,^{7,14} slightly lower rates compared with our case series.

Cortical SAH has been described in up to 34%,^{7,14} and posterior reversible encephalopathy syndrome, in 9%–38% of patients with RCVS. For the latter, vasoconstriction is believed to be causative for the characteristic vasogenic edema.^{7,20,21} Several authors have hypothesized that RCVS and posterior reversible encephalopathy syndrome have an overlapping pathophysiology because both occur in the setting of sympathetic overactivity and endothelial dysfunction leading to disturbances of the vascular tone.^{20,22,23}

We observed clinical worsening in 4 of 11 patients despite empiric administration of glucocorticoids and/or cyclophosphamide. Empiric use of immunosuppressant therapy is common, given the clinical and angiographic similarities between primary angiitis of the central nervous system and RCVS and emphasizes the limited experience with this disease entity.^{17,24,25} Use of glucocorticoids in RCVS treatment has been described as associated with poor outcome and is therefore controversial.^{1,26-29} A possible explanation for deterioration following steroids is glucocorticoid-induced noradrenaline hypersensitivity in vascular smooth-muscle cells, though the exact mechanisms are not yet known.³⁰

All our patients had at least 1 known RCVS trigger in their clinical history (autoimmune diseases: 3 patients; bone marrow transplantation: 2 patients; postpartum state: 2 patients; head trauma: 1 patient; exhaustive exercise/postcoital: 2 patients; blood transfusions: 1 patient; narcotic use/binge drinking: 5 patients).¹ RCVS is known to be associated with autoimmune diseases and immunosuppressive treatment following transplantation. Endothelial damage and activation occur in both of these conditions and are believed to trigger the disease.^{1,31} While women are more predisposed to the disorder per se, the incidence rate in those who gave birth recently is even higher.^{1,32}

Currently, there is no guideline for the use of IA treatment in RCVS. Nevertheless, IA treatment with calcium channel blockers has not only been recognized as an important treatment adjunct for severe refractory RCVS but has also been proposed as a differential diagnostic tool.^{8,9,27,33-36} At our institutions, there is an increased awareness of the entity in general and a lower threshold for intervention. As opposed to systemic administration of high-dose oral calcium channel blockers, this targeted therapy approach may avoid sustained hypotension, which can further precipitate cerebral infarction in the

border zones.³³ Slow injection rates of large doses and proximal IA administration of verapamil have been reported to be safe and effective in patients with vasospasm due to aneurysmal SAH in conjunction with monitored anesthesia care and were noted to be able to reduce the need for angioplasty in these cases.^{11,37}

Similar to the treatment of aneurysmal SAH-induced vasospasm, IA verapamil provided an improvement of the arterial caliber during angiographic studies, and all our patients demonstrated improvement clinically. This outcome can be interpreted as an early confirmation of the reversible nature of the vasoconstriction. Several authors have suggested that IA treatment might not only be an effective treatment option but may also serve as a diagnostic tool, crucial to guiding acute management.^{34,35} The improvement in vessel caliber is not angiographically immediate and is better observed at least 10 minutes after infusion.¹² Furthermore, as with vasospasm from SAH, IA treatment is not durable and multiple treatments during the hospital course were necessary in 5 of 11 of our patients because the vasoconstriction tended to recur. Recurrence of vasoconstriction in this setting with the need for repeat IA treatment is not infrequent and has been reported.²⁷ Nevertheless, there is evidence that in patients with vasospasm from SAH, a preventative strategy using frequent and early endovascular treatment seems to reduce the risk of delayed cerebral ischemia.³⁸

CONCLUSIONS

RCVS remains a challenging diagnosis, and its severity can be underestimated. Careful clinical and imaging evaluation is crucial, and a high index of suspicion for possible complications must be maintained to guide optimal management. Angiographic evaluation may be necessary in patients with fulminant RCVS, not only because of its superiority as the criterion standard for vascular imaging but also as a provocative diagnostic maneuver in the setting of potential IA treatment. This clinical report adds evidence for the effectiveness of IA verapamil as a treatment escalation in RCVS and confirms its favorable safety profile. In light of the growing evidence, we suggest a low threshold when considering IA verapamil injection not only as a therapeutic option but also as an early diagnostic tool for patients with oral treatment-refractory presumed RCVS.

Disclosures: Richard Jung—UNRELATED: Travel/Accommodations/Meeting Expenses Unrelated to Activities Listed: Penumbra PEER Meeting, Comments: September 28–29, 2018; attendance at a conference paid for by Penumbra.* *Money was paid to the individual.

ACKNOWLEDGMENTS

We thank Dr Selina Ackermann from the University Hospital Basel for editorial assistance.

REFERENCES

- Ducros A. **Reversible cerebral vasoconstriction syndrome.** *Lancet Neurol* 2012;11:906–17 CrossRef Medline
- Ducros A, Boukobra M, Porcher R, et al. **The clinical and radiological spectrum of reversible cerebral vasoconstriction syndrome: a prospective series of 67 patients.** *Brain* 2007;130:3091–3101 CrossRef Medline
- Nowak DA, Rodiek SO, Henneken S, et al. **Reversible segmental cerebral vasoconstriction (Call-Fleming syndrome): are calcium channel inhibitors a potential treatment option?** *Cephalalgia* 2003;23:218–22 CrossRef Medline
- Calabrese LH, Dodick DW, Schwedt TJ, et al. **Narrative review: reversible cerebral vasoconstriction syndromes.** *Ann Intern Med* 2007;146:34–44 CrossRef Medline
- Chen SP, Fuh JL, Chang FC, et al. **Transcranial color Doppler study for reversible cerebral vasoconstriction syndromes.** *Ann Neurol* 2008;63:751–57 CrossRef Medline
- Singhal AB, Topcuoglu MA, Fok JW, et al. **Reversible cerebral vasoconstriction syndromes and primary angitis of the central nervous system: clinical, imaging, and angiographic comparison.** *Ann Neurol* 2016;79:882–94 CrossRef Medline
- Singhal AB, Hajj-Ali RA, Topcuoglu MA, et al. **Reversible cerebral vasoconstriction syndromes: analysis of 139 cases.** *Arch Neurol* 2011;68:1005–12 CrossRef Medline
- Elstner M, Linn J, Muller-Schunk S, et al. **Reversible cerebral vasoconstriction syndrome: a complicated clinical course treated with intra-arterial application of nimodipine.** *Cephalalgia* 2009;29:677–82 CrossRef Medline
- Al-Mufti F, Dodson V, Wajswol E, et al. **Chemical angioplasty for medically refractory reversible cerebral vasoconstriction syndrome.** *Br J Neurosurg* 2018;32:431–35 CrossRef Medline
- Jun P, Ko NU, English JD, et al. **Endovascular treatment of medically refractory cerebral vasospasm following aneurysmal subarachnoid hemorrhage.** *AJNR Am J Neuroradiol* 2010;31:1911–16 CrossRef Medline
- Keuskamp J, Murali R, Chao KH. **High-dose intraarterial verapamil in the treatment of cerebral vasospasm after aneurysmal subarachnoid hemorrhage.** *J Neurosurg* 2008;108:458–63 CrossRef Medline
- Sehy JV, Holloway WE, Lin SP, et al. **Improvement in angiographic cerebral vasospasm after intra-arterial verapamil administration.** *AJNR Am J Neuroradiol* 2010;31:1923–28 CrossRef Medline
- Ansari SA, Rath TJ, Gandhi D. **Reversible cerebral vasoconstriction syndromes presenting with subarachnoid hemorrhage: a case series.** *J NeuroInterv Surg* 2011;3:272–78 CrossRef Medline
- Ducros A, Fiedler U, Porcher R, et al. **Hemorrhagic manifestations of reversible cerebral vasoconstriction syndrome: frequency, features, and risk factors.** *Stroke* 2010;41:2505–11 CrossRef Medline
- Sattar A, Manousakis G, Jensen MB. **Systematic review of reversible cerebral vasoconstriction syndrome.** *Expert Rev Cardiovasc Ther* 2010;8:1417–21 CrossRef Medline
- Noda K, Fukae J, Fujishima K, et al. **Reversible cerebral vasoconstriction syndrome presenting as subarachnoid hemorrhage, reversible posterior leukoencephalopathy, and cerebral infarction.** *Intern Med* 2011;50:1227–33 CrossRef Medline
- Chen SP, Fuh JL, Lirng JF, et al. **Recurrent primary thunderclap headache and benign CNS angiopathy: spectra of the same disorder?** *Neurology* 2006;67:2164–69 CrossRef Medline
- Cappelen-Smith C, Calic Z, Cordato D. **Reversible cerebral vasoconstriction syndrome: recognition and treatment.** *Curr Treat Options Neurol* 2017;19:21 CrossRef Medline
- Ducros A, Wolff V. **The typical thunderclap headache of reversible cerebral vasoconstriction syndrome and its various triggers.** *Headache* 2016;56:657–63 CrossRef Medline
- Bartynski WS. **Posterior reversible encephalopathy syndrome, Part 2: controversies surrounding pathophysiology of vasogenic edema.** *AJNR Am J Neuroradiol* 2008;29:1043–49 CrossRef Medline
- Chen SP, Fuh JL, Wang SJ, et al. **Magnetic resonance angiography in reversible cerebral vasoconstriction syndromes.** *Ann Neurol* 2010;67:648–56 CrossRef Medline
- Bartynski WS, Boardman JF. **Catheter angiography, MR angiography, and MR perfusion in posterior reversible encephalopathy syndrome.** *AJNR Am J Neuroradiol* 2008;29:447–55 CrossRef Medline

23. Chen SP, Yang AC, Fuh JL, et al. **Autonomic dysfunction in reversible cerebral vasoconstriction syndromes.** *J Headache Pain* 2013;14:94 CrossRef Medline
24. Calabrese LH, Gragg LA, Furlan AJ. **Benign angiopathy: a distinct subset of angiographically defined primary angiitis of the central nervous system.** *J Rheumatol* 1993;20:2046–50 Medline
25. Kadkhodayan Y, Alreshaid A, Moran CJ, et al. **Primary angiitis of the central nervous system at conventional angiography.** *Radiology* 2004;233:878–82 CrossRef Medline
26. Chen SP, Fuh JL, Wang SJ. **Reversible cerebral vasoconstriction syndrome: current and future perspectives.** *Expert Rev Neurother* 2011;11:1265–76 CrossRef Medline
27. French KF, Hoesch RE, Allred J, et al. **Repetitive use of intra-arterial verapamil in the treatment of reversible cerebral vasoconstriction syndrome.** *J Clin Neurosci* 2012;19:174–76 CrossRef Medline
28. Katz BS, Fugate JE, Ameriso SF, et al. **Clinical worsening in reversible cerebral vasoconstriction syndrome.** *JAMA Neurol* 2014;71:68–73 CrossRef Medline
29. Singhal AB, Topcuoglu MA. **Glucocorticoid-associated worsening in reversible cerebral vasoconstriction syndrome.** *Neurology* 2017;88:228–36 CrossRef Medline
30. Rascher W, Dietz R, Schomig A, et al. **Modulation of sympathetic vascular tone by prostaglandins in corticosterone-induced hypertension in rats.** *Clin Sci* 1979;57(Suppl 5):235s–37s. CrossRef Medline
31. Leroux G, Sellam J, Costedoat-Chalumeau N, et al. **Posterior reversible encephalopathy syndrome during systemic lupus erythematosus: four new cases and review of the literature.** *Lupus* 2008;17:139–47 CrossRef Medline
32. Kumai Y, Seguchi O, Sato T, et al. **Reversible cerebral vasoconstriction syndrome after heart transplantation: a case report.** *Transplant Proc* 2017;49:2415–18 CrossRef Medline
33. Farid H, Tatum JK, Wong C, et al. **Reversible cerebral vasoconstriction syndrome: treatment with combined intra-arterial verapamil infusion and intracranial angioplasty.** *AJNR Am J Neuroradiol* 2011;32:E184–87 CrossRef Medline
34. Laneuville M, Ding J, Shamy M, et al. **Intra-arterial milrinone may differentiate fulminant RCVS from vasculitis.** *Neurology* 2017;89:1093–94 CrossRef Medline
35. Linn J, Fesl G, Ottomeyer C, et al. **Intra-arterial application of nimodipine in reversible cerebral vasoconstriction syndrome: a diagnostic tool in select cases?** *Cephalalgia* 2011;31:1074–81 CrossRef Medline
36. Bouchard M, Verreault S, Garipey JL, et al. **Intra-arterial milrinone for reversible cerebral vasoconstriction syndrome.** *Headache* 2009;49:142–45 CrossRef Medline
37. Albanese E, Russo A, Quiroga M, et al. **Ultrahigh-dose intraarterial infusion of verapamil through an indwelling microcatheter for medically refractory severe vasospasm: initial experience. Clinical article.** *J Neurosurg* 2010;113:913–22 CrossRef Medline
38. Jabbarli R, Pierscianek D, Rolz R, et al. **Endovascular treatment of cerebral vasospasm after subarachnoid hemorrhage: more is more.** *Neurology* 2019;93:e458–66 CrossRef Medline

Artery of Davidoff and Schechter Supply in Dural Arteriovenous Fistulas

K.D. Bhatia, H. Kortman, T. Wälchli, I. Radovanovic, V.M. Pereira, and T. Krings



ABSTRACT

SUMMARY: The artery of Davidoff and Schechter is a dural branch of the posterior cerebral artery that can supply the meninges close to the falcotentorial junction. It is usually not identified on angiography except when enlarged in the setting of a dural AVF or meningioma. The impact on treatment of the artery of Davidoff and Schechter supply to a fistula is not well-described in the literature. Our retrospective analysis of patients with dural AVFs treated at the Toronto Western Hospital between 2006 and 2018 identified 6 patients with dural AVFs receiving supply from artery of Davidoff and Schechter (of a total of 173 patients with dural AVFs). All patients were initially treated by transarterial embolization using liquid embolic agents. Three patients required a second endovascular procedure partly due to residual supply from artery of Davidoff and Schechter, and in all cases, angiographic cure was obtained. The treatment approach, challenges encountered, and potential complications of treating such fistulas are described.

ABBREVIATIONS: ADS = artery of Davidoff and Schechter; PCA = posterior cerebral artery; SCA = superior cerebellar artery

The artery of Davidoff and Schechter (ADS) is a dural branch that arises from the posterior cerebral artery and supplies the falcotentorial junction.¹ It is usually not identified on angiography except when enlarged in the setting of dural AVFs,^{2,3} meningiomas,⁴ or, rarely, cerebellar tumors.⁵ The ADS is the only dural branch of the posterior cerebral artery (PCA),¹ and unlike most other arteries that provide dural supply, it has an intradural origin.⁶ The first description was by Wollschlaeger and Wollschlaeger,⁷ in 1965, based on postmortem barium angiography, and they named the artery to honor their mentors in neuroradiology.¹

The ADS may originate from the superior surface of the P1–2 junction or the proximal P2 segment and extends posterolaterally across the ambient cistern between the superior cerebellar artery (SCA) superiorly and the trochlear nerve inferiorly,

adjacent to the free edge of the tentorium.¹ It supplies a 3- to 4-cm width region on the inferior surface of the posterior medial tentorium as it approaches the falcotentorial junction,^{1,7} reinforcing the more anterior supply from the artery of Bernasconi and Cassinari (a branch of the meningohypophyseal trunk).^{6,7} Uniting with its contralateral partner at the falcotentorial junction, the ADS then pierces the dura and extends superiorly along the falx cerebri toward its attachment with the superior sagittal sinus (Fig 1).^{1,8}

While a PCA origin of the ADS is most common, a similar branch arising from the SCA was identified in the original 1965 study (reporting an SCA anastomosis to the PCA dural branch in 1 cadaver)⁷ and reported in 5 patients with tentorial AVFs by Byrne and Garcia in 2013⁹ and later eponymously named as the artery of Wollschlaeger and Wollschlaeger by Tayebi Meybodi et al,¹⁰ in 2017.¹¹ The literature is variable in describing the SCA dural branch as a variant of the ADS versus an entirely separate artery.^{9,11–13} Because we have previously described a tentorial AVF with a coexistent pial-to-dural arterial supply from both the PCA and SCA,¹⁴ for the purposes of this study, we defined the ADS as being solely of PCA origin.

Endovascular treatment has become progressively prominent in the treatment of intracranial dural AVFs.¹⁵ The direct communication of the ADS between the dural arterial network and the intradural posterior circulation poses a potential risk of iatrogenic stroke related to reflux of liquid embolic agents toward pial vessels.^{2,9} Given the overall rarity of falcotentorial AVFs, the impact that the ADS supply has on the treatment of

Received September 25, 2019; accepted after revision November 20.

From the Division of Neuroradiology (K.D.B., H.K., V.M.P., T.K.), Joint Department of Medical Imaging, and Division of Neurosurgery (T.W., I.R., V.M.P., T.K.), Department of Surgery, Toronto Western Hospital, Toronto, Ontario, Canada; Department of Fundamental Neurobiology (T.W., I.R.), Krembil Research Institute, Toronto Western Hospital, University Health Network, University of Toronto, Toronto, Ontario, Canada; Group of CNS Angiogenesis and Neurovascular Link, and Physician-Scientist Program (T.W.), Institute for Regenerative Medicine, Neuroscience Center Zurich, Zurich, Switzerland; Department of Health Sciences and Technology (T.W.), Swiss Federal Institute of Technology, Zurich, Zurich, Switzerland; and Division of Neurosurgery Program (T.W.), University Hospital Zurich, Zurich, Switzerland.

Please address correspondence to Kartik Dev Bhatia, MD, Division of Neuroradiology, Level 3, Toronto Western Hospital, 399 Bathurst St, Toronto, M5T 2S8, ON, CANADA; e-mail: Kartik.bhatia@uhn.ca

Indicates article with supplemental on-line tables.

<http://dx.doi.org/10.3174/ajnr.A6380>

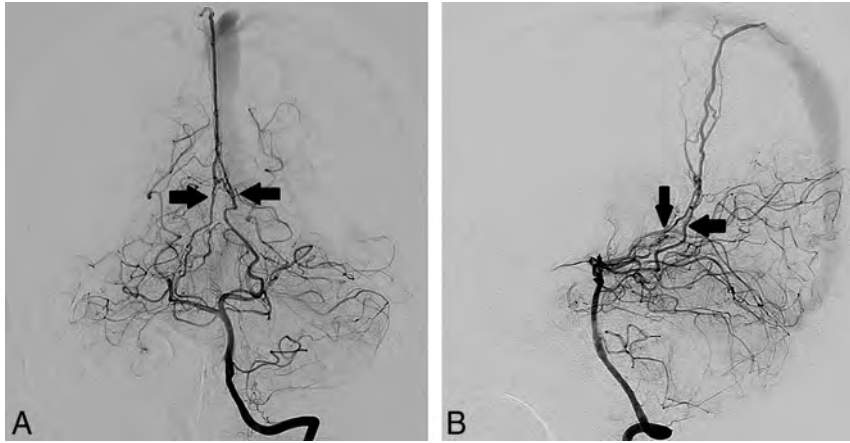


FIG 1. A, Cerebral DSA (patient 3) via a left vertebral artery injection demonstrating arterial supply to a superior sagittal sinus dural AVF by enlarged bilateral arteries of Davidoff and Schechter. Anterior-posterior projection in the arterial phase shows a bilateral enlarged ADS arising from the superior aspect of the P1–2 junctions of the posterior cerebral arteries and converging (black arrows) into an enlarged falx artery at the falcotentorial junction, with early venous filling of the superior sagittal sinus. Note the presence of cortical venous reflux. B, Lateral projection shows a bilateral enlarged ADS (black arrows) extending posteriorly along the free edges of the tentorium cerebelli and converging adjacent to the falcotentorial junction.

these fistulas is not well-described. In this study, we aimed to assess the angioarchitecture, treatment strategies, and clinical outcomes for intracranial dural AVFs that receive arterial supply from the ADS. This study builds on our previously published analysis of intracranial dural AVFs with a pial artery supply.¹⁴

MATERIALS AND METHODS

Ethics approval for this study was granted by the Research Ethics Board of the University Health Network, Toronto (approval No. 19–5018). Retrospective cohort review was undertaken of all patients with intracranial AVFs managed at Toronto Western Hospital between 2006 and 2018. Inclusion criteria were a confirmed diagnosis of dural AVF on DSA, follow-up time-resolved MRA or DSA after interventional or conservative management, and a demonstrated arterial supply to the AVF from ADS. Clinical presentation and clinical outcomes were obtained from the electronic patient records.

Imaging Assessment

Baseline and follow-up DSA (and MRA when available) imaging for each patient was analyzed independently by 2 reviewers, both fellowship-qualified in interventional neuroradiology (K.D.B. and H.K.). Disagreements were resolved by a senior reviewer (T.K.). The following characteristics were assessed on DSA: fistula location, arterial supply, venous drainage, classifications of Borden et al¹⁶ and Cognard et al,¹⁷ endovascular treatment approach, embolic agent used, number of endovascular procedures required, residual supply from the ADS after the first embolization, and final angiographic outcome.

RESULTS

Diagnosis

Between 2006 and 2018 at Toronto Western Hospital, 173 patients with 192 fistulas were identified with a confirmed diagnosis of dural AVF on DSA and follow-up imaging available. Of these, 6

patients (3 women and 3 men; mean age, 46.5 years) with 6 fistulas demonstrated arterial supply to the AVF from the ADS (3.5% of patients, 3.1% of fistulas) (see On-line Table 1 for individual patient demographics, clinical presentations, and angiographic analysis results). One patient presented with subarachnoid hemorrhage. Four patients were diagnosed with falcotentorial fistulas (all Cognard type IV); 1 patient, with a parasagittal fistula (Cognard III); and 1 patient, with a superior sagittal sinus fistula (Cognard Ila+b) (Fig 1). Patients 1 and 6 were previously included in our published analysis of AVFs with pial artery supply.¹⁴

Treatment Planning

Following multidisciplinary discussion among radiosurgery, cerebrovascular neurosurgery, and interventional neurology,

the consensus opinion in all 6 cases was for initial endovascular transarterial embolization based on the angiographic features, the extensive vascular structures involved, the deep location, and the perceived natural history.

Endovascular Treatment

All 6 patients initially underwent transarterial embolization using liquid embolic agents (On-line Table 2). Three patients required a second embolization session, in part due to residual supply to the fistula from the ADS. Two patients specifically underwent microcatheter cannulation of the ADS (Figs 2 and 3), and patient 2 underwent embolization via the ADS. All patients demonstrated cure of the fistula on the final DSA (Figs 2E, -F and 3E, -F). No procedural complications were encountered; in particular, we did not encounter reflux to the PCA.

DISCUSSION

Published Literature

Based on our review of the literature, this is the largest reported series of dural AVFs supplied by the ADS treated by endovascular techniques (the existing literature predominantly being case reports; On-line Table 3).^{1–3,18} The ADS supply may not be appreciated on angiography due to competitive flow from multiple arterial feeders (Fig 3A, -B) and thus may not always have been recognized in large series of tentorial AVFs.^{9,19} Tentorial fistulas constitute <3% of cranial AVFs but are 6 times more likely than nontentorial AVFs to present with hemorrhage,²⁰ likely a result of the direct cortical venous drainage seen with these AVFs.^{3,13,20}

Surgical Approach to Falcotentorial AVFs

Most tentorial AVFs carry a high risk of hemorrhage²⁰ and endovascular approaches can be challenging; thus, some cases may require microsurgical disconnection.^{13,21} The primary surgical goal for tentorial AVFs is the same as for all AVFs—occlusion of

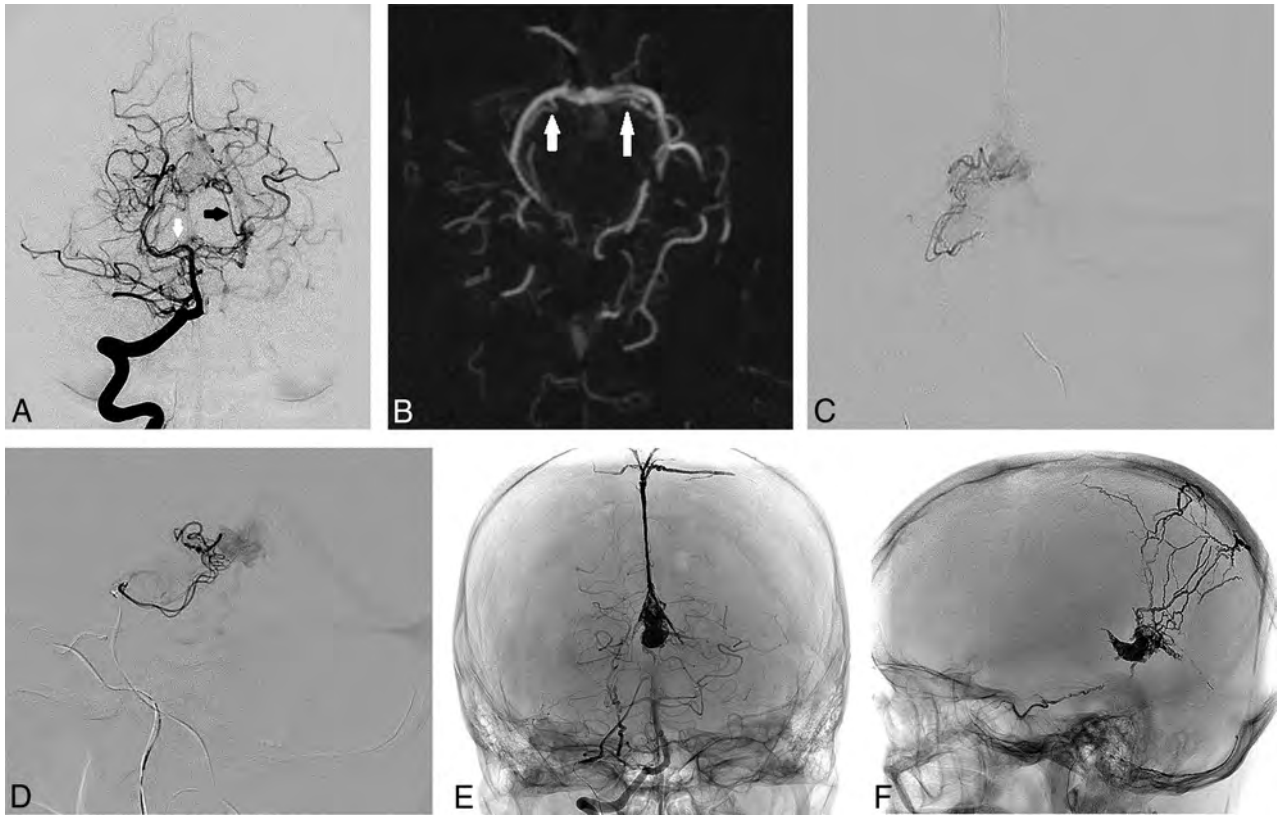


FIG 2. A, Cerebral DSA and endovascular treatment (patient 1) of a falcotentorial dural AVF supplied by the bilateral arteries of Davidoff and Schechter. Anterior-posterior projection of a right vertebral artery injection in the arterial phase shows an enlarged left ADS (*black arrow*) with early filling of the vein of Galen. Note the mildly enlarged right ADS arising from the right P1–2 junction (*white arrow*) and the infratentorial venous reflux. B, Axial MIP reconstruction of a 3D rotational angiogram performed via right vertebral artery injection shows the bilateral origins of the ADS from the P1–2 junctions of the posterior cerebral arteries (*white arrows*). C, Anterior-posterior projection of a microcatheter injection within the right ADS shows early venous filling along the straight and left transverse sinuses. D, Lateral projection of a microcatheter injection within the right ADS shows the course of the vessel along the free edge of the tentorium to the falcotentorial junction, with early venous filling into the vein of Galen. E, Nonsubtracted anterior-posterior projection during right vertebral artery injection after a second-stage transvenous embolization shows no residual early venous filling, with an Onyx cast filling the vein of Galen. F, Spot lateral radiograph of the skull shows the Onyx cast following transarterial and transvenous embolizations.

the proximal portion of the draining vein.²¹ In principle, the operative strategy is based on an optimal surgical approach with an ideally adapted patient position allowing gravity to retract the brain, open subarachnoid planes, and shorten dissection times to expose and interrupt the draining vein.^{13,21}

Lawton et al,¹³ in 2008, created a surgical classification of tentorial AVFs based on their experience with 31 cases, differentiating 6 types based on fistula location, dural base, associated sinuses, and direction of venous drainage. Among those 31 patients, arterial supply from branches of the SCA or PCA (including the ADS) was identified in 8 patients.¹³ Six of these 8 patients had the Galenic subtype, located adjacent to the falcotentorial junction with drainage to the vein of Galen either directly or via cortical veins, requiring a posterior interhemispheric surgical approach after initial transarterial embolization.¹³ Preoperative embolization is often undertaken to minimize blood loss due to the extensive adjacent arterial and deep venous structures in the operative field.^{13,22} If a cure can be achieved by endovascular means, this may be preferable to a surgical approach.²¹

In our overall cohort of 173 patients with intracranial AVFs, only 4 patients had falcotentorial Galenic subtype AVFs¹³ (2.3%).

All 4 patients demonstrated an ADS supply and were included in this study; this finding is consistent with the known high rates of SCA or PCA supply to this AVF subtype.¹³ All 4 patients underwent endovascular treatment with angiographic cure, and none required surgical intervention.

Endovascular Approaches to Falcotentorial AVFs with ADS Supply

Both transarterial^{2,3,18} and transvenous²³ approaches with the use of liquid embolic agents have been described for the successful treatment of falcotentorial AVFs, with a treatment goal of occlusion of the fistulous point and foot of the draining vein to achieve cure. In our series, all patients initially underwent transarterial embolization using liquid embolics (On-line Table 2), with excellent outcomes, thus eliminating the need for potentially more invasive surgical approaches.

In patient 2, the initial embolization procedure also required microcatheter selection and embolization from the ADS itself (Fig 3) once competitive flow from the middle meningeal artery was excluded. In this instance, a highly distal position was achieved with the microcatheter, allowing deposition of small coils to minimize reflux followed by administration of Onyx

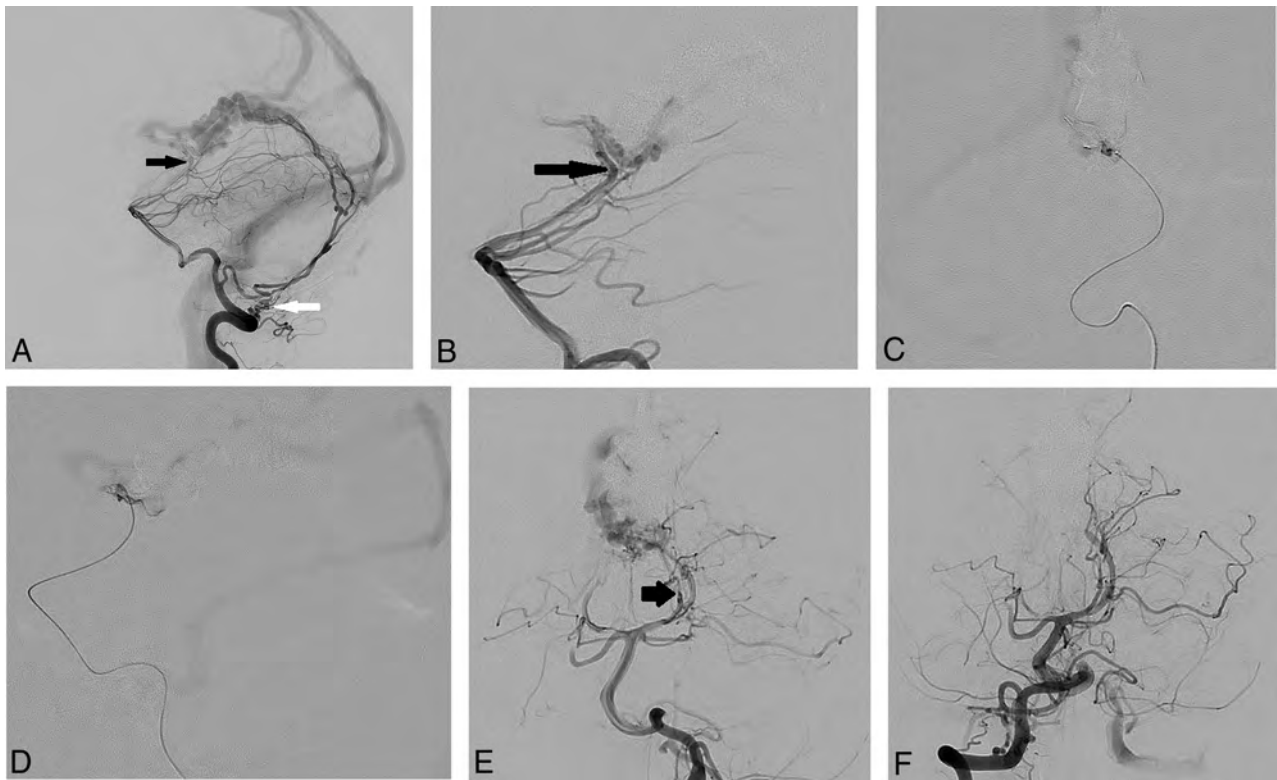


FIG 3. A, Cerebral DSA and endovascular treatment (patient 2) of a falcotentorial dural AVF supplied by the bilateral arteries of Davidoff and Schechter. Lateral projection of a left vertebral artery injection shows supply to the dural AVF by the left posterior meningeal artery (*white arrow*) and faint supply from the ADS (*black arrow*). B, Lateral projection of a left vertebral artery injection after embolization using Onyx from the posterior meningeal artery shows the residual ADS supply (*black arrow*) to the inferior surface of the vein of Galen more clearly, with reduced competitive flow. C, Anterior-posterior projection of a microcatheter injection via the left ADS distally shows the remnant fistulous flow to the junction of the vein of Galen and straight sinus at the falcotentorial junction. D, Lateral projection of a microcatheter injection via the left ADS distally shows the residual supply to the dural AVF with deep venous reflux. E, Anterior-posterior projection of a left vertebral artery injection in the arterial phase shows the residual supply to the dural AVF by the enlarged left ADS (*black arrow*). F, Anterior-posterior projection of a right vertebral artery injection after embolization of the left ADS distal supply using coils and Onyx shows no residual early venous filling with cure of the AVF.

Table: Risk-reduction strategies for endovascular treatment of falcotentorial dural AVFs

Category	Risk-Reduction Strategy	Patients Treated
Anatomic assessment; to identify supply from ADS	Magnified high-frame-rate angiography	1-6
	3D rotational angiography with multiplanar reconstructions	1-6
Transarterial embolization; strategies to avoid reflux across ADS	Initial embolization from non-ADS arterial supplies (to reduce competitive flow)	1-6
	Close monitoring for linear reflux anteriorly from the vein of Galen (along the expected course of ADS)	1-6
Embolization directly via ADS; strategies to treat via ADS while avoiding reflux	Direct cannulation of ADS with embolization if distal access achieved (pressure-cooker technique to minimize reflux)	2
	Aborting embolization attempts from ADS if distal access not achieved (insufficient safety margin)	1
Strategies for residual ADS supply	Staged embolization over multiple sessions as required	1, 3, 5
	Transvenous approach (eg, reverse pressure-cooker technique)	1

(Covidien, Irvine, California) directly to the fistulous point using a modified pressure-cooker technique. Understanding the complex arterial anatomy and using imaging-based treatment were the keys to a complete, safe, and successful endovascular treatment approach in this case. In patient 1, the right ADS was

cannulated with a microcatheter (Fig 2), but a distal position adjacent to the fistula could not be obtained. Our opinion was that successful injection of a liquid embolic agent from this proximal position would require initial formation of a long plug of embolic agent, thus increasing the risk of reflux into the PCA and basilar artery. This patient was subsequently cured by transvenous embolization.

Impact of ADS Supply on the Endovascular Approach

The key to avoiding reflux across the ADS was initial recognition of its supply to the AVF. Given the poten-

tial difficulties of identifying the ADS supply when there is competitive flow (Fig 3) and the high likelihood of pial supply from the SCA or PCA to a Galenic-type tentorial AVFs,¹³ it would be reasonable to assume that most fistulas in this location have potential ADS supply. Therefore, care should be taken to assess

the ADS supply with magnified, high-frame-rate DSA and MPRs of 3D rotational angiography (Fig 2B) when treating these fistulas. Even if such a supply is not identified, care should still be taken during embolization to assess any linear reflux anteriorly from the vein of Galen and along the expected course of the free tentorial edge, because this could represent reflux back toward the PCA and basilar artery. We have summarized the strategies we used to avoid dangerous reflux across ADS in the Table.

Study Limitations

This study is limited by the small sample size, retrospective design, and the already-discussed difficulties associated with identifying the ADS supply (potentially underestimating the true rate of supply). The requirement for follow-up imaging may have excluded patients with low-grade fistulas (less of a concern in tentorial AVFs, which are usually high-grade).

CONCLUSIONS

Dural AVFs supplied by the ADS are rare and difficult to treat by surgical or endovascular means. Endovascular treatment can be successfully undertaken by incorporating detailed anatomic assessment with risk-reduction strategies. Recognition of the ADS supply to falcotentorial junction fistulas is key to avoiding iatrogenic posterior circulation stroke.

Disclosures: Kartik D. Bhatia—UNRELATED: Employment: University Health Network, Toronto, Comments: Clinical Fellow in interventional neuroradiology. Vitor Mendes Pereira—UNRELATED: Consultancy: Stryker, Medtronic, Philips Healthcare, Balt, Cerenovus.* Timo Krings—UNRELATED: Consultancy: Stryker, Medtronic, Penumbra; Royalties: Thieme; Stock/Stock Options: Marblehead.*Money paid to the institution.

REFERENCES

- Griessenauer CJ, Loukas M, Scott JA, et al. **The artery of Davidoff and Schechter: an anatomical study with neurosurgical case correlates.** *Br J Neurosurg* 2013;27:815–18 CrossRef Medline
- Puri AS. **Dural arteriovenous fistula supplied by the artery of Davidoff and Schechter.** *Radiol Case Rep* 2010;5:375 CrossRef Medline
- Gioppo A, Farago G, Caldiera V, et al. **Medial tentorial dural arteriovenous fistula embolization: single experience with embolic liquid polymer SQUID and review of the literature.** *World Neurosurg* 2017;107:1050.e1–57 CrossRef Medline
- Hart JL, Davagnanam I, Chandrashekar HS, et al. **Angiography and selective microcatheter embolization of a falcine meningioma supplied by the artery of Davidoff and Schechter: case report.** *J Neurosurg* 2011;114:710–13 CrossRef Medline
- Uchino A, Ohno M. **Cerebellar hemangioblastoma supplied by the artery of Davidoff and Schechter: a case report.** *Nihon Igaku Hoshasen Gakkai Zasshi* 1986;46:1194–97 Medline
- Martins C, Yasuda A, Campero A, et al. **Microsurgical anatomy of the dural arteries.** *Neurosurgery* 2005;56(2 Suppl):211–51; discussion 211–51 Medline
- Wollschlaeger PB, Wollschlaeger G. **An infratentorial meningeal artery [in German].** *Radiologe* 1965;5:451–52 Medline
- Weinstein M, Stein R, Pollock J, et al. **Meningeal branch of the posterior cerebral artery.** *Neuroradiology* 1974;7:129–31 CrossRef Medline
- Byrne JV, Garcia M. **Tentorial dural fistulas: endovascular management and description of the medial dural-tentorial branch of the superior cerebellar artery.** *AJNR Am J Neuroradiol* 2013;34:1798–804 CrossRef Medline
- Tayebi Meybodi A, Vigo V, Lawton MT, et al. **The artery of Wollschlaeger and Wollschlaeger: an anatomical-clinical illustration.** *Br J Neurosurg* 2017;31:593–95 CrossRef Medline
- Krafft PR, Liu SS, Agarwalla PK, et al. **The meningeal branch of the superior cerebellar artery.** *Br J Neurosurg* 2018;32:273–75 CrossRef Medline
- Umeoka K, Takusakawa Y, Kominami S, et al. **The meningeal branches of the superior cerebellar artery: a surgical observation study.** *J Neurosurg* 2016;124:244–47 CrossRef Medline
- Lawton MT, Sanchez-Mejia RO, Pham D, et al. **Tentorial dural arteriovenous fistulae: operative strategies and microsurgical results for six types.** *Neurosurgery* 2008;62:110–24; discussion 124–25 Medline
- Osada T, Krings T. **Intracranial dural arteriovenous fistulas with pial arterial supply.** *Neurosurgery* 2019;84:104–15 CrossRef Medline
- Signorelli F, Gory B, Maduri R, et al. **Intracranial dural arteriovenous fistulas: a review of their current management based on emerging knowledge.** *J Neurosurg Sci* 2017;61:193–206 CrossRef Medline
- Borden JA, Wu JK, Shucart WA. **A proposed classification for spinal and cranial dural arteriovenous fistulous malformations and implications for treatment.** *J Neurosurg* 1995;82:166–79 CrossRef Medline
- Cognard C, Gobin YP, Pierot L, et al. **Cerebral dural arteriovenous fistulas: clinical and angiographic correlation with a revised classification of venous drainage.** *Radiology* 1995;194:671–80 CrossRef Medline
- Choudhri O, Marks MP. **Endovascular treatment of a tentorial dural arteriovenous fistula.** *Neurosurg Focus* 2014;37:1 CrossRef Medline
- Tomak PR, Cloft HJ, Kaga A, et al. **Evolution of the management of tentorial dural arteriovenous malformations.** *Neurosurgery* 2003;52:750–60; discussion 760–62 CrossRef Medline
- Hiramatsu M, Sugiu K, Hishikawa T, et al. **Epidemiology of dural arteriovenous fistula in Japan: analysis of Japanese Registry of Neuroendovascular Therapy (JR-NET2).** *Neurol Med Chir (Tokyo)* 2014;54:63–71 CrossRef Medline
- Radovanovic I, Wallace M. **Cranial dural arteriovenous fistula disconnection.** In: Jandial R, McCormick P, Black P, eds. *Core Techniques in Operative Neurosurgery.* Philadelphia: Elsevier; 2019
- Zhou LF, Chen L, Song DL, et al. **Tentorial dural arteriovenous fistulas.** *Surg Neurol* 2007;67:472–81; discussion 481–82 CrossRef Medline
- Beer-Furlan A, Dasenbrock HH, Joshi KC, et al. **Transarterial and transvenous approaches for embolization of tentorial dural arteriovenous fistula.** *Neurosurg Focus* 2019;46(Suppl 2):V10 CrossRef Medline

Asymptomatic Cerebral Vasoconstriction after Carotid Artery Stenting

C.H. Kang, J. Roh, J.A. Yeom, S.H. Ahn, M.G. Park, K.P. Park, and S.K. Baik



ABSTRACT

BACKGROUND AND PURPOSE: Carotid artery stent placement is widely performed for treatment of carotid stenosis. The purpose of this study is to present our observations on cerebral vasoconstriction in ipsilateral anterior circulation during immediate poststenting angiography in patients with near-total occlusion of the proximal ICA.

MATERIALS AND METHODS: We retrospectively reviewed patient data from December 2008 to December 2018. There were 28 patients with carotid near-total occlusion. Two neuroradiologists reviewed the final cerebral angiographic finding of carotid artery stent placement to evaluate the presence of vasoconstriction or vasodilation.

RESULTS: A total of 28 patients with near-total occlusion (mean \pm standard deviation age, 69.0 \pm 6.5 years; 92.9% male) were analyzed. Ten patients showed vasoconstriction in the treated territory, and 18 patients did not show vasoconstriction after carotid artery stenting. There were no statistically significant differences in comorbidity, frequency of symptomatic lesions, antiplatelet medication, mean procedure time, and initial NIHSS and baseline modified Rankin scale scores between the 2 groups. However, vasoconstriction is more likely to happen in patients with isolated territory from the contralateral anterior and posterior circulation (66.7% in the isolated territory group and 12.5% in the not-isolated territory group; $P < .05$). No headache or neurologic deficit was noted in all 10 patients with cerebral vasoconstriction.

CONCLUSIONS: Cerebral vasoconstriction may occur after carotid artery stenting more frequently than expected. It occurs more frequently in patients with near-total occlusion and with isolation of the cerebral circulation. A large-scale study is necessary to assess the clinical implications of cerebral vasoconstriction after carotid artery stenting.

ABBREVIATIONS: CAS = carotid artery stenting; CPP = cerebral perfusion pressure; HPS = hyperperfusion syndrome; NTO = near-total occlusion

Carotid artery stenting (CAS) and carotid endarterectomy are widely performed for the treatment of carotid stenosis to improve cerebral perfusion and prevent stroke recurrence. Both the morphology of the stenotic vessel and hemodynamics of cerebral perfusion change after CAS. Some changes are immediately notable based on postprocedural angiographic finding, among which is cerebral vasoconstriction. Cerebral vasoconstriction cases after carotid endarterectomy have often been reported.¹⁻⁶ In

contrast, cerebral vasoconstriction cases after CAS have rarely been reported.⁷⁻¹² The purpose of this retrospective study is to present our observation on cerebral vasoconstriction in the ipsilateral anterior circulation during immediate poststenting angiography in patients with near-total occlusion (NTO) of the proximal ICA.

MATERIALS AND METHODS

Design and Patient Selection

We retrospectively reviewed patient data from December 2008 to December 2018. A total of 361 stent placement procedures (in 286 patients) were performed in our hospital. Of these, there were 296 carotid stent placement procedures (in 221 patients) for carotid atherosclerotic stenosis and 28 patients with carotid NTO (Fig 1). NTO was defined as ipsilateral distal ICA less than the contralateral distal ICA, or ipsilateral distal ICA equal to or less than the ipsilateral external carotid artery.¹³

Two interventional neuroradiologists (S.K. Baik and J. Roh) reviewed the final cerebral angiographic finding of CAS to

Received August 13, 2019; accepted after revision December 1.

From the Departments of Radiology (C.H.K., J.R., J.A.Y., S.K.B.) and Neurology (S.H.A., M.G.P., K.P.P.), Pusan National University Yangsan Hospital, Pusan National University School of Medicine, Yangsan, Korea.

This work was supported by a 2-year research grant of Pusan National University.

Please address correspondence to Seung Kug Baik, MD, PhD, Department of Radiology, Research Institute for Convergence of Biomedical Science and Technology, Pusan National University Yangsan Hospital, Pusan National University School of Medicine, 20 Geumo-ro, Mulgeum-eup, Yangsan 50612, Korea; e-mail: skbaik9@gmail.com.

Indicates article with supplemental on-line tables.

<http://dx.doi.org/10.3174/ajnr.A6385>

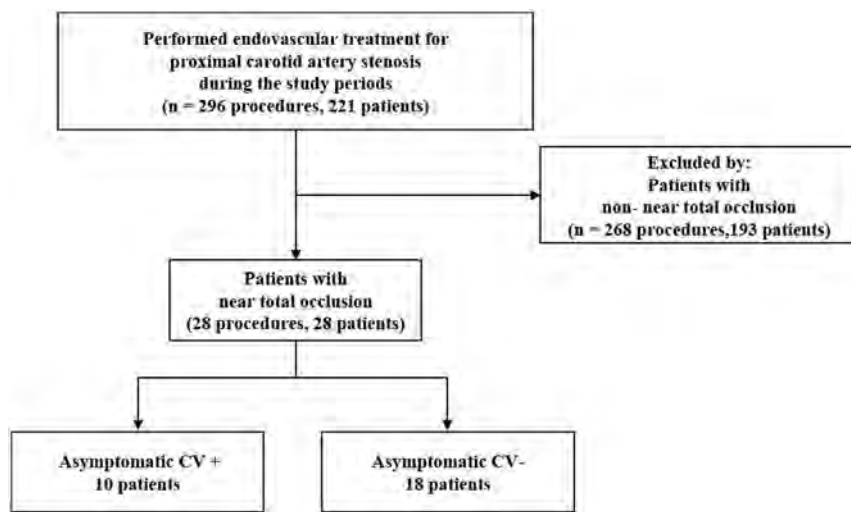


FIG 1. Patient flow diagram. CV indicates cerebral vasoconstriction; +, presence; –, absence.

evaluate the presence of vascular changes, such as vasoconstriction or vasodilation. Moreover, preprocedural DSA or MRA images were reviewed to determine if the vascular territory was isolated from the contralateral anterior or posterior circulation. Isolated circulation was defined as 1) signal intensity drop of the ipsilateral MCA-ICA territory, and 2) absence of an ipsilateral A1 segment and posterior communicating artery when evaluated on TOF-MRA. In 24 of the 28 patients (85.7%), the results of independent review from the 2 radiologists (S.K. Baik and J. Roh) showed complete agreement, and the discrepancies in 4 patients were resolved after consensus meeting of the 2 neuroradiologists (S.K. Baik and J. Roh).

Data Collection

Demographic data and medical history (including age, sex, hypertension, diabetes mellitus, cigarette smoking, alcohol drinking, hyperlipidemia, atrial fibrillation, coronary artery disease, active cancer, and previous stroke) were collected. Procedural data collected were laterality, procedure time, deployed stents, balloon catheters, and embolic protection devices. In addition, data on the presence of symptoms caused by carotid stenosis, antiplatelet medication, plaque echogenicity on carotid Doppler ultrasonography, and initial NIHSS and baseline modified Rankin scale scores were collected. Moreover, data on the incidence of postprocedural parenchymal hemorrhage and discharge NIHSS and 3-month modified Rankin scale scores were collected.

Procedural Technique

All CAS procedures were performed by using a biplane angiography unit (Axiom Artis zee Biplane; Siemens, Erlangen, Germany). All the patients received aspirin (100 mg/day) and clopidogrel (75 mg/day) treatment at least 7 days before the procedure. All procedures were performed with the patient under local anesthesia. A bolus of IV heparin (50 IU/kg of body weight, 3000–5000 IU) was injected after the placement of the guide catheter. Subsequently, 1000 IU/h infusion was administered among all the patients.

The Guider Softip XF Catheter (Boston Scientific, Fremont, California) was used as a guide catheter in all patients, except in 2, in whom the Envoy Catheter (Codman & Shurtleff, Raynham, Massachusetts) was used. Distal embolic protection devices were deployed in all patients except 1. The types of embolic protection device were Spider FX (Covidien, Plymouth, Minnesota), FilterWire EZ (Boston Scientific, Natick, Massachusetts), and Emboshield NAV6 (Abbott Laboratories, Abbott Park, Illinois). We applied pre- and poststenting dilation in all the patients except 2. Only prestenting balloon dilation was performed in 1 patient, and only poststenting balloon dilation was performed in another patient.

The Ryujin balloon catheter (Terumo, Tokyo, Japan) and UltraSoft SV (Boston Scientific) were applied until 2011. Afterward, the Sterling balloon catheter (Boston Scientific) was used.

We applied open-cell type stents in all the patients and a combination of open- and closed-cell type stents in 1 patient. In most cases, Precise (Cordis, Fremont, California) was applied. However, in some cases, Protégé (Covidien), Acculink (Guidant, St. Paul, Minnesota), and Carotid Wallstent (Boston Scientific) were applied. After CAS, angiography of the proximal ICA and intracranial area and immediate postprocedural CT were performed in all patients.

Statistical Analysis

Statistical analysis was performed by using the Statistical Package for Social Sciences version 18.0 software for Windows (IBM, Armonk, New York). The patients were classified into 2 groups based on the presence of cerebral vasoconstriction. Univariate analysis was carried out by using the Mann-Whitney U test for continuous variables and the Fisher exact test for categorical variables. A *P* value of <.05 was considered as statistically significant.

RESULTS

The patients' baseline characteristics are shown in On-line Table 1. A total of 28 patients with NTO were analyzed. Of those, 26 patients (92.9%) were men, and the mean \pm standard deviation age was 69.0 ± 6.5 years (range, 51–81 years). The left ICA was treated in 15 patients (53.6%), and 17 patients (60.7%) had symptomatic stenosis. Ten patients showed multifocal vascular narrowing considered as vasoconstriction in the treated territory, whereas 18 patients did not show vasoconstriction after CAS. There were no statistically significant differences in comorbidity, frequency of symptomatic lesions, antiplatelet medication, mean procedure time, and initial NIHSS and baseline modified Rankin scale scores between the 2 groups. None of the 28 patients were taking vasoactive drugs.

However, vasoconstriction is more likely to happen in patients with isolated territory from the contralateral anterior

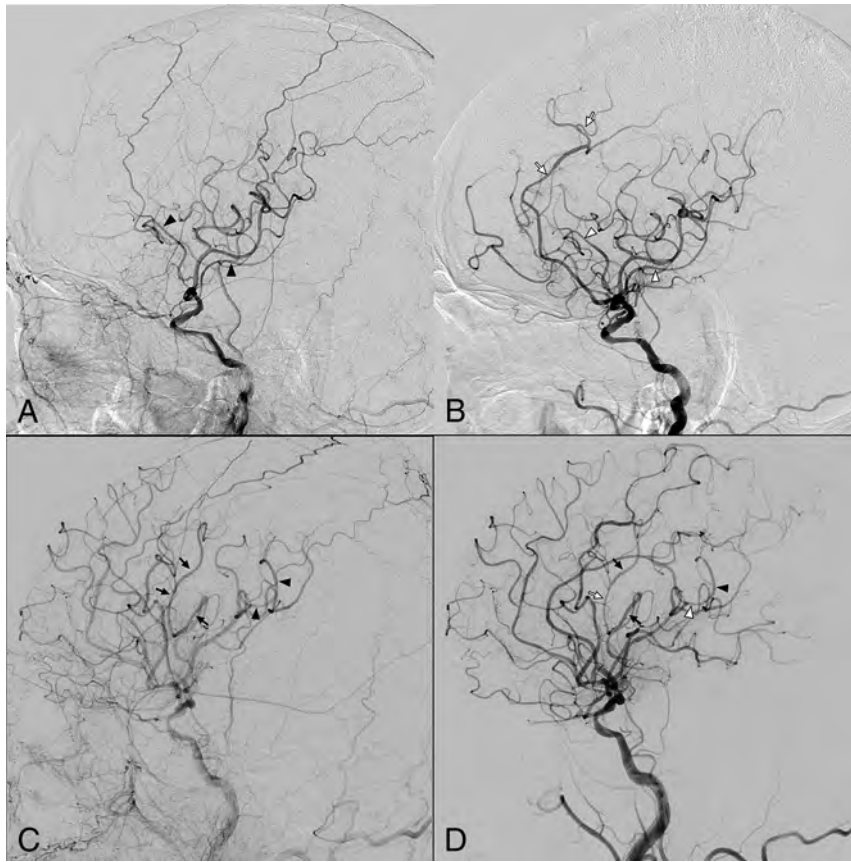


FIG 2. Two representative cases of vasoconstriction after revascularization therapy (A and B, patient 10; C and D, patient 24). A, On prestenting angiography, the distal branches of the left MCA are marked with *black arrowheads*, and the left ACA is invisible due to decreased cerebral blood flow. B, On poststenting angiography, these segments appear to be constricted (*white arrowheads*). The left ACA is visible, and the narrowed (believed to be constricted) segments are also observed in the left ACA. C and D, A superior division branch of the left MCA is marked with *black arrows*. C, An inferior division branch (*arrowheads*) on the angiography image before stent placement. D, On poststenting angiography, those branches are showing a narrowing and dilation appearance, and the narrowed (believed to be constricted) segments are marked with a *white arrow* and *white arrowhead*, respectively. Vasoconstriction phenomenon can be seen in arteries other than the marked branches. There is notable discrepancy of full/filling phase on pre- and poststenting angiography images, especially when compared with the external carotid artery filling. Note:—ACA indicates anterior cerebral artery.

and posterior circulation (66.7% in the isolated territory group and 12.5% in the not-isolated territory group; $P < .05$). Vasoconstriction was observed in a larger number of the patients than expected (10/28 [35.7%]). Small- and medium-sized vessels of the ipsilateral M2–3 and A2–3 were noted, and these changes were mostly multifocal. All the patients with vasoconstriction were asymptomatic.

The characteristics of 10 patients with asymptomatic cerebral vasoconstriction after CAS are shown in On-line Table 2. The characteristics of 18 patients without asymptomatic cerebral vasoconstriction after CAS are shown in On-line Table 3. There was no significant association between the types of embolic protection devices and cerebral vasoconstriction. No headache or neurologic deficit was noted in any of the 10 patients with cerebral vasoconstriction. There was no postprocedural hemorrhage in any of the 28 patients with NTO who underwent CAS, and no patient had a worsened NIHSS score by more than 2 points or

worsened modified Rankin scale score at discharge. In addition, no patient had a decreased modified Rankin scale score at 90 days, except for 4 patients who were lost to follow-up. Cerebral vasoconstriction after CAS in 2 patients (cases 10 and 24) is shown in Fig 2.

DISCUSSION

There have been many reports of changes in hemodynamic status or cognitive function after CAS; however, few report the morphologic changes in intracranial vasculature after CAS. Morphologic changes of the intracranial artery were noted immediately after CAS in patients with NTO, and smooth vascular narrowing was observed. In our study, all the patients with vasoconstriction were asymptomatic, which indicated that these morphologic changes in the intracranial vasculature are physiologic responses to increased cerebral perfusion, which is a type of autoregulation.

Cerebral autoregulation is a homeostatic process that regulates and maintains constant CBF in a range of blood pressures. In healthy adults, CBF is constantly maintained between 50 and 150 mm Hg cerebral perfusion pressure (CPP). The vascular adjustments that underlie autoregulation consist of constriction of cerebral resistance vessels when CPP increases and vasodilation of these vessels when CPP decreases.¹⁴ However, during cerebral ischemia, these mechanisms become dysfunctional and fail to compensate for CBF reduction.¹⁵

Moreover, autoregulation is impaired by stenosis or occlusion of the ICA. Two investigations by using transcranial Doppler sonography found that cerebral autoregulation is impaired in patients with severe ICA stenosis or occlusion.^{16,17} A correlation between the degree of stenosis and loss of autoregulation was noted in both groups.^{16,17} Of these, Reinhard et al¹⁷ found that cerebral autoregulation is most severely impaired in patients without Willisian collaterals. Furthermore, Haubrich et al¹⁸ demonstrated that impaired cerebral autoregulation may recover after CAS.

Compensatory mechanisms maintain cerebral perfusion in the initial stages of CBF reduction. Powers¹⁹ categorized these cerebrovascular adjustments into 3 stages: stage 0, when CPP is normal; stage 1, when CPP is reduced and autoregulation dilates the cerebral vessels to maintain CBF; and stage 2, when the compensatory capacity for cerebral vasodilation exceeds

Previous cases of CV after CAS

Study	Age (y)	Sex	Laterality	Onset from CAS	Infarction	Outcome
Arai et al ⁷	72	M	R	13 h	Present	No deficit
Shiraga et al ¹²	62	M	R	1.5 days	Present	No deficit
Soltanolkotabi et al ¹¹	49	F	L	14 days	Present	No deficit
Aghaebrahim et al ⁸	60	M	R	1 mo	Not available	No deficit
Watanabe et al ⁹	74	M	R	17 days	Present	No deficit
Higashi et al ¹⁰	73	M	L	Immediately	Present	Right hemiparesis, higher brain dysfunction

Note.—CV indicates cerebral vasoconstriction; R, right; L, left.

the limit, CBF begins to decrease, and cerebrovascular autoregulation is disrupted.

In patients with carotid NTO, CBF in the ipsilateral intracranial circulation is reduced. In response to CBF reduction, the cerebral vessels may be dilated to maintain cerebral perfusion. Likewise, autoregulation may be impaired in proportion to the severity of the stenosis. Immediately after CAS, a large amount of blood flows into the cerebral vessels, where autoregulation is impaired. We thought that cerebral vessels become uniformly constricted under normal autoregulation. Nevertheless, as in our patients, multifocal vasoconstriction may occur because of partial disruption of the autoregulation. Therefore, asymptomatic vasoconstriction in our patients is considered as a type of autoregulation or the boundary between autoregulation and pathologic condition. If the autoregulation is completely disrupted, then the cerebral vessels cannot constrict and are dilated. This condition is thought to be more vulnerable to hyperperfusion syndrome (HPS).

In our study, vasoconstriction occurred more frequently in patients with isolation of the cerebral circulation, which is consistent with the finding of Reinhard et al,¹⁷ that autoregulation is further impaired in patients without Willisian collaterals. This is probably because the cerebral hemodynamic reserve is further reduced, and autoregulation is subsequently further impaired in patients with isolation of the cerebral circulation. These changes are expected to return to normal when autoregulation is restored over time after CAS.

Six case reports of cerebral vasoconstriction after CAS have been published so far (Table). In these reports, cerebral vasoconstriction frequently occurred immediately after CAS and up to 1 month after CAS. In our study, we observed only the development of cerebral vasoconstriction immediately after CAS. In these 6 reports, the symptoms were mild in some patients and severe in the other cases.

However, in our study, all the patients with vasoconstriction were asymptomatic. This may be attributed to the location and degree of vasoconstriction, and susceptibility between individuals is different. Vasoconstriction after CAS has a broad spectrum of manifestations, depending on the severity of autoregulation impairment. If the autoregulation impairment is mild, then vasoconstriction is not prominent and the patients are asymptomatic. It may be a physiologic response, which is a type of autoregulation. Otherwise, if autoregulation impairment is severe, then vasoconstriction is prominent and may cause severe symptoms. It may be a pathologic condition, causing severe headache or stroke.

After CAS, impaired autoregulation of CBF also causes HPS.²⁰ Both cerebral vasoconstriction and HPS are caused by abrupt increased blood flow into the cerebral vessels that are

dilated by a compensatory response to severe carotid stenosis. Cerebral vasoconstriction probably occurs because the cerebral artery constricts abnormally. However, HPS probably occurs because the cerebral arteries cannot constrict and are dilated. Both are caused by impairment of cerebral autoregulation. To our knowledge, there have been no reports or studies on the morphologic changes of intracranial vessels in HPS after CAS.

After CAS, aside from HPS, cerebral vasoconstriction may occur. In the previous case report, the patient's symptom deterioration after CAS was misdiagnosed as HPS and antihypertensive medications were administered. Left MCA vasoconstriction was later observed. This caused severe disability in the patient.¹⁰ Therefore, when the patient's symptoms worsen after CAS, the possibility of cerebral vasoconstriction should be considered. It should be differentiated and treated appropriately. In previous reports, administration of calcium channel blockers, such as oral lomerizine hydrochloride¹⁰ or intra-arterial verapamil,^{8,11} was effective in the treatment of vasoconstriction after CAS. This study had some limitations. First, this was retrospective study. Second, the sample size was small.

CONCLUSIONS

Cerebral vasoconstriction may occur after CAS more frequently than expected. It occurs more frequently in patients with NTO and with isolation of the cerebral circulation. A large-scale study is necessary to assess the clinical implications of cerebral vasoconstriction after CAS.

Disclosures: Seung Kug Baik—RELATED: Grant: This work was supported by a 2-year research grant from Pusan National University.

REFERENCES

1. Brick JF, Dunker RO, Gutierrez AR. **Cerebral vasoconstriction as a complication of carotid endarterectomy.** *J Neurosurg* 1990;73:151–53 CrossRef Medline
2. Lopez-Valdes E, Chang HM, Pessin MS, et al. **Cerebral vasoconstriction after carotid surgery.** *Neurology* 1997;49:303–04 CrossRef Medline
3. Rosenbloom MH, Singhal AB. **CT angiography and diffusion-perfusion MR imaging in a patient with ipsilateral reversible cerebral vasoconstriction after carotid endarterectomy.** *AJNR Am J Neuroradiol* 2007;28:920–22 Medline
4. Wu TY, Frith RW, Barber PA. **Reversible cerebral vasoconstriction following carotid endarterectomy.** *J Clin Neurosci* 2011;18:1725–28 CrossRef Medline
5. Causey MW, Amans MR, Han S, et al. **Reversible cerebral vasoconstriction syndrome is a rare cause of stroke after carotid endarterectomy.** *J Vasc Surg* 2016;64:1847–50 CrossRef Medline
6. Fitas D, Carvalho M, Castro P, et al. **Cerebral vasoconstriction after carotid endarterectomy.** *Pract Neurol* 2018;18:378–81 CrossRef Medline

7. Arai M, Kuwayama N, Koide K, et al. **Transient right hemisphere hypoperfusion following right carotid artery stenting: a case report (in Japanese).** *NOUSHINKEI KEKKANNAI TIRYOU* 2013;7:119–26 CrossRef
8. Aghaebrahim A, Jadhav AP, Saeed Y, et al. **Reversible cerebral vasoconstriction syndrome following carotid stenting.** *Neurology* 2014; 83:570–71 CrossRef Medline
9. Watanabe Y, Takechi A, Kajiwaru Y, et al. **Reversible cerebral vasoconstriction syndrome following carotid artery stenting: a case report.** *Jpn J Stroke* 2017;39:299–303 CrossRef
10. Higashi E, Uwatoko T, Mizokami T, et al. **Reversible cerebral vasoconstriction complicated with brain infarction immediately after carotid artery stenting.** *Interv Neuroradiol* 2018;24:688–92 CrossRef Medline
11. Soltanolkotabi M, Ansari S, Patel B, et al. **Reversible cerebral vasoconstriction syndrome following carotid artery stenting.** *J NeuroIntervent Surg* 2012;4:A49–A50 CrossRef
12. Shiraga S, Akai T, Takata H, et al. **Possible cerebral infarction due to multiple segmental cerebral vasospasms after carotid artery stenting: a case report [in Japanese].** *No Shinkei Geka* 2015;43:1081–89 CrossRef Medline
13. Fox AJ, Eliasziw M, Rothwell PM, et al. **Identification, prognosis, and management of patients with carotid artery near occlusion.** *AJNR Am J Neuroradiol* 2005;26:2089–94 Medline
14. Kontos HA, Wei EP, Navari RM, et al. **Responses of cerebral arteries and arterioles to acute hypotension and hypertension.** *Am J Physiol* 1978;234:H371–83 CrossRef Medline
15. Langfitt TW, Weinstein JD, Kassell NF. **Cerebral vasomotor paralysis as a cause of brain swelling.** *Trans Am Neurol Assoc* 1964;89:214–15 Medline
16. Gooskens I, Schmidt EA, Czosnyka M, et al. **Pressure-autoregulation, CO₂ reactivity and asymmetry of haemodynamic parameters in patients with carotid artery stenotic disease. A clinical appraisal.** *Acta Neurochir (Wien)* 2003;145:527–32; discussion 532 CrossRef Medline
17. Reinhard M, Müller T, Roth M, et al. **Bilateral severe carotid artery stenosis or occlusion – cerebral autoregulation dynamics and collateral flow patterns.** *Acta Neurochir (Wien)* 2003;145:1053–60; discussion 1059–60 CrossRef Medline
18. Haubrich C, Kruska W, Diehl RR, et al. **Recovery of the blood pressure–cerebral flow relation after carotid stenting in elderly patients.** *Acta Neurochir (Wien)* 2007;149:131–36; discussion 137 CrossRef Medline
19. Powers WJ. **Cerebral hemodynamics in ischemic cerebrovascular disease.** *Ann Neurol* 1991;29:231–40 CrossRef Medline
20. Buhk JH, Cepek L, Knauth M. **Hyperacute intracerebral hemorrhage complicating carotid stenting should be distinguished from hyperperfusion syndrome.** *AJNR Am J Neuroradiol* 2006;27:1508–13 Medline

Characterization of Carotid Plaque Components by Quantitative Susceptibility Mapping

 M. Azuma,  K. Maekawa,  A. Yamashita,  K. Yokogami,  M. Enzaki,  Z.A. Khant,  H. Takeshima,  Y. Asada,  Y. Wang, and  T. Hirai



ABSTRACT

BACKGROUND AND PURPOSE: Intraplaque hemorrhage in the carotid artery is related to an increased risk of cerebrovascular ischemic events. We aimed to investigate whether quantitative susceptibility mapping can characterize carotid artery plaque components and quantify the severity of intraplaque hemorrhage.

MATERIALS AND METHODS: For this ex vivo quantitative susceptibility mapping study, 9 carotid endarterectomy specimens were imaged on a 3T MR imaging scanner using a 3D multi-echo gradient-echo sequence and a microscopy coil. The samples were examined histologically using immunostains, including glycophorin A and Prussian blue. The areas of erythrocytes, iron deposits, calcification, and fibrous matrices observed on stained sections were compared with quantitative susceptibility mapping findings and their mean susceptibility values.

RESULTS: Intraplaque hemorrhage and iron deposits were observed only in areas hyperintense on quantitative susceptibility mapping; calcifications and fibrous matrices were prevalent in hypointense areas. The mean susceptibility values for necrotic cores with intraplaque hemorrhage but no iron deposits, cores with iron deposits but no intraplaque hemorrhage, cores without either intraplaque hemorrhage or iron deposits, and cores with calcification were 188 ± 51 , 129 ± 49 , -11 ± 17 , and -158 ± 78 parts per billion, respectively. There was a significant difference in the mean susceptibility values among the 4 histologic components ($P < .01$). The mean susceptibility values of the whole plaque positively correlated with the percentage area positive for glycophorin A ($r = 0.65$, $P < .001$) and Prussian blue ($r = 0.47$, $P < .001$).

CONCLUSIONS: Our findings suggest that quantitative susceptibility mapping can characterize the composition of carotid plaques and quantify the degree of intraplaque hemorrhage and iron deposits.

ABBREVIATIONS: CR = contrast ratio; GYPA = glycophorin A; ICH = intracranial hemorrhage; IPH = intraplaque hemorrhage; QSM = quantitative susceptibility mapping; SV = susceptibility value

Vulnerable atherosclerotic plaques in carotid arteries are obviously correlated with cerebrovascular ischemic events such as ischemic stroke and transient ischemic attacks.^{1,2} The characteristics of vulnerable plaques are intraplaque hemorrhage (IPH), lipid-rich necrotic cores, thin fibrous caps, and, to a lesser extent,

plaque calcification.² IPH in the carotid artery is related to an increased risk of plaque rupture; it plays a critical role in stratifying the risk of future events in patients with carotid atherosclerosis.^{3,4} In a meta-analysis, the presence of IPH increased the risk of cerebrovascular events 5- to 7-fold.⁵ While carotid endarterectomy or carotid artery stent placement helps prevent future stroke, it may elicit intraoperative embolic complications, especially when plaques contain many vulnerable components such as IPH or lipids.⁶ Therefore, a method for characterizing the intraplaque components is needed for the prediction of cerebrovascular ischemic events and perioperative complications.

Imaging modalities for the evaluation of IPH should be noninvasive and easily accessible in daily clinical practice. There are various noninvasive imaging methods to recognize carotid vulnerable plaques in vivo. However, ultrasonography including contrast-enhanced sonography, shear wave elastography, and CT including contrast-enhanced CT cannot accurately diagnose IPH.⁷

Received August 15, 2019; accepted after revision November 14.

From the Departments of Radiology (M.A., Z.A.K., T.H.), Pathology (K.M., A.Y.), and Neurosurgery (K.Y., H.T., Y.A.), Faculty of Medicine, University of Miyazaki, Miyazaki, Japan; Radiology Section (M.E.), University of Miyazaki Hospital, Miyazaki, Japan; and Department of Radiology (Y.W.), Weill Medical College of Cornell University, New York, New York.

M. Azuma and K. Maekawa contributed equally to this work.

This work was supported, in part, by the National Institutes of Health (R01NS105144).

Please address correspondence to Minako Azuma, MD, Department of Radiology, Faculty of Medicine, University of Miyazaki, 5200 Kihara, Kiyotake, Miyazaki 889-1692, Japan; e-mail: minako_azuma@med.miyazaki-u.ac.jp

 Indicates open access to non-subscribers at www.ajnr.org

<http://dx.doi.org/10.3174/ajnr.A6374>

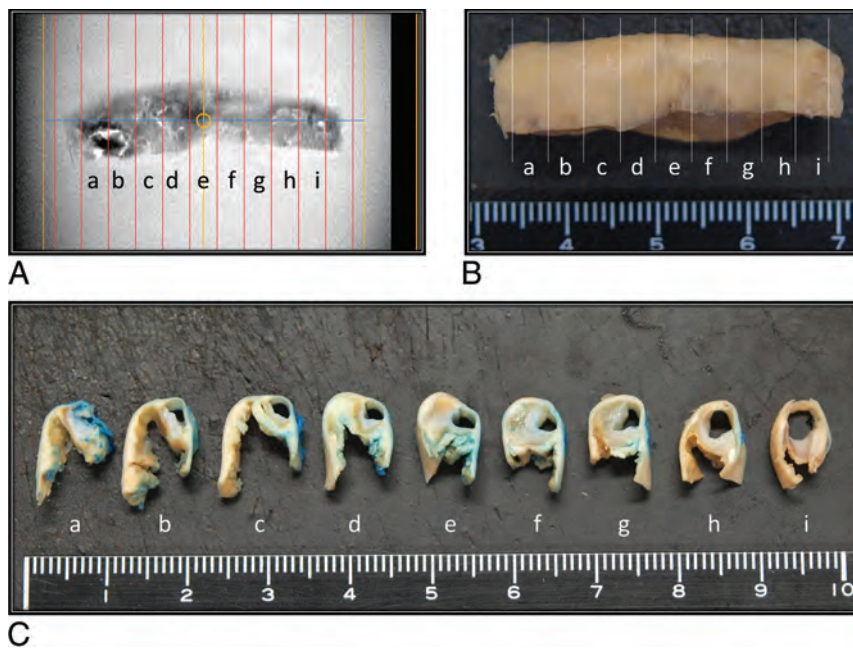


FIG 1. Resected carotid artery specimen from a 72-year-old man. Tissue preparation for MR imaging and histology studies. Formalin-fixed carotid endarterectomy tissue specimens (B and C) were cut into 3-mm-thick sections and matched at 3-mm intervals against the corresponding MR image (A). Blue dye was used for plaque orientation (C).

Multiparametric qualitative MR imaging can help visualize components that render plaques vulnerable to rupture.^{8–12} T1-weighted and fat- and flow-suppressed sequences are the preferred imaging modalities to evaluate IPH because they exploit methemoglobin-induced T1-shortening.^{13,14} However, it can be difficult to differentiate IPH from the lipid-rich necrotic core.¹⁵ The disadvantages of these qualitative and semiquantitative approaches include their operator dependency, the need for reference tissue, and their lack of specificity for the identification of plaque components.

Quantitative susceptibility mapping (QSM) is a quantitative imaging technique that has been used to assess hemorrhage, iron, and calcification in the brain.^{16–19} To our knowledge, no earlier studies correlated histopathologic findings with QSM data on carotid plaque components, including IPH. Therefore, we investigated whether QSM can be used to characterize the composition of carotid plaques and to quantify the degree of intraplaque hemorrhage.

MATERIALS AND METHODS

The institutional review board of the University of Miyazaki Hospital approved our retrospective, observational study and waived the requirement for informed consent.

Patients and Carotid Plaque Specimens

This study included 9 carotid specimens of 9 male patients ranging in age from 63 to 83 years (mean age, 73 years) who underwent carotid endarterectomy with en bloc excision at the University of Miyazaki Hospital or affiliated hospitals between March 2015 and March 2017. Of these patients, 8 had symptomatic stenosis of 60%–95% and 1 patient had asymptomatic

stenosis of 60%. The percentage diameter of stenosis was determined using the NASCET criteria on contrast-enhanced CT angiography.²⁰ The clinical profiles of the patients included hypertension ($n = 6$), diabetes mellitus ($n = 2$), and hyperlipidemia ($n = 1$).

The specimens were fixed in formaldehyde immediately after carotid endarterectomy. The time from fixation to MR imaging ranged from 9 to 60 days (mean, 35.5 ± 16.1 days). Formalin-fixed samples were placed on a 5-mm-thick 2% agarose gel layer in 10-cm petri dishes. The dorsal surface was marked for proper orientation, and the samples were carefully embedded in 2% agarose gel to remove all air.

MR Imaging Protocol

Agarose-embedded samples were subjected to MR imaging on a 3T scanner (Inginia 3T CX; Philips Healthcare, Best, the Netherlands) using dStream

Microscopy coil (47 mm, Philips Healthcare) (Fig 1). A 3D multiecho gradient echo sequence was acquired in the axial plane; the parameters were the following: TE = 7.2/13/20/26/32/38 ms; FOV = 100×100 mm; matrix = 216×216 mm²; voxel size = $0.2 \times 0.2 \times 1.0$ mm³; scan time = 9 minutes 32 seconds. 3D multiecho gradient echo data were used for QSM using complex data and a morphology-enabled dipole inversion method.²¹

The MR imaging protocol also included 3D T1-weighted MPRAGE sequences; the parameters were the following: TR/TE = 7/2.8 ms; FOV = 100×100 mm; matrix = 256×256 mm²; voxel size = $0.2 \times 0.2 \times 0.6$ mm³; scan time = 5 minutes 20 seconds.

Histologic and Immunohistochemical Analysis

Carotid endarterectomy tissue specimens were cut into 3-mm-thick slices to match the corresponding MR imaging scans (Fig 1); they were embedded in paraffin, cut into 3- μ m-thick sections, and stained with H&E. Azan trichrome was used to visualize the fibrous collagen matrix. Prussian blue staining was performed to visualize ferric iron (Fe^{3+}) to identify hemosiderin deposits indicative of chronic hemorrhage. To detect erythrocytes, we stained sections with an antibody against glycophorin A (GYPA) (Dako, Glostrup, Denmark), a sialoglycoprotein on the erythrocyte membrane and visualized with EnVision system (Dako). We also applied 3,3'-diaminobenzidine tetrahydrochloride and performed counterstaining with Meyer hematoxylin. The immunostaining controls included nonimmune mouse immunoglobulin G instead of the primary antibody. Erythrocytes and Fe^{3+} deposits were localized by a combination of immunohistochemistry for GYPA and Prussian blue staining, respectively.

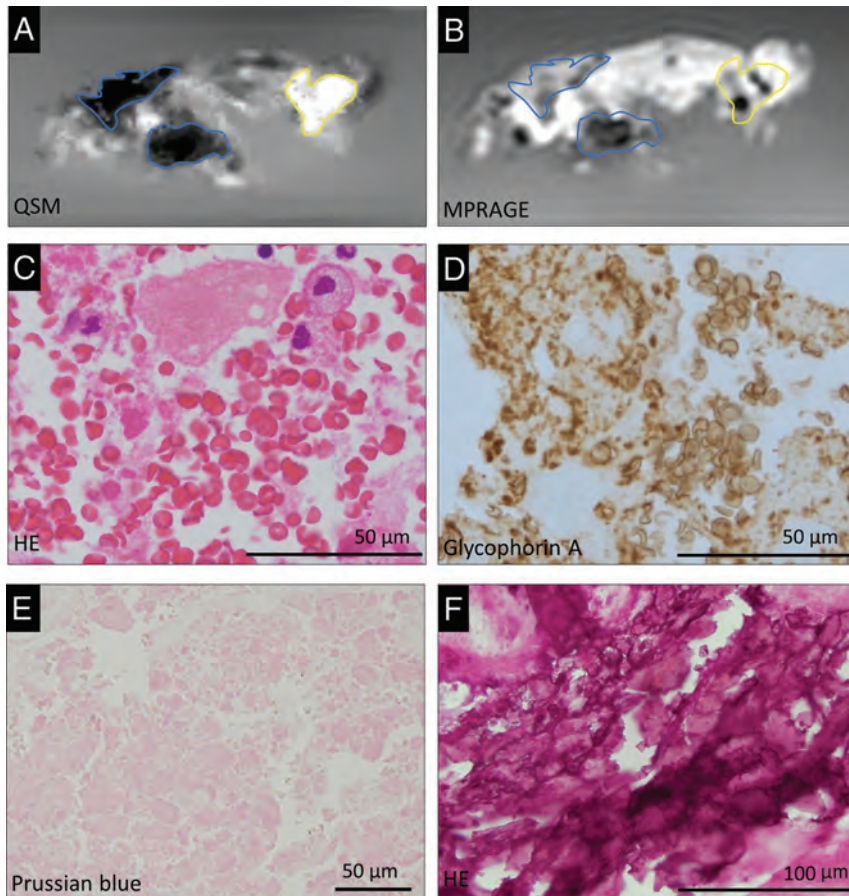


FIG 2. Representative QSM (A) and MPRAGE (B) images of carotid plaques and corresponding histologic images (C–F) in a 77-year-old man. Carotid plaque with both hyper- and hypointense areas on the QSM image (A) and corresponding MPRAGE image (B). The hyperintense ROI (A, yellow outline) corresponds with histologic evidence of intraplaque hemorrhage and erythrocytes in the atherosclerotic necrotic core (C, H&E stain). The glycophorin-A-positive erythrocytes and erythrocyte fragments are abundant in the plaque (D). In the hyperintense ROI (yellow outline) on the QSM image (A), Prussian blue staining shows no iron deposition (E). Two hypointense ROIs (blue outline) on the QSM image (A) correspond with basophilic calcification in the plaque (F, H&E stain). The corresponding blue and yellow outlines are placed on the MPRAGE image (B).

Assessment of Plaque Composition with QSM

To characterize the plaque composition with QSM, 2 radiologists (M.A., T.H.) first consensually selected foci that were hyperintense or hypointense relative to the 2% agarose gel background and manually set ROIs (Figs 2A and 3A). Then 1 pathologist (K.M.) and 1 radiologist (M.A.) consensually assessed the corresponding areas on histologic sections for spatial agreement or disagreement between the histologic sections and the QSM images. The plaque configuration and areas with specific plaque components and calcification were considered for coregistration between QSM and histology sections. Sections were excluded from further analysis when the MR images failed to match the histologic sections due to gross sample deformation during histologic processing. Also excluded were segments with histologic processing errors (damaged or inappropriately-cut plane samples) and histologic sections with spatial disagreement between histologic sections and MR images. For the final selection of histologic sections, 2 pathologists (K.M., Y.A.) consensually checked for the presence or absence of IPH, iron deposits,

calcification, fibrous matrix components, dense inflammatory infiltrates, and necrotic cores without intraplaque hemorrhage in hyper- and hypointense areas on QSM images.

IPH was defined as the presence of intact and/or fragmented erythrocyte foci in atherosclerotic plaques²² detected by H&E and GYPA staining; calcification, as basophilic deposits on H&E-stained sections; and fibrous matrix components, as blue foci on Azan trichrome-stained sections. Dense inflammatory infiltrates were identified by the accumulation of mononuclear cells. When erythrocyte foci in a necrotic core were absent or undetectable, the designation was necrotic core without IPH.

To measure the susceptibility value of the main plaque components on QSM images, 1 pathologist (K.M.) first assessed all H&E-, GYPA-, and Prussian blue-stained sections and selected ROIs containing a necrotic core with IPH but no Fe^{3+} deposits; Fe^{3+} deposits (chronic hemorrhage) without IPH; calcification; and a necrotic core with neither IPH nor Fe^{3+} deposits. Then 2 radiologists (M.A., T.H.) consensually drew ROIs on QSM images that matched the histologic sections. The susceptibility values in the ROIs were determined using ImageJ (National Institutes of Health, Bethesda, Maryland). Exclusion criteria were the same as those in the qualitative evaluation.

On MPRAGE images, 2 radiologists (M.A., T.H.) also put ROIs in the areas corresponding to the same histologic components and adjacent background with the 2% agarose gel. The signal intensities of the ROIs on MPRAGE were determined using ImageJ. The contrast ratio (CR) of each plaque component was calculated by dividing the signal intensity of each component by the background signal intensity.

Correlation between Intraplaque Erythrocytes and Iron Deposits and the Susceptibility Value on QSM Images

The extent of erythrocyte/iron deposits on histologic sections was correlated with the mean susceptibility value (SV) of the whole plaque on QSM images. One pathologist (K.M.) first manually traced whole plaque on histologic sections. Areas positive for GYPA (erythrocyte component) or Fe^{3+} staining (iron deposits) were quantified using Win-ROOF Color Image Analysis Software (Mitani, Fukui, Japan) (Fig 4A, -B). To quantify the degree of hemorrhage/iron deposition in carotid plaques on histopathologic sections, the software calculated the percentage of the area with

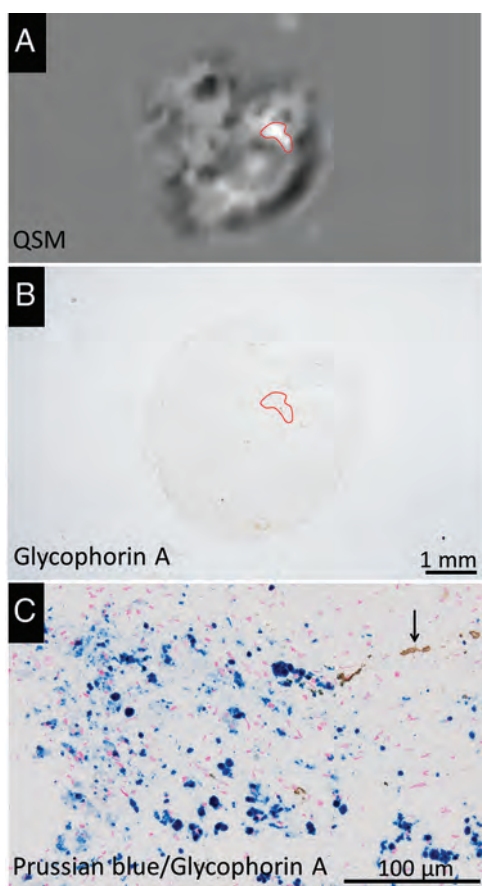


FIG 3. Representative QSM image (A) of carotid plaques of a 79-year-old man and corresponding histologic images (B and C). Carotid plaque with a hyperintense area on the QSM image (A, red outline), which contained few GYPA-positive erythrocyte components in the corresponding histologic ROI (B, red outline). There are many intracellular hemosiderin deposits (blue) and a few erythrocytes (brown, arrow) in the ROI (C).

GYPA- or Fe^{3+} -positive relative to the whole plaque in each section. Then, QSM images matching the histologic sections were selected and consensually segmented by 2 radiologists (M.A., T.H.), and the SV in the ROIs was determined using ImageJ (Fig 4C).

Statistical Analysis

GraphPad Prism 5 (GraphPad Software, San Diego, California) was used for drawing graphs and statistical analysis. We used the Fisher exact test for contingency table analysis to compare the incidence of identical histologic findings in hyper- and hypointense areas on QSM images. To compare the mean SV and mean CR among the pathology components, we used 1-way ANOVA and the Scheffe test. The relationship between the degree of erythrocyte/iron deposition on histologic sections and the mean susceptibility values on QSM images was analyzed with the Spearman correlation test.

RESULTS

Comparison of Histologic and QSM Findings

As shown in the Table, histology was compared with 26 hyper- and 9 hypointense areas on QSM images. Of the 26 hyperintense areas, 19 (73%) manifested IPH and 20 (77%) contained Fe^{3+} deposits (Figs 2A–C and 3). Of these areas, 14 featured both IPH

and Fe^{3+} deposits; 5 showed only IPH; and 6, only Fe^{3+} deposits. Immunohistochemistry for GYPA highlighted the presence of intact and fragmented erythrocytes (Fig 2B). Of the 9 hypointense areas on QSM images, all exhibited a fibrous matrix, and 8 (89%) had calcifications (Fig 2A, -C). All 8 hypointense areas with calcification had large, platelike calcifications, while 6 of 7 hyperintense areas with calcification had dotlike calcifications that were smaller than the voxel size of QSM images. The incidence of calcifications and fibrous matrices was significantly higher in hypo- than in hyperintense areas ($P < .05$); no hypointense areas contained IPH or Fe^{3+} deposits. With respect to dense inflammatory infiltrates and necrotic cores without intraplaque hemorrhage, there was no significant difference in the incidence of the components between hyper- and hypointense areas.

For quantitative analysis, we assessed 5 typical atherosclerotic necrotic cores with IPH but no Fe^{3+} deposits, 7 cores with Fe^{3+} deposits but no IPH, 7 cores with neither IPH nor Fe^{3+} deposits, and 10 cores with calcification. The mean SV in foci of the necrotic core with IPH was 188 ± 51 parts per billion (ppb), it was 129 ± 49 ppb in cores with Fe^{3+} deposits without IPH, -11 ± 17 ppb in cores without IPH or Fe^{3+} deposits, and -158 ± 78 ppb in cores with calcification (Fig 5A). The mean SV in foci of necrotic cores with IPH and in cores with Fe^{3+} deposits but no IPH was significantly larger than but did not overlap with the SV of necrotic cores without either IPH or Fe^{3+} deposits or with the SV of cores with calcifications ($P < .01$). There was no significant difference in the mean SV of necrotic cores with IPH and necrotic cores with Fe^{3+} deposits without IPH.

The summary of the mean CR of each component on MPRAGE images is shown in Fig 5B. There were no significant differences in the mean CR among necrotic cores with IPH but no Fe^{3+} deposits, necrotic cores with Fe^{3+} deposits but no IPH, and necrotic cores with neither IPH nor Fe^{3+} deposits. The mean CR was significantly lower for calcification than the other 3 components ($P < .05$).

Correlation between the Degree of Erythrocyte/Iron Deposition and Its Susceptibility on QSM Images

The relationship between erythrocytes and iron deposits observed on histologic sections and the mean SV of a whole plaque region on QSM images is shown in Fig 6. There was a moderately positive correlation in GYPA-positive areas ($r = 0.65$, $n = 34$, $P < .001$) (Fig 6A) and a weak positive correlation with areas positive for Fe^{3+} ($r = 0.47$, $n = 34$, $P < .01$) (Fig 6B). Fe^{3+} -positive areas tended to be much smaller than areas positive for GYPA. Some areas with a relatively high mean SV were observed at nearly zero areas positive for Fe^{3+} (Fig 6B). There was no significant correlation between Prussian blue–stained areas and GYPA-positive areas ($r = 0.28$, $n = 34$, $P = .1$) (Fig 6C).

DISCUSSION

For characterization of carotid plaques, qualitative analysis showed IPH and Fe^{3+} deposits in hyper- but not in hypointense areas on QSM images. The incidence of calcification and fibrous matrix deposits was higher in hypo- than in hyperintense areas. All calcified foci with hypointensity on QSM had large platelike calcifications with diamagnetic properties. Although calcifications

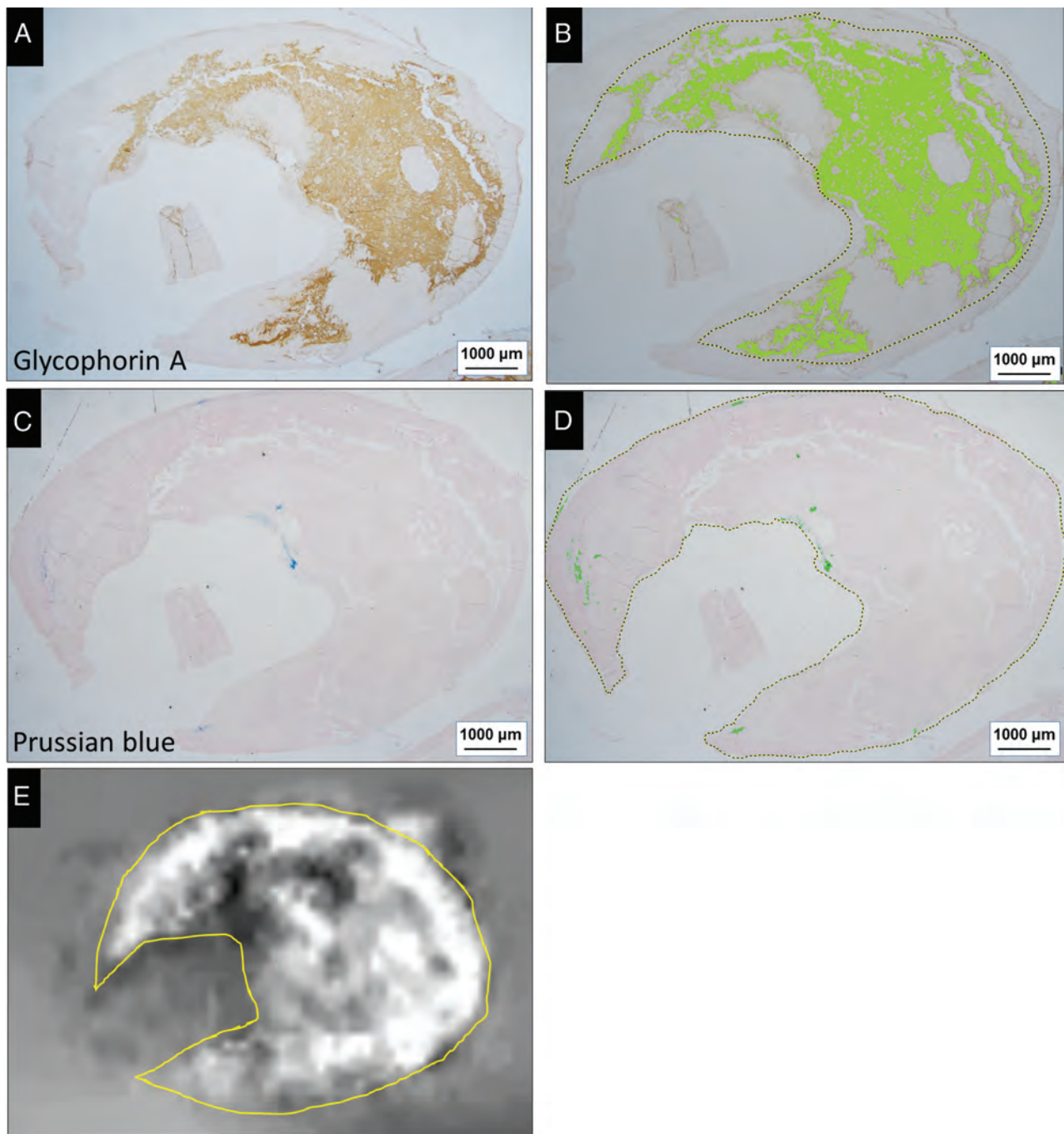


FIG 4. Correlative analysis of erythrocytes and iron deposits on histologic sections from a 73-year-old man (A–D) and the SV on the QSM image of whole plaque (E). Areas positive for GYPA staining (A) and color extraction (B) were relatively well-correlated with the distribution of hyperintensity on the QSM image (E). There are a few small areas positive for Prussian blue staining (C) and color extraction (D). Positively stained areas were extracted under specific protocols using the hue of the color and its lightness and saturation. Data are expressed as the ratio (percentage) of extracted green areas relative to the whole plaque (*dashed outline* in B and D). The ROI on the QSM image (*yellow outline*, E) is matched with the histologic ROI for measuring the mean SV of the whole plaque.

were also observed in hyperintense areas, they tended to be smaller than the voxel size of the QSM images. This finding suggests that paramagnetic hemoglobin or hemosiderin or both exert stronger effects than diamagnetic calcifications. Quantitative analysis showed that the mean SV was significantly higher for cores with IPH or Fe^{3+} deposits than cores without either IPH or Fe^{3+} deposits and cores with calcifications. The SV for necrotic cores

with IPH and for cores with Fe^{3+} deposits did not overlap the SV of necrotic cores without either IPH or Fe^{3+} deposits or the SV of cores with calcifications. Our findings indicate that the qualitative and quantitative assessment of carotid plaques on QSM images may help facilitate the identification of their composition.

Although QSM and gradient echo phase imaging have been reported to be useful for the differentiation of intracranial

Comparison of histologically identified plaque components in hyper- and hypointense areas on QSM images^a

Plaque Components	Hyperintense Area (n = 26)	Hypointense Area (n = 9)	P Value
Intraplaque hemorrhage	19 (73)	0 (0)	.0002
Iron deposition	20 (76.9)	0 (0)	<.0001
Calcification	7 (26.9)	8 (88.9)	.002
Fibrous matrix deposits	9 (34.6)	9 (100)	.001
Dense inflammatory infiltrates	10 (38.5)	4 (44.4)	1.0
Necrotic core without intraplaque hemorrhage	5 (19.2)	1 (11.1)	1.0

^aData in parentheses are percentages.

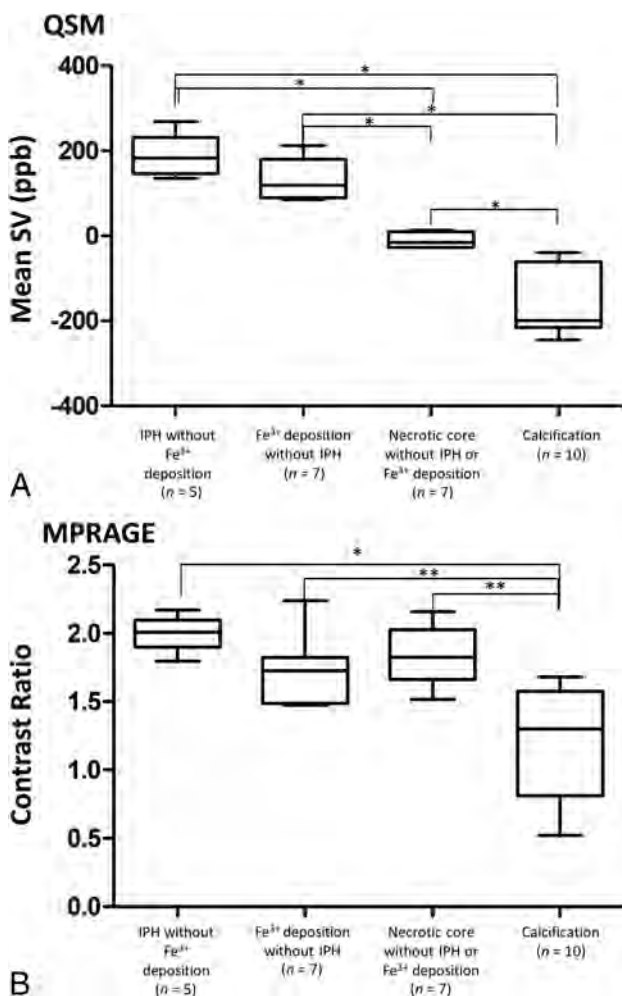


FIG 5. Comparison of the mean SV on QSM images (A) and the CR on MPRAGE images (B) among 4 typical atherosclerotic components. Analysis was with 1-way ANOVA with the Scheffe test (asterisk, $P < .001$; double asterisks, $P < .01$).

calcifications and hemorrhage,²³⁻²⁶ QSM may be superior. We document that QSM also distinguishes between hemorrhage and calcification in carotid artery plaques. The inferiority of gradient echo phase imaging to QSM can be explained by the underlying physics: the phase is determined by the product of the TE and the magnetic field, which is a nonlocal parameter or a convolution of

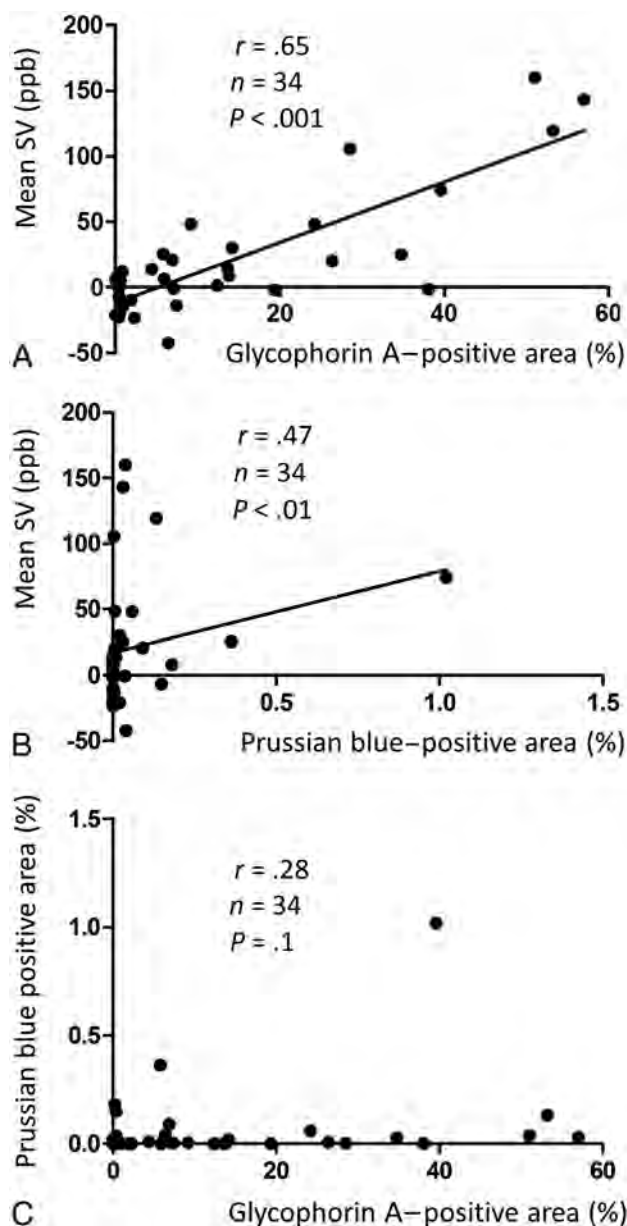


FIG 6. Relationship between the mean magnetic SV and areas positive for GYPA (A, erythrocytes) or Fe³⁺ (B). Relationship between Prussian blue-stained areas and GYPA-positive areas (C).

all surrounding tissue magnetic susceptibility sources. Imaging parameters, including TE, field strength, object orientation, and object size, can change the appearance of gradient recalled-echo phase images.^{27,28} The high-pass filtering that is commonly used in susceptibility-weighted imaging, makes the phase image noisy and difficult to interpret.

In the mean CR on MPRAGE images, there were no significant differences among necrotic cores with IPH but no Fe³⁺ deposits, cores with Fe³⁺ deposits without IPH, and necrotic cores with neither IPH nor Fe³⁺ deposits. Formalin fixation shortens the relaxation time of tissues with time.^{29,30} In the current ex vivo study, all plaque components except calcification could not be differentiated on MPRAGE images. The relaxation times of plaque tissues on MPRAGE images seemed to be

shortened. This effect must have affected the results on MPRAGE images.

In our study, the SV of IPH in the carotid artery detected on QSM images is 201 ± 115 ppb. This value overlaps the lower end of the SV range of cerebral cavernous malformations (125–750 ppb)³¹ and is much lower than the SV range of intracranial hemorrhage (ICH, 570–1380 ppb) in the hyperacute-to-chronic stage.^{18,32} This difference may be explained by differences in the microenvironment of the brain parenchyma and the carotid artery wall.

The susceptibility for intracranial hemorrhage depends on the magnetic status of hemoglobin iron in degraded erythrocytes; it varies greatly with the hemorrhage size and stage.^{18,24,33} ICH occurs when a massive number of erythrocytes rapidly burst out of an artery. The fast degradation of these cells results in a high SV due to the presence of deoxyhemoglobin in hyperacute hematomas and of methemoglobin during erythrocyte lysing.¹⁸ The influx of macrophages results in iron phagocytosis and either iron clearing from degraded erythrocytes in the late subacute stage or in iron storage in hemosiderin in the chronic ICH stage.¹⁸ The former event results in a susceptibility reduction, while the latter increases susceptibility due to the formation of a superparamagnetic domain. Cerebral cavernous malformations are characterized by slow, small hemorrhages at the capillary level; consequently, SV increases more slowly and remains lower than in the presence of ICH.³⁴ Bleeding in the necrotic core of carotid plaques may be even less and slower than in cerebral cavernous malformations, and it may be recurrent due to disruption of the vasa vasorum³⁵ and plaque fissure/rupture.³⁶ IPH and Fe^{3+} deposits (ie, hemosiderin) tended to coexist in hyperintense areas on our QSM images. Because the presence of hemosiderin is indicative of chronic hemorrhage, hyperintense areas in carotid plaques may reflect different hemorrhagic stages. IPH can contribute to the progression of atheroma via the deposition of free cholesterol derived from the erythrocyte membrane,²² and it may change the macrophage phenotype in advanced atherosclerotic lesions. Hyperintense areas on QSM images may be associated with atheroma progression.

The quantification of erythrocytes and Fe^{3+} deposits in whole plaques showed that the mean susceptibility values were positively correlated with GYPA- and Fe^{3+} -positive areas. However, the Fe^{3+} -positive areas were much smaller than the GYPA-positive areas. This difference may be attributable to differences in the size and abundance of erythrocytes compared with hemosiderin, an aggregate of ferritin protein, and also may lead to a weak correlation between Fe^{3+} -positive areas and SVs. Even small amounts of iron affected the mean SV on QSM images, probably due to the superparamagnetic susceptibility of hemosiderin, in which iron forms a magnetic domain.³³ In addition, there was no significant difference in the mean SV between cores with IPH but no iron deposits and cores with iron deposits but no IPH. These results support high susceptibility on QSM images, reflecting both hemoglobin content and hemosiderin deposition. On the basis of our findings, we think that carotid plaque components with positive susceptibility on QSM images reflect erythrocyte and/or iron deposits at different hemorrhage stages (ie, deoxyhemoglobin, methemoglobin, and hemosiderin).

Quantification of changes in the IPH volume in asymptomatic individuals may help to identify new risk factors for the development and progression of IPH and may yield further clues for the prevention of cerebrovascular events.³⁷ Because the mean SV of whole plaques was correlated with the degree of IPH, quantification of the IPH volume on QSM images may be useful for assessing the initial IPH volume and subsequent changes.

Our study has some limitations. It did not include in vivo images, and our sample size was relatively small. Although imaging of in vivo QSM for the extracranial carotid artery seems to be challenging, an in vivo QSM study of carotid plaques was recently reported.³⁸ Future studies using in vivo carotid QSM are needed to clarify the usefulness of the in vivo imaging. Evia et al³⁹ showed the strong linear correlation in susceptibility on QSM between in vivo and ex vivo brain tissues. Therefore, our results may be valuable for translation of ex vivo QSM findings to in vivo ones.

We did not perform an in vivo comparison of MPRAGE with QSM. This is also needed to clarify whether the image quality of QSM is similar to that of MPRAGE for clinical use and to evaluate whether QSM is more useful for characterization of plaque components than MPRAGE. The time from fixation of samples to MR imaging was relatively long; the mean time was 36 days. Evia et al³⁹ reported that susceptibility in gray and white matter measured ex vivo with QSM does not change in the first 6 weeks after death and fixation. Therefore, the effect of the time from fixation to MR imaging may have been small. Last, the sections visualized on our QSM images are not completely comparable with the histology sections because the section thickness was 1 mm on QSM and 3 μm on histologic images. Therefore, the histologic images may reflect only a part of the QSM images.

CONCLUSIONS

Our ex vivo study suggests that QSM can be used to help characterize the composition of carotid plaque (ie, IPH, Fe^{3+} deposition, necrotic core, and calcification). It may facilitate the quantification of erythrocytes and Fe^{3+} deposits in plaques and differentiate these deposits from necrotic cores and calcification.

Disclosures: Kazunari Maekawa—UNRELATED: Employment: university salary. Yi Wang—RELATED: Grant: National Institutes of Health, Comments: R01NS105144*; UNRELATED: Employment: Cornell University; Stock/Stock Options: Medimagetric LLC, Comments: a Cornell spin-off company. *Money paid to the institution.

REFERENCES

1. Takaya N, Yuan C, Chu B, et al. **Association between carotid plaque characteristics and subsequent ischemic cerebrovascular events: a prospective assessment with MRI—initial results.** *Stroke* 2006;37:818–23 CrossRef Medline
2. Liu XS, Zhao HL, Cao Y, et al. **Comparison of carotid atherosclerotic plaque characteristics by high-resolution black-blood MR imaging between patients with first-time and recurrent acute ischemic stroke.** *AJNR Am J Neuroradiol* 2012;33:1257–61 CrossRef Medline
3. Hellings WE, Peeters W, Moll FL, et al. **Composition of carotid atherosclerotic plaque is associated with cardiovascular outcome: a prognostic study.** *Circulation* 2010;121:1941–50 CrossRef Medline

4. Altaf N, Daniels L, Morgan PS, et al. **Detection of intraplaque hemorrhage by magnetic resonance imaging in symptomatic patients with mild to moderate carotid stenosis predicts recurrent neurological events.** *J Vasc Surg* 2008;47:337–42 CrossRef Medline
5. Saam T, Hetterich H, Hoffmann V, et al. **Meta-analysis and systematic review of the predictive value of carotid plaque hemorrhage on cerebrovascular events by magnetic resonance imaging.** *J Am Coll Cardiol* 2013;62:1081–91 CrossRef Medline
6. Altaf N, Beech A, Goode SD, et al. **Carotid intraplaque hemorrhage detected by magnetic resonance imaging predicts embolization during carotid endarterectomy.** *J Vasc Surg* 2007;46:31–36 CrossRef Medline
7. Zhou T, Jia S, Wang X, et al. **Diagnostic performance of MRI for detecting intraplaque hemorrhage in the carotid arteries: a meta-analysis.** *Eur Radiol* 2019;29:5129–38 CrossRef Medline
8. Toussaint JF, LaMuraglia GM, Southern JF, et al. **Magnetic resonance images lipid, fibrous, calcified, hemorrhagic, and thrombotic components of human atherosclerosis in vivo.** *Circulation* 1996;94:932–38 CrossRef Medline
9. Yuan C, Mitsumori LM, Ferguson MS, et al. **In vivo accuracy of multispectral magnetic resonance imaging for identifying lipid-rich necrotic cores and intraplaque hemorrhage in advanced human carotid plaques.** *Circulation* 2001;104:2051–56 CrossRef Medline
10. Watanabe Y, Nagayama M. **MR plaque imaging of the carotid artery.** *Neuroradiol* 2010;52:253–74 CrossRef Medline
11. Bitar R, Moody AR, Symons S, et al. **Carotid atherosclerotic calcification does not result in high signal intensity in MR imaging of intraplaque hemorrhage.** *AJNR Am J Neuroradiol* 2010;31:1403–07 CrossRef Medline
12. Wasserman BA, Smith WI, Trout HH, 3rd, et al. **Carotid artery atherosclerosis: in vivo morphologic characterization with gadolinium-enhanced double-oblique MRI imaging: initial results.** *Radiology* 2002;223:566–73 CrossRef Medline
13. Bitar R, Moody AR, Leung G, et al. **In vivo 3D high-spatial-resolution MR imaging of intraplaque hemorrhage.** *Radiology* 2008;249:259–67 CrossRef Medline
14. Moody AR, Murphy RE, Morgan PS, et al. **Characterization of complicated carotid plaque with magnetic resonance direct thrombus imaging in patients with cerebral ischemia.** *Circulation* 2003;107:3047–52 CrossRef Medline
15. Chu B, Kampschulte A, Ferguson MS, et al. **Hemorrhage in the atherosclerotic carotid plaque: a high-resolution MRI study.** *Stroke* 2004;35:1079–84 CrossRef Medline
16. Liu T, Surapaneni K, Lou M, et al. **Cerebral microbleeds: burden assessment by using quantitative susceptibility mapping.** *Radiology* 2012;262:269–68 CrossRef Medline
17. Langkammer C, Liu T, Khalil M, et al. **Quantitative susceptibility mapping in multiple sclerosis.** *Radiology* 2013;267:551–59 CrossRef Medline
18. Chang S, Zhang J, Liu T, et al. **Quantitative susceptibility mapping of intracerebral hemorrhages at various stages.** *J Magn Reson Imaging* 2016;44:420–25 CrossRef Medline
19. Chen W, Zhu W, Kovanlikaya I, et al. **Intracranial calcifications and hemorrhages: characterization with quantitative susceptibility mapping.** *Radiology* 2014;270:496–505 CrossRef Medline
20. Eisenmenger LB, Aldred BW, Kim SE, et al. **Prediction of carotid intraplaque hemorrhage using adventitial calcification and plaque thickness on CTA.** *AJNR Am J Neuroradiol* 2016;37:1496–503 CrossRef Medline
21. Schweser F, Sommer K, Deistung A, et al. **Quantitative susceptibility mapping for investigating subtle susceptibility variations in the human brain.** *Neuroimage* 2012;62:2083–100 CrossRef Medline
22. Kolodgie FD, Gold HK, Burke AP, et al. **Intraplaque hemorrhage and progression of coronary atheroma.** *N Engl J Med* 2003;349:2316–25 CrossRef Medline
23. Schweser F, Deistung A, Lehr BW, et al. **Differentiation between diamagnetic and paramagnetic cerebral lesions based on magnetic susceptibility mapping.** *Med Phys* 2010;37:5165–78 CrossRef Medline
24. Gupta RK, Rao SB, Jain R, et al. **Differentiation of calcification from chronic hemorrhage with corrected gradient echo phase imaging.** *J Comput Assist Tomogr* 2001;25:698–704 CrossRef Medline
25. Yamada N, Imakita S, Sakuma T, et al. **Intracranial calcification on gradient-echo phase image: depiction of diamagnetic susceptibility.** *Radiology* 1996;198:171–78 CrossRef Medline
26. Zhu WZ, Qi JP, Zhan CJ, et al. **Magnetic resonance susceptibility weighted imaging in detecting intracranial calcification and hemorrhage.** *Chin Med J* 2008;121:2021–25 CrossRef Medline
27. de Rochefort L, Liu T, Kressler B, et al. **Quantitative susceptibility map reconstruction from MR phase data using Bayesian regularization: validation and application to brain imaging.** *Magn Reson Med* 2010;63:194–206 CrossRef Medline
28. Li J, Chang S, Liu T, et al. **Reducing the object orientation dependence of susceptibility effects in gradient echo MRI through quantitative susceptibility mapping.** *Magn Reson Med* 2012;68:1563–69 CrossRef Medline
29. Thelwall PE, Shepherd TM, Stanisz GJ, et al. **Effects of temperature and aldehyde fixation on tissue water diffusion properties, studied in an erythrocyte ghost tissue model.** *Magn Reson Med* 2006;56:282–89 CrossRef Medline
30. Pfefferbaum A, Sullivan EV, Adalsteinsson E, et al. **Postmortem MR imaging of formalin-fixed human brain.** *Neuroimage* 2004;21:1585–95 CrossRef Medline
31. Tan H, Zhang L, Mikati AG, et al. **Quantitative susceptibility mapping in cerebral cavernous malformations: clinical correlations.** *AJNR Am J Neuroradiol* 2016;37:1209–15 CrossRef Medline
32. Sun H, Klahr AC, Kate M, et al. **Quantitative susceptibility mapping for following intracranial hemorrhage.** *Radiology* 2018;288:830–39 CrossRef Medline
33. Gomori JM, Grossman RI. **Mechanisms responsible for the MR appearance and evolution of intracranial hemorrhage.** *Radiographics* 1988;8:427–40 CrossRef Medline
34. Mikati AG, Tan H, Shenkar R, et al. **Dynamic permeability and quantitative susceptibility: related imaging biomarkers in cerebral cavernous malformations.** *Stroke* 2014;45:598–601 CrossRef Medline
35. Barger AC, Beeuwkes R, 3rd, Lainey LL, et al. **Hypothesis: vasa vasorum and neovascularization of human coronary arteries: a possible role in the pathophysiology of atherosclerosis.** *N Engl J Med* 1984;310:175–77 CrossRef Medline
36. Daemen MJ, Ferguson MS, Gijzen FJ, et al. **Carotid plaque fissure: an underestimated source of intraplaque hemorrhage.** *Atherosclerosis* 2016;254:102–08 CrossRef Medline
37. van den Bouwhuisen QJ, Selwaness M, Tang H, et al. **Change in carotid intraplaque hemorrhage in community-dwelling subjects: a follow-up study using serial MR imaging.** *Radiology* 2017;282:526–33 CrossRef Medline
38. Ikebe Y, Ishimaru H, Imai H, et al. **Quantitative susceptibility mapping for carotid atherosclerotic plaques: a pilot study.** *Magn Reson Med Sci* 2019 May 31. [Epub ahead of print] CrossRef Medline
39. Evia AM, Kotrotsou A, Tamhane AA, et al. **Ex-vivo quantitative susceptibility mapping of human brain hemispheres.** *PLoS One* 2017;12:e0188395 CrossRef Medline

Standard Diffusion-Weighted Imaging in the Brain Can Detect Cervical Internal Carotid Artery Dissections

G. Adam, J. Darcourt, M. Roques, M. Ferrier, R. Gramada, Z. Meluchova, S. Patsoura, A. Viguier, C. Cognard, V. Larrue, and F. Bonneville



ABSTRACT

BACKGROUND AND PURPOSE: The ICA is the most common site of cervical artery dissection. Prompt and reliable identification of the mural hematoma is warranted when a dissection is clinically suspected. The purpose of this study was to assess to capacity of a standard DWI sequence acquired routinely on the brain to detect dissecting hematoma related to cervical ICA dissections.

MATERIALS AND METHODS: This was a retrospective study of a cohort of 110 patients younger than 55 years of age (40 women; mean age, 46.79 years) admitted at the acute phase of a neurologic deficit, headache, or neck pain and investigated by at least a standard 3T diffusion-weighted sequence of the brain. Among them were 50 patients (14 women; mean age, 46.72 years) with subsequently confirmed ICA dissection. In the whole anonymized cohort, both a senior and junior radiologist separately assessed, on the DWI sequences only, the presence of a crescent-shaped or circular hypersignal projecting on the subpetrosal segment of the ICA arteries, assuming that it would correspond to a mural hematoma related to an ICA dissection.

RESULTS: The senior radiologist found 46 subpetrosal hyperintensities in 43/50 patients with ICA dissection and none in patients without dissection (sensitivity, 86%; specificity, 100%). The junior radiologist found 48 subpetrosal hyperintensities in 45/50 patients with dissection and none in patients without dissection (sensitivity, 90%; specificity, 100%).

CONCLUSIONS: In our cohort, a standard DWI sequence performed on the brain at the acute phase of a stroke or for a clinical suspicion of dissection detected nearly 90% of cervical ICA dissections.

ABBREVIATION: FS = fat-saturated

Cervical artery dissection is defined by the spontaneous or posttraumatic onset of a hematoma in the wall of an artery. The cervical ICA is the most common site for dissection of supra-aortic trunks.¹ While cervical artery dissections are responsible for nearly 25% of ischemic strokes in young or middle-aged adults,² dissections may be diagnosed without or before the onset of a stroke. These ischemic complications occur in 82% of patients in the first week following dissection.³ It is, therefore, essential to be able to diagnose cervical artery dissection as soon as possible following the appearance of a mural hematoma to implement an adapted treatment, medical or endovascular, and

reduce the risk of thromboembolic or hemodynamic complications.⁴ In this context of dissection and in case of stroke due to a large-vessel occlusion, noninvasive imaging of the extra- and intracranial arteries is essential for planning, if necessary, an endovascular recanalization strategy, both cervical and cerebral,^{5,6} because tandem occlusions may occur and can be treated at the same time.⁷

MR imaging allows the diagnosis of cervical artery dissection by directly visualizing the wall hematoma through fat-saturated (FS) T1WI. It appears as a crescent-shaped hypersignal around an eccentric residual arterial lumen. This T1 hyperintensity is associated with the presence of intracellular and extracellular methemoglobin in the hematoma.⁸ Because these hemoglobin-degradation products only appear 72 hours after the formation of the hematoma, T1 hypersignal is only visible after this period. Before 72 hours, oxyhemoglobin and deoxyhemoglobin appear isointense on T1-weighted sequences; this feature makes diagnosis difficult in the acute phase and can be the cause of false-negatives.⁹ The sensitivity of the FS T1WI is, therefore, more reliable after the first 72 hours of the onset of a dissection.¹⁰

Received April 4, 2019; accepted after revision November 27.

From the Departments of Diagnostic and Therapeutic Neuroradiology (G.A., J.D., M.R., M.F., R.G., Z.M., S.P., C.C., F.B.) and Neurology (A.V., V.L.), Centre Hospitalier Universitaire Toulouse, Pierre-Paul Riquet Hospital, Toulouse, France.

Please address correspondence to Fabrice Bonneville, MD, CHU Toulouse, Pierre-Paul Riquet Hospital, Place du Docteur Baylac, TSA 4003131059 Toulouse, France; e-mail: bonneville.f@chu-toulouse.fr

Indicates article with supplemental on-line table.

<http://dx.doi.org/10.3174/ajnr.A6383>

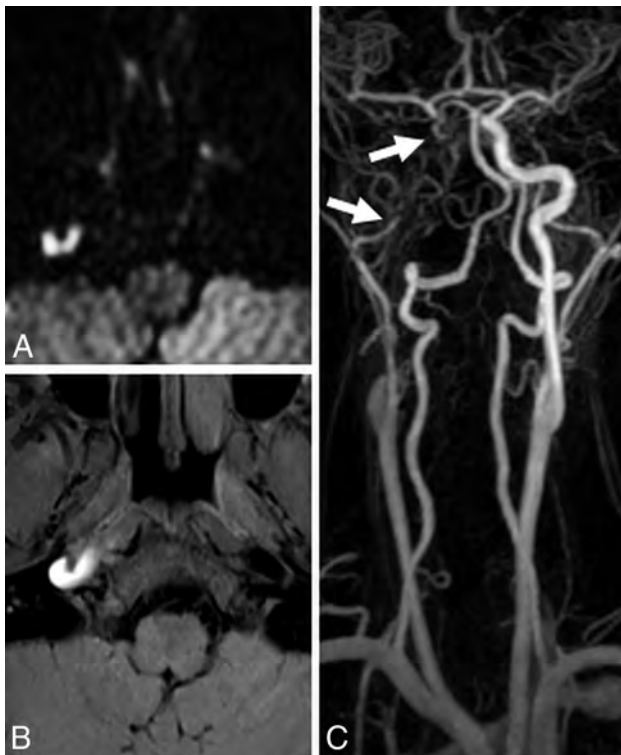


FIG 1. DWI (A) and FS T1WI (B) show a crescent-shape hypersignal of a mural hematoma of a right carotid artery dissection. MR angiography (C) shows the subsequent near-occlusion stenosis of the arterial lumen.

DWI is generally the first sequence acquired during a brain MR imaging performed to explore an acute neurologic deficit to identify early signs of cerebral ischemia. On this sequence, acute cerebral hemorrhage also appears hyperintense¹¹ and wall hematomas of cervical artery dissections are sometimes also visible as a hypersignal.^{12,13} Brain MR imaging usually covers the subpetrous segment of the ICA, where the wall hematoma of the dissections is most frequently seen.¹

In our experience, DWI shows a crescent or circular hypersignal in the projection of the subpetrous ICA in cases of dissection (Fig 1), even during the hyperacute phase of a stroke, while FS T1WI is usually not acquired, to minimize the overall acquisition time of the examination, or the findings were negative because it was performed too early.

The aim of this work was to evaluate the capacity of DWI alone, without knowledge of other sequences, to detect wall hematomas of ICA dissections.

MATERIALS AND METHODS

Patients

From June 2014 to December 2016, we retrospectively included 50 consecutive patients younger than 55 years of age from a register of our university hospital (14 women; mean age, 46.72 years; range, 21–65 years) with a final diagnosis of carotid dissection. This diagnosis was confirmed secondarily, either by Doppler sonography when an intimal flap or a parietal hematoma was visible (10 patients, 20%), or by MR imaging showing a hyperintense parietal wall hematoma on FS T1WI (22 patients, 44%), or finally

during follow-up showing either restoration to the original condition of the caliber of the cervical ICA, which presented at the acute phase with a postbulbar irregular stenosis (18 patients, 36%), or the development of a pseudoaneurysm (14 patients, 28%). Patients were admitted to the neurovascular emergency department due to neck pain (18 patients, 36%), headache (35 patients, 70%), Horner syndrome (28 patients, 56%), or neurologic deficit (30 patients, 60%) such as visual disturbances (14 patients, 28%), speech disorders (12 patients, 24%), or sensory (13 patients, 26%) or motor disorders (24 patients, 48%) (On-line Table). The average NIHSS score on arrival at the neurovascular emergency department was 5 (range, 0–24). The patients were examined with at least routine DWI on a 3T MR imaging. Among these 50 patients, 28 patients (56%) had acute cerebral ischemic injury on initial MR imaging. The time between the onset of any symptoms reported by the patient (ie, neck pain, headaches, or neurologic deficit), considering that it might correspond to the onset of the internal carotid artery wall hematoma, and acquisition of MR imaging was calculated for each patient.

A control group of 60 individuals had the same distribution in sex and age. This group consisted of 2 subgroups: 35 patients (11 women; mean age, 47.91 years; range, 20–65 years) who had an ischemic stroke unrelated to carotid dissection and 25 patients (15 women; mean age, 45.36 years; range, 21–65 years) who had a clinical suspicion of carotid dissection due to aggressive symptoms such as neck pain or Horner syndrome, but for whom the dissection diagnosis was rejected by the complete radiologic assessment. The final diagnoses for those patients were ischemic stroke (35/60 patients, 58%); functional disorder (9/60 patients, 15%); transient ischemic attack (7/60 patients, 12%); migraine with aura (5/60 patients, 8%); ear, nose, and throat pathology (2/60 patients, 3%); rupture of an aneurysm (1/60 patients, 2%); and a vasovagal episode (1/60 patients, 2%). The control population was admitted during the same period and underwent the same 3T cerebral DWI as the 50 patients with carotid dissection not have been consecutively enrolled to match with the dissection group in age and sex and presence of stroke on DWI.

The 50 patients with a final diagnosis of carotid dissection and the 60 controls without dissection showed no significant difference regarding the presence of ischemic stroke: Twenty-eight of 50 (56%) patients with carotid dissection had an ischemic stroke, while 35/60 (58%) patients from the control group had one ($P = .4$). Two patients (4%) had a transient ischemic attack in the “dissection” group. In the control group, 35 patients (58%) had acute cerebral ischemic lesions and 7 patient (12%) had a transient ischemic attack.

MR Imaging

All brain MRIs included at least 1 DWI sequence with 4-mm-thick sections on 3T magnets, either a Magnetom Skyra (Siemens, Erlangen, Germany) (TR/TE: 5300/96 ms; matrix: 110 × 110; acquisition time: 53 seconds) or an Achieva TX (Philips Healthcare, Best, the Netherlands) (TR/TE: 2756/57 ms; matrix: 112 × 89; acquisition time: 33 seconds), from the vertex to the upper part of the second cervical vertebra, including the distal, subpetrous cervical segment of the cervical internal carotid arteries.

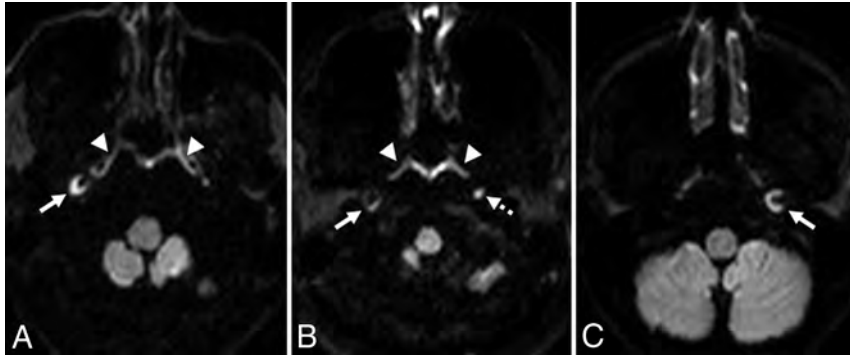


FIG 2. DWI in 3 different patients with cervical internal carotid artery dissections. Crescent-shaped hypersignal of wall hematomas (A–C, *solid arrows*), ring-shaped hypersignal of a wall hematoma (B, *solid arrow*), linear hyperintensity of pharyngeal lymphoid tissue (A and B, *arrowheads*), and nodular hypersignal of a ganglion (B, *dashed arrow*).

MR Imaging Analysis

The DWIs of patients and controls were isolated from the rest of the examinations, grouped together, anonymized, randomized, and randomly numbered.

Two observers, a senior radiologist (F.B.) and a junior radiologist (G.A.), with no knowledge of the patients or controls, the other sequences, and the clinical information, independently analyzed the DWI sequences separately. They had to determine whether a hypersignal with a crescent or ring shape suggestive of a wall hematoma was present in the projection of the distal cervical internal carotid arteries (Fig 2).

Other DWI high signal intensities, either located at a distance from the subpetrous segments of internal carotid arteries or of different shapes, were not retained. In particular, pharyngeal lymphoid tissue and lymph nodes, respectively, in the form of linear and nodular hypersignals, were not taken into account (Fig 2).

In a second step, among patients with dissections, after anonymity was waived, we calculated the time between the onset of symptoms and MR imaging; and when FS T1WI was performed, we compared it visually with the DWI sequence to evaluate their respective capacities in detecting a wall hematoma. Among the 50 patients with dissections, we also analyzed the shape of the DWI hyperintensities of those who had an occlusion based on MRA or CTA data (On-line Table 1).

Statistical Analysis

We calculated the sensitivity and specificity of the crescent- or ring-shaped DWI hypersignal along the expected wall of the subpetrosal ICA for the detection of carotid dissections. A κ coefficient was calculated to measure the interobserver agreement between the senior and the junior radiologists in the detection of crescent- or ring-shaped DWI hyperintensities.

RESULTS

The senior radiologist found 46 abnormal DWI hyperintensities in the projection of the distal portion of cervical internal carotid arteries in 43/50 patients with carotid artery dissection (bilateral hypersignal for 3 patients) and none in patients without dissection (sensitivity, 86%, specificity 100%). The junior radiologist found 48 abnormal DWI hyperintensities in the distal portion of

internal carotid arteries in 45/50 patients with carotid dissection (bilateral hypersignal for 3 patients) and none in patients without dissection (sensitivity 90%; specificity 100%).

The κ coefficient was calculated at 0.99, meaning excellent interobserver agreement.

Finally, after consensus, 90% (45/50) of patients with dissections could be correctly diagnosed due to the DWI sequence alone, and none of the subjects of the control group were misclassified. For patients who had a dissection, the time between the onset of their symptoms and their MR imaging was <24 hours for 24/50 patients (48%), between 24 and 72 hours for

11/50 patients (22%) and >72 hours for 15/50 patients (30%).

FS T1WI was part of the initial MR imaging protocol in 26/50 (52%) patients with dissection. For these MR images, the wall hematoma appeared hyperintense on both DWI and FS T1WI in 20/26 (77%) patients. It was visible only on DWI in 4/26 (15%) patients (Fig 3). These MR images were obtained, on average, 15 hours 20 minutes after the onset of symptoms (range, 80 minutes to 32 hours). On the other hand, the hyperintensity of the wall hematoma was only visible on FS T1WI in 2/26 (8%) patients; these MRIs were performed, on average, 6 days after the onset of symptoms (5–7 days).

DISCUSSION

The primary result of our study is that 90% of cervical ICA dissections could be detected by a standard, routine DWI sequence, acquired of the brain in the event of clinical suspicion of ischemic stroke or cervical artery dissection. Other authors¹ had already investigated the possibility of diagnosing a dissection of the upper cervical portions of the internal and vertebral carotid arteries by analyzing 5 different brain sequences (sagittal T1 WI, axial FLAIR imaging, axial gradient recalled-echo T2-weighted imaging, DWI, and 3D time-of-flight angiography of the circle of Willis). In that study, the dissection diagnosis was made if the hematoma was seen on 3 different sequences. The authors showed that 59/77 (77.6%) patients with a cervical artery dissection included in the field covered during the brain acquisition had a correct diagnosis using this method. The diagnosis was more frequent for carotid dissections (54/58 patients, 93.1%) than for vertebral dissections (5/19 patients, 26.3%). The sensitivity of each sequence assessed independently for detecting wall hematomas was not indicated. Our study shows comparable sensitivity of the DWI sequence alone in the detection of ICA dissections, independent of FS T1WI in particular.

However, contrary to this previous study, we analyzed not only the carotid dissections that were included in the field of acquisition of the DWI, but we included all carotid dissections without prejudging their locations and their extensions to subpetrosal segments of the cervical ICA. Our results would, therefore, suggest that most carotid dissections reach the distal,

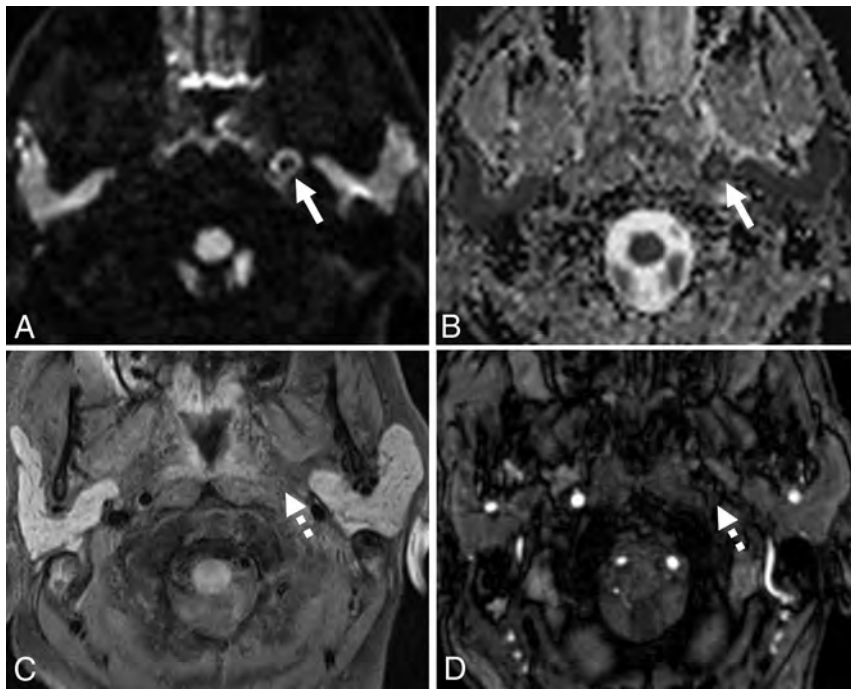


FIG 3. Hyperacute dissection with a wall hematoma appearing hyperintense on DWI (A, arrow), with apparent diffusion coefficient restriction (B, arrow), not visible on FS T1WI (C, dotted arrow) or the axial source image of time-of-flight MR angiography (D, dotted arrow).

subpetrous segments of the internal carotid arteries. Curiously, there are scant data in the literature regarding the accurate frequency of damage of the subpetrous segment in carotid dissections, even if it appears to be affected “in most cases.”¹⁴ According to some authors, dissections usually originate 2 cm above the carotid bulb and extend over a variable length, often up to the carotid canal, covering the subpetrous segment.¹⁵

In our study, 1 dissection of 10 was not diagnosed by DWI, either due to the absence of hyperintensity despite a subpetrous topography included in the field of acquisition or because the hematoma was likely situated lower in the wall of the cervical ICA. The association between the tortuosity of cervical arteries and dissections is known.¹⁶ In 1 study,¹⁷ these loops were shown in 22% of dissections compared with 8% in healthy controls. In view of our results, these loops were often subpetrous, therefore included in the field of exploration, but some might be postbulbar and, therefore, not included in the field, and this feature may explain some of the false-negatives of the routine DWI brain sequences.

Among cervical artery dissections reported in the study of Naggara et al,¹⁶ 67 ICA dissections were included in the fields of acquisition of brain MRIs and 21 carotid dissections were excluded, 76% of high dissections. This determination was made by analyzing axial FS T1WI performed on 1.5T magnets. Compared with our results, which indicate 90% of ICA dissections seen on subpetrous segments, it is possible that the findings of their sequence were faulty, particularly for the small wall hematomas or hematomas seen early, before 72 hours, and there were, in actuality, more carotid dissections included in the fields of acquisition of brain MRIs but not detected by their restrictive method. Although no studies have shown the superiority of 3T MR imaging compared with 1.5T in the detection of cervical

artery dissections, with the intensity of the MR imaging signal being directly proportional to the intensity of the primary magnetic field, the signal-to-noise ratio is higher on a sequence performed at 3T than at 1.5T. It is likely that the wall hematomas of our series were more visible on 3T. Several studies have also shown interest in 3T MR imaging using T1 Cube (GE Healthcare)¹⁸ or black-blood¹⁹ sequences for detecting wall hematomas of dissections, but without comparing them with 1.5T.

In our study, DWI at 3T revealed a parietal hematoma of ICA dissection very early because most of our patients with a dissection were examined by MR imaging within 24 hours after the onset of their symptoms. DWI was even better than FS T1WI in detecting wall hematoma in 15% of our patients, having undergone both sequences on their initial MR imaging performed, on average, 15 hours 20 minutes after the onset of symptoms. On the other hand, the later the MRIs were performed, the more likely it was that DWI findings were faulty. The hyperintensity of the wall hematoma was only visible on FS T1WI in 2/26 (8%) patients; these MRIs were then performed, on average, 6 days after the onset of symptoms (range, 5–7 days). The intracerebral hematoma signal intensity on DWI is the lowest during the early subacute phase of intracellular methemoglobin (between 4 and 7 days) before increasing again in the late subacute phase (after 7 days).¹¹ This phenomenon could, therefore, explain the poorer sensitivity of DWI in detecting dissecting hematomas during this subacute phase.

The DWI and FS T1WI sequences, therefore, appear complementary in detecting ICA dissections: DWI could detect wall hematomas in the acute phase, even before the appearance of a FS T1WI hypersignal, while the latter could enable diagnosis of dissections beyond 72 hours and later than DWI. These considerations about the temporality are accurate if the wall hematoma occurs at the same time as the first symptoms of patients, which is not always the case.

Our study showed not only the very good sensitivity of DWI in the detection of ICA dissections but also an excellent specificity with no false-positives. Crescent- or ring-shaped hypersignals were likely to represent wall hematomas of dissections, not hemorrhagic plaques, because these are not supposed to appear with DWI hypersignal²⁰ and are not usually located in the subpetrosal aspect of the distal ICA. However, it is important to learn to distinguish crescent- or ring-shaped dissections of hematomas from linear and nodular hyperintensities of pharyngeal lymphoid tissue and lymph nodes. Once this sign is learned, it enables detection of wall hematomas with excellent specificity and excellent interobserver agreement. In clinical routine, the radiologist will

naturally be aided by other classic protocol sequences such as FLAIR and gradient recalled-echo T2* to more easily locate the hypersignal on DWI. However, in practice, in view of our results, if the hematoma clearly appears hyperintense on DWI at the acute phase of a neurologic deficit or neck pain, then the specificity of our sign can be obtained without FS T1WI and thus save acquisition time. It also does not appear necessary to re-examine the patient later to confirm the presence of a dissection if the hypersignal of the hematoma is visible in DWI on the initial MR imaging.

The primary limitation of our study is its retrospective nature, including 50 patients with dissections and 60 patients without dissections, a prevalence of 45% dissections in our total population, or an overrepresentation of dissections compared with the general stroke population. However, knowing this prevalence, if the sensitivity was increased, the observers would also have seen more hematomas than there were in reality, with a consequent decrease in specificity. This did not occur, as no false-positives were found.

Some patients with dissections had visible cerebral ischemic lesions on DWI. This could have been a bias in the analysis of the presence of a crescent- or ring-shaped hypersignal along the expected wall of the subpetrosal ICA, particularly if this hypersignal was on the same side as the ischemic lesions. This bias was removed by the same proportion of ischemic lesions in the dissection group as in the control group.

We chose to investigate ICA dissections; we do not know the sensitivity and specificity of DWI in the detection of vertebral artery dissections. One study¹² observed DWI hyperintensity in connection with vertebral dissections in a small cohort of 4 patients on 1.5T MR imaging. A future study, including a greater number of patients and performed with 3T MR imaging will analyze the capacity of DWI in detecting wall hematomas of vertebral dissections. Finally, this following study may also compare the respective sensitivities and specificities of DWI and FS T1WI sequences in detecting cervical artery dissections as a function of the time of onset of symptoms.

CONCLUSIONS

In our study, a standard diffusion-weighted sequence routinely performed on the brain at the acute phase of a stroke or for a clinical suspicion of cervical artery dissection detected nearly 90% of cervical ICA dissections by showing a crescent- or ring-shaped hypersignal along the expected wall of the subpetrosal ICA. This sign, present on the first sequence generally acquired during MR imaging performed for a suspicion of acute ischemic stroke, makes it possible to confidently discuss the dissection diagnosis and initiate medical treatment adapted to very quickly reduce the risk of thromboembolic complications, and also to better predict the material necessary for a potential endovascular procedure.

Disclosures: Christophe Cognard—UNRELATED: Consultancy: Medtronic, Stryker, MicroVenton, Cerenovus, MIVI. Zuzana Meluchova—UNRELATED: Employment: University Hospital Toulouse.

REFERENCES

1. Naggara O, Soares F, Touze E, et al. Is it possible to recognize cervical artery dissection on stroke brain MR imaging? A matched case-

- control study. *AJNR Am J Neuroradiol* 2011;32:869–73 CrossRef Medline
2. Schievink WI. Spontaneous dissection of the carotid and vertebral arteries. *N Engl J Med* 2001;344:898–906 CrossRef Medline
3. Biousse V, D'Anglejan-Chatillon J, Touboul PJ, et al. Time course of symptoms in extracranial carotid artery dissections: a series of 80 patients. *Stroke* 1995;26:235–39 CrossRef Medline
4. Hoving JW, Marquering HA, Majoie C. Endovascular treatment in patients with carotid artery dissection and intracranial occlusion: a systematic review. *Neuroradiology* 2017;59:641–47 CrossRef Medline
5. Rotzinger DC, Mosimann PJ, Meuli RA, et al. Site and rate of occlusive disease in cervicocerebral arteries: a CT angiography study of 2209 patients with acute ischemic stroke. *AJNR Am J Neuroradiol* 2017;38:868–74 CrossRef Medline
6. Wei D, Mascitelli JR, Nistal DA, et al. The use and utility of aspiration thrombectomy in acute ischemic stroke: a systematic review and meta-analysis. *AJNR Am J Neuroradiol* 2017;38:1978–83 CrossRef Medline
7. Marnat G, Bühlmann M, Eker OF, et al. Multicentric experience in distal-to-proximal revascularization of tandem occlusion stroke related to internal carotid artery dissection. *AJNR Am J Neuroradiol* 2018;39:1093–99 CrossRef Medline
8. Bradley WG Jr. MR appearance of hemorrhage in the brain. *Radiology* 1993;189:15–26 CrossRef Medline
9. Bissleret D, Khalil A, Favrole P, et al. Spontaneous cervical artery dissection: role of a SE-T1-weighted fat-sat volume acquisition. *Diagn Interv Imaging* 2014;95:443–46 CrossRef Medline
10. Provenzale JM, Morgenlander JC, Gress D. Spontaneous vertebral dissection: clinical, conventional angiographic, CT, and MR findings. *J Comput Assist Tomogr* 1996;20:185–93 CrossRef Medline
11. Silvera S, Oppenheim C, Touzé E, et al. Spontaneous intracerebral hematoma on diffusion-weighted images: influence of T2-shine-through and T2-blackout effects. *AJNR Am J Neuroradiol* 2005;26:236–41 Medline
12. Choi KD, Jo JW, Park KP, et al. Diffusion-weighted imaging of intramural hematoma in vertebral artery dissection. *J Neurol Sci* 2007;253:81–84 CrossRef Medline
13. Haussen DC, Henninger N, Selim M. Diffusion-weighted imaging of intramural hematoma in internal carotid artery dissection. *Acta Neurol Belg* 2013;113:109–10 CrossRef Medline
14. Ben Hassen W, Machet A, Edjlali-Goujon M, et al. Imaging of cervical artery dissection. *Diagn Interv Imaging* 2014;95:1151–61 CrossRef Medline
15. Guillon B, Bousser MG. Epidemiology and pathophysiology of spontaneous cervical artery dissection. *J Neuroradiol* 2002;29:241–49 Medline
16. Kim BJ, Yang E, Kim NY, et al. Vascular tortuosity may be associated with cervical artery dissection. *Stroke* 2016;47:2548–52 CrossRef Medline
17. Kim ST, Brinjikji W, Lehman VT, et al. Association between carotid artery tortuosity and carotid dissection: a case-control study. *J Neurosurg Sci* 2018;62:413–17 CrossRef Medline
18. Edjlali M, Roca P, Rabrait C, et al. 3D fast spin-echo T1 black-blood imaging for the diagnosis of cervical artery dissection. *AJNR Am J Neuroradiol* 2013;34:E103–06 CrossRef Medline
19. Hunter MA, Santosh C, Teasdale E, et al. High-resolution double inversion recovery black-blood imaging of cervical artery dissection using 3T MR imaging. *AJNR Am J Neuroradiol* 2012;33:E133–37 CrossRef Medline
20. Yao B, Yang L, Wang G, et al. Diffusion measurement of intraplaque hemorrhage and intramural hematoma using diffusion weighted MRI at 3T in cervical artery. *Eur Radiol* 2016;26:3737–43 CrossRef Medline

MRI Patterns of Extrapontine Lesion Extension in Diffuse Intrinsic Pontine Gliomas

L. Makepeace, M. Scoggins, B. Mitrea, Y. Li, A. Edwards, C.L. Tinkle, S. Hwang, A. Gajjar, and Z. Patay



ABSTRACT

BACKGROUND AND PURPOSE: Diffuse intrinsic pontine glioma is a devastating childhood cancer that despite being primarily diagnosed by MR imaging alone, lacks robust prognostic imaging features. This study investigated patterns and quantification of extrapontine lesion extensions as potential prognostic imaging biomarkers for survival in children with newly diagnosed diffuse intrinsic pontine glioma.

MATERIALS AND METHODS: Volumetric analysis of baseline MR imaging studies was completed in 131 patients with radiographically defined typical diffuse intrinsic pontine gliomas. Extrapontine tumor extension was classified according to the direction of extension: midbrain, medulla oblongata, and right and left middle cerebellar peduncles; various extrapontine lesion extension patterns were evaluated. The Kaplan-Meier method was used to estimate survival differences; linear regression was used to evaluate clinical-radiographic variables prognostic of survival.

RESULTS: At least 1 extrapontine lesion extension was observed in 125 patients (95.4%). Of the 11 different extrapontine lesion extension patterns encountered in our cohort, 2 were statistically significant predictors of survival. Any extension into the middle cerebellar peduncles was prognostic of shorter overall survival ($P = .01$), but extension into both the midbrain and medulla oblongata but without extension into either middle cerebellar peduncle was prognostic of longer overall survival compared with those having no extension ($P = .04$) or those having any other pattern of extension ($P < .001$).

CONCLUSIONS: Within this large cohort of patients with typical diffuse intrinsic pontine gliomas, 2 specific extrapontine lesion extension patterns were associated with a significant overall survival advantage or disadvantage. Our findings may be valuable for risk stratification and radiation therapy planning in future clinical trials.

ABBREVIATIONS: DIPG = diffuse intrinsic pontine glioma; EPLE = extrapontine lesion extension; ETV = extrapontine tumor volume; MCP = middle cerebellar peduncle; OS = overall survival; PFS = progression-free survival; PTV = pontine tumor volume; RT = radiation therapy; TTV = total tumor volume

High-grade gliomas comprise 10%–15% of pediatric brain tumors and cause half of the deaths occurring as a result of CNS neoplasms in children.^{1,2} Of pediatric high-grade gliomas, those occurring in the pons, formerly referred to as diffuse intrinsic pontine glioma (DIPG), are most common and have the worst prognosis, with a 2-year survival rate of <10%.^{2,3}

DIPGs present with characteristic MR imaging features,⁴ explaining the high accuracy of the initial diagnostic imaging work-up (>95%)^{5,6} and the low rates of biopsies required before treatment. On MR imaging, the typical DIPG appears as an expansile, dominantly T2-hyperintense, usually inhomogeneous, intra-axial brain stem mass involving most of the pons but originating from the ventral pons (or basis pontis).¹ These tumors often show some signal enhancement after IV injection of gadolinium-based contrast agents and ventral exophytic growth, leading to engulfing of the basilar artery.⁷ Extrapontine lesion extensions (EPLEs) are also common in DIPG.

Although outcomes in DIPG remain grim overall, differences in disease course across patients are also well-known. Therefore, the need for imaging features that can inform noninvasive biologic characterization, aid early prognostication, and guide the development of risk-stratification schemes for future clinical trials persists. Hence, the quest for robust conventional (or

Received November 1, 2018; accepted after revision December 10, 2019.

From the Departments of Diagnostic Imaging (L.M., M.S., B.M., A.E., S.H., Z.P.), Biostatistics (Y.L.), Radiation Oncology (C.L.T.), and Oncology (A.G.), St. Jude Children's Research Hospital, Memphis, Tennessee.

This work was supported by the National Institutes of Health Cancer Center Support Grant P30 CA21765, the National Cancer Institute grant R25CA23944, and American Lebanese Syrian Associated Charities (ALSAC).

Please address correspondence to Zoltan Patay, MD, PhD, Department of Diagnostic Imaging, St. Jude Children's Research Hospital, 262 Danny Thomas Pl, MS220, Memphis, TN 38105-3678; e-mail: Zoltan.Patay@STJUDE.ORG

Indicates open access to non-subscribers at www.ajnr.org

<http://dx.doi.org/10.3174/ajnr.A6391>

advanced) prognostic imaging biomarkers of DIPG continues in the pediatric neuroimaging and neuro-oncology communities.

In 2008, Hargrave et al⁵ studied several conventional MR imaging features, including local extension, exophytism, percentage of pontine volume affected, T1 or T2 signal heterogeneity, metastasis, tumor dimension, and margin definition and found none to be predictive of survival. Jackson et al⁶ have also attempted to describe imaging characteristics of long-term survivors of DIPG, but the value of the findings was somewhat limited by the small number of long-term survivors. In 2015, Jansen et al⁸ suggested that the duration of clinical symptoms before diagnosis, age at diagnosis, and ring enhancement within the tumor lesion in postcontrast T1-weighted images may have prognostic value in DIPG. Others have suggested that ADC or ADC histogram metrics derived from diffusion-weighted MR imaging may identify prognostically distinct subgroups and correlate with survival in patients with DIPG.^{9,10} Most recently in 2018, Hoffman et al² assessed clinical-radiographic characteristics and their relationship with outcomes in a collaborative study that included >1000 patients with DIPG. In the largest population of DIPGs ever studied, they identified increased craniocaudal tumor dimension and higher rates of EPLE, tumor necrosis, and ring enhancement at diagnosis as significantly associated with shorter overall survival (OS) on univariate analysis, but only ring enhancement was significantly associated with OS on multivariate analysis. This outcome contrasts with the findings of Poussaint et al¹¹ in which larger tumor volumes were associated with longer survival (in that study, EPLEs were not analyzed separately but were presumably included), though enhancement at diagnosis was associated with shorter survival in their cohort as well.

Although prior studies, including the last 2 references cited above, suggest that EPLE may be relevant to and explain some of the differences in the clinical course and OS in patients with DIPG, methodologic differences hamper the unambiguous interpretation of these findings. Therefore, we sought to revisit this matter and clarify, in more specific terms, the potential prognostic value of EPLE at diagnosis in DIPG. To that end, we conducted a retrospective study using systematic and standardized analysis of imaging data focusing on the descriptive (ie, patterns) and quantitative (ie, overall burden) evaluation of EPLE and correlated those factors with key survival metrics in the largest, single-center cohort of patients with radiographically confirmed typical DIPG to date.

MATERIALS AND METHODS

Study Population

We identified all patients (younger than 18 years of age) with newly diagnosed DIPG who were evaluated at our institution at the time of diagnosis during the 17-year period between January 1, 2000, and December 31, 2017 (193 patients). Patients who had been previously treated or had metastatic disease at diagnosis were not included. For the purposes of this review, we requested approval from our institutional review board to retrospectively evaluate the clinical and imaging data collected during the treatment and follow-up of patients. This request, in conjunction with

a waiver of repeat consenting when the patient had been enrolled in a clinical trial, was granted.

Patients who did not have an adequate baseline MR imaging examination suitable for segmentation and coregistration were excluded ($n = 36$). Additionally, patients who were alive on May 1, 2018, were excluded because final survival data could not be collected for them ($n = 24$). Two of the remaining 133 patients were excluded because in retrospect, they were determined to have non-DIPG tumors of the brain stem (ie, not fulfilling the imaging criteria of the typical DIPG). One patient exhibited supratentorial tumor spread diffusely into the cerebral hemispheres with a gliomatosis cerebri growth pattern and a mixed glial/neuronal histopathologic phenotype, and 1 patient underwent surgical resection, which revealed a high-grade glioma of the medulla oblongata. Overall, 131 patients were included in our retrospective chart review and diagnostic MR imaging review study; 108 patients were enrolled in a total of 8 different therapeutic clinical trials, and 23 patients were treated on individualized treatment plans. Details of the 3 clinical trials accounting for the largest patient accrual sources, including treatment protocols and outcomes, have been reported previously.¹²⁻¹⁴

Clinical Variables

Clinical information was extracted from the patients' medical records, including demographics, age at diagnosis, progression-free survival (PFS), and OS. Age at diagnosis was defined as the time from the date of birth to the diagnostic MR imaging study performed at our institution; PFS was defined as the time from diagnosis to disease progression as determined by a combination of clinical and radiologic parameters, with minor differences across treatment protocols. Typically, progressive disease was defined by any of the following: 1) neurologic abnormalities or worsening neurologic status not explained by causes unrelated to tumor progression (eg, seizures, anticonvulsant toxicity, electrolyte disturbances, sepsis); 2) a >25% increase in the product of the maximum perpendicular diameters of the tumor lesion by imaging; 3) the presence of new metastatic disease; or 4) increasing doses of dexamethasone required to maintain a stable neurologic status. OS was defined as the time from diagnosis to death from any cause. The presence or absence of metastasis at the time of progression was recorded as well as the distribution pattern of metastasis: intracranial, intraspinal, or both.

Image Processing

Baseline MR imaging studies of the brain (ie, first diagnostic MR imaging examinations at our institution) were obtained for all patients within 2 weeks before initiation of treatment. After the baseline MR imaging study, patients either consented to participate in a therapeutic clinical trial or elected an individualized, nonprotocol treatment plan. Most studies ($n = 114$) were performed on 3T magnets (the remaining on 1.5T) and under various forms of anesthesia. Standard brain MR imaging was performed in all patients, including axial T1WI, postcontrast axial T1WI, and postcontrast 3D-T1WI. Postcontrast axial FLAIR imaging was also available for all except 4 patients for whom sagittal 3D-FLAIR imaging was used for segmentation. For 1 patient, who had no axial T2WI, sagittal 3D-T2WI

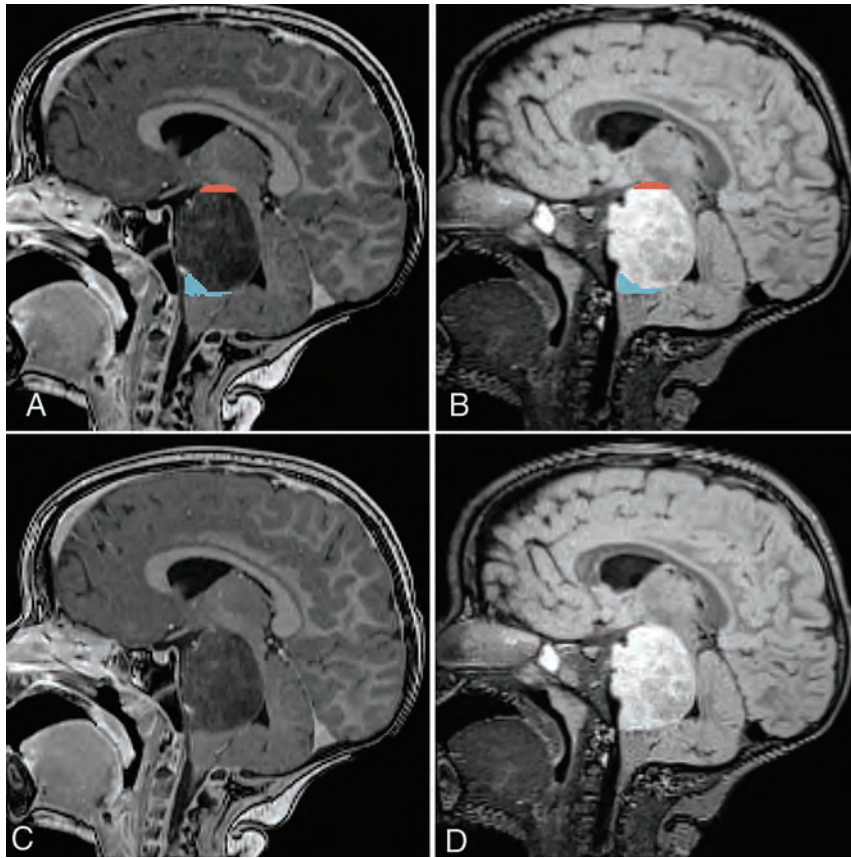


FIG 1. Vertical extrapontine lesion extensions in a patient with DIPG on sagittal postcontrast T1WI (A and C) and T2WI FLAIR (B and D) scans. Segmented (A and B) lesion extensions into the midbrain and medulla oblongata are highlighted in red and blue, respectively.

was used for segmentation. Voxel size for the 3D acquisitions was isotropic ($1 \times 1 \times 1$ mm). The section thickness for 2D imaging sequences was consistently 4 mm without a gap; however, subsequently, all axial 2D images were interpolated to isotropic voxels ($1 \times 1 \times 1$ mm) and coregistered to the postcontrast 3D T1 images.

The total tumor volume (TTV) was automatically estimated using a machine learning–based segmentation tool that we modeled after the work of Wang et al,¹⁵ which uses anisotropic convolutional neural networks to segment the entire tumor on the basis of precontrast T1-weighted and T2-weighted and postcontrast T1-weighted and FLAIR images. Postcontrast T2-weighted images were used for 2 subjects for whom precontrast T2-weighted images were unavailable. Subsequently, the images (including the TTV) were normalized to the Montreal Neurological Institute brain atlas. In the Montreal Neurological Institute space, the pons was segmented using SPM 12 software (<http://www.fil.ion.ucl.ac.uk/spm/software/spm12>); then, the resultant intrapontine tumor volume (pontine tumor volume [PTV]) was returned to the patient's space.

Radiologic Variables

After the automated segmentation of the tumors, each set of images and segmentations was evaluated and processed manually

by a single, trained observer under the supervision of a board-certified neuroradiologist. Using the automatically detected TTV as a starting point, the TTV was adjusted in 3D Slicer (<http://www.slicer.org>) to correct any misclassification of image voxels.¹⁶ The median smoothing tool, with a 2- to 3-voxel radius, depending on the accuracy of each segment at the tumor borders, was used on individual segments during the adjustment process.¹⁷ Once the entire tumor was segmented, the PTV was isolated from the TTV using anatomic boundaries and landmarks. Any exophytism (typically ventral) that arose from the pons was included in the PTV. Often, the primarily intrapontine tumor had an exophytic component that prolapsed downward ventrally to the medulla, but a direct extension into the upper aspect of the medulla was also present. In these cases, sagittal and coronal views were used to distinguish the exophytic portion of the PTV and EPLE toward the medulla oblongata. Extrapontine tumor volume (ETV) was defined as the discordance between the PTV and the TTV. ETV was then further classified by location into extensions

of the midbrain, medulla oblongata (collectively vertical EPLE), and right and left middle cerebellar peduncles (MCPs, collectively horizontal EPLE) (Figs 1 and 2). In addition to TTV, the cranio-caudal dimension of the tumor was extracted from the segmented volume by subtracting the location of the most inferior section that contained the TTV from the most superior one. The presence of postcontrast enhancement was recorded for each extension as well as the pontine component of each tumor. The presence of ring enhancement was also recorded for each tumor.

Statistical Analysis

Descriptive statistics were calculated for variables of interest. Kaplan-Meier estimates were calculated to estimate the 1-, 2- and 5-year OS and PFS rates and respective 95% confidence intervals. The association between possible prognostic factors and OS data was explored by performing univariate linear regression because the data were not censored. Cox regression models were used to model the relationship between PFS and possible prognostic factors. Two-sample *t* tests were used to assess whether imaging parameters were different between age categories (3 years or older at diagnosis versus younger than 3 years at diagnosis, age groups commonly used by other investigators). Patients were classified into 3 survival groups by their survival status (OS > 2 years, OS between 1 and 2 years, and OS < 1 year). Continuous variables of ETVs were

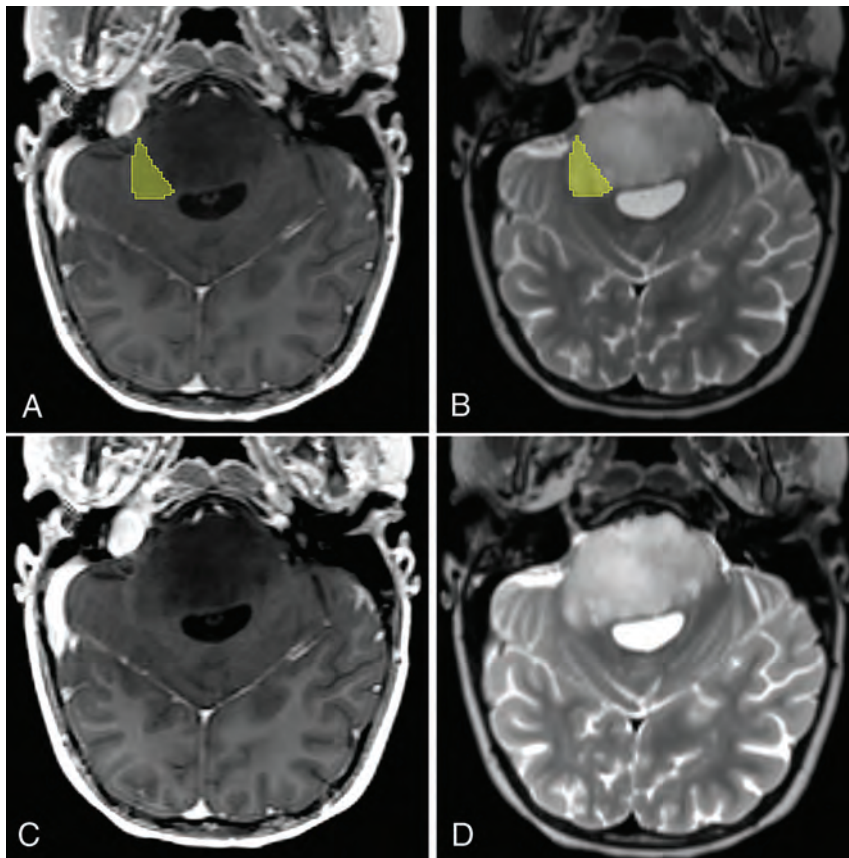


FIG 2. Unilateral horizontal extrapontine lesion extension in a patient with DIPG in transverse postcontrast TIWI (A and C) and T2WI (B and D). The segmented (A and B) extrapontine lesion extension toward the right middle cerebellar peduncle is highlighted in yellow.

Table 1: Patient characteristics

Variable/Category	No. (%)
Age at diagnosis	
3 yr or older	120 (91.6)
Younger than 3 yr	11 (8.4)
Sex	
Female	78 (59.6)
Male	53 (40.4)
Ethnicity	
Asian	2 (1.5)
Asian and white	1 (0.8)
Black	18 (13.8)
Black and white	3 (2.3)
Multiple	5 (3.8)
Other	2 (1.5)
Unknown	2 (1.5)
White	98 (74.8)
Metastasis at the end of progression-free survival?	
Yes	24 (18.3)
Spinal	7 (5.3)
Intracranial	4 (3.1)
Intracranial + spinal	13 (9.9)
No	112 (85.5)

compared among survival groups by performing ANOVA, and categorical variables of extrapontine extension were compared by performing χ^2 testing. To evaluate the association between categorical variables (pattern of metastasis and EPLE pattern or pattern

of metastasis and ETV), we used the Fisher exact test because there are cells in frequency tables with expected counts of <5 . ANOVA was applied when evaluating the association between continuous variables (TLV and ETV) and categorical variables (pattern of metastasis, ring enhancement, and enhancement). A 2-sample *t* test was performed to test the association between dichotomous enhancement pattern-related variables and continuous variables (global TLV/aggregate volume). All analyses were evaluated using SAS, Version 9.4 (SAS Institute, Cary, North Carolina).

RESULTS

Survival Outcomes

Of the 131 patients meeting the inclusion criteria, the median age at diagnosis was 6.4 years (interquartile range, 4.6 to 8.2). Ninety-eight (74.8%) patients were white; 18 (13.8%), black; demographics of the remaining 15 (12%) are shown in Table 1. Seventy-eight (59.6%) patients were female and 53 (40.4%) were male, resulting in a female-to-male sex ratio of 1.5:1. The median PFS time was 6.8 months (interquartile range, 5.8 to 9.1). The respective 1-, 2-, and 5-year PFS rates were 16.20% (95% CI, 10.44%–

23.09%), 3.44% (95% CI, 1.14%–7.90%), and 0.86% (95% CI, 0.08%–4.25%). At the time of progression, metastatic disease had developed in 24 patients (18.3%), 7 with intracranial metastasis, 4 with spinal metastasis, and 13 with both spinal and intracranial metastasis. The presence of metastasis at progression was significantly associated with shorter PFS ($P = .01$), but not with OS ($P = .09$), pattern of extension ($P = .89$), TTV ($P = .95$), or ETV ($P = .39$). Patient characteristics are summarized in Table 1. The median OS time was 10.3 months (interquartile range, 7.4–14.9 months). The respective 1-, 2-, and 5-year OS rates were 38.20% (95% CI, 29.89%–46.39%), 8.40% (95% CI, 4.45%–13.92%), and 0.76% (95% CI, 0.07%–3.82%). Kaplan-Meier curve OS rates of the cohort are shown in Fig 3. Analysis showed no difference in survival between age groups ($P = .65$).

Extrapontine Lesion Extension

Baseline tumor volumes are summarized in Table 2. On the initial diagnostic MR imaging, 95.4% ($n = 125$) of the tumors had at least 1 EPLE. The mean TTV, PTV, and ETV were 40.0279 cm³ (range, 8.9750–110.8010 cm³), 36.1874 cm³ (range, 8.9750–100.8550 cm³), and 4.03311 cm³ (range, 0.2840–16.9780 cm³), respectively (Table 2). The most common extension of EPLE was into the midbrain 83.2% ($n = 109$), and the least common extension of EPLE, though still present in 61.8% of tumors, was into the MCPs ($n = 81$). Only 5.3% ($n = 7$) of tumors had

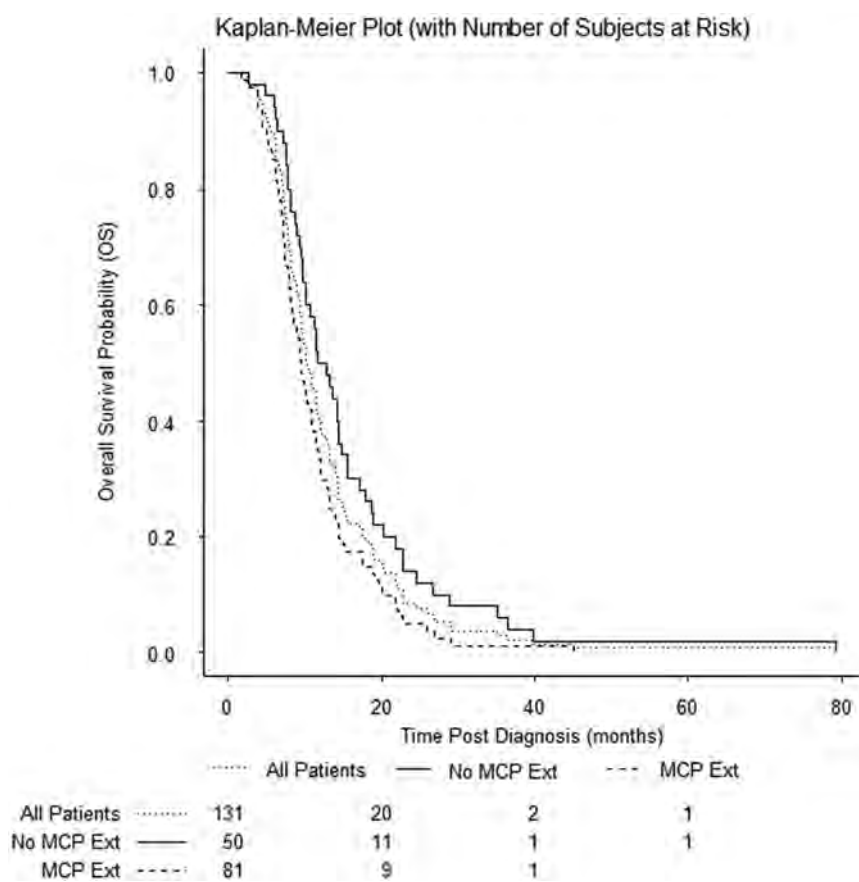


FIG 3. Kaplan-Meier plot of OS of the cohort. Any extension (Ext) into the middle cerebellar peduncles was prognostic of shorter overall survival ($P = .01$).

Table 2: Tumor volumes at baseline

VOI	No. (%)	Mean Volume (cm ³) (Range)	No. Enhancing (%)
TTV	131 (100.0)	40.0279 (8.9750–110.8010)	106 (80.92)
PTV	131 (100.0)	36.1874 (8.9750–100.8550)	
ETV	125 (95.4)	4.03311 (0.2840–16.9780)	42 (33.6)
EPL, medulla oblongata	101 (77.1)	0.96112 (0.1910–4.5400)	9 (8.91)
EPL, right MCP	44 (33.6)	1.9368 (0.0410–7.4560)	14 (31.1)
EPL, left MCP	44 (33.6)	1.7811 (0.0750–7.8440)	6 (11.54)
EPL, any MCP	81 (61.8)	2.0196 (0.0410–7.8440)	18 (22.22)
EPL, midbrain	109 (83.2)	2.23375 (0.1380–11.9460)	23 (21.50)

both right and left MCP extensions. Of the 16 potential combination patterns (>1 EPL associated with a tumor), 11 were present in the study population as shown in Fig 4. Most interesting, no horizontal EPL was present without the concurrent presence of at least 1 vertical EPL, either into the medulla oblongata or the midbrain.

The presence of any MCP extension was associated with shorter survival ($P = .01$) on univariate analysis, but the volume of EPL into the MCPs was not significant as a predictor of poorer OS ($P = .07$). When we compared patterns of EPL, patients with tumors with both vertical EPLs without horizontal EPL experienced significantly longer survival than did patients with any other pattern of EPL ($P < .001$) or those without any EPL ($P = .04$). The TTV, ETV (overall EPL burden), and PTV were not significantly associated with OS.

Postcontrast Enhancement

At diagnosis, 80.92% of tumors ($n = 106$) had some degree of postcontrast enhancement. Of those with enhancement, 50.9% ($n = 54$) were ring-enhancing lesions. A number of tumors (22.1%, $n = 29$) also showed occult enhancement, which we have previously identified as a potential marker of angiogenesis.⁷ Of 125 tumors with EPL, 33.6% ($n = 42$) showed enhancement in at least 1 EPL. The presence of postcontrast enhancement in individual EPLs is summarized in Table 3. Enhancement of individual EPLs was not associated with OS, PFS, an EPL pattern, or TTV. The presence of any postcontrast enhancement at diagnosis was associated with increased ETV ($P = .02$) and shorter OS ($P = .01$), and enhancement of an EPL into the midbrain was associated with increased ETV ($P = .01$). The presence of ring enhancement was also associated with increased ETV ($P = .01$). The presence of an MCP extension was not associated with the presence of enhancement ($P = .36$), ring enhancement ($P = .82$), or metastatic disease at progression ($P = 1.00$).

DISCUSSION

Our study, capitalizing on the largest single-center patient cohort to date, demonstrates that EPLs are very common in DIPG and that their identification and quantitative analysis are feasible and, potentially, worthwhile in the clinical setting. Semiautomated segmentation enabled us to efficiently determine the frequency of the individual forms of EPL and the various patterns defined by their possible combinations. We then found statistically significant correlations between horizontal EPL (toward the MCPs) and shorter OS and vertical EPL and longer survival, findings that have not been reported previously. We, therefore, submit that vertical and horizontal EPLs should be evaluated separately because their effects on survival appear to have different, possibly opposing influences. Beyond their prognostic value, these findings may have implications for the targeting and dosing strategies used in fractionated conformal radiation therapy (RT), which provide only temporary relief but are the cornerstone of current treatment for DIPG. We think that these findings are meaningful additions to the existing body of the clinical and imaging knowledge base in DIPG.

The current overhaul of the definition of DIPG, including the poorly understood clinical implications, represents a limitation of

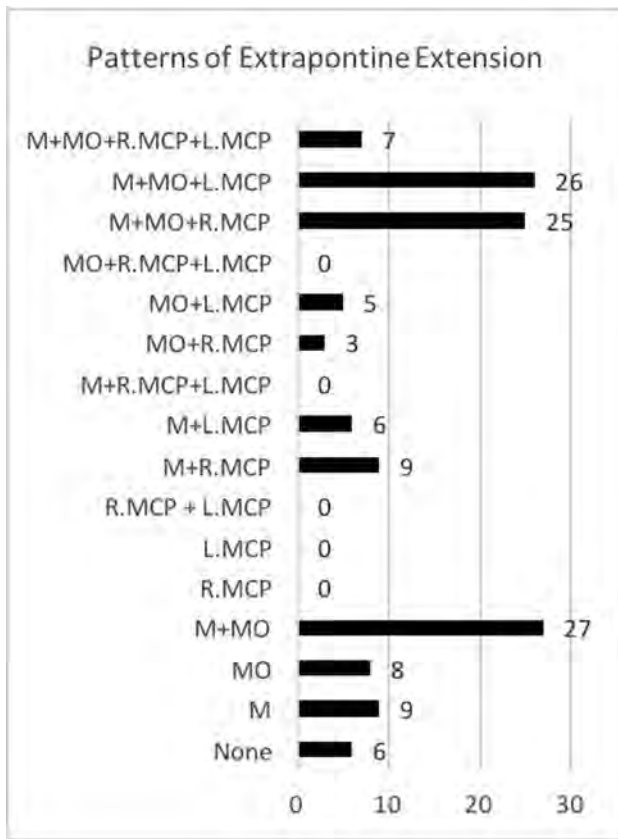


FIG 4. Frequency of patterns of extrapontine lesion extension. M indicates midbrain; MO, medulla oblongata; L.MCP indicates left middle cerebellar peduncle; R.MCP, right middle cerebellar peduncle.

Table 3: Postcontrast enhancement in individual EPLEs

VOI	No. Enhancing (%)
EPLE, medulla oblongata	9 (8.91)
EPLE, right MCP	14 (31.11)
EPLE, left MCP	6 (11.54)
EPLE, any MCP	18 (22.22)
EPLE, midbrain	23 (21.50)

our study. Because our study was retrospective and based on historical data, we used the now-obsolete term DIPG. This is, however, true for all previous similar studies, and we anticipate that large-scale prospective studies using the current, integrated approach introduced in the latest World Health Organization classification may not be available for several years. Another limitation of our study stems from the evolution of treatment regimens explored in our patients during the 17-year review period.^{12,13} While the course of treatment was not analyzed in this study, changing protocols and the use of different chemotherapeutic or other tumor-targeted agents across the cohort should be considered. We found no significant difference in OS between patients treated in the 2 largest trials included in the cohort ($P = .480$). After all, treatment heterogeneity is inevitable, given that no effective treatments for DIPG beyond RT have been identified and that new trials using novel agents must be constantly developed.

Approximately 80% of tumors radiographically diagnosed as DIPG in the past are thought to correspond to diffuse

midline glioma H3 K27M-mutant neoplasms. Potentially clinically relevant, differences among H3 wild-type, H3.1-, and H3.3-mutant tumors have been recognized recently in several reports.^{2,18} Unfortunately, the imaging and some of the biologic correlates of these tumor subgroups are still poorly understood because no consistent imaging features have been found to identify H3 K27M-mutant high-grade gliomas or to distinguish those from H3 wild-type tumors within the pons or elsewhere. This distinction depends on the availability of a biopsy at diagnosis or retrospectively at the time of postmortem examination; despite the recent advances in our understanding of the molecular and epigenetic underpinnings of DIPG (and other pediatric high-grade gliomas), the diagnosis of pediatric brain stem malignancies continues to rely heavily on imaging because of the persistently low rates of tissue biopsy at presentation (<15%) in most countries, including the United States.

The lack of biopsy in our cohort represents a limitation of our study too. However, recent reports demonstrating the feasibility and accuracy of detecting H3 mutations in circulating tumor DNA within biofluids in these patients hold promise for minimally invasive diagnostic approaches in the future.^{19,20} In the meantime, the devastating nature of DIPG, and the lack of therapeutic advances necessitate the continued search for robust imaging biomarkers in pediatric DIPG/DMG in the pursuit of enhanced prognostication and risk stratification at the time of diagnosis.

In prior studies, the methods for evaluating tumor volume have been inconsistent, while the description of the various EPLE patterns and the quantitative determination of the overall EPLE burden have been lacking. It is, therefore, difficult to estimate the contribution of EPLE to the overall lesion volume and its potential prognostic impact in those studies because the various forms and patterns of EPLE are not explicitly specified.⁵

In contrast, the strengths of our study include consistent imaging protocols across various patient subcohorts, a robust and highly automated imaging data analysis and processing pipeline, and the systematic use of tumor volume quantification instead of the descriptive approach used in prior studies. We also report demographic, expanded survival, and other data that have been sparsely available (eg, the frequency of leptomeningeal metastatic spread at the end of PFS). We report specific patterns of metastasis intracranially, intraspinally, or both and their prevalence in this cohort as well as a significant relationship between the presence of metastatic disease in the brain and spinal cord at progression with shorter PFS ($P = .01$). The significance of this relationship is difficult to determine because the presence of metastatic disease was a criterion for progression in this cohort.

We have quantified the presence of postcontrast lesion enhancement in this cohort and identified relationships between the presence of any enhancement at diagnosis and increased TLV and ETV as well as between enhancement at diagnosis and poorer OS.

Our research confirms that EPLE into the midbrain, the medulla oblongata, and the MCPs is common in DIPG and suggests

that differences in survival outcomes exist among various patterns of EPLE. We propose 2 specific patterns of EPLE as predictors of OS in newly diagnosed DIPG; thus, our findings may be valuable for risk stratification in future clinical trials for children with newly diagnosed DIPG.

The findings of shorter survival in patients with any horizontal extension into the cerebellar peduncles and an apparent survival benefit in patients with craniocaudal EPLE without horizontal EPLE may have ramifications for RT targeting and treatment planning. It is possible that only the presence or absence of horizontal EPLE is the prognostically determinant factor. On the basis of limited postmortem examinations and patterns-of-failure studies, focal irradiation rather than whole-brain RT has been most commonly recommended for patients with DIPG.²¹⁻²³ In the era of 3D conformal RT, clinical target volumes have ranged between 1 and 2 cm and have been expanded in an isotropic fashion.^{13,23} Although further work is needed to evaluate the patterns of failure and routes of spread after conformal RT, findings from this study suggest that a potential avenue of treatment intensification could include a “boost” dose RT to horizontal tumor extensions. Additionally, these data provide the opportunity to examine the extent of EPLE across these 3 principal directions of spread at diagnosis, with the goal of identifying rational nonisotropic clinical target volume margins.

CONCLUSIONS

EPLE in newly diagnosed DIPG is common. In a large cohort of patients with newly diagnosed DIPGs, we determined that the presence of EPLE into either MCP is predictive of shorter OS. We conclude that the identification and quantitative analysis of EPLEs in DIPG are feasible, with potential clinical uses in the prognostication of DIPG at diagnosis and in the targeting and dosing strategies used in fractionated conformal RT.

Disclosures: Lydia Makepeace—*RELATED: Grant:* National Institutes of Health, National Cancer Institute, *Comments:* National Institutes of Health Cancer Center Support Grant P30 CA21765, Pediatric Oncology Education grant paid to me; National Cancer Institute grant R25CA23944, institutional grant.* Christopher L. Tinkle—*UNRELATED: Payment for Manuscript Preparation:* UpToDate, ependymoma chapter. Scott Hwang—*UNRELATED: Employment:* I am employed as a neuroradiologist; *Grants/Grants Pending:* National Institutes of Health. *Comments:* Five percent of my effort is supported by a grant for sickle cell anemia; 9% of my effort is supported by a grant for looking at sleep apnea in Hodgkin lymphoma survivors who received radiation therapy*; *Stock/Stock Options:* I have stocks. None of these has any relationship to the research in the article; *Travel/Accommodations/Meeting Expenses Unrelated to Activities Listed:* My employer provides a small fund for professional development, which includes travel and room and board for Continuing Medical Education and other academic conferences. None was used for this article. Zoltan Patay—*RELATED: Grant:* National Institutes of Health, ALSAC, *Comments:* This work was supported by the National Institutes of Health Cancer Center Support Grant P30 CA21765, the National Cancer Institute grant R25CA23944, and ALSAC*; *UNRELATED: Consultancy:* Guerbet, *Comments:* Guerbet Medical Advisory Meeting, Chicago, July 17, 2016, honorarium; *Travel/Accommodations/Meeting Expenses Unrelated to Activities Listed:* National Hospital for Neurology and Neurosurgery, University College, London, UK; Radiological Society of Sao Paulo; Hungarian Society of Neuroradiology; Turkish Society of Neuroradiology; European Congress of Magnetic Resonance in Neuropediatrics; European Society of Neuroradiology, *Comments:* visiting professorship, National Hospital for Neurology and Neurosurgery, University College, London, UK; invited speaker, Radiological Society of Sao Paulo, Brazil; invited

speaker, Hungarian Society of Neuroradiology; invited speaker, Turkish Society of Neuroradiology; invited speaker, European Congress of Magnetic Resonance in Neuropediatrics; invited speaker, European Society of Neuroradiology. *Money paid to the institution.

REFERENCES

- Dang M, Phillips PC. **Pediatric brain tumors.** *Continuum (Minneapolis)* 2017;23:1727–57 CrossRef Medline
- Hoffman LM, Veldhuijzen van Zanten SE, Colditz N, et al. **Clinical, radiologic, pathologic, and molecular characteristics of long-term survivors of diffuse intrinsic pontine glioma (DIPG): a collaborative report from the International and European Society for Pediatric Oncology DIPG Registries.** *J Clin Oncol* 2018;36:1963–72 CrossRef Medline
- Tisnado J, Young R, Peck KK, et al. **Conventional and Advanced Imaging of Diffuse Intrinsic Pontine Glioma.** *J Child Neurology* 2016;31:1386–93
- Barkovich AJK, Kun J, Packer LE, et al. **Brain stem gliomas: a classification system based on magnetic resonance imaging.** *Pediatr Neurosurg* 1990–1991;16:73–83 CrossRef Medline
- Hargrave D, Chuang N, Bouffet E. **Conventional MRI cannot predict survival in childhood diffuse intrinsic pontine glioma.** *J Neurooncol* 2008;86:313–19 CrossRef Medline
- Jackson S, Patay Z, Howarth R, et al. **Clinico-radiologic characteristics of long-term survivors of diffuse intrinsic pontine glioma.** *J Neurooncol* 2013;114:339–44 CrossRef Medline
- Conway AE, Reddick WE, Li Y, et al. **“Occult” post-contrast signal enhancement in pediatric diffuse intrinsic pontine glioma is the MRI marker of angiogenesis?** *Neuroradiology* 2014; 56:405–12 CrossRef Medline
- Jansen MH, Veldhuijzen van Zanten SE, Sanchez Aliaga E, et al. **Survival prediction model of children with diffuse intrinsic pontine glioma based on clinical and radiological criteria.** *Neuro Oncol* 2015;17:160–66 CrossRef Medline
- Lober RM, Cho YJ, Tang Y, et al. **Diffusion-weighted MRI derived apparent diffusion coefficient identifies prognostically distinct subgroups of pediatric diffuse intrinsic pontine glioma.** *J Neurooncol* 2014;117:175–82 CrossRef Medline
- Poussaint TY, Vajapeyam S, Ricci KI, et al. **Apparent diffusion coefficient histogram metrics correlate with survival in diffuse intrinsic pontine glioma: a report from the Pediatric Brain Tumor Consortium.** *Neuro Oncol* 2016;18:725–34 CrossRef Medline
- Poussaint TY, Kocak M, Vajapeyam S, et al. **MRI as a central component of clinical trials analysis in brainstem glioma: a report from the Pediatric Brain Tumor Consortium (PBTC).** *Neuro Oncol* 2011;13:417–27 CrossRef Medline
- Broniscer A, Baker JN, Tagen M, et al. **Phase I study of vandetanib during and after radiotherapy in children with diffuse intrinsic pontine glioma.** *J Clin Oncol* 2010;28:4762–68 CrossRef Medline
- Broniscer A, Baker SD, Wetmore C, et al. **Phase I trial, pharmacokinetics, and pharmacodynamics of vandetanib and dasatinib in children with newly diagnosed diffuse intrinsic pontine glioma.** *Clin Cancer Res* 2013;19:3050–58 CrossRef Medline
- Wetmore C, Turner D, Kun L, et al. **PDCT-10: First in Pediatrics Phase I Study of Crenolanib Besylate (CP-868, 596-26) Administered During and After Radiation Therapy (RT) in Newly-Diagnosed Diffuse Intrinsic Pontine Glioma (DIPG) and Recurrent High Grade Glioma (HGG).** *Neuro Oncol* 2016;18:v147–48
- Wang G, Li W, Ourselin S, Vercauteren T. **Automatic brain tumor segmentation using convolutional neural networks with test-time augmentation.** In: Crimi A, Bakas S, Kuijff H, Keyvan F, Reyes M, van Walsum T. eds. *Brainlesion: Glioma, Multiple Sclerosis, Stroke and Traumatic Brain Injuries.* BrainLes 2018, LNCS, 11384. Cham: Springer, 2019;61–72
- Fedorov A, Beichel R, Kalpathy-Cramer J, et al. **3D Slicer as an image computing platform for the Quantitative Imaging Network.** *Magn Reson Imaging* 2012;30:1323–41 CrossRef Medline

17. 3D Slicer. 2018. <http://www.slicer.org>. Version 4.4.0 (2016)
18. Castel D, Philippe C, Calmon R, et al. **Histone H3F3A and HIST1H3B K27M mutations define two subgroups of diffuse intrinsic pontine gliomas with different prognosis and phenotypes.** *Acta Neuropathol* 2015;130:815–27 CrossRef Medline
19. Aboian MS, Solomon DA, Felton E, et al. **Imaging characteristics of pediatric diffuse midline gliomas with histone H3 K27M mutation.** *AJNR Am J Neuroradiol* 2017;38:795–800 CrossRef Medline
20. Huang TY, Piunti A, Lulla RR, et al. **Detection of histone H3 mutations in cerebrospinal fluid-derived tumor DNA from children with diffuse midline glioma.** *Acta Neuropathol Commun* 2017;5:28 CrossRef Medline
21. Mantravadi RV, Phatak R, Bellur S, et al. **Brain stem gliomas: an autopsy study of 25 cases.** *Cancer* 1982;49:1294–96 CrossRef Medline
22. Halperin EC. **Pediatric brain stem tumors: patterns of treatment failure and their implications for radiotherapy.** *Int J Radiat Oncol Biol Phys* 1985;11:1293–98 CrossRef Medline
23. Haas-Kogan DA, Banerjee A, Kocak M, et al. **Phase I trial of tipifarnib in children with newly diagnosed intrinsic diffuse brainstem glioma.** *Neuro Oncol* 2008;10:341–47 CrossRef Medline

Frequency, Extent, and Correlates of Superficial Siderosis and Ependymal Siderosis in Premature Infants with Germinal Matrix Hemorrhage: An SWI Study

M.S. Albayram, G. Smith, F. Tufan, and M.D. Weiss

ABSTRACT

BACKGROUND AND PURPOSE: Germinal matrix intraventricular hemorrhage is a common complication of prematurity. An underrecognized complication of germinal matrix intraventricular hemorrhage is superficial siderosis, and the clinical consequences of superficial siderosis are not well-known. We aimed to investigate the prevalence, anatomic distribution, and severity of superficial siderosis and ependymal siderosis in premature infants with germinal matrix intraventricular hemorrhage using SWI.

MATERIALS AND METHODS: In this retrospective study, we included 88 patients across all grades of germinal matrix intraventricular hemorrhage who underwent MR imaging at term-equivalent age. Images were evaluated for the presence, distribution, and severity of superficial siderosis and ependymal siderosis. Univariate and multivariate logistic regression analyses were performed to determine factors associated with superficial siderosis and ependymal siderosis. The agreement among T1, T2, and SWI sequences was examined.

RESULTS: Seventy-two patients had brain stem superficial siderosis, and 79 patients had ependymal siderosis. The presence, extent, and severity of superficial siderosis and ependymal siderosis were closely related to the grade of germinal matrix intraventricular hemorrhage and intraventricular hematoma volume. Brain stem superficial siderosis had a stronger correlation with intraventricular hemorrhage than with cerebellar hemorrhage. Compared with SWI, T1 and T2 sequences detected only small proportions of patients with superficial siderosis (12.5% and 6.9%, respectively).

CONCLUSIONS: The incidence of superficial siderosis and ependymal siderosis is very high in preterm infants with germinal matrix intraventricular hemorrhage when assessed by SWI at term-equivalent age. The presence and extent of superficial siderosis and ependymal siderosis are closely related to germinal matrix intraventricular hemorrhage grade and intraventricular hematoma volume. Additional prospective studies using SWI are needed to clearly determine the clinical consequences of germinal matrix intraventricular hemorrhage with superficial siderosis and ependymal siderosis.

ABBREVIATIONS: CN = cranial nerve; ES = ependymal siderosis; GM-IVH = germinal matrix intraventricular hemorrhage; HUS = head ultrasound; SS = superficial siderosis; TVHV = total ventricular hematoma volume

Superficial siderosis (SS) of the CNS is a disease characterized by deposition of hemosiderin, a by-product of the breakdown of red blood cells, into subpial layers of CNS tissue caused by chronic or recurrent bleeding into the subarachnoid space.^{1,2} In adults, most cases of CNS SS present with sensorineural hearing loss and cerebellar ataxia. Myelopathy, polyradiculopathy, anosmia, and dementia may also be present.^{1,2} Despite the attention

afforded to imaging findings and clinical sequelae of adult SS, few studies have described SS, ependymal siderosis (ES), or similar pathology occurring after germinal matrix intraventricular hemorrhage (GM-IVH) in premature infants.³⁻⁵ To the best of our knowledge, no previous study has investigated the relationship of GM-IVH to SS or ES using primarily SWI, the most sensitive MR imaging for the detection of hemorrhage and siderosis.⁶⁻⁸

This study aimed to investigate the prevalence and anatomic distribution of SS and ES in premature infants with GM-IVH of different severities using SWI to assess the relationship of GM-IVH grade with the presence of SS in the cranial nerve (CN) VII/VIII complex and to determine the factors primarily associated with brain stem SS. We hypothesized that GM-IVH grade and volume would be positively related to the severity of SS and ES.

Received September 23, 2019; accepted after revision November 12.

From the Departments of Radiology (M.S.A., G.S.) and Pediatrics (M.D.W.) University of Florida College of Medicine, Gainesville, Florida; and Silivrikapi mh Hisaralti cd. Fatih sitesi A1/9 (F.T.), Fatih, Istanbul, Turkey.

Please address correspondence to Mehmet Sait Albayram, MD, Department of Radiology, University of Florida College of Medicine, PO Box 100374, Gainesville, FL 32610-0374; e-mail: albaym@radiology.ufl.edu
<http://dx.doi.org/10.3174/ajnr.A6371>

MATERIALS AND METHODS

Study Population

Patients with GM-IVH who underwent MR imaging in our institution (Department of Radiology, University of Florida College of Medicine) between 2011 and 2018 were identified by a search in our electronic data base for the key words “germinal matrix hemorrhage.” The study was approved by the institutional review board, and parental informed consent was obtained. Sex, birth weight, and gestational age at birth were noted. Inclusion criteria were as follows: 1) a history of GM-IVH diagnosed on head ultrasound (HUS) within 3 weeks after birth, and 2) the availability of at least 1 MR imaging study of diagnostic quality including axial SWI, T1, and T2-weighted imaging at term-equivalent age. Patients were excluded from the study if the quality of imaging was insufficient to recognize the presence of SS, if additional clinical diagnoses such as meningitis or abscess were present, or if MR imaging was performed before term-equivalent age. Patients in whom GM-IVH was detected on HUS but not MR imaging were also excluded.

Image Acquisition

MR imaging was performed on a 1.5T scanner (Avanto; Siemens, Erlangen, Germany) or a 3T scanner (Verio; Siemens) between 2011 and 2018 with a multichannel head coil in our radiology department. At our institution, MR imaging in neonates is routinely performed without sedation or general anesthesia. MR imaging was typically performed at term-equivalent age before discharge. For each patient, axial SWI was performed. Magnitude images, SWI, and SWI–minimum-intensity-projection images were obtained automatically from the scanner.

Image Analysis

Analysis of all images was performed by M.S.A., a neuroradiology attending physician with extensive experience in neuroimaging research. GM-IVH grading and measurements of hematoma size were performed using the patients' HUS studies during the acute GM-IVH phase for the purpose of this study. The Papile classification was used for grading of GM-IVH with respect to the findings of the HUS examination in which hemorrhage was detected.⁹ GM-IVH and cerebellar hemorrhage dimensions (anterior-posterior [AP], craniocaudal [CC], and transverse diameter) were recorded in each hemisphere, and GM-IVH volume was calculated by the ellipsoid volume formula $AP \times CC \times \text{transverse} \times \pi/6$ for each hemisphere.¹⁰ Total dimensions of the ventricular hematoma included both germinal matrix and ventricular hemorrhage values combined. All calculations, visual evaluations, and measurements were performed on the PACS software (Visage; <http://www.visageimaging.com>). The presence of SS and ES was visually determined using magnitude, SWI, and minimum-intensity-projection SWI. Measurements of SS or ES depth were made using SWI.

The presence or absence of siderosis and maximal siderosis depth measurements were recorded from the bilateral lateral ventricles, bilateral lateral ventricular choroid plexuses, ependyma of the third ventricle, choroid plexus of the third ventricle, ependyma of the fourth ventricle, choroid plexus of the fourth ventricle, vermis of the cerebellum, bilateral cerebellar hemispheres,

pons, mesencephalon, medulla oblongata, and spinal cord. The presence or absence of SS in the CN VII/VIII complex was also noted. Last, the distributions of SS in the spinal cord, medulla oblongata, pons, and mesencephalon were visually estimated as 0°, 90°, 180°, 270°, or 360° (0° denoting no SS and 360° denoting SS around the entire perimeter of a structure).

Statistics

Statistical analysis was performed using SPSS 20.0 (IBM, Armonk, New York). The normality of distribution of continuous data was assessed with the Kolmogorov-Smirnov or Shapiro-Wilk tests. Categorical variables were presented as frequencies and percentages, and continuous variables were presented as mean \pm SD or median (minimum-maximum) when appropriate. Categorical variables were compared using χ^2 and Fisher exact tests, and continuous variables were compared using Mann-Whitney *U*, Student *t*, ANOVA, or Kruskal-Wallis tests. The correlations between variables were assessed using Pearson or Spearman correlation tests. Binary logistic regression was performed to determine factors independently associated with the presence of SS in the brain stem. The variables associated with brain stem SS in univariate analyses were included in logistic regression models. Because of the strong correlation between GM-IVH grade and total ventricular hematoma volume (TVHV), 2 separate logistic-regression models were used, each including one of these factors. The level of agreement between MR imaging sequences in the detection of brain stem SS was analyzed using κ analysis. Statistical significance was established at $P < .05$.

RESULTS

A total of 88 patients (52 males and 36 females) with GM-IVH were included. The mean gestational age at birth was 27.5 ± 2.9 weeks. The mean birth weight was 1110.6 ± 505.6 g. The mean durations between birth and HUS and MR imaging examinations were 6.1 ± 3.3 days and 68.5 ± 32.7 days, respectively. There were 22 patients in each GM-IVH grade group. While 33 patients had cerebellar hematoma (median volume, 14.7 mm^3 ; minimum-maximum volume, $0.5\text{--}6333 \text{ mm}^3$), siderosis was present in the ependymal zone of 79 (Fig 1), brain stem of 72 (Fig 2), cerebellar vermis of 53, cerebellum of 31, and CNs VII and VIII of 42. All patients with brain stem SS and 6/15 of patients without brain stem SS had ES. All patients with cerebellar SS also had cerebellar vermis SS, and all patients with cerebellar vermis SS also had brain stem SS. Supratentorial SS was detectable in 34% (30/88), mainly in the Sylvian fissures bilaterally. Convexity SS was present only in 2 patients (2.2%). Table 1 documents the relationship of GM-IVH grade to patient demographics, presence or absence of siderosis, and depth of siderosis in different anatomic locations.

Brain stem SS and ES were significantly more common in the GM-IVH grades II, III, and IV compared with the GM-IVH grade I group ($P < .001$ for all comparisons). The depth of brain stem SS increased with higher GM-IVH grades (for grades I–III, $P < .001$ for all comparisons) and was similar between patients with grade III and grade IV GM-IVH. Brain stem SS distribution and ventricular ependymal SS depth also increased in parallel

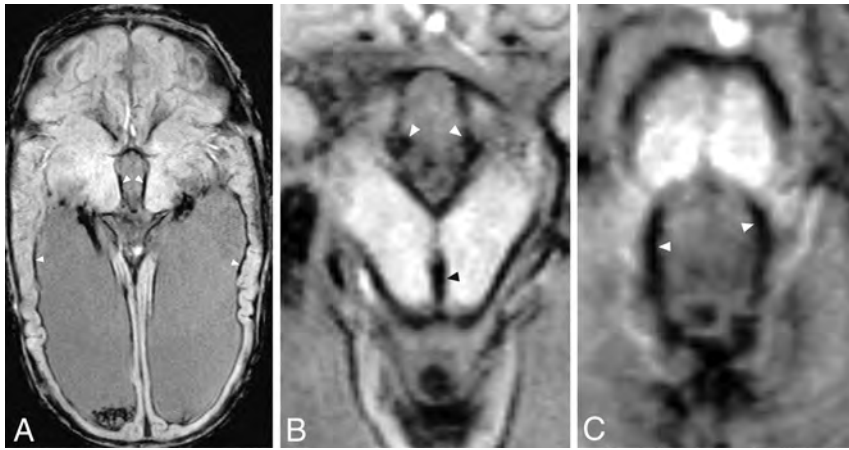


FIG 1. Axial SWI of a premature male infant born at 30 weeks' gestation diagnosed with grade III GM-IVH shows significant siderosis in the ependymal surfaces at the level of the lateral ventricles (A, arrowheads), third ventricle (B, white arrowheads), cerebral aqueduct (B, black arrowhead), and fourth ventricle (C, arrowheads). MR imaging was performed 14 weeks after birth. Note significant SS around the mesencephalon and pons.

with the severity of GM-IVH grade ($P < .001$ for all comparisons, Table 1 and Fig 3). While the incidence of cerebellar SS tended to be greater in higher GM-IVH grades ($P = .009$), the incidence of cerebellar hematoma was similar among GM-IVH grade groups. The median cerebellar SS depth increased in parallel with the severity of GM-IVH grade ($P = .001$, Table 1). While the TVHV significantly increased in higher GM-IVH grade groups ($P < .001$), there was no such trend for cerebellar hematoma volume ($P = .12$).

In the present study, we detected a significant SWI signal decrease, suggestive of blood products, on the surface of the CN VII and VIII complex (Fig 4). This finding was seen in 47% of patients in the present study (42/88).

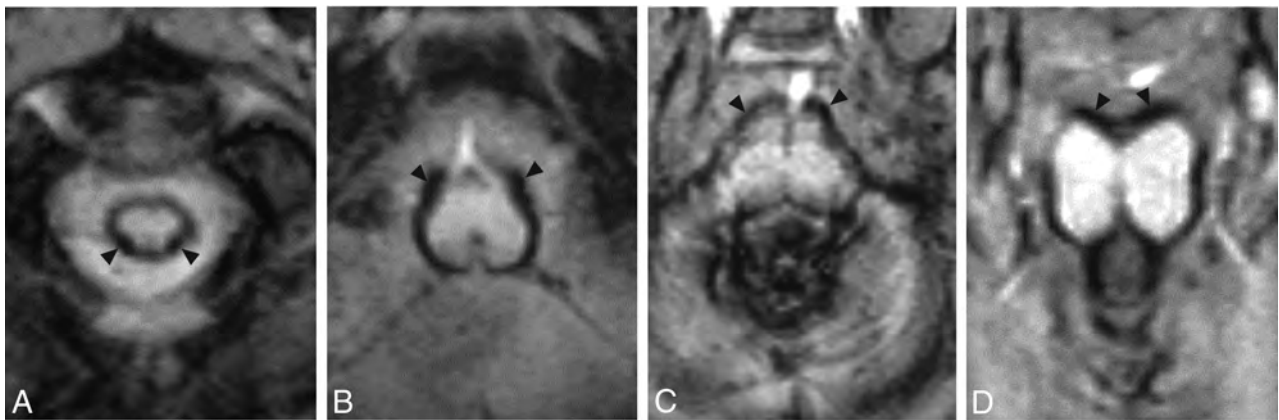


FIG 2. Axial SWI depicting SS in the same patient as in Fig 1 at the level of the cervical spinal cord (A), medulla oblongata (B), pons (C), and mesencephalon (D). Arrowheads indicate the point of maximal SS depth within each structure. Note the circumferential distribution of SS around each of these brain stem structures and significant vermian SS.

Table 1: Comparison of GM-IVH groups for study variables^a

GM-IVH Grade	I	II	III	IV	P
Brain stem SS (%)	45.5	95.5	95.5	95.5	<.001
Brain stem SS distribution	0 (140.6)	168.8 (140.6)	213.8 (106.9)	247.5 (163.1)	<.001
Spinal cord SSD (mm)	0 (0–0.8)	0.65 (0–1.1)	0.8 (0–1.5)	0.75 (0–1.5)	<.001
Medulla oblongata SSD (mm)	0 (0–0.8)	0.75 (0–1.2)	1 (0–1.7)	1 (0–2)	<.001
Pons SSD (mm)	0 (0–1.2)	0.6 (0–1.1)	0.8 (0–1.7)	0.85 (0–1.8)	<.001
Mesencephalon SSD (mm)	0 (0–0.9)	0.6 (0–1.1)	0.8 (0–1.6)	0.8 (0–2.3)	<.001
Lateral ventricle SSD (mm)	0.5 (0–1)	0.9 (0–3.3)	1 (0–2)	0.95 (0.4–2.5)	<.001
Third ventricle SSD (mm)	0 (0–0.2)	0 (0–1.6)	0 (0–2.2)	0.6 (0–1.2)	<.001
Fourth ventricle SSD (mm)	0 (0–0.8)	0.1 (0–0.9)	0.4 (0–1.9)	0.65 (0–2.2)	<.001
CN VII/VIII siderosis (%)	9.1	54.5	72.7	54.5	<.001
Total ventricular HV on HUS (mm ³)	64.9 (79.8)	491.1 (358.7)	2168.7 (2469)	4319.4 (9731.5)	<.001
Total cerebellar HV (mm ³)	0 (0–13.6)	0 (0–6333)	0 (0–530)	0.5 (0–1123)	.12
Cerebellar SS present (%)	31.8	77.3	72.7	59.1	.009
Cerebellar SS depth (mm)	0 (0–0.25)	0.3 (0–2)	0.35 (0–2.1)	0.43 (0–2.2)	.001
Cerebellar hematoma present (%)	27.3	45.5	27.3	50	.26

Note:—HV indicates hematoma volume; SSD, superficial siderosis depth.

^aNumeric variables are presented as median (minimum–maximum).

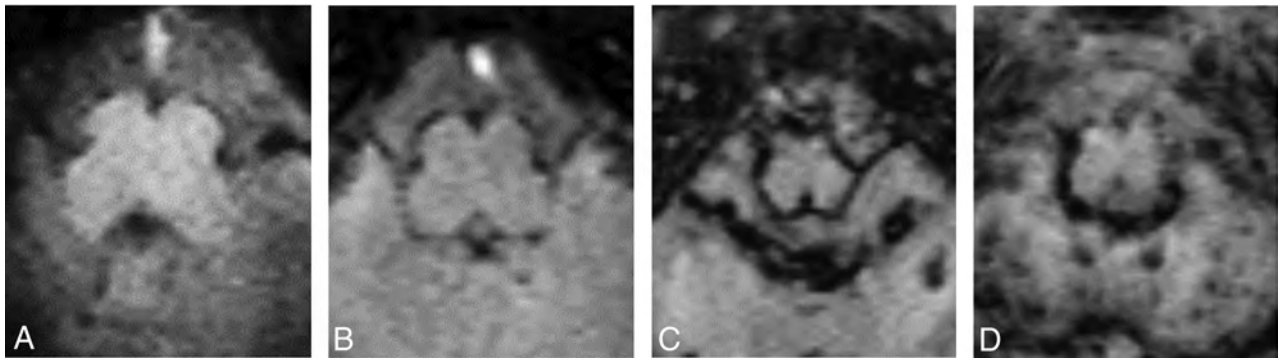


FIG 3. Sample axial SWI views at the level of the medulla oblongata in infants diagnosed with GM-IVH grades I (A), II (B), III (C), and IV (D). Note that severity of SS, measured by SS depth and distribution, increases from lower grade to higher grade GM-IVH. Also note the multiple punctate hemorrhages seen in the cerebellum in grades III and IV GM-IVH.

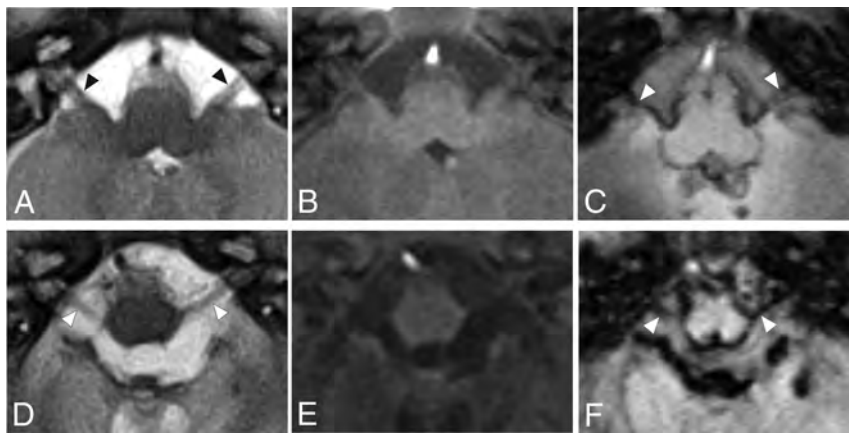


FIG 4. Axial MR images from 2 patients at the level of CNs VII and VIII seen on T2-weighted imaging (A and D), T1-weighted imaging (B and E), and SWI (C and F). The arrowhead indicates the positions of the cisternal segment of CNs VII and VIII. Leptomeningeal thickening and significant iron accumulation can be seen in CNs VII and VIII bilaterally. Images were obtained from a boy born at 28 weeks' gestation with grade III GM-IVH (A–C) and a boy born at 24 weeks' gestation with grade III GM-IVH (D–F).

The incidence of CN VII and VIII SS increased in parallel with GM-IVH grades for grades I–III (linear-by-linear association $P < .001$), but the grade IV group had a rate equivalent to that of the grade II group (Table 1). The strongest correlations with the presence of CN VII and VIII SS were siderosis of the lateral ventricle ($r = 0.62$, $P < .001$) and choroid plexus of the fourth ventricle ($r = 0.6$, $P < .001$).

The GM-IVH grade and TVHV had moderate-to-strong positive correlations with brain stem (r range, 0.52–0.6; $P < .001$ for all), cerebellar ($r = 0.37$, $P < .001$), and ventricular ES depth (r range, 0.4–0.67; $P < .001$ for all) (Table 2). Cerebellar hematoma volume had positive-but-weak correlations with brain stem SS depth measurements (r range, 0.2–0.34; P range, .001–.06) and a moderate and positive correlation with cerebellar SS depth ($r = 0.46$, $P < .001$).

The patients with brain stem SS had a significantly higher GM-IVH grade ($P < .001$), ventricular SS depth ($P < .001$), incidence of CN VII and VIII SS ($P < .001$), TVHV ($P < .001$), cerebellar vermis SS depth ($P < .001$), and cerebellar SS depth ($P = .002$) (Table 3). The patients with and without brain stem SS

had similar rates and volumes of cerebellar hematoma and cerebellar vermis hematoma ($P > .05$ for all comparisons).

The binary logistic regression analysis indicated that both GM-IVH grade (model $r^2 = 0.48$; OR = 5.9; 95% CI, 2.1–16.3; $P = .001$) and total ventricle volume (model $r^2 = 0.36$; OR = 1.001; 95% CI, 1–1.003; $P = .04$) had independent and significant associations with the presence of brain stem SS.

Among the patients with brain stem SS, the T1 sequence detected 9/72 patients (12.5%), while the T2 sequence detected 5/72 patients (6.9%). The level of agreement for the presence of brain stem SS between SWI and T1 sequences was 0.049 ($P = .15$), and the level

of agreement between SWI and T2 sequences was 0.026 ($P = .30$).

DISCUSSION

Intracortical injection of ferrous or ferric chloride into the rat or cat cortex causes transient epileptiform discharge, focal edema, and cavitory gliosis.^{11,12} Repeat subarachnoid bleeding and incident circulation of heme in the CSF can result in SS,¹³ a rare disorder characterized by intra- and extracellular hemosiderin deposition into subpial tissues.^{14–16} Neuropathology studies show that SS particularly affects the ventricular ependyma, choroid plexus epithelium, inferior temporal lobes, cerebellum, brain stem, spinal cord, and CNs VII and VIII.^{14–16} Microscopically, the meninges may be thickened and fibrotic,¹⁶ and hemosiderin-laden macrophages and extracellular iron granules can be identified in the subpial brain stem parenchyma, spinal cord, and cerebellum.^{14–16} Cases of brown-staining subpial siderosis and ES have been found extending approximately 2 mm in the spinal cord and 1–3 mm in the brain stem inward into the neural parenchyma.^{14,16} Central chromatolysis in the anterior horn cells and

Table 2: Correlations between GM-IVH grades and hematoma volumes with SS^a

	GM-IVH Grade		Total Ventricular HV (mm ³)		Cerebellar HV (mm ³)	
	<i>r</i>	<i>P</i>	<i>r</i>	<i>P</i>	<i>r</i>	<i>P</i>
	Spinal cord SSD (mm)	0.55	<.001	0.55	<.001	0.29
Medulla oblongata SSD (mm)	0.60	<.001	0.63	<.001	0.30	.005
Pons SSD (mm)	0.52	<.001	0.61	<.001	0.20	.06
Mesencephalon SSD (mm)	0.59	<.001	0.62	<.001	0.34	.001
Brain stem SS distribution	0.54	<.001	0.62	<.001	0.25	.018
Lateral ventricle SSD (mm)	0.48	<.001	0.51	<.001	0.32	.02
Third ventricle SSD (mm)	0.46	<.001	0.66	<.001	0.28	.009
Fourth ventricle SSD (mm)	0.44	<.001	0.59	<.001	0.21	.049
Choroid lateral ventricle SSD (mm)	0.67	<.001	0.72	<.001	0.26	.013
Choroid third ventricle SSD (mm)	0.61	<.001	0.73	<.001	0.32	.003
Choroid fourth ventricle SSD (mm)	0.40	<.001	0.47	<.001	0.23	.03
Cerebellar SSD (mm)	0.37	<.001	0.50	<.001	0.46	<.001
Total ventricular HV on HUS (mm ³)	0.85	<.001	n/a	n/a	0.22	.04
Cerebellar HV (mm ³)	0.17	.11	0.22	.04	n/a	n/a

Note:—n/a indicates not applicable; HV, hematoma volume; SSD, superficial siderosis depth; HUS, head ultrasound.

^a GMH-IVH hemorrhage was detected by HUS and classified by using the Papile classification.

Table 3: Comparison of patients with and without brain stem SS

	Brain Stem SS Absent (n = 15)	Brain Stem SS Present (n = 73)	<i>P</i>
Gestational age at birth (wk)	28.6 ± 2.9	27.3 ± 2.9	.11
Sex (% male)	53.3	60.3	.62
Birth weight (g)	1299.5 ± 830	1071.7 ± 407.4	.11
GM-IVH grade	I (0)	III (2)	<.001
Total ventricular HV on HUS (mm ³)	91.6 (96.3)	935.1 (2978.8)	<.001
Cerebellar hematoma (%)	20	35.6	.24
Cerebellar HV (mm ³)	0 (0)	0 (7.9)	.12
CV hematoma + (%)	0	19.2	.12
CV HV (mm ³)	0 (0)	0 (0)	.07
Cerebellar SS + (%)	0	42.5	.001
Lateral ventricle SSD (mm)	0 (0–1)	0.9 (0–3.3)	<.001
Third ventricle SSD (mm)	0 (0–0)	0 (0–2.2)	<.001
Fourth ventricle SSD (mm)	0 (0–0)	0.4 (0–2.2)	<.001
CV SS + (%)	0	72.6	<.001
CN VII/VIII SS + (%)	0	57.5	<.001
CV SS depth (mm)	0 (0–0)	0.4 (0–2.8)	<.001
Cerebellar SS depth (mm)	0 (0–0)	0 (0–2.5)	.002

Note:—CV indicates cerebellar vermis; GM-IVH, Germinal matrix intraventricular hemorrhage; HV, hematoma volume; SS, superficial siderosis; CN, cranial nerve; +, positive, pathology found; SSD, superficial siderosis depth.

^a Numeric variables are presented as mean ± SD or median (minimum-maximum) where appropriate.

ovoid/spheroid bodies (a marker distinctive of SS) may also be present between the myelinated axons in the brain stem and in the subpial white matter in the spinal cord.^{13,16} SS commonly presents with hearing impairment,^{1,2} which appears to be related to the vulnerability of CN VIII to SS.

Due to the limited number of human studies of SS and the indolent course of disease progression, studies of SS in animal models have been critical to establish disease pathophysiology and the timing required for pathologic features of the disease to emerge. Studies in which autologous washed blood cells were injected weekly during 3–6 months into the cisterna magna of rabbits identified distinct patterns of iron accumulation extending 1–2 mm in the brain parenchyma after 3 months.^{17,18} These animal studies indicate that bolus infusions of blood products into the ventricular

system are sufficient to induce patterns of neuropathology similar to those seen in human SS within approximately 2–3 months.

Previous studies have documented neuropathologic findings of short-term survivors of intraventricular hemorrhage. One study found that of 20 infants with verified intraventricular hemorrhage who survived for at least 1 week, 9 were found to have clotted blood filling dilated ventricles, suggesting severe GM-IVH and posthemorrhagic hydrocephalus.¹⁹ In all except 1 of these 9 cases, an accumulation of blood pigment was noted in the subarachnoid space. This study did not describe the location of subarachnoid blood products in the posterior fossa. Non-protein-bound iron has been found frequently and at high levels in CSF from preterm infants as early as 2–3 weeks after GM-IVH.²⁰ In premature infants, GM-IVH may also precipitate SS.^{3–5} SS secondary to neonatal intraventricular hemorrhage was first described by Gomori et al,⁴ who reported findings on T2-weighted imaging of superficial hypointensity of the medulla, tectal region, and Sylvian fissures in a neonate patient with bilateral GM-IVH. A later study identified low signal patterns on heavily T2WI consistent with SS in the basal cisterns, along the tentorium, covering the brain stem, and in the Sylvian fissures of 7 infants with previous peri-/intraventricular hemorrhage.³ More recently, Yilmaz et al⁵ reported SS in a retrospective study of 37 patients with a history of GM-IVH. SS was detected using T2-weighted imaging or SWI in 67.6% (25/37) of patients, was present

infratentorially in all 25 patients with SS, with additional supratentorial SS in 27% (10/37). There was no discussion provided about the presence or distribution of SS in the posterior fossa, CNs, brain stem, cerebellum, or spinal cord or the relationship between the severity of GM-IVH and the severity of SS.

In the present study, 81% of preterm infants with GM-IVH showed some degree of SS in the posterior fossa, and 90% showed supratentorial SS. Supratentorial SS was detected in only 34% of cases, mainly in the Sylvian fissures and, rarely (2%), in the cerebral convexities. The study by Yilmaz et al⁵ reported a frequency of SS higher than that of our study but did not include cases of grade I GM-IVH. Our study noted a higher frequency of posterior fossa SS than the study of Yilmaz et al, which we believe is most likely related to our exclusive

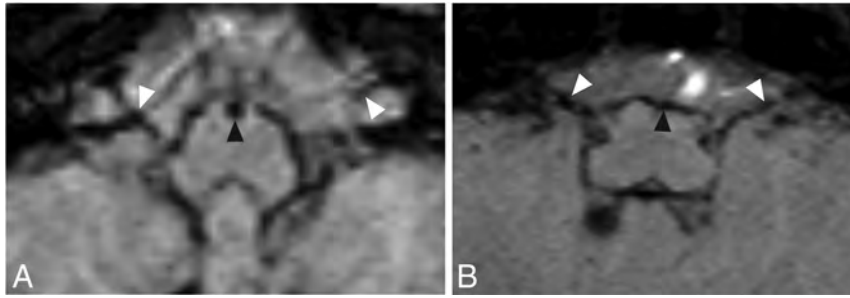


FIG 5. Initial axial SWI shows significant SS as early as 12 days after birth in a male patient with grade IV GM-IVH in the medulla oblongata (A, black arrowhead) and the CN VII/VIII complex (A, white arrowheads). Follow-up axial SWI of this patient reveals significant residual SS in the medulla oblongata (B, black arrowhead) and CN VII/VIII complex (B, white arrowheads) at 235 days after birth. Note that significant residual SS can also be seen in the CN VII/VIII complex at both time points.

use of SWI, which appears to be more sensitive to SS. We detected SS in the cerebellar vermis of 60% (53/88) of patients and in the cerebellar hemispheres of 35% (31/88). Hemispheric cerebellar SS in our population was less common than vermian SS. We believe this is related to the close proximity of the vermis to the mesencephalon and supravermian cistern. In the present study, SS in the posterior fossa was most frequent and severe within the brain stem. The depth of SS was greatest at the level of medulla oblongata, which is adjacent to both the foramen of Luschka and fourth ventricle outlets. SS was less severe in the mesencephalon. The timing at which MRIs were collected for the present study (mean, 68.5 ± 32.7 days) aligns with the timeframe during which we would expect iron accumulation and parenchymal destruction following GM-IVH, based on experimental studies as discussed earlier. It is not clear, however, how long SS remains detectable in infants after the initial hemorrhage. One case showed evidence of significant residual SS at 235 days after GM-IVH (Fig 5), suggesting that toxic effects of SS could be present, in some cases, for several months before resolution.

We found that both GM-IVH grade and TVHV were closely associated with SS depth in the brain stem, ventricle surfaces, cerebellum, and spinal cord. Multivariate regression analysis suggested that the presence of brain stem SS was associated with GM-IVH grade and TVHV, independent of birth weight, gestational age at birth, and cerebellar hematoma volume. Furthermore, cerebellar and vermis SS were present in many cases without cerebellar or vermis hemorrhage. This finding suggests that rather than cerebellar germinal matrix hemorrhage, intraventricular hemorrhage is the main factor underlying both brain stem and cerebellar SS.

In the present study, ES was common in both the supratentorial and infratentorial regions and was closely associated with GM-IVH grade, TVHV, and brain stem SS. Notably, all patients with brain stem SS and 40% of patients without brain stem SS had ES. These findings suggest that ES is a common consequence of GM-IVH. Chronic or subacute iron accumulation in the ependymal surfaces may have a deleterious effect on subsequent brain development, in addition to the effects of GM-IVH itself, due to the close proximity of these structures to the germinal matrix. The germinal matrix, which is a key source of

oligodendroglial precursor cells, produces myelin in the cerebral white matter.^{21,22} Infants with posthemorrhagic hydrocephalus have been found to exhibit ferritin-positive reactive microglia in the fourth ventricular wall before 2 weeks of age, in addition to hemosiderin deposits, nodular gliosis, ependymal cell loss, and subependymal rosettes in the fourth ventricular wall after 2 weeks of age.²³ Further studies are needed to investigate the clinical significance of ES and possible damage to the germinal matrix.

CN VIII is especially vulnerable to iron accumulation in adult SS, corresponding to the clinical presentation

of hearing loss in most adult patients with SS.¹ In 1 postmortem case study of an adult with SS and sensorineural hearing loss, pathologic examination revealed severe bilateral degeneration of the organ of Corti and spiral ganglion cells, with iron deposits noted in the glial and other cells of the cochlear nucleus in the brain stem near its CSF-facing surface.²⁴ There is concern that similar patterns of SS may contribute adversely to neurodevelopmental outcomes in premature infants. A recent cohort study of extremely preterm infants reported higher rates of hearing loss at 2- to 3-years' corrected age in infants with GM-IVH (I-IV included) compared with infants without GM-IVH.²⁵ In the present study, we detected significant iron accumulation on the surfaces of the CN VII/VIII complex. This finding was seen in 47% of patients in the present study (42/88). The incidence increased from grade I to III, but the grade IV group had a rate equivalent to that of the grade II group. The features most strongly correlated with the presence of CN VII/VIII SS were lateral ventricle ES and fourth ventricle choroid plexus ES. This finding is likely related to the close proximity of CNs VII and VIII and the lateral fourth ventricle outlets, in which the fourth ventricle choroid plexuses are present bilaterally.

The SWI sequence is the MR imaging sequence most sensitive to hemorrhage and SS⁷ and was used in all patients of this study. Previous imaging studies of GM-IVH generally used the T1, T2, or gradient T2 sequence to detect SS. In the present study, T1 and T2 sequences detected only a small proportion of the patients with SS. These findings suggest that SWI is more sensitive and efficient for detecting the presence and severity of SS compared to T1 and T2 weighted imaging.

The present study is limited by its retrospective design, the use of 2 different MR imaging machines, and the absence of a second radiologist to determine interrater reliability. Last, given the findings of neuropathologic studies, we cannot exclude the blooming artifacts of the SWI sequence; thus, the exact depth of SS might have been overestimated.

CONCLUSIONS

In the present study, we found a high rate of widespread SS and ES in premature infants with GM-IVH. As hypothesized, the

presence and extent of SS were closely and independently related to TVHV and GM-IVH grade. Notably, SS of the CN VII/VIII complex seems to be a very common complication of GM-IVH. Brain stem and cerebellar SS seem to be related to intraventricular hemorrhage, rather than to cerebellar hemorrhage. Although the deleterious effects of excessive iron on neuronal tissues are well-known, studies in premature infants with GM-IVH are limited and mostly retrospective. Prospective studies in preterm infants with GM-IVH are needed to clearly determine the clinical consequences of neonatal SS, especially relating to hearing impairment.

Disclosures: Garrett Smith—UNRELATED: Employment: University of Florida. Comments: I am an MD/PhD candidate at the University of Florida. I receive a regular stipend for this engagement.

REFERENCES

1. Kumar N, Cohen-Gadol AA, Wright RA. **Superficial siderosis.** *Neurology* 2006;66:1144–52 CrossRef Medline
2. Kumar N. **Neuroimaging in superficial siderosis: an in-depth look.** *AJNR Am J Neuroradiol* 2010;31:5–14 CrossRef Medline
3. Glasier CM, Garcia-Thomas GI, Allison JW. **Superficial CNS siderosis in the newborn: MR diagnosis.** *Pediatr Radiol* 1999;29:76–77 CrossRef Medline
4. Gomori JM, Grossman RI, Goldberg HI, et al. **High-field spin-echo MR imaging of superficial and subependymal siderosis secondary to neonatal intraventricular hemorrhage.** *Neuroradiology* 1987;29:339–42 CrossRef Medline
5. Yilmaz U, Meyer S, Gortner L, et al. **Superficial siderosis after germinal matrix hemorrhage.** *AJNR Am J Neuroradiol* 2016;37:2389–91 CrossRef Medline
6. Mittal S, Wu Z, Neelavalli J, et al. **Susceptibility-weighted imaging: technical aspects and clinical applications, Part 2.** *AJNR Am J Neuroradiol* 2009;30:232–52 CrossRef Medline
7. Tong KA, Ashwal S, Obenaus A, et al. **Susceptibility-weighted MR imaging: a review of clinical applications in children.** *AJNR Am J Neuroradiol* 2008;29:9–17 CrossRef Medline
8. Intrapromkul J, Northington F, Huisman T, et al. **Accuracy of head ultrasound for the detection of intracranial hemorrhage in preterm neonates: comparison with brain MRI and susceptibility-weighted imaging.** *J Neuroradiol* 2013;40:81–88 CrossRef Medline
9. Papile LA, Burstein J, Burstein R, et al. **Incidence and evolution of subependymal and intraventricular hemorrhage: a study of infants with birth weights less than 1,500 gm.** *J Pediatr* 1978;92:529–34 CrossRef Medline
10. Tomayko MM, Reynolds CP. **Determination of subcutaneous tumor size in athymic (nude) mice.** *Cancer Chemother Pharmacol* 1989;24:148–54 CrossRef Medline
11. Willmore LJ, Hiramatsu M, Kochi H, et al. **Formation of superoxide radicals after FeCl₃ injection into rat isocortex.** *Brain Res* 1983;277:393–96 CrossRef Medline
12. Willmore LJ, Sypert GW, Munson JB. **Recurrent seizures induced by cortical iron injection: a model of posttraumatic epilepsy.** *Ann Neurol* 1978;4:329–36 CrossRef Medline
13. Koeppen AH, Michael SC, Li D, et al. **The pathology of superficial siderosis of the central nervous system.** *Acta Neuropathol* 2008;116:371–82 CrossRef Medline
14. Hughes JT, Oppenheimer DR. **Superficial siderosis of the central nervous system: a report on nine cases with autopsy.** *Acta Neuropathol* 1969;13:56–74 CrossRef Medline
15. Kellermier H, Wang G, Wiley C. **Iron localization in superficial siderosis of the central nervous system.** *Neuropathology* 2009;29:187–95 CrossRef Medline
16. Koeppen AH, Barron KD. **Superficial siderosis of the central nervous system. A histological, histochemical and chemical study.** *J Neuropathol Exp Neurol* 1971;30:448–69 CrossRef Medline
17. Koeppen AH, Borke RC. **Experimental superficial siderosis of the central nervous system. I: morphological observations.** *J Neuropathol Exp Neurol* 1991;50:579–94 CrossRef Medline
18. Koeppen AH, Hurwitz CG, Dearborn RE, et al. **Experimental superficial siderosis of the central nervous system: biochemical correlates.** *J Neurol Sci* 1992;112:38–45 CrossRef Medline
19. Armstrong DL, Sauls CD, Goddard-Finegold J. **Neuropathologic findings in short-term survivors of intraventricular hemorrhage.** *Am J Dis Child* 1987;141:617 CrossRef Medline
20. Savman K, Nilsson UA, Blennow M, et al. **Non-protein-bound iron is elevated in cerebrospinal fluid from preterm infants with post-hemorrhagic ventricular dilatation.** *Pediatr Res* 2001;49:208–12 CrossRef Medline
21. Back SA, Luo NL, Borenstein NS, et al. **Late oligodendrocyte progenitors coincide with the developmental window of vulnerability for human perinatal white matter injury.** *J Neurosci* 2001;21:1302–12 CrossRef Medline
22. Rakic P. **Elusive radial glial cells: historical and evolutionary perspective.** *Glia* 2003;43:19–32 CrossRef Medline
23. Fukumizu M, Takashima S, Becker LE. **Glial reaction in periventricular areas of the brainstem in fetal and neonatal posthemorrhagic hydrocephalus and congenital hydrocephalus.** *Brain Dev* 1996;18:40–45 CrossRef Medline
24. Nadol JB, Adams JC, O'Malley JT. **Temporal bone histopathology in a case of sensorineural hearing loss caused by superficial siderosis of the central nervous system and treated by cochlear implantation.** *Otol Neurotol* 2011;32:748–55 CrossRef Medline
25. da Silva LS, Ribeiro GE, Montovani JC, et al. **The effect of periventricular hemorrhage on the auditory pathway of infants.** *Int J Pediatr Otorhinolaryngol* 2018;112:24–26 CrossRef Medline

Macrocerbellum in Achondroplasia: A Further CNS Manifestation of *FGFR3* Mutations?

H.M. Pascoe, J.Y.-M. Yang, J. Chen, A.M. Fink, and S. Kumbla

ABSTRACT

SUMMARY: Achondroplasia is the result of a mutation in the *fibroblast growth factor receptor 3* gene (*FGFR3*). Appearances suggestive of macrocerbellum have not been described in this patient group. We retrospectively reviewed MR imaging studies of the brain in 23 children with achondroplasia. A constellation of imaging findings that are recognized in macrocerbellum was observed, including cerebellar hemisphere enlargement (inferior and superior extension, wrapping around the brainstem); an effaced retro- and infravermian cerebellar subarachnoid CSF space; a shortened midbrain; distortion of the tectal plate; and mass effect on the brainstem. All MR imaging studies exhibited some of these findings. Quantitative analysis confirmed an increased cerebellar volume compared with age- and sex-matched controls. We hypothesized that this may be due to direct effects of the *FGFR3* mutation on cerebellar morphogenesis.

ABBREVIATIONS: PCF = posterior cranial fossa; PCFBV = posterior cranial fossa brain volume; STBV = supratentorial brain volume

Achondroplasia is the most common form of inherited disproportionate short stature affecting approximately 250,000 people worldwide. It is an autosomal dominant condition. The responsible mutation is almost always a glycine-to-arginine substitution at codon 380 in the transmembrane domain of the *fibroblast growth factor receptor 3* (*FGFR3*) gene, which results in overactivation of the receptor. Neuroimaging is frequently performed in children with achondroplasia because there are known associated intracranial abnormalities.¹⁻⁴

Macrocerbellum, an abnormally enlarged cerebellum, while rare, is associated with many syndromic conditions⁵⁻¹² and has also been described as an isolated finding.¹³⁻¹⁵ It has, however, never been reported in achondroplasia. We suspected an increased cerebellar volume in patients with achondroplasia based on observed qualitative MR imaging findings. However,

given the high incidence of skull base deformities in achondroplasia, the possibility that these were contributing to the MR imaging appearances by causing crowding of the posterior cranial fossa (PCF) structures was considered. Skull base deformation occurs due to impaired endochondral ossification and premature fusion of the posterior fossa synchondroses.^{1,3} A recent quantitative study of the PCF in patients with achondroplasia, however, did not show a decreased bony PCF volume compared with controls but did confirm an increased cerebellar volume.³

We hypothesized that the appearances described in macrocerbellum are present to varying degrees in patients with achondroplasia and that these are due to a true increase in the cerebellar volume rather than secondary to skull base changes. In our case series, we describe the qualitative imaging features suggestive of macrocerbellum and use volumetric analysis to confirm our findings.

Received August 14, 2019; accepted after revision November 2.

From the Departments of Medical Imaging (H.M.P., A.M.F., S.K.) and Neurosurgery (J.Y.-M.Y.), The Royal Children's Hospital, Parkville, Victoria, Australia; Neuroscience Research (J.Y.-M.Y.) and Developmental Imaging (J.Y.-M.Y., J.C.), Murdoch Children's Research Institute, Parkville, Victoria, Australia; Department of Paediatrics (J.Y.-M.Y.), University of Melbourne, Parkville, Victoria, Australia; Department of Perinatal Medicine (A.M.F.), Mercy Hospital for Women, Heidelberg, Victoria, Australia; and Department of Diagnostic Imaging (S.K.), Monash Health, Clayton, Victoria, Australia.

Dr Joseph Yuan-Mou Yang receives grant support from the Royal Children's Hospital Foundation (RCHI000).

Please address correspondence to Heather Michelle Pascoe, MD, Department of Medical Imaging, The Royal Children's Hospital, 50 Flemington Rd, Parkville, Victoria, Australia, 3052; e-mail: pascoeh@gmail.com

<http://dx.doi.org/10.3174/ajnr.A6369>

Case Series

A retrospective MR imaging data base search was conducted using the Radiology Information System at the Medical Imaging Department, The Royal Children's Hospital, Melbourne, Australia. We identified all children (from birth to 18 years of age) who had a diagnosis of achondroplasia and an MR imaging study of the brain performed for any indication between January 2000 and November 2018. The study was approved by our institutional Human Research Ethics Committee as a clinical audit.

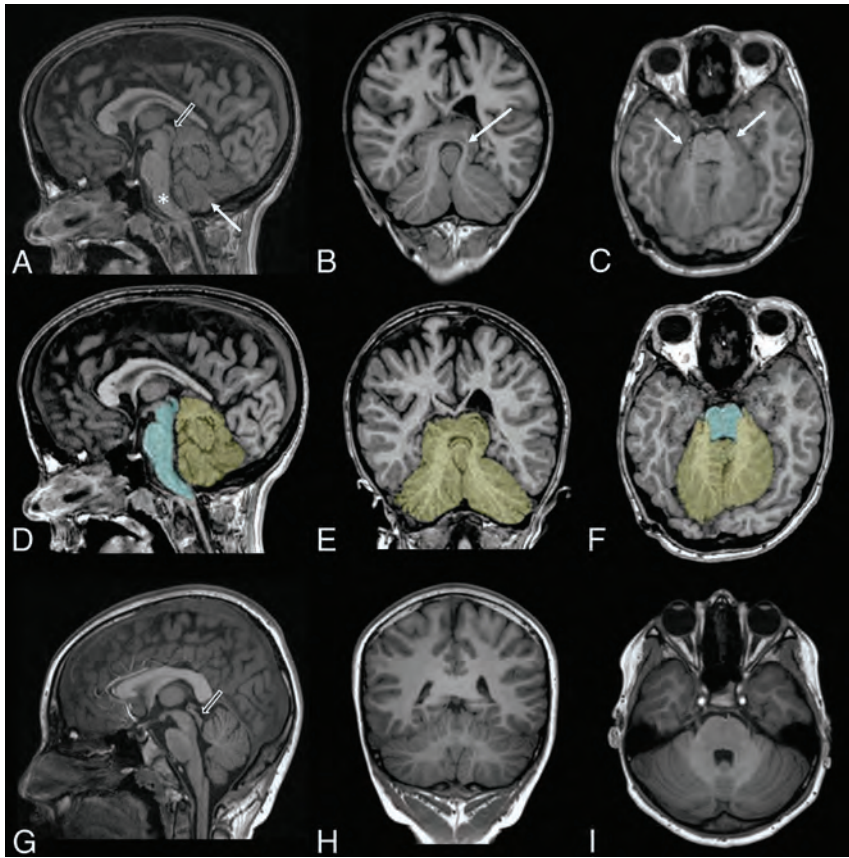


FIG 1. T1WIs of an 11-year-old child with achondroplasia (A–C) and the same T1WIs with superimposed cerebellum (yellow) and brainstem (cyan) segmentations (D–F). T1WIs from a healthy 11-year-old child (G–I) are provided for comparison. Extension of the cerebellar hemispheres inferior to the vermis is seen on the midsagittal plane (*arrow* in A); extension of the superomedial portions of the hemispheres above the tentorium cerebelli is seen on the coronal plane (*arrow* in B); and wrapping of the cerebellar hemispheres around the brainstem with extension around the lateral aspects of the brainstem at the level of the middle cerebellar peduncles is seen on the axial plane (*arrows* in C). Also seen on the midsagittal plane (A) are effacement of the retro- and infravermian subarachnoid CSF spaces, mass effect on the brainstem (which is anteriorly bowed [*asterisk*] with narrowing of the prepontine cistern and partial effacement of the fourth ventricle), and shortening of the midbrain with distortion of the tectal plate (*open arrow*). Note the normal morphology of the midbrain and tectal plate in G (*open arrow*).

The inclusion criteria were a diagnosis of achondroplasia and the availability of a diagnostic-quality MR examination of the brain in the study period. If the patient had >1 MR imaging in the study period, the most recent MR imaging was used. Twenty-three patients were included (12 boys and 11 girls). Ages ranged from 3 months to 15 years. An age- and sex-matched healthy control was selected for each patient. The controls were identified from the MR imaging database at The Royal Children’s Hospital using the following criteria: 1) normal brain anatomy, and 2) absence of a neurologic disorder. Reasons for their MR imaging referral were either sensorineural hearing loss or headache. MR imaging studies were performed on a 1.5 or 3T scanner.

Both qualitative and quantitative analyses were performed.

For qualitative analysis, the volumetric T1WIs were retrospectively evaluated by a pediatric radiology fellow (H.M.P.) and 2 pediatric neuroradiologists (S.K. and A.M.F.), and the results were

consensus-based. The presence of the following qualitative imaging features (Fig 1A–C) was assessed:

1. Extension of the cerebellar hemispheres inferior to the vermis (on the midsagittal plane; Fig 1A).
2. Extension of the superomedial portions of the cerebellar hemispheres above the tentorium cerebelli (on the coronal plane; Fig 1B).
3. Wrapping of the cerebellar hemispheres around the brainstem with extension around the lateral aspects of the brainstem at the level of the middle cerebellar peduncles (on the axial plane; Fig 1C).
4. Effacement of the retro- and infravermian subarachnoid CSF spaces (on the midsagittal plane; Fig 1A).
5. Apparent shortening of the midbrain with or without distortion of the tectal plate (on the midsagittal plane; Fig 1A).
6. Mass effect on the brainstem (on the midsagittal plane; Fig 1A). The features assessed were anterior bowing of the brainstem, narrowing of the prepontine cistern, and effacement of the fourth ventricle.

Quantitative analysis of the cerebellar and brainstem volumes was performed in each patient and the age- and sex-matched healthy control using automated brain tissue segmentation. T2WIs were used for analyzing patients younger than 1 year of age, and T1WIs for patients older than 1 year of age. All T2WIs used for the younger subjects had 0.4-mm in-plane resolution and 4-mm slice thickness. All 3D T1WIs had similar (0.5–0.9 mm) in-plane resolution and 0.9-mm slice thickness. The imaging sequence used and the resolution were comparable between the patient and the paired control to avoid introducing bias in our quantitative analysis. Morphologically Adaptive Neonatal Tissue Segmentation (MANTIS) software (<https://www.mantissoftware.com/>)¹⁶ was used in the younger group, and a surface-based brain parcellation software, FreeSurfer Version 6.0 (<http://surfer.nmr.mgh.harvard.edu>),¹⁷ was used in the older group. Manual editing was subsequently performed to ensure anatomic accuracy. This was performed by the neurosurgery fellow (J.Y.-M.Y.) and reviewed by a pediatric radiology fellow (H.M.P.) and a pediatric neuro-radiologist (S.K.). The cerebellar segmentation included both the cerebellar hemispheres and vermis. The brainstem segmentation included the midbrain, pons, and medulla. The posterior cranial fossa brain volume (PCFBV) was derived by summing the cerebellum and brainstem volumes.

Table 1: Summary of the qualitative features of macrocerebellum in patients with achondroplasia

Macrocerebellum Imaging Features on Different Imaging Planes	No. of Patients with Imaging Features Present (% Total) (Total = 23 Patients)
Extension of the cerebellar hemispheres inferior to the vermis (midsagittal)	23 (100.0)
Extension of the superomedial portions of the hemispheres above the tentorium cerebelli (coronal)	16 (69.6)
Wrapping of the cerebellar hemispheres around the brainstem (axial)	20 (87.0)
Effacement of the retro- and infravermian subarachnoid CSF spaces (midsagittal)	22 (95.7)
Shortening of the midbrain (midsagittal)	8 (34.8)
Distortion of the tectal plate (midsagittal)	3 (13.0)
Mass effect on the brain stem (midsagittal)	7 (30.4)

Table 2: Quantitative analysis of the cerebellum and brainstem

Variables	Patient (Mean ± SD)	Control (Mean ± SD)	P Value ^a
Age (yr)	5.38 ± 4.39	5.43 ± 4.46	.43
Cerebellum (mL)	137.85 ± 29.55	127.00 ± 27.78	.009 ^a
Brainstem (mL)	19.28 ± 3.96	19.56 ± 4.91	.92
PCFBV (mL)	157.14 ± 33.30	146.55 ± 32.16	.02 ^a
STBV (mL)	1097.56 ± 171.54	1001.05 ± 187.58	<.001 ^a

Note:—PCFBV indicates posterior cranial fossa brain volume; STBV, supratentorial brain volume; SD, standard deviation.

^a Statistical significance ($P < .05$).

The supratentorial brain volume (STBV) was also calculated for all cases. This was performed using the brain tissue classification tool from SPM12 (<http://www.fil.ion.ucl.ac.uk/spm/software/spm12>)¹⁸ to calculate the total brain volume, and the PCFBV was then subtracted from this.

Statistical analysis was performed using the R statistical and computing software and graphics (<http://www.r-project.org>). Group summary statistics were expressed in means and SDs. Comparison between the patients and their age- and sex-matched controls was analyzed using the paired Wilcoxon rank sum test. P values $< .05$ were considered statistically significant.

Results of the qualitative neuroimaging features of macrocerebellum are summarized in Table 1. Each of the MR imaging findings was recorded as present or not. Figure 1A–C demonstrates the qualitative MR imaging findings, with a healthy control for comparison shown in Fig 1G–I.

The results of quantitative analysis are summarized in Table 2. Figure 1D–F demonstrates the cerebellar and brainstem segmentations in standard orthogonal 2D MR imaging planes. Figure 2 demonstrates the cerebellar and brainstem segmentation as a 3D volume rendering.

The achondroplasia patients had a significantly larger PCFBV compared with their age- and sex-matched healthy controls ($P = .02$). This volume difference was due to a larger cerebellum ($P = .009$). There was no brainstem volume difference between the 2 study groups ($P = .92$). The patients with achondroplasia also had significantly larger STBVs compared with their age- and sex-matched healthy controls ($P < .001$).

DISCUSSION

The prevalence of skull base changes in patients with achondroplasia is well-documented; however, the morphology of the PCF content has not been widely reported.³ In particular, appearances described in macrocerebellum,¹⁹ such as those we observed, have not been described in this patient group.

The cerebellar enlargement in macrocerebellum has been reported to mainly involve the cerebellar hemispheres^{13,15} and has been described as an isolated finding^{13–15} as well as in many syndromic conditions.^{5–12} As a consequence of the cerebellar hemispheric enlargement, the hemispheres extend into available surrounding spaces, resulting in wrapping around the brainstem as well as upward and/or downward herniation.¹⁵ All of the patients with achondroplasia in our study demonstrated some of these qualitative signs of apparent cerebellar hemisphere enlargement. Ancillary changes of apparent macrocerebellum observed in the PCF were the following: effacement of the retro- and infravermian subarachnoid CSF spaces; apparent shortening of the midbrain, with associated distortion of the tectal plate in severe cases; and mass effect on the brainstem. Most of these features have been previously described in macrocerebellum.^{5,19}

On the basis of our qualitative results, it remained possible that deformation of the bony PCF causing overcrowding could be responsible for the MR imaging appearance of an apparent macrocerebellum. However, in line with the findings by Calandrelli et al,³ we confirmed that compared with healthy controls, cerebellar volumes were increased in patients with achondroplasia, indicating true macrocerebellum. In contradistinction to Calandrelli et al, however, we found no difference in the brainstem volume between patients and controls. This may be due to the small number of cases in both series; thus, larger series would be needed to establish whether there is any brainstem involvement in achondroplasia.

Fibroblast growth factor receptors are transmembrane tyrosine kinases that are expressed in the developing brain.²⁰ They are encoded by 4 genes (*FGFR1–4*),²¹ including the *FGFR3* gene, which is mutated in achondroplasia. Fibroblast growth factors bind to the fibroblast growth factor receptors, and this signaling is an important regulator of cerebral cortex development.²² Studies have demonstrated malformations involving the cerebral cortex, such as expansion of the occipitotemporal cortex²² and oversulcation of the mesiotemporal lobes⁴ in the presence of activating *FGFR3* mutations. These findings may also explain our finding of significantly higher supratentorial brain volume in patients with achondroplasia compared with healthy controls.

Less well-known is that fibroblast growth factor signaling has also been shown in mice to have an important role in regulating the formation of the cerebellum from the early embryonic period into early postnatal life.²³ Three neural layers are present in the adult cerebellar cortex (the molecular, Purkinje cell, and granular

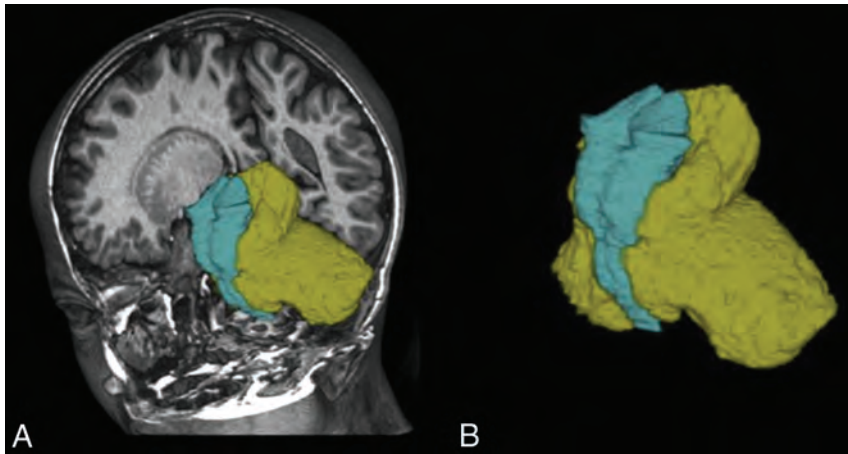


FIG 2. Cerebellum (yellow) and brainstem (cyan) segmentations of the same patient with achondroplasia as in Fig 1, shown as 3D volume renders.

cells layers), and most of the cerebellar neurons migrate to the cortex from the ventricular zone during the early embryonic period under the influences of molecular signaling, including fibroblast growth factor signaling. In the mouse cerebellum, *FGFR3* has been detected in the cerebellum as early as embryonic day 12.5. *FGFR3* is then expressed at varying levels in different parts of the cerebellar nuclei and cortical layers throughout the remainder of the prenatal period extending to 21 days postnatally.²³ Shazeeb et al²⁴ reported no *FGFR3* expression in the cerebellum of 3-week-old mice.

There is no current literature on the appearance of the cerebellum in achondroplasia. However, given our qualitative and quantitative findings, the known expression of *FGFR3* in the cerebellum during early development in mice, and the known growth-promoting effects of *FGFR3* mutations in the supratentorial compartment, we hypothesized that macrocerebellum in achondroplasia may be due to the direct effects of the *FGFR3* mutation on cerebellar morphogenesis. Further genetic and pathologic studies are required to substantiate or refute this hypothesis.

A major limitation of our study is that it is retrospective, with a relatively small sample size. The prevalence of macrocerebellum in patients with achondroplasia can thus not be established from this study. Additionally, segmenting the cerebellar hemispheres and vermis separately was beyond the scope of the methodology of this study; thus, the relative contribution of each to the enlarged cerebellum cannot be determined.

CONCLUSIONS

Our study is the first to describe macrocerebellum with its typical appearance in children with achondroplasia. We confirmed an increase in the cerebellar volume quantitatively through volumetric analysis and hypothesized that macrocerebellum may be due to the direct effects of the *FGFR3* mutation. Thus, macrocerebellum can be inferred when the qualitative imaging appearances we described are identified. These features should be sought when imaging patients with achondroplasia, alongside the other previously reported PCF

and supratentorial features. Further pathologic and genetic studies will be required to gain a better understanding of our observations.

ACKNOWLEDGMENTS

We thank the support from The Royal Children's Hospital Foundation, Murdoch Children's Research Institute, The University of Melbourne Department of Pediatrics, and the Victorian Government's Operational Infrastructure Support Program.

REFERENCES

1. Kao SC, Waziri MH, Smith WL, et al. **MR imaging of the craniocervical junction, cranium, and brain in children with achondroplasia.** *AJR Am J Roentgenol* 1989;153:565–69 CrossRef Medline
2. Pauli RM. **Achondroplasia: a comprehensive clinical review.** *Orphanet J Rare Dis* 2019;14:1 CrossRef Medline
3. Calandrelli R, Panfili M, D'Apolito G, et al. **Quantitative approach to the posterior cranial fossa and craniocervical junction in asymptomatic children with achondroplasia.** *Neuroradiology* 2017;59:1031–41 CrossRef Medline
4. Manikkam SA, Chetcuti K, Howell KB, et al. **Temporal lobe malformations in achondroplasia: expanding the brain imaging phenotype associated with FGFR3-related skeletal dysplasias.** *AJNR Am J Neuroradiol* 2018;39:380–84 CrossRef Medline
5. Alqahtani E, Huisman TA, Boltshauser E, et al. **Mucopolysaccharidosis type I and II: new neuroimaging findings in the cerebellum.** *Eur J Paediatr Neurol* 2014;18:211–17 CrossRef Medline
6. Poretti A, Snow J, Summers AC, et al. **Joubert syndrome: neuroimaging findings in 110 patients in correlation with cognitive function and genetic cause.** *J Med Genet* 2017;54:521–29 CrossRef Medline
7. Shiohama T, Fujii K, Miyashita T, et al. **Brain morphology in children with nevoid basal cell carcinoma syndrome.** *Am J Med Genet A* 2017;173:946–52 CrossRef Medline
8. Schaefer GB, Bodensteiner JB, Buehler BA, et al. **The neuroimaging findings in Sotos syndrome.** *Am J Med Genet* 1997;68:462–65 CrossRef Medline
9. Gripp KW, Hopkins E, Doyle D, et al. **High incidence of progressive postnatal cerebellar enlargement in Costello syndrome: brain overgrowth associated with HRAS mutations as the likely cause of structural brain and spinal cord abnormalities.** *Am J Med Genet A* 2010;152:1161–68 CrossRef Medline
10. Jones W, Hesselink J, Courchesne E, et al. **Cerebellar abnormalities in infants and toddlers with Williams syndrome.** *Dev Med Child Neurol* 2002;44:688–94 CrossRef Medline
11. van der Knaap MS, Salomons GS, Li R, et al. **Unusual variants of Alexander's disease.** *Ann Neurol* 2005;57:327–38 CrossRef Medline
12. Kau T, Karlo C, Gungör T, et al. **Increased cerebellar volume in the early stage of fucosidosis: a case control study.** *Neuroradiology* 2011;53:509–16 CrossRef Medline
13. Bodensteiner JB, Schaefer GB, Keller GM, et al. **Macrocephallism: neuroimaging and clinical features of a newly recognized condition.** *J Child Neurol* 1997;12:365–68 CrossRef Medline
14. D'Arco F, Ugga L, Caranci F, et al. **Isolated macrocephallism: description of six cases and literature review.** *Quant Imaging Med Surg* 2016;6:496–503 CrossRef Medline

15. Izbudak I, Acer N, Poretti A, et al. **Macrocerbellum: volumetric and diffusion tensor imaging analysis.** *Turk Neurosurg* 2015;25:948–53 Medline
16. Beare RJ, Chen J, Kelly CE, et al. **Neonatal brain tissue classification with morphological adaptation and unified segmentation.** *Front Neuroinform* 2016;10:12 CrossRef Medline
17. Fischl B. **FreeSurfer.** *Neuroimage* 2012;62:774–81 CrossRef Medline
18. Ashburner J, Friston KJ. **Unified segmentation.** *Neuroimage* 2005;26:839–51 CrossRef Medline
19. Poretti A, Mall V, Smitka M, et al. **Macrocerbellum: significance and pathogenic considerations.** *Cerebellum* 2012;11:1026–36 CrossRef Medline
20. Hevner RF. **The cerebral cortex malformation in thanatophoric dysplasia: neuropathology and pathogenesis.** *Acta Neuropathol* 2005;110:208–21 CrossRef Medline
21. Zhang X, Ibrahimi OA, Olsen SK, et al. **Receptor specificity of the fibroblast growth factor family: the complete mammalian FGF family.** *J Biol Chem* 2006;281:15694–700 CrossRef Medline
22. Thomson RE, Kind PC, Graham NA, et al. **FGF receptor 3 activation promotes selective growth and expansion of occipitotemporal cortex.** *Neural Dev* 2009;4:4 CrossRef Medline
23. Yaguchi Y, Yu T, Ahmed MU, et al. **Fibroblast growth factor (FGF) gene expression in the developing cerebellum suggests multiple roles for FGF signaling during cerebellar morphogenesis and development.** *Dev Dyn* 2009;238:2058–72 CrossRef Medline
24. Shazeeb MS, Cox MK, Gupta A, et al. **Skeletal characterization of the FGFR3 mouse model of achondroplasia using micro-CT and MRI volumetric imaging.** *Sci Rep* 2018;8:469 CrossRef Medline

Considerations for Mean Upper Cervical Cord Area Implementation in a Longitudinal MRI Setting: Methods, Interrater Reliability, and MRI Quality Control

C. Chien, V. Juenger, M. Scheel, A.U. Brandt, and F. Paul



ABSTRACT

BACKGROUND AND PURPOSE: Spinal cord atrophy is commonly measured from cerebral MRIs, including the upper cervical cord. However, rescan intraparticipant measures have not been investigated in healthy cohorts. This study investigated technical and rescan variability in the mean upper cervical cord area calculated from T1-weighted cerebral MRIs.

MATERIALS AND METHODS: In this retrospective study, 8 healthy participants were scanned and rescanned with non-distortion- and distortion-corrected MPRAGE sequences (11–50 sessions in 6–8 months), and 50 participants were scanned once with distortion-corrected MPRAGE sequences in the Day2day daily variability study. From another real-world observational cohort, we collected non-distortion-corrected MPRAGE scans from 27 healthy participants (annually for 2–4 years) and cross-sectionally from 77 participants. Statistical analyses included coefficient of variation, smallest real difference, intraclass correlation coefficient, Bland-Altman limits of agreement, and paired *t* tests.

RESULTS: Distortion- versus non-distortion-corrected MPRAGE-derived mean upper cervical cord areas were similar; however, a paired *t* test showed incomparability ($t = 11.0$, $P = <.001$). Higher variability was found in the mean upper cervical cord areas calculated from an automatic segmentation method. Interrater analysis yielded incomparable measures in the same participant scans ($t = 4.5$, $P = <.001$). Non-distortion-corrected mean upper cervical cord area measures were shown to be robust in real-world data ($t = -1.04$, $P = .31$). The main sources of variability were found to be artifacts from movement, head/neck positioning, and/or metal implants.

CONCLUSIONS: Technical variability in cord measures decreased using non-distortion-corrected MRIs, a semiautomatic segmentation approach, and 1 rater. Rescan variability was within $\pm 4.4\%$ for group mean upper cervical cord area when MR imaging quality criteria were met.

ABBREVIATIONS: CoV = coefficient of variation; HP = healthy participants; ICC = intraclass correlation coefficient; MUCCA = mean upper cervical cord area; SC = spinal cord; SCT = Spinal Cord Toolbox; SRD = smallest real difference; UCC = upper cervical cord; DND = Day2day non-distortion corrected; DDC = Day2day distortion corrected cross-sectional; CNDC = clinical non-distortion corrected cross-sectional; D'AD = asymptotic test of equality; LoA = Bland-Altman limits of agreement; SEM = standard error of measurement

Spinal cord (SC) atrophy occurs often in neuroinflammatory diseases and can be measured using structural MRI.^{1–3} Several studies have identified cervical SC atrophy as predictive of disease progression and/or disability in patients with multiple sclerosis and related diseases; thus, it is of great interest to measure SC atrophy longitudinally.^{1,4,5} One of the most common SC atrophy

measurement methods is the mean upper cervical cord area (MUCCA).^{6–8} MUCCA has been found to be robust at the C1–C2 and C2–C3 intervertebral levels.^{9,10} However, there is little consensus on how reliable it is longitudinally or whether SC atrophy measures are ready for use as a clinical trial end point and/or for patient monitoring in neuroinflammatory diseases,^{11,12} SC injury,^{13,14} or degenerative cervical myelopathy,¹⁵ among other diseases affecting the SC. Most studies of MR imaging–based SC

Received September 9, 2019; accepted after revision December 4.

From the Experimental and Clinical Research Center (C.C., V.J., A.U.B., F.P.), Max Delbrück Center for Molecular Medicine & Charité–Universitätsmedizin Berlin, corporate member of Freie Universität Berlin, Humboldt-Universität zu Berlin, and Berlin Institute of Health, Berlin, Germany; NeuroCure Clinical Research Center (C.C., V.J., M.S., A.U.B., F.P.) and Departments of Neuroradiology (V.J., M.S.) and Neurology (F.P.), Charité–Universitätsmedizin Berlin, corporate member of Freie Universität Berlin, Humboldt-Universität zu Berlin, and Berlin Institute of Health, Berlin, Germany; and Department of Neurology (A.U.B.), University of California, Irvine, Irvine, California.

Funding for this work was provided by the Deutsche Forschungsgemeinschaft DFG (EXC 257), awarded to F.P. and A.U.B.

Please address correspondence to Friedemann Paul, MD, NeuroCure Clinical Research Center, Charité–Universitätsmedizin Berlin, Charitéplatz 1, 10117 Berlin, Germany; e-mail: friedemann.paul@charite.de

Indicates open access to non-subscribers at www.ajnr.org

Indicates article with supplemental on-line tables.

Indicates article with supplemental on-line photos.

<http://dx.doi.org/10.3174/ajnr.A6394>

atrophy comparisons of diseased with healthy SC measures have relied on interindividual variability calculated from cross-sectional data.¹⁶ Intraindividual variability in healthy participants (HP) is often ignored or assumed to be equivalent to the mean change (or SD) in SC atrophy measures.⁹ The utility of using cerebral 3D MRIs, including the upper cervical cord (UCC), as a source of MUCCA calculations is based on the availability of this sequence in most patients. These scans can be used for both detection of abnormalities in the brain and the retrospective analysis of SC atrophy.⁸ Although some methods for reducing variability in MUCCA have been described, these methods require extra calculations and effort that are not implemented in many SC atrophy studies, as of yet.¹⁷ Thus, investigations of raw MUCCA in HP are still required for making considerations for MRI sequence and analysis methods in prospective SC atrophy studies. Technical and rescan variability in HP must be evaluated to understand the pathologic changes in raw MUCCA in a longitudinal setting.

In this study, we hypothesized that the raw MUCCA will differ in HP, dependent on several factors: 1) non-distortion- versus distortion-corrected source MRIs, 2) analysis software used for MUCCA calculation, 3) interrater biases, and 4) MR imaging artifacts/positioning. The aim of our study was to identify factors that impact healthy rescan MUCCA in a longitudinal intraparticipant manner using rescan cerebral distortion- and non-distortion-corrected MPRAGE images, while also accounting for interparticipant variations using cross-sectional cerebral distortion and non-distortion-corrected MPRAGE images.

MATERIALS AND METHODS

The local institutional review board (NeuroCure Clinical Research Center, Charité-Universitätsmedizin Berlin) approved this retrospective study, and written informed consent was obtained from all participants.

Cohort

We performed a retrospective analysis of data of HP collected from the Day2day daily variability study,¹⁸ and an ongoing observational single-center cohort (EA1/163/12). Inclusion criteria were as follows: a minimum of 18 years of age and no presence of any neurologic/psychiatric disorders, contraindications for an MR imaging examination, or incidental MR imaging findings. Participants who had undergone a full MR imaging scan protocol between January 2015 and January 2019 were eligible. Age and sex were collected for each healthy participant.

MR Imaging Acquisition

All images were acquired with 2 distinct 3T systems (Magnetom Trio; Siemens, Erlangen, Germany). From the Day2day study, we collected distortion- and non-distortion-corrected 3D MPRAGE sequences, including the upper cervical cord ($1 \times 1 \times 1$ mm resolution, TR = 2500 ms, TE = 4.77 ms, acquisition time [altogether] = 9:20 minutes, plane = sagittal). Eight HP (female/male = 6:2, mean age = 28.4 ± 2.97 years) were scanned with this MPRAGE protocol weekly for 6–8 months (11–50 scans per healthy participant), and 50 HP (female/male = 50:0, mean age = 24.9 ± 3.10 years) were scanned with the distortion-corrected 3D

MPRAGE sequence once in the Day2day study, all with the same scanner at the Max Planck Institute for Imaging Research, Berlin. From the observational study, we collected a non-distortion-corrected 3D MPRAGE sequence including the UCC ($1 \times 1 \times 1$ mm resolution, TR = 1900 ms, TE = 3.03 ms, acquisition time = 4:26 minutes, plane = sagittal) all with the same scanner at the Berlin Center of Advanced Imaging. Twenty-seven HP (female/male = 18:9, mean age = 36.8 ± 14.3 years) were scanned annually for 2–4 years (2–4 scans per healthy participant), and 77 HP (female/male = 49:28, mean age = 34.5 ± 12.0 years) were scanned using this non-distortion-corrected MPRAGE sequence once in the observational study.

Image Postprocessing

All images were reoriented with `fslreorient2std` (<https://www.rdocumentation.org/packages/fslr/versions/2.24.1/topics/fslreorient2std>) to match the Montreal Neurological Institute 152 standard template, which only applies 0°, 90°, 180°, or 270° rotations (FSL; Analysis Group, FMRIB, 2019; Version 5.0.9; open source: <https://fsl.fmrib.ox.ac.uk/fsl/fslwiki/>), and N4 bias field corrected (Advanced Normalization Tools; 2019; Version 0.0.8; open source: <http://stnava.github.io/ANTs/>).¹⁹ Longitudinal/rescan images were not coregistered because the SC region is not the center of registration, and in most coregistration pipelines, brain extraction is required, which cuts off the UCC.

Image Analysis

MUCCA was measured in all postprocessed MPRAGE images using the active surface method²⁰ using Jim software (2019; Version 7.0; http://www.xinapse.com/Manual/cord_intro.html) at the C2/C3 intervertebral space level (MUCCA-Jim), where the mean of cross-sectional areas in 5 consecutive slices of each MPRAGE image were obtained by an experienced rater (C.C.). Three center-of-cord seeds were marked by the rater, 1 at the most superior section of the C2/C3 intervertebral space, 1 after moving 2 slices down (center of C2/C3 intervertebral space), and the last seed after moving 2 more slices down in the cervical cord. Jim Cord Finder tool was set to a nominal cord diameter of 10 mm, with the number of shape coefficients set to 20 coefficients, a default order of longitudinal variation of 6, and the “cord is hypointense to CSF” setting not checked (for a T1 image). The active surface model takes into account the angulation of the cord by calculating cross-sectional areas in a plane perpendicular to the local cord centerline. Unfolded cervical cord images from each MPRAGE image were created using the same 5 consecutive slices, in which the setting for “create an unfolded image of the spinal cord” was checked in the Spinal Cord Finder Tool in Jim 7.0 so that during the calculation of the cross-sectional areas of the cord outline an unfolded image is automatically saved. The unfolded images are straightened cord centerline images, where cord image section planes are perpendicular to the straightened cord centerline.²¹ The unfolded cervical cord images were used as input for automatic MUCCA segmentation (MUCCA-SCT) using the Spinal Cord Toolbox (SCT; PropSeg; 2019; version 4.1.0 https://sourceforge.net/p/spinalcordtoolbox/wiki/correction_PropSeg/).²² The comparison of the 2 segmentation methods is valuable because the

semiautomatic Jim requires roughly 2–3 minutes of manual marking and quality checks per scan after reorienting to standard Montreal Neurological Institute space, while the automatic PropSeg requires only about 3 seconds of computation time after creating unfolded cervical cord images. If no unfolded cervical cord images are created, PropSeg is able to segment full cervical cords in roughly 15 seconds.

For interrater analysis, V.J. (trainee) measured MUCCA-Jim in the same MPRAGE scans from 1 healthy participant, using the same settings and methodology as described above.

Of the 308 rescan MRIs from 8 HP in the Day2day study, 37 (13%) distortion-corrected and 28 (9%) non-distortion-corrected MPRAGE scans were excluded from analyses due to motion artifacts and/or rescan differences in participant positioning in the scanner. From the ongoing observational cohort of 27 HP, we collected 66 longitudinal MRIs, of which 15 (7 HP, 23%) were excluded due to motion and/or metallic implant artifacts and/or differences in positioning in the scanner. In total, 28 HP with 600 longitudinal/rescan MPRAGE scans were included in statistical analysis.

Statistical Analysis

For age and sex comparison between HP from the Day2day study and our center, Kruskal-Wallis rank sum and χ^2 tests were performed, respectively. Group baseline MUCCAs calculated from different MR imaging scans were compared using an ANOVA test. Effect sizes between groups were evaluated with bootstrapped ($n = 5000$) confidence intervals.²³ Comparisons between MUCCAs derived from distortion- and non-distortion-corrected MPRAGE scans and from Jim versus SCT were performed using the coefficient of variation (CoV) asymptotic test of equality,²⁴ smallest real difference (SRD),²⁵ Bland-Altman limits of agreement, and paired t tests. The SRD (Equation 1) is a statistical method that estimates a true difference in measures and accounts for the 95% confidence interval of true observed differences among measures (1.96) using the difference in variances of measures ($\sqrt{2}$) and the standard error of measurement (SEM). SEM is calculated using intraclass correlation (ICC) metrics (Equation 2), as shown below.

$$1) \quad SRD = 1.96 \times \sqrt{2} \times SEM$$

$$2) \quad SEM = \sqrt{(Total\ Variance)(1 - ICC)}$$

Interrater MUCCAs were compared using the CoV, ICC, SRD, and a paired t test. ICCs were calculated with consistency from a 2-way mixed model. Because the number of longitudinal/rescan MUCCAs differed among HP, we calculated the CoV for each individual participant. All statistics and graphs were produced using R (Version 3.4.0; <http://www.r-project.org>),²⁶ and statistical significance was set to $P < .05$.

RESULTS

Cohort Demographics

Of the 28 participants with rescan MUCCAs, 21 (75%) were women, and of the 127 participants with cross-sectional MUCCAs,

99 (78%) were women. All relevant demographic data are shown in On-line Table 1.

There were significant differences between the cross-sectional HP' sex ($\chi^2 = 21.3$, $P = <.001$) and age ($\chi^2 = 33.1$, $P = <.001$) distributions. A significant difference in the baseline mean MUCCA-Jim when comparing rescan, longitudinal, and cross-sectional data from the Day2day and clinical participants ($F = 14.7$, $P = <.001$) was observed (On-line Table 1). However, little difference in the effect sizes of mean MUCCA-Jim derived from distortion- versus non-distortion-corrected MPRAGE scans was found (Fig 1).

Larger effect sizes from differences in MUCCA-Jim seemed to be the result of small sample sizes when subtracting the mean MUCCAs of a small cohort of 8 HP from the mean MUCCAs of 20 HP. However, when larger cohorts were compared, MUCCAs from distortion- and non-distortion-corrected MPRAGE scans (Day2day distortion-corrected cross-sectional and clinical non-distortion-corrected cross-sectional scans), a much smaller effect size was seen.

Rescan MUCCA from Distortion versus Non-Distortion-Corrected MPRAGE Sequences

Rescan MUCCA-Jims derived from the Day2day distortion- and non-distortion-corrected MPRAGE scans were compared. The CoVs in repeat MUCCAs for each participant are shown in the Table. An asymptotic test for the equality of the CoV between distortion- and non-distortion-derived MUCCA-Jim was non-significant (asymptotic test of equality = $<.0001$, $P = .98$). The SRD range in distortion-corrected derived MUCCA-Jim was $\pm 3.5 \text{ mm}^2$ ($\pm 4.8\%$ of the mean group MUCCA), while it was $\pm 3.2 \text{ mm}^2$ ($\pm 4.4\%$ of the mean group MUCCA) for non-distortion-corrected derived MUCCA-Jim. Bland-Altman limits of agreement (-2.9 to 6.0 mm^2) showed a predisposition for MUCCA-Jim to have a lower value when measured from non-distortion-corrected MPRAGE scans. This result was corroborated when the rescan MUCCA-Jim was evaluated using a paired t test ($t = 10.98$, $P = <.001$). Fig 2 and On-line Fig 1 illustrate the differences between each rescan MUCCA.

Although CoVs from most non-distortion-corrected MPRAGE-derived MUCCA-Jims were lower than those derived from distortion-corrected derived MUCCA-Jims, it can be seen, along with Fig 1, that participants with a similar number of scans analyzed had similar CoVs from both types of scans (eg, participants 1, 2, 4, 5, 7, and 8). CoVs from a similar number of scans analyzed were mostly lower in non-distortion-corrected derived MUCCA-Jims, and because the mean follow-up scan time per healthy participant was 5.2 days, this finding suggests that these measures are more robust than those from distortion-corrected cerebral scans.

Rescan MUCCA from Semiautomatic-versus-Automatic Segmentation

Variability in non-distortion-corrected MPRAGE-derived MUCCA was tested using the semiautomatic Jim (MUCCA-Jim) and the fully automatic PropSeg (MUCCA-SCT) segmentation methods. The CoVs in MUCCA for each participant from the Day2day cohort are shown in On-line Table 2.

An asymptotic test for the equality of CoV between MUCCA-Jim and MUCCA-SCT was significant (asymptotic test of equality = 130.1, $P = <.001$). The SRD range for MUCCA-Jim was $\pm 3.2 \text{ mm}^2$ ($\pm 4.4\%$ of the mean group MUCCA-Jim), while it was $\pm 9.5 \text{ mm}^2$ ($\pm 14.5\%$ of the mean group MUCCA-SCT) for MUCCA-SCT. Bland-Altman limits of agreement (-2.3 to 16.0 mm^2) showed a predisposition for MUCCA-Jim to have a higher value than MUCCA-SCT, which was also evident when evaluating the rescan MUCCA-Jim and MUCCA-SCT with a paired t test ($t = 24.42$, $P = <.001$). Since PropSeg

was optimized on MR imaging acquired with a spine coil instead of a head-neck coil, as used in this study, differences in the CSF to SC contrast-to-noise ratios may cause an underestimation of this segmentation method.²⁷ On-line Figure 2 shows the Bland-Altman and paired t test results when comparing MUCCA-Jim and MUCCA-SCT, as well as sample segmentations by Jim and PropSeg.

Single- versus Multirater Rescan MUCCA-Jim

To evaluate the robustness of using nondistortion MPRAGE scans and semiautomatic software to measure the MUCCA, we performed an interrater analysis for the same participant with 50 weekly scans from the Day2day study. Rater 1 (C.C.) has several years of experience with MUCCA segmentation, while rater 2 (V.J.) has never segmented MUCCA before this study. The CoVs in rescan MUCCA-Jim for healthy participant the same HP from rater 1 and rater 2 were 1.38% and 1.64%, respectively. An asymptotic test for the equality of CoV was nonsignificant (asymptotic test of equality = 1.5, $P = .23$). The ICC was 0.74, and the SRD range in MUCCA-Jim from the 2 raters was $\pm 2.8 \text{ mm}^2$ ($\pm 3.8\%$ of the mean group MUCCA-Jim). The rescan MUCCA-Jim when compared using a paired t test still showed a significant difference ($t = 4.54$, $P = <.001$). On-line Figure 3 illustrates the paired t test comparison of rescan MUCCA-Jim, from the same participant, measured by 2 raters.

Real-World Data Confirmation

To validate the findings from our analysis of the Day2day study cohort, we compared, cross-sectionally, 50 Day2day HP MUCCA-Jim derived from distortion-corrected MPRAGE scans with 77 observational HP MUCCA-Jim derived from non-

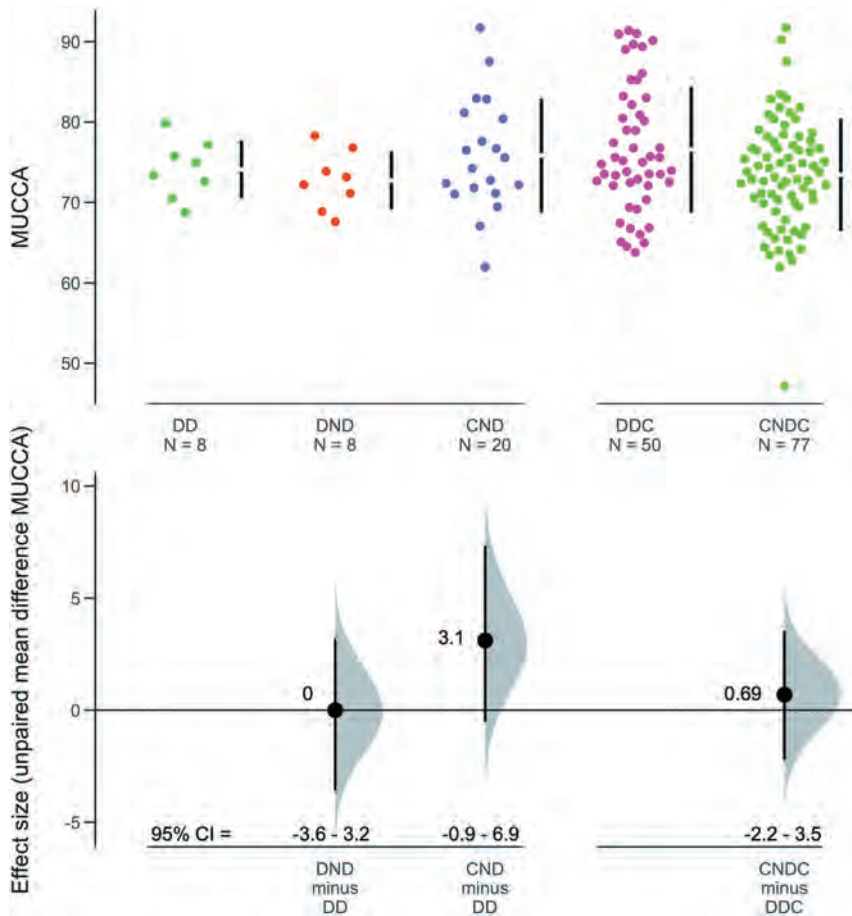


FIG 1. Comparison of effect sizes of differences between baseline MUCCA-Jim derived from the participants with longitudinal Day2day distortion-corrected (DD) DD and Day2day non-distortion-corrected (DND), clinical non-distortion-corrected (CND), Day2day distortion-corrected cross-sectional, and clinical non-distortion-corrected cross-sectional (CNDC) MPRAGE scans. Vertical lines beside dot plots indicate SDs around the means.

CoVs for each Day2day participant MUCCA-Jim derived from distortion- and non-distortion-corrected MPRAGE scans

Participant	No. of Rescan MPRAGE Scans Collected	No. of Distortion-Corrected Derived MUCCAs Analyzed	CoV for Distortion-Corrected Derived MUCCA	No. of Non-Distortion-Corrected Derived MUCCAs Analyzed	CoV for Non-Distortion-Corrected Derived MUCCA
1	50	50	1.36	50	1.38
2	13	10	1.89	10	1.72
3	50	37	3.09	43	2.03
4	11	11	1.39	10	1.35
5	45	40	1.40	41	1.33
6	47	36	1.91	42	1.55
7	43	43	1.35	41	1.55
8	49	42	1.55	43	1.40

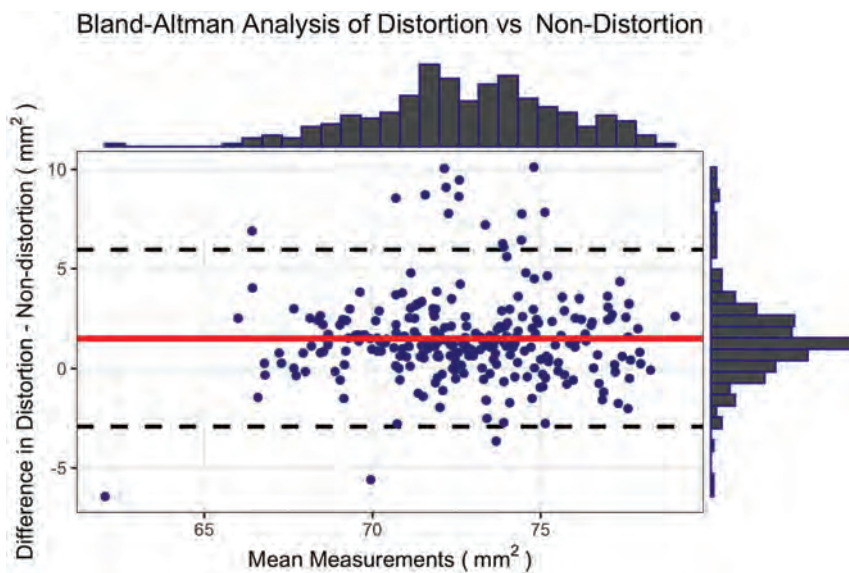


FIG 2. Bland-Altman graph showing larger distortion-corrected MPRAGE-derived MUCCA-Jim values than non-distortion-corrected MPRAGE derived MUCCA-Jim, with relatively normally distributed mean values.

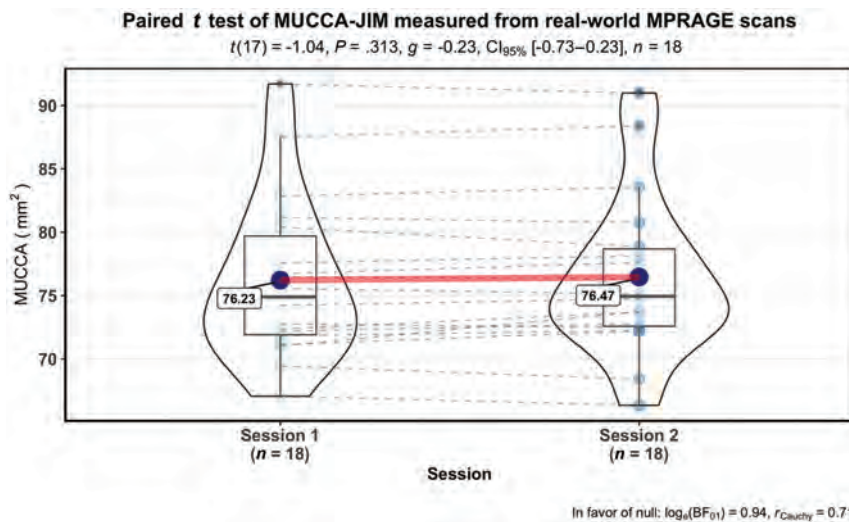


FIG 3. Paired *t* test showing that the mean rescan MUCCA-Jim is quite stable when measured by an experienced rater from real-world non-distortion-corrected MPRAGE scans obtained, on average, 1 year apart.

distortion-corrected MPRAGE scans. Again, we found that the CoV was smaller in MUCCAs derived from non-distortion-corrected versus distortion-corrected MPRAGE scans (9.5% versus 10.2%, respectively). However, the CoV values were not significantly different when tested with an asymptotic test for equality (asymptotic test of equality = 0.10, $P = .75$). A 2-sample *t* test showed a slight difference between MUCCA-Jim (derived from distortion-corrected: mean = $76.6 \pm 7.8 \text{ mm}^2$; from non-distortion-corrected: mean = $73.4 \pm 7.0 \text{ mm}^2$; $t = 2.32$, $P = .02$) from the 2 cohorts. Because the 50 HP from the Day2day study were all women with a small range in age, one would expect less variation in interparticipant MUCCAs in

this cohort. However, our finding that there was a higher (though slightly higher) CoV in the MUCCA-Jim from this cohort suggests that a “normal range” of MUCCA may be larger when using distortion-corrected scans for SC atrophy evaluation.

We also tested rescan MPRAGE MUCCA-Jim from the observational cohort to evaluate the feasibility of using the raw MUCCA in a longitudinal, real-world setting. The CoVs in rescan MUCCA-Jim for each participant are shown in On-line Table 3. The SRD range for MUCCA-Jim was $\pm 2.4 \text{ mm}^2$ ($\pm 3.1\%$ of the mean group MUCCA-Jim). The ICC for longitudinal MUCCA-Jim was 0.97. A paired *t* test of MUCCA-Jim measured between 2 consecutive imaging time points showed that the MUCCA were stable ($t = -1.04$, $P = .31$), as illustrated in Fig 3.

Sources of Exclusion from Analysis (MPRAGE Quality Control)

On inspection of large variations in consecutive MUCCA-Jim from the Day2day and observational cohort, several artifacts were identified to give inadequate rescans MUCCAs for comparison. Participants with largely variable MUCCAs most often had ≥ 1 of the following MR imaging qualities: 1) motion artifacts seen in the brain or neck region, 2) head and neck positions being different between sessions, and/or 3) metal implants in the mouth causing artifacts (eg, retainer, braces, and so forth). Head and neck positioning differences included head tilt angle and different levels of UCC included in the scan FOV. All of these qual-

ities can be observed in postprocessed MPRAGE images, as shown in Fig 4.

DISCUSSION

We investigated rescan MUCCA variability in HP on the basis of the following: 1) scan settings for source MRIs, 2) segmentation software, 3) interrater bias, and 4) imaging artifacts. Rescan MUCCA was found to be less variable when measured from 3T, non-distortion-corrected cerebral 3D MPRAGE scans. We also showed that using a semiautomatic segmentation approach (Jim 7.0 Cord Finder Tool) gave a robust MUCCA in participants compared with fully automatic segmentation (SCT PropSeg) in

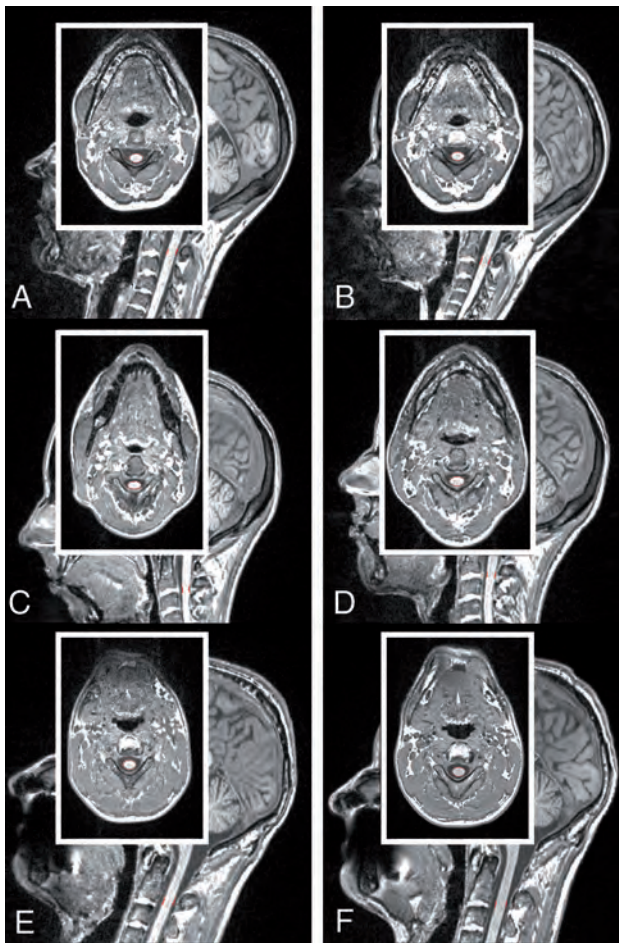


FIG 4. Consecutive sagittal MPRAGE scans. *A* and *B*, Large motion artifacts (session 1 MUCCA-Jim = 67.8 mm², session 2 MUCCA-Jim = 53.1 mm²). *C* and *D*, Different head and neck (vertebrae level cutoff) positioning (session 1 MUCCA-Jim = 47.1 mm², session 2 MUCCA-Jim = 64.3 mm²). *E* and *F*, Metal implants in the mouth region (session 1 MUCCA-Jim = 73.8 mm², session 2 MUCCA-Jim = 79.7 mm²). Inlays show axial MUCCA regions, where the SC does not immediately seem different, but surrounding head/neck regions are often sliced differently. *Red outline* in images indicates the location of MUCCA segmentation.

the exact same MR imaging slices. Interrater bias evaluation revealed that MUCCA from a single rater is more consistent, and if measured by different raters, a systematic bias could occur. Finally, several sources of highly variable rescan MUCCAs were found through quality control analysis of postprocessed MPRAGE scans. These included imaging artifacts in the brain/mouth/neck regions and, most noticeably, when participants were positioned differently (ie, different head tilt, different levels of vertebrae in the FOV) and/or had metal implants in the mouth.

Few studies publish whether MR imaging sequences are distortion- or non-distortion-corrected using a phantom. MUCCA has been shown to be more robust when normalized with a factor calculated from a cylindrical phantom that represents the UCC.¹⁷ However, we found that raw MUCCA derived from distortion-corrected MPRAGE scans yielded more variable (higher CoVs and SDs) within-participant rescan measures than those derived

from non-distortion-corrected MPRAGE scans. This finding suggests that without an SC-specific phantom for distortion correction, non-distortion-corrected cerebral scans yield less variable and more robust raw MUCCAs for longitudinal SC atrophy evaluation. We would recommend, in retrospective studies, using non-distortion-corrected cerebral MPRAGE for higher longitudinal reproducibility, as seen from the results of our real-world clinical data. Furthermore, to reduce variability in repeat MUCCAs as much as possible, when using cerebral MPRAGE scans, we propose a strict quality control step before inclusion in a study, which involves the removal of participants with any metallic implants and scans that have any brain-movement artifacts. It would be also beneficial to standardize the positioning of patients in the scanner to achieve cervical cord placement as straight as possible and include a minimum number of vertebral levels.

We compared 2 common SC segmentation tools used to calculate the MUCCA: the semiautomatic Jim Cord Finder and the fully automatic SCT PropSeg. Jim uses an active surface method,²⁰ and SCT uses an iterative propagation of a deformable adaptive contrast method.²² One study found good correlation between Jim and PropSeg using a normalization factor,²⁸ while another study found a systematic difference in the 2 outputs.²⁷ We confirmed this systematic bias in raw MUCCA, in which PropSeg yielded significantly smaller and more variable segmentations than Jim, with higher intraparticipant variability and low consistency in paired measures. Because we segmented MUCCAs using the exact same MR imaging slices for this analysis, our study shows that raw MUCCAs measured by these 2 methods are not comparable. SCT has another functionality, namely DeepSeg (<https://github.com/neuropoly/spinalcordtoolbox>), which is based on a convolutional neural network algorithm that segments the spinal cord, with the capability of also segmenting intramedullary multiple sclerosis lesions.²⁹ This method was shown to better segment MR imaging scans, including the brain, than PropSeg; however, raw MUCCAs were still significantly different between DeepSeg and Jim.⁷ Thus, when one compares results from different studies using different segmentation methods, absolute MUCCA cannot be used; rather, we propose the evaluation of effect sizes from the change in the MUCCA from each study.

Many studies have used Jim for MUCCA segmentation, but they had either 1 experienced rater for multiple centers³⁰ or no raters were mentioned.³¹ We found only a moderate intraclass correlation between MUCCAs segmented by 2 raters. The less experienced rater also had higher variability in the MUCCA, as evidenced by large differences in paired measures. These results highlight the need for disclosure of raters in MUCCA studies, standardized training of individuals performing SC segmentation, and/or using 1 rater for longitudinal studies.

We validated our findings in real-world clinical data. In distortion versus non-distortion MPRAGE-derived MUCCA, stability of the rescan MUCCA was shown to be a smallest real difference of roughly $\pm 4\%$ change. This is in line with a recent study that found high reproducibility of the MUCCA within 1 scanner with 1 measurement method, but no comparability among scanners or methods.²⁷ One large metadata study found,

on average, that patients with multiple sclerosis lose 1.78%/year of their cervical SC area.¹⁶ We do not need to assume that SC atrophy during 1 year in HP would be zero; however, a large study with >1200 asymptomatic participants spanning 20–80 years in age found that in both men and women the C2/C3 intervertebral level cross-sectional area had a minimum decrease of about 1% and a maximum decrease of roughly 4.5% spanning several decades.³² Thus, we can be fairly certain that during the course of a 1-year follow-up, normal SC atrophy would, most likely, not surpass 1.5%. Our study shows that annual MUCCA may not give enough signal over noise; thus, we suggest that MUCCA be monitored for >24 months to assess SC atrophy.

The limitations of our study include the small sample size of HP scanned longitudinally. Because our study was performed with retrospective data, we could not evaluate dedicated SC sequences, which may give more robust SC atrophy measurements using fast, automated methods such as PropSeg or DeepSeg. A future direction would be to collect a large amount of healthy participant SC MR imaging for further longitudinal testing. It would be ideal to scan many HP with a wide age range, to truly validate whether there is an effect of age or sex on the MUCCA. One study did find an effect of age, sex, height, and weight on the lower cervical volume of HP, however, with very small effect sizes for their models.³³ We were also not able to investigate the time of day of MR imaging acquisition or hydration levels of HP, which may lead to further fluctuations in the MUCCA. These factors have been found to affect brain morphometric measures³⁴ and SC area.³⁵ However, due to the robustness of our real-world longitudinal MUCCA analysis, we can postulate that these factors play a smaller role in MUCCA variability.

CONCLUSIONS

Our study illustrates some technical and rescan factors important in longitudinal SC atrophy studies using MUCCA: type and correction of source MR imaging, segmentation method, rater training, and MR imaging quality controls should be addressed, because all these factors contribute to increased rescan variability in the MUCCA. With these considerations, the MUCCA has the potential to be used in a longitudinal setting to evaluate and track SC atrophy.

ACKNOWLEDGMENTS

We would like to thank Dr Simone Kühn for her large contributions of high-quality data from the Day2day study. Also, we thank all participants who volunteered for these observational studies, the study nurses, MR imaging technicians (S. Pikol and C. Kraut), and residents who aided in collecting the clinical data.

Disclosures: Michael Scheel—UNRELATED: Patents (Planned, Pending or Issued): patent for 3D printing method; Royalties: from education books from Elsevier. Alexander Brandt—RELATED: Grant: BMBF, Comments: Neu2 ADVISIMS*; UNRELATED: Patents (planned, pending or issued): Retinal Image Analysis, Multiple sclerosis serum biomarkers, perceptive visual computing; Stock/stock options: Motognosis GmbH Nocturne GmbH, Friedemann Paul—OTHER RELATIONSHIPS: FP has received research support from Bayer, Novartis, Biogen Idec, Teva, Sanofi-Aventis/Genzyme, Merck Serono, Alexion, Chugai, Arthur Arnstein Foundation Berlin,

Guthy Jackson Charitable Foundation and the US National Multiple Sclerosis Society; has received travel funding and/or speaker honoraria from Bayer, Novartis, Biogen Idec, Teva, Sanofi-Aventis/Genzyme and Merck Serono; and has consulted for Sanofi Genzyme, Biogen Idec and MedImmune; none of this is related to the present study. *Money paid to the institution.

REFERENCES

1. Brownlee WJ, Altmann DR, Alves Da Mota P, et al. **Association of asymptomatic spinal cord lesions and atrophy with disability 5 years after a clinically isolated syndrome.** *Mult Scler* 2017;23:665–74 CrossRef Medline
2. Tsagkas C, Magon S, Gaetano L, et al. **Preferential spinal cord volume loss in primary progressive multiple sclerosis.** *Mult Scler* 2019; 25:947–57 CrossRef Medline
3. Chien C, Scheel M, Schmitz-Hübsch T, et al. **Spinal cord lesions and atrophy in NMOSD with AQP4-IgG and MOG-IgG associated autoimmunity.** *Mult Scler* 2019;25:1926–36 CrossRef Medline
4. Zeydan B, Gu X, Atkinson EJ, et al. **Cervical spinal cord atrophy: an early marker of progressive MS onset.** *Neurol Neuroimmunol Neuroinflamm* 2018;5:e435 CrossRef Medline
5. Ciccarelli O, Cohen JA, Reingold SC, et al; International Conference on Spinal Cord Involvement and Imaging in Multiple Sclerosis and Neuromyelitis Optica Spectrum Disorders. **Spinal cord involvement in multiple sclerosis and neuromyelitis optica spectrum disorders.** *Lancet Neurol* 2019;18:185–97 CrossRef Medline
6. Sinnecker T, Granziera C, Wuerfel J, et al. **Future brain and spinal cord volumetric imaging in the clinic for monitoring treatment response in MS.** *Curr Treat Options Neurol* 2018;20:17 CrossRef Medline
7. Alcaide-Leon P, Cybulsky K, Sankar S, et al. **Quantitative spinal cord MRI in radiologically isolated syndrome.** *Neurol Neuroimmunol Neuroinflamm* 2018;5:e436 CrossRef Medline
8. Chien C, Brandt AU, Schmidt F, et al. **MRI-based methods for spinal cord atrophy evaluation: a comparison of cervical cord cross-sectional area, cervical cord volume, and full spinal cord volume in patients with aquaporin-4 antibody seropositive neuromyelitis optica spectrum disorders.** *AJNR Am J Neuroradiol* 2018;39:1362–68 CrossRef Medline
9. Moccia M, Ruggieri S, Ianniello A, et al. **Advances in spinal cord imaging in multiple sclerosis.** *Ther Adv Neurol Disord* 2019;12: 1756286419840593 CrossRef Medline
10. Valsasina P, Aboulwafa M, Preziosa P, et al. **Cervical cord T1-weighted hypointense lesions at MR imaging in multiple sclerosis: relationship to cord atrophy and disability.** *Radiology* 2018;288: 234–44 CrossRef Medline
11. Filippi M, Rocca MA, Ciccarelli O, et al; MAGNIMS Study Group. **MRI criteria for the diagnosis of multiple sclerosis: MAGNIMS consensus guidelines.** *Lancet Neurol* 2016;15:292–303 CrossRef Medline
12. Prados F, Barkhof F. **Spinal cord atrophy rates: ready for prime time in multiple sclerosis clinical trials?** *Neurology* 2018;91:157–58 CrossRef Medline
13. Lammertse D, Dungan D, Dreisbach J, et al; National Institute on Disability and Rehabilitation. **Neuroimaging in traumatic spinal cord injury: an evidence-based review for clinical practice and research.** *J Spinal Cord Med* 2007;30:205–14 CrossRef Medline
14. Seif M, Wheeler-Kingshott CA, Cohen-Adad J, et al. **Guidelines for the conduct of clinical trials in spinal cord injury: neuroimaging biomarkers.** *Spinal Cord* 2019;57:717–28 CrossRef Medline
15. Nouri A, Martin AR, Mikulis D, et al. **Magnetic resonance imaging assessment of degenerative cervical myelopathy: a review of structural changes and measurement techniques.** *Neurosurg Focus* 2016; 40:E5 CrossRef Medline
16. Casserly C, Seyman EE, Alcaide-Leon P, et al. **Spinal cord atrophy in multiple sclerosis: a systematic review and meta-analysis.** *J Neuroimaging* 2018;28:556–86 CrossRef Medline

17. Papinutto N, Bakshi R, Bischof A, et al; North American Imaging in Multiple Sclerosis Cooperative (NAIMS). **Gradient nonlinearity effects on upper cervical spinal cord area measurement from 3D T1-weighted brain MRI acquisitions.** *Magn Reson Med* 2018;79:1595–601 CrossRef Medline
18. Filevich E, Lisofsky N, Becker M, et al. **Day2day: investigating daily variability of magnetic resonance imaging measures over half a year.** *BMC Neurosci* 2017;18:65 CrossRef Medline
19. Tustison NJ, Avants BB, Cook PA, et al. **N4ITK: improved N3 bias correction.** *IEEE Trans Med Imaging* 2010;29:1310–20 CrossRef Medline
20. Horsfield MA, Sala S, Neema M, et al. **Rapid semi-automatic segmentation of the spinal cord from magnetic resonance images: application in multiple sclerosis.** *Neuroimage* 2010;50:446–55 CrossRef Medline
21. Valsasina P, Horsfield MA, Rocca MA, et al. **Spatial normalization and regional assessment of cord atrophy: voxel-based analysis of cervical cord 3D T1-weighted images.** *AJNR Am J Neuroradiol* 2012;33:2195–200 CrossRef Medline
22. De Leener B, Kadoury S, Cohen-Adad J. **Robust, accurate and fast automatic segmentation of the spinal cord.** *NeuroImage* 2014;98:528–36 CrossRef Medline
23. Ho J, Tumkaya T, Aryal S, et al. **Moving beyond P values: data analysis with estimation graphics.** *Nat Methods* 2019;16:565–66 CrossRef Medline
24. Feltz CJ, Miller GE. **An asymptotic test for the equality of coefficients of variation from k populations.** *Stat Med* 1996;15:646–58 CrossRef Medline
25. Beckerman H, Roebroek ME, Lankhorst GJ, et al. **Smallest real difference, a link between reproducibility and responsiveness.** *Qual Life Res* 2001;10:571–78 CrossRef Medline
26. Core Team R. *R: A language and environment for statistical computing.* Vienna; R Foundation for Statistical Computing; 2019
27. Weeda MM, Middelkoop SM, Steenwijk MD, et al. **Validation of mean upper cervical cord area (MUCCA) measurement techniques in multiple sclerosis (MS): high reproducibility and robustness to lesions, but large software and scanner effects.** *Neuroimage Clin* 2019;24:101962 CrossRef Medline
28. Yiannakas MC, Mustafa AM, De Leener B, et al. **Fully automated segmentation of the cervical cord from T1-weighted MRI using PropSeg: application to multiple sclerosis.** *Neuroimage Clin* 2016;10:71–77 CrossRef Medline
29. Gros C, De Leener B, Badji A, et al. **Automatic segmentation of the spinal cord and intramedullary multiple sclerosis lesions with convolutional neural networks.** *Neuroimage* 2019;184:901–15 CrossRef Medline
30. Liu Y, Lukas C, Steenwijk MD, et al. **Multicenter validation of mean upper cervical cord area measurements from head 3D T1-weighted MR imaging in patients with multiple sclerosis.** *AJNR Am J Neuroradiol* 2016;37:749–54 CrossRef Medline
31. Valsasina P, Rocca MA, Horsfield MA, et al. **A longitudinal MRI study of cervical cord atrophy in multiple sclerosis.** *J Neurol* 2015;262:1622–28 CrossRef Medline
32. Kato F, Yukawa Y, Suda K, et al. **Normal morphology, age-related changes and abnormal findings of the cervical spine, Part II: magnetic resonance imaging of over 1,200 asymptomatic subjects.** *Eur Spine J* 2012;21:1499–507 CrossRef Medline
33. Yanase M, Matsuyama Y, Hirose K, et al. **Measurement of the cervical spinal cord volume on MRI.** *J Spinal Disord Tech* 2006;19:125–29 CrossRef Medline
34. Trefler A, Sadeghi N, Thomas AG, et al. **Impact of time-of-day on brain morphometric measures derived from T1-weighted magnetic resonance imaging.** *Neuroimage* 2016;133:41–52 CrossRef Medline
35. Wang C, Tam RC, Mackie E, et al. **Dehydration affects spinal cord cross-sectional area measurement on MRI in healthy subjects.** *Spinal Cord* 2014;52:616–20 CrossRef Medline

Renal Excretion of Contrast on CT Myelography: A Specific Marker of CSF Leak

S. Behbahani, J. Raseman, H. Orłowski, A. Sharma, and R. Eldaya



ABSTRACT

BACKGROUND AND PURPOSE: The purpose of this study was to evaluate the sensitivity and specificity of renal/ureteric opacification on postmyelographic CT as a sign of CSF leak.

MATERIALS AND METHODS: We performed a retrospective review of postmyelographic CT scans from 49 consecutive patients seen between January 2008 and August 2018 with imaging and/or clinical findings related to intracranial hypotension. Each scan was evaluated by both a neuroradiology fellow and a board-certified neuroradiologist for the presence of contrast in the renal excretory system. A similar assessment was also performed on 90 consecutive control subjects who underwent CT myelography for alternative indications.

RESULTS: Among the 49 patients with suspected CSF leak, 21 (43%) had an overt CSF leak on postmyelographic CT (group 1) and 28 (57%) did not (group 2). Overall, renal contrast was identified in 7/49 patients (14.3%): 5 (24%) patients in group 1, and 2 (7%) patients in group 2. Renal contrast was not seen in any of the 90 controls on postmyelographic CT.

CONCLUSIONS: Renal contrast was exclusively seen in patients with a clinically or radiographically suspected CSF leak. Given its 100% specificity, identification of this finding should prompt a second look for subtle myelographic contrast extravasation or an underlying CSF-venous fistula. Our results suggest that this sign may be considered an additional diagnostic criterion for CSF leak in the absence of an identifiable leak.

ABBREVIATIONS: CTM = CT myelogram; CVF = CSF-venous fistula; ICH = intracranial hypotension

Spinal CSF leaks resulting in intracranial hypotension are an important and common cause of chronic postural, and often debilitating, headaches¹⁻³ in young and middle-aged individuals. Causes of spinal CSF leak include iatrogenic (operation, epidural injections, and fluoroscopically guided spinal interventions) or noniatrogenic traumatic injury to the dura, degenerative changes (ie, osteophytes), and the recently described CSF-venous fistula (CVF). Imaging plays a central role both in establishing the diagnosis of intracranial hypotension and in identifying the location of a CSF leak.⁴⁻⁸ However, despite the advances in imaging, the number of cases without an identifiable cause remain high and can reach 46%–55% of cases in spontaneous

intracranial hypotension (SIH).^{9,10} For optimal management of these patients, it is important that a firm diagnosis of intracranial hypotension and underlying CSF leak be established, even in the absence of an overt CSF leak.

Schievink et al⁴ have proposed 3 diagnostic criteria for spontaneous CSF leak and intracranial hypotension, which are independently diagnostic: A, B, and C. Criterion A is demonstration of spinal CSF leak on any spinal imaging. Criterion B is demonstration of cranial MR imaging related to intracranial hypotension such as a subdural fluid collection and brain sagging plus the presence of at least 1 of the following: low opening pressure (60 mm H₂O or less), spinal meningeal diverticulum, or improvement of symptoms after epidural blood patching. Criterion C is the presence of all of the following or the presence of orthostatic headache and at least 2 of the following: low opening pressure (60 mm H₂O or less), spinal meningeal diverticulum, and/or improvement of symptoms after epidural blood patching.⁴

CT myelography is often used to establish the source of spinal CSF leak, given its wide availability and relative ease of interpretation across different subspecialties compared with

Received June 29, 2019; accepted after revision December 9.

From the Mallinckrodt Institute of Radiology, Washington University School of Medicine, St. Louis, Missouri.

Please address correspondence to Siavash Behbahani, MD, Washington University School of Medicine, Mallinckrodt Institute of Radiology, Neuroradiology Section, Campus Box 8131, 510 S. Kingshighway Boulevard, St. Louis, MO 63110-1076; e-mail: Siabeh@gmail.com

Indicates article with supplemental on-line table.

<http://dx.doi.org/10.3174/ajnr.A6393>

Table 1: Distribution of cases with clinical and/or imaging concern for CSF leak and the control group

	Cases (n = 49)	Controls (n = 90)
Inclusion criteria	Clinical suspicion and/or imaging concerning for CSF leak	Degenerative changes, spinal canal stenosis, radiculopathy, preoperative planning, and so forth
Age (yr) (range)	19–75 (mean, 49)	25–90 (mean, 58)
Sex	M = 14, F = 35	M = 33, F = 57

MR myelography and radionuclide cisternography. We have anecdotally observed opacification of the renal excretory system on CT myelograms obtained in patients with a suspected CSF leak. The purpose of this retrospective study was to assess whether the opacification of the renal excretory system could be used as an additional diagnostic sign of underlying CSF leak on CT myelograms (CTMs).

MATERIALS AND METHODS

An approval from the institutional review board at the Washington University in Saint Louis was obtained for this Health Insurance Portability and Accountability Act–compliant retrospective case-control research project.

Patient Selection

From our spine procedure data base, all consecutive adult patients (older than 18 years of age) who had undergone CT myelography between January 2008 and August 2018 in the setting of imaging and/or clinical findings of intracranial hypotension were included (Table 1). We additionally included 90 consecutive controls (Table 1) in whom lumbar CT myelography had been performed for indications other than suspected CSF leak. Patients who had received intravenous iodinated or gadolinium-based contrast within 48 hours preceding myelography were excluded. Studies that did not include the CT images of the lumbar spine or kidneys were also excluded. Indications for myelography in the control group were back pain ($n = 79$), radiculopathy ($n = 4$), spinal stenosis ($n = 3$), lower extremity weakness ($n = 2$), scoliosis ($n = 1$), fracture ($n = 1$), postfusion hardware failure ($n = 1$), and myelopathy ($n = 1$).

The 49 cases with imaging and/or clinical signs concerning for a spinal CSF leak that met the inclusion but not exclusion criteria were divided into 2 groups: Group 1 patients had CTM evidence of a CSF leak, and group 2 patients did not have any CTM evidence of a CSF leak. Group 2 was further assessed with respect to the presence or absence of imaging evidence of intracranial hypotension (ICH) on cranial MR imaging or a fluid collection on spinal MR imaging. These groups were then further evaluated for a response to the epidural blood patch and other pertinent clinical information.

Imaging Review and Statistical Analysis

Each CTM had initially been interpreted by a neuroradiology fellow and a board-certified neuroradiologist to evaluate a CSF leak. A neuroradiology fellow and a neuroradiology attending physician re-assessed these imaging studies for evidence of renal contrast, as evidenced by subjective visual recognition of

opacification of the renal excretory system (ie, calyces, renal pelvis, ureters, or urinary bladder). In addition, the average Hounsfield unit of renal pelvises was calculated by averaging the Hounsfield unit of each renal pelvis as determined by placing a circular ROI measuring between 8 and 10 mm within it. ROIs were placed centrally unless an off-center location had to be

selected due to the presence of streak artifacts or partial collapse of the central aspect of the renal pelvis. The Hounsfield unit value was not recorded if the small size of the renal pelvis or the presence of artifacts prevented placement of an ROI of >8 mm.

Both readers recorded the location of the CSF leak and epidural collection if they were present. They also reviewed other pertinent clinical and imaging records for categorization of patients based on the diagnostic criteria proposed by Schievink et al.⁴ The time from the start of the procedure (ie, initial fluoroscopic image obtained before access to the intrathecal space) to the time when the CT for the CTM was performed was recorded for all patients.

The mean and SD were calculated for the Hounsfield unit for patients with (groups 1 and 2) suspicion of CSF leak and for controls. Differences between these groups were tested for significance using an unpaired 2-sample *t* test. A *P* value $< .05$ was considered significant.

All the examinations were performed as single-energy CT on a Somatom Definition (Siemens, Erlangen, Germany) 128-section scanner with the following parameters: pitch = 0.9, kilovolt = 120, milliampere-second = 400, section thickness = 2 mm with a multiplane reconstruction increment of 1 mm. Both soft-tissue and bone kernels were included.

RESULTS

Of the 49 total patients with imaging and/or clinical signs concerning for a spinal CSF leak, 41 patients demonstrated clinical symptoms of headaches, orthostatic headaches, chronic headaches, and/or positional headaches with the remainder demonstrating various nonspecific symptoms of back pain, gait problems, falls, and so forth.

Direct evidence of CSF leak on CTM was seen in 21 patients (Fig 1, group 1: 7 men; mean age, 47.7 years; and 14 women; mean age, 45.8 years). Of these, 12 (57%) demonstrated cranial MR imaging findings of intracranial hypotension (Fig 2), whereas 5 (23%) did not. The remaining 4 patients did not have MR imaging of the brain. In 16/21 group 1 patients, an intraspinal epidural CSF leak was seen. The leak was foraminal in location in remaining 5 cases. Renal contrast on the CT myelogram was seen in 5/21 (23%) group 1 patients (On-line Table).

Those patients with a clinically suspected CSF leak without confirmatory evidence on CTM (group 2) included 8 men (average age, 37.9 years) and 20 women (average age, 55.5 years). Of these 28 patients, 8 patients met criterion B for the diagnosis of ICH and spinal CSF leak.⁴ Of the remaining 20 patients, 10 met neither criterion B nor C for the diagnosis of spinal CSF leak or ICH, and the other 10 could not be characterized using the criteria due to a lack of MR imaging or clinical data.

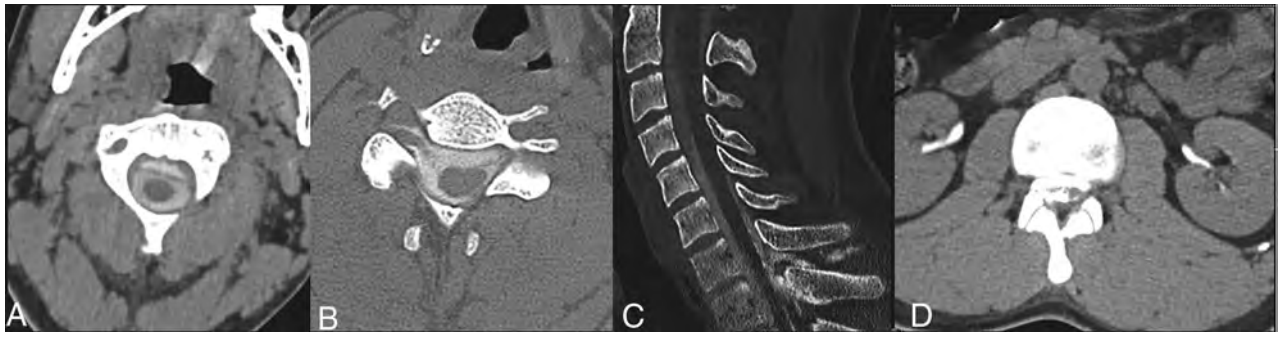


FIG 1. A 35-year-old man with trauma and MR imaging demonstrating a spinal fluid collection worrisome for CSF leak. Postmyelographic CT (A and B) reveals a ventral epidural fluid collection in the cervical spinal canal with right foraminal extension corresponding to an epidural CSF. A sagittal postmyelographic CT image (C) reveals gross extravasation of contrast into the interspinous space at C7–T1 at the suspected site of a ligamentum flavum injury. Axial images in soft-tissue windows demonstrate contrast in both renal collecting systems in this CTM without visualized intravenous contrast.

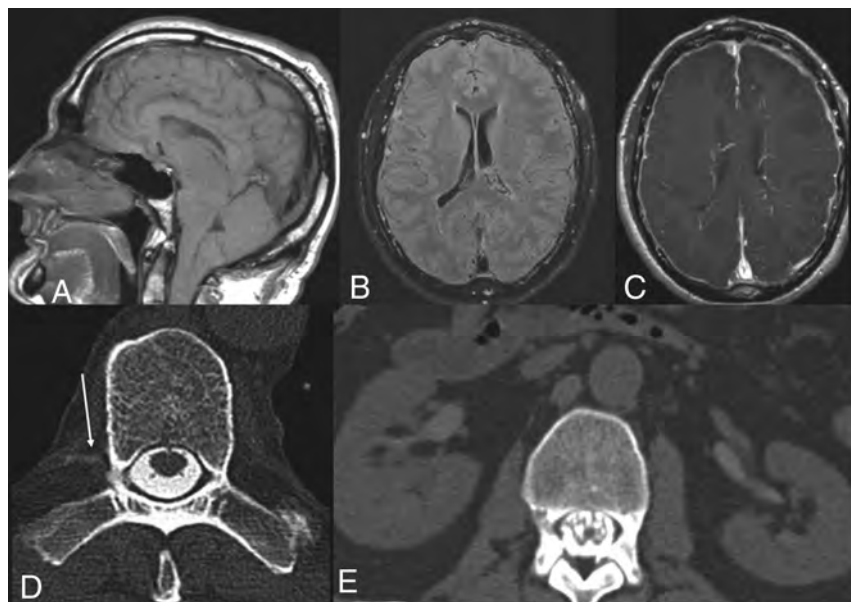


FIG 2. Upper images demonstrate signs of intracranial hypotension on brain MR imaging as demonstrated by cerebellar tonsillar descent through the foramen magnum (A), dilated venous sinuses (B), and diffuse pachymeningeal thickening and enhancement (C). Lower images demonstrate a CT myelogram in the same patient with a subtle CSF-venous fistula in the thoracic spine (arrow) and opacified renal collecting systems.

Only 2/28 (7.1%) patients in group 2 demonstrated renal contrast, both of whom met criterion B as demonstrated by MR imaging evidence of ICH as well as clinical symptom improvement with the epidural blood patch procedure. The first patient underwent an additional nuclear medicine examination for evaluation of a CSF leak, which demonstrated findings consistent with persistent CSF leak, confirming the diagnosis (On-line Table).

None of the controls demonstrated any renal or ureteric opacification on CT (Fig 3).

Successful measurement of Hounsfield units of the renal collecting system could be performed in 68 controls and 34 patients (including 7 in whom the presence of excreted contrast in the collecting system was visually evident). Patients in whom myelography was performed to look for CSF leaks had higher mean

Hounsfield units of the renal pelvises compared with the control group (Table 2, $P < .001$). Even patients without visually evident opacification of the renal collecting system had higher mean Hounsfield units compared with the control group (Table 2, $P < .001$).

The time between intrathecal contrast administration and CT examination ranged between 45 and 74 minutes with a mean of 57 minutes for our cases positive for renal contrast. The average time from the first fluoroscopy image obtained to the CT scan was 57 minutes in the patients with a suspected CSF leak and without renal contrast and 58 minutes in the control group. There was no statistical difference for the fluoroscopy-to-CT scan time interval among all 3 groups, with the P values for cases positive for renal contrast and the control group being .94, the control group and suspected CSF leak without contrast being .81, and suspected CSF leak without contrast and contrast-positive cases being .89.

DISCUSSION

CSF leak is a source of substantial patient morbidity and remains a challenging diagnosis. While most patients present with typical postural headaches, a subset of patients present with vague or atypical symptoms that can result in a delay in diagnosis. Additionally, not all patients demonstrate the classic intracranial or spinal MR imaging findings of ICH. The acknowledgment of such diagnostic challenges and yet the need for rapid and definitive diagnosis of CSF leak and ICH have recently led to increased use of and dependence on imaging to establish the diagnosis with incorporation of imaging in the diagnostic criteria of ICH.^{4,11}

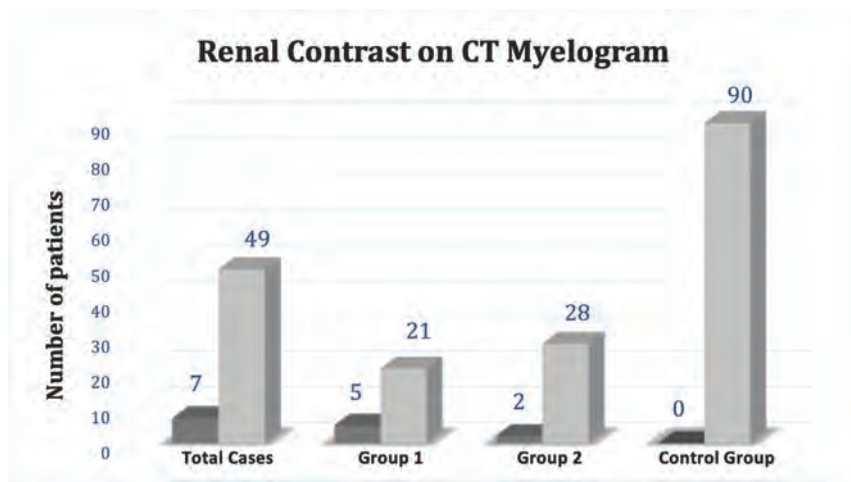


FIG 3. Contrast seen in the renal excretory system (renal contrast) in dark gray and total cases in each group in light gray.

Table 2: Mean Hounsfield unit values of the renal collecting systems for each group

Group	Mean HU in Right Renal Pelvis	Mean HU in Left Renal Pelvis	Mean HU in Renal Pelvises ^a
Control	68	3.2	1.8
Clinical- or imaging-suspected CSF leak with no contrast visualized in the renal collecting system	27	11.7	13.0
Suspected CSF leak with contrast visualized in the collecting system	7	132.8	128.5
			131

^aThe mean for each group was rounded to the next whole number for simplification.

Reliance on imaging to detect spinal sources of CSF leak will continue to increase, given the recent evidence suggesting that most spontaneous intracranial hypotension can be predominantly attributed to spinal sources (mechanical tears, CVFs, and leaking nerve root sleeves) and the increased rate of detection of a CSF leak with dynamic CT myelography.^{6,8,12-19} Despite these advances, detection of the site of CSF leak continues to remain elusive, and in some cases, establishing the diagnosis of CSF leak or ICH remains uncertain.

The primary goal of imaging of patients with positional headaches or suspected ICH is to establish the diagnosis of CSF leak, and if possible, the source of the leak. Our study suggests that visualization of contrast within the renal collecting system or ureters (renal contrast) on CT myelography can serve to firmly establish the diagnosis of a CSF leak. Contrast opacification of the renal collecting excretory system was 100% specific for CSF leak. This subjective visual assessment was further confirmed objectively by a statistically significant difference between the mean Hounsfield unit in the collecting system between the control group and group 2. The objective measurement of the collecting system Hounsfield unit further adds validity to this finding and can, in combination with the visual assessment, serve as an additional sign of CSF leak.

Renal and ureteric renal opacification was noted in patients across multiple pathophysiologies, including traumatic dural

tears, degenerative mechanical tears, CVF, and no identifiable CSF leak source. Renal and ureteric contrast opacification was also noted in patients with and without brain MR imaging findings of ICH and in patients with or without spinal fluid collections on MR imaging (slow or fast leak). This consistency across multiple pathophysiologies and positive or negative MR imaging findings supportive of CSF leak and/or ICH combined with 100% specificity makes this finding excellent for confirmation of a leak and an extremely valuable marker for occult spinal CSF leaks. As a result, renal contrast on CT myelography can be used as a definitive predictor or a major component of the diagnostic criteria for CSF leak.

Kinsman et al¹² have recently shown similar results with renal contrast on CT myelography only detected in patients with spontaneous intracranial hypotension. However, in their study, renal contrast visualization was highly correlated with the presence of CSF venous fistulas in patients with spontaneous intracranial hypotension and was noted less frequently in patients with dural tears. This find-

ing differs from those in our retrospective study because our study found that only 1 of the 7 cases was due to a CSF-venous fistula. However, because both studies are limited by power, studies with larger numbers of case series or a large-volume literature meta-analysis are needed to estimate the relative proportion of each etiology before associating this specific finding with a particular pathophysiology of CSF leak.

The underlying pathophysiology of this finding remains unclear. A potential explanation is the presence of direct communication between CSF and the venous system and, thus, rapid clearance of contrast by the collecting system as noted in CVF. However, the lack of consistency of this finding in all patients with CVF suggests an additional mechanism for this finding.¹² Also, the presence of this finding, in our series and of that of Kinsman et al,¹² in patients without CVF further supports additional factors contributing to the rapid renal clearance of CSF in selective patients with CSF leak. An interesting observation in our study is that subjective contrast opacification of the renal system on CT myelography was detected only in patients meeting the Schievink diagnostic criteria A or B, with none seen in patients meeting criterion C. This finding was similar to that of Kinsman et al because their study showed contrast opacification in patients with a detected leak on CT myelography (criterion A), patients with findings of ICH (criterion B), and patients with CVF.

Quantitative Hounsfield unit assessment revealed significant differences between the control group (average 3 Hounsfield units) and patients with suspected CSF leak without visually apparent renal contrast (average of 12 Hounsfield units). There was also a significant difference between the mean Hounsfield unit of the collecting system between groups 1 and 2. This may indicate that the extent of renal contrast excretion occurring by the time a postmyelogram CT is obtained is also a function of how much contrast ends up extravasating from the thecal sac. While arguing for measuring Hounsfield units of the renal pelvises, it also suggests the possible role of techniques such as dual-energy CT myelography in bringing out these inherent subtle contrast differences.^{20,21}

Recognition of this sign has important implications in the management of patients with suspected ICH. It is well-recognized that identification and localization of a CSF leak can sometimes require multiple imaging studies, especially in patients who end up being diagnosed with CVF. Our results suggest that recognition of renal contrast on CT myelography should prompt a thorough review of CT myelography for subtle signs of CSF leak, and if not found, an active pursuit with additional imaging, including digital subtraction myelography to look for underlying pathology including a CVF or focal dural tear, should be performed.^{8,10,22}

Limitations and Future Research

While our study highlights an important finding that can aid in establishing the diagnosis of spinal leak, prompting a search for a leak source in subtle or occult cases, we acknowledge several limitations. The first limitation was the relatively small sample size of the patient population. While we acknowledge that the sensitivity of our study for detection of CSF leak may be low, given the high specificity of the positive findings and the relatively large control group, these were not thought to limit the significance of the finding. Furthermore, the high specificity of this finding may prove helpful when applied to larger populations of patients. However, the small sample size limits association of this finding with specific CSF leak pathophysiology. Second, the recorded time between intrathecal contrast injection and the CT examination start was longer than the actual interval between the 2 examinations because the myelographic examination start was recorded from the first fluoroscopic acquisition rather than from the time of intrathecal contrast injection. However, this difference was not a significant limitation because the time interval between the 2 examinations remained relatively short and there was no significant difference in the time interval among all 3 groups. Third, a direct CSF leak was not detected on CT myelography in many of the cases; this finding may have been, at least partially, due to a combination of interval resolution of the presumed spinal CSF leak between initial symptom presentation and CTM acquisition and/or clinical misdiagnosis. Last, in the study design, the attending neuroradiologist and neuroradiology fellow who designed and completed this retrospective project were not blinded to the study and data collection. However, the conclusion derived by this nonblinded review is firmly supported by the objective, quantitative Hounsfield unit measurements.

CONCLUSIONS

Renal contrast was exclusively seen in the presence of CSF leak. Given its 100% specificity, identification of this finding should prompt a closer second look for subtle myelographic contrast extravasation or an underlying CVF. Our results suggest that this sign may be considered as an additional diagnostic criterion for CSF leak in the absence of an identifiable leak. This could be used in conjunction with known diagnostic criteria of CSF leak in SIH.⁴

REFERENCES

1. Schievink WI. **Spontaneous spinal cerebrospinal fluid leaks: a review.** *Neurosurg Focus* 2000;9:9 CrossRef Medline
2. Schievink WI. **Spontaneous spinal cerebrospinal fluid leaks and intracranial hypotension.** *JAMA* 2006;295:2286–96 CrossRef Medline
3. Mokri B. **Spontaneous low pressure, low CSF volume headaches: spontaneous CSF leaks.** *Headache* 2013;53:1034–53 CrossRef Medline
4. Schievink WI, Maya MM, Louy C, et al. **Diagnostic criteria for spontaneous spinal CSF leaks and intracranial hypotension.** *AJNR Am J Neuroradiol* 2008;29:853–56 CrossRef Medline
5. Halkar R, Pettigrew R, Lipman C, et al. **Rapid transit of tracer to the kidneys and urinary bladder in radionuclide cisternography: a sign of CSF leak.** *Clin Nucl Med* 1997;22:121–23 CrossRef Medline
6. Dillon WP. **Challenges in the diagnosis and treatment of spontaneous intracranial hypotension.** *Radiology* 2018;289:773–74 CrossRef Medline
7. Kranz PG, Tanpitukpongse TP, Choudhury KR, et al. **How common is normal cerebrospinal fluid pressure in spontaneous intracranial hypotension?** *Cephalalgia* 2016;36:1209–17 CrossRef Medline
8. Farb RI, Nicholson PJ, Peng PW, et al. **Spontaneous intracranial hypotension: a systematic imaging approach for CSF leak localization and management based on MRI and digital subtraction myelography.** *AJNR Am J Neuroradiol* 2019;40:745–53 CrossRef Medline
9. Sencakova D, Mokri B, McClelland RL. **The efficacy of epidural blood patch in spontaneous CSF leaks.** *Neurology* 2001;57:1921–23 CrossRef Medline
10. Luetmer PH, Schwartz KM, Eckel LJ, et al. **When should I do dynamic CT myelography? Predicting fast spinal CSF leaks in patients with spontaneous intracranial hypotension.** *AJNR Am J Neuroradiol* 2012;33:690–94 CrossRef Medline
11. Headache Classification Subcommittee of the International Headache Society. **The International Classification of Headache Disorders, 2nd ed.** *Cephalalgia* 2004;24(Suppl 1):9–160 Medline
12. Kinsman KA, Verdoorn JT, Luetmer PH, et al. **Renal contrast on CT myelography: diagnostic value in patients with spontaneous intracranial hypotension.** *AJNR Am J Neuroradiol* 2019;40:376–81 CrossRef Medline
13. Schievink WI, Moser FG, Maya MM. **CSF-venous fistula in spontaneous intracranial hypotension.** *Neurology* 2014;83:472–73 CrossRef Medline
14. Kranz PG, Amrhein TJ, Schievink WI, et al. **The “hyperdense paraspinous vein” sign: a marker of CSF-venous fistula.** *AJNR Am J Neuroradiol* 2016;37:1379–81 CrossRef Medline
15. Clark MS, Diehn FE, Verdoorn JT, et al. **Prevalence of hyperdense paraspinous vein sign in patients with spontaneous intracranial hypotension without dural CSF leak on standard CT myelography.** *Diagn Interv Radiol* 2018;24:54–59 CrossRef Medline
16. Schievink WI, Maya MM, Jean-Pierre S, et al. **A classification system of spontaneous spinal CSF leaks.** *Neurology* 2016;87:673–79 CrossRef Medline

17. Kranz PG, Gray L, Amrhein T. **Spontaneous intracranial hypotension: 10 myths and misperceptions.** *Headache* 2018;58:948–59 CrossRef Medline
18. Kranz PG, Malinzak MD, Amrhein TJ, et al. **Update on the diagnosis and treatment of spontaneous intracranial hypotension.** *Curr Pain Headache Rep* 2017;21:37 CrossRef Medline
19. Kranz PG, Amrhein TJ, Gray L. **CSF venous fistulas in spontaneous intracranial hypotension: imaging characteristics on dynamic and CT myelography.** *AJR Am J Roentgenol* 2017;209:1360–66 CrossRef Medline
20. Watanabe Y, Tsukabe A, Kunitomi Y, et al. **Dual-energy CT for detection of contrast enhancement or leakage within high-density haematomas in patients with intracranial haemorrhage.** *Neuroradiology* 2014;56:291–95 CrossRef Medline
21. Kaza RK, Platt JF, Cohan RH, et al. **Dual-energy CT with single- and dual-source scanners: current applications in evaluating the genitourinary tract.** *Radiographics* 2012;32:353–69 CrossRef Medline
22. Hoxworth JM, Patel AC, Bosch EP, et al. **Localization of a rapid CSF leak with digital subtraction myelography.** *AJNR Am J Neuroradiol* 2009;30:516–19 CrossRef Medline

Long-Term Outcome of Patients with Spinal Dural Arteriovenous Fistula: The Dilemma of Delayed Diagnosis

F. Jablawi, G.A. Schubert, M. Dafotakis, J. Pons-Kühnemann, F.-J. Hans, and M. Mull



ABSTRACT

BACKGROUND AND PURPOSE: The impact of various radiologic and clinical features on the long-term outcome in spinal dural arteriovenous fistulas is still unclear; thus, they are the purpose of this study.

MATERIALS AND METHODS: We retrospectively analyzed our medical data base for all patients treated for spinal dural arteriovenous fistula in our institution between 2006 and 2016. Patient age, neurologic status at the time of diagnosis, the duration of symptoms from onset to diagnosis, and follow-up information were evaluated. The extent of medullary T2WI hyperintensity, intramedullary contrast enhancement, and elongation of perimedullary veins on MR imaging at the time of diagnosis were additionally analyzed.

RESULTS: Data for long-term outcome analysis were available in 40 patients with a mean follow-up of 52 months (median, 50.5 months; range, 3–159 months). The mean age at the time of diagnosis was 69.27 ± 9 years (median, 71 years; range, 53–84 years) with a male predominance ($n = 32$; 80%). The mean duration of symptoms was 20.2 months (median, 10 months; range, 1–120 months). Shorter duration of symptoms at the time of diagnosis was significantly correlated with better outcome of symptoms ($P < .05$).

CONCLUSIONS: Spinal dural arteriovenous fistulas are characterized by interindividually variable clinical presentations, which make a determination of specific predictors for long-term outcome more difficult. Fast and sufficient diagnosis might result in a better outcome after treatment. The diagnosis of spinal dural arteriovenous fistula remains markedly delayed, reflecting an ongoing lack of knowledge and awareness among treating physicians of this rare-but-serious disease.

ABBREVIATIONS: AL-score = Aminoff-Logue disability score; CE-MRA = contrast-enhanced MRA; sdAVF = spinal dural arteriovenous fistula

Spinal dural arteriovenous fistulas (sdAVFs) usually become symptomatic in elderly men, who are affected 5 times more often than women.¹ Symptoms caused by sdAVF comprise gait disturbances with or without paresis, sensory disturbances in the lower extremities, pain, and sphincter and erectile dysfunctions.² An estimation based on a series assessed previously in RWTH Aachen University Hospital revealed an incidence rate for sdAVF of up to 5–10 million per year in the general population.³

The predictive value of several radiologic and clinical factors in patients with sdAVF has been controversially discussed in the

past.^{4,5} The existence of a plethora of case series implies a lack of universal consensus on possible predictors for long-term outcome.⁵

Because sdAVF is a particularly rare disease and is frequently misdiagnosed for several months to years, gathering a sufficient number of patients for a meaningful analysis is an inherent challenge. At the same time, gathering long-term outcome data of a predominantly elderly and comorbid patient population is associated with several logistic difficulties. Moreover, a comparative analysis of various studies to dramatically increase sample size is hampered by relevant variations in diagnostic and therapeutic strategies in different referral centers.^{3,5} Thus, our current study aims to fill this gap by providing clinical and radiologic features as well as follow-up information of a considerable cohort of microsurgically treated sdAVFs.

MATERIALS AND METHODS

We retrospectively analyzed our medical data base for all patients treated for sdAVF at RWTH Aachen University Hospital between 2006 and 2016.

Received September 24, 2019; accepted after revision November 06.

From the Departments of Diagnostic and Interventional Neuroradiology (F.J., M.M.), Neurosurgery (G.A.S.), and Neurology (M.D.), RWTH Aachen University Hospital, Aachen, Germany; Department of Neurosurgery (F.J.), and Medical Statistics, Institute for Medical Informatics (J.P.-K.), Justus-Liebig-University, Giessen, Germany; and Department of Neurosurgery (F.-J.H.), Paracelsus Kliniken, Osnabrück, Germany.

Please address correspondence to Michael Mull, MD, Department of Diagnostic and Interventional Neuroradiology, RWTH Aachen University Hospital, Pauwelsstr 30, 52074 Aachen, Germany; e-mail: mmull@ukaachen.de
<http://dx.doi.org/10.3174/ajnr.A6372>

Aminoff-Logue disability score for gait

Grade of Gait Disturbances	Characteristics
0	Normal
1	Leg weakness, abnormal walk or stance, but no restriction of activity
2	Restricted activity
3	Requiring 1 cane for walking
4	Requiring 2 canes, crutches, or walker
5	Confined to wheelchair

The diagnosis of sdAVF was performed on the basis of the following criteria: 1) myelopathic symptoms, including gait disturbances with or without vegetative urinary dysfunctions; 2) findings of congestive myelopathy with or without engorged perimedullary veins on MR images; and 3) angiographic confirmation of an sdAVF.

Clinical data including patient age, neurologic status at diagnosis, and duration of symptoms from onset to diagnosis were assessed by the treating physicians and re-evaluated for this study. Radiologic data were electronically available and reviewed accordingly. Clinical data were obtained by chart review and/or telephone survey.

We routinely aim to perform an early postoperative MR imaging during the inpatient stay, 3–6 months after discharge, and annually in the first three years after treatment for all patients with sdAVFs. In case of persistence or deterioration of clinical symptoms and/or radiologic findings indicative of congestive myelopathy, we additionally perform spinal MRA and DSA to rule out residual or recurrent fistulas.

Neurologic status at time of diagnosis and at last follow-up was assessed using the Aminoff-Logue disability score for gait (AL-score) (Table).⁶ The long-term outcome was assessed on the basis of changes of the AL-score across time and was rated as improved, stable, or aggravated. To analyze the significance of the duration of symptoms on long-term outcome, we categorized the time from onset to diagnosis as follows: 1) ≤ 6 months, 2) 7–18 months, and 3) > 18 months. The extent of medullary edema, intramedullary contrast enhancement, and engorgement of perimedullary veins on MR imaging at diagnosis was recorded and rated according to the number of affected vertebral levels. The location of the sdAVF verified by spinal DSA was categorized as follows: 1) thoracic: T3–T9; 2) thoracolumbar: T10–L4; and 3) deep lumbosacral: below L4.⁷

Statistics

Data were expressed as means \pm SD and median and range. Correlation analysis and group comparisons were performed with nonparametric statistics. Data analysis was performed with SPSS Statistics for Windows, Version 25.0 (IBM, Released 2017, Armonk, New York).

RESULTS

A total of 59 patients with sdAVFs were identified. Data for long-term outcome analysis were available in 40 patients, with the remaining 19 patients being lost to follow-up due to unknown changes of address ($n = 11$) or incomplete clinical

and radiologic data ($n = 8$). Twenty-eight (70%) of these 40 patients were referred to our center from elsewhere due to clinically and radiologically suspected spinal arteriovenous pathology with nonconclusive MR imaging and/or DSA examinations. All 28 patients underwent at least 1 spinal MR imaging, and 17 of them underwent at least 1 spinal DSA before admission to our institution.

After angiographic visualization of the sdAVF in our center, all 40 patients were treated via microsurgical disconnection of the intradural drainage vein. Only 1 patient was found to have a residual fistula on early postoperative DSA, which was occluded surgically 2 days after the initial operation. Procedure-related complications were observed in 2 (5%) patients. One patient developed a wound infection, and 1 patient was treated for postoperative CSF leakage.

Clinical Features

The mean age at diagnosis ($n = 40$) was 69.27 ± 9 years (median, 71 years; range, 53–84 years) with a male predominance ($n = 32$, 80%). The mean duration of symptoms from onset to diagnosis was 20.2 months (median, 10 months; range, 1–120 months). Gait disturbances were present in all 40 patients. Paraparesis was observed in various manifestations in 29/40 (73%) patients. Another 11/40 (27%) patients had ataxia or neurogenic claudication without overt paresis in the lower extremities. The mean AL-score for gait at diagnosis was 3 ± 1.6 (median, 3; range, 0–5).

Radiologic Findings

Preoperative MR imaging ($n = 40$) and additional spinal contrast-enhanced MRA (CE-MRA) ($n = 34$) examinations were available for this analysis. Medullary edema was detected in 35/40 (88%), extending, on average, over 5.5 ± 3 vertebral levels (median, 6 vertebral levels; range, 1–12 vertebral levels). Intramedullary contrast enhancement was observed in 30/40 (75%), on average extending over 4 ± 2.4 vertebral levels (median, 4 vertebral levels; range, 1–8 vertebral levels). Engorged perimedullary veins in the thoracic and/or thoracolumbar region were observed in all 40 patients, with a mean extension of 7.5 ± 4.6 vertebral levels (median, 7 vertebral levels; range, 1–18 vertebral levels). On DSA, 17 sdAVFs were located in the thoracic, and 19, in the thoracolumbar region. Four fistulas were located in the deep lumbosacral region.

Long-Term Outcome

After a mean follow-up of 52 ± 37 months (median, 50.5 months; range, 3–159 months), the mean AL-score was 2.5 ± 1.8 (median, 3; range, 0–5). Clinical follow-up outcome was improved in 21/40 (53%), stable in 11/40 (28%), and aggravated in 8/40 (20%) patients. Chances for good long-term outcome were not influenced by patient age ($P = .152$) or by the neurologic status at diagnosis ($P = .324$) (Fig 1). A longer duration of symptoms from onset to diagnosis was significantly associated with worse long-term outcome ($P = .008$). Patients with a shorter clinical course (≤ 6 months) had an improvement of their gait disturbances up to 1 grade on the AL-score (Fig 1). No significant correlation was observed

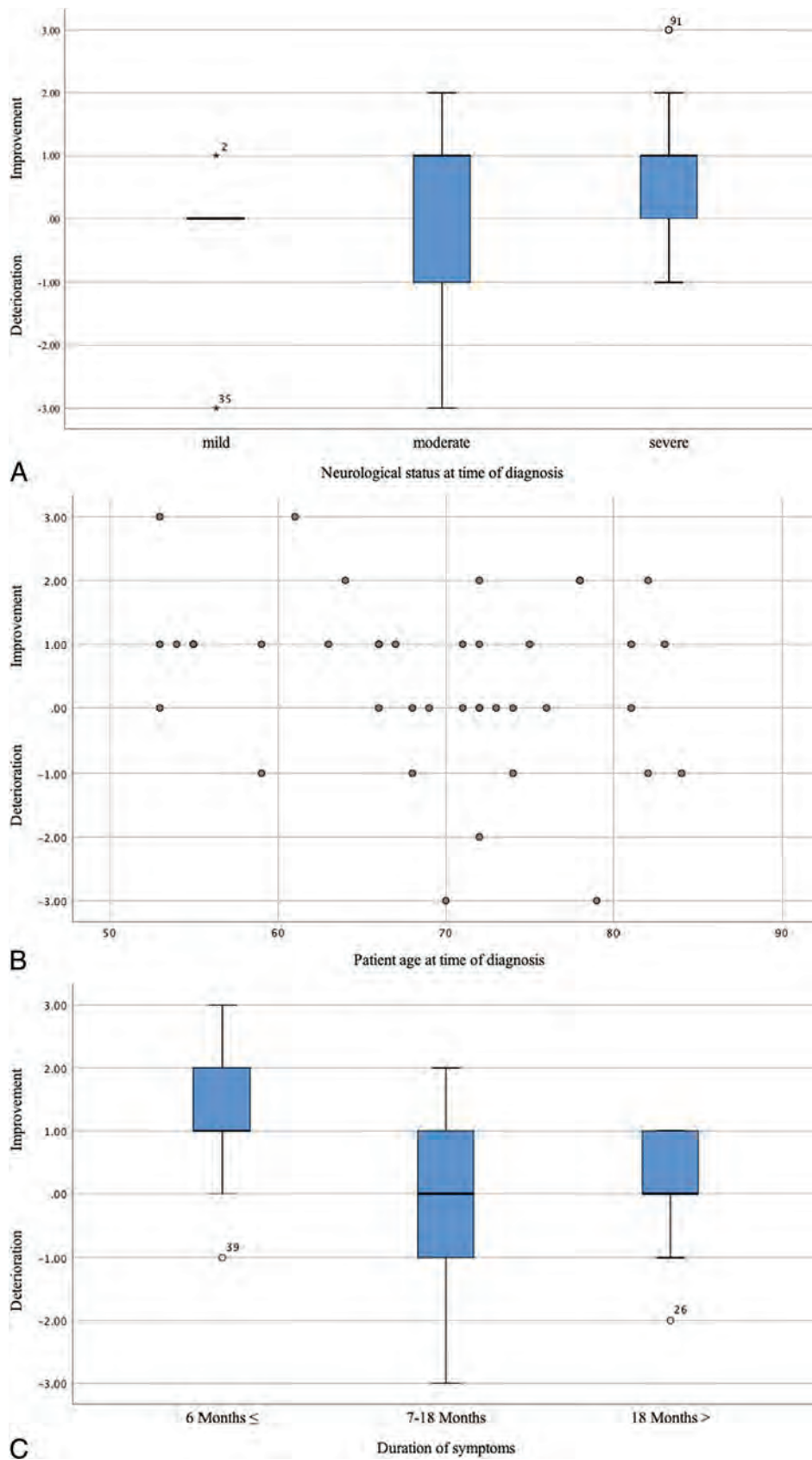


FIG 1. A, Boxplot demonstrates the correlation between long-term outcome and neurologic status at diagnosis evaluated by the AL-score and dichotomized into mild: AL-score 0–1; moderate: AL-score 2–3; and severe: AL-score: 4–5. B, Scatterplot demonstrates the relationship between long-term outcome and patient age at diagnosis. C, Boxplot demonstrates the correlation between long-term outcome and the duration of symptoms at diagnosis. The x-axis indicates the initial and follow-up AL-scores.

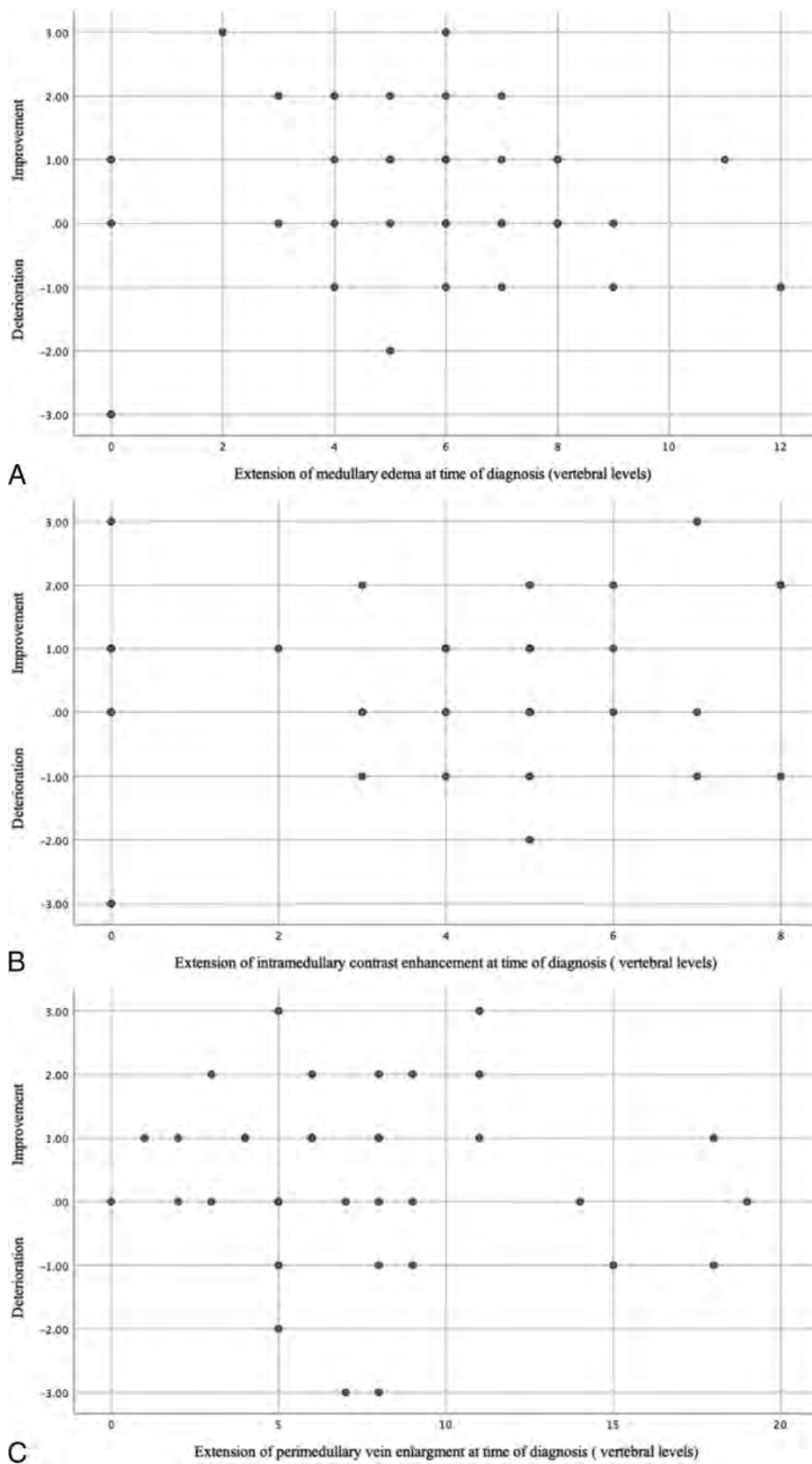


FIG 2. Scatterplot demonstrates the relationship between long-term outcome and extension of medullary edema (A), intramedullary contrast enhancement (B), and perimedullary vein enlargement at diagnosis (C). The x-axis indicates the initial and follow-up AL-scores.

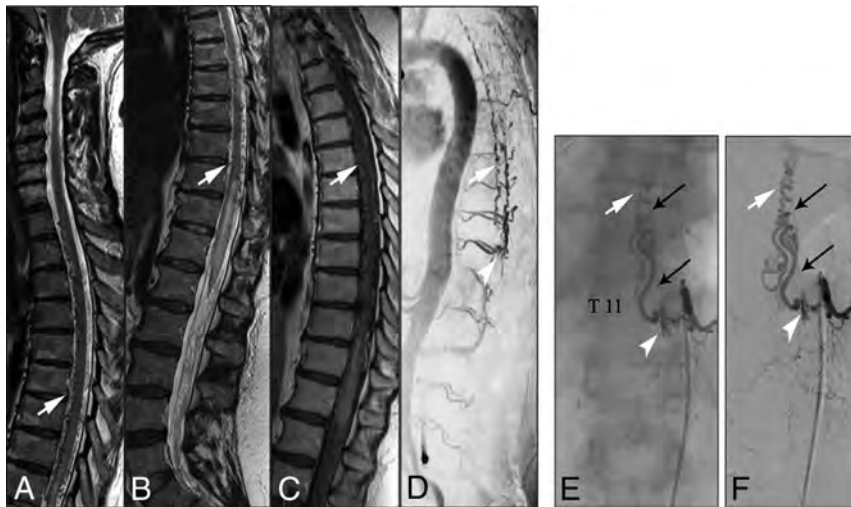


FIG 3. A–C, T2- and T1-weighted MR images demonstrate elongated perimedullary veins (*white arrows*) associated with medullary edema and centro-medullary contrast enhancement in the lower thoracic region. *D*, CE-MRA image shows the arterialized perimedullary veins in the thoracic region (*white arrow*) and depicts the shunt zone at the T11 vertebral level (*white arrowhead*). *E* and *F*, Spinal DSA examination (posterior-anterior projection) of the left T11 segmental artery shows the hypervascularized fistula zone (*white arrowhead*) with a dilated and elongated intradural drainage vein. Note the origin of the Adamkiewicz artery from the same fistula side (*small black arrows*).

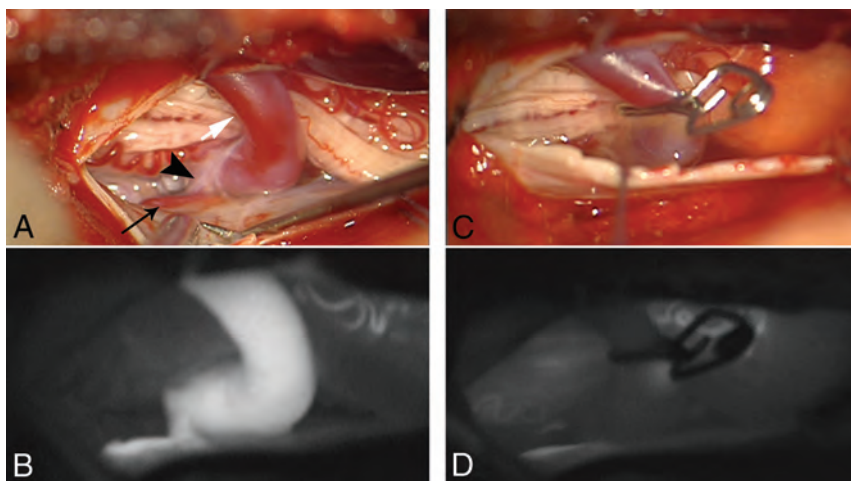


FIG 4. *A*, Intraoperative images show the fistula zone (*black arrowhead*), a narrow arterial feeder (*small black arrow*), and the elongated radicular drainage vein (*white arrow*). *B*, Indocyanine green images confirm the pathologic arterialization of the elongated radicular vein. *C* and *D*, The radicular drainage vein is disconnected via clip ligation, and indocyanine green videoangiography confirms the interruption of the pathologic arterialization.

between long-term outcome and the extent of medullary edema ($P = .638$), intramedullary contrast enhancement ($P = .425$), and engorgement of the perimedullary veins ($P = .672$) (Fig 2). There was also no relationship between the fistula location and the long-term outcome in our cohort.

Long-term follow-up MR imaging examinations were available for 21 patients with a mean follow-up of 14.5 ± 11.6 months (median, 12 months; range, 1–44 months). All 21 patients demonstrated a regression of the medullary venous congestion, reflecting a sufficient interruption of the arteriovenous shunt.

DISCUSSION

Clinical Features

Among all analyzed clinical factors in our current cohort, only a shorter duration of symptoms before treatment (≤ 6 months) was associated with a better long-term outcome. Patient age and the neurologic status at diagnosis had no influence on the long-term outcome.

Most surprising, the most stunning finding among patients in our current cohort was the long duration of symptoms of almost 2 years from onset to definite diagnosis. This was unchanged

The clinical and/or radiologic follow-up examinations were performed by their local physicians in the remaining 19 patients. No clinical/radiologic findings suggesting a recurrent sdAVF were re-reported in any of these patients.

Illustrative Case

A 56-year-old woman presented with progressive gait disturbances during the past 4 months. Neurologic examinations at the time of admission showed spinal ataxia, proximal accentuated paraparesis, and hypoesthesia below T10. In the initial CE-MRA in our center, T2WI and T1WI showed centro-medullary edema and contrast enhancement extending from the T10 vertebral level to the conus medullaris (Fig 1). Arterialized perimedullary veins were detected in the thoracic region dorsally as well as ventral to the myelon. Further MRA sequences suggested an arteriovenous shunt at the level of the T11 segmental artery. The subsequent DSA was primarily focused on this region. A sdAVF could be identified at the level of the left T11 nerve root receiving arterial supply via radiculomeningeal branches of the left T11 segmental artery. The venous drainage into the perimedullary venous plexus occurred via the elongated left T11 radicular vein (Fig 3). After left-sided hemilaminectomy at the T11 vertebral level, the hypervascularized fistula zone and the elongated radicular drainage vein were identified. The drainage vein was disconnected via clip ligation (Fig 4). In the annual follow-up examinations after treatment, gait disturbances and paraparesis had improved markedly. MR images showed a complete regression of medullary congestion (Fig 5).



FIG 5. Follow-up T2-weighted MR image and CE-MRA 3 years after treatment show a complete regression of medullary edema and alteration of perimedullary veins.

compared with an older cohort from our group (91 patients diagnosed between 1988 and 2002, mean duration of symptoms of 20 ± 19 months; $P = .533$).⁸ Moreover, to the best of our knowledge, a mean duration of symptoms of <1 year has never been reported in any of the large representative series in the literature.^{4,5,9}

Because high-quality MR imaging/MRA and DSA are more readily available currently than in the past, we assume that our actual observation is reflecting an ongoing lack of awareness and experience in dealing with this rare disease of nonspecific clinical and radiologic presentations. This may also explain the relatively high rate of patients who were referred to our center with nonconclusive clinical and radiologic findings (28/40), despite repetitive MR imaging and/or DSA examinations performed in their local hospitals.

In the early phase of the disease, the diffuse symptoms of sdAVF are commonly confused with more frequent disease entities such as spinal degenerative diseases or polyneuropathy. In cases with the above-mentioned, nonspecific symptoms but a lack of

typical findings of degeneration or polyneuropathy, we recommend imaging the whole spine with T2WI. Whenever a medullary congestion with or without elongated perimedullary vessels is present, further spinal MRA and/or DSA examinations should be considered.

Radiologic Findings

There is a universal consensus in the literature that medullary venous hypertension is the basic pathomechanism behind the symptomatology of sdAVF. If the fistula is left untreated, induced congestive myelopathy usually progresses to medullary ischemia, leading to disturbances of the spinal cord–blood barrier.¹⁰ These pathophysiologic changes induce typical-but-nonspecific medullary edema and contrast enhancement with or without engorgement of perimedullary veins on MR images.^{1,11}

Regardless of the treatment technique, the prognostic impact of initial neuroradiologic findings on long-term outcome in patients with sdAVFs is still a matter of dispute.^{12,13} Hetts et al¹⁴ demonstrated in a series of 31 patients, a positive correlation between early functional recovery after treatment and the extent of elongated perimedullary veins at diagnosis. In a cohort of 65 patients treated either microsurgically or endovascularly with a mean follow-up of 6 months reported by Cenzato et al,¹⁵ sdAVFs in the lower thoracic segments (T9–T12) were associated with more severe symptoms but tended to improve more after treatment. Midthoracic (above T9) and lumbar (below T12) fistulas in their series were associated with a lower incidence of improvement.¹⁵ In contrast, Dhandapani et al¹⁶ reported a higher improvement rate in patients with sdAVFs below the T9 level in 22 microsurgically treated patients within a mean follow-up of 7 months.

Compared with the rather short follow-up periods in these studies, our current analysis had a mean follow-up of 52 ± 37 months and showed no correlation between the extensions of medullary edema, centro-medullary contrast enhancement, or elongation of perimedullary veins, and the long-term outcome. Also, the fistula location showed no influence on the long-term outcome in our analysis.

We assume that the chronic pathologic arterialization of the spinal venous system could induce irreversible changes of medullary venous outflow that may significantly affect the functional recovery, even after sufficient interruption of the arteriovenous shunt.^{2,17}

In a previous analysis by our group, we found that the elongation of perimedullary veins on MR images is more dominant in the earlier phase of this disease.² These dilated veins may maintain the medullary venous outflow, reflecting a better compensation of the medullary venous hypertension and result in a better outcome if the sdAVF was sufficiently diagnosed and treated in this phase of the disease. A sufficient visualization of the spinal venous system is, however, still associated with major diagnostic difficulties. It could clarify several unclear aspects of this disease and should be the subject of further studies.

Limitations

Our study has several limitations. First, because our institution is a tertiary referral center for spinal vascular diseases, there is a

high risk of referral bias in our current analysis, resulting in a longer duration from symptom onset to diagnosis. Another risk of bias is the retrospective approach of this study, which may provoke speculative interpretation of our data to some extent. Another limitation is that we retrospectively determined the Aminoff-Logue disability scale through chart review. The AL-score itself has a limited value in the interpretation of neurologic status.

CONCLUSIONS

Spinal dural arteriovenous fistulas are characterized by interindividually variable clinical presentations that make a determination of specific predictive factors for the long-term outcome more difficult. Our current analysis implies the importance of early diagnosis for a better neurologic outcome. However, despite major developments in neuroradiologic noninvasive diagnostic tools in the past decades, the diagnosis of sdAVF remains markedly delayed. Our current study may raise the awareness of neurologists of this rare disease and emphasize the importance of early diagnosis in these patients.

Disclosures: Gerrit Alexander Schubert—UNRELATED: Consultancy: Carl Zeiss Meditec AG, Jena, Germany. Manuel Dafotakis—UNRELATED: Board Membership: Merz Pharma, Comments: dystonia and spasticity; Payment for Lectures Including Service on Speakers Bureaus: Merz Pharma, Ipsen, Allergan, Comments: botulinum toxin therapy.

REFERENCES

1. Thron AK. Applications in spinal dural AV fistulas. In: Thron AK. *Vascular Anatomy of the Spinal Cord: Radioanatomy as the Key to Diagnosis and Treatment*. 2nd ed. Cham: Springer-Verlag International Publishing; 2016
2. Jablawi F, Mull M. **The clinical value of venous drainage in patients with spinal dural arteriovenous fistula.** *J Neurol Sci* 2019;397:50–54 CrossRef Medline
3. Behrens S, Thron A. **Long-term follow-up and outcome in patients treated for spinal dural arteriovenous fistula.** *J Neurol* 1999;246:181–85 CrossRef Medline
4. Saladino A, Atkinson JL, Rabinstein AA, et al. **Surgical treatment of spinal dural arteriovenous fistulae: a consecutive series of 154 patients.** *Neurosurgery* 2010;67:1350–57; discussion 1357–58
5. Steinmetz MP, Chow MM, Krishnaney AA, et al. **Outcome after the treatment of spinal dural arteriovenous fistulae: a contemporary single-institution series and meta-analysis.** *Neurosurgery* 2004;55:77–87; discussion 87–88 Medline
6. Aminoff MJ, Barnard RO, Logue V. **The pathophysiology of spinal vascular malformations.** *J Neurol Sci* 1974;23:255–63 CrossRef Medline
7. Jablawi F, Nikoubashman O, Schubert GA, et al. **Clinical and radiologic characteristics of deep lumbosacral dural arteriovenous fistulas.** *AJNR Am J Neuroradiol* 2018;39:392–98 CrossRef Medline
8. Mull M. **Durchblutungsstörungen des Rückenmarks: Neurologische Untersuchungen zur Pathogenese und Strategien der Diagnosesicherung.** Department of Diagnostic and Interventional Neuroradiology, University Hospital Aachen; 2004. https://www.researchgate.net/publication/33987973_Durchblutungsstorungen_des_Ruckenmarks_neuroradiologische_Untersuchungen_zur_Pathogenese_und_Strategien_der_Diagnosesicherung. Accessed June 30, 2003
9. Sherif C, Gruber A, Bavinszki G, et al. **Long-term outcome of a multidisciplinary concept of spinal dural arteriovenous fistulae treatment.** *Neuroradiology* 2008;50:67–74 CrossRef Medline
10. Hurst RW, Kenyon LC, Lavi E, et al. **Spinal dural arteriovenous fistula: the pathology of venous hypertensive myelopathy.** *Neurology* 1995;45:1309–13 CrossRef Medline
11. Mull M, Nijenhuis RJ, Backes WH, et al. **Value and limitations of contrast-enhanced MR angiography in spinal arteriovenous malformations and dural arteriovenous fistulas.** *AJNR Am J Neuroradiol* 2007;28:1249–58 CrossRef Medline
12. Yen PP, Ritchie KC, Shankar JJ. **Spinal dural arteriovenous fistula: correlation between radiological and clinical findings.** *J Neurosurg Spine* 2014;21:837–42 CrossRef Medline
13. Koenig E, Thron A, Schrader V, et al. **Spinal arteriovenous malformations and fistulae: clinical, neuroradiological and neurophysiological findings.** *J Neurol* 1989;236:260–66 CrossRef Medline
14. Hetts SW, Moftakhar P, English JD, et al. **Spinal dural arteriovenous fistulas and intrathecal venous drainage: correlation between digital subtraction angiography, magnetic resonance imaging, and clinical findings.** *J Neurosurg Spine* 2012;16:433–40 CrossRef Medline
15. Cenzato M, Versari P, Righi C, et al. **Spinal dural arteriovenous fistulae: analysis of outcome in relation to pretreatment indicators.** *Neurosurgery* 2004;55:815–22; discussion 822–23 Medline
16. Dhandapani S, Gupta A, Singh J, et al. **Spinal dural arterio-venous fistula: clinico-radiological profile and outcome following surgical occlusion in an Indian neurosurgical center.** *Neurol India* 2013;61:406–10 CrossRef Medline
17. Jablawi F, Nikoubashman O, Mull M. **Arterial hypertension is associated with symptomatic spinal dural arteriovenous fistulas.** *World Neurosurg* 2017;103:360–63 CrossRef Medline

Differentiation between Tuberculous and Pyogenic Spondylodiscitis: The Role of the Anterior Meningovertebral Ligament in Patients with Anterior Epidural Abscess

S.B. Strauss, S.R. Gordon, J. Burns, J.A. Bello, and S.E. Slasky

ABSTRACT

BACKGROUND AND PURPOSE: Differentiation between tuberculous and pyogenic spondylodiscitis is a diagnostic challenge because imaging often does not reliably distinguish the 2 entities and percutaneous biopsies are often culture-negative. The purpose of this study was to determine whether violation of the anterior meningovertebral ligament in the setting of anterior epidural abscess discriminates between these entities.

MATERIALS AND METHODS: This was a retrospective cohort study of all patients with acid-fast bacillus testing and anterior epidural abscess diagnosed on spinal MR imaging between May 2014 and September 2019, with a final diagnosis of tuberculous or pyogenic spondylodiscitis. Six cases of tuberculous spondylodiscitis (mean age, 45.5 years; 80% male) and 35 cases of pyogenic spondylodiscitis were evaluated (mean age, 56.6 years; 49% male). Demographic characteristics were recorded. Cases were assessed for anterior meningovertebral ligament destruction on MR imaging, as demonstrated by the shape of the epidural collection. Segmental location of the infection was also assessed. Independent 2-sample *t* tests and χ^2 tests of independence were performed to evaluate the significance of the difference between the groups.

RESULTS: Five of 6 (83.3%) cases of tuberculous epidural abscess had an intact anterior meningovertebral ligament, and 0/35 cases of pyogenic epidural abscess demonstrated an intact ligament ($P < .001$). The presence of an intact anterior meningovertebral ligament had 83.3% sensitivity and 100% specificity for tuberculous spondylodiscitis, a 100% positive predictive value, and a 97.2% negative predictive value.

CONCLUSIONS: The presence of an intact anterior meningovertebral ligament has high sensitivity and specificity for tuberculous spondylodiscitis-associated epidural abscess, though these results should be validated in a larger sample.

ABBREVIATIONS: TB = tuberculosis; CSF = cerebrospinal fluid

Infectious spondylodiscitis is an infection of the vertebral body and intervertebral disc and can be classified as either granulomatous (eg, mycobacterial and fungal), pyogenic (other bacterial organisms), or parasitic depending on responsible pathogen and the host response.¹ There may be associated paraspinal soft-tissue infection or epidural abscess, though this is not required for a diagnosis of infectious spondylodiscitis. *Staphylococcus aureus* is the causative organism in >75% of cases of bacterial spondylodiscitis,² resulting from either hematogenous spread or direct

extension from trauma or adjacent infection.³ Granulomatous spondylodiscitis, specifically tuberculous (TB) spondylodiscitis, is less common than pyogenic spondylodiscitis, with an estimated incidence of only 0.05/100,000 in the United States,⁴ though the incidence is higher in endemic regions.⁵ Differentiation of pyogenic and tuberculous spondylodiscitis is critical because early, targeted treatment can decrease mortality and long-term neurologic morbidity.

The posterior longitudinal ligament is apposed to the posterior vertebral body with direct fixation to the outer annulus fibrosis of the intervertebral disc. At the level of the midvertebral body, there is a midline, sagittally oriented septum (meningovertebral ligament) anchoring the posterior longitudinal ligament to the periosteum, effectively dividing the anterior epidural space into 2 discrete compartments to the right and left of the midline septum (Fig 1).^{6,7} The anatomy and composition of the multiple meningovertebral ligaments in both the anterior and posterior epidural spinal compartments were well-delineated in a study

Received September 9, 2019; accepted after revision November 3.

From the Department of Radiology (S.B.S.), Weill Cornell Medical Center, New York, New York; and Department of Radiology (S.R.G., J.B., J.A.B., S.E.S.), Montefiore Medical Center, Albert Einstein College of Medicine, Bronx, New York.

Scientific abstract previously presented at: Annual Meeting of the American Society of Neuroradiology, May 18–23, 2019; Boston, Massachusetts.

Please address correspondence to Shira E. Slasky, MD, Montefiore Medical Center, Department of Radiology, 111 East 210th St, Bronx, NY 10467; e-mail: sslasky@montefiore.org; @ShiraSlaskyMD
<http://dx.doi.org/10.3174/ajnr.A6370>

using data from in vivo imaging, postmortem anatomy, and microscopy, in which they were found to comprise compact collagen attached to an area of thickened vertebral body periosteum.⁸ Geers et al⁷ demonstrated that the polygonal, stellar, or y-shaped deformation of the dural sac seen in patients with epidural lipomatosis is attributable to the presence of meningovertbral ligaments. These ligaments, and particularly the anterior meningovertbral ligament, are variably affected by pathology involving the epidural space. Kim et al⁹ demonstrated that whereas epidural hematoma and pyogenic infection disrupt the ventral meningovertbral ligament, a neoplasm leaves this anterior septum intact. The purpose of this study was to determine whether the identification of the ventral meningovertbral ligament on MR imaging can help differentiate between TB and pyogenic spondylodiscitis. It is thought that unlike pyogenic spondylodiscitis, TB spondylodiscitis spares the intervertebral disc in the setting of early infection because it lacks the proteolytic enzymes necessary to breach the disc. We hypothesize that similarly, TB spondylodiscitis will

not affect the anterior meningovertbral ligament in the setting of anterior epidural abscess.

MATERIALS AND METHODS

This Health Insurance Portability and Accountability Act–compliant retrospective cohort study was performed with approval of the institutional review board of Montefiore Medical Center. We identified all patients who had MR imaging of the cervical, thoracic, or lumbar spine between May 2014 and September 2019 performed in the inpatient or emergency department setting who also had any acid-fast bacillus lab test performed (culture or stain, derived from abscess, body fluid, blood culture, bone marrow, CSF, respiratory, tissue, or wound) using the Looking Glass clinical analytics (Streamline Health, Atlanta, Georgia). Four hundred seventy-one patients were identified, of whom 85 had epidural abscess as per the radiology report. Final pathology and chart review were performed, and cases were further classified as either pyogenic or TB spondylodiscitis established by positive culture or gram stain. Cases were excluded if there was a dorsal epidural abscess alone without ventral involvement ($n = 11$), postoperative/post traumatic infection ($n = 5$), no definite final diagnosis (patient lost to follow-up or died) ($n = 3$), no organism identified on culture ($n = 14$), phlegmon rather than organized abscess on imaging ($n = 11$), or final pathology demonstrated a noninfectious process ($n = 1$). The remaining 40 patients demonstrating a ventral epidural collection at the level of the vertebral body were included in the study. Demographics recorded included age, sex, and ethnicity and are provided in Table 1.

Spinal MRIs were acquired at multiple inpatient sites in our institution, using various 1.5T and 3T imaging systems including 1.5T Achieva, 1.5T Ingenia, 3T Intera, and 3T Ingenia MR imaging scanners (Philips Healthcare, Best, the Netherlands). Gadavist (gadobutrol) 0.1 mmol/kg (Bayer Schering Pharma, Berlin, Germany) intravenous contrast was administered. MR imaging sequences reviewed for each patient included axial and sagittal T2WI and T1WI with and without contrast. The imaging review was conducted by a team consisting of a Certificate of Added Qualification board-certified neuroradiologist (S.E.S. with 14 years' experience) and a fourth-year radiology resident (S.B.S. with 4 years' experience) using consensus review; a third Certificate of Added Qualification board-certified neuroradiologist (J.B. with 13 years' experience) adjudicated the differences when consensus could not be reached.

The third reviewer was necessary in 3 cases. All reviewers were blinded to the final diagnosis. A unanimous determination was made regarding whether the anterior meningovertbral ligament was intact versus violated.

An intact anterior meningovertbral ligament was defined as an epidural abscess at the level of the vertebral body with an umbilicated, bilobed, or unilobed appearance (Figs 2 and 3), whereas a destroyed ligament was defined as a collection along the posterior aspect of the vertebral body with a

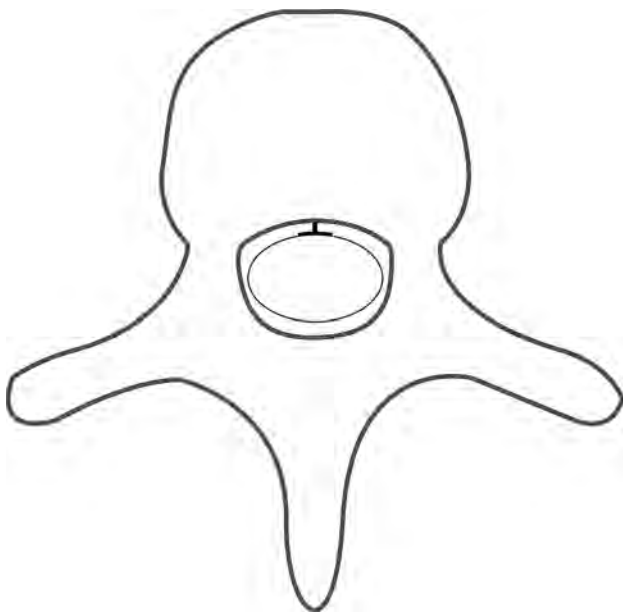


FIG 1. Graphic representation of normal anatomy. The anterior meningovertbral ligament anchors the periosteum to the posterior longitudinal ligament, effectively creating 2 distinct compartments.

Table 1: Demographic and clinical characteristics^a

	<i>M Tuberculosis</i> (<i>n</i> = 5)	<i>Pyogenic</i> (<i>n</i> = 35)	<i>P</i> Value
Age (mean) (SD, range) (yr)	45.5 (29.6, 11.4–82)	56.6 (15.8, 11.4–76)	.45
Sex			.19
Male (No.) (% total)	4 (80%)	17 (49%)	
Female (No.) (% total)	1 (20%)	18 (51%)	
Race/ethnicity (self-reported)			.97
White	2 (40%)	9 (26%)	
Black	2 (40%)	14 (40%)	
Hispanic	0	6 (17%)	
Other/unknown	1 (20%)	6 (17%)	
Duration of symptoms (mean) (SD, range) (days)	31.6 (23.6, 9–56)	22 (16, 1–67)	.15

^a For categorical variables, the frequency (No.) and percentage are reported. For continuous variables, the mean (SD) are reported.

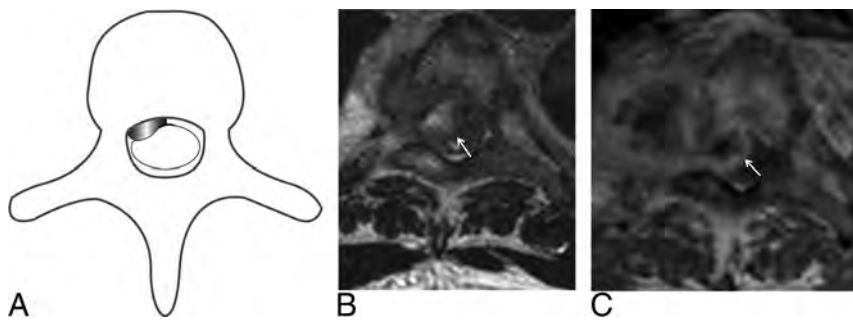


FIG 2. Preserved anterior meningeal ligament with a unilobed anterior epidural abscess. Graphic representation of a unilobed anterior epidural space abscess (A). Axial T2WI (B) and contrast-enhanced T1WI (C) show a unilobed appearance of the epidural abscess.



FIG 3. Preserved anterior meningeal ligament in 2 patients with bilobed anterior epidural abscess. Graphic representation of a bilobed anterior epidural space abscess (A). Axial T2WI (B) and contrast-enhanced T1WI (C) show a bilobed appearance of the epidural abscess in the setting of a preserved anterior meningeal ligament (*arrow*).

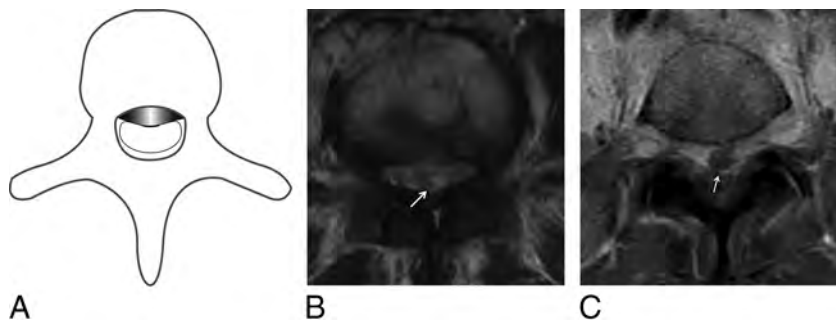


FIG 4. Destruction of the anterior meningeal ligament in 2 patients. Graphic representation of destruction of the anterior meningeal ligament (A). Axial T2WI (B) demonstrates destruction of the anterior meningeal ligament (*arrow*). Axial contrast-enhanced T1WI (C) in a different patient similarly demonstrates destruction of the anterior meningeal ligament (*arrow*). The apices of the collections are midline and convex and do not respect left-right boundaries.

dorsally convex midline apex and direct communication between the right and left compartments of the epidural space (Fig 4). Thus, the anterior meningeal ligament was not directly visualized, but rather, its status was inferred on the basis of the shape of the anterior epidural abscess. In addition, the segmental location of the anterior epidural abscess (cervical, thoracic, or lumbar) was recorded.

Statistical analyses were performed using SPSS (Versions 24 and 25; IBM, Armonk, New York). Demographic and imaging characteristics were compared between the groups with TB spondylodiscitis and pyogenic spondylodiscitis. A χ^2 test of

independence was used to assess significant difference in race/ethnicity between the 2 groups and segmental location of epidural abscess. Independent 2-sample *t* tests were performed to test for significant differences between the 2 groups in age. Sensitivity, specificity, and positive and negative predictive values were determined, and their confidence intervals were calculated using the Jeffreys method with EpiTools epidemiological calculators (2019 Ausvet; <http://epitools.ausvet.com.au/content.php?page=home>).

RESULTS

The demographic features of patients with TB spondylodiscitis and pyogenic spondylodiscitis are shown in Table 1. There were no significant differences between the 2 groups in age, sex, race/ethnicity, or segmental location of anterior epidural abscess. All patients included in the study had laboratory confirmation of the pathogen. Eighteen of 35 (51%) patients classified as having pyogenic osteomyelitis had laboratory confirmation of the pathogen based on biopsy, and 17/35 (49%) patients classified as having pyogenic osteomyelitis had confirmation of the pathogen based on positive blood cultures. The biopsy results are summarized in Table 2 several patients had >1 pathogen isolated. Of note, one of the patients with TB spondylodiscitis had 2 separate abscesses at remote spinal levels, which were counted as 2 different abscesses.

Prevalence of imaging features associated with tuberculous and pyogenic anterior epidural abscesses in the studied cohort are detailed in Table 3. There was a significant differ-

ence between the 2 groups in terms of the appearance of the meningeal ligament, with 5/6 (83.3%) cases of tuberculous-associated anterior epidural abscess demonstrating an intact meningeal ligament, and 0/35 (0%) cases with pyogenic osteomyelitis-associated infection demonstrating an intact meningeal ligament ($P < .001$). The single case of tuberculosis with a destroyed meningeal ligament also demonstrated extensive vertebral body collapse (75% loss of vertebral body height). The presence of an intact anterior meningeal ligament had 83.3% sensitivity (95% confidence interval, 44.2%–98.1%), 100% specificity (95% confidence interval,

Table 2: Pyogenic Biopsy and Culture Results

Organisms Isolated	No.
<i>Staphylococcus</i> species	23
<i>Streptococcus</i> species	6
<i>Escherichia coli</i>	2
Other: <i>Klebsiella</i> , <i>Bacillus cereus</i> , <i>Proteus</i> , <i>Hemophilus</i> species, <i>Enterococcus</i> , <i>Enterobacter</i>	8

Table 3: Imaging features associated with TB-versus-pyogenic anterior epidural space abscess

	<i>M Tuberculosis</i> (n = 6)	Pyogenic (n = 35)	P Value
Anterior septum violated	1 (16.7%)	35 (100%)	<.001
Location			.90
Cervical	0	5 (14.3%)	
Thoracic	4 (66.7%)	8 (22.9%)	
Lumbar	1 (16.7%)	19 (54.3%)	
Thoracolumbar	1 (16.7%)	1 (2.9%)	
Lumbosacral	0	2 (5.7%)	

93%–100%), 100% positive predictive value (95% confidence interval, 62.1%–1%), and 97.2% negative predictive value (95% confidence interval, 88%–1%) for TB spondylodiscitis.

DISCUSSION

Mycobacterium tuberculosis is a Gram-positive acid-fast bacillus, which can primarily infect bone or secondarily spread to the axial skeleton via the Batson venous plexus from remote sites of disease. Several patterns of vertebral body infection are described in *M tuberculosis* spondylodiscitis, including central, anterior, posterior, and paradiscal. Tuberculosis occurs more often in the thoracic spine, followed by the lumbar spine.¹⁰ Late in the disease, osteolysis results from bone necrosis, causing spinal instability and the typical gibbus deformity to develop.¹⁰ Epidural abscess may be present in TB spondylodiscitis, particularly in association with paradiscal infection and can be difficult to differentiate from pyogenic osteomyelitis in the absence of other stereotypical features.¹⁰

Differentiation between pyogenic and TB spondylodiscitis is often a diagnostic challenge because few imaging features are shown to reliably distinguish the 2 entities. Moreover, approximately 43%–70% of percutaneous biopsies are culture-negative in the setting of pyogenic and TB spondylodiscitis, even with high clinical and radiologic suspicion, with only marginally improved percentages reported for open biopsies.^{11,12} In this study, we found that preservation of the anterior meningovertbral ligament had high sensitivity (83.3%) and specificity (100%) for the diagnosis of tuberculous infection in the setting of anterior epidural abscess, though these results must be interpreted with some degree of caution given the small sample size. The single case of culture-positive TB infection with a destroyed anterior meningovertbral ligament also demonstrated extensive vertebral body height loss (75% loss of vertebral body height). We postulate that the vertebral body damage itself was likely responsible for injury to the anterior meningovertbral ligament, rather than primary destruction due to the infection.

Several prior studies have examined imaging features that differentiate pyogenic from TB spondylodiscitis. Features favoring TB infection over typical pyogenic infection include intervertebral disc space sparing, posterior element involvement, extensive paraspinal soft-tissue involvement, multiple vertebral body involvement, a heterogeneous vertebral body enhancement pattern, and subligamentous spread.^{1,5,13,14} The status of the anterior meningovertbral ligament represents a novel addition to the existing body of literature and may serve as collateral information in cases in which both diagnoses are being entertained.

The anterior meningovertbral ligament has been shown to have an impact on the spread of disease in the context of noninfectious pathology. In the setting of degenerative disease, the anterior meningovertbral ligament limits transverse migration of extruded disc material.⁸ Schellinger et al⁶ initially described progressive destruction of this midline septum in the setting of infection and neoplasm, and Kim et al⁹ showed that a unilobed or bilobed appearance of a ventral epidural collection had a 76%–82% sensitivity and 73%–80% specificity in identifying neoplastic compared with nonneoplastic anterior epidural space lesions, including hematoma and infection. Hong et al¹⁵ noted that TB associated anterior paraspinal abscess of the thoracic spine will not encase the intercostal arteries due to an inability to breach the anterior longitudinal ligament. In the current study, the observed destruction of the anterior midline meningovertbral ligament in the setting of pyogenic spondylodiscitis is consistent with that previously reported; the observed preservation of the ligament in TB suggests that mycobacterial infection behaves more similar to neoplasm than to trauma or bacterial infection.

The pathophysiologic basis of the observed effects on the anterior meningovertbral ligament is likely related to the unique features of the microorganism. An explanation commonly given for the observed sparing of the intervertebral disc during early stages of infection is that TB characteristically lacks proteolytic enzymes.^{16–18} Additionally, as an aerobic organism, *M tuberculosis* requires greater arterial supply to survive and is therefore more slow-growing than other infectious organisms,¹⁹ taking up to 11.2 months before clinical signs present, compared with 6.4 months in patients with pyogenic spondylodiscitis.¹ Lack of proteolytic enzymes is an important factor that may explain why *M tuberculosis* infection typically spares the anterior meningovertbral ligament. Although the meningovertbral ligament varies in thickness between different spinal segments, increasing in thickness at the level of the lumbar spine, we found no significant difference between the pyogenic and TB cases in terms of segmental involvement.

There are several limitations to this study. First, the sample size is limited, with only 15% of total cases positive for tuberculosis. However, this limitation reflects the relatively low prevalence of tuberculosis in the studied population. The relatively high number of pyogenic cases improves the specificity and negative predictive value of this finding, while reducing the sensitivity and positive predictive value. Of note, the search criteria used to develop the cohort included only patients who underwent acid-fast bacillus testing. Therefore, while we did not capture all epidural abscesses in our institution during the study period; the study specifically addresses those cases in which both pyogenic and TB

infections were differential considerations and in which a radiologic sign might be of greatest utility in discriminating the 2 organisms. Finally, although all studies were performed at the same institution, not all studies were performed on the same scanner or with identical parameters, and the variability in image quality may potentially impact interpretation.

CONCLUSIONS

The presence of an intact anterior meningeovertebral ligament on spinal MR imaging has high specificity, sensitivity, and negative predictive value for the diagnosis of TB spondylodiscitis, though these results remain to be validated in a larger sample. Attention to this subtle imaging feature might facilitate early pathogen-directed treatment and ultimately reduce morbidity and the length of stay in the setting of otherwise inconclusive clinical parameters.

ACKNOWLEDGMENTS

We thank Dr Victoria Chernyak for her contributions to data mining and Dr Kenny Ye for his assistance with statistical analysis.

REFERENCES

1. Lee KY. Comparison of pyogenic spondylitis and tuberculous spondylitis. *Asian Spine J* 2014;8:216–23 CrossRef Medline
2. Kumar Y, Gupta N, Chhabra A, et al. Magnetic resonance imaging of bacterial and tuberculous spondylodiscitis with associated complications and non-infectious spinal pathology mimicking infections: a pictorial review. *BMC Musculoskelet Disord* 2017;18:244 CrossRef Medline
3. Darouiche RO. Spinal epidural abscess. *N Engl J Med* 2006;355:2012–20 CrossRef Medline
4. De la Garza Ramos R, Goodwin CR, Abu-Bonsrah N, et al. The epidemiology of spinal tuberculosis in the United States: an analysis of 2002–2011 data. *J Neurosurg Spine*. 2017;26:507–12 CrossRef Medline
5. Jung NY, Jee WH, Ha KY, et al. Discrimination of tuberculous spondylitis from pyogenic spondylitis on MRI. *AJR Am J Roentgenol* 2004;182:1405–10 CrossRef Medline
6. Schellinger D, Manz H, Vidic B, et al. Disk fragment migration. *Radiology* 1990;175:831–36 CrossRef Medline
7. Geers C, Lecouvet FE, Behets C, et al. Polygonal deformation of the dural sac in lumbar epidural lipomatosis: anatomic explanation by the presence of meningeovertebral ligaments. *AJNR Am J Neuroradiol* 2003;24:1276–82 Medline
8. Scapinelli R. Anatomical and radiologic studies on the lumbosacral meningo-vertebral ligaments of humans. *J Spinal Disord* 1990;3:6–15 CrossRef Medline
9. Kim DH, Rosenblum JK, Panghaal VS, et al. Differentiating neoplastic from nonneoplastic processes in the anterior extradural space. *Radiology* 2011;260:825–30 CrossRef Medline
10. Rivas-Garcia A, Sarria-Estrada S, Torrents-Odin C, et al. Imaging findings of Pott's disease. *Eur Spine J* 2013;22:567–78 CrossRef Medline
11. Colmenero J, Jimenez-Mejias M, Reguera J, et al. Tuberculous vertebral osteomyelitis in the new millennium: still a diagnostic and therapeutic challenge. *Eur J Clin Microbiol Infect Dis* 2004;23:477–83 CrossRef Medline
12. Gras G, Buzele R, Parienti J, et al. Microbiological diagnosis of vertebral osteomyelitis: relevance of second percutaneous biopsy following initial negative biopsy and limited yield of post-biopsy blood cultures. *Eur J Clin Microbiol Infect Dis* 2014;33:371–75 CrossRef Medline
13. Arizono T, Oga M, Shiota E, et al. Differentiation of vertebral osteomyelitis and tuberculous spondylitis by magnetic resonance imaging. *Int Orthop* 1995;19:319–22 CrossRef Medline
14. Frel M, Bialecki J, Wieczorek J, et al. Magnetic resonance imaging in differential diagnosis of pyogenic spondylodiscitis and tuberculous spondylodiscitis. *Pol J Radiol* 2017;82:71 CrossRef Medline
15. Hong SH, Choi JY, Lee JW, et al. MR imaging assessment of the spine: infection or an imitation? *Radiographics* 2009;29:599–612 CrossRef Medline
16. Chang MC, Wu HT, Lee CH, et al. Tuberculous spondylitis and pyogenic spondylitis: comparative magnetic resonance imaging features. *Spine* 2006;31:782–88 CrossRef Medline
17. Smith AS, Weinstein MA, Mizushima A, et al. MR imaging characteristics of tuberculous spondylitis vs vertebral osteomyelitis. *AJR Am J Roentgenol* 1989;153:399–405 CrossRef Medline
18. Almeida Á. Tuberculosis of the spine and spinal cord. *Eur J Radiol* 2005;55:193–201 CrossRef Medline
19. Moorthy S, Prabhu NK. Spectrum of MR imaging findings in spinal tuberculosis. *AJR Am J Roentgenol* 2002;179:979–83 CrossRef Medline

Intraoperative MR and Synthetic Imaging

In the past 2 decades, intraoperative MRI (ioMRI) has been implemented in surgery for pituitary tumors, low-grade gliomas,¹ epilepsy, and deep brain stimulation. In neuro-oncological surgery, the adjunct of ioMRI improves the extent of resection, which eventually results in improved overall and progression-free survival.² However, despite encouraging results, there are no specific sequences dedicated to ioMRI to our knowledge.

In the neuroradiologist's point of view, one of the main difficulties is to find the most useful and time-effective sequence to guide the surgeon in determining the existence of residual tumor tissue. Often, multiple series before and after the administration of a contrast agent are used. In our opinion, this time-consuming step is not compatible with a surgical context in which time for imaging is limited. This restricts the neuroradiologist, especially in complex cases. One potential solution might reside in the use of so-called synthetic imaging (SyntheticMR; SyntheticMR, Linköping, Sweden), which allows us to obtain 1) different types of contrast, and 2) quantitative information, such as T1 and T2 mapping of the tissues.^{3,4}

The use of SyntheticMR in low-grade tumors could represent a real shift of paradigm. Due to edema, air, blood, and immediate postoperative changes, these lesions do not allow a clear delimitation of the tumor border solely by visual analysis, and remaining tumor may thus be missed. Having multiple contrasts in a single sequence by using SyntheticMR may aid the interpretation, in a reduced acquisition time (7 min). The quantitative values may also be of great interest; indeed, synthetic imaging provides several types of cartography, such as cerebral cortex, CSF, white matter, and other tissues, as shown in Fig 1. Quantitative values of T1, T2, and proton density of the tissues are also available. It has already been shown that relaxation rates can be used to grade gliomas,⁵ but, at that time, there were no sequences with short acquisition times. Recently, this finding was confirmed with an MR fingerprinting technique.⁶ The latter sequence is under development and therefore, not fully available, contrary to SyntheticMR. In Fig 2, we show that T2 measured with SyntheticMR in the case of a World Health Organization grade I left occipital meningioma is different between the lesion and the cerebral cortex. In our

opinion, this principle could be used to help delineate remnant tumor tissue also in low-grade tumors.

We, therefore, think that SyntheticMR could be beneficial for ioMRI by providing multiple contrasts and relaxation-rate quantification to give a reliable interpretation of the presence of residual tumor, thus improving patient care.

Disclosures: None.

ACKNOWLEDGEMENT

The authors thank IMRIS. The SyntheticMR sequence (MDME) was provided by Karolinska University Hospital, developed in collaboration with Synthetic MR AB and Frederik Testud, Siemens Healthcare AB, Sweden.

REFERENCES

1. Coburger J, Merkel A, Scherer M, et al. **Low-grade glioma surgery in intraoperative magnetic resonance imaging: results of a multicenter retrospective assessment of the German study group for intraoperative magnetic resonance imaging.** *Neurosurgery* 2016;78:775–86 CrossRef Medline
2. Senft C, Bink A, Franz K, et al. **Intraoperative MRI guidance and extent of resection in glioma surgery: a randomised, controlled trial.** *Lancet Oncol* 2011;12:997–1003 CrossRef Medline
3. Warntjes JBM, Leinhard OD, West J, et al. **Rapid magnetic resonance quantification on the brain: Optimization for clinical usage.** *Magn. Reson. Med.* 2008;60:320–9 CrossRef Medline
4. Granberg T, Uppman M, Hashim F, et al. **Clinical Feasibility of Synthetic MRI in Multiple Sclerosis: A Diagnostic and Volumetric Validation Study.** *Am. J. Neuroradiol.* 2016;37:1023–9 CrossRef Medline
5. Newman S, Haughton VM, Yetkin Z, et al. **T1, T2 and proton density measurements in the grading of cerebral gliomas.** *Eur Radiol* 1993;49–52
6. Badve C, Yu A, Dastmalchian S, et al. **MR fingerprinting of adult brain tumors: initial experience.** *AJNR Am J Neuroradiol* 2017;38:492–99 CrossRef Medline

 M.I. Vargas

Division of Neuroradiology

 B.M.A. Delatte

Division of Radiology

 P. Vayssiere

 M. Corniola

 T. Meling

Division of Neurosurgery

Geneva University Hospital and Faculty of Medicine of Geneva
Geneva, Switzerland

Please address correspondence to Maria Isabel Vargas, MD, Division of Diagnostic and Interventional Neuroradiology, Geneva University Hospitals, Rue Gabrielle-Perret-Gentil 4, 1211 Genève 14, Switzerland; e-mail: maria.i.vargas@hcuge.ch; @maiva96

<http://dx.doi.org/10.3174/ajnr.A6373>

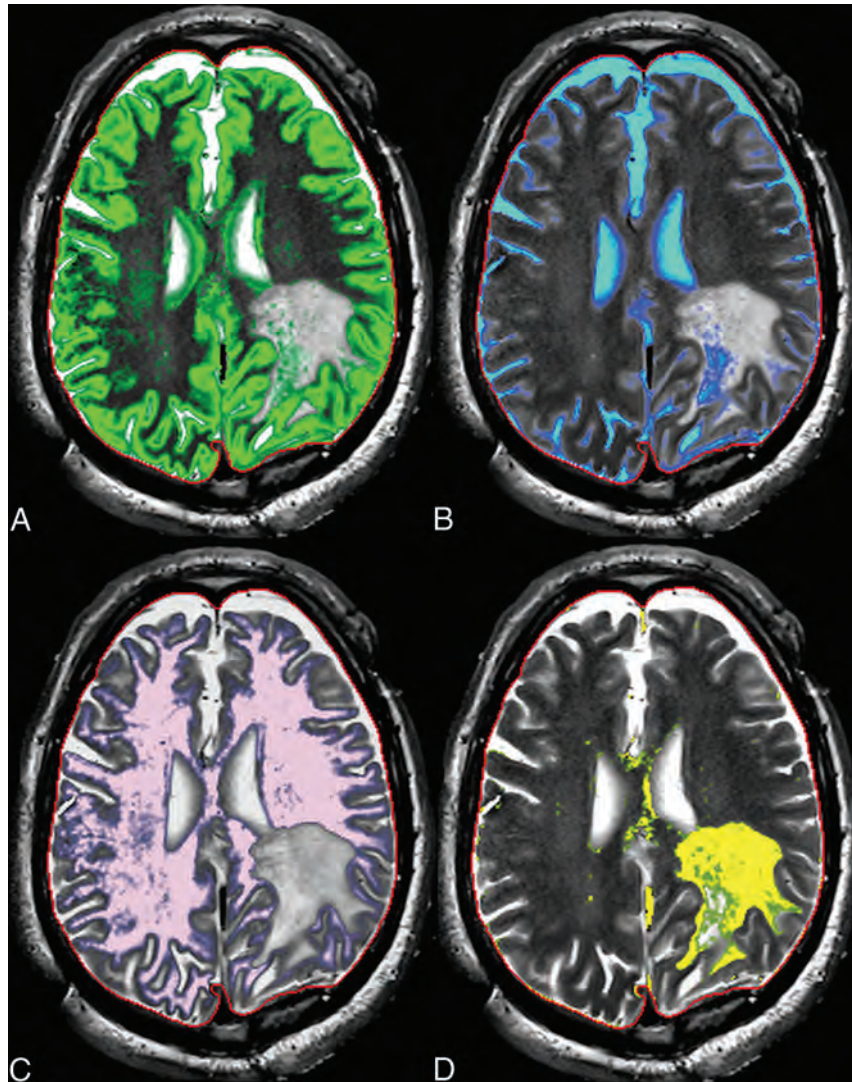


FIG 1. Intraoperative Synthetic MR cartographies illustrating gray matter (green in *A*), CSF (blue in *B*), white matter (pink in *C*), and edema (yellow in *D*).

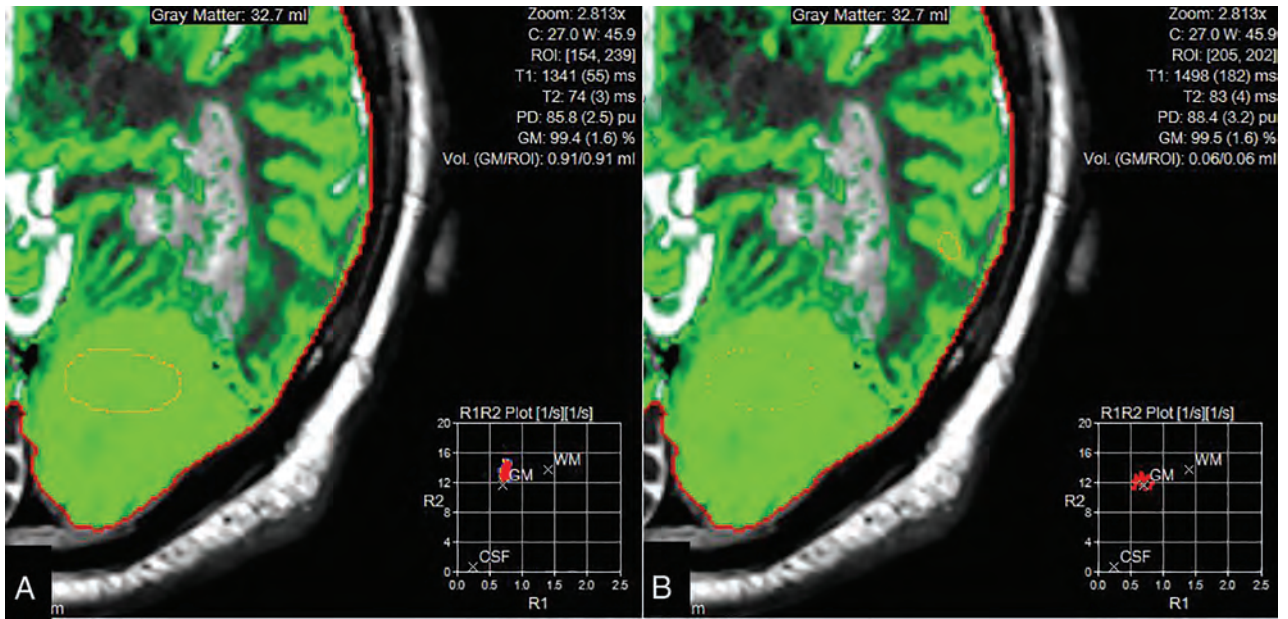


FIG 2. Region of interest in the tumor (A), showing decreased T2 values in rapport to gray matter (B) and, on the contrary, T1 values similar to the gray matter.

Comments on “Prolonged Microgravity Affects Human Brain Structure and Function”

This letter addresses the article, “Prolonged Microgravity Affects Human Brain Structure and Function.”¹ To investigate whether brain structural changes (which can be observed after long-term space missions) are associated with alterations in motor or cognitive function, Roberts et al¹ retrospectively analyzed brain MR images of National Aeronautics and Space Administration astronauts to quantify pre- to postflight alterations in brain structure. They showed that brain structural changes were linked to changes in cognitive and motor test scores as well as the development of spaceflight-associated neuro-optic syndrome. However, due to the small sample size and number of comparisons, they suggested that their findings should be interpreted with caution.

Although this article has certain strengths, it has at least 1 major shortcoming that stems from ignoring the key point that in long-duration deep space missions, astronauts are exposed to multiple stressors ranging from psychological stress due to the confined environment to ionizing radiation and gravitational changes. It is not well-understood whether these stressors impact the central nervous system only individually or in combination (ie, synergistically). However, what we are fully aware of is the key role of space radiation on human brain function, according to Parihar et al,² “The Mars mission will result in an inevitable exposure to cosmic radiation that has been shown to cause cognitive impairments in rodent models, and possibly in astronauts engaged in deep space travel.” Cucinotta et al³ have also confirmed galactic cosmic ray (GCR)-induced alterations in astronauts’ cognitive function, “Galactic cosmic rays may alter astronauts, cognition during space missions.” Cucinotta et al also reported that exposure to GCRs can be associated with increased risk of CNS disorders, “GCR[s] may increase central nervous system risks including Alzheimer disease.” Most important, Krukowski et al⁴ reported that novel pharmaceutical agents are being explored for their ability to protect memory function in rodents exposed to simulated cosmic radiation, “Now neuroscientists have identified a potential treatment for the brain damage caused by cosmic rays, a drug that prevents memory impairment in mice exposed to simulated space radiation.” In summary, this omission has possi-

bly affected the validity of the findings of the study conducted by Roberts et al.¹

Disclosures: James Welsh—UNRELATED: Grant: I have a Small Business Innovation Research grant from the National Institutes of Health, but it is related to proton radiography and proton beam CT scanning; Consulting Fee or Honorarium: I am an advisor to TAE Life Sciences for boron neutron capture therapy.* Membership: Coqui Pharma, Comments: I have received no financial remuneration; Employment: Department of Veterans Affairs, Comments: This is my primary employer; Patents (Planned, Pending or Issued): I hold a patent for a method to reduce adverse effects of reirradiation by adjusting the effective dose rate. So far, I have received no financial benefit; Royalties: Prometheus Books, Comments: I am the author of *Sharks Get Cancer, Mole Rats Don't: How Animals Might Hold the Key to Cancer Immunity*. This was published in 2016. *Money paid to the institution.

REFERENCES

1. Roberts DR, Brown TR, Nietert PJ, et al. **Prolonged microgravity affects human brain structure and function.** *AJNR Am J Neuroradiol* 2019;40:1878–85 CrossRef Medline
2. Parihar VK, Allen BD, Caressi C, et al. **Cosmic radiation exposure and persistent cognitive dysfunction.** *Sci Rep* 2016;6:34774 CrossRef Medline
3. Cucinotta FA, Alp M, Sulzman FM, et al. **Space radiation risks to the central nervous system.** *Life Sciences in Space Research* 2014;2:54–69 CrossRef
4. Krukowski K, Feng X, Paladini MS, et al. **Temporary microglia-depletion after cosmic radiation modifies phagocytic activity and prevents cognitive deficits.** *Sci Rep* 2018;8:7857 CrossRef Medline

© J.J. Bevelacqua
Bevelacqua Resources
Richland, Washington

© J. Welsh
Department of Radiation Oncology
Edward Hines Jr VA Hospital
Hines, Illinois

© S.M.J. Mortazavi
Diagnostic Imaging Department
Fox Chase Cancer Center
Philadelphia, Pennsylvania
Medical Physics Department
School of Medicine
Shiraz, Iran

<http://dx.doi.org/10.3174/ajnr.A6387>

REPLY:

We thank Drs Bevelacqua, Welsh, and Mortazavi for their interest in our article, “Prolonged Microgravity Affects Human Brain Structure and Function.” We disagree, however, that we have ignored the multiple unique features of the spaceflight environment to which astronauts are exposed and that “this omission has possibly affected the validity of the findings.”

As we stated in the article, many factors affect individual astronaut performance. These factors include psychological stress, gravitational changes, and radiation exposure as highlighted in the letter of Drs Bevelacqua, Welsh, and Mortazavi. Other unique characteristics of the spaceflight environment include elevated carbon dioxide levels, cephalad fluid shifts, and unique microbial habitats among others. Any of these factors may act individually or in synergy to result in the changes in brain structure and cognitive function that we have documented in astronauts after spaceflight.

Our study highlights the need for further investigations of human brain adaptation to spaceflight to disentangle the relative contribution that each factor, including radiation exposure, may

have on brain health. This work will be important in guiding the development of effective countermeasures protecting brain function in support of future human spaceflight.

 **D.R. Roberts**

 **D. Asemani**
Department of Radiology and Radiological Science

 **P.J. Nietert**

Department of Public Health

 **M.A. Eckert**

Department of Otolaryngology - Head and Neck Surgery

 **D.C. Inglesby**

Department of Radiology and Radiological Science
Medical University of South Carolina
Charleston, South Carolina

 **J.J. Bloomberg**

Neurosciences Laboratory
NASA Johnson Space Center
Houston, Texas

 **M.S. George**

Department of Psychiatry and Behavioral Sciences
Medical University of South Carolina
Charleston, South Carolina
Ralph H. Johnson VA Medical Center
Charleston, South Carolina

 **T.R. Brown**

Department of Radiology and Radiological Science
Medical University of South Carolina
Charleston, South Carolina

<http://dx.doi.org/10.3174/ajnr.A6400>

The authors regret that in the article “MR Imaging Features of Histologically Diagnosed Supratentorial Primitive Neuroectodermal Tumors and Pineoblastomas in Correlation with Molecular Diagnoses and Outcomes: A Report from the Children’s Oncology Group ACNS0332 Trial” (*AJNR Am J Neuroradiol* 2019;40:1796–1803), an item in Table 3 was inadvertently changed from “0.080” to “0.80” when annotating proofs. The corrected table is reproduced below.

<http://dx.doi.org/10.3174/ajnr.A6406>

Table 3: MR imaging features by tumor group (all patients, n = 56)

	Group				P Value	All Patients	
	PBL/ET		Non-ET			No.	%
	No.	%	No.	%		No.	%
Size (cm)					<.001		
Median	3.6	—	6.2	—		4.3	—
Minimum	1.1	—	2.7	—		1.1	—
Maximum	9.1	—	9.3	—		9.3	—
% Enhancement					.17 ^a , .080 ^b		
None	1	2.7	0	0		1	1.8
0–25	3	8.1	3	15.8		6	10.7
25–75	6	16.2	7	36.8		13	23.2
>75	27	73.0	9	47.4		36	64.3
Margins					<.001		
Well-defined	37	100.0	13	68.4		50	89.3
Ill-defined	0	0	6	31.6		6	10.7
Presence of edema					<.001 ^c		
Absent	32	86.5	5	26.3		37	66.1
<2 cm from tumor margin	4	10.8	13	68.4		17	30.4
>2 cm from tumor margin	1	2.7	1	5.3		2	3.6
Presence of cyst/necrosis					.22		
Absent	12	32.4	3	15.8		15	26.8
Present	25	67.6	16	84.2		41	73.2
Presence of calcification or hemorrhage					.26		
Absent	16	43.2	5	26.3		21	37.5
Present	21	56.8	14	73.7		35	62.5
DWI					—		
Bright	28	75.7	15	78.9		43	76.8
Dark	1	2.7	0	0		1	1.8
Intermediate	5	13.5	3	15.8		8	14.3
Artifact or not available	3	8.1	1	5.3		4	7.1
Metastasis					—		
Intracranial	1	2.7	0	0		1	1.8
Spinal	5	13.5	0	0		5	8.9
Intracranial and spinal	6	16.2	0	0		6	10.7
None	25	67.6	19	100.0		44	78.6
All patients	37	100.0	19	100.0		56	100.0

Note:— indicates no data available.

^a Comparison of none versus 0%–25% versus 25%–75% versus >75%.

^b Comparison of >75% versus ≤75%.

^c Comparison of absent versus present.